

TECHNICAL AND ENVIRONMENTAL ISSUES IN THE PRODUCTION OF UNCONVENTIONAL SHALE GAS RESOURCES

*Onuoha F. Wopara*

*Engineering, Rivers State University, Port Harcourt, Nigeria*

Received April 4, 2018; Accepted June 27, 2018

---

### Abstract

The current global upsurge in the development of unconventional shale gas and tight oil starting from the United States is resulting in increased economic benefits, including significant rise in job creation, lower energy costs and improved security, new sources of government revenue, and improved energy security. Also, there is a substantial decrease in greenhouse gas (GHG) emissions due to the development of this unconventional natural gas resource. Increasing technological advances in directional drilling, hydraulic fracturing and fracturing fluids have led to increases in unconventional shale gas development, raising questions about health impacts. This paper gives a brief review of the physics and thermodynamics of gas flow in such a low porosity and low to ultra-low permeability reservoirs. It also looks at effects of such phenomena a gas desorption/desorption process, non-Darcy flow, gas slippage (Klinkenberg effect), rock deformation caused by change in effective stress in ultra-low permeability reservoirs, hydraulic fracturing and environmental impact of flowback and produced fluids.

**Keywords:** *Unconventional reservoirs; shale gas; shale reservoir parameters, hydraulic fracturing; fracturing fluids.*

---

## 1. Introduction

Unconventional reservoirs such as shale, hydrates, tight sand, ultra tight sand and coal bed methane reservoirs serves as alternative sources to meet the increasing demand for energy all over the world. The exploitation of unconventional gas reservoirs has become an integral part of the global gas supply chain. The economic viability of many unconventional gas developments hinges on the effective stimulation of extremely low porosity and ultra-low permeability reservoir rocks. Global shale gas reservoirs are thought to contain large amount of natural gas resources and are therefore attractive targets for energy development. Global estimate of the gas originally in place in these reservoirs are quoted to be around 7,576.6 trillion cubic feet (TCF), while tight oil is estimated at about 418.9 billion barrels [1]. This huge energy resources need to be exploited for the benefit of sustaining global energy supply and the economy. Figure 1 shows global spread of technically recoverable shale gas reserves as at 2016 [2].

Shale gas reservoirs are organic-rich petroleum system wherein the same rock formation acts simultaneously as source, reservoir rock, sealing rock and the trap. Kerogen (organic matter) is the precursor for tight oil and gas in shale. The pores contain mature oil and gas Kerogen (organic matter) is the precursor for tight oil and gas in shale. The pores contain mature oil and gas Gas is stored in the limited pore space of the rock and migrates solely in a micro-scale. A sizeable fraction of gas is adsorbed on the organic materials [3-6]. Figure 2 shows Scanning Electron Micrograph (SEM) of kerogen rapped within organically rich shale [7]. Gas is highly dispersed in the micropores of the reservoir rock, rather than occurring in concentrated underground locations. Many studies and a lot of progress have been made on the development and production of shale gas reservoirs in North America, China and other countries, but the fundamental physics of flow in shale gas rocks and the engineering of fracturing shale gas reservoirs are not yet fully understood. It is therefore essential to develop a critical

understanding of the factors that underlie the complex behavior of gas flow in the reservoir with a view to choosing the appropriate methods for optimal gas production from a given shale system.

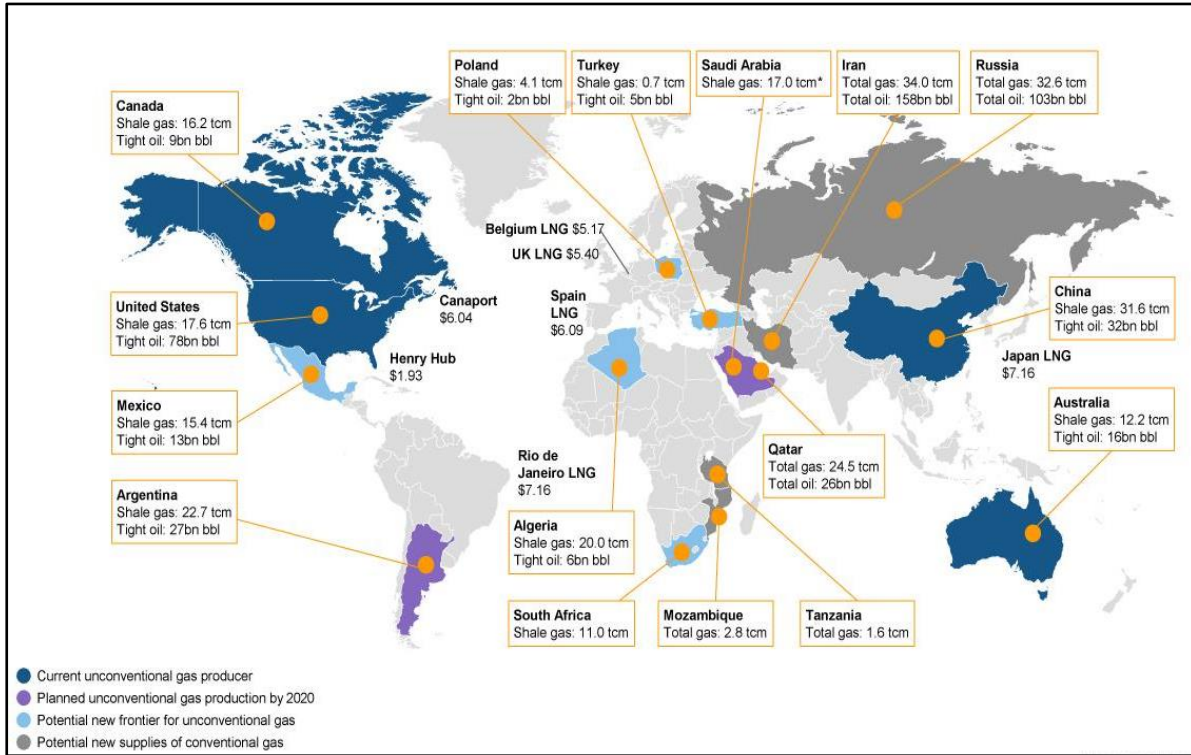


Figure 1. New supply landscape of technically recoverable reserves [2]

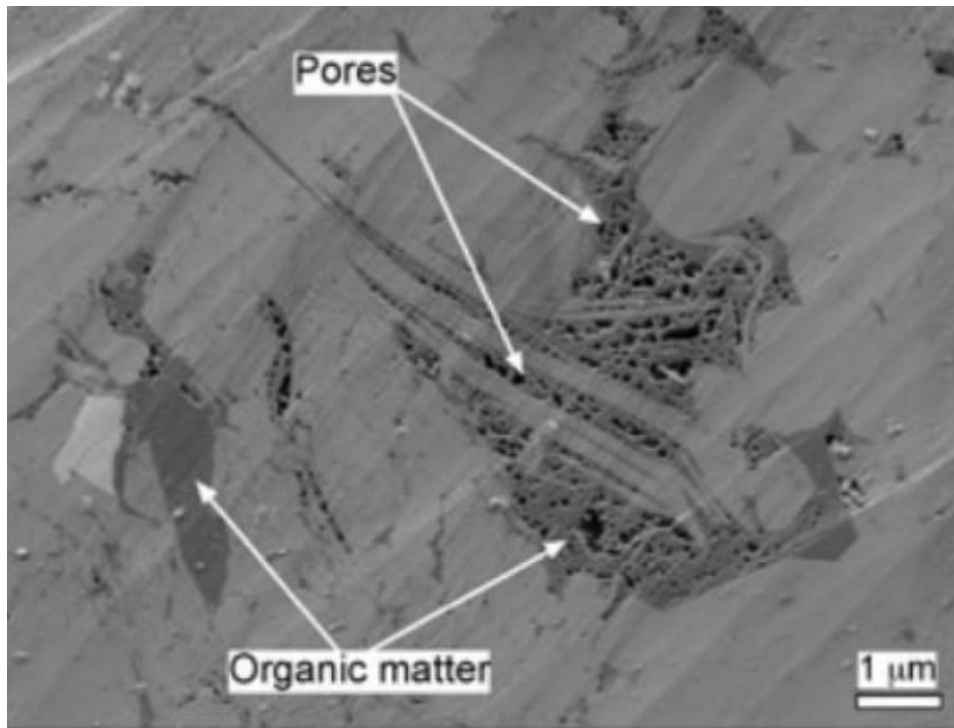


Figure 2. SEM of kerogen rapped within organically rich shale [7]

## 2. Technical issues

### 2.1. Petrophysical parameters: porosity and permeability

The reservoir parameters necessary for shale gas accumulations include thermal maturity, reservoir thickness, total organic carbon (TOC), adsorbed gas, free gas within the pores and fractures, porosity and permeability [8-9]. Thermal maturity is commonly measured in core analysis and reservoir thickness is routinely derived from analysis of logs. Shale gas reservoirs are complex and exhibit significant variations in their petro-physical characteristics (mineralogy, porosity, permeability, gas content, and pressure). In order to characterize the petro-physical properties of the rocks with regard to capability to accumulate and transport reservoir fluids, it is necessary to determine the values of these parameters, particularly porosity and permeability.

Porosity of shale gas formations is key parameter that directly affects the volume of gas initially in place in the reservoir. Together with the desorption characteristics of the shale rock, it plays very significant role in the gas delivery potential of the reservoir. There are three components of total porosity of a shale gas reservoir: porosity within natural fractures, which provide flow conduits to a wellbore, intergranular porosity, which contains electrochemically-bound water, capillary-bound water, and free fluids that are mostly presumed to comprise gas (intergranular porosity is non-zero in the (petrophysical) effective porosity system only if the shale is not electrochemically and compositionally 'perfect': it is always nonzero in the total porosity system, and porosity associated with the organic content. Total porosity provides an estimate of the total gas in place [10].

Producibility of a shale gas reservoir depends greatly on permeability which is a key parameter for stimulation design and prediction of its flow capacity. Shale gas reservoirs have unique characteristics due to their very low and ultra-low permeabilities. Permeability is enhanced by the presence, density, and continuity of natural, open fractures [11]. Permeability is associated with the presence of natural cracks/fractures in the rock which enable the flow of reservoir fluids between pore spaces. Successful development generally entails hydraulic fracturing in order to connect these natural fractures to the wellbore. Permeability coefficient is dependent on the size of pores, relative configuration of the rock-building grains, grain grading and cementation, and rock fracture networks. Porosity and permeability in shales are highly dependent on mineral composition, organic matter distribution, quantitative (%) content of organic matter, and thermal maturity of organic matter. Shale rocks, because of their extremely low permeability (0.001 to 0.0001 mD), basically prevent any unrestrained flow of hydrocarbons and therefore stimulation (fracturing) must be performed in order to connect the pores to the borehole and allow for an unrestrained flow of gas.

### 2.2. Pore-network structure

Understanding of the internal structure of a shale rock sample is needed to calculate flow in the bulk system [12]. Numerical simulation methods, using X-ray computed microtomography (micro-CT) to scan internal structure of the rock sample from which a pore network is extracted, coupled with digital rock physics analysis (DRP), will be useful in characterizing the shale gas reservoir in terms of absolute and relative permeability and in quantifying the effects of the pertinent factors on multiphase flow and well performance for long-term gas recovery [13]. Knowing the pore network structure also helps in estimating other parameters such as spatial configuration of fluids in the pore spaces, wettability and its distribution, adsorption and desorption, precipitation and dissolution, biocide fouling and biomass growth. Molecular simulations have been gaining wide applications and are proving successful for the study gas adsorption in shale gas reservoirs.

### 2.3. Gas adsorption

Knowledge of gas transport process in shale matrix is of great importance in designing development strategies and in formulating appropriate predictive mathematical models for the

complex multiphase behavior of the system. Knowing the contribution of each gas source to gas transport history and to ultimate gas recovery is of great importance to design and management of gas development project.

Gas desorption is essential in understanding the production capacity of a shale gas reservoir [14-18]. This is because, the shale can hold significant quantity of gas adsorbed on the surface of organic matter (including clay) in shale formations [19-20]. In shale, methane molecules are mainly on the carbon-rich components, eg kerogen, which is usually quantified in terms of total organic carbon (TOC). As the pressure decreases due to continuous gas production from the reservoir, more adsorbed gas is released from solid to the gas phase, contributing to flow and production. Mathematical models show that gas desorption rate varies and can be divided into three stages: slow desorption stage, the large desorption stage, and the final desorption stage [21]. It is critical to understand the multistage gas desorption process in order to adequately analyze shale gas transport phenomena and reservoir flow capacity necessary for designing production scheme for sustained economic gas recovery.

## 2.4. Geomechanics role

The effect of geomechanics is important and critical in gas production from shale formations. It is therefore necessary to properly characterize the geomechanical properties of a producing formation. Stress direction, optimum well trajectory and fracture orientation, relationship between matrix permeability, natural fracture permeability, and induced fracture permeability, and are of importance in designing stimulation schemes for increased gas production and minimization of environmental impact of fracturing operations. Achieving reasonable gas production rates requires to significantly lower well pressure to maximize pressure drops in order to mobilize more gas to the well. This creates a large change in pressure field, leading to change in effective stress that may cause large rock deformation. As a result, the aperture and permeability of the micro channels and fractures is altered, leading to significant decrease in both fracture and matrix permeability and subsequent reduction in gas production [22-23]. Understanding the geomechanical behavior of unconventional shale gas systems throughout the production period is gaining increasing importance. Geomechanical analysis of the stress state in the reservoir leads to improved understanding of how to place and design wells for maximum gas production efficiency and project stability.

## 2.5. Shale gas reservoir simulation

The behavior of shale gas reservoirs and the complex fracture networks are mainly poorly understood. This poses a huge challenge for the petro-physicists who have to use more advanced techniques of research, especially in the nano- and macro-scale, and to the field engineers whose function it is to design effective stimulation schemes for economic development of the reservoirs. Different reservoir characterization methods for different scales are required for better understanding of individual shale gas reservoirs.

The last decade has witnessed increased studies and developments for shale gas reservoir resources [24-26]. Comprehensive review of flow mechanisms in unconventional shale gas reservoirs can be found in Blasingane [27], Gensterblum [28] and Wang *et al.* [29]. Commercial reservoir simulators and integrated workflow have been used to study gas production from shale gas reservoirs [30-32]. However, current understanding of gas flow and effective tools for the development of shale gas reservoirs is still far behind the industry needs. It is therefore very essential to identify the most critical parameters to be considered in shale-gas flow modeling for the development of stimulation tools adequate for a given reservoir.

## 3. Hydraulic fracturing and fracturing fluids

### 3.1. Hydraulic fracturing

Hydraulic fracturing has become a very common and widespread technique for practical exploitation of shale gas reservoirs. Figure 3 presents a schematic diagram of shale formation

for natural gas. As the formation is fractured, gas flows from the non-Darcy scale to the complex fracture network and then to the well for production. According to Lee and Kim [33], the features that characterize the non-linear behavior of the reservoir flow dynamics include natural fracture system, adsorption/desorption of gas, diffusion in nano-pores, gas slippage (Klinkenberg effect), non-Darcy flow, and rock deformation caused by change in effective stress. Figure 3 shows a schematic depiction of hydraulic fracturing for shale gas [34].

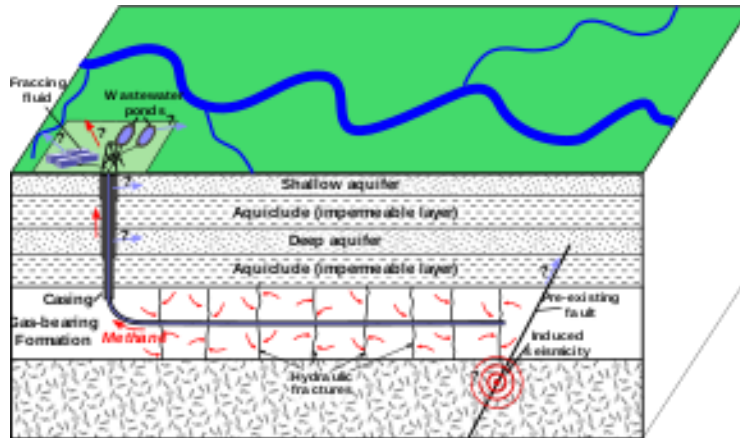


Figure 3. Schematic depiction of hydraulic fracturing for shale gas [34]

An improved understanding of hydraulic fracture geometry and shale rock mechanics enables reservoir engineers optimize stimulation design and completion strategy, improve stimulation performance, well productivity, and gas recovery. Gas production performance depends on nature and degree of fracture complexity fracture width: fracture spacing, and number of fractures. This is known as stimulated reservoir volume (SRV). A large stimulated reservoir volume (SRV) is very vital to enhanced gas production rate [35]. Simulation of the complex fracture network (natural and man-made) is a major problem for reservoir simulation approach. An adequate and valid simulation model is needed for sensitivity analysis of gas production- reservoir parameters relationship.

Hydraulic fracturing is performed by injecting fluid into a target rock formation at a pressure higher than the compressive strength or fracture pressure of the rock. The interval to be stimulated or fractured is isolated top and bottom with retrievable plugs and then pressured to rock breakdown pressure. The fractures formed stimulate the flow of natural gas or oil, increasing the volumes that can be recovered. However, the fundamental science and engineering of fracturing shale gas reservoirs are not yet fully understood and hence it is essential to develop a critical understanding of the factors that underlie optimal stimulation methods.

### 3.2. Hydraulic fracturing fluids

Hydraulic fracturing uses high pressure to force fluid consisting of water, sand and chemical additives into the shale formation. This pressurized fluid causes the rock to fracture, creating fissures or cracks in the formations. Gas (and oil) are released and flow through the fracture channels to the wellbore. Different types of chemical additives are added to fracturing fluids. These include: dilute acids, biocides, breakers, corrosion inhibitors, crosslinkers, friction reducers, gels, potassium chloride, oxygen scavengers, pH adjusting agents, scale inhibitors, and surfactants. Biocides are added to prevent microorganism growth and to reduce biofouling in the fractures; oxygen scavengers and other stabilizers prevent corrosion of metal pipes; and acids that are used to remove drilling mud damage within the near-wellbore area [36]. These fluids aid not only in creating the fractures but also they carry the proppants (sand, aluminum shot or ceramic beads) which frequently injected to hold the fractures open after the pressure treatment.

Figure 4 shows the level of baseline water stress in 20 countries with the largest volumes of technically recoverable shale gas resources. The volume of water injected during hydraulic fracturing affects the availability and consumptive use of freshwater resources, volumes of wastewater, the wastewater disposal and treatment procedures available, and the ultimate fate of this water [37]. Analysis of historical data indicates the importance of well borehole orientation, drilling date, and target gas resource on hydraulic fracturing water volumes [37] and could account for the wide range of estimates. Individually, these previous studies provided only partial information needed to fully understand the complexity of hydraulic fracturing water use across different geologic basins. There is a need to better understand the spatial variability of water use in hydraulic fracturing in aggregate, taking into consideration well types and target gas reservoirs.

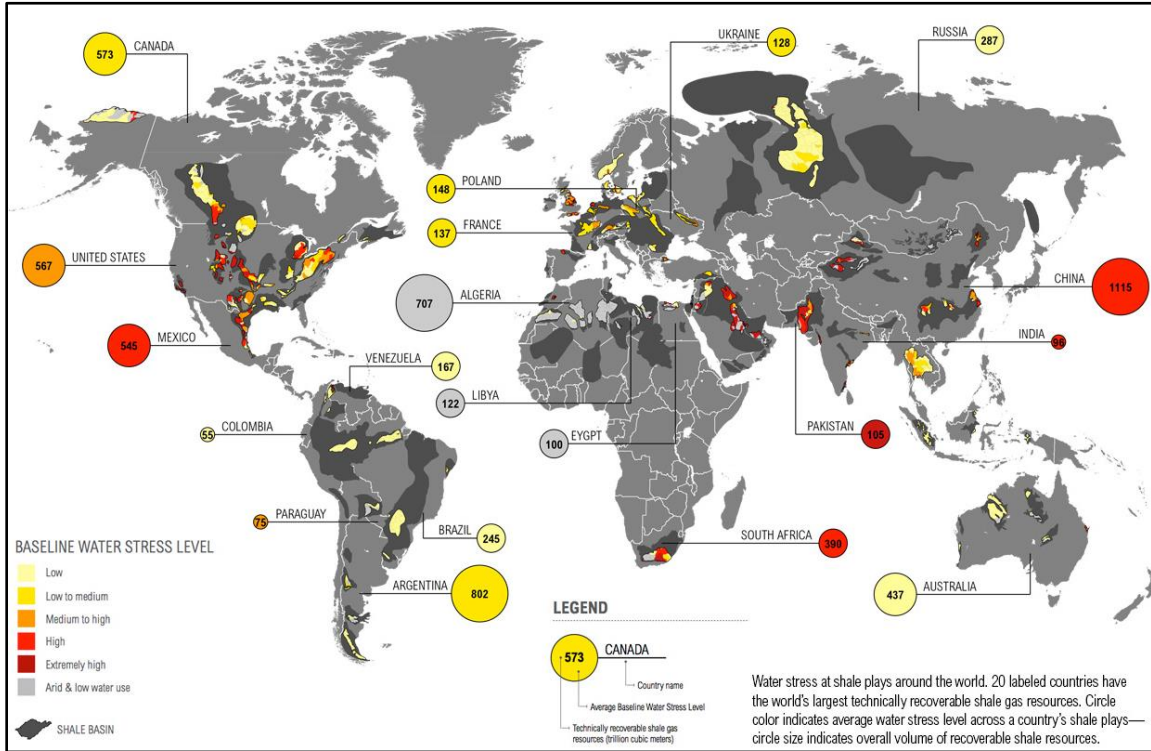


Figure 4. Baseline water stress level for hydraulic fracturing [38]

## 4. Environmental issues

### 4.1. Flowback and produced water

Although the make-up of fracturing fluid varies from one geologic basin or formation to another, the environmental issues associated with fracturing projects are the same or similar. These include water and soil contamination that result from the processes and handling of the fluids as well as the large quantities of water necessary to undertake fracturing and seismic activity that might be induced. Large volumes of freshwater are mixed with the above stated chemical additives and proppants in varying quantities depending on the geological location or well and reservoir properties. Millions of gallons of water may be injected per site, generating very large volumes of flowback and produced waters. Flowback waters are those that return to the surface after the pressure is released. They are extremely complex matrices composed of hydrolytic fracturing fluids and chemical additives that were injected and the recovered hydrocarbons from the deep formations, highly saline, with large amounts of total dissolved solids. They may contain various hydrocarbons, organic acids, al-

cohols, radionuclides, and metals. Figure 4 shows global baseline water stress level for hydraulic fracturing in the 20 countries with the largest shale gas and tight oil resources, as analyzed by World Resources Institute [38]. For shale gas, it was found that 40 percent of these countries face high water stress or arid conditions: China, Algeria, Mexico, South Africa, Libya, Pakistan, Egypt, and India

The large volumes of water used in fracturing invariably leads to large volumes of wastewater produced and ultimately to potential environmental impacts, including public water availability, water quality, wastewater disposal, aquatic ecology, and possible wastewater injection-induced earthquakes ecology [39-44]. More localized and technology-specific risks are coupled with degradation of air quality and water resources, induced seismic activity, and methane emissions which can increase the overall risk of climate change due to their increased potency relative to other fossil fuels [45].

On a regional basis, the average water volume used per well for hydraulic fracturing will depend on the number and locations of wells accessing shale gas reservoirs within a geologic basin [37]. Differences in local geology, well borehole configuration, resource type, target gas reservoir characteristics, well completion time, hydrology, and proximity to freshwater sources, existence and location of water treatment facilities, chemical makeup of flowback and produced wastewaters, management practices, land availability for surface storage, and availability of deep-disposal wells, coupled with differences in volumes of water injected could translate into possible differences in the potential for environmental impacts [46]. Development of better technological approaches that will serve as potential solutions to the problems posed by the complex matrices inherent to flowback and produced waters is needed.

## 4.2. Wastewater composition

Apart from the chemical additives to be managed, the natural water that is surfaced may contain very high levels of dissolved solids (TDS), toxic metals, radionuclides and hydrocarbons. In addition to the high content of sodium and chloride, the salts content can include elevated concentrations of bromide, bicarbonate, sulfate, calcium, magnesium, barium, strontium, radium, organic chemicals and heavy metals. The management challenge is to safely dispose, treat, or reuse those waters without damaging the local groundwater or downstream surface waters and potential drinking water sources [47-48].

The number of hydraulic fracturing shale oil and gas wells in the US, and worldwide, continues to increase. This will result to increased stress on surface water and groundwater supplies to complete the fracturing process. Equally important is the large volumes of wastewater generated (up to 60% of the water injected into a well) as flowback or produced water during fracturing of wells. This wastewater needs to be captured, and disposed of or recycled.

Water being the base fluid and biggest component used in hydraulic fracturing, its importance remains a critical factor in the operation and economics of shale oil and gas production. However, significant and growing water management challenges are impacting hydraulic fracturing [49-51]. Therefore, oil and gas companies, faced with growing concern of proper water utilization activities, need to adopt a more unified and proactive perspective on their water life-cycle management.

With the already significant fracturing industry set for further rapid expansion in the US and other countries, the demands on fresh water supplies are mounting, as is the need to process the large volumes of flowback and produced wastewater discharged during fracturing operations. Centralized treatment of wastewater is emerging as a viable solution for long-term efficiency in managing water sources and wastewater treatment in hydraulic fracturing [52].

A word on regulatory requirements – the type of chemical additives to be used in hydraulic fracturing projects and the information about their chemical characteristics should conform to regulatory requirements. Material Safety Data Sheets should be provided by the additives manufacturers [44]. Also to be provided are:

- the potential health and environmental risks of each of the additives be assessed by the operating company or suitably qualified third party selected by the operating company;
- operational procedures and controls specific to the selected additive(s) determined to manage the potential health and environmental risks identified by the risk assessment, as appropriate;
- written risk management plans incorporated into the well-specific hydraulic fracturing program;
- confirmed execution of the risk management program and actual additives used prior to program initiation and at program completion.

## 5. Conclusion

After many years of unconventional shale gas development and production the industry is not grappling with technical and environmental issues that impact on economic gas production. Existing science and technology data on shale gas formations are not adequate for describing complex flow and transport phenomena occurring in the reservoir. More research is needed to help improve understanding of the peculiar characteristics of individual shale gas reservoir adequate for determining stimulation technologies for economic gas development and recovery. Numerical simulation methods, coupled with digital rock physics analysis (DRP), will aid in characterizing individual shale gas reservoirs and quantifying the effects of pertinent factors on multiphase flow and well performance for long-term gas recovery. Knowledge generated from such studies will enable engineers to better design fracture treatments and operators to better manage the wells in a shale gas reservoir.

Regional variations in regulatory structures also mean that decisions regarding hydraulic fracturing including wastewater management and disposal practices, recycling, and underground fluid injection may fall under different regulations and jurisdictions. Because hydraulic fracturing is not a one-size-fits-all operation, assumptions and generalizations regarding water use in hydraulic fracturing operations and the potential for environmental impacts should be made with caution. More efforts are needed to develop a one-stop approach to managing environmental issues associated with freshwater usage for hydraulic fracturing operations and for managing the large volumes of flowback and produced waters generated in fracturing projects.

## Acknowledgement

I express my sincere appreciation to Professor Sunny E. Iyuke of the School of Chemical and Metallurgical Engineering, University of the Witwatersrand, Johannesburg, South Africa for his material support during the preparation of this manuscript.

## References

- [1] Energy Information Administration 2015. <https://www.eia.gov/analysis/studies/worldshalegas/>. Accessed March 24, 2018.
- [2] World Energy Council: World Energy Resources - Unconventional-gas-a-global-phenomenon-World-Energy-Resources Full-report 2016. Accessed March 31, 2018.
- [3] Lu XC, Li FC, Watson A. Adsorption studies of natural gas storage in devonian shales. SPE Form. Evaluation 1995; 10: 109-113.
- [4] Cheng AL, Huang WL. Selective adsorption of hydrocarbon gases on clays and organic matter. Org. Geochem., 2004; 35: 413-423.
- [5] Busch A, Alles S, Gensterblum Y, Prinz D, Dewhurst DN, Raven MD, Stanjek H, Krooss BM. Carbon dioxide storage potential of shales. Int. J. Greenh. Gas Control 2008; 2: 297-308.
- [6] Jin Z, Firoozabadi A. Methane and carbon dioxide adsorption in claylike slit pores by monte carlo simulations. Fluid Phase Equilibria 2013; 360: 456-465.
- [7] Eagleford shale. <http://goeaglefordshale.com/forum/topics/pearsall-shale-what-area-does-it-over?id=6447762:Topic:30747&page=3>.
- [8] Bustin AMM, Bustin RM. Importance of rock properties on the producibility of gas shales. Intl J. Coal Geol., 2012; 103: 132-147.

- [9] Pang Y, Soliman MY, Deng H, Emadi H. Analysis of effective porosity and effective permeability in shale-gas reservoirs with consideration of gas adsorption and stress effects. Society of Petroleum Engineers 2017. doi:10.2118/180260-PA.
- [10] Bust VK, Majid AA, Oletu JU, Worthington PF. The petrophysics of shale gas reservoirs: Technical challenges and pragmatic solutions. *Petroleum Geoscience* 2013; 19: 91–103.
- [11] Lewis R, Ingraham D, Percy M, Williamson J, Sawyer W, Frantz J. New evaluation techniques for gas shale reservoirs. Reservoir 2004, Schlumberger. (accessed March 20, 2018).
- [12] Leu L, Georgiadis A, Blunt MJ, Busch A, Bertier P, Schweinar K, Liebi M, Menzel A, Ott H. Multiscale description of shale pore systems by scanning SAXS and WAXS microscopy. *Energy Fuels*, 2016; 30: 10282–10297.
- [13] Wopara FO, Iyuke SE. Prediction of flow and transport properties in porous media. *Int. J. Oil, Gas and Coal Technology*, 2018; 17, 3: 284–303.
- [14] Lane HS, Lancaster DE, Watson AT. Characterizing the role of desorption in gas production from Devonian shales. *Energy Sources*, 1991; 13(3): 337-359.
- [15] Passey QR. Characterization of shale-gas reservoirs. International Oil and Gas Conference and Exhibition. SPE-131350-MS, 8-10 June, 2010, Beijing, China. doi.org/10.2118/131350-MS.
- [16] Yang T, Li X, Zhang D. Quantitative dynamic analysis of gas desorption contribution to production in shale gas reservoirs. *Journal of Unconventional Oil and Gas Resources*, 2015; 9: 18-30.
- [17] Wang J, Chen L, Kang Q, Rahman SS. Apparent permeability prediction of organic shale with generalized lattice Boltzmann model considering surface diffusion effect. *Fuel*, 2016; 181: 478–490.
- [18] Tang X, Jiang Z, Jiang S, Cheng L, Zhang Y. Characteristics and origin of in-situ gas desorption of the Cambrian Shuijingtuo Formation shale gas reservoir in the Sichuan Basin, China. *Fuel* 2017, 187(11): 285-295.
- [19] Mengal SA, Wattenbarger RA. Accounting for adsorbed gas in shale gas reservoirs. Paper presented at the SPE Middle East Oil and Gas Show and Conference. SPE 141085, 25-28 September, 2011, Manama. doi.org/10.2118/141085-MS.
- [20] Guo C, Wei M, Liu H. Modeling of gas production from shale reservoirs considering multiple transport mechanisms. *PLOS ONE*, 2015; 10(12): e0143649.
- [21] Chen S, Du L, Yong Q, Zhao J, Zhang Q. Numerical description of shale gas desorption stages. *Energy Exploration & Exploitation*, 2017; 35(6) 734–747.
- [22] Bustin RM, Bustin AMM, Cui A, Ross D, Pathi VM. Impact of shale properties on pore structure and storage characteristics. Society of Petroleum Engineers Shale Gas Production Conference, SPE 119892S, Fort Worth, Texas, USA, November 16 2008, 18, 28. doi: 10.2118/119892-MS.
- [23] Wang J, Yang Z, Dong M, Gong H, Sang Q, Li Y. Experimental and numerical investigation of dynamic gas adsorption/desorption-diffusion process in shale. *Energy Fuels*, 2016, 30(12): 10080–10091.
- [24] Leahy-Dios A, Das M, Agarwal A, Kaminsky R. Modeling of transport phenomena and multi-component sorption for shale gas and coalbed methane in an unstructured grid simulator. SPE Paper 147352, Presented at SPE Annual Technical Conference and Exhibition, Denver, Colorado, USA, October 30- November 2 2011. doi.org/10.2118/147352-MS.
- [25] Darishchev A, Rouvroy P, Lemouzy P. On simulation of flow in tight and shale gas reservoirs. SPE-163990-MS. SPE Unconventional Gas Conference and Exhibition, 28-30 January, Muscat, Oman. 2013. doi: 10.2118/163990-MS.
- [26] Szott W, Milek K. Methods to determine drainage area in shale formations produced by stimulated horizontal wells using reservoir simulation modelling. *Nafta-Gaz*, 2015; 71(12): 992-997.
- [27] Blasingame TA. The Characteristic flow behavior of low-permeability reservoir systems. SPE 11416. SPE Unconventional Reservoirs Conference Keystone 2008, CO, U.S.A.
- [28] Gensterblum Y, Ghaizadeh A, Cuss RJ, Amann-Hildenbrand A, Kross BM, Clarkson CR, Harrington JF, Zoback MD. Gas transport and storage capacity in shale gas reservoirs. A review Part A: Transport processes. *Journal of Unconventional Oil and Gas Resources*, 2015; 12: 87-122.
- [29] Wang L, Torres A, Xiang L, Fei X, Naido A, Wu W. Technical review on shale gas production and unconventional reservoirs modeling. *Natural Resources*, 2015; 6: 141-151.
- [30] Dahaghi AK, Mohaghegh SD. Numerical simulation and multiple realizations for sensitivity study of shale gas reservoirs. Production and Operations Symposium, 27-29 March 2011. Oklahoma City, Oklahoma. doi.org/10.2118/141058-MS.

- [31] Mirzaei M, Cipolla CLA. Workflow for modeling and simulation of hydraulic fractures in unconventional gas reservoir. Paper SPE 153022, 2012. Presented at the SPE Middle East Unconventional Gas Conference and Exhibition held in Abu Dhabi, UAE.
- [32] Gouth F, Collell J, Galliero G, Wang J. Molecular simulation to determine key Shale gas parameters, and their use in a commercial simulator for production forecasting. Society of Petroleum Engineers 2013. Richardson, TX, USA.
- [33] Lee KS, Kim TH. Integrative understanding of shale gas reservoirs, Springer briefs in: Applied Sciences and Technology, 2016. doi: 10.1007/978-3-319-29296-0\_2.
- [34] Wikipedia. [https://en.wikipedia.org/wiki/Hydraulic\\_fracturing](https://en.wikipedia.org/wiki/Hydraulic_fracturing)
- [35] Guo C, Xu J, Wu K, Wei M, Liu S. Study on gas flow through nanopores of shale gas reservoirs. Fuel, 2015; 143: 107-117.
- [36] Schlumberger. PowerSTIM Well Optimization Service 2017, (accessed March 21, 2018).
- [37] Gallegos TJ, Varela BA, Haines SS, Engle MA. Hydraulic fracturing water use variability in the United States and potential environmental implications. Water Resour. Res., 2015; 51: 5839-5845.
- [38] World Resources Institute. [www.wri.org/water-for-shale](http://www.wri.org/water-for-shale). Accessed March 31, 2018.
- [39] Jackson RB, Vengosh A, Darrah TH, Warner NR, Down A, Poreda RJ, Osborn SG, Zhao K, Karr JD. Increased stray gas abundance in a subset of drinking water wells near Marcellus shale gas extraction. PNAS, 2011; 110: 11250-11255.
- [40] Vidic RD, Brantley SL, Vandenbossche JM, Yoxheimer D, Abad JD. Impact of shale gas development on regional water quality. Science, 2013; 340(6134): 1235009.
- [41] Jackson RB, Vengosh A, Carey JW, Darrah TH, O'Sullivan F, Pétron G. The Environmental Costs and Benefits of Fracking. Annual Rev Environm Resour., 2014; 39: 1.
- [42] Nicot JP, Scanlon BR, Reedy RC, Costley RA. Source and fate of hydraulic fracturing water in the Barnett Shale: A historical perspective. Environ. Sci. Technol., 2014, 48(4), 2464-2471
- [43] Blewett TA, Weinrauch AM, Delompré PLM, Goss GG. The effect of hydraulic flowback and produced water on gill morphology, oxidative stress and antioxidant response in rainbow trout. Scientific Reports, 2016; 7: 46582.
- [44] Vengosh V, Kondash A, Harkness J, Lauer N, Warner N, Darrah TH. The geochemistry of hydraulic fracturing fluids. Procedia Earth and Planetary Science, 2017; 17: 21 - 24.
- [45] McKenzie LM, Witter RZ, Newman LS, Adgate JL. Human health risk assessment of air emissions from development of unconventional natural gas resources. Sci Total Environ., 2012; 124:79-87.
- [46] Mauter MS, Alvarez PJJ, Burton A, Cafaro DC, Chen W, Gregory KB, Jiang G, Li Q, Pittock J, Reible D, Schnoor JL. Regional variation in water-related impacts of shale gas development and implications for emerging international plays. ES&T., 2014, 48(15): 8298-8306.
- [47] Warner NR, Christie CA, Jackson RB, Vengosh A. Impacts of shale gas wastewater disposal on water quality in western Pennsylvania. ES&T, 2013; 47: 11849-11857.
- [48] Adgate JL, Goldstein BD, McKenzie LM. Potential public health hazards, exposures and health effects from unconventional natural gas development. ES&T., 2014; 48(15): 8307-20.
- [49] Garth T, Llewellyn GT, Dormanb F, Westlandb JL, Yoxtheimerc D, Grievenc P, Sowersc T, Humston-Fulmerd E, Brantleyc SL. Evaluating a groundwater supply contamination incident attributed to Marcellus Shale gas development. PNAS, 2015; 112(20): 6325-6330.
- [50] Vandecasteele I, Rivero IM, Sala S, Baranzelli C, Barranco R, Batelaan O, Lavalley C. Impact of Shale Gas Development on Water Resources: A Case Study in Northern Poland. Environ Manage., 2015; 55(6): 1285-1299.
- [51] Yu M, Weinthal E, Patiño-Echeverri D, Deshusses MA, Zou C, Ni Y, Vengosh A. Water availability for shale gas development in Sichuan Basin, China. ES&T, 2016; 50: 2837-2845.
- [52] Easton J. Fracking Wastewater management. Water and Wastewater International 2018. <http://www.waterworld.com/articles/wwi/print/volume-28/issue-5/regional-spotlight-us-caribbean/fracking-wastewater-management.html> (accessed 28 March, 2018).

To whom correspondence should be addressed: Dr. Onuoha F. Wopara, Engineering, Rivers State University, Port Harcourt, Nigeria, [wopara.fidelis@ust.edu.ng](mailto:wopara.fidelis@ust.edu.ng)

## MODELLING, SIMULATION AND DYNAMIC MATRIX CONTROL OF A METHANOL-TO-ETHENE PROCESS

Abdulwahab Giwa<sup>1\*</sup>, Chioma Miriam Chijioko<sup>2</sup>, Saidat Olanipekun Giwa<sup>3</sup>

<sup>1,2</sup> *Chemical and Petroleum Engineering Department, College of Engineering, Afe Babalola University, Afe Babalola Way, Ado-Ekiti, Ekiti State, Nigeria*

<sup>3</sup> *Chemical Engineering Department, Faculty of Engineering and Engineering Technology, Abubakar Tafawa Balewa University, Tafawa Balewa Way, Bauchi, Nigeria*

Received July 5, 2018; Accepted September 28, 2018

---

### Abstract

This research has been carried out to develop a model for the methanol-to-ethene process, simulate it and carry out its dynamic matrix control by investigating the effects of some tuning parameters on the control system. In order to achieve this aim, the methanol-to-ethene (MTE) process was modelled and simulated with the aid of ChemCAD for both steady state and dynamics. The dynamics data showing the response of ethene mole fraction to a change in reflux ratio were extracted from the ChemCAD dynamic simulation of the developed process model and used to develop a first-order transfer function relation between ethene mole fraction and reflux ratio via the System Identification Toolbox of MATLAB. Furthermore, the open loop simulation of the process was carried out in MATLAB environment. Thereafter, the closed loop response of the system was obtained using different values of control horizon, prediction horizon, model length, and control weighting as the tuning parameters of the dynamic matrix controller while the set point of the process was made to be the achievement of a mole fraction of 0.95 for ethene. It was revealed from the results obtained that the ChemCAD and the transfer function models developed for the process were valid ones because the ethene mole fractions obtained at their steady states upon the application of a final value of 2 to the reflux ratio, which was the input variable of the process, were very close. Also, the simulations of the closed-loop system of the dynamic matrix control of the process showed that there were significant effects of the control horizon, prediction horizon, and control weighting on the dynamic matrix control of the methanol-to-ethene process whereas the effect of the model length was found to be insignificant. Therefore, it has been discovered that control horizon, prediction horizon, and control weighting were the main tuning parameters for the dynamic matrix control of the methanol-to-ethene process.

**Keywords:** *Methanol; ethene; ChemCAD; dynamic matrix control; MATLAB; control horizon; prediction horizon; control weighting.*

---

## 1. Introduction

To meet the ever-increasing demand for oil-based chemicals despite waning oil reserves, the development of new technologies from alternative feedstock is a general concern for both scientific and industrial communities [1]. One of the most prominent emerging technologies is the methanol-to-olefin (MTO) process that is catalyzed by acidic zeolites, such as H-ZSM-5, or by nanoporous zeotype materials, such as H-SAPO-34 [2].

Olefins can be produced using several processes and feedstocks. In every process, a range of products and byproducts are formed. The percentage of the different products depending on the process and the feedstock used. Currently, there are three main sources of olefins for petrochemicals, viz. steam cracking of hydrocarbons (naphtha, ethane, gas oil and liquefied petroleum gas), fluid catalytic cracking in oil refineries and paraffin dehydrogenation. In addition to these commercial processes, there are some non-commercial technologies under

various phases of development such as oxidative coupling of methane, oxidative dehydrogenation of paraffins and methanol-to-olefins process [3], which is being considered in this work.

According to the information from the research of Keil [4], the conversion of methanol to hydrocarbons, including methanol-to-olefin, was discovered by two teams of Mobil scientists working on unrelated projects. They discovered, by accident, the formation of hydrocarbons from methanol over the synthetic zeolite ZSM-5 in early 1970. The group at Mobil Chemical in Edison, New Jersey, had been trying to convert methanol to ethene oxide, while workers at Mobil Oil's Central Research Laboratory in Princeton were attempting to methylate isobutene with methanol in the presence of ZSM-5. Neither of the reactions yielded the expected result. Instead, aromatic hydrocarbons were formed.

The methanol-to-olefin process converts methanol into light olefins, such as ethene - an important feedstock for the production of many types of polymers, which serve as basic building blocks for petrochemical industries and polymerization processes in particular. As a result, ethene and propene are increasingly in demand [1] in process industries.

Recent interest in the methanol-to-olefin mechanism was further fueled by a surge in oil prices. methanol-to-olefin conversion allows the petrochemical industry to bypass crude oil as a fundamental feedstock because methanol can be made from synthesis gas, which, in turn, can be formed from almost any gasifiable carbonaceous species, such as natural gas, coal, biomass and organic waste [1]. This process has some advantages over the current steam cracking of natural gas liquids, naphtha or other light fractions of petroleum, due to the fact that methanol-to-olefin process can provide a wider and more flexible range of ethene to propene ratio relative to those of conventional processes to meet market demand [2].

For the purpose of this research work, the interest will be limited to the production of the simplest olefin, which is ethene. The methanol-to-ethene (MTE) process was got from the methanol-to-olefin process. The former was launched solely for ethene production. In both processes, methanol that is produced mainly from synthesis gas is used as the feed of the process [5].

Due to the fast development of the process industries, one of which is a methanol-to-ethene process, improving the plant efficiency is very challenging owing to the fact that the scale of processes has become larger and process complexity has increased dramatically. This has led to the demand of a very robust controller design strategy, both in theory and practice [2].

Based on that, Richalet [6] has classified the controllers for the control problems into four hierarchical levels:

1. first level controllers used for the control problems dealing with some ancillary systems, in which proportional-integral-derivative (PID) controller could be a very good choice,
2. the second level controller used for problems involving multivariable dynamic process, which is interfered by some unmeasured perturbations,
3. third level controllers used for optimization problems based on the minimization of cost functions; a model predictive controller (MPC) is in this level, and
4. fourth level controllers consisting of those time and space scheduling production problems that include the feasible research and have the best economic benefits.

As a result of the simple structure, low cost, convenient manipulation and the satisfaction for most of the production control, proportional-integral-derivative has become the major controller used in the family of level one. However, the economic benefits induced by level one and two are usually negligible [6].

The model predictive controller works in a different manner in the sense that instead of using the past error between the output of the system and the desired value like a proportional-integral-derivative controller would do, it controls the system by predicting the value of the output in a short time, so the system output is as closer as possible to its desired value for these moments. In process control today, more than 95% of the control loops are of proportional-integral-derivative type [7-8]. Also, it is stated that more than 90% of industrial controllers are still implemented based on proportional-integral-derivative algorithms [9]. However, the proportional-integral-derivative seems not to be robust and effective in some cases involving a methanol-to-olefin process.

Owing to that, it has been realized that there is the need to incorporate an advanced controller type such as the dynamic matrix control that is based on model predictive control technology to processes like the one of methanol-to-olefin type because it can bring about many improvements in the economics of the system, can easily deal with multivariable cases and can also be used to handle the process if there are delays. Therefore, the aim of this research work is to apply dynamic matrix control to a methanol-to-ethene process by taking the mole fraction of ethene obtained from the process and the reflux ratio as the controlled and the manipulated variables respectively.

## 2. Methodology

The methods adopted in accomplishing the control of the methanol-to-ethene (MTE) process are as outlined in the following subsections.

### 2.1. Steady State modeling and simulation of the MTE process

The process was modelled and simulated using ChemCAD [10] process simulator through the following steps:

- Component Selection:** The chemical components involved in the process were chosen from the ChemCAD database, and they were:
  - Methanol
  - Dimethyl ether
  - Ethene
  - Water
- Thermodynamic Package Selection:** Based on the components involved in the process, UNIQUAC Functional-group Activity Coefficients (UNIFAC) method was chosen as the thermodynamic package for the simulation.
- Flowsheet Development:** The different unit of the process flowsheet was selected from the Palette of the simulator and connected accordingly. The equilibrium reactor having one feed stream was connected to the kinetic reactor which was in turn connected to the Simultaneous Correction Distillation System (SCDS) column with two product streams, see Figure 1. The dehydration of methanol to dimethyl ether represented by Equation (1) was incorporated into the equilibrium reactor while the conversion of dimethyl ether to ethene and water, which is represented by Equation (2), was incorporated into the kinetics reactor using the kinetics expressions given in Equation (3) and (4) and the parameters contained in Table 5.
- Feed Stream Specification:** The conditions of the feed streams were specified as given in Table 1.
- Equipment Specification:** The conditions of the equilibrium reactor, kinetic reactor and SCDS column were specified using the operating parameters given in Tables 2 – 4 respectively.



Table 1. Operating parameters for feed stream

Parameter	Description/Value
Stream name	Methanol
Temperature (oC)	60
Pressure (atm)	1
Total flow (kmol/hr)	100
Methanol (mole fraction)	1

Table 2. Operating parameters of the equilibrium reactor

Parameter	Description/Value
Reactor type	General equilibrium reactor
Number of reactions	1
Thermal mode	Isothermal
Calculation mode	Approach delta T = 5 (°C)
Liquid Keq model	Keq = Kx

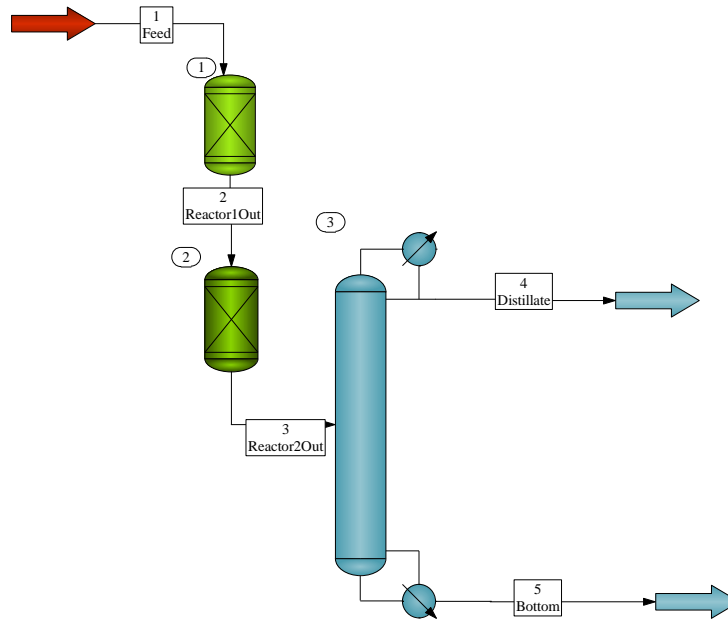


Figure 1. ChemCAD model of the methanol-to-ethene process

Table 3. Operating parameters of the kinetics reactor

Parameter	Description/Value
Reactor type	Plug flow
Number of reactions	1
Thermal mode	Adiabatic
Calculation mode	Volume specification and conversion calculation
Reactor volume	10 m3

Table 4. Operating parameters of the SCDS column

Parameter	Description/Value
Condenser type	Total
Number of stages	11
Feed stage for column feed stream	5
Reflux ratio	1
Reboiler duty (kJ/sec)	0.1

The rate of reaction for the conversion of dimethyl ether to ethene is given as,

$$r = k_2 C_{DME} \tag{3}$$

where DME denotes dimethyl ether, and the rate constant is given as

$$k = k_0 e^{-\frac{E}{RT}} \tag{4}$$

The kinetic data for modeling the reaction was obtained from the work of Jianglong and Huixin [11] as given in Table 5.

Table 5. Kinetics data for the conversion of dimethyl ether to ethane

Parameter	Value
$k_0$ (hr <sup>-1</sup> )	$9.18 \times 10^7$
E (J/mol)	89478

Source: Jianglong and Huixin [11]

After developing the steady-state process model using ChemCAD, it was run using the 'Run All' icon on the ChemCAD flowsheet ribbon until convergence before converting it to the type used in the dynamic simulation.

## 2.2. Process dynamics simulation

The dynamic simulation of the methanol to ethene process was carried out using the following steps:

1. *Conversion of the steady-state model to dynamics type:* Using the developed converged steady state MTE model, the dynamics option was selected from the 'Steady state/Dynamics' drop-down menu found under "run" menu.
2. *Dynamics simulation:* The dynamic model was simulated at two run time steps:
  - First run time step: A time of 5 min with a 0.01 min interval was used, and the dynamic simulation was run from the initial steady state in this case.
  - Second run time step: A time of 1.5 hr with a 0.05 min interval was used for the second run time step from the current steady state. In this case, the reflux ratio of the column was changed to a final value of 2.
3. *Dynamics data extraction:* The dynamics data obtained were for the mole fraction of ethene in the column distillate stream (stream 4). The run time plot for the mole fraction of ethene in stream 4 was obtained using the 'Plot Dyn Streams' icon on the ChemCAD flowsheet ribbon. From the plot, the dynamic data were extracted to an excel worksheet by clicking the 'Data to Excel CSV file' option from the 'Chart' drop-down menu.

## 2.3. Process transfer function formulation

The process transfer function model used in this work was formulated by developing the relationship between ethene mole fraction (output variable) and reflux ratio (input variable) using the data generated from the developed ChemCAD model with the aid of the System Identification Toolbox of MATLAB [12] using codes written. By running the script, the dynamics data of the simulated MTE process was called from the Microsoft Excel Spreadsheet and exported to the System Identification Toolbox interface of the MATLAB. On the System Identification Toolbox interface, a transfer function model of the form shown in Equation 5 was specified and developed.

$$G_p(s) = \frac{K_p e^{-T_d s}}{(1 + T_p s)} \quad (5)$$

## 2.4. Dynamic Matrix Control of the MTE Process

### 2.4.1. Formulation of control objective function

The dynamic matrix control (DMC) of the methanol-to-ethene process was accomplished using the method described by Bequette [13] in which the least-squares objective function for a control horizon of  $nc$  and a prediction horizon of  $np$  was as defined in Equation (6),

$$\Phi = \sum_{i=1}^{np} (y_{sp} - \hat{y}_{k+i})^2 + w \sum_{i=0}^{nc-1} (\Delta u_{k+i})^2 \quad (6)$$

where  $y_{sp}$  is the setpoint,  $\hat{y}_{k+i}$  is the model prediction at time  $k+i$ ,  $w$  is the control weighting and  $u_{k+i}$  is the manipulated input at time step  $k+i$ .

The method was, actually, based on step response model that has the form given in Equation (7),

$$\hat{y}_k = \sum_{i=1}^{N-1} s_i \Delta u_{k-i} + s_N u_{k-N} \quad (7)$$

where  $\hat{y}_k$  is the model prediction at time step  $k$ ,  $s_i$  represents the step response coefficient for the  $i$ th sample after the unit step input change,  $u_{k-i}$  is the manipulated input  $i$  steps in the past and  $u_{k-N}$  is the manipulated input  $N$  steps in the past.

As such, the control objective function was written as given in Equation (8),

$$\Phi = (E - S_f \Delta u_f)^T (E - S_f \Delta u_f) + (\Delta u_f)^T W \Delta u_f \quad (8)$$

where  $E$  is the unforced error vector,

$$S_f = \begin{bmatrix} s_1 & 0 & 0 & \cdots & 0 & 0 \\ s_2 & s_1 & 0 & \cdots & 0 & 0 \\ \vdots & \vdots & & & & \\ s_j & s_{j-1} & s_{j-2} & \cdots & \cdots & s_{j-M+1} \\ \vdots & \vdots & \vdots & & & \vdots \\ s_p & s_{p-1} & s_{p-2} & \cdots & \cdots & s_{p-M+1} \end{bmatrix} \quad (9)$$

$$\Delta u_f = \begin{bmatrix} \Delta u_k \\ \Delta u_{k+1} \\ \vdots \\ \Delta u_{k+M-2} \\ \Delta u_{k+M-1} \end{bmatrix} \quad (10)$$

and

$$W = \begin{bmatrix} w & 0 & 0 & 0 \\ 0 & w & 0 & 0 \\ 0 & 0 & \ddots & 0 \\ 0 & 0 & 0 & w \end{bmatrix} \quad (11)$$

The solution of the objective function was thus, also, carried out in MATLAB environment.

### 2.4.2. Tuning and simulation of the control system

The tuning parameters (control horizon, prediction horizon, model length, and control weighting) of the dynamic matrix control system were varied, and their effects on the control performance were investigated with the aid of MATLAB *mfile* codes written. It should be noted that, before tuning and controlling the system, the first-order-plus-delay-time transfer function of the system was approximated to an ordinary first order system using Pade approximation in order to convert the model to the form required by the approach of Bequette [13], which was the one adopted in this work.

## 3. Results and discussion

### 3.1. ChemCAD Steady-State simulation output

The results obtained from the steady-state simulation of the developed ChemCAD process model of the methanol-to-ethene (MTE) process were as given in Tables 6. Based on the information given in the table, the production of ethene using the process was a successful one because the mole fraction of ethene obtained was approximately 0.73 while the other main component present in the product was water with a mole fraction of approximately 0.25. The mole fractions of the other chemicals (methanol and dimethyl ether) involved in the process were found to be negligible. Based on the results of the steady-state simulation of the process, it was observed that a high concentration of the main product (ethene) could be obtained.

Table 6. Steady-state product stream component mole fraction

Component	Mole fraction
Methanol	0.01925
Dimethyl Ether	6.7166e-08
Ethene	0.7318
Water	0.2489

### 3.2 ChemCAD dynamic simulation output

Having ensured that the developed ChemCAD model of the process converged under steady state, it was converted to a dynamic type and simulated accordingly. The results of the dynamic simulation of the process are given in Figure 2 when a step change was applied to the reflux ratio, which was the input variable of the process, to make its final value to be 2.

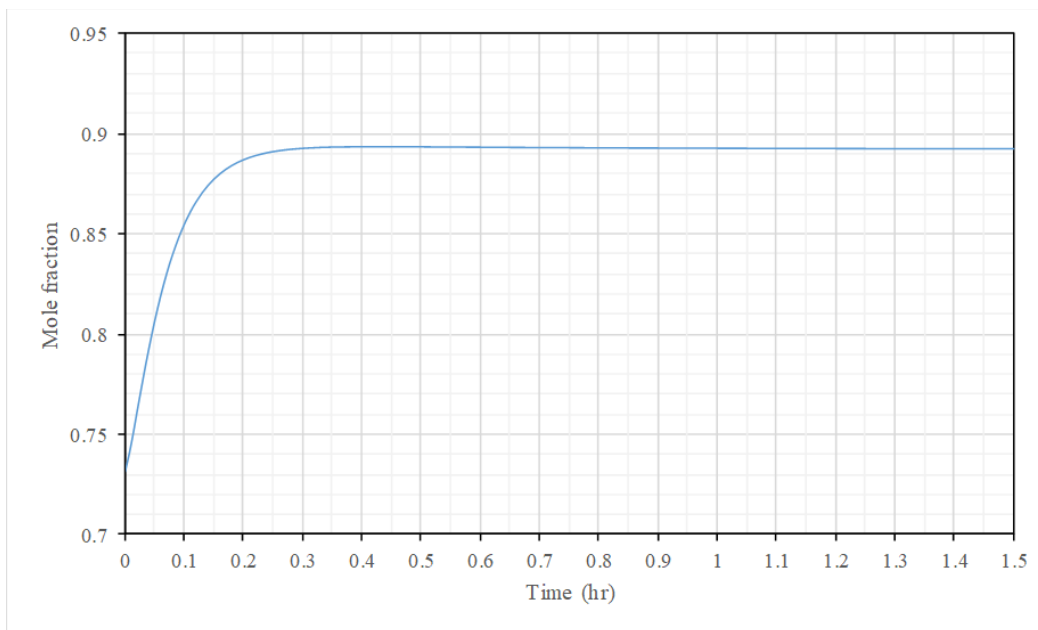


Figure 2. Dynamic response of the system in terms of the mole fraction of ethene mole fraction against time

It can be seen from Figure 2 that ethene mole fraction was affected by the change in the reflux ratio because it (ethene mole fraction) was found to vary from its initial steady state value of 0.7318 to another final steady state of approximately 0.8920. Therefore, it can be said that a change in the column reflux ratio has caused a change in the dynamic response of ethene mole fraction. In other words, the reflux ratio was an appropriate input variable for the process.

### 3.3. Transfer function modelling and Open-Loop simulation response

A first order transfer function with time delay was developed with the aid of System Identification Toolbox of MATLAB Using the data generated from the dynamic simulation of the process. The developed transfer function relating the ethene mole fraction (output variable) to the reflux ratio (input variable) in Laplace transforms was as given in Equation (12).

$$x(s) = \frac{0.44738}{7.3869s+1} e^{-0.25s} R(s) \quad (12)$$

The open-loop simulation of the developed transfer function model of the process was also carried with the aid of MATLAB *mfile* by applying a step change with a final value of 2 to the reflux ratio, and the dynamic response obtained is given in Figure 3.

From the open loop response shown in Figure 3, it was again confirmed that the system was a stable one as it could attain an ethene steady-state value of approximately 0.8942 within 50 min of the simulation period. This steady-state value was found to be in agreement with the one obtained from the ChemCAD dynamic simulation of the process. Though the system was found to be a stable one, in order to obtain an ethene mole fraction higher than the one obtained from the open-loop steady-state simulation, there was the need for its proper control using an advanced control method known as dynamic matrix control.

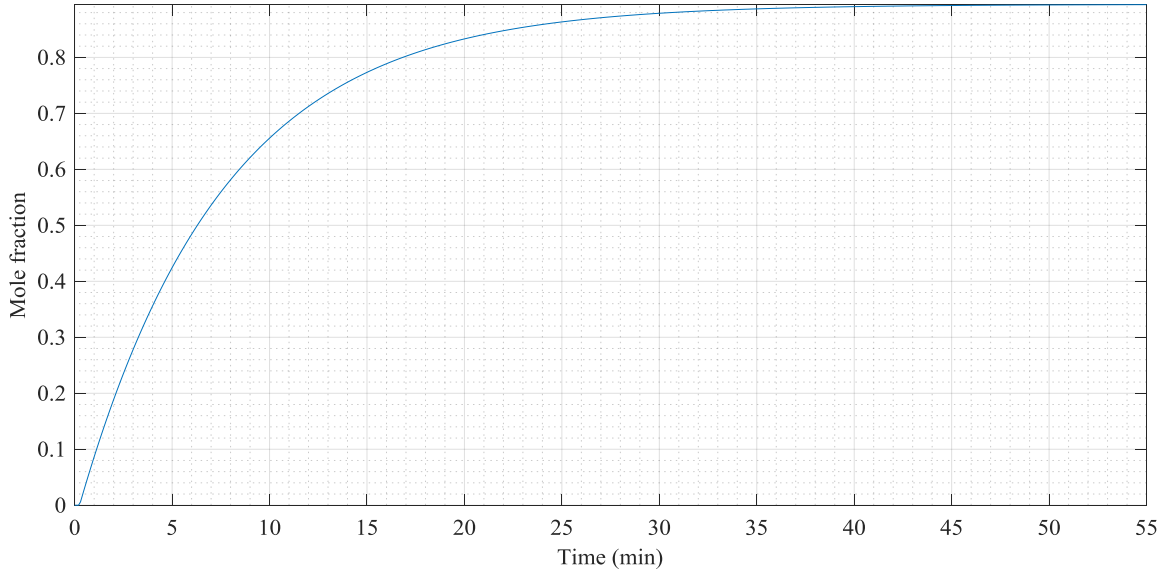


Figure 3. Open loop response of the process to a unit step change in reflux ratio

### 3.4. Dynamic matrix control simulation

The dynamic matrix control of the methanol-to-ethene process was carried out by investigating the effects of the tuning parameters (control horizon, prediction horizon, model length, and control weighting) on the performance of the system towards giving ethene mole fraction of 0.95 as the controlled variable while the reflux ratio was taken as the manipulated variable.

#### 3.4.1. Effect of control horizon

Control horizon refers to the sequence of control moves required to satisfy the specified optimization objective of minimizing the predicted deviation of the process output from the target over the prediction horizon and the expenditure of control effort in driving the process output to the target in the presence of prespecified operating constraints. Since this variable is used in the optimization of the control function, it means it is very important to the performance of the control system. As such, it is worth investigating how it affects the dynamic matrix control of the methanol-to-ethene process. The results of the investigation carried out by making the value of the control horizon to be 1 and 5 are given in Figure 4. According to the results given in the figure, the response of the control system was found not to have any overshoot when the control horizon was 1 whereas that of the control horizon of 5 had overshoot. However, the response of the control horizon of 5 was observed to get settled faster than that of the control horizon of 1.

Table 7. Performance criteria values for effects of control horizon

Criterion	Control horizon = 1	Control horizon = 5
SAE	7.3294	5.8830
MAE	0.1018	0.0817
SSE	4.3084	4.1008
MSE	0.0598	0.0570

In order to further know the effect of the control horizon on the performance of the control system, some performance criteria, which were sum of absolute error (SAE), mean of absolute error (MAE), sum of squared error (SSE) and mean of squared error (MSE), were calculated for the two cases considered in this work, and the results obtained are given in Table 7. The values of the criteria given in the table revealed that the performance of the control system when the control horizon was 5 was better than that of the control horizon of 1 because all

the values of the performance criteria of the control horizon of 5 were less than those of the control horizon of 1, keeping other tuning parameters constant.

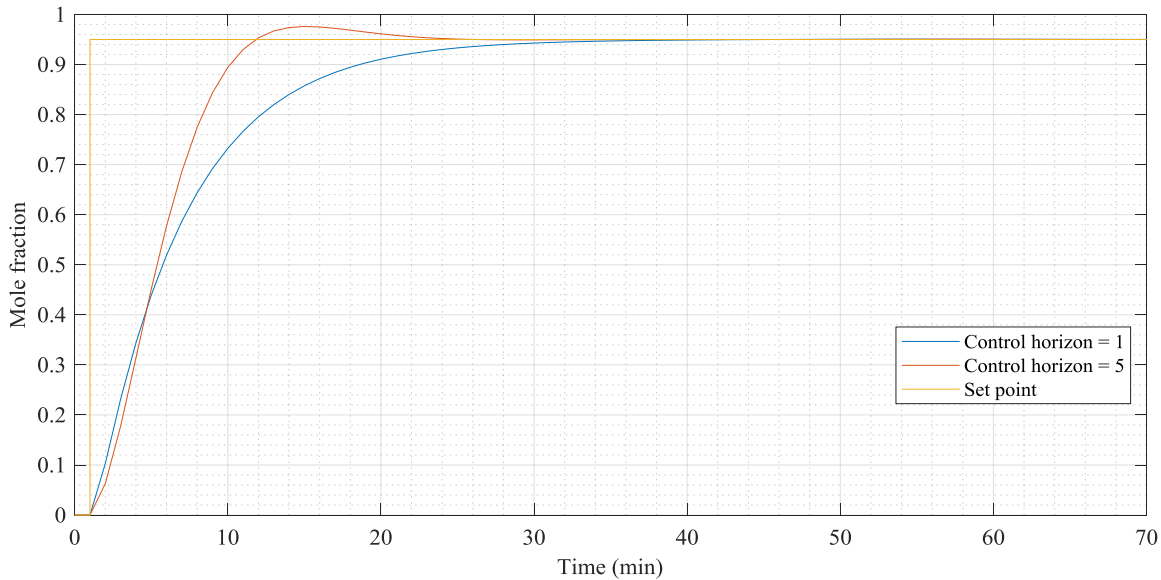


Figure 4. Closed-loop response of the MTE process to a step change of 0.95 in ethene mole fraction and variation in control horizon; prediction horizon = 25, model length = 50, control weighting = 0.3

### 3.4.2. Effect of the prediction horizon

The prediction horizon is the number of a prediction made on the process over a predetermined time horizon beyond the extent of the control action, and it is another tuning parameter that affects the response obtained from the dynamic matrix control system. The investigation of its effect on the dynamic matrix control of the methanol-to-ethene process was carried out by varying its value from 15 to 35, and the responses obtained were as given in Figure 5. The responses in the figure showed that the variation in the closed-loop dynamic response of the process was not much despite the 20-unit difference in the values of the prediction horizon, as compared to the response obtained when the control horizon was changed from 1 to 5. This is to say that the response of the dynamic matrix control of this process was more sensitive to the control horizon than to the prediction horizon.

In an attempt to know how the change in the prediction horizon was affecting the control system involving the methanol-to-ethene process, the selected performance criteria were also calculated in this case, and the results are given in Table 8. The closeness of the performances of the control systems with prediction horizons of 15 and 35 could also be seen from the performance criteria results because the values of SAE, MAE, SSE and MSE for the two cases considered were found to be close for each criterion.

Table 8. Performance criteria values for effects of prediction horizon

Criterion	Prediction horizon = 15	Prediction horizon = 35
SAE	6.1494	6.3923
MAE	0.0854	0.0888
SSE	4.2396	4.3601
MSE	0.0589	0.0606

Moreover, however, the importance of the prediction horizon was shown clearly by comparing the responses in Figures 4 and 5 because it was clearly observed that the responses obtained when the prediction horizon was varied could get settled faster than those obtained when the control horizon was varied.

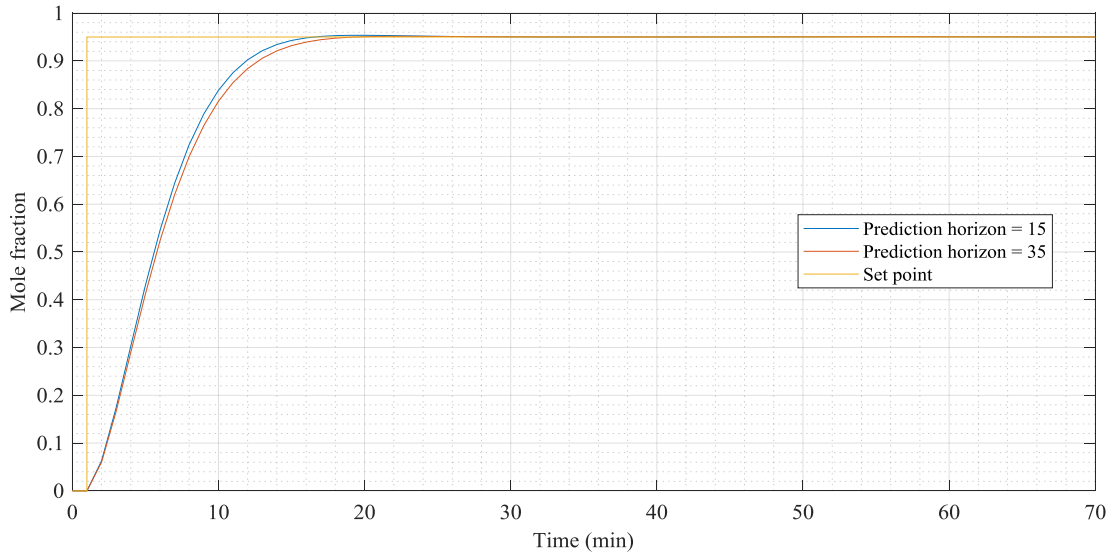


Figure 5. Closed-loop response of the MTE process to a step change of 0.95 in ethene mole fraction and variation in prediction horizon; control horizon = 3, model length = 50, control weighting = 0.3

**3.4.3. Effect of model length**

Another parameter affecting the responses obtained from dynamic matrix control is the model length. The model length of a dynamic matrix control should be selected in such a way that it is approximately the time required for the system to get to a new steady state. According to the information obtained from the literature, the model length for most systems is approximately 50 coefficients. That value of 50 was taken as the middle value in this work, and the simulation of the control system was carried out using a model length of 35 and 65 successively, and the results obtained are given in Figure 6. From the figure, it could be observed that the two responses obtained overlapped each other almost throughout the simulation time used for the dynamics. This is showing that the effect of model length chosen for the dynamic matrix control of this process is not significant.

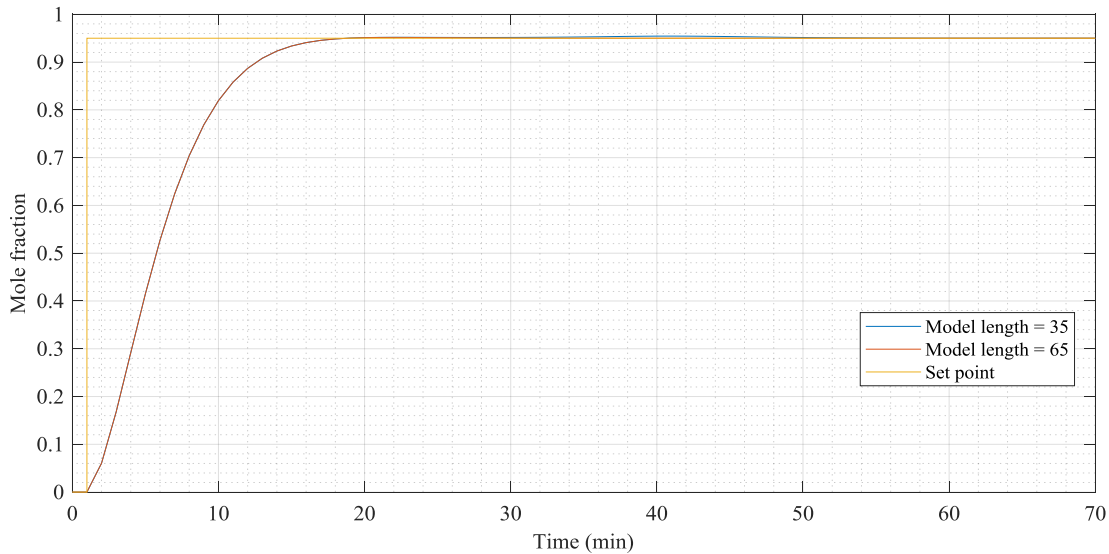


Figure 6. Closed-loop response of the MTE process to a step change of 0.95 in ethene mole fraction and variation in model length; control horizon = 3, prediction horizon = 25, control weighting = 0.3

Table 9. Performance criteria values for effects of model length

Criterion	Prediction horizon = 35	Prediction horizon = 65
SAE	6.4119	6.3408
MAE	0.0891	0.0881
SSE	4.3393	4.3391
MSE	0.0603	0.0603

This argument was also found to be supported by the values of the performance criteria that were calculated to be very close to each other for each criterion (see Table 9).

#### 3.4.4. Effect of control weighting

Another parameter used in tuning the dynamic matrix control for this methanol-to-olefin process was the weighting factor. In this case, it was varied from 0.1 to 0.5 and the results obtained were as given in Figure 7.

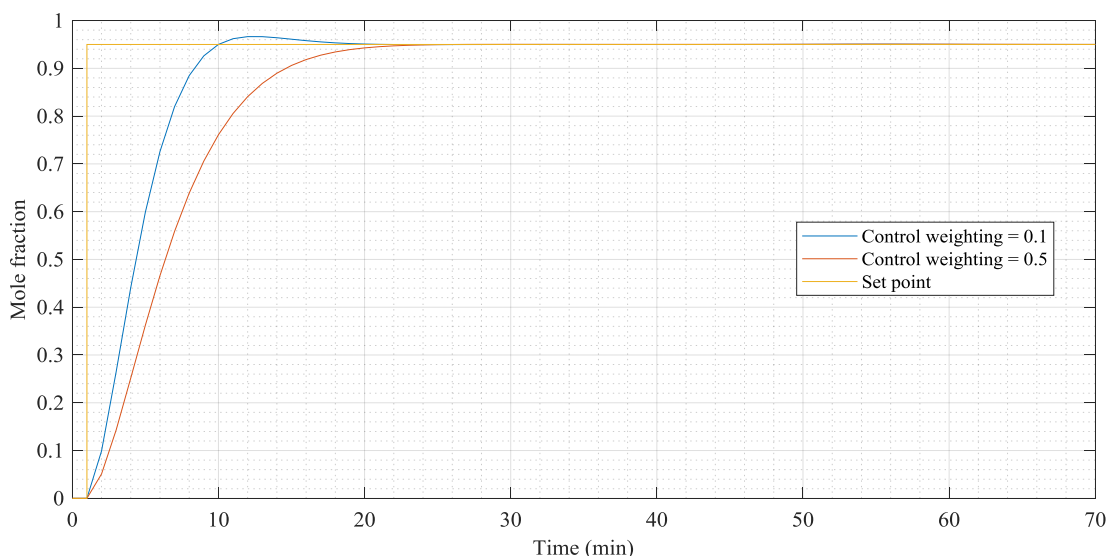


Figure 7. Closed-loop response of the MTE process to a step change of 0.95 in ethene mole fraction and variation in control weighting; control horizon = 3, prediction horizon = 25, model length = 50

Table 10. Performance criteria values for effects of control weighting

Criterion	Control weighting = 0.1	Control weighting = 0.5
SAE	4.8363	7.0623
MAE	0.0672	0.0981
SSE	3.4539	4.7237
MSE	0.0480	0.0656

From the results shown in Figure 7, it was clear that there is a dependency of the performance of dynamic matrix control on the control weighting because there was a clear difference between the two responses obtained when the values of the weighting factor were made to be 0.1 and 0.5.

The criteria values calculated for the variation of the control weighting showed that the performance of the dynamic matrix control was better when the control weighting was 0.1 than when it was 0.5 because all the performance criteria values of control weighting of 0.1 were less than those of the control weighting of 0.5.

## 4. Conclusion

The results obtained from the simulations carried out on the ChemCAD and the transfer function process models developed for the methanol-to-ethene production showed that the

models were valid ones because the steady-state values of ethene mole fraction given by the two models when the final value of the reflux ratio, which was the input variable, was 2 were very close. Furthermore, the closed-loop simulations of the dynamic matrix control system formulated for the process for investigating the effects of some tuning parameters (control horizon, prediction horizon, model length and control weighting) revealed that the control horizon, prediction horizon, and control weighting showed significant effects on the performance of the control system while the effect of the model length was found not to be significant for the methanol-to-ethene process. In addition, in all the cases, the process was observed to get settled within 45 min. Therefore, it can be inferred that the dynamic matrix control exhibited good control ability on the methanol-to-ethene process considered in this work.

### Acknowledgement

Special thanks go to Aare Afe Babalola, LL.B, FFPA, FNIALS, FCIArb, LL.D, SAN, OFR, CON – The Founder and President, and the Management of Afe Babalola University, Ado-Ekiti, Ekiti State, Nigeria for providing a very conducive environment and pieces of equipment that enabled the accomplishment of this research work.

### References

- [1] Lesthaeghe D, Mynsbrugge JV, Vandichel M, Waroquier M, and Speybroeck VV. Full theoretical cycle for both ethene and propene formation during methanol-to-olefin conversion in H-ZSM-5. *ChemCatChem*, 2011; 3(1): 208-212.
- [2] Chijioke CM. Dynamic Matrix Control of a Methanol-to-Ethene Process. Undergraduate Thesis. Afe Babalola University, Ado-Ekiti, Ekiti State, Nigeria, 2018, 68 pages.
- [3] Al Wahabi SM, Conversion of methanol to light olefins on SAPO-34: kinetic modeling and reactor design. Ph.D. Thesis. A & M University, Texas, 2003.
- [4] Keil FJ. Methanol-to-hydrocarbons: process technology. *Microporous and Mesoporous Materials*, 1999; 29(1-2): 49-66.
- [5] Hadi N, Niaei A, Nabavi SR, Farzi A, and Shirazi, M. N. Development of a new kinetic model for methanol to propylene process on Mn/H-ZSM-5. *Catalyst*, 2014; 28(1): 53-63.
- [6] Richalet JA, Rault A, Testud JD, and Papon J. Model predictive heuristic control: applications to industrial processes. *Automatica*, 1978; 14: 413-428.
- [7] Iruthayarajan MW, and Baskar S. Evolutionary algorithms based design of multivariable PID controller. *Expert Systems with Applications*, 2009; 36: 9159-9167.
- [8] Ang KH, Chong G, and Li Y. PID control system analysis, design, and technology. *IEEE Transaction on Control Systems Technology*, 2005; 13(4): 2005.
- [9] Moharam A, El-Hosseini MA, and Ali HA. Design of optimal PID controller using hybrid differential evolution and particle swarm optimization with an aging leader and challengers. *Applied Soft Computing* 2016; 38: 727-737.
- [10] Chemstations. ChemCAD 7.1.2.9917, Chemstations Inc, Texas, 2017.
- [11] Jianglong P, Huixin W. Kinetic modeling of methanol to olefins (MTO) process on the SAPO-34 catalyst. *China Petroleum Processing and Petrochemical Technology*, 2013; 15(3): 86-90.
- [12] MathWorks. MATLAB, The Language of Technical Computing, The MathWorks, Inc., Natick, 2017.
- [13] Bequette BW. Process Control: Modeling, Design, and Simulation. Prentice Hall, New Jersey, 2003.

*To whom correspondence should be addressed: Dr. Abdulwahab Giwa, Chemical, and Petroleum Engineering Department, College of Engineering, Afe Babalola University, Afe Babalola Way, Ado-Ekiti, Ekiti State, Nigeria*

## AIR QUALITY INDEX PATTERN OF CRITERIA AIR POLLUTANTS AROUND A HAULAGE TRUCK STOP

M. A Lala<sup>1</sup>, O. A. Adesina<sup>1\*</sup>, A.S. Yusuff<sup>1</sup>, L. A. Jimoda<sup>2</sup>, J. A. Sonibare<sup>3</sup>

<sup>1</sup> Department of Chemical and Petroleum Engineering Afe Babalola University, Ado Ekiti, Nigeria

<sup>2</sup> Department of Chemical Engineering, Ladoke Akintola University of Technology Ogbomoso, Nigeria

<sup>3</sup> Environmental Engineering Research Laboratory Department of Chemical Engineering, Obafemi Awolowo University, Ile-Ife, Nigeria

Received July 5, 2018; Accepted September 28, 2018

---

### Abstract

This study investigated the air quality index (AQI) pattern of criteria pollutants around a haulage truck-stop in southwestern part of Nigeria using carbon monoxide (CO) and nitrogen dioxide (NO<sub>2</sub>) as indicators. Concentrations of these pollutants were quantified at five different sampling points using ToxiRAE II Gas Monitor. The results showed the 8-hours averaging period mean concentrations of carbon monoxide (CO) ranged between 0.0875 and 0.4556 ppm, while the extrapolated 1-hour averaging period mean concentration of nitrogen dioxide (NO<sub>2</sub>) were of the range 121.60 – 633.14 ppb. The mean AQI concentrations determined indicates good and moderate AQI categories for CO while the AQI categories of NO<sub>2</sub> indicates unhealthy for sensitive groups at all sampled point. This study establishes that vehicular activities at the truck-stop could pose great impact on the ambient air quality with sensitive groups most at risk.

**Keywords:** Air quality index; breakpoint; criteria pollutants; vehicular activities; haulage truck-stop; mixing ratio; airshed.

---

### 1. Introduction

Air pollution has continued to receive attention worldwide due to its harmful effects on human health, especially in many urban areas around the world. Anthropogenic sources of air pollution are major contributors to ambient air pollution [1-4], these include emission from industries, homes and internal combustion engines exhaust [5]. Automotive pollution has been established to account for gas and other air toxics in ambient air along motorways and urban sites [6]. Emission from products of incomplete combustion (PIC) of vehicular engine has been identified to be responsible for about 90-95% of the ambient CO levels, 80-90% of the NO<sub>x</sub> and hydrocarbons and a large portion of the particulates which poses a significant threat to human health and natural resources [7].

The air quality index (AQI) is an index for reporting daily air quality. It is a tool for communicating air quality status to people in simple terms, it also transforms complex air quality data of various pollutants into a single number, nomenclature and colour [8]. These index informs the public on how clean or unhealthy the ambient air is with all the associated health effects which might be of concern [9]. It has therefore proven to provide a clearer picture of local air quality to the general public and has been adopted effectively in many nations [9-10]. AQI index is a tool that present complex air quality data of six common air pollutants (PM<sub>2.5</sub>, PM<sub>10</sub>, CO, NO<sub>2</sub>, SO<sub>2</sub> and O<sub>3</sub>) in a single number and colour with respect to the effects on human health [11-13]. Fakinle [1] and Sonibare [9] analyzed the air quality index pattern of particulate around a haulage vehicle park in southwestern Nigeria and around petroleum production facilities in Niger Delta sub region of Nigeria, respectively. AQI was also adopted by [14] to analyze the evolution of air pollution in a space of two decades in Germany, also [12,15] used

the tool for air quality assessments for Naples in Italy and Athens, respectively. However not much work has been done on the usage of the tool for air quality assessment in Sub-Saharan Africa especially in Nigeria. Due to the undeveloped railway system in Nigeria, major goods and petroleum product are being conveyed to the major cities by trucks which could cause a great deal of air pollution [7]. There are many truck stop in the Nigeria designated to provides refuelling, rest and other services to motorists and truck drivers. Due to large number of the trucks, these truck stops have become hot-spots experiencing frequent exceedance in pollutant ambient air limit. Hence the present study investigated the air quality index pattern of criteria air pollutants around a truck-stop using carbon monoxide (CO) and nitrogen dioxide (NO<sub>2</sub>) as indicators, these is with a view of assessing ambient air quality around the truck-stop.

## 2. Methodology

### 2.1. Study area

The study area was a truck-stop located in Ogere along popular Lagos –Ibadan highway, Ogun State of Southwestern part of Nigeria. Ogere is situated in a hilly area and on geographical coordinate 6° 56' 0" North and 3° 38' 0" East. Ogere truck-stop is about 0.6km<sup>2</sup> area is located between 56 kilometer and 59 kilometer of Lagos-Ibadan expressway and has remained a major stop-over for long-haul trucks and other haulage vehicles. Air sample were taken in five locations which is labeled A, B, C, D and E where considered for the study. Figure 1 shows the map of the study region with sampling points.

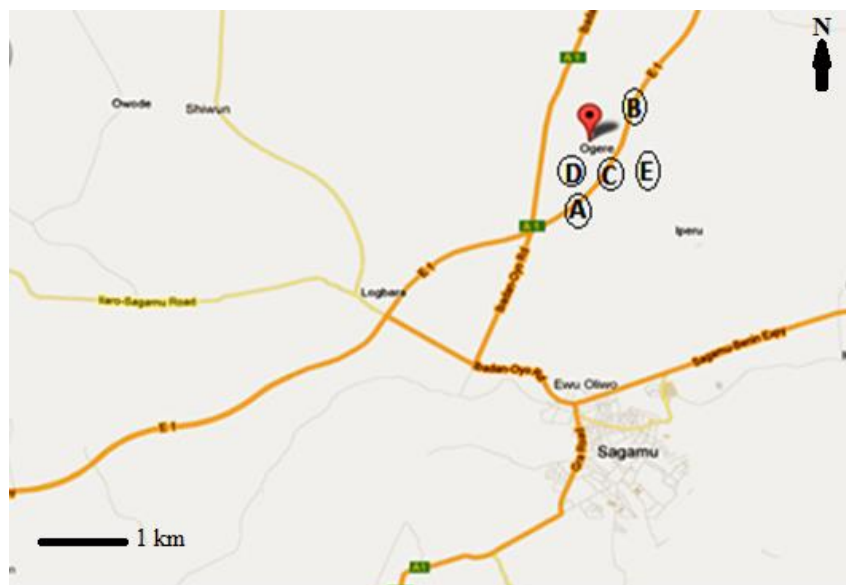


Figure 1. Map of Ogere truck-stop

### 2.2. Criteria air pollutant sampling

Sampling of carbon monoxide (CO) and nitrogen dioxide (NO<sub>2</sub>) in the airshed of Ogere truck-stop were carried out using ToxiRAE II Gas Monitor for CO and NO<sub>2</sub>, respectively. Sampling was done for 15 consecutive days with averaging time of 8 hours per day. The Gas monitors were positioned on a sampling stands of 1m height above the ground level to prevent measurement of fugitive gases mobilized by tides. Also four (4) principal meteorological parameters - temperature, wind speed, relative humidity and pressure were determined using Kestrel 4000 Pocket Weather Tracker. Sampled concentration data obtained in ppm were converted to ppb using Equation 1 and also converted from ppm to  $\mu\text{g}/\text{m}^3$  using concentration

unit conversion formula [16-17] given in Equation 2, for easy comparison with some air quality standards.

$$ppb = ppm * 1000 \tag{1}$$

$$\mu g/m^3 = \frac{PM_i}{RT} x(ppm) * (1000) \tag{2}$$

where  $\mu g/m^3$  is the concentration in microgram per cubic meter,  $ppm$  is the concentration in parts per million,  $ppb$  is the concentration in parts per billion,  $P$  is the sampled atmospheric pressure,  $T$  is the sampled ambient temperature,  $M_i$  is the molecular weight of the gaseous pollutant and  $R$  is the universal gas constant.

The concentration data for NO where extrapolated from the sampled 8-hours averaging time to 24-hours averaging time and also from 24-hours averaging time to 1-hour averaging time using an atmospheric stability dependent equation [1,18] Equation 3.

$$C_0 = C_1 * \left(\frac{T_1}{T_0}\right)^n \tag{3}$$

where  $C_0$  is the shorter averaging time concentration,  $C_1$  is the longer averaging time concentration,  $T_1$  is the longer averaging time,  $T_0$  is shorter averaging time and  $n$  is the stability dependent exponent given as 0.28 for the conversion from 8-hours averaging time to 24-hours averaging time [1] and 0.2 for extrapolating between 1-hours and 24-hours averaging time [18].

### 2.3. The air quality index (AQI)

AQI for CO and NO<sub>2</sub> were calculated using the EPA (2016) method with the equation given as Equation 4.

$$I_p = \frac{I_{HI} - I_{LO}}{BP_{HI} - BP_{LO}} (C_p - BP_{LO}) + I_{LO} \tag{4}$$

where  $I_p$  is the index value of pollutant  $p$ ,  $C_p$  is the concentration of pollutant  $p$ ,  $BP_{HI}$  is the breakpoint that is greater than or equal to  $C_p$  as given in Table 5,  $BP_{LO}$  is the breakpoint that is less than or equal to  $C_p$  as given in Table 5,  $I_{HI}$  is the AQI value corresponding to  $BP_{HI}$  and  $I_{LO}$  is the AQI value corresponding to  $BP_{LO}$ . Concentrations of CO (ppm) were truncate to 1 decimal place and NO<sub>2</sub> (ppb) truncate to integer [19]. Table 1 show AQI breaking points for CO and NO<sub>2</sub>.

Table 1. Air quality index breaking points

Breaking points		AQI	AQI category
CO (ppm) 8-hour	NO <sub>2</sub> (ppb) 1-hour		
0.0 - 4.4	0 - 53	0 - 50	Good
4.5 - 9.4	54 - 100	51 - 100	Moderate
9.5 - 12.4	101 - 360	101 - 150	Unhealthy for sensitive groups
12.5 - 15.4	361 - 649	151 - 200	Unhealthy
15.5 - 30.4	650 - 1249	201 - 300	Very unhealthy
30.5 - 40.4	1250 - 1649	301 - 400	Hazardous
40.5 - 50.4	1650 - 2049	401 - 500	Hazardous

### 3. Results and discussion

The daily sampled 8-hours averaging period of NO<sub>2</sub> concentrations ranged, 0.0875 - 0.4556 ppm (Table 2). The minimum daily sampled and minimum average concentration of NO<sub>2</sub> were observed at sampling point D, this may be due to low vehicular activity at this region as it is a mini-park within the truck-stop, also the maximum daily sampled and maximum average concentration of NO<sub>2</sub> were noticed at sampling point B. Sampling point B is located along the road side with higher volume of trucks compared to other points. Sampled data obtained in ppm for CO were converted to  $\mu g/m^3$  (Table 3), also NO<sub>2</sub> data were extrapolated from 8-hours

averaging period to 24-hours and 1-hour averaging period as presented in Table 4, Table 5 and Table 6.

Table 2. Sampled 8-hours averaging period concentration with standard error of mean

SP	Gaseous pollutants					
	NO <sub>2</sub> (ppm)			CO (ppm)		
	Day 1	Day 2	Day 3	Day 1	Day 2	Day 3
A	0.1333±0.11	0.3208±0.0913	0.2458±0.06	5.7917±0.75	6.0000±0.38	5.8333±0.09
B	0.5750±0.11	0.3250±0.0848	0.4667±0.06	6.8333±0.53	7.0000±0.36	6.2083±0.36
C	0.1542±0.07	0.3583±0.1082	0.2250±0.07	7.0417±0.89	5.7917±0.54	6.6250±1.45
D	0.0292±0.02	0.1083±0.0510	0.1250±0.05	1.5833±0.42	1.0000±0.36	1.1667±0.37
E	0.1667±0.09	0.1667±0.0932	0.3333±0.18	1.7083±0.47	1.2917±0.42	1.8750±0.47

Table 3. 8-hours averaging period mean concentration for sampling points

Sam- pling point	Gaseous pollutants concentration							
	NO <sub>2</sub> (ppm)				CO (ppm)			
	Day 1	Day 2	Day 3	Average	Day 1	Day 2	Day 3	Average
A	0.1333	0.320	0.2458	0.2333	5.7916	6.00	5.8333	5.8750
B	0.5750	0.3250	0.4667	0.4556	6.8333	7.00	6.2083	6.6805
C	0.1542	0.3583	0.2250	0.2458	7.0417	5.79	6.6250	6.4856
D	0.0292	0.1083	0.1250	0.0875	1.5833	1.00	1.1667	1.2500
E	0.1667	0.1667	0.3333	0.2222	1.7083	1.29	1.8750	1.6244

Table 4. 8-hours averaging period concentration of CO (µg/m<sup>3</sup>)

Sampling point	CO (µg/m <sup>3</sup> )			
	Day 1	Day 2	Day 3	Average
A	6379.05	6596.32	6434.88	6470.08
B	7538.30	7646.50	6762.05	7315.62
C	7696.29	6314.95	7366.24	7125.83
D	1729.64	1094.07	1271.78	1365.16
E	1856.35	1410.09	2044.24	1770.23

Table 5. Extrapolated 24-hours averaging period concentration for NO<sub>2</sub> (µg/m<sup>3</sup>)

Sampling point	CO (µg/m <sup>3</sup> )			
	Day 1	Day 2	Day 3	Average
A	6379.05	6596.32	6434.88	6470.08
B	7538.30	7646.50	6762.05	7315.62
C	7696.29	6314.95	7366.24	7125.83
D	1729.64	1094.07	1271.78	1365.16
E	1856.35	1410.09	2044.24	1770.23

Table 6. Extrapolated 1-hour averaging period concentration of NO<sub>2</sub> (ppb)

Sampling point	NO <sub>2</sub> (ppb)			
	Day 1	Day 2	Day 3	Average
A	185.29	445.86	341.63	324.26
B	799.08	451.65	648.67	633.14
C	214.23	497.97	312.68	341.63
D	40.54	150.55	173.71	121.60
E	231.62	231.62	463.23	308.83

Table 7. Extrapolated 1-hour averaging period concentration of NO<sub>2</sub> (µg/m<sup>3</sup>)

Sampling Point	NO <sub>2</sub> (µg/m <sup>3</sup> )			
	Day 1	Day 2	Day 3	Average
A	339.26	803.10	618.59	586.98
B	1454.84	814.20	1159.43	1142.82
C	383.52	890.98	571.28	615.26
D	74.67	269.13	311.21	218.34
E	414.88	414.37	825.57	551.60

Table 8. Air quality index rating for the study region

Sampling point	AQI for CO 8-hours (ppm)	AQI category	AQI for NO <sub>2</sub> 1-hour (ppb)	AQI category
A	64.75	Moderate	143.24	Unhealthy for sensitive groups
B	72.81	Moderate	197.30	Unhealthy
C	70.86	Moderate	146.52	Unhealthy for sensitive groups
D	14.20	Good	104.90	Unhealthy for sensitive groups
E	18.46	Good	140.32	Unhealthy for sensitive groups

When compared with 24-hours averaging standards of 75- 113 µg/m<sup>3</sup> and 150 µg/m<sup>3</sup> set by Nigeria Federal Ministry of Environment [20] and World Bank [21] respectively, all extrapolated daily sampled concentration of NO<sub>2</sub> at all locations exceeded the standards except Day 1 and Day 2 sampling at location D which were below the World Bank set limit. The average concentrations were also greater than the set limits at all sampling points except point D which is slightly below the World Bank standard. When compared with 1-hour averaging standard of 200 µg/m<sup>3</sup> set by World Health Organization WHO [21] and World Bank [22], extrapolated average concentrations at all sampling point exceeded the set limit. Daily sampled 8-hours averaging period concentration of CO for sampling point A to E ranged between 1365.16 – 7315.62 µg/m<sup>3</sup> (Exhibit 4), these concentrations are far below the set limit of 22,800 µg/m<sup>3</sup> given by Nigeria Federal Ministry of Environment [20] and 10,000 µg/m<sup>3</sup> limit given by World Bank [21] and World Health Organization [22]. The reason associated to these is as of readily conversion of CO to CO<sub>2</sub> when it is emitted into air. Figure 2 shows the distribution of pollutant at the various sampling locations, the trend showed the concentrations both pollutants were high at sampling points A, B and C these could be as a result of the large number of the truck parked at that location and their proximity to the high way. However relatively lower concentrations of these pollutants were observed at the sampling point D and E, these could be connected with the fewer number of the trucks and vehicular activities at these points.

The AQI indicates the level of ambient air pollution with respect to health effect associated with few hours or days after breathing the polluted air. EPA [20] method was to calculate the AQI, Table 7 shows Air quality index rating for the study region. The AQI of CO for the sampled region ranges from 14.20 to 72.81 which indicates good to moderate AQI category. The air quality Indexes at the sampling points D and E are good while AQI at sampling points A, B and C are moderate. For NO<sub>2</sub>. The AQI ranges from 104.90 to 143.24, sampling points A, C, D and E fall to AQI category of unhealthy for sensitive groups while sampling point B falls to a more serious category of unhealthy represented. At every location within the sampling region, people with asthma, children, and older adults are most at risk [1,20]. The colour representation of AQI is depicted in Figure 3 and 4.

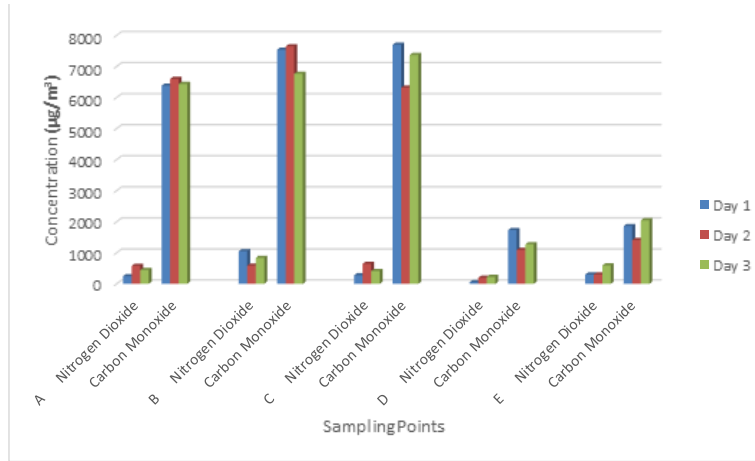


Figure 2. Distribution average sampled concentration of pollutant at the various sampling locations

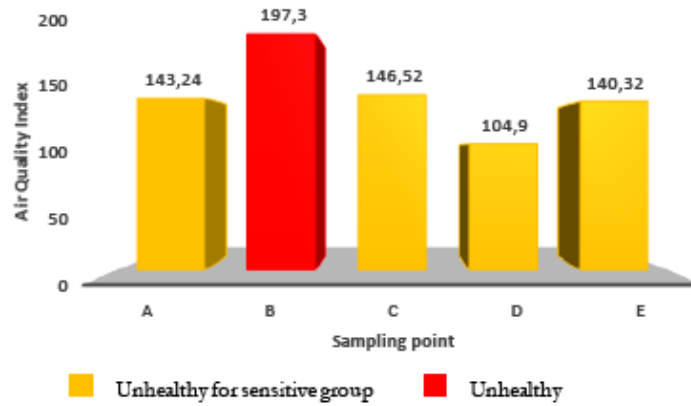


Figure 3. Air quality index pattern for NO<sub>2</sub> around Ogere truck-stop

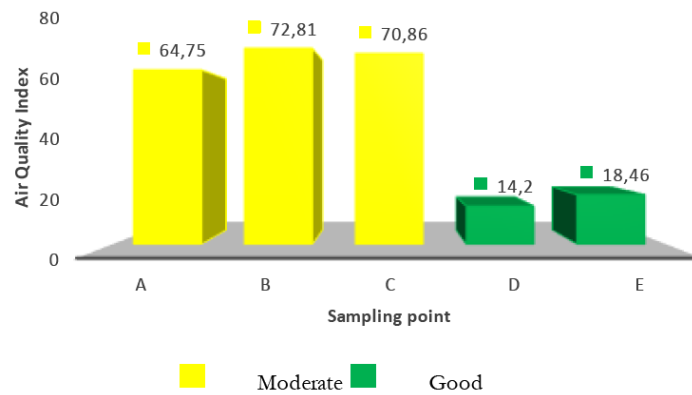


Figure 4. Air quality index pattern for CO around Ogere truck-stop

#### 4. Conclusion

The air quality index pattern of criteria pollutants around a truck-stop was investigated in this study using carbon monoxide (CO) and nitrogen dioxide (NO<sub>2</sub>) as indicators. The studied area is a typical truck-stop located between 56 kilometer and 59 kilometer Lagos-Ibadan expressway of Southwestern part of Nigeria. Concentrations of the criterial air pollutants were

quantified at five (5) selected sampling points using ToxiRAE II Gas Monitor. The results indicated that the extrapolated 24-hours and 1-hour average period concentration of NO<sub>2</sub> at almost all the sampled point exceeded the limits set by Nigeria Federal Ministry of Environment, World Health Organization and World Bank, while 8-hours averaging period concentrations of CO at all sampled point were below the set limits. The AQI pattern obtained for the studied region show further that AQI of CO ranges from 14.20 to 72.81 which indicates good to moderate AQI category with no known health effects. The AQI for NO<sub>2</sub> ranges from 104.90 to 143.24 indicating AQI category of unhealthy for sensitive groups to unhealthy, therefore people with respiratory or heart disease, the elderly and children should be prevented from this region. The study established that vehicular activities at the truck-stop could pose great impact on the ambient air quality with sensitive groups most at risk.

## Reference

- [1] Fakinle BS, Sonibare JA, Okedere OB, Jimoda LA, Ayodele CO. Air quality index pattern of particulate around a haulage vehicle park. *Cogent Environmental Science*, 2016; 34(1):1–7.
- [2] Shukla JB, Misra AK, Sundar S, Naresh, R. Effect of rain on removal of a gaseous pollutant and two different particulate matters from the atmosphere of a city. *Mathematical and Computer Modelling*, 2008; 48, 832–844.
- [3] Udia C. The environmental pollution consequences of the Niger Delta Wetland occasioned by gas flaring. *Journal of Land Use and Development Studies*, 2005; 1:12–20.
- [4] Campbell GW, Stedman JR, Stevenson K. A Survey of Nitrogen dioxide concentrations in the United Kingdom using diffusion tubes. *Atmos. Environ*, 1994; 28:477–486.
- [5] Park, K. Preventive and Social Medicine (18th ed). Journal Pur, India: M / S Banarsidas Bhanot publishers, 2005.
- [6] Obioh IB, Olise FS, Owoade OK, Olaniyi HB. Chemical characterization of suspended particulates along air corridors of motorways in two Nigerian cities. *J. Appl. Science*, 2005; 5: 347–350.
- [7] Saville SB. Automotive Options and Air Quality Management in Developing Countries. United Nations Environment Programme Industry and Environment, 1993; 16:20, 32.
- [8] Central Pollution Control Board, Ministry of Environment, Forests & Climate Change, Government of India. [www.cpcb.nic.in](http://www.cpcb.nic.in), 2014
- [9] Sonibare JA, Adebisi FM, Obanijesu EO, Okelana OA. Air quality index pattern around petroleum production facilities. *Management of Environmental Quality: An International Journal*, 2010; 21, 379–392.
- [10] Ontario. A review of the Ontario air quality index and air quality health index system. ISBN 978-1-4606-0936-1. Air Resource Branch, Ontario Ministry of the Environment, Toronto, Ont., Canada, 2013.
- [11] Bishoi B, Prakash A, Jain, V K. A Comparative Study of Air Quality Index Based on Factor Analysis and US-EPA Methods for an Urban Environment, May, 2014.
- [12] Murena F. Measuring Air Quality over Large Urban Areas: Development and Application of an Air Pollution Index at the Urban Area of Naples. *Atmos. Environ*, 2004; 38: 6195–6202.
- [13] Bortnick, SM., Coutant, BW, Eberly S.I. Using Continuous PM<sub>2.5</sub> Monitoring Data to Report an Air Quality Index. *J. Air Waste Manage. Assoc.*, 2002; 52: 104–112.
- [14] Mayer H, Holst J, Schindler D, Ahrens D. Evolution of the air pollution in SW Germany evaluated by the long-term air quality index LAQx. *Atmospheric Environment*, 2008; 42(20): 5071–5078.
- [15] Kyrkilis G, Chaloulakou A, Kassomenos PA. Development of an aggregate Air Quality Index for an urban Mediterranean agglomeration: Relation to potential health effects. *Environment International*, 2007; 33(5):670–676.
- [16] Richard CF, John HS. Fundamentals of Air Pollution Engineering. Satoshi, N. and Eldred, T.T. (2012). Monitoring the levels of toxic air pollutants in the ambient air of Freetown, Sierra Leone. *African Journal of Environmental Science and Technology*, 1988; 6(7): 283–292.
- [17] Boguski, T. K. Understanding Units of Measurement. *Environmental Sci and Tech Brief for citizen*, 2006; 1–2.
- [18] Smadi BM, Al-Zboon KK, Shatnawi KM. Assessment of Air Pollutants Emissions from a Cement Plant: A Case Study in Jordan, *Jordan Journal of Civil Engineer*, 200; 3(3), 265–282.
- [19] U.S. Environmental Protection Agency. Air Quality Index: A Guide to Air Quality and Your Health. February, EPA-456/F-14-002, 2016.

- [20] Federal Environmental Protection Agency, Lagos (FEPA). Guidelines and Standards for Environmental Pollution Control in Nigeria, 1991; 33:103.
- [21] World Bank. Petroleum refining, Pollution Prevention and abatement handbook. World Bank group, Washington D.C. 1998; 337-380.
- [22] World Health Organization [WHO].WHO Air quality guidelines for particulate matter, ozone, nitrogen dioxide and sulphur dioxide Global update. Summary of risk 62:351-352. 860296, 2005.

---

*To whom correspondence should be addressed: Dr. O. A. Adesina, Department of Chemical and Petroleum Engineering Afe Babalola University, Ado Ekiti, Nigeria*

## SYNTHESIS OF Pt-Re-Sn NANO-CATALYST: ROLE OF NANO-PARTICLE SIZE ON ACTIVITY AND SELECTIVITY IN N-HEPTANE REFORMING

Ali Karimi<sup>2</sup>, Haniieh Karimi<sup>1</sup>, Ahmad Tavasoli<sup>1</sup>

<sup>1</sup> School of Chemistry, College of Science, University of Tehran, Tehran, Iran

<sup>2</sup> Research Institute of Petroleum Industry, Catalyst Division, Tehran, Iran

Received July 8, 2018; Accepted September 28, 2018

---

### Abstract

The bimetallic and trimetallic 0.3 wt. % Pt–0.3 wt. % Re–x wt. % Sn/Al<sub>2</sub>O<sub>3</sub> catalysts (x = 0, 0.07, 0.2, 0.3, 0.4) were prepared through impregnation technique and applied in n-heptane reforming as a model fuel. The catalysts were characterized using ICP-AES, BET, TPR, H<sub>2</sub> chemisorption, and Volhard–Charpentier method. All catalysts were assessed in terms of their activity, selectivity and products' yield in a fixed bed micro reactor for n-heptane reforming process. The results showed that the most appropriate percentage of tin metal, as a promoter, was 0.3%. At least the trimetallic catalyst was synthesized using Chemical Vapor Deposition (CVD) technique with the optimized catalyst compositions. According to TEM pictures, the catalysts produced with CVD technique have smaller particles with very narrow particle size distributions. The nano-particles synthesized by the proposed CVD technique increased catalyst activity (g HC/g cat. hr) and the selectivity of isoparaffin to both of aromatics and undesirable light gaseous products from 37% and 39.5% to 51% and 51.62% respectively, and the selectivity of methane decreased from 1.23% to 0.71%.

**Keywords:** -Heptane reforming; Impregnation; CVD, Pt-Re-Sn/Al<sub>2</sub>O<sub>3</sub> catalyst; Dispersion.

---

## 1. Introduction

The naphtha reforming process is very important in the petroleum refining and petrochemical industries because it is one of the main suppliers of high octane gasoline and aromatic hydrocarbons. Great improvements in the process have been occurred since 1949 when a bifunctional metal–acid catalyst was introduced [1-2]. The metal function is provided by Pt, which is supported over the acid function, chlorinated gamma alumina. Alumina support has important industrial applications in the petroleum industry in reforming and hydrotreating processes. The catalytic properties of Pt can be improved by the addition of another metal, such as Re, Sn or Ge. The major reactions promoted by bifunctional catalysts are hydrogenation, dehydrogenation, isomerization, cyclization and hydrocracking, Therefore, the reaction to produce aromatic compounds is bifunctional since it uses both the metal and the acid sites [3-4]. The adverse effect of hydrogenolysis reaction that generate light and volatile hydrocarbons stops by sulphidation. Sulphidation venoms the hydrogenolysis active sites and the catalyst activity decreases, also sulphidation is costly operation and catalyst need to rebuild. Recently, trimetallic catalysts were studied in order to replace the sulphidation of the metallic Pt–Re [1, 4-6]. The wet impregnation method has traditionally been used to prepare bimetallic reforming catalysts. It seems necessary to do studies to improve the catalysts performance through employing different methods of synthesis. In this sense, the Chemical Vapor Deposition (CVD) method has been reported as an alternative to produce better catalysts. The CVD process includes reactions of gaseous reactant in an active environment such as heat, light,

plasma which is used to form a stable solid product. The CVD technique for catalyst preparation, enables the control of metal particle size with a narrow particle size distribution, regardless of metal content [7-11].

Bilone and Helle mentioned that with increasing in the distribution of metal particles, dehydrogenation reaction increases [1, 12]. Gaseous light product was decreased and liquid product and the selectivity of isoparaffin to both of aromatics and undesirable light gaseous increased by CVD synthesized catalysts. This matter can be attributed to the high dispersion and uniform distribution of active metal particles on the support in CVD synthesized catalyst in comparison to impregnated catalysts [13-18].

In this study bimetallic and trimetallic 0.3 wt.% Pt–0.3 wt.% Re–x wt.% Sn/Al<sub>2</sub>O<sub>3</sub> catalysts (x =0, 0.07, 0.2, 0.3, 0.4) were prepared through impregnation technique. The catalysts were assessed in terms of their activity, selectivity, stability and products' yield in a fixed bed micro reactor at 500°C and 1 bar for n-heptane reforming as model fuel. The results showed that the most appropriate percentage of tin metal, as a promoter. At least the trimetallic catalyst was synthesized using CVD technique with the optimized catalyst compositions. All catalysts also were characterized by BET, TPR, H<sub>2</sub> chemisorption, ICP-AES, XRD and Volhard–Charpentier method.

## 2. Experimental

### 2.1. Catalysts preparation

The support used was a commercial high-purity  $\gamma$ -alumina (Cyanamid Ketjen CK300) and main impurities were Na (5 ppm), Fe (150 ppm) and S (50 ppm). The extruded alumina pellets were sieved and the 35–80 mesh fractions was separated and dried at 70°C for 8 hr, 120°C overnight and then calcined at 450°C for 3 hr under flow of air (60 cm<sup>3</sup>/min.gr). The specific surface area of this support was 212.40 m<sup>2</sup>g<sup>-1</sup>, the pore volume 0.57 cm<sup>3</sup>. Impregnation method was used in order to synthesize 0.3 wt.% Pt–0.3 wt.% Re–x wt.% Sn/Al<sub>2</sub>O<sub>3</sub> (x= 0, 0.07, 0.2, 0.3, 0.4) catalysts. The concentration of Pt and Re and Sn were adjusted using aqueous solutions of H<sub>2</sub>PtCl<sub>6</sub> and HReO<sub>4</sub> and SnCl<sub>2</sub> (Merck). The catalysts prepared by means of this protocol were denoted as Cat<sub>1</sub>–Cat<sub>5</sub>. Next, the catalyst was dried at 120°C and calcined at 370°C for 3 hr and slowly exposed to an oxygen atmosphere during the cooling step. The catalyst with the optimum percentage of tin (x= 0.3 wt%) synthesized by the CVD method through direct liquid injection (DLICVD). Precursor used in this method is SnCl<sub>4</sub> and was adsorbed on catalyst surface and the catalyst was dried, calcined according to above procedure. The catalyst prepared by this method, denoted as Cat<sub>6</sub>. The compositions in all calcined catalysts were verified by an ICP-AES system. The catalysts nomenclature and properties are listed in Table 1.

Table 1. Chemical composition and chlorine content of the catalysts

Catalyst	Targeted composition (wt. %)				Measured composition (wt. %)			
	Pt	Re	Sn	Cl	Pt	Re	Sn	Cl
Cat <sub>1</sub>	0.3	0.3	0	0.8	0.291	0.289	0	0.78
Cat <sub>2</sub>	0.3	0.3	0.07	0.8	0.291	0.292	0.067	0.77
Cat <sub>3</sub>	0.3	0.3	0.2	0.8	0.289	0.295	0.19	0.78
Cat <sub>4</sub>	0.3	0.3	0.3	0.8	0.296	0.297	0.294	0.78
Cat <sub>5</sub>	0.3	0.3	0.4	0.8	0.290	0.293	0.398	0.79
Cat <sub>6</sub>	0.3	0.3	0.3	0.8	0.288	0.293	0.288	0.84

### 2.2. Catalyst characterization

Morphology of all catalysts (Cat<sub>1</sub>–Cat<sub>6</sub>) were characterized by Volhard–Charpentier method, BET, TPR, and H<sub>2</sub> chemisorptions according to procedure previously reported [1].

### 2.3. Catalyst activity and selectivity

One gram of each catalyst (diluted with 4 g quartz) was charged in an Inconel fixed bed reactor of 2.54cm internal diameter, forming a bed of 54cm height. The catalyst was reduced in situ with hydrogen (60 ml/min) for 4 h at 500°C. Then n-heptane (Merck, 99.9%) as a model fuel (molar ratio of H<sub>2</sub>/n-heptane =7.5) was injected to the reactor and the reaction was carried out for 6 hr at 500°C, 0.1 MPa. The reaction products were analyzed in a HP 5890 SERIES II Gas Chromatograph equipped with flame ionization and thermal conductivity detectors. The products' yields were obtained from the chromatographic data. The yield or the percentage of n-heptane converted into any product is calculated as [1-2]:

$$\text{Yield}_i = \frac{\%C_i 100X}{\sum \%C_i} \quad (1)$$

where X is the total conversion; the notification i is any compound concentration in the reaction products;  $\sum \%C_i$  the sum of concentration of all reaction products (n-heptane is not included).

For each experiment, the sum of all the C<sub>i</sub> yields was in agreement with the n-heptane conversion. The Carbon balance was considered satisfactory when the error was < 3 %. Fig. 1 shows a schematic view of experimental setup.

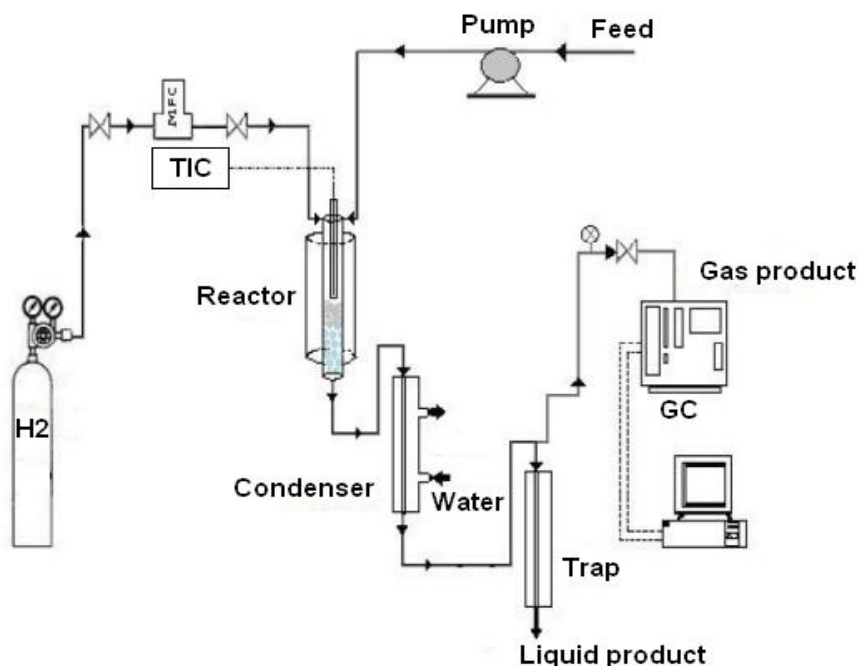


Fig. 1. Schematic view of experimental setup

## 3. Result and discussion

### 3.1. Catalyst characterization

The chlorine content and elemental compositions of the calcined catalysts, measured by Volhard–Charpentier [1, 19] and ICP method, are given in Table 1. The measured metal loadings were found to be slightly lower compared to the targeted values. As shown, the chlorine content in the catalyst prepared by CVD technique is higher than the targeted value. This can be due to the presence of chloride in precursor (SnCl<sub>4</sub>) used for catalyst preparation.

Table 2 presents the surface morphological characterization results for support, the bimetallic and trimetallic catalysts synthesized in both CVD and impregnation methods. The results

of BET surface area ( $S_{\text{BET}}$ ) in this table show that in all cases the metal incorporation reduced the specific surface area of the catalysts when compared to the support. Lower  $S_{\text{BET}}$  and pore volume of the Cat<sub>1</sub>-Cat<sub>6</sub> catalysts indicate some pore blockage due to Pt-Re loading on the support. However, this table shows that the amount of pore blockage is lower in the case of the catalyst prepared by CVD technique. In case of Cat<sub>4</sub> and Cat<sub>6</sub> catalysts, with equal amount of active metals and promoter loading, have different  $S_{\text{BET}}$ , which is attributed to synthesis technique of catalysts. The CVD technique increased the dispersion and caused the promoter particles on the support were distributed and formed a film on the entire surface. The uniform and small metal particles size produced through CVD technique increases the efficiency of the catalyst and also prevents sintering of active metals particles [16-18, 20-22].

Table 2. Textural properties of the catalysts

Sample	Preparation procedure	$S_{\text{BET}}$ ( $\text{m}^2/\text{g}$ )	pore volume ( $\text{mL/g}$ )	Average pore diameter ( $\text{\AA}$ )
Cat1	Impregnation	209.45	0.53	80.89
Cat2	Impregnation	208.66	0.52	79.40
Cat3	Impregnation	205.15	0.51	75.36
Cat4	Impregnation	203.14	0.49	73.20
Cat5	Impregnation	192.59	0.48	65.45
Cat6	CVD	206.25	0.50	67.50
Support	-	212.40	0.57	99.80

The reducibility of the catalysts in  $\text{H}_2$  atmosphere was determined by TPR experiments. The TPR spectra of the calcined catalysts are shown in Fig. 2.

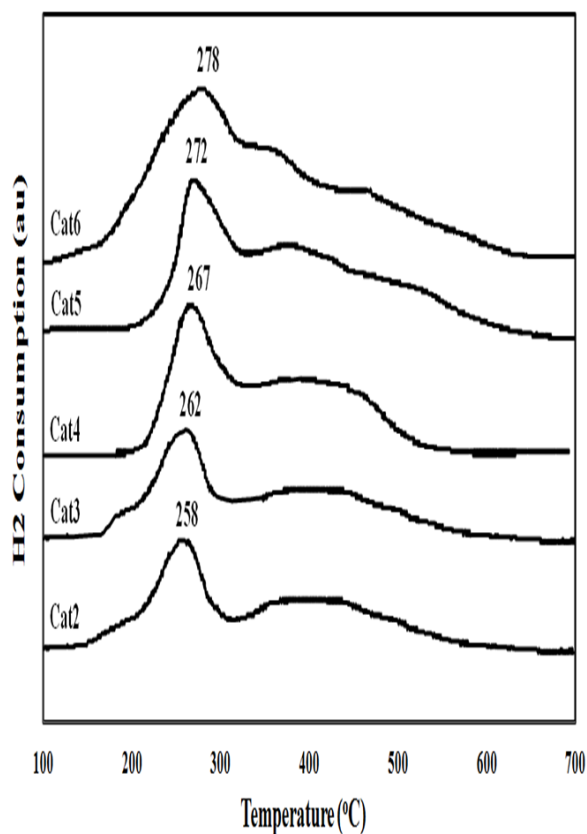


Fig. 2. TPR curves for catalysts

The Cat<sub>4</sub> & Cat<sub>6</sub> which contain the same contents of active metals and promoter have different hydrogen consumption and the hydrogen consumption of Cat<sub>6</sub> was more than Cat<sub>4</sub>. This

TPR peak temperatures and the TPR area for all samples are presented in Table 3. This technique allows getting information about the interaction of the metal components by means of the measurement of the hydrogen consumption during the reduction of the oxides at a constant heating rate. The temperature at which reduction occurs and the number of reduction peaks depend on the oxidation state of the metals, the interaction of the metal oxides with each other and with the support. As shown, the TPR peak for tin oxide is very broad, starting at  $150^\circ\text{C}$  and ending at  $550^\circ\text{C}$ , with two main reduction regions in the  $200\text{--}300^\circ\text{C}$  and  $380\text{--}520^\circ\text{C}$  ranges. This is an indication of interaction of Sn oxide with alumina that is able to produce tin aluminates. According to this figure the reduction peak of catalyst synthesized by CVD technique (Cat<sub>6</sub>) shifted to higher temperature compared to the catalyst prepared by impregnation method (Cat<sub>4</sub>), This can be attributed to difficult reduction for small particles produced in this method. In TPR spectra, the peak area is assigned to hydrogen uptake of each catalyst, so results of Table 3 show the hydrogen consumption increases when the promoters' content increase.

is attributed to small metal particles size and more and regular distribution of tin metal nano-particles in CVD synthesized catalyst which prevents sintering of active metals particles [21-24].

Table 3. Hydrogen consumption and TPR results of catalysts

Catalysts	TPR peak (oC) Sn+4→Sn0	TPR area peak	Catalysts	TPR peak (oC) Sn+4→Sn0	TPR area peak
Cat2	258	2 721	Cat5	372	4 522
Cat3	262	3 063	Cat6	378	4 017
Cat4	367	3 556			

The results of H<sub>2</sub> chemisorption are given on Table 4. As shown, changes in catalyst synthesis method from impregnation to CVD increase the percentage dispersion. In CVD preparation technique the promoter particles on the support were distributed through gases and sediments of atoms and formed a film on the entire surface. This method of sedimentation can produce high purity materials with structural nanometer.

Table 4. H<sub>2</sub> chemisorption results

Catalyst	Dispersion (%)
Cat4	15.1
Cat6	37

### 3.2. Reaction

Table 5 shows the results of catalysts activity and the different products' yield in n-heptane reforming reaction. The tin was added to the bimetallic catalyst to increase the isomerization step and decrease gaseous undesirable products. In the presence of tin, n-heptane is broken mostly from intermediate carbons instead of the first and last carbons of molecules [2, 6]. In case of Cat<sub>1</sub>-Cat<sub>4</sub> catalysts prepared by impregnation technique, with increasing the percentage of tin promoter the activity of catalysts increased from 20.48 to 37.65, and then the catalyst activity decreased. The activity (g HC/g cat.hr) of proposed catalyst synthesized by CVD technique (Cat<sub>6</sub>) was 51.25 compared to 37.65 for traditionally impregnated catalyst (Cat<sub>4</sub>) with the equal amount of Sn loading. The Cat<sub>6</sub> is approximately two times more active, and it can be attributed to small and uniform particles size and consequently the higher dispersion of metals particles on the surface of CVD synthesized catalyst [16-18]. Comparative studies of Cat<sub>4</sub> & Cat<sub>6</sub> catalysts show that Cat<sub>6</sub> have smaller particle size, less pore blockage, higher S<sub>BET</sub>; pore volume and percentage of dispersion which can be responsible for it's higher catalyst activity [16-18, 25].

Table 5 also shows Cat<sub>6</sub> synthesized through CVD technique with smaller Pt-Re ensembles (a site composed of a large number of contiguous active metal atoms) has a methane yield of 0.71% compared to the Cat<sub>4</sub> catalyst with methane yield of 1.23%. This is logical, since hydrogenolysis occurs better on a large ensemble, so decrease in the metals particle size is effective in inhibiting the hydrogenolytic activity of the Pt-Re ensembles [1, 26].

It must be taken into account that methane is produced mainly from a hydrogenolysis reaction catalyzed by the metal sites, while propane is formed by a bifunctional mechanism controlled by the acid function of the catalyst. As shown in this table, for impregnated catalysts series (Cat<sub>1</sub>-Cat<sub>4</sub>), with increasing percentage of tin from 0.07 to 0.3 wt%, gaseous light and undesirable products decreased. Comparing the product yields for impregnation catalysts (Cat<sub>1</sub>-Cat<sub>4</sub>), it can be seen that, benzene and toluene and methyl cyclohexane yields increased from 3.28%, 2.78% and 2.39% to 10.87%, 5.54% and 9.74% respectively. In this catalysts series, higher benzene, toluene and methyl cyclohexane yields belong to Cat<sub>4</sub> and it is related to the increase in dehydrogenation step through the catalytic process.

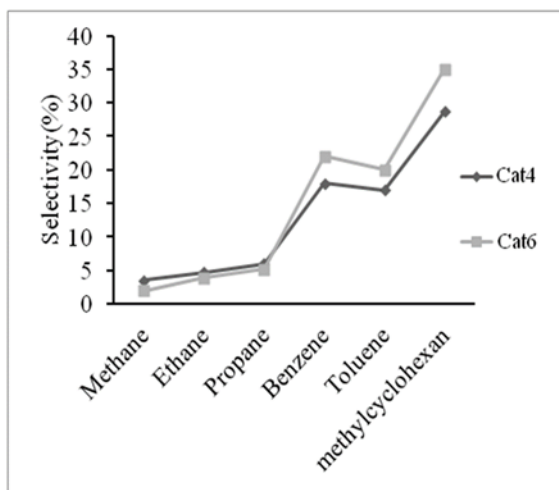


Fig. 3. Comparison selectivity of Cat4 and Cat6

As shown in Table 5 and Fig 3, Cat<sub>6</sub> decreased gaseous light, increased liquid products with high octane number and selectivity of isoparaffins to aromatics, in comparison to Cat<sub>4</sub>. This matter can be attributed to the high dispersion and uniform distribution of active metal particle on the support in CVD synthesized catalyst in comparison to impregnated catalysts, which can cause to increase dehydrogenation reactions through n-heptane reforming. On the other hand, uniform distribution of small active metal particles causes olefin intermediate molecules produced on a metal site easily adsorb on adjacent metal site and don't traverse long trajectory and possible expos to existing acidic sites (capable to cracking reaction) on

the catalyst support. Therefore in CVD synthesized catalyst the possibility of two-factor reactions that lead to the production of gaseous undesirable products reduced.

Table 5. Catalysts' activity and yield of different products in n-heptane reforming reaction

Catalyst	Activity (g HC/g cat. h)	Yield (%)					
		Benzene	Toluene	Ethane	Methane	Propane	MCyH*
Cat1	20.48	3.28	2.78	5.45	3.87	7.52	2.39
Cat2	29.52	5.54	3.36	4.74	3.22	6.51	4.46
Cat3	31.36	9.63	4.70	3.65	2.24	4.45	7.32
Cat4	37.65	10.87	5.54	3.09	1.23	3.23	9.74
Cat5	35.2	10.10	5.32	3.1	1.54	3.18	8.82
Cat6	51.25	12.60	7.52	1.84	0.71	2.31	14.25

\*MCyH –methyl cyclohexane

#### 4. Conclusion

The bimetallic and trimetallic 0.3 wt.% Pt–0.3 wt.% Re–x wt.% Sn/Al<sub>2</sub>O<sub>3</sub> (x = 0, 0.07, 0.2, 0.3, 0.4) catalysts were synthesized by impregnation and 0.3%Pt-0.3%Re-0.3%Sn/Al<sub>2</sub>O<sub>3</sub> (optimized catalyst compositions) was synthesized by CVD method and applied in n-heptane reforming process as a model fuel. According to H<sub>2</sub> chemisorptions data and S<sub>BET</sub>, the CVD technique produces small and uniform nano-particles and consequently increases the dispersion of nano-particles on the alumina supports. According to TPR profile, these Pt-Re nano-particles were reduced at higher temperatures due to increasing metal-support interactions. It was also found that activity and selectivity of the catalysts are dependent to the synthesize method. The proposed Pt-Re-Sn nano-catalyst synthesized by CVD technique increased the catalyst activity and the yield of benzene; toluene; and methyl cyclohexane. Also the yields of undesirable products like methane decreased.

#### 5. Acknowledgements

The authors are thankful to the Iran National Science Foundation (INSF) for their support of this work.

#### References

- [1] Asrami MR, Nejati B, Tavasoli A, Karimi A. *Pet. Coal*, 2016; 58(1): 56-65.
- [2] D'Ippolito SA, Vera CR, Epron F, Samoila P, Especel C, Marecot P, Gutierrez LB, Pieck CL. *Appl. Catal. A: Gen.*, 2009; 370: 34-41.
- [3] Nabgan W, Rashidzadeh M, Nabgan B. *Environ. Chem. Let.*, 2018; 16: 507-522

- [4] Carvalho LS, Conceição KCS, Mazzieri VA, Reyes P, Pieck CL, Rangel MDC. Appl. Catal. A: Gen., 2012; 419–420: 156–163.
- [5] Jahel A, Avenier P, Lacombe S, Olivier J, Fourcade JC. J. Catal., 2010; 272: 275–286.
- [6] Mazzieri VA, Grau JM, Vera CR, Yori JC, Parera JM, Pieck CL. Appl. Catal. A: Gen. , 2005; 296: 216–221
- [7] Pierson HO. HANDBOOK OF CHEMICAL VAPOR DEPOSITION (CVD) Principles, Technology and Application, New Jersey, USA (2001).
- [8] Badisch E, Fontalvo GA, Stoiber M and Mitterer C. Surf. Coat. Tech., 2003; 163–164: 585.
- [9] Zhang H, Qiu J, Liang C, Li Z, Wang X. Catal. Lett., 2005; 101: 211–214.
- [10] D Lee, GS Jung, HCh Lee, JS. Lee, Catal. Today, 2006; 111: 373–378.
- [11] Parnian M.J., Khodadadi A.A., Taheri Najafabadi A., Mortazavi Y., Appl. Catal. A: Gen., 2014; 470: 221– 231.
- [12] Biloen P, Helle JN, Verbeek H, Dautzenberg FM, Sachtler WMH. J. Catal., 1980; 63: 112–118.
- [13] Spear KE. Proc. of the 7th Int. Conference on CVD, (Sedgwick TO, and Lydtin H., eds.), p. 6, The Electrochemical Society, Pennington, NJ (1979).
- [14] Bernard C. Proc. of the 8th Int'l. Conf. on CVD, (Blocher, Jr. JM, Vuillard GE, and Wahl G. eds.), p. 3, The Electrochemical Society, Pennington, NJ (1981).
- [15] Lindstrom N and Schachner H. Proc. of the 3rd European Conf on CVD, (1996) 208.
- [16] Faust M, Enders M, Bruns M, Bräse S, Gao K, Seipenbusch M. Sur. Coat. Tech., 2013; 230: 284–289.
- [17] dal Santo V, Mondelli C, de Grandi V, Gallo A, Recchia S, Sordelli L, Psaro R. Appl. Catal. A: Gen., 2008; 346: 126–133.
- [18] Parnian MJ, Khodadadi AA, Najafabadi AT, Mortazavi Y. Appl. Catal. A: Gen., 2014; 470: 221–231
- [19] Carvalho LS, Conceição KCS, Mazzieri VA, Reyes P, Pieck CL, Rangel MdC. Appl. Catal. A: Gen., 2012; 419–420: 156–163.
- [20] Spear KE. Proc. of the 7th Int. Conference on CVD, (T. O. Sedgwick and H. Lydtin, eds.), p. 6, The Electrochemical Society, Pennington, NJ (1979).
- [21] Karimi S, Tavasoli A, Mortazavi Y, Karimi A. Appl. Catal. A., 2015; 499: 188–196.
- [22] Karimi S, Tavasoli A, Mortazavi Y, Karimi A. Chem. Eng. Res. and Des., 2015; 104: 713–722.
- [23] Carvalho LS, Pieck CL, Rangel MC, Figoli NS. Appl. Catal. A: Gen., 2004; 269: 91–103.
- [24] Pieck CL, Vera CR, Parera JM, Gimenez GN, Serra LR, Carvalho LS, Rangel MC. Catal. Today, 2005; 107–108: 637–642.
- [25] Carnevillier C, Epron F, Marecot P. Appl. Catal. A: Gen., 2004; 275: 25–33.
- [26] Augustine SM, Sachtler WMH. The J. of Phys. Chem., 1987; 91: 5953–5956.

---

*To whom correspondence should be addressed: prof. Ali Karimi, School of Chemistry, College of Science, University of Tehran, Tehran, Iran, [karimial@ripi.ir](mailto:karimial@ripi.ir)*

## STUDY THE FLUID LOSS AND RHEOLOGICAL BEHAVIORS OF BENTONITE DRILLING MUD CONTAMINATED WITH SALT AND USED MOTOR OIL

*Aram Mohammed Raheem*

*Civil Engineering Department, University of Kirkuk, Kirkuk, Iraq*

Received July 14, 2018; Accepted October 17, 2018

---

### **Abstract**

In this study, the fluid loss and rheological behaviors of 6% bentonite drilling mud contaminated individually with 6% salt and 6% used motor oil have been investigated. Two models represented by API static and kinetic fluid loss models have been used to examine the behavior of experimentally uncontaminated 6% bentonite drilling mud tested at room temperature and lasted for 120 minutes. In addition, both API and kinetic models were used to study the behavior of experimentally 6% bentonite drilling mud contaminated independently with 6% salt and 6% used motor oil tested under similar conditions as uncontaminated drilling mud. All the fluid loss tests have been performed under two different applied pressures represented by 25 psi (172 kPa) and 90 psi (621 kPa). Moreover, four different models represented by a power law, Bingham, Herschel- Buckley (H-B), and hyperbolic models were used to investigate the rheological behavior of experimentally uncontaminated 6% drilling mud tested under two different temperatures represented by 25°C and 50°C. The similar rheological study has been performed on experimentally 6% bentonite drilling mud contaminated separately with 6% salt and 6% used motor oil tested under similar conditions as uncontaminated drilling mud. For the applied pressure of 25 psi, it was shown that the maximum fluid loss is increased by 244% and 31% as the salt and used motor oil contaminations increased from 0% to 6% respectively. Furthermore, it was shown that the maximum shear stresses for 6% bentonite drilling mud tested at 50°C increased by 104% and 59% as the salt and oil contaminations increased from 0% to 6% respectively. Finally, the kinetic model was better than API for fluid loss prediction and the hyperbolic model was the best for rheological properties evaluation with the highest  $R^2$  of 0.98 and lowest RMSE of 0.14 Pa.

**Keywords:** *fluid loss; rheological behavior; bentonite drilling mud; contamination; salt; used motor oil; kinetic model; API model; hyperbolic model; temperature; Bingham; power law; Herschel- Buckley.*

---

## **1. Introduction**

Boring mud or drilling fluid is a thick, viscous fluid combination that is used in oil and gas drilling progressions to carry rock cuttings to the surface and to lubricate and cool the drill bit [1]. In the drilling processes, the hydrostatic pressure prevents the collapse of unstable strata into the borehole and the infiltration of water from water-bearing strata that might be confronted [2]. The mud or drilling fluid system is the single constituent of the well-construction advancement that remains in contact with the wellbore during the entire drilling operation. The drilling-fluid systems are designed to exhibit severe wellbore conditions [3]. New enhancements in drilling-fluid expertise have made it attainable to reach a cost-effective, suitable-for-purpose system for every step in the well construction practice [4]. There are different types of drilling fluids based on their composition and uses. Three main factors affect the type of drilling fluid represented by the cost, technical implementation, and environmental influence. The annual classification of fluid schemes includes several categories of drilling fluids such as freshwater systems, saltwater system, oil or synthetic based systems, and pneumatic fluid system [5-6]. Oil based systems have been developed in the early 1960s to handle several drilling problems including clay swelling, the reaction between clay and formation, slough after exposure to

water based fluid systems, increasing downhole temperature, stuck pipe, contaminants, torque, and drag [7].

Commonly, saltwater drilling fluids are used for drilling salt formations and shale inhabitation [8]. This type of drilling fluids is established to restrain the formation to be similar as ice-type hydrates and accumulate around subsea wellheads and well-control equipment, blocking lines and impeding critical operations. The most used type of drilling mud is the water-based mud that is used frequently all around the world where the composition is mainly water and bentonite. The bentonite has the ability to add some degree of viscosity to the drilling mud and assists to carry drilled cuttings up the annulus of the well bore, and hence, it is being added to water based drilling mud [9].

In addition, clay or polymers can be added to generate the viscosity in the water based drilling mud. The clay is the cheapest and most broadly used additive for viscosity control in the water-based mud [10]. In the drilling mud, the clay is responsible for intensifying viscosity to enhance the lifting capacity of the mud to transport cuttings to the surface, especially in larger holes where annular velocity is low. Furthermore, the clay can facilitate to build a wall filter cake in permeable zones to prevent fluid loss [11].

The contamination in the drilling mud is extremely a serious problem that can happen during drilling operation [12]. Mud can be contaminated when any foreign material appears the mud system and produces unfavorable changes in the mud properties such as the viscosity, the density, and filtration. Water based mud systems are highly exposed to contamination among other kinds of drilling muds. Mud contamination can be caused by over treating the mud system with additives or from the material entering into the mud during drilling. The most frequent contaminants of water-based drilling mud systems are solids gypsum/anhydrite, makeup water, soluble sulfides, cement/lime, salt / saltwater flow, and soluble bicarbonates and carbonates.

The most affected characteristics are the rheological properties including yield stress, plastic viscosity, filter cake, and gel strength, stability against contamination, and stability under different operating conditions [13]. A number of factors can affect the rheological properties of the drilling mud such as pressure, temperature, and contaminants [14]. In the drilling operations, the drilling mud is polluted with different contaminants such as salts, cement, and drill solids. Salt contamination can come from salt beds during drilling or from formation water influx. At high temperature, the drilling mud remedy is required since the mud is unable to tolerate the contaminants [15]. The drilling fluid efficiency and performance in drilling operation is influenced by its rheological properties, so it is required to investigate the drilling mud rheological properties and parameters at the downhole conditions [16].

The rheological properties of two drilling muds have been studied, and the results have shown that the drilling mud with stable properties is needed at high pressures and temperatures [13]. The effect of NaCl salt as a contaminant on the rheological properties of bentonite drilling mud has been studied where both plastic viscosity and electrical resistivity were decreased with increasing salt content [17]. It was shown that the contamination could increase the filter loss by 30% and decrease the electrical resistivity by 86% compared to the same sample with no contamination [18]. The effect of different electrolyses on the viscosity of water based drilling mud at different testing conditions has been investigated [19]. This study has concluded that NaCl salt contamination increases the shear stress versus shear strain rate relationship whereas KCl contamination decreases the shear stress versus shear strain rate relationship of water based drilling mud. The effect of polyelectrolyte in salt-free and salt contaminated drilling fluid systems have been examined [14]. The polyelectrolyte is a super fluid loss reducer and might be used as a stabilizer for bentonite drilling mud by building good temperature resistance with anti-aging performance. The effects of pressure and temperature on the drilling mud properties have been studied by many researchers [20-21]. In addition, the effect of salt contamination on the drilling fluid has been examined by some researchers [22].

The main objective of this study is to investigate the effects of salt and used motor oil contaminations on the behavior of bentonite drilling mud. The specific objectives are as follows:

1. Study the effect of salt and used motor oil contaminations on the fluid loss behavior of 6% bentonite drilling mud tested at room temperature under the effect of two applied pressures represented by 25 psi (172 kPa) and 90 psi (621 kPa) and all the tests lasted for 120 minutes. In addition, API and kinetic models were used to predict the fluid loss behavior.
2. Examine the effect of salt and used motor oil contaminations on the rheological behavior of 6% bentonite drilling mud tested under two different temperatures represented by 25° C and 50° C. Moreover; power law, Bingham, Herschel- Buckley (H-B), and hyperbolic models were used to evaluate the rheological behavior.

## **2. Materials and methods**

### **2.1. Material**

#### **2.1.1. Bentonite**

The mineral bentonite is found all around the world. It is the result of volcanic ash weathering. Bentonite has the ability to react as a fluid when mechanically stressed especially when it is shaken or stirred. Nevertheless, it hardens in inactive condition due to the viscosity increase. In this study, unaltered light commercial sodium bentonite was used to prepare water based drilling mud with 6% bentonite (w/w) content. The hydraulic conductivity of the bentonite was  $1 \times 10^{-9}$  m/sec.

#### **2.1.2. Salt**

Sodium chloride or salt is an ionic compound with a chemical formula of NaCl representing a 1:1 ratio of sodium and chloride ions. Sodium chloride is the responsible for the salinity of seawater, and it is generally used as a condiment and food preservative.

#### **2.1.3. Used motor oil**

Crude oil or petroleum (in this study "heavy used engine oil"), is unprocessed oil found deep beneath the surface of the earth. Its color ranges from clear to black and found as a liquid or solid. The overall properties of the crude oils are dependent upon their chemical compositions and structure. The crude oil consists of hydrocarbons compounds. The main hydrocarbons exist in crude oil are aliphatics, alicyclics and Polycyclic Aromatic Hydrocarbons (PAH).

## **2.2. Methods**

### **2.2.1. OFITE model 900 viscometer**

The OFITE model 900 viscometer is a small portable fully automated system used for measuring fluid viscosity. It is made of cylindrical rotational viscometer, which uses a transducer to determine the induced angle of rotation of the bob by a fluid sample. The tested fluid is contained in the shear gap or annular space between the rotor and bob, which is connected to a shaft with a spring.

The viscous drag generated by the fluid produces a torque on the bob that is observed by the transducer that computes the angular displacement of the bob.

### **2.2.2. Filter press**

The series 300 LPLT filter press (API Filter Press) is the most used means for measuring the filtration properties of the drilling muds and cement slurries. LPLT filter press assemblies contain a mud reservoir mounted in a frame, pressure source, filtering medium, and a graduated cylinder for collecting filtrate. As specified by the American Petroleum Institute (API), the working pressure is 100 psi (689 kPa), and the filtering area is 7.1 in<sup>2</sup> (46 cm<sup>2</sup>). The filter press design features a cell body to hold the mud sample, a pressure inlet, and a base

cap with screen and filter press. These units have been used by the industry for field and laboratory uses.

### 2.2.3. Drilling mud mixer

Drilling fluid formulations are normally mixed using different shearing devices having either fixed or variable speeds. API recommends single mud impeller blade where the blades can be in different forms such as rounded propellers, waveform shapes, and sharp blades. These mixers can also be used to mix cement for laboratory or field-testing

## 3. Modeling

### 3.1. Modeling of the rheological properties

#### 3.1.1. Power law

The power law model is a fluid model that used to define a non-Newtonian fluid where there an exponential relationship between shear stress and shear strain rate as follows:

$$\tau = K_1 \gamma^{n_1} \quad (1)$$

where:  $K_1$  = is the fluid consistency unit;  $n_1$  = is the power law exponent.

$$\frac{d\tau}{d\gamma} = K_1 n_1 \gamma^{n_1-1} \quad (2)$$

$$\frac{d^2\tau}{d\gamma^2} = (n_1 - 1)n_1 K_1 \gamma^{n_1-2} \quad (3)$$

$$\text{When } \gamma = \infty \Rightarrow \tau_{\max} = \infty \quad (4)$$

Thus, the upper shear stress limit condition is not satisfied when power law model is used.

#### 3.1.2. Bingham model

Bingham model is a two-parameter rheological model that is widely used to describe the flow characteristics of many types of drilling muds. The mathematical form of the model is as follows:

$$\tau = Y_p + P_v * \gamma \quad (5)$$

where:  $\tau$  = shear stress,  $\gamma$  = shear rate,  $Y_p$  = yield point,  $P_v$  = plastic viscosity.

Fluid obeys the Bingham model exhibit a linear shear stress-shear strain rate behavior. The plastic viscosity ( $P_v$ ) clearly identifies the slope of the line, and the yield point ( $Y_p$ ) is the threshold shear stress.  $P_v$  is kept as low as possible for fast drilling to minimize colloidal solids.  $Y_p$  should be high enough to transport cuttings out of the hole, but not so large as to create extreme pump pressure as the mudflow starts.  $Y_p$  is controlled using different choices of mud treatment.

#### 3.1.3. Herschel–Bulkley model (H-B model)

The Herschel–Bulkley model is defined a fluid using three parameters that can be represented mathematically as follows [24]:

$$\tau = \tau_{02} - K_2 \dot{\gamma}^{n_2} \quad (6)$$

where  $\tau, \tau_{02}, \dot{\gamma}, K_2$  and  $n_2$  represent the shear stress (Pa), yield stress (Pa), shear strain rate (1/s), correction parameter and flow behavior index respectively.

For the rigid material; the model assumes that below the yield stress ( $\tau_0$ ), the slurry behaves as a rigid solid similar to Bingham plastic model. For the material flows as a Power law fluid, the exponent  $n$  describes the shear thinning and shear thickening behavior. Slurries are considered as shear thinning when  $n < 1$  and shear thickening when  $n > 1$ . A fluid becomes shear thinning when the apparent viscosity decreases with the increase in shear strain rate.

Thus, the model should satisfy the following conditions:

$$\frac{d\tau}{d\dot{\gamma}} = K_2 n_2 \dot{\gamma}^{(n_2-1)} > 0 \Rightarrow K_2 n_2 > 0 \quad (7)$$

$$\frac{d^2\tau}{d\dot{\gamma}^2} = K_2 n_2 (n_2 - 1) \dot{\gamma}^{(n_2-2)} \Rightarrow K_2 n_2 (n_2 - 1) < 0$$

$$\text{when } \dot{\gamma} \rightarrow \infty \Rightarrow \tau_{\max} = \infty \tag{8}$$

Hence, Herschel–Bulkley model does not satisfy the upper limit condition for the shear stress limit.

**3.1.4. Hyperbolic model**

Relationship between shear stress and shear strain rate of water based drilling mud was inspected. Based on the investigation of the laboratory tested data, the following hyperbolic relationship can be proposed:

$$\tau - \tau_0 = \frac{A}{A + D\dot{\gamma}} \tag{9}$$

where  $\tau_0$  is the yield stress (Pa),  $A(\text{Pa s})^{-1}$ , and  $D(\text{Pa})^{-1}$ , are model parameters and  $\dot{\gamma}$  is the shear strain rate ( $\text{s}^{-1}$ ).

$$\frac{d\tau}{d\dot{\gamma}} = \frac{(A + D\dot{\gamma})(0) - AD}{(A + D\dot{\gamma})^2} = \frac{-AD}{(A + D\dot{\gamma})^2} > 0 \Rightarrow A > 0$$

$$\frac{d^2\tau}{d\dot{\gamma}^2} = \frac{-2AD^2}{(A + D\dot{\gamma})^3} < 0 \Rightarrow D > 0$$

$$\text{when } \dot{\gamma} = \infty \Rightarrow \tau_{\max} = \frac{1}{D} + \tau_0 \tag{10}$$

It is clearly shown that this model has a limit on the maximum shear stress, which can be produced by the fluid at a relatively high rate of shear strains.

**3.2. Modeling of the filtering process**

**3.2.1. General model**

The traditional method to calculate the infiltration through filter cake is given by the following equations [25-26]. The filter press is used to determine: (1) the filtration rate in a standard filter paper, and (2) the rate of mud cake thickness increase on the standard filter paper. Based on Darcy’s law, the rate of infiltration is given by:

$$\frac{dv_f}{dt} = \frac{k(t)A_0\Delta P}{\mu(T)h_{mc}} > 0 \tag{11}$$

During the filtration process, the volume of infiltrated solids in the mud is equal to the volume of deposited solids in the filter cake:

$$f_{sm}(t)V_m = f_{sc}(t)h_{mc}A_0 \tag{12}$$

where  $f_{sm}$  = volume fraction of solids in the mud and  $f_{sc}$  = volume fraction of solids in the cake.

$$f_{sm}(t)(h_{mc}A_0 + V_f) = f_{sc}(t)h_{mc}A_0 \tag{13}$$

$$h_{mc} = \frac{f_{sm}(t)V_f}{A_0(f_{sc}(t) - f_{sm}(t))} = \frac{V_f}{A_0\left(\frac{f_{sc}}{f_{sm}}(t) - 1\right)} \tag{14}$$

Substituting Eq. (14) into Eq. (11):

$$\int_0^{V_f} V_f dV_f = \int_0^t \frac{k(t)A_0\Delta P}{\mu(T)} A_0 \left(\frac{f_{sc}}{f_{sm}}(t) - 1\right) dt \tag{15}$$

**3.2.2. Static model (API model)**

The static model has been build based on the following assumptions:

1. It was assumed that the filter cake is formed initially; however, this is not true since at the start there is no cake formation in either experimental or real field situation.
2. The percentage of solids in the cake to the solids in the mud is constant, but in fact, it increases with time to a limiting value when the flow is stopped.
3. The cake permeability is constant, but in reality, it should decrease with the time.

By applying these assumptions to equation (15) and performing the integration with the initial condition, the following equation is obtained:

$$V_f - V_0 = \sqrt{2k\Delta P \left(\frac{f_{sc}}{f_{sm}} - 1\right) A_0} \frac{\sqrt{t}}{\sqrt{\mu}} \tag{16}$$

Equation (16) can be re-written as follows:

$$v_f - v_0 = M * \sqrt{t} \tag{17}$$

where:  $V_f$  = volume of fluid loss ( $\text{cm}^3$ ),  $v_0$  = initial volume of fluid loss ( $\text{cm}^3$ ),  $k$  = drilling mud permeability (Darcy),  $k_0$  = initial permeability of drilling mud (Darcy),  $\Delta P$  = applied pressure (atm),  $f_{sc}$  = Volume fraction of solid in the cake,  $f_{sm}$  = volume fraction in mud,  $V_m$  = volume of solids in mud,  $A_0$  = filter area ( $\text{cm}^2$ ),  $t$  = time (minute),  $\mu$  = mud viscosity (cp),  $h_{mc}$  = the thick-

ness of the filter mud cake (cm),  $M = \sqrt{\frac{2k\Delta P(f_{sc}-1)}{\mu}} A_0$ .

If the time is considered to be ( $\infty$ ) in Eq. (17), the volume of the fluid loss will be ( $\infty$ ), and this cannot happen in reality. Hence, static (API) model does not satisfy the total filtration volume.

### 3.2.3. New kinetic (hyperbolic) model

This model is developed based on the fact that the rate of infiltration is dependent on several factors such as the permeability of the filter cake, the ratio of the solid content in the cake to the solid content in the mud, and the time [27].

$$\frac{dv}{dt} = f\left(k(t), \frac{f_{sc}}{f_{sm}}(t)\right) = Nk^L \left(\frac{f_{sc}}{f_{sm}}\right)^p \quad (18)$$

This model has the following features:

1. The rate of change in the permeability can be quantified as shown in Eq. 19 with  $L=1$ :

$$k = \frac{2A_1 * k_0}{(A_1 + B_1 t)^2} \quad (19)$$

2. The ratio of the solid content in the cake to the solid content in the mud as a volume fraction is a function of time shown in Eq. 20 with  $p=1$ :

$$\left(\frac{f_{sc}}{f_{sm}} - 1\right) = \frac{\alpha_0 t}{A_1 + B_1 t} \quad (20)$$

3. The final form of the filtration equation exhibits the form of hyperbolic function after substituting Eqs. (19) and (20) into Eq. (15) and performing integration of the equation with applying the initial conditions:

$$V_f - V_0 = N * \frac{t}{A_1 + B_1 t} \quad (21)$$

where:  $A_1$  = fluid loss parameter,  $B_1$  = arbitrary constant (1/min),  $\alpha_0$  = arbitrary constant (1/min),  $A_0$  = filter area ( $\text{cm}^2$ ),  $V_0$  = Initial value of drilling mud infiltration ( $\text{cm}^3$ ),

$$N = \sqrt{\frac{2 * k_0 * \alpha_0 * \Delta P}{\mu(T)}} * A_0.$$

The parameter  $A_1$  represents the initial rate of the infiltration, while the constant  $B_1$  represents the final stage of infiltration. Moreover, Eq. (21) satisfies the following criteria:

1. The total infiltration volume has a limiting value where no more infiltration could happen because the particle is blocking all the open porous in the filter cake medium.
2. None of the mentioned properties can be checked in the API model; however, these changes in the properties can be monitored in the field or the laboratory. In addition, this model can be used to model both short and long term infiltration-time relationships.
3. Both  $A_1$  and  $B_1$  are functions of pressure and time.

### 3.3. Comparison of model predictions

In order to evaluate the accuracy of any model predictions in the study, both the root mean square error (RMSE) and the coefficient of determination ( $R^2$ ) as defined in Eqs. (22) and (23) were quantified using [28]:

$$RMSE = \sqrt{\frac{\sum_{i=1}^n (y_i - x_i)^2}{N_2}} \quad (22)$$

$$R^2 = \left( \frac{\sum_i (x_i - \bar{x})(y_i - \bar{y})}{\sqrt{\sum_i (x_i - \bar{x})^2} \sqrt{\sum_i (y_i - \bar{y})^2}} \right)^2 \quad (23)$$

where  $y_i$  is the actual value;  $x_i$  is the calculated value from the model;  $\bar{y}$  is the mean of actual values;  $\bar{x}$  is the mean of calculated values and  $N_2$  is the number of data points.

## 4. Results and analysis

### 4.1. General

The results and analysis of 28 laboratory experimental tests conducted on water based drilling mud where 14 experiments have done to model the filtration phenomenon and the rest have been performed for the rheological properties. For the fluid loss experiments, two set of tests have been performed using pressures of 25 psi and 90 psi on 6% uncontaminated bentonite drilling mud and the tests have lasted for 120 minutes. The same fluid loss experimental tests have been done on 6% bentonite drilling mud contaminated separately with salt and used motor oil using pressures of 25 psi and 90 psi and the tests have lasted for 120 minutes. For the rheological experiments, two set of tests have been performed at two different temperatures at 25°C and 50°C on 6% uncontaminated bentonite drilling mud. Similar rheological experimental tests have been performed on 6% bentonite drilling mud contaminated individually with salt and used motor oil at two different temperatures at 25°C and 50°C.

### 4.2. Filtration experimental tests

The validity of both kinetic hyperbolic and API models was considered for long-term results ( $t > 30$  min). Most of the real laboratory or field tests can be performed for more than 30 min; therefore, it is important to check the filtration phenomenon for more than 30 min where implicit changes occur in cake permeability, so the lid content ratio in the cake to the mud, and cake porosity.

The variation of fluid loss with time for uncontaminated 6% bentonite drilling mud under two different applied pressures of 25 psi and 90 psi have shown in Fig. 1. The experimental tests have done at room temperature and lasted for 120 minutes. With increasing the time, the API model prediction increased with no limit on the fluid loss compared to the kinetic hyperbolic model that limited the maximum fluid loss to  $(V_0 + N/B)$ . The effect of applied pressure is ignored in the API model whereas both A and B parameters include the effect of applied pressure in the kinetic hyperbolic model. Experimental tests have shown that the maximum fluid loss for the 6% bentonite drilling mud at the final tested time of 120 min were 35  $\text{cm}^3$  and 42  $\text{cm}^3$  at applied pressures of 90 psi and 25 psi respectively. As the applied pressure increased from 25 psi to 90 psi, the maximum fluid loss increased by 20% because fluid flow increased under the effect of higher applied pressure.

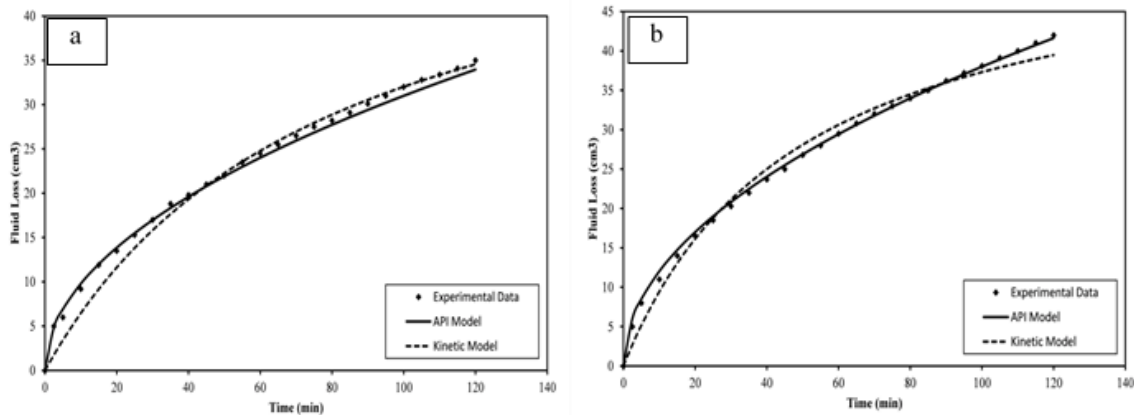


Figure 1. The variation of fluid loss with time for uncontaminated 6% bentonite drilling mud at room temperature under two different applied pressures of (a) applied pressure = 25 psi, and (b) applied pressure = 90 psi

Similarly, the variation of fluid loss with time for 6% bentonite drilling mud contaminated with 6% salt under two different applied pressures of 25 psi and 90 psi have shown in Fig. 2. The experimental tests have done at room temperature and lasted for 120 minutes. Experimental tests have shown that the maximum fluid loss for the 6% bentonite drilling mud contaminated with 6% salt at the final tested time of 120 min was 120.5  $\text{cm}^3$  and 132.8  $\text{cm}^3$  at

applied pressures of 90 psi and 25 psi respectively. As the applied pressure increased from 25 psi to 90 psi, the maximum fluid loss increased by 10% because fluid flow increased under the effect of higher applied pressure. For the applied pressure of 25 psi, the maximum fluid loss is increased by 244% as the salt contamination increased from 0% to 6%. For the applied pressure of 90 psi, the maximum fluid loss is increased by 216% as the salt contamination increased from 0% to 6%. The salt has the tendency to increase the fluid loss since the salt increases the flocculation of clay particles that leads to more particles settlement in a shorter time.

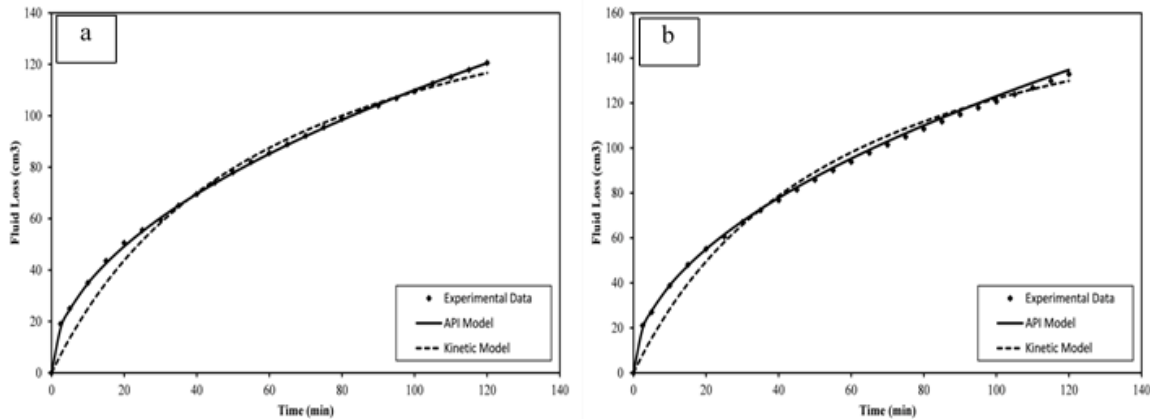


Figure 2. The variation of fluid loss with time for 6% bentonite drilling mud contaminated with 6% salt at room temperature under two different applied pressures of (a) applied pressure = 25 psi, and (b) applied pressure = 90 psi

Similarly, the variation of fluid loss with time for 6% bentonite drilling mud contaminated with 6% used motor oil under two different applied pressures of 25 psi and 90 psi have shown in Fig. 3.

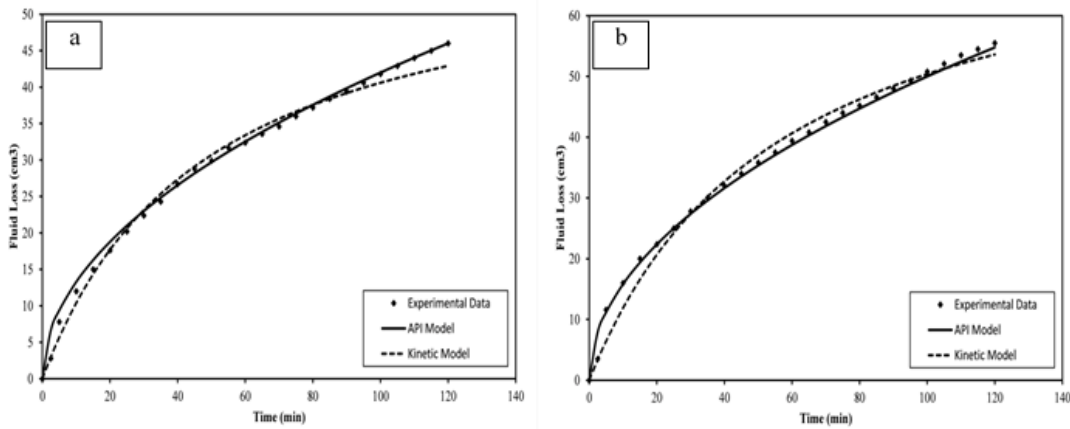


Figure 3. The variation of fluid loss with time for 6% bentonite drilling mud contaminated with 6% used motor oil at room temperature under two different applied pressures of (a) applied pressure = 25 psi, and (b) applied pressure = 90 psi

The experimental tests have done at room temperature and lasted for 120 minutes. Experimental tests have shown that the maximum fluid loss for the 6% bentonite drilling mud contaminated with 6% used motor oil at the final tested time of 120 min were 46 cm<sup>3</sup> and 55.5 cm<sup>3</sup> at applied pressures of 90 psi and 25 psi respectively. As the applied pressure increased from 25 psi to 90 psi, the maximum fluid loss increased by 21% because fluid flow increased under the effect of higher applied pressure. For the applied pressure of 25 psi, the maximum fluid loss is increased by 31% as the used oil contamination increased from 0% to 6%. For the applied pressure of 90 psi, the maximum fluid loss is increased by 32% as the used oil contamination increased from 0% to 6%. The oil has the tendency to increase the fluid loss

since the oil decreases the friction between the clay particles that leads to more particles settlement in a shorter time.

### 4.3. Rheological properties analysis

The rheological experimental tests have been performed on uncontaminated 6% bentonite drilling mud under two different temperatures of 25°C and 50°C. In addition, similar experimental tests have been performed on 6% bentonite drilling mud contaminated separately with 6% salt and 6% used motor oil.

### 4.4. Experimental tests at 25°C

The variation of shear stress with a shear strain rate of uncontaminated 6% bentonite drilling mud at 25°C has shown in Fig. 4. Four different models including power law, Bingham, Herschel-Buckley (H-B), and Hyperbolic models have been used. All the model parameters with their accuracy predictions have summarized in Table 1. The maximum measured shear stress for uncontaminated 6% bentonite drilling mud at 25°C was 8.6 Pa at a shear strain rate of 1700 (1/s). All the models predicted the maximum shear stress very well with the highest R<sup>2</sup> of 0.97 and lowest RMSE of 0.3 Pa.

Table 1. Models prediction parameters for uncontaminated 6% bentonite drilling mud tested at 25°C

Bentonite (%)	Salt (%)	Oil (%)	Power law					Bingham				
			$\tau_0$ (Pa)	K	n	RMSE (Pa)	R <sup>2</sup>	$\tau_0$ (Pa)	$\mu$ (cP)	RMSE (Pa)	R <sup>2</sup>	
6	0	0	1.9	0.8	0.62	0.46	0.93	2.1	0.0035	0.3	0.97	-
Bentonite (%)	Salt (%)	Oil (%)	Herschel- Buckley (H-B)				Hyperbolic					
			$\tau_0$ (Pa)	k (Pa.s)	n	RMSE (Pa)	R <sup>2</sup>	$\tau_0$ (Pa)	A (Pa <sup>-1</sup> )	B (Pa) <sup>-1</sup>	RMSE (Pa)	R <sup>2</sup>
6	0	0	1.79	0.06	0.66	0.35	0.93	2.5	255	0.008	0.3	0.97

The variation of shear stress with a shear strain rate of 6% bentonite drilling mud contaminated with 6% salt at 25° C has shown in Fig. 5. Four different models including power law, Bingham, Herschel-Buckley (H-B), and Hyperbolic models have been used. All the model parameters with their accuracy predictions have summarized in Table 2. The maximum measured shear stress for 6% bentonite drilling mud contaminated with 6% salt at 25°C was 5.8 Pa at a shear strain rate of 1700 (1/s). All the models predicted the maximum shear stress very well, and the hyperbolic model was the best with the highest R<sup>2</sup> of 0.98 and lowest RMSE of 0.14 Pa. The maximum shear stress for 6% bentonite drilling mud tested at 25° C decreased by 48% as the salt contamination increased from 0% to 6% because the salt causes dispersion between clay particles leads to lower measured maximum shear stress.

Table 2. Models prediction parameters for 6% bentonite drilling mud contaminated with 6% salt tested at 25°C

Bentonite (%)	Salt (%)	Oil (%)	Power law					Bingham				
			$\tau_0$ (Pa)	K	n	RMSE (Pa)	R <sup>2</sup>	$\tau_0$ (Pa)	$\mu$ (cP)	RMSE (Pa)	R <sup>2</sup>	
6	6	0	1.4	0.06	0.62	0.3	0.93	1.8	0.0027	0.18	0.97	-
Bentonite (%)	Salt (%)	Oil (%)	Herschel- Buckley (H-B)				Hyperbolic					
			$\tau_0$ (Pa)	k (Pa.s)	n	RMSE (Pa)	R <sup>2</sup>	$\tau_0$ (Pa)	A (Pa <sup>-1</sup> )	B (Pa) <sup>-1</sup>	RMSE (Pa)	R <sup>2</sup>
6	6	0	1.8	0.055	0.62	0.3	0.93	2	380	0.008	0.14	0.98

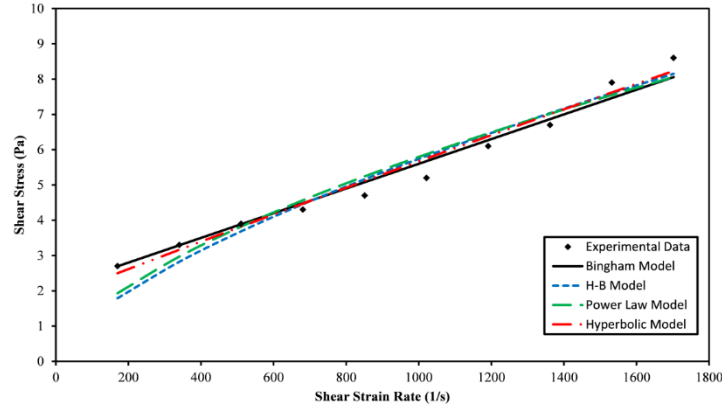


Figure 4. The variation of shear stress with shear strain rate for uncontaminated 6% bentonite drilling mud tested at 25°C

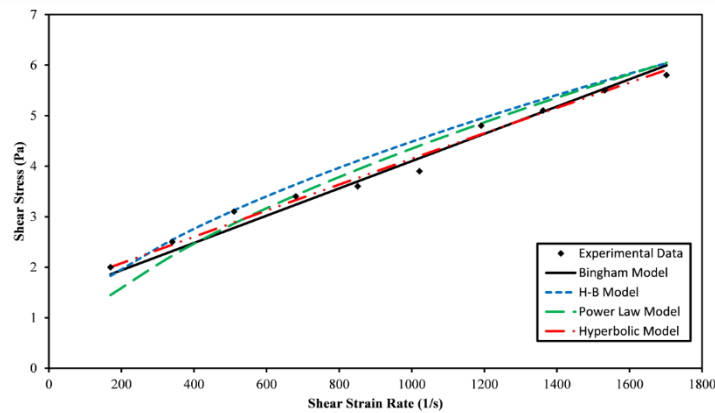


Figure 5. The variation of shear stress with shear strain rate for 6% bentonite drilling mud contaminated with 6% salt tested at 25°C

The variation of shear stress with a shear strain rate of 6% bentonite drilling mud contaminated with 6% used motor oil at 25°C has shown in Fig. 6. Four different models including power law, Bingham, Herschel-Buckley (H-B), and Hyperbolic models have been used. All the model parameters with their accuracy predictions have summarized in Table 3. The maximum measured shear stress for 6% bentonite drilling mud contaminated with 6% used motor oil at 25°C was 12.2 Pa at a shear strain rate of 1700 (1/s). Almost all the models predicted the maximum shear stress very well, and both the Bingham and hyperbolic models were the best with the highest  $R^2$  of 0.95 and lowest RMSE of 0.48 Pa. The maximum shear stress for 6% bentonite drilling mud tested at 25°C increased by 42% as the used motor oil contamination increased from 0% to 6% because the used motor oil has lower density than clay particles that make the medium to have more clay particles in less volume leads to higher measured maximum shear stress.

Table 3. Models prediction parameters for 6% bentonite drilling mud contaminated with 6% used motor oil tested at 25°C

Bentonite (%)	Salt (%)	Oil (%)	Power law					Bingham				
			$\tau_0$ (Pa)	K	n	RMSE (Pa)	$R^2$	$\tau_0$ (Pa)	$\mu$ (cP)	RMSE (Pa)	$R^2$	
6	0	6	4.86	0.94	0.32	1.12	0.78	4.42	0.0044	0.48	0.95	-
Bentonite (%)	Salt (%)	Oil (%)	Herschel- Buckley (H-B)				Hyperbolic					
			$\tau_0$ (Pa)	k (Pa.s)	n	RMSE (Pa)	$R^2$	$\tau_0$ (Pa)	A (Pa <sup>-1</sup> )	B (Pa <sup>-1</sup> )	RMSE (Pa)	$R^2$
6	0	6	4.45	0.085	0.62	0.79	0.89	4.5	230	0.004	0.53	0.95

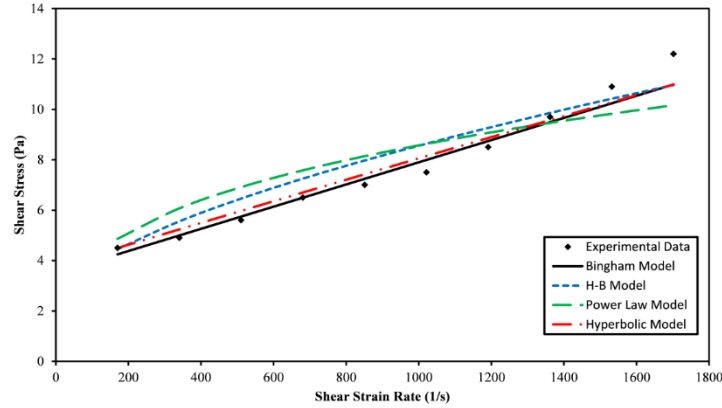


Figure 6. The variation of shear stress with shear strain rate for 6% bentonite drilling mud contaminated with 6% used motor oil tested at 25°C

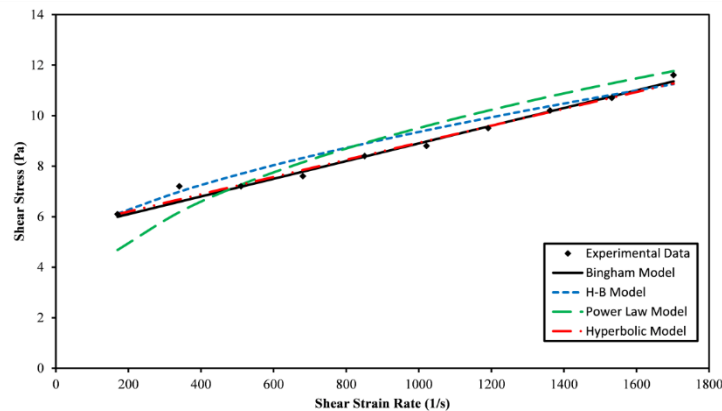


Figure 7. The variation of shear stress with shear strain rate for uncontaminated 6% bentonite drilling mud tested at 50° C

#### 4.5. Experimental tests at 50°C

The variation of shear stress with a shear strain rate of uncontaminated 6% bentonite drilling mud at 50°C has shown in Fig. 8. Four different models including power law, Bingham, Herschel-Buckley (H-B), and Hyperbolic models have been used. All the model parameters with their accuracy predictions have summarized in Table 4. The maximum measured shear stress for uncontaminated 6% bentonite drilling mud at 50°C was 11.6 Pa at a shear strain rate of 1700 (1/s). All the models predicted the maximum shear stress very well with the highest R<sup>2</sup> of 0.98 and lowest RMSE of 0.22 Pa. The maximum shear stress for uncontaminated 6% bentonite drilling mud increased by 35% as the testing temperature increased from 25° C to 50°C.

Table 4. Models prediction parameters for uncontaminated 6% bentonite drilling mud tested at 50° C

Bentonite (%)	Salt (%)	Oil (%)	Power law					Bingham				
			$\tau_0$ (Pa)	K	n	RMSE (Pa)	R <sup>2</sup>	$\tau_0$ (Pa)	$\mu$ (cP)	RMSE (Pa)	R <sup>2</sup>	
6	0	0	4.6	0.6	0.4	0.73	0.80	5.9	0.0035	0.22	0.98	-
Bentonite (%)	Salt (%)	Oil (%)	Herschel- Buckley (H-B)				Hyperbolic					
			$\tau_0$ (Pa)	k (Pa.s)	n	RMSE (Pa)	R <sup>2</sup>	$\tau_0$ (Pa)	A (Pa <sup>-1</sup> )	B (Pa) <sup>-1</sup>	RMSE (Pa)	R <sup>2</sup>
6	0	0	6.11	0.067	0.62	0.42	0.93	6.1	290	0.004	0.22	0.98

The variation of shear stress with a shear strain rate of 6% bentonite drilling mud contaminated with 6% salt at 50°C has shown in Fig. 9. Four different models including power law,

Bingham, Herschel-Buckley (H-B), and Hyperbolic models have been used. All the model parameters with their accuracy predictions have summarized in Table 5. The maximum measured shear stress for 6% bentonite drilling mud contaminated with 6% salt at 50°C was 5.7 Pa at a shear strain rate of 1700 (1/s). All the models predicted the maximum shear stress very well, and the hyperbolic model was the best with the highest R<sup>2</sup> of 0.98 and lowest RMSE of 0.16 Pa. The maximum shear stress for 6% bentonite drilling mud tested at 50°C decreased by 104% as the salt contamination increased from 0% to 6%. The maximum shear stress for 6% bentonite drilling mud contaminated with 6% salt decreased by 2% as the testing temperature increased from 25°C to 50°C.

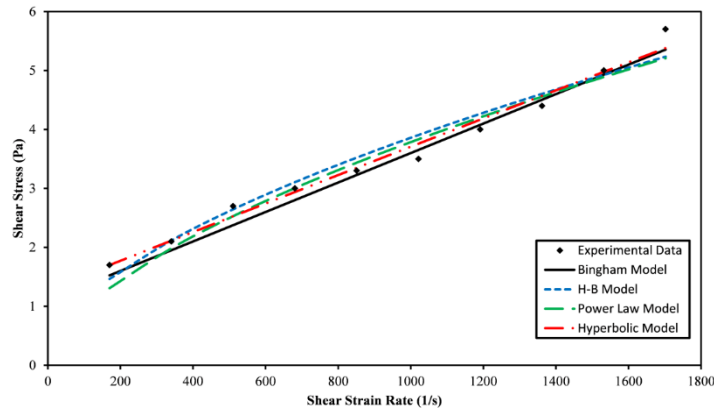


Figure 8. The variation of shear stress with shear strain rate for 6% bentonite drilling mud contaminated with 6% salt tested at 50°C

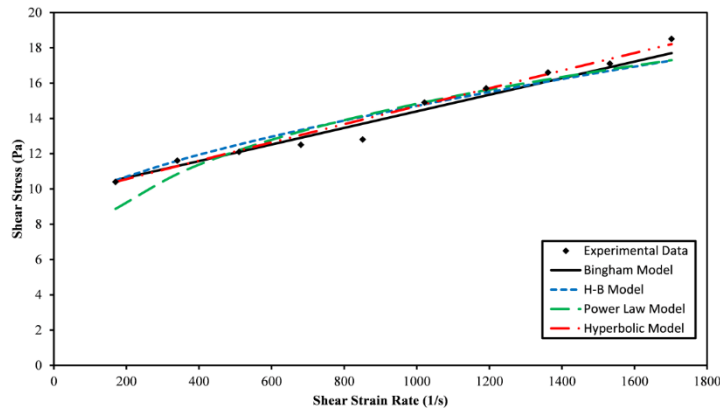


Figure 9. The variation of shear stress with shear strain rate for 6% bentonite drilling mud contaminated with 6% used motor oil tested at 50°C

Table 5. Models prediction parameters for 6% bentonite drilling mud contaminated with 6% salt tested at 50°C

Bentonite (%)	Salt (%)	Oil (%)	Power law					Bingham				
			$\tau_0$ (Pa)	K	n	RMSE (Pa)	R <sup>2</sup>	$\tau_0$ (Pa)	$\mu$ (cP)	RMSE (Pa)	R <sup>2</sup>	
6	6	0	1.3	0.06	0.6	0.25	0.95	1.5	0.0025	0.19	0.97	-
Bentonite (%)	Salt (%)	Oil (%)	Herschel- Buckley (H-B)				Hyperbolic					
			$\tau_0$ (Pa)	k (Pa.s)	n	RMSE (Pa)	R <sup>2</sup>	$\tau_0$ (Pa)	A (Pa <sup>-1</sup> )	B (Pa) <sup>-1</sup>	RMSE (Pa)	R <sup>2</sup>
6	6	0	1.4	0.058	0.6	0.24	0.95	1.7	410	0.004	0.16	0.98

The variation of shear stress with a shear strain rate of 6% bentonite drilling mud contaminated with 6% used motor oil at 50°C has shown in Fig. 9. Four different models including

power law, Bingham, Herschel-Buckley (H-B), and Hyperbolic models have been used. All the model parameters with their accuracy predictions have summarized in Table 6. The maximum measured shear stress for 6% bentonite drilling mud contaminated with 6% used motor oil at 50°C was 18.5 Pa at a shear strain rate of 1700 (1/s). All the models predicted the maximum shear stress very well, and the hyperbolic model was the best with the highest R<sup>2</sup> of 0.97 and lowest RMSE of 0.43 Pa. The maximum shear stress for 6% bentonite drilling mud tested at 50°C increased by 59% as the used motor oil contamination increased from 0% to 6%. The maximum shear stress for 6% bentonite drilling mud contaminated with 6% used motor oil increased by 52% as the testing temperature increased from 25°C to 50°C.

Table 6. Models prediction parameters for 6% bentonite drilling mud contaminated with 6% used motor oil tested at 50°C

Bentonite (%)	Salt (%)	Oil (%)	Power law					Bingham				
			$\tau_0$ (Pa)	K	n	RMSE (Pa)	R <sup>2</sup>	$\tau_0$ (Pa)	$\mu$ (cP)	RMSE (Pa)	R <sup>2</sup>	
6	0	6	8.87	2	0.29	0.83	0.89	10.5	0.0047	0.48	0.96	-

Bentonite (%)	Salt (%)	Oil (%)	Herschel- Buckley (H-B)				Hyperbolic					
			$\tau_0$ (Pa)	k (Pa.s)	n	RMSE (Pa)	R <sup>2</sup>	$\tau_0$ (Pa)	A (Pa <sup>-1</sup> )	B (Pa <sup>-1</sup> )	RMSE (Pa)	R <sup>2</sup>
6	0	6	10.9	0.064	0.66	0.67	0.93	10.4	190	0.004	0.43	0.97

### 5. Conclusions

Based on the experimental results and model predictions of this study, the following conclusions can be advanced:

1. For the fluid loss prediction, the API model prediction increased nonlinearly with time where no limit on the maximum fluid loss has been encountered whereas the kinetic hyperbolic model limited the maximum fluid loss to the quantity  $(V_0 + N/B)$ . In addition, the effect of applied pressure has been neglected in the API model, but the kinetic hyperbolic model has taken into account the effect of applied pressure.
2. For the uncontaminated 6% bentonite drilling mud, the maximum fluid loss is increased by 20% as the applied pressure increased from 25 psi to 90 psi.
3. For the 6% bentonite drilling mud contaminated with 6% salt, the maximum fluid loss is increased by 10% as the applied pressure increased from 25 psi to 90 psi.
4. For the applied pressure of 25 psi, the maximum fluid loss is increased by 244% as the salt contamination increased from 0% to 6%. For the applied pressure of 90 psi, the maximum fluid loss is increased by 216% as the salt contamination increased from 0% to 6%.
5. For the 6% bentonite drilling mud contaminated with 6% used motor oil, the maximum fluid loss is increased by 21% as the applied pressure increased from 25 psi to 90 psi.
6. For the applied pressure of 25 psi, the maximum fluid loss is increased by 31% as the used oil contamination increased from 0% to 6%. For the applied pressure of 90 psi, the maximum fluid loss is increased by 32% as the used oil contamination increased from 0% to 6%.
7. The maximum measured shear stresses for uncontaminated 6% bentonite drilling mud were 8.6 Pa and 11.6 Pa at 25°C and 50°C respectively. However, the maximum measured shear stresses for 6% bentonite drilling mud contaminated with 6% salt were almost the same represented by 5.8 Pa and 5.7 Pa at 25°C and 50°C respectively.
8. The maximum measured shear stresses for 6% bentonite drilling mud contaminated with 6% used motor oils were 12.2 Pa and 18.5 Pa at 25° C and 50° C respectively.
9. The maximum shear stresses for 6% bentonite drilling mud tested at 25° C increased by 48% and 42% as the salt and oil contaminations increased from 0% to 60% respectively. The maximum shear stresses for 6% bentonite drilling mud tested at 50° C increased by 104% and 59% as the salt and oil contaminations increased from 0% to 60% respectively.

10. All the used models to predict the maximum shear stress were very good and the hyperbolic model was the best with the highest  $R^2$  of 0.98 and lowest RMSE of 0.14 Pa.

### Acknowledgements

The author would like to thank all the staff at the Drilling Laboratory in the Petroleum Engineering Department at the University of Kirkuk.

### Symbols

$\tau$	Shear stress	$V_m$	Volume of solids in mud
$\gamma$	Shear strain rate	$A_o$	Filter area
$K_1$	Fluid consistency unit	$t$	Time
$n_1$	Power law exponent	$\mu$	Mud viscosity
$Y_P$	Yield point	$h_{mc}$	Thickness of the filter mud cake
$P_v$	Plastic viscosity	$f_{sm}$	Volume fraction of solids in the mud
$\tau_{o1}$	Yield stress	$f_{sc}$	Volume fraction of solids in the cake
$\dot{\gamma}$	Shear strain rate	$L$ and $p$	Arbitrary constants
$K_2$	Correction parameter	$A_1$	Fluid loss parameter
$n_2$	Flow behavior index	$B_1$	Arbitrary constant
$\tau_{max}$	Maximum shear stress	$\alpha_o$	Arbitrary constant
$A$ and $D$	Model parameters	$V_o$	Initial value of drilling mud infiltration
$V_f$	Volume of fluid loss	RMSE	Root mean square error
$v_o$	Initial volume of fluid loss	$R^2$	Coefficient of determination
$k$	Drilling mud permeability	$y_i$	The actual value
$k_o$	Initial permeability of drilling mud	$x_i$	The calculated value from the model
$\Delta P$	Applied pressure	$\bar{y}$	The mean of actual values;
$f_{sc}$	Volume fraction of solid in cake	$\bar{x}$	The mean of calculated values
$f_{sm}$	Volume fraction in mud	$N_2$	The number of data points
$M$	$\sqrt{\frac{2k\Delta P \left( \frac{f_{sc}}{f_{sm}} - 1 \right)}{\mu} A_o}$	$N$	$\sqrt{\frac{2 * k_o * \alpha_o * \Delta P}{\mu(T)} * A_o}$

### References

- [1] Makhoukhi B. Design of experiments on sodic activation of bentonite for using as water-based drilling fluids. *Pet Coal*, 2016; 58 (3): 368-381.
- [2] Sami NA. Effect of magnesium salt contamination on the behavior of drilling fluids. *Egyptian Journal of Petroleum*, 2016; 25: 453-458.
- [3] Azim RA. Evaluation of production potential of fractured geothermal systems due to cold fluid circulation under poro-thermo elastic conditions. *Pet Coal*, 2017; 59(6): 975-990.
- [4] Vipulanandan C, Raheem AM. Characterizing ultra-soft soils and anchor-soil interaction for deepwater applications. *Proceedings of the Twenty-fifth International Ocean and Polar Engineering Conference, Kona, Big Island, Hawaii, USA, June 21-26, pp. 1048-1054.*
- [5] Shadravan A, Amani M. HPHT 101-what petroleum engineers and geoscientists should know about high pressure high temperature wells environment. *Energy Science and Technology*, 2012; 4(2): 36-60.
- [6] Aremu MO, Arinkoola AO, Salam KK, Ogunmola EO. Potential of local pH control additives for corrosion inhibition in water base drilling fluids. *Pet Coal*, 2017; 59(5): 611-619.
- [7] Shijun N, Bin F, Shibin L, Xiang S, Xuan Z, Bing L. Technical measures for improving compatibility of cement slurry with CO<sub>2</sub> contaminated drilling fluid: a case study. *Nat Gas Ind*, 2013; 33(9): 91-96.
- [8] Avci E. Effect of Salinity on flow properties of Drilling Fluids: an experimental approach. *Pet Coal*, 2018; 60(2): 232-235.
- [9] Ming L., Wei W., Youzhi Z., Xiaowei C., Bin D., Xiaoyang G. Impact of drilling fluid additives on performance of the cement slurry by single-factor. *Chem Eng Oil Gas*, 2014; 43(3): 297-301.

- [10] Amede VG, Alfazazi U. Optimal drilling fluid rheological considerations for avoiding stuck pipe and fluid loss under HT horizontal well condition: Gulf of Guinea as a scenario. *Pet Coal*, 2017; 59(5): 703-709.
- [11] Fakhreldin YE, Sharji H, Aghbari SA, Al-Rashdi S. Novel technique to determine cement contamination,.In: SPE/IADC Middle East Drilling Technology Conference and Exhibition, 24-26 October 2011, Muscat, Oman.
- [12] Youzhia Z, Chaoyia S, Kunquanc Y, Xiaoyangd G, Hualia Z, Taa Y, Mingd L. (2015). Contamination effects of drilling fluid additives on cement slurry. *Natural Gas Industry B*, 2015; 2: 354-359.
- [13] Amani M, Al-Jubouri M, Shadravan A. Comparative study of using oil-based mud versus water-based mud in HPHT fields. *Adv Pet Explor Dev*, 2012; 4: 18–27.
- [14] Nagre RD, Lin Zhao, Owusu PA. Thermosaline resistant acrylamide-based polyelectrolyte as filtration control additive in aqueous-based mud. *Pet. Coal*, 2014; 56(3): 222–230.
- [15] Darley HCH, Gray GR. Composition and properties of drilling and completion Fluids. Fifth ed., Gulf Professional Publishing 1988, Houston, Texas, USA.
- [16] Nasser J, Jesil A, Mohiuddin T, Al Rugheshi M, Devi G, Mohataram S. Experimental investigation of drilling fluid performance as nanoparticles. *World Journal of Nano Science and Engineering*, 2013; 3: 57-61.
- [17] Ali K, Vipulanandan C, Richardson D. Salt (NaCl) contamination on the resistivity and plastic viscosity of a bentonite drilling mud. *Proceedings of CIGMAT Conference & Exhibition 2013*.
- [18] Basirat B, Vipulanandan C, Richardson D. Filtration loss in 4% bentonite drilling mud with xanthan gum. *Proceedings of THC-IT Conference & Exhibition 2013*.
- [19] Hassiba KJ, Amani M. The effect of salinity on the rheological properties of water based mud under high temperatures for drilling offshores and deep wells. *Earth Sci. Res. J.*, 2013; 2(1): 175–186.
- [20] Adekomaya OA, Anifowose DM, Wale T. Experimental study of the effect of temperature on the flow properties of normal oil based muds in Niger delta formation. *Pet. Coal*, 2011; 53(2): 140–145.
- [21] Wang F, Tan X, Wang R, Sun M, Wang L, Liu J. High temperature and high pressure rheological properties of high-density water-based drilling fluids for deep wells. *Pet. Sci.*, 2012; 9: 354–362.
- [22] Alaskari MKG, Teymoori RN. Effects of salinity, pH and temperature on CMC polymer and XC polymer performance. *IJE Tran. B: Appl.*, 2007; 20(3): 283-290.
- [23] Studds PG, Stewart DI, Cousens TW. (1998). The effects of salt solutions on the properties of bentonite-sand mixtures. *Clay Minerals*, 1998; 33: 651-660.
- [24] Tang H, Kalyon D. Estimation of the parameters of Herschel–Bulkley fluid under wall slip using a combination of capillary and squeeze flow viscometers. *Rheol. Acta*, 2004; 43: 80–88.
- [25] Bourgoyne AT, Millheim KK, Chenevert ME, Young FS. *Applied drilling engineering*. SPE Foundation 1991, pp. 508.
- [26] Andrea SV, Hau G, Gerard DB, Pavel B, Pacelli LJ. A CT scan aided core-flood study of the leak-off process in oil-based drilling fluids. *SPE International Symposium and Exhibition 2012*, Louisiana, USA, pp.1-25.
- [27] Vipulanandan C, Raheem AM, Basirat B, Mohammed A, Richardson D. New kinetic model to characterize the filter cake formation and fluid loss in HPHT process. *OTC*, 25100-MS, Houston, TX, 5-8 May 2014, pp. 1-17.
- [28] Steel RGD, Torrie JH. *Principles and procedures of statistics with special reference to the biological sciences*. McGraw Hill 1960.

*To whom correspondence should be addressed: Dr. Aram Mohammed Raheem, University of Kirkuk, Civil Engineering Department, Kirkuk, Iraq*

SYNTHESIS AND EVALUATION OF MAGNETIC ZEOLITE NANO-COMPOSITE FOR REMOVAL OF RU FROM AQUEOUS SOLUTIONS

Leila Eskandari<sup>1\*</sup>, Farshad Kheiri<sup>1</sup>, Mozhgan Irawani<sup>2</sup>, Mohammad Sirousazar<sup>1</sup>

<sup>1</sup> Faculty of Chemical Engineering, Urmia University of Technology, Urmia, Iran

<sup>2</sup> Faculty of Chemistry, University of Isfahan, 81746-73441 Isfahan, Iran

Received September 17, 2018; Accepted October 14, 2018

---

## Abstract

Ruthenium compounds are distinctly toxic and carcinogenic, and its treatment has received much attention. Within the present studies, a singular magnetic nano zeolite composite (MZNC) became organized. Natural clinoptilolite tuff changed into nanoparticles by the use of a mechanical technique. The samples had been carried out to signify the adsorbents by XRD, XRF, FT-IR, DTG, SEM, and VSM. The nanocomposites were evaluated for Ruthenium (Ru) removal from aqueous solutions. The outcomes of the analytical variables, inclusive of pH, preliminary ion concentration, contact time, and temperature have been investigated. The saturation magnetization of the nano-composite turned into measured as  $19.50 \text{ emu g}^{-1}$  through which the magnetic separations of the samples have been facilitated after the adsorption procedure. The thermodynamic values of  $\Delta G^\circ$  and  $\Delta H^\circ$  represented the endothermic and spontaneous natures of Ru elimination.

**Keywords:** *Magnetic nanocomposite, Nano clinoptilolite, Ruthenium, Isotherm.*

---

## 1. Introduction

The environmental effect of the release of poisonous and radioactive pollutions from the nuclear industry has brought about a wide kind of studies on the removal of such pollutants. Therefore, to protect human health and the surroundings from risks resulting from radioactive waste and to keep away from any undue burden on future generations, radioactive waste needs to be controlled responsibly. Ion exchange process is one of the most effective approaches to the remedy of heavy metals [1-5]. Amongst distinct ion exchangers zeolites have received considerable attention for contaminant removal owing to their high exchange capacity, low cost and worldwide abundance [6-10]. Considering the largescale utilizations, natural zeolites seem more ascendant than synthetic ones, due to their low cost, abundant and much less chemical pollutants during production [11]. In comparison to the micro-sized zeolites, nano-crystalline zeolites have greater ion-exchange abilities, quicker exchange kinetics, larger surface areas, and more adjustable porosities. Yet, in spite of these advantages, separating them from the medium is the main challenge. This can be coped with by using magnetic separation technique. By applying nano-magnetic composites, these new methods open a simpler, faster, and more accurate way to the removal of elements [12]. Despite the fact that different methods have been reported for the synthesis of nano zeolites, as an alternative technique, the zeolite particle size may be decreased mechanically using particularly designed ball mills [13-17]. In spite of these advantages, separation of ion exchangers with the particle size in nanoscale from the medium is very difficult. This problem could be overcome by using a magnetic separation technique. This technique facilitates nano zeolite separation from solution in synthesis and usage steps since magnetic composites can be separated by efficient, simple, and fast magnetic separation process. For this kind of separation, extensive researches have been performed. The present study, magnetic nanocomposite was synthesized and characterized for studying their efficiencies of Ru removal from aqueous solutions. Meanwhile, the

effects of varied parameters, including pH, initial ion concentration, contact time, and temperature were evaluated and 4 optimized. Moreover, for the experimental data assessment, different kinetic and isotherm models were employed.

## 2. Experimental procedure

### 2.1. Reagents and methods

All the chemical reagents used in this study were of analytical reagent grade [AR Grade].  $\text{FeCl}_3 \cdot 6\text{H}_2\text{O}$  (Aldrich 98%),  $\text{FeCl}_2 \cdot 4\text{H}_2\text{O}$  (Aldrich 99%), and ammonium hydroxide (Aldrich 28–30% of ammonia) were applied for magnetic particle preparation, and Ru ions were supplied as ruthenium trichloride hydrate (also from Merck, Darmstadt, Germany). The natural clinoptilolite tuff belonged to Semnan region in the north-east of Iran. Identifications of the structural phases of the nanocomposite were achieved by usage of a Bruker D8 Advance X-ray diffractometer. The chemical compositions of the samples were determined through PANalytical Magix XRF spectrometry. An IR Prestige-21 Model spectrophotometer (Shimadzu, Japan) was utilized to obtain FT-IR spectra. Thermo-Gravimetric Analysis (TGA) of the samples was performed using a Mettler TG-50 Thermal Analyzer with a heating rate of  $10^\circ\text{C min}^{-1}$ . A vibrating sample magnetometer (Meghnatis Daghigh Kavir Company, Iran) was used to characterize MZNC magnetic properties. A Philips EM-208S transmission electron microscope was utilized to take the relevant images. Also, ICP-AES technique (Integra XL by GBC Australia) was employed to specify Ru concentration. The prepared nanocomposite was separated with the aid of a permanent magnet. Finally, the product was washed four times with deionized–deoxygenated water and then dried at  $50^\circ\text{C}$  for 5 h. The nanocomposite was prepared by adding the amount of nano zeolite clinoptilolite Fig. 1.

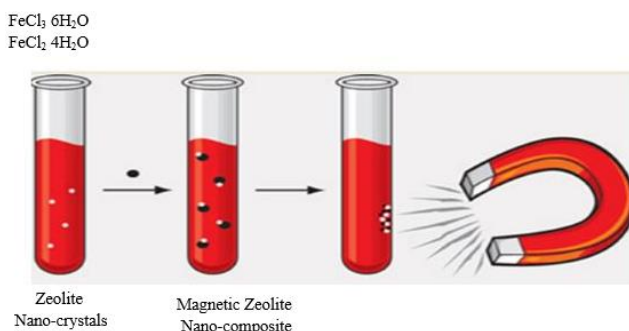


Fig. 1. Scheme of synthesis procedure of the nanocomposite

### 2.2. Adsorption experiments

The adsorption of Ru was studied by a batch technique to discover the optimum conditions. A sample of 0.05 g of nano zeolite or nanocomposite was equilibrated with 10 mL of Ru solution of known concentration at the fixed temperature for a known period of time. After equilibration, filtration of the solid phase was followed by centrifugation of the filtrate (3000 rpm for 5 min) while the nano-composite separation from liquid phase was followed with efficient, simple, and fast filtering. 10 mL of the supernatant solution was then taken for Ru measurement. The adsorbed amount of Ru was calculated from the difference in concentrations before and after adsorption.

$$q = (C_i - C_f) \times V/m \quad (1)$$

where  $q$  is the adsorbed amount of metal ions by a unit mass of zeolite ( $\text{meq g}^{-1}$ );  $C_i$  and  $C_f$  are the initial and final Ru concentrations ( $\text{meq L}^{-1}$ ), respectively;  $m$  is the used amount of zeolite (g), and  $V$  is the volume of Ru solution (L). The effects of different parameters, which is included initial Ru concentration, the solution pH, the contact time, and the temperature were investigated.

### 3. Results and discussion

#### 3.1. Characterization of M ZNC

The XRD patterns of raw nano-clinoptilolite (NCP) and magnetite zeolite nano-composite (MZNC) are shown in Figure 2. The characteristic lines at  $2\theta$  values of  $10.1^\circ$ ,  $11.4^\circ$ ,  $17.3^\circ$ ,  $23^\circ$ ,  $26^\circ$ ,  $28.2^\circ$ ,  $30.2^\circ$ ,  $32^\circ$ ,  $35^\circ$ ,  $37^\circ$  and  $39^\circ$  in the pattern (a) can be attributed to clinoptilolite crystalline structure data [18]. This confirms that the sample used in this work has a typical clinoptilolite phase as the microporous component. The diffraction line of iron oxide was observed at  $2\theta$  values of  $35.9^\circ$ ,  $42^\circ$  and  $73^\circ$  in the XRD pattern of MZNC sample (b) shows the formation of iron oxide in the zeolite structure [19]. The relative line intensity and line position related to zeolite clinoptilolite remained unchanged, which represented that the crystal structure of zeolite had been stable during the preparation of composite. Through Scherrer's equation [20], the magnetite particle size of the composite was appeared to be 22.4 nm.

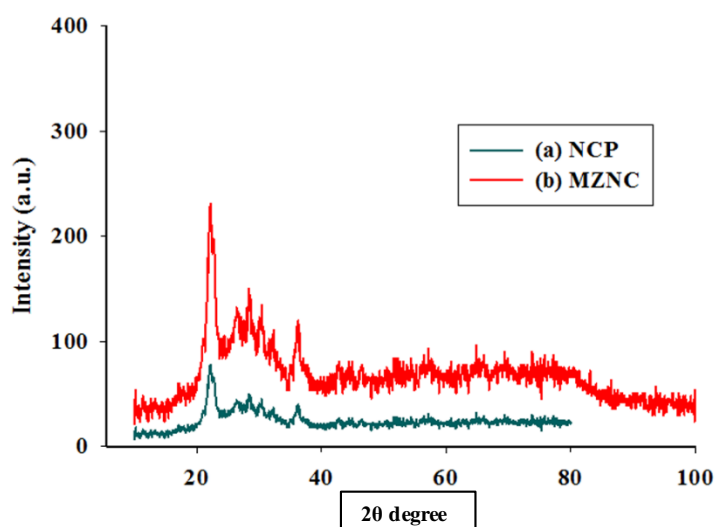


Fig 2. XRD patterns of the nano zeolite (matched with a reference pattern of clinoptilolite) (a), and MZNC (b)

Zeolite and MZNC chemical compositions (Table 1) were obtained by the XRF method. The composite consisted of 19.86 wt.%  $\text{Fe}_2\text{O}_3$ . The Si/Al ratio of the present zeolite sample was 4.85, which was consistent with the previous findings placing the ratio within a range of 4-5.5 [21]. The sum of the exchangeable ions estimated Theoretical Cation Exchange Capacity (TCEC),  $\text{Na}^+$ ,  $\text{K}^+$ ,  $\text{Ca}^{2+}$ , and  $\text{Mg}^{2+}$  in the zeolite included. The disparity between TCEC and Cation Exchange Capacity (CEC) (Table 1) was owing to the fact that some counter-ion sites in the zeolite particles were not available for cation exchange.

Table 1. Chemical compositions of zeolite and MZNC obtained through XRF analysis

	SiO <sub>2</sub>	Al <sub>2</sub> O <sub>3</sub>	Na <sub>2</sub> O	TiO <sub>2</sub>	K <sub>2</sub> O	CaO	MgO
CLI	67.41	11.82	2.66	0.10	2.44	1.31	0.71
MZNC	53.21	9.28	1.92	1.096	1.48	1.25	0.71
	SrO	Fe <sub>2</sub> O <sub>3</sub>	LOI <sup>a</sup>	Total	Si/Al	TCEC <sup>c</sup>	CEC <sup>c</sup>
CLI	0.13	1.32	11.46	99.54	4.85	1.736	1.561
MZNC	n.d. <sup>b</sup>	19.86	12.01	99.81	4.87	1.335	1.218

CLI-clinoptilolite; <sup>a</sup> Loss on ignition; <sup>b</sup> Not detected; <sup>c</sup> (meq g<sup>-1</sup>)

The FT-IR spectra of the samples, zeolite, and composite, were reported under a range of 400-4000 cm<sup>-1</sup> (Fig. 3). Absorption bands of water at 1638 cm<sup>-1</sup> in the range of 3000-3600 cm<sup>-1</sup> confirmed significant hydrations of the zeolite. The band at 1070 cm<sup>-1</sup> was attributed to the

asymmetric stretching vibration modes of the internal T-O bonds in TO<sub>4</sub> tetrahedra (T=Si and Al). The 609 and 465 cm<sup>-1</sup> bands risen from the stretching vibration modes of O-T-O groups and the vibration modes of bending of T-O bonds, respectively [22]. About the zeolite, the regions corresponding to (Si-O and Al-O) and (O-Si-O and O-Al-O) showed strong bands, which indicate an increase within the surface areas and aluminosilicate bonds of the zeolite. The characteristically related band to Fe-O-Fe bond of iron oxide must have appeared at 584 cm<sup>-1</sup> [19].

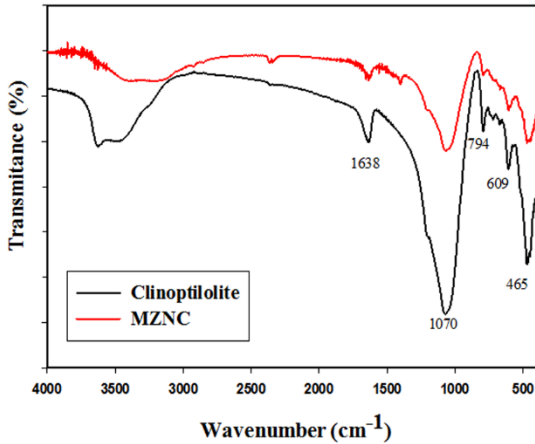


Figure 3. FTIR spectra of clinoptilolite and MZNC

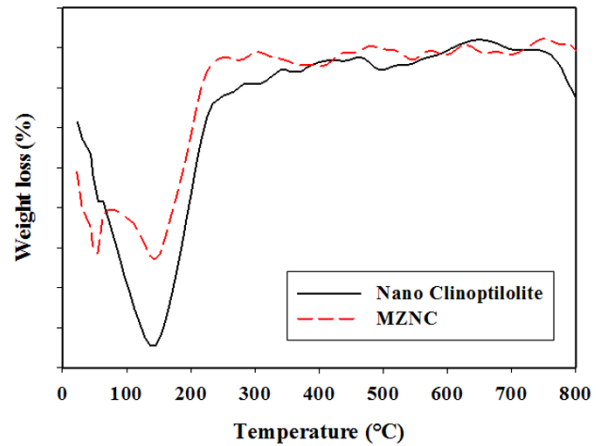
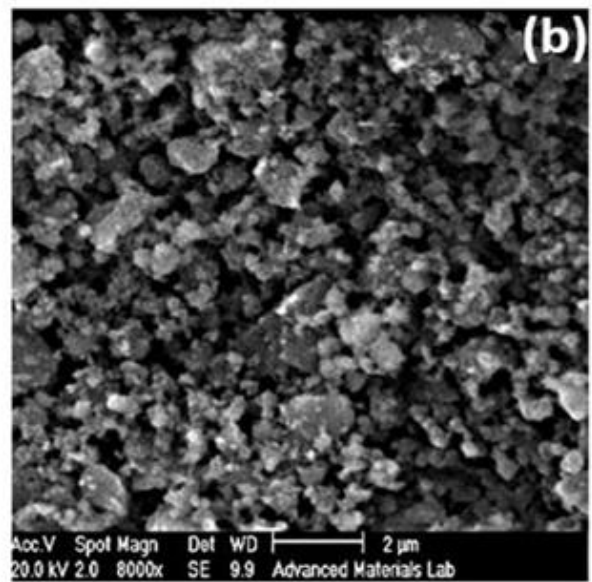
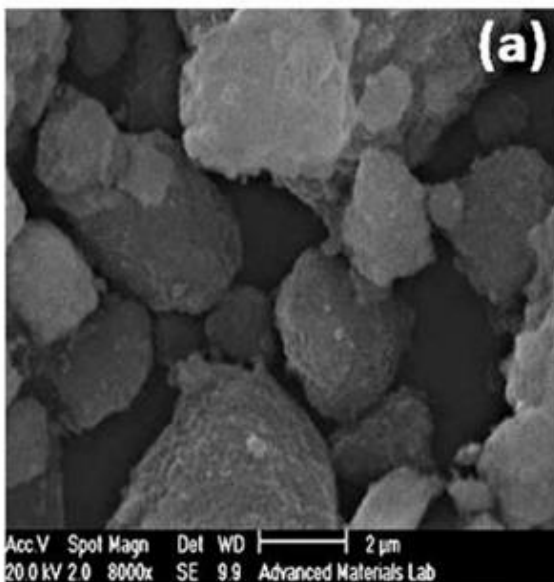


Figure 4. DTG curves of Nano clinoptilolite and MZNC

In the DTG curves of the nano-zeolite clinoptilolite and MZNC, two weight-loss peaks occurring between 50°C and 120°C were assigned to the loss of the adsorbed water Fig. 4. After 280°C, the adsorbents exhibited no dehydration peaks up to 800°C, which means that the samples were thermally stable.

The disparity between the amorphous surface structures of the sample of natural zeolite and nano-zeolite clinoptilolite with a uniform surface was visible in accordance with SEM images Fig 5 (a and b). Owing to the scarcity of monotony and extensive range of particle dimensions, determination of the particle size distribution not be able to accurately carried out for micro-sized clinoptilolite, according to (Fig. 5a), but for nano-sized particles given in Fig 5b. Also, TEM images illustrated iron oxide particles to have been nano-sized and bound to the aluminosilicate framework of nano-zeolite (Fig 5c).



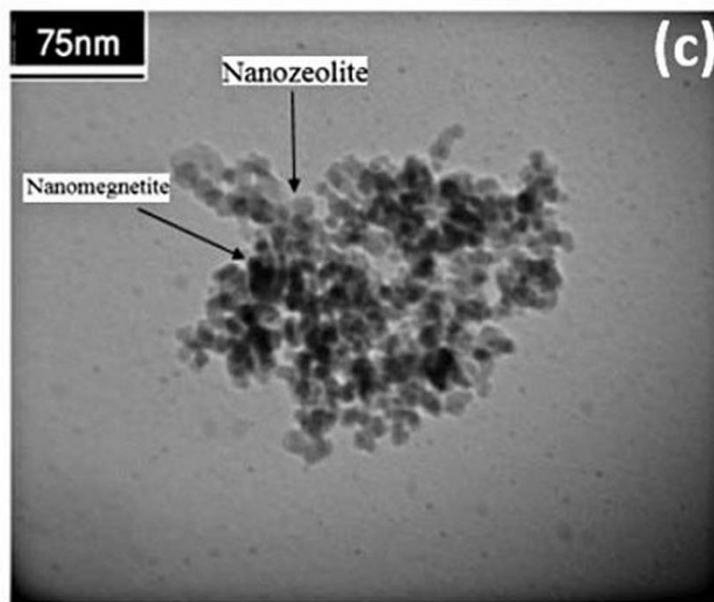


Figure 5 (a, b). SEM images of zeolite clinoptilolite (a) and nano clinoptilolite (b).

Figure 5 (c). The MZNC TEM images

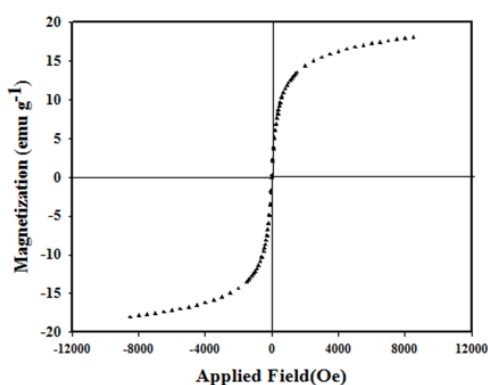


Figure 6. The hysteresis loops of MZNC

This new composite's feature was its magnetic property, which means that it was characterized by a sample of the vibrating magnetometer in this study Fig 6. The magnetic curve illustrated no hysteresis loop and remanence, which indicate the good super-paramagnetic properties of MZNC. The zero amount of remanence certified that the composite had not retained magnetization after being exposed to an external magnetic field and they could be thus re-dispersed after removing the magnetic field. Nanocomposite exhibited the saturation magnetizations of approximately  $19.50 \text{ emu g}^{-1}$  at 298K. This value verified the adequate magnetic properties of MZNC to be appealed by a permanent magnet.

## 3.2. Optimization of conditions

### 3.2.1. Effect of pH

The adsorption of Ru species was at its greatest at pH 2 (Figure. 7), so the present adsorption studies were performed at that pH. The study of electrochemical and spectral on  $\text{RuCl}_3$  in aqueous solution in the pH of 0.4-2.0 have shown that Ru (III) may exist as four major species,  $[\text{RuCl}_4(\text{H}_2\text{O})_2]$ ,  $[[\text{RuCl}_3(\text{H}_2\text{O})_3]$ ,  $[\text{RuCl}_2(\text{H}_2\text{O})_4]^+$ , and/or  $[\text{RuCl}(\text{H}_2\text{O})_5]^{2+}$ . They are referred to here as species 1, 2, 3, and 4, respectively. At pH 2, only species 3 was present [23]. The charge repulsion between the zeolite surface and negatively charged species of Ru at  $\text{pH} < 2.0$  may be one of the reasons for poor adsorption at these pH values. Competition with  $\text{H}_3\text{O}^+$  is another possible reason. At higher pH values, hydroxyl ions are introduced gradually to the coordination sphere and negatively charged Ru complexes are produced.

### 3.2.2. Effect of contact time

The results show that as contact time increased, Ru adsorption increased initially, but then approached a constant value rapidly (Figure. 8). Equilibrium was attained after 24 h, after

which time no further significant increase occurred in the level of adsorption. After just 15 h, 92% of the adsorption amount at equilibrium had been achieved. A shaking time of 24 h employed for all of the equilibrium adsorption studies was sufficient to ensure that adsorption equilibrium was reached.

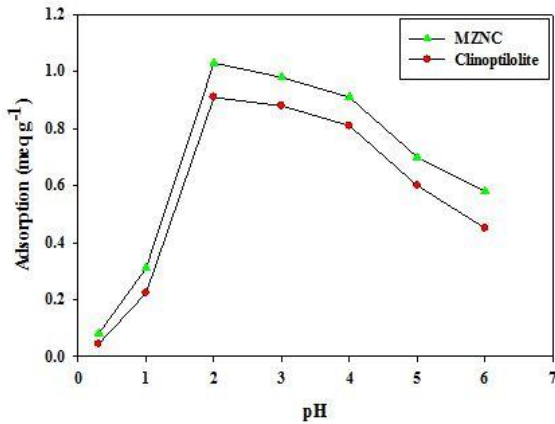


Figure 7. pH effect on sorption of Ru

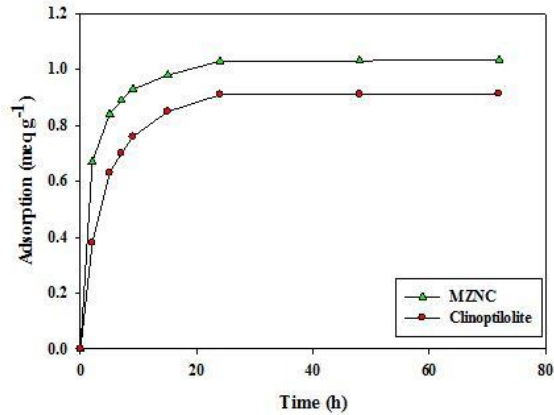


Figure 8. Contact time effect on adsorption of Ru onto clinoptilolite and MZNC

### 3.3. Adsorption kinetics and thermodynamics

The kinetics of adsorption was evaluated by applying four different models including the pseudo-first-order equation, the pseudo-second-order equation, Elovich equation, and intra-particle diffusion model. These models were tested to fit experimental data obtained by batch experiments.

The pseudo-first-order equation is generally expressed as follows:

$$\ln (q_e - q_t) = \ln q_e - k_1 t \tag{2}$$

where  $q_e$  and  $q_t$  are the ions adsorbed amount per unit mass of the adsorbent at equilibrium and at any time  $t$ , respectively and  $k_1$  is the rate constant of pseudo-first-order sorption ( $\text{min}^{-1}$ ).

The values of  $k_1$  and  $q_e$  were regulated from the slope and the intercept of plotting of  $\log (q_e - q_t)$  vs.  $t$ . The results are listed in Table. 2. Although no extremely low values were obtained for R2, the calculated  $q_e$  was not consistent with that of experimental data. Hence, the adsorption process did not follow a pseudo-first-order model. The linear form of the pseudo-second-order kinetic model is written as follow:

$$t/q_t = 1/(k_2 q_e^2) + (1/q_e)t \tag{3}$$

The initial sorption rate can be calculated by the following formula:

$$h = k_2 q_e^2 \tag{4}$$

where  $k_2$  is the rate constant of pseudo-second-order kinetic sorption ( $\text{g/mg/min}$ ). The calculated values of  $k_2$ ,  $q_e$ , and  $h$  values and the correlation coefficients (R2) are listed in table 2. The comparison of  $k_2$  values indicated faster ion adsorption onto MZNC is faster than on clinoptilolite.

Table 2. Kinetic parameters of pseudo-first-order and pseudo-second-order kinetic models

sorbents	$q_e$ (exp.) ( $\times 10^{-1}$ ) ( $\text{meq g}^{-1}$ )	pseudo-first-order model			pseudo-second-order model			
		$k_1$ ( $\times 10^{-1}$ ) ( $\text{h}^{-1}$ )	$q_e$ (theor.) ( $\times 10^{-1}$ ) ( $\text{meq g}^{-1}$ )	R <sup>2</sup>	$k_2$ ( $\text{meq}^{-1} \text{h}^{-1}$ )	$q_e$ ( $\times 10^{-1}$ ) ( $\text{meq g}^{-1}$ )	$h$ ( $\times 10^{-1}$ ) ( $\text{meq g}^{-1} \text{h}^{-1}$ )	R <sup>2</sup>
Clinoptilolite	9.1	1.775	77.49	0.9868	0.4695	9.4993	4.2366	0.9994
MZNC	10.3	1.881	63.02	0.9132	0.8468	10.5407	9.4085	0.9999

### 3.3.1. Sorption thermodynamics

The effect of sorption temperature on Ru removal was investigated at five different temperatures. The adsorption capacity enhanced with increasing temperature (Fig 9). The thermodynamic parameters, including enthalpy change ( $\Delta H^\circ$ ) and entropy change ( $\Delta S^\circ$ ), can be obtained using the Van't Hoff equation.

$$\ln K_d = - (\Delta H^\circ/RT) + (\Delta S^\circ/R) \tag{5}$$

A plot of  $\ln K_d$  vs.  $1/T$  is shown in Fig 10. The free energy change of the adsorption ( $\Delta G^\circ$ ) is calculated as follows:

$$\Delta G^\circ = \Delta H^\circ - T\Delta S^\circ \tag{6}$$

The calculated thermodynamic parameters are summarized in Table 3. Since  $\Delta H^\circ$  values are positive, the adsorption process is endothermic in nature.

Table 3. Thermodynamic parameters of Ru adsorption

Sorbent	$\Delta H^\circ$ (kJ/mol)	$\Delta S^\circ$ (kJ/mol/K)	$\Delta G^\circ$ (kJ/mol)			
			298(K)	313(K)	328(K)	343(K)
CLI	2.312	29.74	-6.55	-6.99	-7.44	-7.88
MZNC	3.744	30.99	-5.49	-5.95	-6.42	-6.88

CLI- clinoptilolite

The positive values of  $\Delta S^\circ$  suggested that the randomness at the solid/solution interface had increased during the sorption process. The negative values of  $\Delta G^\circ$  indicated that Ru adsorption reaction was spontaneous. The decrease in  $\Delta G^\circ$  values with increasing temperature showed that the spontaneous nature of sorption was directly proportional to temperature. Therefore, the adsorption process was favored when the temperature was augmented. The greater absolute values of  $\Delta G^\circ$  for MZNC compared to clinoptilolite revealed that the adsorption of the former on Ru had been more favored.

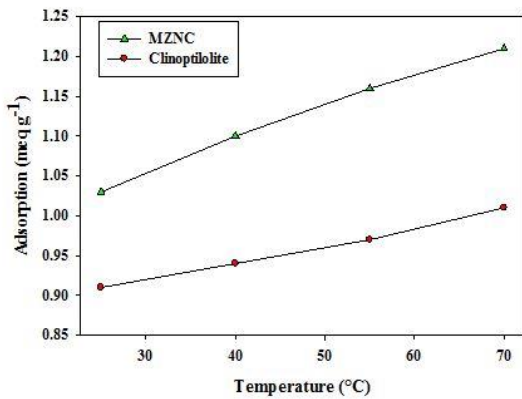


Figure 9. Temperature effect on Ru adsorption onto clinoptilolite and MZNC

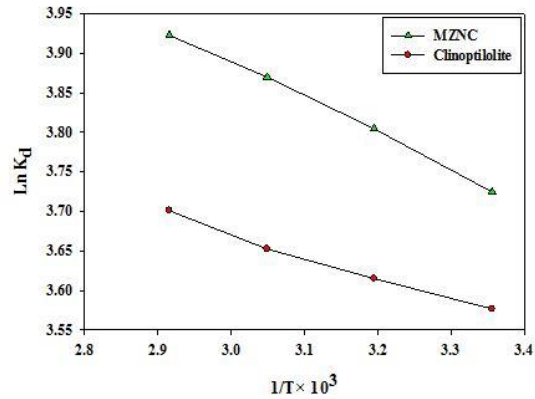


Figure 10. Van't Hoff plot for adsorption of Ru

### 3.3.2. Sorption isotherm

To investigate the effect of initial concentration, various concentrations of Ru solution were equilibrated with constant amounts of the adsorbents (Fig 11). The initial fast adsorption was followed by a slow approach to equilibrium at a higher concentration. Three isotherm models, including Langmuir, Freundlich, and Dubinin-Radushkviech (D-R) models were employed to examine the experimental data.

### 3.3.3. Langmuir isotherm model

Langmuir isotherm assumes that the sorption occurs at specific homogeneous sites within the adsorbent. This model is expressed by:

$$C_e/q_e = 1/(Q_0b) + C_e/Q_0 \tag{7}$$

where  $Q_0$  denotes the saturation adsorption capacity (mg/g), and  $b$  represents the Langmuir constant related to the free energy of adsorption calculated from the slope and intercept (Table 4). The plot of  $C_e/q_e$  vs.  $C_e$  is shown in Fig 12. The important parameter of Langmuir isotherm is the dimensionless constant,  $RL$ , which can be calculated as follows:

$$R_L = 1 / (1 + bC_0) \tag{8}$$

where  $C_0$  stands for the highest initial metal ion concentration (mg/L).

Table 4. Adsorption isotherm parameters for Ru adsorption

Isotherm	Sorbent	Model parameters			
		$Q_0$ (mg/g)	$b \times 10^3$ (L/mg)	$RL \times 10^3$	$R^2$
Langmuir	Clinoptilolite	131.4	19.849	0.01	0.7812
	MZNC	405.5	43.759	0.045	0.9998
Freundlich	Sorbent	Model parameters			
		$n$	$K_f$ (mg/g)	$R^2$	
Freundlich	Clinoptilolite	0.152	262.84	0.9524	
	MZNC	0.336	928.53	0.9644	
D-R	Sorbent	Model parameters			
		$\beta \times 10^{-9}$ (mol <sup>2</sup> /kJ <sup>2</sup> )	$q_m$ (mmol/g)	$E$ (kJ/mol)	$R^2$
D-R	Clinoptilolite	6.38	2.974	12.7	0.9970
	MZNC	8.45	3.126	16.0	0.9530

The values of this parameter indicate the unfavorable ( $RL > 1$ ), linear ( $RL = 1$ ), favorable ( $0 < RL < 1$ ), and irreversible ( $RL = 0$ ) types of the adsorption isotherm.

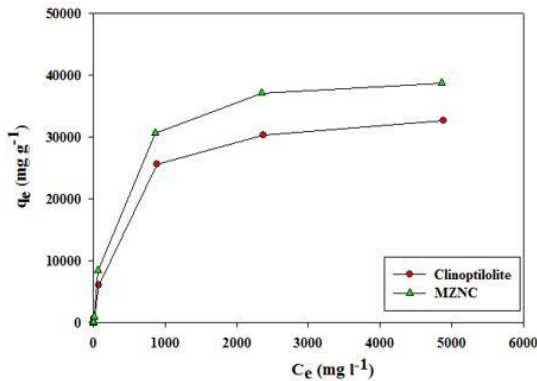


Figure 11. Different initial ion concentration effect on Ru adsorption onto clinoptilolite and MZNC

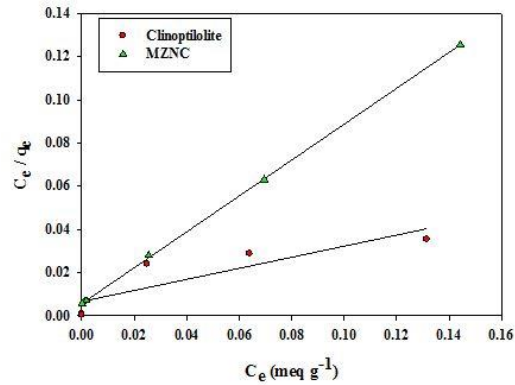


Figure 12. Langmuir isotherm plots for adsorption of Ru onto clinoptilolite and MZNC

### 3.3.4. Freundlich isotherm model

Freundlich isotherm model makes the assumption that multi-layer sorption occurs at a heterogeneous surface. This model was used to estimate the intensity of the adsorption process and the relative sorption capacity. A linear form of the Freundlich equation is shown as follows:

$$\log q_e = \log K_f + 1/n \log C_e \tag{9}$$

where  $K_f$  denotes the Freundlich constant relevant to the adsorbent capacity, and  $n$  displays the constant related to the intensity of the adsorption process.

The Freundlich isotherm is shown in Fig 13, and their constants are represented in Table 4. The Freundlich constant ( $n$ ) was greater than its unity, indicating that an increasing tendency of the adsorption process had occurred with the elevation of ion concentration.  $K_f$  value of MZNC was higher compared to clinoptilolite, corroborating a greater adsorption tendency of the adsorbents towards MZNC.

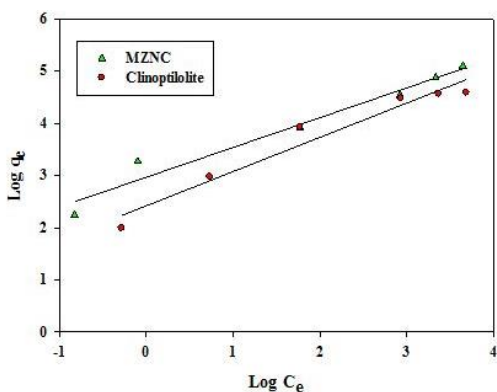


Figure 13. Freundlich isotherm plots for adsorption of Ru onto clinoptilolite and MZNC

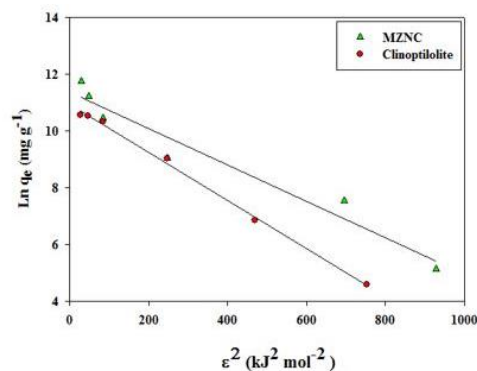


Figure 14. D-R isotherm plots for adsorption of Ru onto clinoptilolite and MZNC

### 3.3.5. Dubinin–Radushkviech isotherm model

D–R isotherm was used to distinguish between the physical and chemical adsorptions of the ions and estimate the apparent free energies of adsorption. The related equation is given as follows:

$$\ln q_e = \ln q_m - \beta \varepsilon^2 \quad (10)$$

where  $q_m$  is the maximum adsorption capacity (mequiv/g),  $b$  is the D–R constant related to the sorption energy ( $\text{mol}^2/\text{K/J}^2$ ), and  $e$  is the Polanyi potential:

$$\varepsilon = RT \ln(1 + 1/C_e) \quad (11)$$

where  $R$  is the gas constant ( $\text{kJ}\cdot\text{mol}^{-1}\cdot\text{K}$ ), and  $T$  is the absolute temperature (K).

The D–R isotherm is plotted in Fig. 14 and the obtained parameters are represented in Table 5. In a solution, when 1 mol of an ion is transferred to the surface of an adsorbent from infinity, its free energy is called the mean energy of adsorption ( $E$ ), which is calculated as follows:

$$E = (2\beta)^{-1/2} \quad (12)$$

The magnitude of  $E$  within a range of 8–16 kJ/mol demonstrates that the sorption process is done through an ion exchange interaction. The reaction mechanism can be related to the magnitude of  $E$ . When  $E$  value is within the range of 8–16 kJ/mol, the sorption process is followed by ion exchange, but when  $E < 8.0$  kJ/mol, physical forces are responsible for the process [25].

## 4. Conclusion

The magnetite-zeolite nano- composite was synthesized, characterized, and evaluated for Ru removal from aqueous solutions. The nano-composite represented a high cation exchange capacity, high selectivity towards Ru, and rapid adsorption kinetics as compared to the zeolite itself. The nano-composite displayed a 34.9% increase in adsorption capacity. The results of the kinetic studies suggested that the initial sorption rate and rate constant were greater when using the nano-composite instead of the zeolite. The VSM results verified the sufficient magnetic strengths of the nanocomposite to be attracted by a magnetic field. The Pseudo-Second Order model gave a better correlation with the experimental kinetic data compared to the pseudo-first-order model, confirming the dominant process of the chemical sorption. The values of the thermodynamic parameters demonstrated the endothermic and spontaneous natures of the adsorption process.

## References

- [1] Sharma P, Sharma M, Tomar R. Na-HEU zeolite synthesis for the removal of Th (IV) and Eu (III) from aqueous waste by a batch process. *Journal of the Taiwan Institute of Chemical Engineers*. 2013; 44(3):480–8.
- [2] Mohseni-Bandpi A, Al-Musawi TJ, Ghahramani E, Zarrabi M, Mohebi S, Vahed SA. Improvement of zeolite adsorption capacity for cephalixin by coating with magnetic Fe<sub>3</sub>O<sub>4</sub> nanoparticles. *Journal of Molecular Liquids*. 2016; 218: 615–24.

- [3] Ltaief OO, Siffert S, Fourmentin S, Benzina M. Synthesis of Faujasite type zeolite from low grade Tunisian clay for the removal of heavy metals from aqueous waste by batch process: Kinetic and equilibrium study. *Comptes Rendus Chimie*. 2015; 18(10):1123-33.
- [4] Gupta P, Khanday WA, Majid SA, Kushwa V, Tomar SS, Tomar R. Study of sorption of metal oxoanions from waste water on surfactant modified analog of laumontite. *Journal of Environmental Chemical Engineering*. 2013; 1(3):510-5.
- [5] Kabiri-Tadi M, Faghihian H. Removal of ruthenium from aqueous solution by clinoptilolite. *Clays and Clay Minerals*. 2011; 59(1):34-41.
- [6] Kong S, Wang Y, Zhan H, Yuan S, Yu M, Liu M. Adsorption/oxidation of arsenic in groundwater by nanoscale Fe-Mn binary oxides loaded on zeolite. *Water Environment Research*. 2014; 86(2):147-55.
- [7] Moamen OA, Ismail IM, Abdelmonem N, Rahman RA. Factorial design analysis for optimizing the removal of cesium and strontium ions on synthetic nano-sized zeolite. *Journal of the Taiwan Institute of Chemical Engineers*. 2015; 55:133-44.
- [8] Noli F, Buema G, Misaelides P, Harja M. New materials synthesized from ash under moderate conditions for removal of toxic and radioactive metals. *Journal of Radioanalytical and Nuclear Chemistry*. 2015; 303(3):2303-11.
- [9] Cretescu I, Soreanu G, Harja M. A low-cost sorbent for removal of copper ions from wastewaters based on sawdust/fly ash mixture. *International Journal of Environmental Science and Technology*. 2015; 12(6):1799-810.
- [10] De Haro-Del Rio DA, Al-Joubori S, Kontogiannis O, Papadatos-Gigantes D, Ajayi O, Li C, Holmes SM. The removal of caesium ions using supported clinoptilolite. *Journal of hazardous materials*. 2015; 289:1-8.
- [11] Nezamzadeh-Ejhieh A, Salimi Z. Heterogeneous photodegradation catalysis of o-phenylenediamine using CuO/X zeolite. *Applied Catalysis A: General*. 2010; 390(1-2):110-8.
- [12] Song W, Li G, Grassian VH, Larsen SC. Development of improved materials for environmental applications: Nanocrystalline NaY zeolites. *Environmental science & technology*. 2005; 39(5):1214-20.
- [13] Charkhi A, Kazemian H, Kazemini M. Optimized experimental design for natural clinoptilolite zeolite ball milling to produce nano powders. *Powder technology*. 2010; 203(2):389-96.
- [14] Chu X, Li X, Dong Y, Qiao H, Bai L. Preparation of Nano-SnO<sub>2</sub> Abrasives and Their Application in Chemical Mechanical Polish of Ruthenium. *Rare Metal Materials and Engineering*. 2013; 42(4):692-5.
- [15] Patra D, Chaaban AH, Darwish S, Saad HA, Nehme AS, Ghaddar TH. Time resolved study of three ruthenium (II) complexes at micellar surfaces: A new long excited state lifetime probe for determining critical micelle concentration of surfactant nano-aggregates. *Colloids and Surfaces B: Biointerfaces*. 2016; 138: 32-40.
- [16] Nezamzadeh-Ejhieh A, Raja G. Modification of nanoclinoptilolite zeolite with hexadecyltrimethylammonium surfactant as an active ingredient of chromate-selective membrane electrode. *Journal of chemistry*. 2013.
- [17] Nezamzadeh-Ejhieh A, Zabihi-Mobarakeh H. Heterogeneous photodecolorization of mixture of methylene blue and bromophenol blue using CuO-nano-clinoptilolite. *Journal of Industrial and Engineering Chemistry*. 2014; 20(4): 1421-31.
- [18] Maity D, Agrawal DC. Synthesis of iron oxide nanoparticles under oxidizing environment and their stabilization in aqueous and non-aqueous media. *Journal of Magnetism and Magnetic Materials*. 2007; 308(1): 46-55.
- [19] Klug HP, Alexander LE. X-ray diffraction procedures: for polycrystalline and amorphous materials. *X-Ray Diffraction Procedures: For Polycrystalline and Amorphous Materials*, 2nd Ed, Wiley-VCH 1974; P.992.
- [20] Breck DW. Zeolite molecular sieves: structure, chemistry and use. Krieger; 1984.
- [21] Jacobs PA, Flanigen EM, Jansen JC, van Bekkum H. Introduction to zeolite science and practice. Elsevier; 2001 Jun 26.
- [22] Taqui Khan MM, Ramachandraiah G, Rao AP. Ruthenium (III) chloride in aqueous solution: electrochemical and spectral studies. *Inorganic Chemistry*. 1986; 25(5): 665-70.
- [23] Mohan D, Chander S. Single, binary, and multicomponent sorption of iron and manganese on lignite. *Journal of Colloid and Interface Science*. 2006; 299(1): 76-87.
- [24] Helfferich FG, Dranoff JS. Ion Exchange. McGraw-Hill, New York. 1962: P.624.

*To whom correspondence should be addressed: Leila Eskandari, Faculty of Chemical Engineering, Urmia University of Technology, Urmia, Iran*

## HYDROGENATION OF LIQUID HYDROCARBON FRACTIONS FOR PRODUCTION OF NON-CONVENTIONAL DIESEL FUEL

*András Peller, Boris Jambor, Elena Hájeková\*, Pavol Hudec, Marcela Hadvinová, Michal Horňáček*

*SLOVAK UNIVERSITY OF TECHNOLOGY in Bratislava, Faculty of Chemical and Food Technology, Institute of Organic Chemistry, Catalysis and Petrochemistry, Radlinského 9, 812 37 Bratislava, Slovak Republic*

Received September 17, 2018; Accepted October 19, 2018

---

### Abstract

Study of kinetics during hydrogenation of hydrocarbon fractions prepared by pyrolysis of waste plastic is presented. Fractions were separated by distillation from oily/wax depolymerizates obtained during pyrolysis of polyethylene and polypropylene from end-of-life vehicles at 450°C in the batch reactor. The hydrogenation of liquid fractions in the boiling range of diesel was studied as a way of upgrading before their addition into fossil diesel fuels. Optimized experimental conditions of hydrogenation and optimized conditions for chromatographic separation are reported. The success rate of hydrogenation based on the alkane/alkene ratio in the samples after hydrogenation was evaluated by chromatography and by IR spectroscopy. Finally, the selected properties prescribed in fuel standards before and after hydrogenation are compared.

**Keywords:** *polyalkene recycling; hydrogenation; diesel fuel; kinetic study; used cars.*

---

## 1. Introduction

The global energy sector, as well as the economy, is still largely based on non-renewable fossil fuels (oil, natural gas, coal). Growth in oil prices creates favourable conditions for renewable energy and recycling technologies. An increasingly important area of recycling technology is becoming waste plastics processing technology, which reflects the fact that the amount of waste plastics produced (50% of annual plastic production: 150 million tonnes [1]) has only a smaller value than the annual production of medium-range petroleum distillates (world-wide daily production [2]).

Interesting is the situation in the automotive industry. In the EU countries, approximately 6 million cars per year become a feedstock for recycling due to the end of their life [3]. The weight of plastic in one car in 2010 amounted to 130 kg, and this number is steadily growing. EU legislation, which came into force on 1 January 2015, aims to increase the recyclability of car parts after the end of life up to 95% of the weight of the vehicle. Polypropylene (17%) and polyethylene (4%) make up the second largest proportion of different types of plastics used in the automotive industry [4]. It is generally known that polyalkenes are the most suitable raw materials for chemical conversion to automotive fuels or chemical feedstock [5].

Pyrolysis, thermal decomposition in the absence of oxygen and the absence of catalysts is a known and technologically controlled process of chemical conversion of polyalkenes to motor fuels [6]. The disadvantage of pyrolysis is the dependence of the quality and amount of individual pyrolysis fractions on the properties of polyalkenes, the type and amount of auxiliary compounds present (e.g., fillers, stabilizers), pyrolysis reactor parameters and pyrolysis conditions [7]. The products of cracking of waste polyalkenes have an unsaturated character and, depending on the additives used in the manufacture of plastics, may also contain sulphur or nitrogen compounds [5, 8].

Hydro-refining belongs to the chemical refining processes which remove unwanted substances from the hydrocarbon fractions. The bonds contained in the unsaturated hydrocarbons are saturated during hydrogenation using suitable catalysts in a hydrogen atmosphere. The unsaturated hydrocarbons are changed to saturated, cyclopentanes are converted to isoalkanes, and the aromatics are hydrogenated to cyclohexanes. The rings are gradually saturated and opened in polycondensed aromatics. Oxygenates, sulphates and nitrogenous substances change gradually through hydrogenation to hydrocarbons, water, sulphate, and ammonia. It is easier to decompose the oxygen and the worst the nitrogen contained substances. The course of the reactions strongly depends on the hydrogenation reaction conditions and the type of used catalyst. The hydrogenation components of the catalysts are metals (Pt, Pd, Ni, Co), their oxides and sulphides. Hydrogenation refinements of the light products are carried out in the vapour phase, liquid or mixed phase. Working conditions may vary depending on the raw material, catalyst, and quality requirements.

Diesel fuels are produced from crude oil fractions, which do not contain unsaturated hydrocarbons. In the case of addition of liquids prepared by pyrolysis of plastics to the diesel fraction, unsaturated hydrocarbons formed during thermal decomposition will decrease the cetane number and worsen colour and oxidation stability of the fuel mixture. For this reason, we have studied the kinetics of hydrogenation of unsaturated hydrocarbons present in products after pyrolysis of waste polyalkenes. The results of hydrogenation should be the better colour stability of liquid motor fuel, smell, and better combustion properties.

## 2. Experimental

### 2.1. Feedstock

Waste polyethylene (PE) and polypropylene (PP) derived from used cars were used for feedstock recycling by pyrolysis in a batch reactor at 450°C. Obtained oil/wax liquid products were separated into fractions by laboratory distillation apparatus. The liquid depolymerizates were first fractionated under atmospheric pressure up to 180°C. Distillation of the residue continued under reduced pressure (1.9 kPa) up to the distillation temperature of 190°C, what corresponds to the temperature of 330°C after calculation to the atmospheric pressure. Prepared distillation fractions with the boiling range of 180 to 330°C correspond to the diesel fuel range, and they were used for subsequent hydrogenation reactions. The detailed description of the laboratory reactor is given in study [5].

### 2.2. Hydrogenation

The hydrogenation was carried out in a batch, mechanically stirred (magnetic transfer, stirrer) pressure reactor. Reactor with volume approx. 100 mL was electrically heated in the shell, and they had a bottom outlet valve with a built-in sampling filter. A powdered hydrogenation catalyst of 3.5% palladium on charcoal was used, which was activated at 300°C for 3 hours before the reaction. Optimized conditions of hydrogenation for individual samples are shown in Tab. 1.

Table 1. Optimized hydrogenation conditions

Parameter / sample	PE	PP
Sample weight, g	55 and 34	50 and 39
Catalyst weight, g	3 and 2	6, 6.6 and 5
Reaction temperature, °C		110 – 120
Reactor pressure, MPa		1.77 – 2.16
Reaction time, h	5 and 6	13 and 14.5
Stirrer speed, rpm		600 – 1100

### 2.3. Gas chromatography

For the analysis of the liquid samples, the Agilent Technologies 7890A GC gas chromatograph with FID detector and HP-5 capillary column (30 m x 0.32 mm, 0.25 µm) was used. A

linear temperature program from 30°C with a ramp of 5°C/min to 200°C and a ramp of 8°C/min to 330°C was applied. Amount of sample represented 0.2 µL, and it was injected into the split/splitless inlet heated to 350°C. For selected samples, components were identified by mass spectrometry (MS, Agilent Technologies, MS 5975C).

## 2.4. FTIR spectroscopy

Infrared spectra were obtained using a Genesis FTIR spectrometer (Mattson-Unicam) in the 400-4000 cm<sup>-1</sup> wavelength range (64 scans, 4 cm<sup>-1</sup>). Liquid samples were measured in a KBr cell of 0.1 mm thickness and thoroughly washed with anhydrous solvents before measurements.

## 3. Results and discussion

### 3.1. Kinetics of hydrogenation

The change in composition and the decrease in the double bond content of the PE and PP samples during hydrogenation was monitored by gas chromatography (GC) using optimized conditions for a good separation of components in liquids. During the hydrogenation, small amounts of sample were taken at regular intervals for GC analysis. For PE liquids, samples were analysed at 1, 2, 3, 4 and 5 hours after the start of the reaction, and the resulting product after approx. 5.33 hours of hydrogenation (PEH). It was more difficult to hydrogenate the liquid from PP pyrolysis under the given conditions. For the analysis of the decrease of the double bonds, sampling was used for longer periods of time: after 2, 4, 6, 8 and 9.25 hours from the start of the hydrogenation and the resulting hydrogenate after 14 hours of reaction (PPH).

The peaks of the unsaturated compounds and their saturated counterparts were selected from the first part (so-called light hydrocarbons) and from the last part (so-called heavier portions) of the chromatogram which have the same number of carbon atoms. These compounds were identified with great certainty based on MS spectrometry and based on available chromatographic data for a similar mixture of compounds from pyrolysis [9]. The peaks of the compounds with the highest weight, meeting the above conditions were also observed and identified. The identified compounds and their retention times are listed in the Tab. 2 and Tab. 3.

Table 2. Identified compounds for monitoring kinetics of PE products hydrogenation

	Label	Retention time /min	Compound	Molecular formula	Mole weight / g mol <sup>-1</sup>
Light fraction	PE1	7.30 – 7.32	<i>1-decene</i>	C10H20	140.27
	PE2	7.53 – 7.55	<i>decane</i>	C10H22	142.28
	PE3	7.69 – 7.72	<i>2-decene</i>	C10H20	140.27
	PE4	7.93 – 7.95			
Main fraction	PE5	21.18 – 21.19	<i>1-pentadecene</i>	C15H30	210.24
	PE6	21.39 – 21.42	<i>pentadecane</i>	C15H32	212.25
	PE7	21.49 – 21.52	<i>2-pentadecene</i>	C15H30	210.24
	PE8	21.73 – 21.76			
Heavy fraction	PE9	35.75 – 35.77	<i>1-docosene</i>	C22H44	308.34
	PE10	35.85 – 35.86	<i>docosan</i>	C22H46	310.36
	PE11	35.91 – 35.94	<i>2-docosene</i>	C22H44	308.34
	PE12	36.13 – 36.15			

The variations in the peak area of the test compounds during hydrogenation are shown in Fig. 1. Alkene peak areas are clearly declining with the time of hydrogenation, on the contrary, the areas of the peaks of the counterpart alkanes in the case of PE are growing. From the signal intensities for the different chromatogram areas, it can be seen that the peak of the compounds at the beginning and at the end of the chromatogram are significantly smaller than the peak intensities of the compounds with the largest proportion. Also, from the similarity of peaks at the beginning and end of the chromatogram, a certain symmetry of the distribution and the peak heights of the compounds results. This is obvious in the case of a PE

sample where the intensity of the main alkanes/alkene peak drops predictably with a decreasing number of carbons from the most intense alkane (C15) and the increasing number of carbon from the most intense alkane (C15). The more complex is the chromatogram for the PP sample, which can also be seen in Fig. 1 for the heavy fraction of PP. This is caused by a larger number of formed mainly branched alkanes and alkenes.

Table 3. Identified compounds for monitoring kinetics of PP products hydrogenation

	Label	Retention time /min	Compound	Molecular formula	Mole weight/g mol <sup>-1</sup>
Light fraction	PP1	12.70 – 12.72	<i>2,4,6-trimethyl-1-nonene</i>	C <sub>12</sub> H <sub>24</sub>	168.32
	PP2	12.81 – 12.83	<i>2,4,6-trimethyl-1-nonene</i>		
Main fraction	PP3	18.99 – 19.03	<i>2,4,6,8-tetramethyl-1-undecene</i>	C <sub>15</sub> H <sub>30</sub>	210.40
	PP4	19.20 – 19.23	<i>2,4,6,8-tetramethyl-1-undecene</i>		
	PP5	19.44 – 19.46	<i>2,4,6,8-tetramethyl-1-undecene</i>		
Heavy fraction	PP6	29.08 – 29.11	<i>2,4,6,8,10,12-hexamethyl-1-pentadecene</i>	C <sub>21</sub> H <sub>42</sub>	294.56
	PP7	29.67 – 29.71	<i>C21-olefine</i>		
	PP8	30.33 – 30.38	<i>C21-olefine</i>		

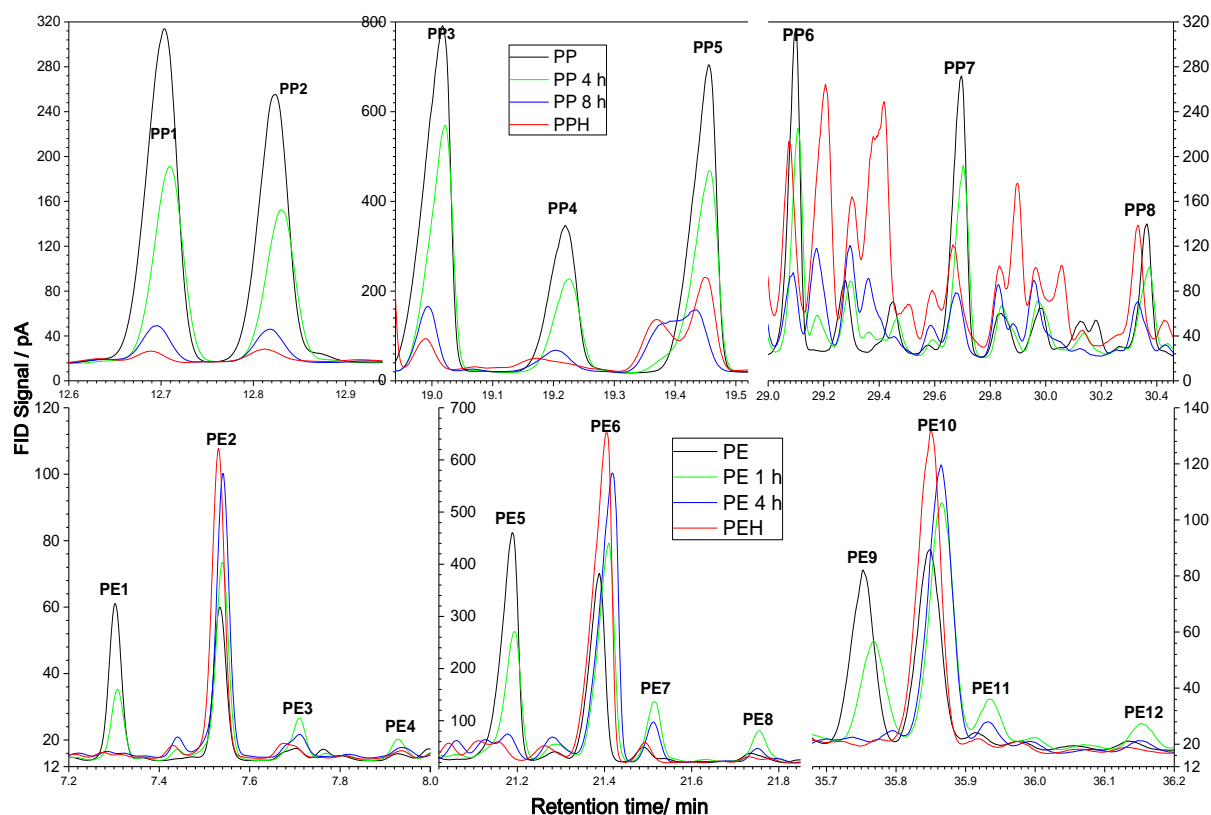


Figure 1. Intensities of selected peaks with increasing hydrogenation time for PE liquid hydrogenation (below) and PP samples (top)

The kinetics of hydrogenation of the PE sample was processed using the time-dependent conversion of a number of alkenes with a given number of carbon to the corresponding alkane ( $X_{\text{alkene}}$ ). We calculated the  $X_{\text{alkene}}$  values based on the sum of the peak areas of the selected

alkenes with the same number of carbons (in particular for C10, C15, C22) to the peak area of the corresponding alkane. In the case of PE, they are all linear hydrocarbons. Another characteristic for hydrogenation kinetics, even in the case of a PP sample, was the time dependence of alkenes with a given number of carbons expressed as a percentage by weight ( $w$ ). We obtained  $w$  values by the sum of the area of the selected alkenes with the same number of carbon atoms (C10, C15, C22 for PE and C12, C15, C21 for PP) to the total area of all peaks of the sample.

The rapid drop in double bonds during PE hydrogenation correlates with a decrease in the ratio of alkenes to alkane  $X_{\text{alkene}}$ . Alkene predominates before hydrogenation; for C15, about 56 % is alkene; for C10 the ratio is equal. At the end of the hydrogenation, the alkene content of the C10, C15 and C22 carbons is less than 10 %. A similarly strong decrease is also observed with the percentage of alkenes ( $w$ ) C10, C12, and C22. These experimental dependencies except  $w$  (C22) can be reliably described by exponential trends with a correlation coefficient greater than 0.96. This indicates the overall behaviour of the kinetics of C10 and C12 alkenes hydrogenation occurs according to the first order. Hydrogenation of longer C22 chains shows different kinetics, a slight increase in hydrogenation rate can be seen on the  $w$  (C22) curve, after 6 hours there is a break and a more severe decrease in the double bond content.

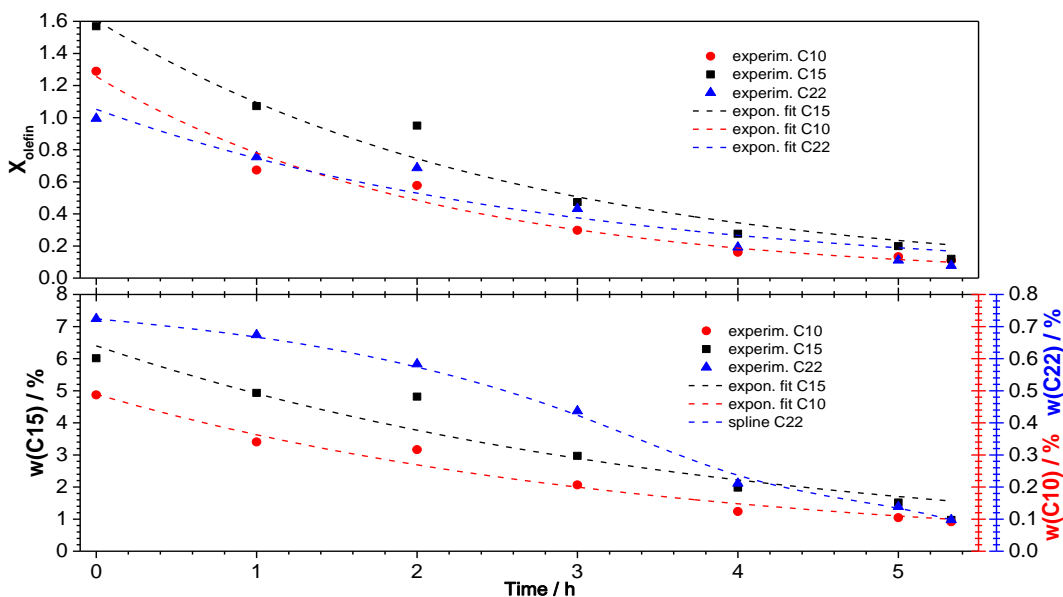


Figure 2. Kinetics of hydrogenation of the PE sample based on  $X_{\text{alkene}}$  and  $w$

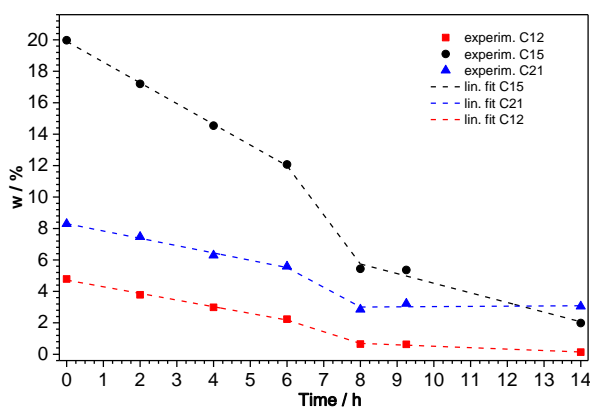


Figure 3. Kinetics of PP hydrogenation based on  $w$  values

Unlike the PE sample, kinetics of hydrogenation of the PP sample were studied only based on  $w$  values. The mass fraction of each selected alkenes is much larger than for a similar number of carbon in the case of PE. From the point of view of the trend of the double bond kinetics, the PP sample manifests itself as according to the kinetics of the zero order. It shows the linear character of the decrease of the double bonds with the time of hydrogenation (correlation coefficient greater than 0.92). At 6 hours there is a break and then continues again with a linear decrease in character. Evidently, it results from the  $w$  values that the hydrogenation of the PP sample compared to the hydro-

genation of the PE sample is significantly slower. While the average number of selected double bonds of PP samples drops after 6 hours of hydrogenation by 42 %, in the case of PE samples, this drop by 49 % in only 3 hours of hydrogenation.

### 3.2. Overall assessment of hydrogenation

The success of hydrogenation can be evaluated based on a change in the total alkene/alkane ratio for selected PE compounds and by the decrease in weight fraction of selected alkenes before and after hydrogenation (both samples PE and PP). If we calculate the  $X_{\text{alkene}}$  value (Figure 2, above) for all selected compounds of the PE sample, we arrive at the total ratio of the selected alkene / selected alkanes. This ratio represents 1.46 for the original, non-hydrogenated sample PE, i.e., about 50 % more is alkenes per the corresponding alkane. At the end of the hydrogenation, this ratio drops to 0.11, meaning that the alkanes already prevailed. A similar decrease is observed in the total weight ratio of double bonds ( $w$ , analogously to Fig. 2), where before hydrogenation it is 7.2 % and after completion of hydrogenation 1.2 %. Thus, a 90% reduction in the weight fraction of the selected alkenes at the end of the hydrogenation is observed. A similar trend is shown by hydrogenation of the PP sample, where the weight fraction of the selected alkenes before hydrogenation is 33.1 % and at the end of the hydrogenation is 5.2 %, representing an 84 % decrease in selected double bonds.

The degree of hydrogenation of both PE and PP samples was also controlled by IR spectra. As a standard to verify the effect of the presence of double bond on the FTIR spectra, 1-tridecene was used, the spectra of which were compared to the alkane n-tridecane. Fig. 4 clearly shows the bands that occur in the FTIR spectra when one double bond is introduced at the 1-position into the n-alkane. For both the alkane and the alkene spectra, common intensive bands at 2800-3000  $\text{cm}^{-1}$  and 1450  $\text{cm}^{-1}$ , which correspond to common vibrations in the saturated hydrocarbon moieties, and the absorbance at 720  $\text{cm}^{-1}$  corresponds to an n-alkane chain having a carbon number of 5 or more. Relatively intense absorbance at 3077  $\text{cm}^{-1}$ , 1640  $\text{cm}^{-1}$ , 991  $\text{cm}^{-1}$  and 909  $\text{cm}^{-1}$  in the 1-tridecene spectrum correspond to vibrations associated with R-CH = CH<sub>2</sub> groups. Also, in the 1-tridecene spectrum, the lower absorbance at 1820, 634 and 552  $\text{cm}^{-1}$  are also present.

In the PE sample, in particular, 1-alkenes in a ratio of about 1:1 with linear alkanes, the FTIR spectra should be close to the 1-tridecene spectrum. In Fig. 4 for the PE sample the intensive absorbance at 3077  $\text{cm}^{-1}$ , 1641  $\text{cm}^{-1}$ , 991  $\text{cm}^{-1}$ , and 909  $\text{cm}^{-1}$  are found to correspond to the double bond in the 1-tridecene. Also less intensive bands at 1821  $\text{cm}^{-1}$ , 634  $\text{cm}^{-1}$  and 552  $\text{cm}^{-1}$  copy the 1-tridecene spectrum. In the FTIR spectra of the hydrogenated PEH sample (Fig. 4), the majority of the strips, corresponding to the presence of the double bond, are reduced to complete extinction. The ratio of integral areas of PEH sample to PE samples for the double bond bands results in 85% conversion of the double bonds. This result is in good agreement with the 90 % conversion of alkenes to alkanes obtained by gas chromatography.

The FTIR spectrum of the PP sample is something more complex than in the previous case, because branched hydrocarbon chains result in more complex spectra, especially in the 700-1,500  $\text{cm}^{-1}$  range. Since we did not have a standard for branched alkenes, we compared the spectra with baseline absorbance at 3077  $\text{cm}^{-1}$  and 1649  $\text{cm}^{-1}$ . Other absorbance corresponding to double bonds are significantly covered by the absorbance of branched hydrocarbon structures, especially in the range of 700-1200  $\text{cm}^{-1}$ , and are also slightly shifted. Absorbance at 3077  $\text{cm}^{-1}$  decreased significantly, but a slight indication of its presence is still visible on the 2800-3000  $\text{cm}^{-1}$  strong shoulder. Absorbance at 1649  $\text{cm}^{-1}$  also dropped significantly after hydrogenation.

Similarly, the absorbance at 1821  $\text{cm}^{-1}$  and 560  $\text{cm}^{-1}$  decreased. By comparing the integral areas for the double bond strips, we proceed to 75 % conversion of the double bonds of the PP sample at the end of the hydrogenation. This result also correlates with the result of chromatographic conversion (84 %), but for the above-mentioned reasons of branched hydrocarbon formation, these results are expected to have greater differences.

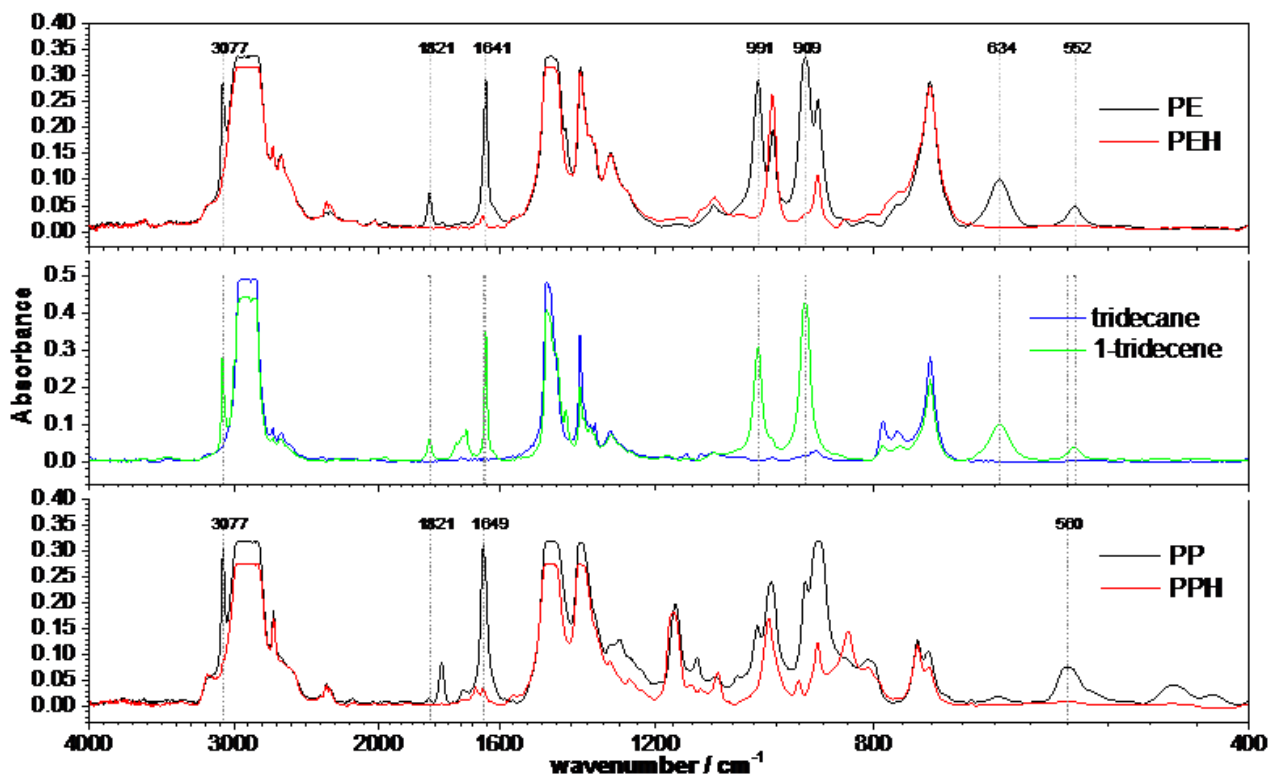


Figure 4. Comparison of samples before and after hydrogenation by IR-spectroscopy

In Tab. 4, the specified values of some of the prescribed performance characteristics of the samples before and after the hydrogenation are also given by the prescribed value. It is evident that, in addition to the density and sulfur content of the samples, they meet the standard values for diesel fuels. Samples have lower density values than the lower density limit specified in the standard. This is due to the minimum content of aromatics in these fractions and the high content of linear or branched alkanes and alkenes depending on the type of plastic. Lower density is typical for diesel fuels of alkanic character, and higher density is typical for more cyclical fuels, possibly fuels containing a higher proportion of aromatics. Lower density is positive for emission reductions, and polyalkenes hydrocarbon fractions could be a good ingredient in engine feeds. The sulfur content exceeds the standard value several times and does not change by hydrogenation. It has been shown that the catalyst used, and the reaction conditions used to saturate the unsaturated hydrocarbon bonds but did not cleave the molecules for the release of the sulfur compounds. It is important to highlight the good low-temperature properties of the hydrogenates, especially the PPH samples. Such a low limitation of filterability ( $-21^{\circ}\text{C}$ ) is achieved in the diesel fuel only after the addition of the depressant.

Table 4. Comparison of some selected sample properties before and after hydrogenation with normalized values for diesel fuels

Sample	PE	PEH	PP	PPH	Standard values	Standard values
Density ( $15^{\circ}\text{C}$ ), $\text{kg}\cdot\text{m}^{-3}$	801	790	794	790	820 - 845	EN ISO 3675
Kinem. viscosity ( $40^{\circ}\text{C}$ ), $\text{mm}^2\cdot\text{s}^{-1}$	2.27	2.35	2.76	2.89	2.00 - 4.50	EN ISO 3104
Water content, $\text{mg}\cdot\text{kg}^{-1}$	52	34	42	24	max. 200	EN ISO 12937
Sulfur content, $\text{mg}\cdot\text{kg}^{-1}$	100	130	147	129	max. 10.0	EN ISO 20884
Pour point, $^{\circ}\text{C}$	-	2-0	-	*1	-	STN EN 23015
Cold filter plugging point, $^{\circ}\text{C}$	-	-2	-	-21	0*2	EN 116

\*1 – sample without mist, viscous, less transparent at  $-24^{\circ}\text{C}$

\*2 – standardized value for moderate climate, diesel Type B

#### 4. Conclusion

PE and PP samples, and in particular PEH and PPH hydrogenates, are the diesel fuel analogues, so they should meet the prescribed engine fuel standard. Prospectively, the plastic recycling unit alone cannot prepare commercial automotive fuels for direct use. However, the aim is to prepare hydrocarbon fractions suitable for further processing in the refinery by using existing fuel production technologies by adding these fractions to refinery streams. Our results show that IR spectroscopy is a quick and reliable method for monitoring the degree of saturation for unsaturated bonds in hydrocarbon liquids from waste polyalkene recycling and this method gave good correlation with results obtained by gas chromatography.

#### Acknowledgement

This work was supported by the Slovak Research and Development Agency under the contract No. APVV-16-0097.

#### References

- [1] <http://www.statista.com/statistics/282732/global-production-of-plastics-since-1950/> (3.4.2015)
- [2] <http://www.bp.com/content/dam/bp/pdf/Energy-economics/statistical-review-2014/BP-statistical-review-of-world-energy-2014-full-report.pdf> (3.4.2015)
- [3] End-of-life vehicle statistics, [https://ec.europa.eu/eurostat/statistics-explained/index.php?title=End-of-life\\_vehicle\\_statistics#undefined](https://ec.europa.eu/eurostat/statistics-explained/index.php?title=End-of-life_vehicle_statistics#undefined), October 2018.
- [4] Duval D, MacLean LH. The role of product information in automotive plastics recycling: a financial and life cycle assessment. *Journal of Cleaner Production*, 2007; 15(11-12): 1158-1168.
- [5] Mlynková B, Bajus M, Hájeková E, Kostrab G, Mravec D. Fuels obtained by thermal cracking of individual and mixed polymers. *Chemical Papers*, 2010; 64(1): 15-24.
- [6] Hájeková E, Špodová L, Bajus M, Mlynková B. Separation and Characterization of Products from Thermal Cracking of Individual and Mixed Polyalkenes. *Chem. Pap.*, 2007; 61(4): 262-270.
- [7] Donahue SW, Brandt CJ. *Pyrolysis: Types, Processes, and Industrial Sources and Products*, Nova Science Publishers, 2009, ISBN-13: 978-1607416692.
- [8] Butler E, Devlin G, McDonnell K. Waste Polyolefins to Liquid Fuels via Pyrolysis: Review of Commercial State-of-the-Art and Recent Laboratory Research. *Waste and Biomass Valorization*, 2011; 2(3): 227-255.
- [9] Soják L, Kubinec R, Jurdáková H, Hájeková E, Bajus M. High resolution gas chromatographic-mass spectrometric analysis of polyethylene and polypropylene thermal cracking products. *J. Anal. Appl. Pyrolysis*, 2007; 78(2):387-399.

*To whom correspondence should be addressed: Assoc. prof. Dr. Elena Hájeková, Slovak University of Technology in Bratislava, Faculty of Chemical and Food Technology, Institute of Organic Chemistry, Catalysis and Petrochemistry, Radlinského 9, 812 37 Bratislava, Slovak Republic*

SYNTHESIS, CHARACTERISTICS AND KINETIC STUDY OF MAGNETIC-ZEOLITE NANO COMPOSITE FOR ADSORPTION OF ZIRCONIUM

Leila Eskandari<sup>1\*</sup>, Farshad Kheiri<sup>1</sup>, Mozghan Irawani<sup>2</sup>, Mohammad Sirousazar<sup>1</sup>

<sup>1</sup> Faculty of Chemical Engineering, Urmia University of Technology, Urmia, Iran

<sup>2</sup> Faculty of Chemistry, University of Isfahan, 81746-73441 Isfahan, Iran

Received September 17, 2018; Accepted October 14, 2018

---

## Abstract

In this research, magnetic-zeolite nano- and micro-composite adsorbents, including nano- and micro-sized zeolite clinoptilolite and iron oxide were synthesized. Natural clinoptilolite tuff was pre-treated and converted into micro- and nano-particles by using a mechanical method. Then, preparation of iron oxide nano-crystals in the presence of nano- and micro-zeolite was followed. The samples were applied to characterize the adsorbents by X-Ray Diffraction, X-Ray Fluorescence, Fourier-Transform Infra-Red spectroscopy, Derivative Thermo-Gravimetry, Scanning Electron Microscopy, Transmission Electron Microscopy, and Vibrating Sample Magnetometry. The nano- and micro-composites were evaluated for Zirconium (Zr) removal from aqueous solutions. The effects of the analytical variables, including pH, initial ion concentration, contact time, and temperature were investigated. The process followed a Pseudo-Second Order (PSO) kinetic model with  $k_2$  values of 1.596 and 1.396  $\text{meq}^{-1} \text{h}^{-1}$  for Magnetic Zeolite Nano-Composite (MZNC) and Magnetic Zeolite Composite (MZC), respectively. The saturation magnetization of the nano-composite was measured as 19.50  $\text{emu g}^{-1}$  by which the magnetic separations of the samples were facilitated after the adsorption process. The thermodynamic values of  $\Delta G^\circ$  and  $\Delta H^\circ$  represented the endothermic and spontaneous natures of Zr removal.

**Keywords:** Micro-composite; Nano-composite; Thermodynamic; Kinetic; Isotherm.

---

## 1. Introduction

Zirconium is one of the rare elements widely used in advanced modern technology. During the past decades, the unique chemical and physical properties of zirconium have led to the widespread use of this element in metallurgy, surgical appliances and the manufacturing of photoflash bulbs. Aside from its ability for industrial applications, Zr is mostly produced today to be applied to water-cooled nuclear reactors. However, fast industrialization to satisfy the population needs by using heavy metals has led to ecosystem contamination. Treatment of heavy metals is of special concern due to their recalcitrance and persistence in the environment [1-2]. Zirconium is a heavy metal with a great risk potential to humans and other organisms in the environment as it has a long half-life. Ion exchange process is one of the most effective approaches to the treatment of heavy metals [3-6]. Among various ion exchangers, zeolites have received considerable attention for removing contaminants due to their high exchange capacities, low costs, and worldwide abundance [6-10]. Considering their large-scale utilizations, natural zeolites seem to be more ascendant than their synthetic counterparts due to their low costs, abundance, and less chemical pollutions caused during their production [11]. Compared to the micro-sized zeolites, nano-crystalline zeolites have greater ion-exchange abilities, quicker exchange kinetics, larger surface areas, and more adjustable porosities. Yet, despite these advantages, separating them from the medium is a major challenge. This can be coped with by the use of magnetic separation method. By applying micro- or nano-magnetic

composites, this new technique opens a simpler, faster, and more accurate way to the removal of elements.

Liu *et al.* synthesized magnetic zeolite NaA to remove  $\text{Cu}^{2+}$  and  $\text{Pb}^{2+}$  [12]. Sharma. *et al.* reported the sorption behavior of nanocrystalline mordenite for  $\text{Th}^{4+}$  and  $\text{Eu}^{+3}$  [13]. E. Chmielewska *et al.* investigated nano-FeO (OH) modified clinoptilolite tuff for antimony removal [14]. Faghihian *et al.* Synthesized a novel PAN-zeolite nano composite for removal of  $\text{Cs}^+$  and  $\text{Sr}^{2+}$  from aqueous solutions [15]. In this work, magnetic nano- and micro-composites were synthesized and characterized for studying their efficiencies of Zr removal from aqueous solutions. Meanwhile, the effects of varied parameters, such as pH, initial ion concentration, contact time, and temperature were evaluated and optimized. Moreover, for the experimental data assessment, different kinetic and isotherm models were employed.

## 2. Experimental procedure

### 2.1. Reagents and methods

All the chemical reagents used in this study were of analytical reagent grade [AR Grade].  $\text{FeCl}_3 \cdot 6\text{H}_2\text{O}$  (Aldrich 98%),  $\text{FeCl}_2 \cdot 4\text{H}_2\text{O}$  (Aldrich 99%), and ammonium hydroxide (Aldrich 28-30% of ammonia) were applied for magnetic particle preparation and Zr was supplied as zirconium chloride by Merck. The natural clinoptilolite tuff belonged to Semnan region in the north-east of Iran. Identifications of the structural phases of nano- and micro-composites were done by using a Bruker D8 ADVANCE X-ray diffractometer. The chemical compositions of the samples were determined through PANalytical Magix XRF spectrometry. An IR Prestige-21 Model spectrophotometer (Shimadzu, Japan) was utilized to obtain FT-IR spectra. Thermo-Gravimetric Analysis (TGA) of the samples was performed using a METTLER TG-50 Thermal Analyzer with a heating rate of  $10^\circ\text{C min}^{-1}$ . To characterize MZNC and MZC magnetic properties, a vibrating sample magnetometer (Meghnatis Daghigh Kavir Company, Iran) was used. A Philips EM-208S transmission electron microscope was utilized to take the relevant images. Also, ICP-AES technique (Integra XL by GBC Australia) was employed to specify Zr concentration.

### 2.2. Pre-treatment of clinoptilolite

Natural clinoptilolite tuff was converted into micron-sized particles by crushing and pulverizing in an agate mortar and sieving using analytical sieves for separating the particle sizes of 200-400  $\mu\text{m}$ . The nanoparticle powders from clinoptilolite were obtained by mechanical ball-mill method (600 rpm, 6 h) of micro-clinoptilolite powder. To remove water-soluble and magnetic impurities, the obtained powders were heated at  $70^\circ\text{C}$  in distilled water on a magnetic stirrer for 8 h. To reach a fixed water content, the powders were stored in a desiccator over a saturated sodium chloride solution for 2 weeks after centrifuging and drying them.

### 2.3. Synthesis of magnetic zeolite nano and micro composite

MZNC and MZC were prepared through the precipitation of Fe (III) and Fe (II) in the presence of nano- and micro-sized zeolite powders. An aqueous ammonia solution (1 M) was placed in a round-bottom flask and the known amounts of nano- or micro-zeolite powders were added to the ammonia solution. The mixture was homogenized by vigorous mechanical stirring and deoxygenated by bubbling of  $\text{N}_2$  gas for 30 min. The solutions of ferric chloride (1 M in water) and ferrous chloride (2 M in HCl 2 M) with a volume ratio of 4:1 were prepared and mixed together. The Fe(III)/Fe(II) solution was added dropwise to the nano- or micro-zeolite/ammonia mixture while stirring the mixture vigorously under  $\text{N}_2$  atmosphere. Separations of the prepared composites were done by using a permanent magnet. Finally, the products were washed four times with deionized-deoxygenated water and then dried at  $50^\circ\text{C}$  for 5 h.

### 2.4. Adsorption experiments

Zr solutions were prepared by dissolving 2.6067 g of zirconium tetrachloride ( $\text{ZrCl}_4$ ) in 1000 mL of distilled water. The initial pH value of 2 underwent an adjustment by adding HCl and NaOH.

The adsorption experiments were performed by agitating 0.05 g of the composites with 10 ml of Zr solution in a thermostat rotary shaker. After each adsorption experiment, the magnetic composites were easily segregated by using a permanent magnet. ICP-AES technique (GBC Integra XL) was utilized to measure Zr after taking a portion of the supernatant solution. The adsorbed Zr amount was calculated with regard to the concentration differences prior and subsequent to the adsorption.

$$q = (C_i - C_f) * V / m \tag{1}$$

The distribution coefficient ( $K_d$ ) was calculated as follows:

$$k_d = (C_i - C_f) / C_f * V / m \tag{2}$$

where:  $q$  is the amount of metal ions adsorbed per unit mass of the adsorbent ( $\text{meq g}^{-1}$ );  $C_i$  and  $C_f$  are the initial and final concentrations ( $\text{meq L}^{-1}$ ), respectively;  $m$  is the adsorbent amount used (g); and  $V$  is the volume of Zr solution (L). The effects of the different parameters, including initial Zr concentration, pH of the solution, contact time, and temperature were determined by changing one parameter at a time and keeping the others constant.

### 3. Results and discussion

#### 3.1. Characterization of M ZNC

The XRD patterns of raw nano- clinoptilolite (NCP) and magnetite zeolite nano-composite (MZNC) are shown in Figure 1. The characteristic lines at  $2\theta$  values of  $10.1^\circ$ ,  $11.4^\circ$ ,  $17.3^\circ$ ,  $23^\circ$ ,  $26^\circ$ ,  $28.2^\circ$ ,  $30.2^\circ$ ,  $32^\circ$ ,  $35^\circ$ ,  $37^\circ$  and  $39^\circ$  in the pattern (a) can be indexed to clinoptilolite crystalline structure data [16]. This confirms that the sample used in this work has a typical clinoptilolite phase as the microporous component. The diffraction line of iron oxide was observed at  $2\theta$  values of  $35.9^\circ$ ,  $42^\circ$  and  $73^\circ$  in the XRD pattern of MZNC sample (b) indicates formation of iron oxide in the zeolite structure [17]. The relative line intensity and line position related to zeolite clinoptilolite remained unchanged, representing that the crystal structure of zeolite had been stable during the composite preparation. Through Scherrer's equation [18], the magnetite particle size of the composite was found to be 22.4 nm.

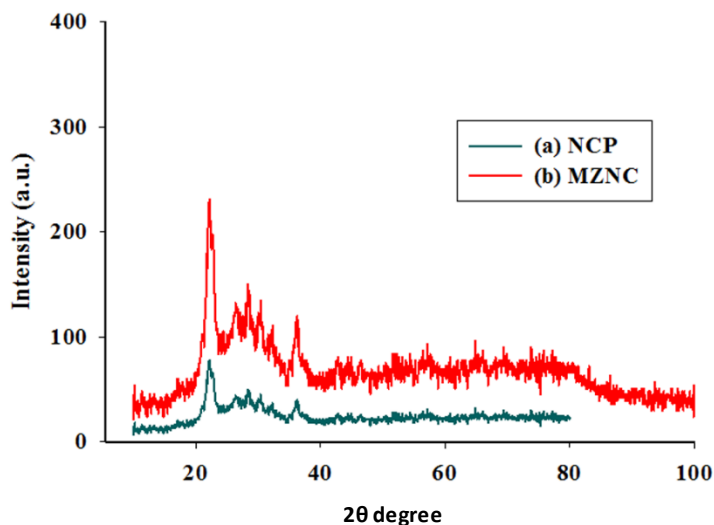


Fig 1. XRD patterns of the nano zeolite (matched with a reference pattern of clinoptilolite) (a), and MZNC (b)

The chemical compositions of zeolite and MZNC (Table 1) were obtained through XRF analysis. The composite consisted of 19.86 wt.%  $\text{Fe}_2\text{O}_3$ . The Si/Al ratio of the present zeolite sample was 4.85, which was consistent with the previous findings placing the ratio within a range of 4-5.5 [19]. The Theoretical Cation Exchange Capacity (TCEC) was estimated by the sum of the exchangeable ions, including  $\text{Na}^+$ ,  $\text{K}^+$ ,  $\text{Ca}^{2+}$ , and  $\text{Mg}^{2+}$  in the zeolite. The difference

between TCEC and Cation Exchange Capacity (CEC) (Table 1) was due to the fact that some counter-ion sites in the zeolite particles were unavailable for cation exchange.

Table 1. Chemical compositions of zeolite and MZNC obtained through XRF analysis

	SiO <sub>2</sub>	Al <sub>2</sub> O <sub>3</sub>	Na <sub>2</sub> O	TiO <sub>2</sub>	K <sub>2</sub> O	CaO	MgO
CLI	67.41	11.82	2.66	0.10	2.44	1.31	0.71
MZNC	53.21	9.28	1.92	1.096	1.48	1.25	0.71
	SrO	Fe <sub>2</sub> O <sub>3</sub>	LOI <sup>a</sup>	Total	Si/Al	TCEC <sup>c</sup>	CEC <sup>c</sup>
CLI	0.13	1.32	11.46	99.54	4.85	1.736	1.561
MZNC	n.d. <sup>b</sup>	19.86	12.01	99.81	4.87	1.335	1.218

CLI-clinoptilolite; <sup>a</sup> Loss on ignition; <sup>b</sup> Not detected; <sup>c</sup> (meq g<sup>-1</sup>)

The FT-IR spectra of the zeolite and composite were recorded over a range of 400-4000 cm<sup>-1</sup> (Fig. 2). Water absorption bands at 1638 cm<sup>-1</sup> within the range of 3000-3600 cm<sup>-1</sup> confirmed significant hydrations of the zeolites. The band at 1070 cm<sup>-1</sup> was assigned to the asymmetric stretching vibration modes of the internal T-O bonds in TO<sub>4</sub> tetrahedra (T=Si and Al). The bands at 609 and 465 cm<sup>-1</sup> arose from the stretching vibration modes of O-T-O groups and the bending vibration modes of T-O bonds, respectively [20]. For the zeolites, the regions corresponding to (Si-O and Al-O) and (O-Si-O and O-Al-O) demonstrated strong bands, indicating an increase in the surface areas and aluminosilicate bonds of the zeolites. The characteristic band related to Fe-O-Fe bond of iron oxide must have appeared at 584 cm<sup>-1</sup> [17].

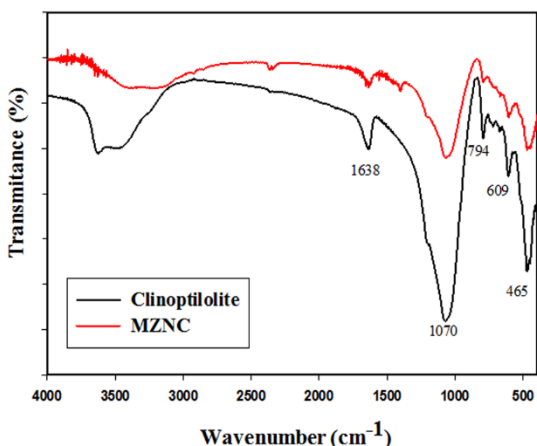


Figure 2. FTIR spectra of clinoptilolite and MZNC

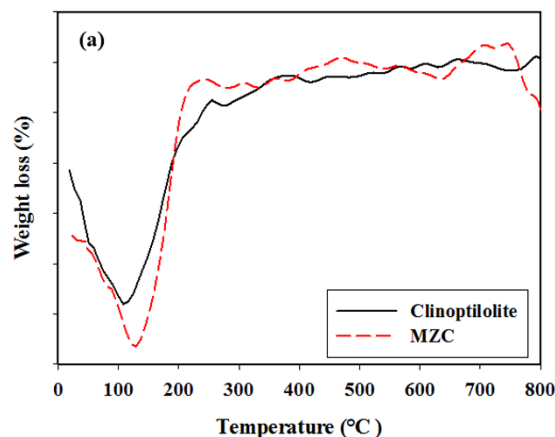


Figure 3a. DTG curves of nano clinoptilolite and MZC

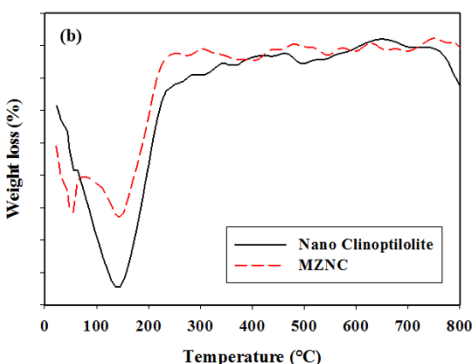


Figure 3 (b). DTG curves of nano clinoptilolite and MZNC

In the DTG curves of the nano-zeolite clinoptilolite and MZNC, two weight-loss peaks occurring between 50°C and 120°C were assigned to the loss of the adsorbed water Fig 3 (a and b). After 280°C, the adsorbents exhibited no dehydration peaks up to 800°C, which means that the samples were thermally stable.



The difference between the amorphous surface structures of the natural zeolite sample and nano-zeolite clinoptilolite with a uniform surface was apparent according to SEM images Fig 4 (a and b). Due to the lack of uniformity and wide range of particle dimensions, determination of the particle size distribution could not be accurately performed for micro-sized clinoptilolite, according to (Fig 4a), but for nano-sized particles depicted in Fig 4b. Also, TEM images showed iron oxide particles to have been nano-sized and bound to the aluminosilicate framework of nano-zeolite (Fig 4c).

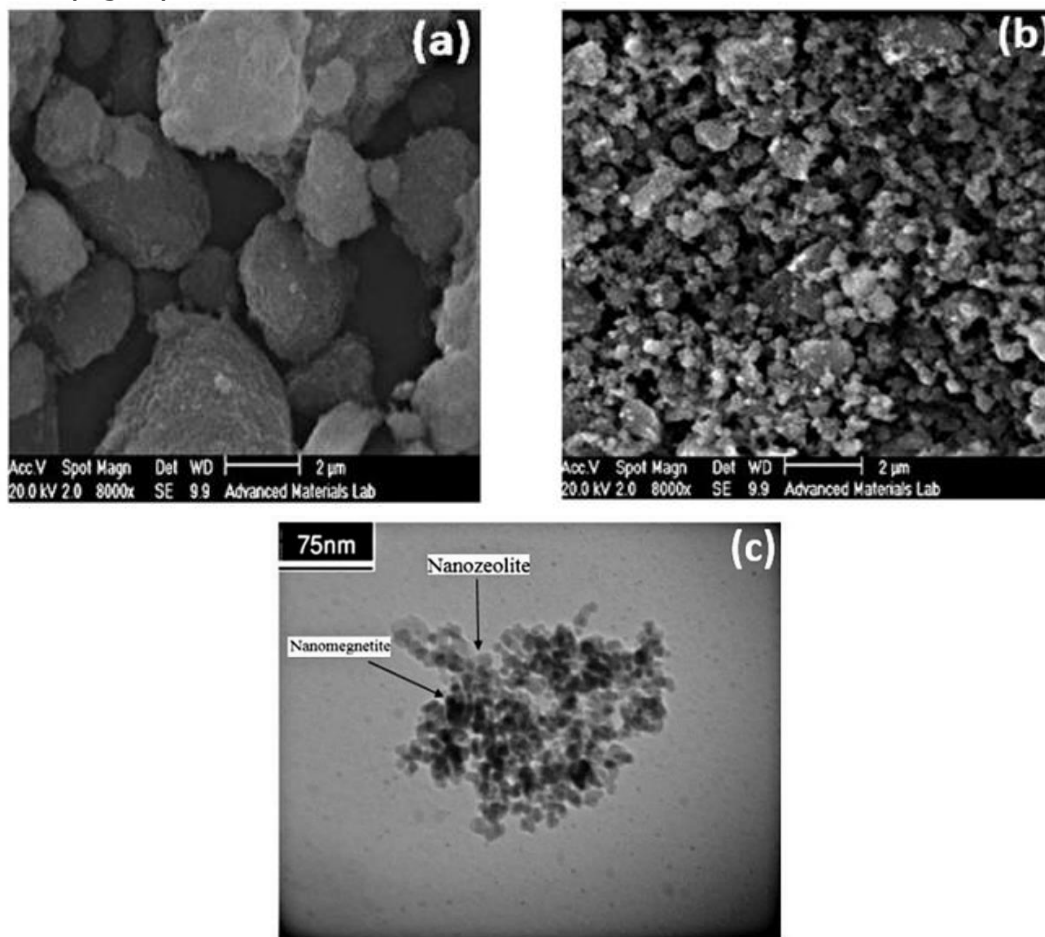


Figure 4 (a, b). SEM images of zeolite clinoptilolite (a) and nano clinoptilolite (b).

Figure 4 (c). The MZNC TEM images

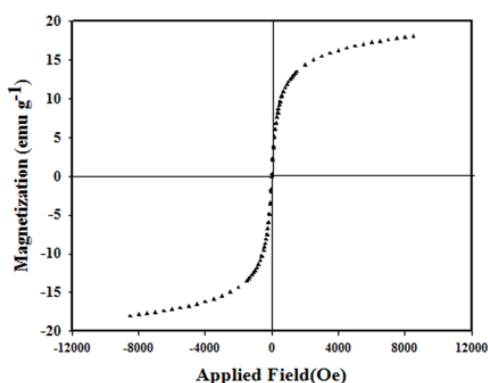


Figure 5. The hysteresis loops of MZNC

This new composite's feature was its magnetic property, which means that it was characterized by a sample of the vibrating magnetometer in this study Fig. 5. The magnetic curve illustrated no hysteresis loop and remanence, which indicate the good super-paramagnetic properties of MZNC. The zero amount of remanence certified that the composite had not retained magnetization after being exposed to an external magnetic field and they could be thus re-dispersed after removing the magnetic field. Nanocomposite exhibited the saturation magnetizations of approximately  $19.50 \text{ emu g}^{-1}$  at 298K. This value verified the adequate magnetic properties of MZNC to be appealed by a permanent magnet.

### 3.2. Optimization of conditions

#### 3.2.1. Effect of pH

The effect of pH on Zr removal by the natural zeolite, MZC, and MZNC at pH<3.5 for [Zr]=1.5–10 mmol L<sup>-1</sup> is shown in Fig. 6. The results revealed an increase in the adsorption capacity with pH enhancement due to the nature of the absorption process. At a constant concentration of 0.01 mol L<sup>-1</sup> for Zr solution, maximum adsorption capacity was observed at pH=2. Higher pH values were not examined due to Zr precipitation at pH>3.5. In the adsorption process using zeolite clinoptilolite, the intense competition between H<sub>3</sub>O<sup>+</sup> and Zr ions for the exchange sites led to the reduced absorption of H<sub>3</sub>O<sup>+</sup> ions because of their small sizes, high ionic mobilities, and consequently high penetration powers, especially at an acidic pH. A decrease and increase in the competition and absorption capacity were expected with the declined concentration of H<sub>3</sub>O<sup>+</sup>. The increasing process of the absorption capacity continued until pH=2 was reached. In the next step, a steady rate of absorption was achieved after eliminating the competition of hydronium ions.

#### 3.2.2. Effect of contact time

The contact time effects of clinoptilolite, MZC, and MZNC on Zr adsorption were studied at a concentration of 0.01 mol L<sup>-1</sup> of Zr solution at 25°C. The results are shown in Fig 7. In all the absorbents, the equilibration was attained after 24 h. From the slopes of the curves, it was concluded that the adsorption rate had been fast at the beginning and become slow with the reaction progress. The absorption rate induced by MZNC was so rapid that more than 80% of the maximum absorption capacity for Zr was obtained during the first 3 hours. Ion exchange reaction with this adsorbent was achieved after 24 h and the sorption capacity was fixed. Therefore, this time was selected as the optimal contact time for the nano-composite. These results indicated that the absorption rate triggered by the nano-composite was faster than those induced by the micro-composite and clinoptilolite. This high absorption rate could be attributed to the nanometer dimensions of zeolite particles.

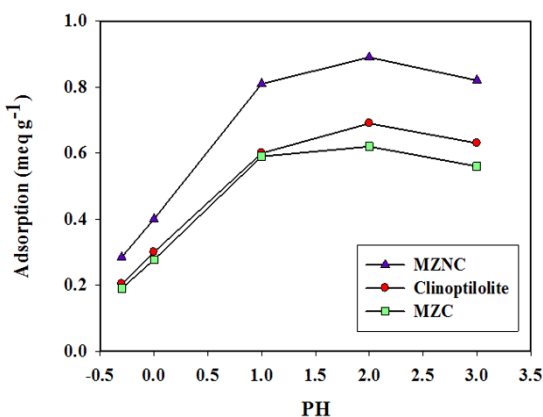


Figure 6. Effect of pH on sorption of Zr

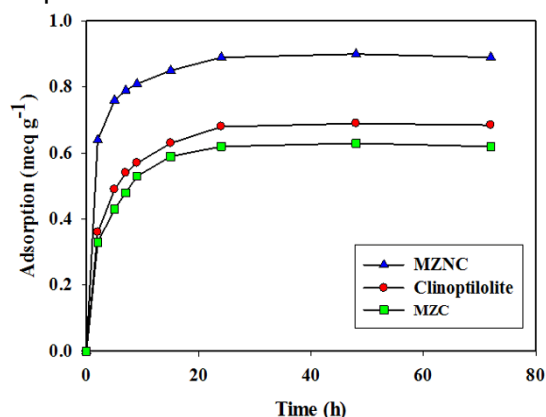


Figure 7. Effect of contact time on adsorption of Zr onto clinoptilolite, MZC and MZNC

### 3.3. Adsorption kinetics and thermodynamics

The kinetics of adsorption was evaluated by applying four different models including the pseudo-first-order equation, the pseudo-second-order equation, Elovich equation, and intra-particle diffusion model. These models were tested to fit experimental data obtained by batch experiments.

The pseudo-first-order equation is generally expressed as follows:

$$\ln (q_e - q_t) = \ln q_e - k_1 t \quad (3)$$

where  $q_e$  and  $q_t$  are the ions adsorbed amount per unit mass of the adsorbent at equilibrium and at any time  $t$ , respectively and  $k_1$  is the rate constant of pseudo-first-order sorption ( $\text{min}^{-1}$ ).

The values of  $k_1$  and  $q_e$  were regulated from the slope and the intercept of plotting of  $\log(q_e - q_t)$  vs.  $t$ . The results are listed in Table. 2. Although no extremely low values were obtained for R2, the calculated  $q_e$  was not consistent with that of experimental data. Hence, the adsorption process did not follow a pseudo-first-order model. The linear form of the pseudo-second-order kinetic model is written as follow:

$$t/q_t = 1/(k_2 q_e^2) + (1/q_e)t \tag{4}$$

The initial sorption rate can be calculated by the following formula:

$$h = k_2 q_e^2 \tag{5}$$

where  $k_2$  is the rate constant of pseudo-second-order kinetic sorption (g/mg/min). The calculated values of  $k_2$ ,  $q_e$ , and  $h$  values and the correlation coefficients (R2) are listed in table 2. The comparison of  $k_2$  values indicated faster ion adsorption onto MZNC is faster than on clinoptilolite.

Table 2. Kinetic parameters of pseudo-first-order and pseudo-second-order kinetic models

sorbents	$q_e$ (exp.) ( $\times 10^{-1}$ ) (meqg <sup>-1</sup> )	pseudo-first-order model			pseudo-second-order model			
		$k_1$ ( $\times 10^{-1}$ ) (h <sup>-1</sup> )	$q_e$ (theor.) ( $\times 10^{-1}$ ) (meqg <sup>-1</sup> )	R <sup>2</sup>	$k_2$ (meq <sup>-1</sup> h <sup>-1</sup> )	$q_e$ ( $\times 10^{-1}$ ) (meq g <sup>-1</sup> )	$h$ ( $\times 10^{-1}$ ) (meq g <sup>-1</sup> h <sup>-1</sup> )	R <sup>2</sup>
Clinoptilolite	6.80	1.644	2.675	0.9575	1.072	7.032	5.3036	0.9990
MZC	6.20	1.285	1.337	0.9647	1.396	6.215	5.393	0.9978
MZNC	8.90	1.863	4.212	0.8648	1.596	9.027	13.005	0.9997

The intra-particle diffusion effect on the total rate of ion exchange was demonstrated by the association of the adsorbed ion amount and the square root of time. The equation of intra-particle diffusion model is exhibited as follows:

$$q_t = k_{diff} t^{1/2} + C \tag{6}$$

where  $K_{diff}$  is the rate constant of intra-particle diffusion (mg/g/min) and C stands for the intercept. As evidenced by the results, intra-particle diffusion cannot provide a rate-determining step in the sorption process (Table 3). Elovich equation is given as follows:

$$q_t = \ln(\alpha\beta)/\beta + 1/\beta \ln t \tag{7}$$

where  $q_t$  is the sorption capacity at time  $t$ ;  $a$  is the initial sorption rate of Elovich equation (mg/g/min); and parameter  $b$  is related to the extent of surface coverage and activation energy for chemisorptions (g/mg). The constants calculated from the slope and the intercept of plot of  $q_t$  vs.  $\ln t$  are listed in Table 3. The comparison of the calculated  $q_e$  and correlation coefficients for the kinetic models revealed that PSO equation best matched with the experimental data. These results demonstrated that the overall sorption rate had been controlled by the chemical sorption process [21].

Table 3. Kinetic parameters of Elovich and intra-particle diffusion models

Sorbents	Elovich model			Intra-particle diffusion model		
	$a$ ( $\times 10^{-1}$ ) (meq g <sup>-1</sup> h <sup>-1</sup> )	$\beta$ (meq <sup>-1</sup> )	R <sup>2</sup>	$k_{diff}$ ( $\times 10^{-2}$ ) (meq g <sup>-1</sup> h <sup>-1/2</sup> )	$C$ ( $\times 10^{-2}$ ) (meq g <sup>-1</sup> )	R <sup>2</sup>
Clinoptilolite	38.904	10.8565	0.9014	6.663	26.82	0.6481
MZC	32.633	11.737	0.8793	6.093	24.33	0.6446
MZNC	14.928	62.037	0.6347	7.436	44.89	0.4914

### 3.3.1. Sorption thermodynamics

The effect of sorption temperature on Ru removal was investigated at five different temperatures. The adsorption capacity enhanced with increasing temperature (Fig. 8). The thermodynamic parameters, including enthalpy change ( $\Delta H^\circ$ ) and entropy change ( $\Delta G^\circ$ ), can be obtained using the Van't Hoff equation.

$$\ln K_d = - (\Delta H^\circ/RT) + (\Delta S^\circ/R) \tag{5}$$

A plot of  $\ln K_d$  vs.  $1/T$  is shown in Fig. 9. The free energy change of the adsorption ( $\Delta G^\circ$ ) is calculated as follows:

$$\Delta G^\circ = \Delta H^\circ - T\Delta S^\circ \tag{6}$$

The calculated thermodynamic parameters are summarized in Table 4. Since  $\Delta H^\circ$  values are positive, the adsorption process is endothermic in nature.

Table 4. Thermodynamic parameters of Zr adsorption

Sorbent	$\Delta G^\circ$ (kJ mol <sup>-1</sup> )	$\Delta S^\circ$ (kJ mol <sup>-1</sup> K <sup>-1</sup> )	$\Delta H^\circ$ (kJ mol <sup>-1</sup> )
Clinoptilolite	-7.21	34.51	3.07
MZC	-6.98	34.87	3.41
MZNC	-8.001	37.10	3.05

The positive values of  $\Delta S^\circ$  suggested that the randomness at the solid/solution interface had increased during the sorption process. The negative values of  $\Delta G^\circ$  indicated that Zr adsorption reaction was spontaneous. The decrease in  $\Delta G^\circ$  values with increasing temperature showed that the spontaneous nature of sorption was directly proportional to temperature. Therefore, the adsorption process was favored when temperature was augmented. The greater absolute values of  $\Delta G^\circ$  for MZNC compared to MZC and clinoptilolite revealed that the adsorption of the former on Zr had been more favored.

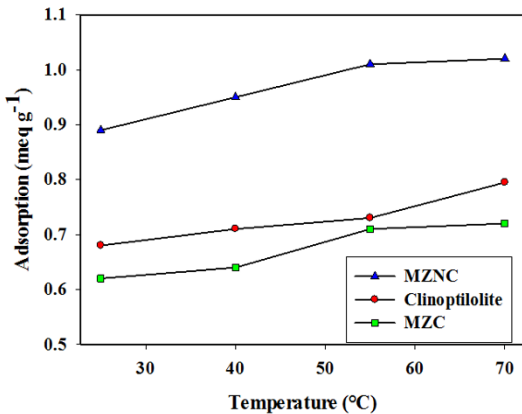


Figure 8. Effect of temperature on Zr adsorption onto clinoptilolite, MZC and MZNC

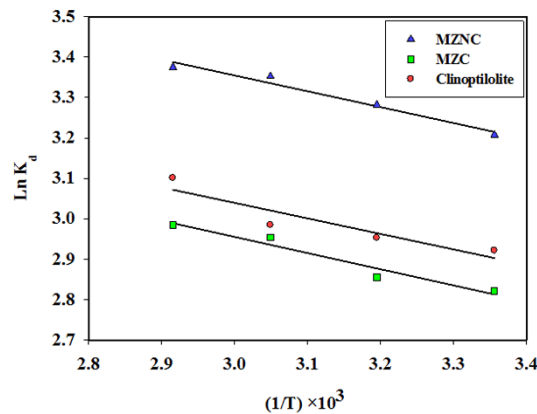


Figure 9. Van't Hoff plot for adsorption of Zr onto clinoptilolite, MZC and MZNC

### 3.4. Sorption isotherm

To investigate the effect of initial concentration, various concentrations of Zr solution were equilibrated with constant amounts of the adsorbents (Fig 10). The initial fast adsorption was followed by a slow approach to equilibrium at a higher concentration. Three isotherm models, including Langmuir, Freundlich, and Dubinin–Radushkviech (D–R) models were employed to examine the experimental data.

#### 3.4.1. Langmuir isotherm model

Langmuir isotherm assumes that the sorption occurs at specific homogeneous sites within the adsorbent. This model is expressed by:

$$C_e/q_e = 1/(Q_0b) + C_e/Q_0 \tag{11}$$

where  $Q_0$  denotes the saturation adsorption capacity (mg/g) and  $b$  represents the Langmuir constant related to the free energy of adsorption calculated from the slope and intercept (Table 5). The plot of  $C_e/q_e$  vs.  $C_e$  is shown in Fig. 11. The important parameter of Langmuir isotherm is the dimensionless constant,  $R_L$ , which can be calculated as follows:

$$R_L = 1/(1 + bC_0) \tag{12}$$

where  $C_0$  stands for the highest initial metal ion concentration (mg/L). The values of this parameter indicate the unfavorable ( $R_L > 1$ ), linear ( $R_L = 1$ ), favorable ( $0 < R_L < 1$ ), and irreversible ( $R_L = 0$ ) types of the adsorption isotherm [22].

The obtained data confirmed that Zr adsorption was favorable. The maximum adsorption capacity of MZNC for Zr removal was compared with those of the other adsorbents reported in the literature (Table 6). MZNC was seen to depict a high adsorption capacity for this ion. On the other hand, the magnetic composites could be easily separated from the solutions using a permanent magnet.

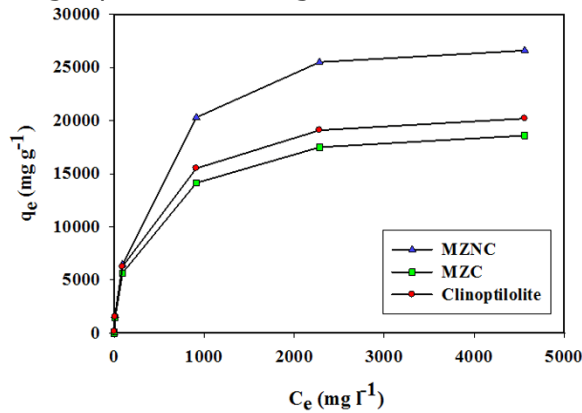


Figure 10. Effect of different initial ion concentration on Zr adsorption onto clinoptilolite, MZC and MZNC

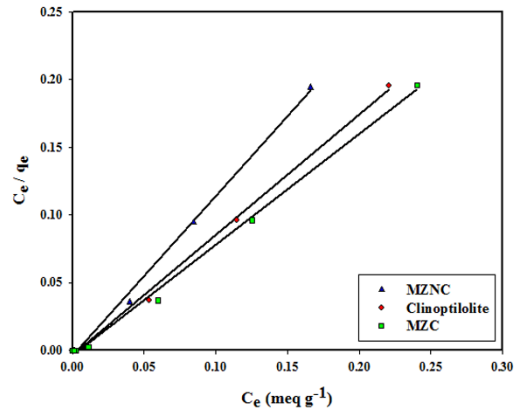


Figure 11. Langmuir isotherm plots for adsorption of Zr onto clinoptilolite, MZC and MZNC

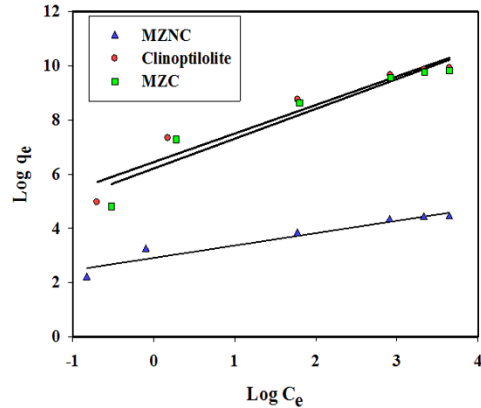


Figure 12. Freundlich isotherm plots for adsorption of Zr onto clinoptilolite, MZC and MZNC

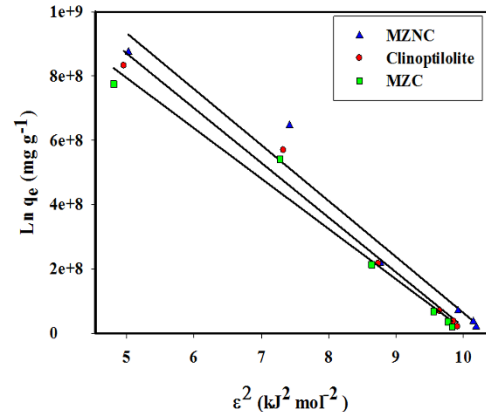


Figure 13. D-R isotherm plots for adsorption of Zr onto clinoptilolite, MZC and MZNC

### 3.4.2. Freundlich isotherm model

Freundlich isotherm model makes the assumption that multi-layer sorption occurs at a heterogeneous surface. This model was used to estimate the intensity of the adsorption process and relative sorption capacity. A linear form of the Freundlich equation is shown as follows:

$$\log q_e = \log k_f + 1/n \log C_e \tag{13}$$

where  $K_f$  denotes the Freundlich constant relevant to the adsorbent capacity and  $n$  displays the constant related to the intensity of the adsorption process. The Freundlich isotherm is

shown in Fig 12 and their constants are represented in Table 5. The Freundlich constant (n) was greater than its unity, indicating that an increasing tendency of the adsorption process had occurred with the elevation of ion concentration.  $K_f$  value of MZNC was higher compared to those of MZC and clinoptilolite, corroborating a greater adsorption tendency of the adsorbents towards MZNC.

Table 5. Adsorption isotherm parameters for Zr adsorption

Isotherm	Sorbents	Model parameters			
		$Q_0$ (mg g <sup>-1</sup> )	$b \times 10^3$ (L mg <sup>-1</sup> )	$R_L \times 10^3$	$R^2$
Langmuir	Clinoptilolite	195.31	11.56	18.6	0.9972
	MZC	188.67	8.096	26.0	0.9964
	MZNC	270.27	8.375	25.0	0.9968
		Model parameters			
		n	$K_f$ (mg g <sup>-1</sup> )	$R^2$	
Freundlich	Clinoptilolite	2.18	630.23	0.9268	
	MZC	2.09	497.0	0.9717	
	MZNC	2.189	808.7	0.9274	
		Model parameters			
		$\beta$ ( $\times 10^{-9}$ )(mol <sup>2</sup> kJ <sup>-2</sup> )	$q_m$ (mmol g <sup>-1</sup> )	E (kJ mol <sup>-1</sup> )	$R^2$
D-R	Clinoptilolite	6.00	1.003	9.32	0.9771
	MZC	6.00	1.001	8.97	0.9717
	MZNC	6.00	1.012	9.506	0.9628

### 3.4.3. Dubinin–Radushkviech isotherm model

D–R isotherm was used to distinguish between the physical and chemical adsorptions of the ions and estimate the apparent free energies of adsorption. The related equation is given as follows:

$$\log q_e = \log k_f + 1/n \log C_e \tag{14}$$

where  $q_m$  is the maximum adsorption capacity (mequiv/g); is the D–R constant related to the sorption energy (mol<sup>2</sup>/K/J<sup>2</sup>); and  $e$  is the Polanyi potential.

$$\epsilon = RT \ln (1 + 1/C_e) \tag{15}$$

where  $R$  is the gas constant (kJ<sup>-1</sup>mol<sup>-1</sup>K) and  $T$  is the absolute temperature (K). The D–R isotherm is plotted in Fig. 13 and the obtained parameters are represented in Table 5. In a solution, when 1 mol of an ion is transferred to the surface of an adsorbent from infinity, its free energy is called the mean energy of adsorption (E), which is calculated as follows:

$$E = (2\beta)^{-1/2} \tag{16}$$

The magnitude of E within a range of 8-16 kJ/mol demonstrates that the sorption process is done through an ion exchange interaction. The reaction mechanism can be related to the magnitude of E. When E value is within the range of 8-16 kJ/mol, the sorption process is followed by ion exchange, but when E < 8.0 kJ/mol, physical forces are responsible for the process [23].

Table 6. Adsorption capacity of Zr by some adsorbents

Sorbent	$Q_m$ (mg.g-1)	Reference
Clinoptilolite	83.12	[6]
<i>Coriolus versicolor</i>	71.00	[24]
Rice bran	50.00	[25]
Citrus peel waste biomass	45.02	[26]
Magnetic zeolite composite	188.67	This work
Magnetic zeolite nano composite	270.27	This work

## 4. Conclusion

The magnetite-zeolite nano- and micro-composites were synthesized, characterized, and evaluated for Zr removal from aqueous solutions. The nano-composite represented a high cation exchange capacity, high selectivity towards Zr, and rapid adsorption kinetics as compared to the micro-composite of zeolite. The nano-composite displayed 26.9% increasing in adsorption capacity. The results of the kinetic studies suggested that the initial sorption rate and rate constant were greater when using the nano-composite instead of the micro-composite. The VSM results verified the sufficient magnetic strengths of the nano- and micro-composites to be attracted by a magnetic field. The PSO model gave a better correlation with the experimental kinetic data compared to the PFO model, confirming the dominant process of the chemical sorption. The values of the thermodynamic parameters demonstrated the endothermic and spontaneous natures of the adsorption process.

## References

- [1] Sounthararajah DP, Loganathan P, Kandasamy J, Vigneswaran S. Removing heavy metals using permeable pavement system with a titanate nano-fibrous adsorbent column as a post treatment. *Chemosphere*. 2017; 168: 467-73.
- [2] Zanin E, Scapinello J, de Oliveira M, Rambo CL, Franscescon F, Freitas L, de Mello JM, Fiori MA, Oliveira JV, Dal Magro J. Adsorption of heavy metals from wastewater graphic industry using clinoptilolite zeolite as adsorbent. *Process Safety and Environmental Protection*. 2017; 105: 194-200.
- [3] Yurekli Y. Removal of heavy metals in wastewater by using zeolite nano-particles impregnated polysulfone membranes. *Journal of hazardous materials*. 2016; 309: 53-64.
- [4] Dulanská S, Remenec B, Gardoňová V, Mátel Ľ. Determination of <sup>93</sup>Zr in radioactive waste using ion exchange techniques. *Journal of Radioanalytical and Nuclear Chemistry*. 2012; 293(2): 635-40.
- [5] Leal M, Martínez-Hernández V, Meffe R, Lillo J, de Bustamante I. Clinoptilolite and palygorskite as sorbents of neutral emerging organic contaminants in treated wastewater: Sorption-desorption studies. *Chemosphere*. 2017; 175: 534-42.
- [6] Faghihian H, Kabiri-Tadi M. Removal of zirconium from aqueous solution by modified clinoptilolite. *Journal of Hazardous Materials*. 2010; (1-3): 66-73.
- [7] Noli F, Buema G, Misaelides P, Harja M. New materials synthesized from ash under moderate conditions for removal of toxic and radioactive metals. *Journal of Radioanalytical and Nuclear Chemistry*. 2015; 303(3): 2303-11.
- [8] Cretescu I, Soreanu G, Harja M. A low-cost sorbent for removal of copper ions from wastewaters based on sawdust/fly ash mixture. *International Journal of Environmental Science and Technology*. 2015; 12(6): 1799-810.
- [9] De Haro-Del Rio DA, Al-Jubouri S, Kontogiannis O, Papadatos-Gigantes D, Ajayi O, Li C, Holmes SM. Corrigendum to "The removal of caesium ions using supported clinoptilolite. *Journal of Hazardous Materials*. 2016; 303: 181-181.
- [10] Ltaief OO, Siffert S, Fourmentin S, Benzina M. Synthesis of Faujasite type zeolite from low grade Tunisian clay for the removal of heavy metals from aqueous waste by batch process: Kinetic and equilibrium study. *Comptes Rendus Chimie*. 2015; 18(10): 1123-33.
- [11] Wen J, Yi Y, Zeng G. Effects of modified zeolite on the removal and stabilization of heavy metals in contaminated lake sediment using BCR sequential extraction. *Journal of environmental management*. 2016; 178: 63-9.
- [12] Liu H, Peng S, Shu L, Chen T, Bao T, Frost RL. Magnetic zeolite NaA: Synthesis, characterization based on metakaolin and its application for the removal of Cu<sup>2+</sup>, Pb<sup>2+</sup>. *Chemosphere*. 2013; 91(11): 1539-46.
- [13] Sharma P, Tomar R. Sorption behaviour of nanocrystalline MOR type zeolite for Th (IV) and Eu (III) removal from aqueous waste by batch treatment. *Journal of colloid and interface science*. 2011; 362(1): 144-56.
- [14] Chmielewska E, Tylus W, Drabik M, Majzlan J, Kravčák J, Williams C, Čaplovičová M, Čaplovič Ľ. Structure investigation of nano-FeO (OH) modified clinoptilolite tuff for antimony removal. *Microporous and Mesoporous Materials*. 2017; 248: 222-33.

- [15] Faghihian H, Iravani M, Moayed M, Ghannadi-Maragheh M. Preparation of a novel PAN–zeolite nanocomposite for removal of Cs<sup>+</sup> and Sr<sup>2+</sup> from aqueous solutions: Kinetic, equilibrium, and thermodynamic studies. *Chemical engineering journal*. 2013; 222: 41-8.
- [16] Treacy MM, Higgins JB. *Collection of simulated XRD powder patterns for zeolites fifth (5th) revised edition*. Elsevier; 2007.
- [17] Maity D, Agrawal DC. Synthesis of iron oxide nanoparticles under oxidizing environment and their stabilization in aqueous and non-aqueous media. *Journal of Magnetism and Magnetic Materials*. 2007; 308(1): 46-55.
- [18] Klug HP, Alexander LE. *X-ray diffraction procedures: for polycrystalline and amorphous materials*. *X-Ray Diffraction Procedures: For Polycrystalline and Amorphous Materials*, 1974, 2nd Edition, p. 992.
- [19] Breck DW, Sieves ZM. *Structure, chemistry and use. Zeolite Molecular Sieves*. Wiley, New York. 1974.
- [20] Bezouhanova CP. Synthesis of aromatic ketones in the presence of zeolite catalysts. *Applied Catalysis A: General*. 2002; 2 29(1-2): 127-33.
- [21] Ho YS, McKay G. Pseudo-second order model for sorption processes. *Process biochemistry*. 1999; 34(5): 451-65.
- [22] Mohan D, Chander S. Single, binary, and multicomponent sorption of iron and manganese on lignite. *Journal of Colloid and Interface Science*. 2006; 299(1): 76-87.
- [23] Helfferich FG, Dranoff JS. *Ion Exchange*. McGraw-Hill, New York (1962), 624 pp.
- [24] Safa Y, Bhatti HN, Sultan M, Sadaf S. Synthesis, characterization and application of wheat bran/zinc aluminium and tea leaves waste/zinc aluminium biocomposites: kinetics and thermodynamics modeling. *Desalination and Water Treatment*. 2016; 57(53): 25532-41.
- [25] Zolfonoun E, Monji AB, Taghizadeh M, Ahmadi SJ. Selective and direct sorption of zirconium from acidic leach liquor of zircon concentrate by rice bran. *Minerals Engineering*. 2010; 23(9): 755-6.
- [26] Sadaf S, Bhatti HN. Response surface methodology approach for optimization of adsorption process for the removal of Indosol Yellow BG dye from aqueous solution by agricultural waste. *Desalination and Water Treatment*. 2016; 57(25): 11773-81.

---

*To whom correspondence should be addressed: Leila Eskandari, Faculty of Chemical Engineering, Urmia University of Technology, Urmia, Iran*

USING SATELLITE IMAGES TO CREATE TRAINING IMAGES FOR MULTIPLE-POINT STATISTICS MODELING OF MEANDERING FLUVIAL RESERVOIRS

*Buhari U. Ardo*

*Department of Geology, Modibbo Adama University of Technology, Yola, Nigeria*

Received July 2 2018; Accepted October 19, 2018

---

## **Abstract**

Geostatistical simulation using multiple-point statistics (MPS) has improved the quality and efficiency of reservoir models by replacing the conventional two-point statistics with multi-point statistics acquired from training images. As a stochastic method, multiple-point statistics requires the training image to satisfy the conditions of stationarity and ergodicity in order to capture patterns from the training image and reproduce them in the reservoir model. This limits the sources of analogue data that can be directly used to create geologically realistic training images. In this paper, I present a workflow for creating training images of meandering fluvial reservoirs from satellite images using the object-based and interactive facies modelling techniques and show that satellite images of modern fluvial depositional environments can serve as a library of analogues for meandering fluvial reservoirs. The workflow describes a simple process of creating stationary training images, which are geologically realistic directly from satellite images. This allows multiple-point statistics to capture the patterns contained in the training images. The extracted patterns, which serve as the main input for simulation of reservoir models, are reproduced in the resulting model.

**Keywords:** *Satellite images; training images; multiple-point statistics; meandering; fluvial; reservoirs.*

---

## **1. Introduction**

Fluvial reservoirs are formed by sedimentary bodies with random, curvilinear geometries such as sinuous sand channels, levees, crevasse splays etc. Such random, complex shapes are poorly reproduced in geostatistical reservoir models using conventional two-point (variogram) statistics [1-4]. This limitation is due to the inability of two-point statistics correlation to adequately capture the irregular pattern and continuity of the facies bodies thus, reservoir connectivity and heterogeneity is often misrepresented. This pixel-based approach however, allows for effective data conditioning. In contrast, object-based modeling provides better and more realistic reproduction of random, curvilinear and highly connected facies geometries but data conditioning, especially with dense data constraints, of the resulting geostatistical model presents a great challenge and is the major limitation of this technique [2,5]. The strengths of these two techniques are combined in the multiple-point statistics (MPS) geostatistical reservoir modelling approach. By combining and utilizing these strengths, MPS is able to reproduce random and complex shapes while also honoring conditioning data.

Multiple-point statistics considers more than two points at a time and builds the model one pixel at a time [3]. It acquires statistics from quantitative, pixel-based, conceptual geological models known as training images [5]. The patterns contained in the training image are extracted and utilized to capture facies geometries and relationships, which are then reproduced during the stochastic simulations.

Training images are preliminary and fundamental requirements for MPS modelling. They describe and quantify spatial facies distribution, facies connectivity, lateral continuity, vertical

stacking pattern etc. They can be constructed based on hand-drawn conceptual models, outcrop mapping or stochastic algorithms and generated using unconditional object-based approach.

Satellite images can serve as a library of analogue data that can be used to generate training images for MPS. High-resolution satellite images of modern fluvial depositional environments capture the facies patterns and geometries expected in meandering fluvial reservoirs. This information is critical for modelling reservoirs and can be imported into MPS reservoir models via training images. Suitable sections of the satellite images can be meticulously selected and directly used to create training images.

## **2. Meandering fluvial systems**

Fluvial environments are characteristically made up of channels and the overbank area. When rivers flow at either low flow stage or high flow stage, they are normally confined to the channels. At low flow stage, the level of water in the channel is far below the level of the channel banks, while at high flow stage, the channel is filled up to the channel banks or close to it. At other times however, the volume of water discharged could be too much for the channel to contain, resulting in flooding over the channel banks and onto the overbank area. For this reason, the overbank area is also known as the floodplain.

Coarser sediments are transported along the channels as bed load, while finer sediments are transported in suspension. The sediments are transported for as long as the energy of the flow is enough to carry them along. As the energy of the flow decreases, coarser sediments are deposited within the channels, while finer sediments subsequently settle out of suspension. During flooding, the sediment – bearing water flows onto the floodplain where the finer sediments settle out of suspension.

In areas of low gradient away from the upland source area (middle to lower parts of the fluvial system), the flow becomes sinuous resulting in the development of the meandering channel pattern. During flooding, suspended sediments carried in water spilled over the channel banks quickly settle out along the banks of the channel where they accumulate to form levees. When there is a rise in water level, the levees are often breached, resulting in the deposition of sediments in a 'fan-shaped' pattern spreading outward from the outer channel meanders to form crevasse splay. As water flows in a sinuous pattern, the outer banks of the channel are eroded and the sediments are deposited along the inner banks, forming point bars and causing the channel to continuously migrate laterally just as the point bar sequence accretes laterally. Over time, the channel meanders become larger and separated by narrow necks, which may eventually be breached, cutting off the meander to form oxbow lakes.

## **3. Training image**

Training images are quantitative and visually explicit conceptual models, showing reservoir facies geometries, patterns, distribution and relationships. They represent the geologist's prior knowledge and understanding of the reservoir. The training image provides a database of the full range of possible patterns and relationships that are believed to be present in the target reservoir [4], from which multipoint statistics are extracted for simulation. It is a conceptual model, which is not conditioned to any data [4,6].

Early advances in MPS simulation proposed the use of 2D digitized outcrop photographs or hand drawn sketches as training images [4,6]. Generating 3D training images by combining 2D information was found to rely on weak assumptions, and introduced errors and uncertainties into the training image [7-8]. Later developments led to the widespread use of object based modeling for generating training images [4]. The object based modeling approach is perhaps the most common and uncomplicated approach for creating 3D training images by generating unconditional realizations. Training images can be generated from several other tools such as outcrop analogues, sequence stratigraphic studies and process-based models [9].

MPS algorithms based on SNESIM require the training image to have similar and repetitive patterns for those patterns to be extracted and reproduced. This principle is referred to as

stationarity [2,10]. By implication, this principle limits the outcrop analogues, models and other tools that can be used to generate training images because many outcrops are made up of non-stationary features and therefore unsuitable for creating training images. Although reservoirs are themselves not entirely stationary, it is good practice to split them into small stationary sections and generate a different training image for each section [9]. Multiple training images may also be required where considerable uncertainty exists regarding facies geometry due to limited geological knowledge [11]. In such situations, multiple training images with variable parameters such as size and orientation of facies, connectivity and heterogeneity should be generated to represent different scenarios.

The size of the training image in relation to the size of the largest feature to be reproduced in the reservoir model is important with regards to ergodicity. Training images should be at least twice the size of the reservoir to be simulated in the direction of the largest continuity due to ergodic fluctuations [10]. These fluctuations, resulting from calculation of parameters from a finite domain, are larger across larger distances over which they are measured. Thus channels, which are usually the largest features in fluvial reservoirs, appear broken along their lengths if the training image is smaller or the same size as the model.

#### 4. General workflow

The following workflow (Figure 1) shows a summary of simple steps to follow to directly use satellite images of modern fluvial depositional environments to create training images for MPS simulation of meandering fluvial reservoirs.

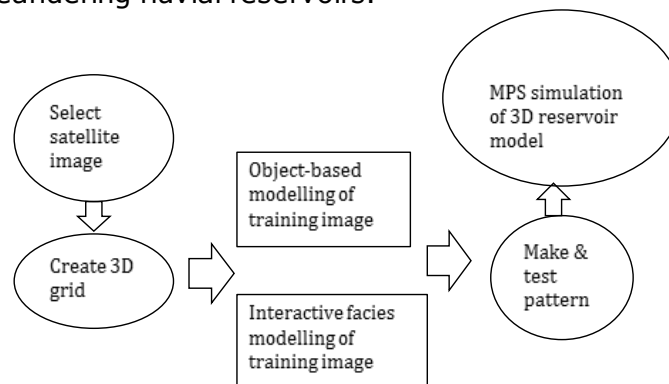


Figure 1. Workflow for using satellite images as analogues to model fluvial reservoirs

#### 4.1. Satellite images

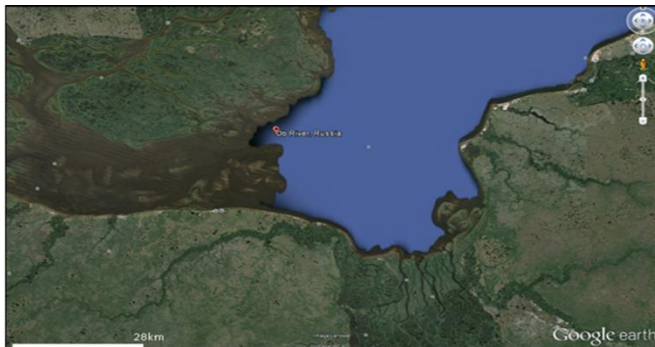


Figure 2. Satellite image of the Ob River area, Russia (Google Earth)

Sections of the satellite image of this area can serve as modern analogues of meandering fluvial reservoirs to create training images. This ensures that the training images, although conceptual, are geologically realistic. The selected sections (Figure 3) show typical meandering channel patterns.



Figure 3. Satellite images of channel patterns in the Ob River area, Russia: (a) Meandering pattern with large meander loops, showing point bars (yellow circles), (b) Meandering pattern with smaller meanders (Google Earth)

#### 4.2. 3D grid

The creation of training images involves creating an empty 3D grid on which the training image would be modeled. This is simplified in Petrel® with the training image and pattern creator, which enables the user to create an empty, simple training image grid (TI grid) by defining the number of cells in the grid, as well as the cell size. The size of the grid may depend on the number, size or complexity of the objects to be populated, and has effects on the execution time. Therefore splitting the reservoir into smaller stationary sections will result in more, but faster training images.

#### 4.3. Object-based training images

One of the most straightforward ways of creating 3D training images is by object-based modelling. This method produces geologically realistic geometries and relationships. Facies modelling under object-based modelling allows the user to select and define facies bodies in the training image (Figure 4). An unconditional training image containing user-defined objects can then be generated to mirror the facies in the satellite image.

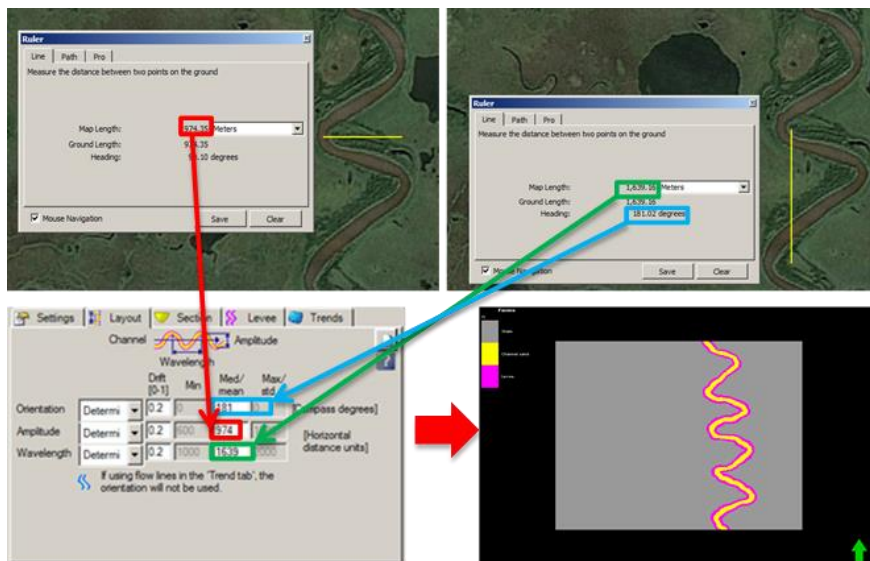


Figure 4. Inputting channel parameters into the object modeling process

The training image (Figure 5) was created using the channel object and associated levees facies bodies. The channel and levee dimensions such as orientation, amplitude, wavelength, width and thickness were defined. The default background facies is shale and so does not require the user to define any parameter for the floodplain.

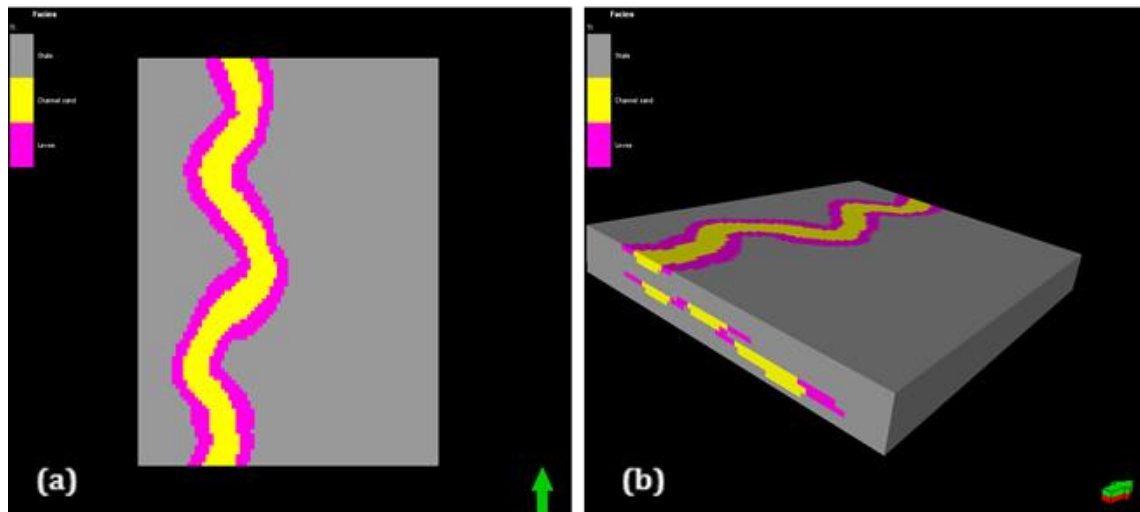


Figure 5. TI 1 – training image showing floodplain (grey), channel (yellow) and levee (pink): (a) map view, (b) oblique view

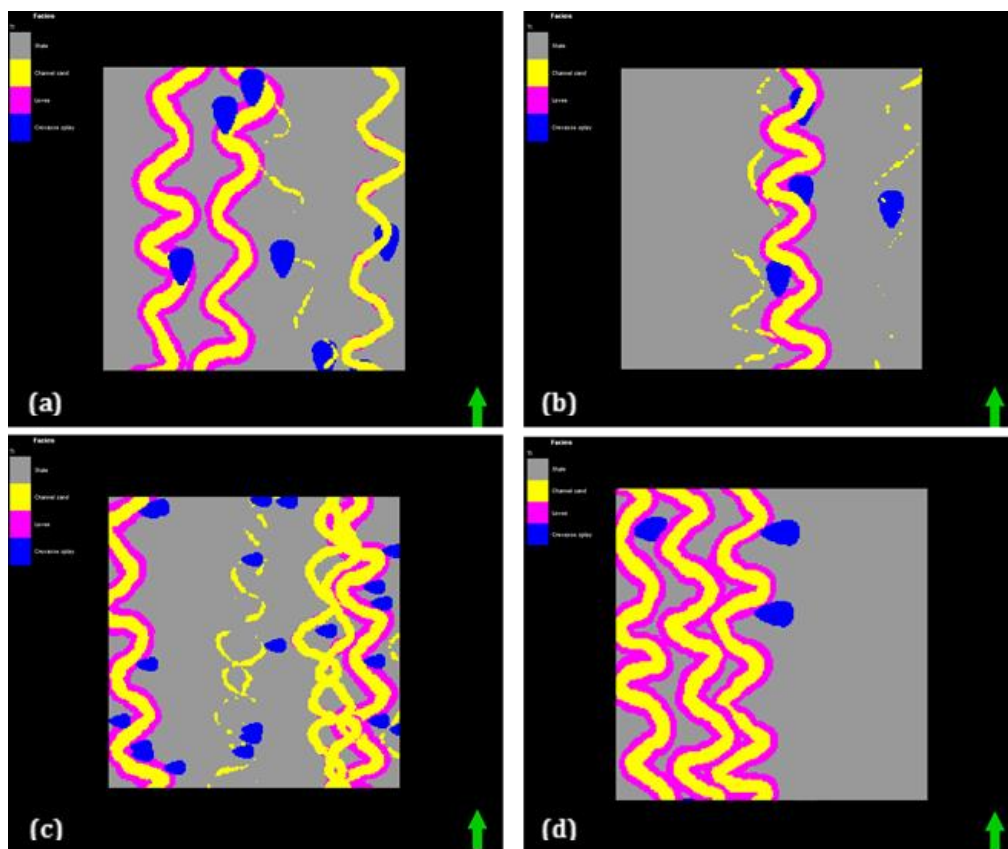


Figure 6. Stages of TI 2 creation process – training image (map view) showing floodplain (grey), channel (yellow), levee (pink) and crevasse splay (blue): (a) erosion rules not defined (b) erosion rules defined, but crevasse splay orientation not defined (c) crevasse splay orientation defined by directional trend property (d) crevasse splay constrained to the outer meanders by object curvature property

Crevasse splay, which form when levees are breached, typically spread outward from the outer meanders. Figure 6 demonstrates the process of creating this relationship. To model the relationship, the erosion rules must be defined for the crevasse splay to erode and overwrite the levees and the floodplain only. Without defining these rules, the crevasse splay are randomly populated in the training image, including within channels (Figure 6a). Defining the erosion rules does not only prevent this, but also attaches the crevasse splay to the levees (Figure 6b). At this stage, it is necessary to generate the directional trend property to define the orientation of the crevasse splay such that they spread outward from the channels (Figure 6c). Generating the object curvature property and using it as a volume probability property constrains the crevasse splays to the outer meanders which have the highest positive curvature values, giving a more geologically realistic relationship (Figure 6d).



The process of adding oxbow lake objects to the training image is similar to that of the crevasse splay. It involves defining the erosion rules for oxbow lake to erode and overwrite floodplain only, and generating the directional trend property to define the orientation of the oxbow lakes (Figure 7). Defining the erosion rules is important to prevent older deposits (oxbow lake) from eroding more recent deposits (channels).

Figure 7. TI 3 – training image (map view) showing floodplain (grey), channel (yellow), levee (pink), crevasse splay (blue) and oxbow lake (orange)



#### 4.4. Interactive facies modelling training images

Interactive facies modeling involves direct painting of facies on the 3D grid. To make the grid visible, a constant value (0) was assigned to the TI grid using the property calculator, which populated the entire grid with background facies (shale). Once this is created, the user can paint the other facies on the TI grid using the facies paintbrush. The user can also filter through the layers of the 3D TI grid and paint the facies on the layers (Figures 8 and 9).

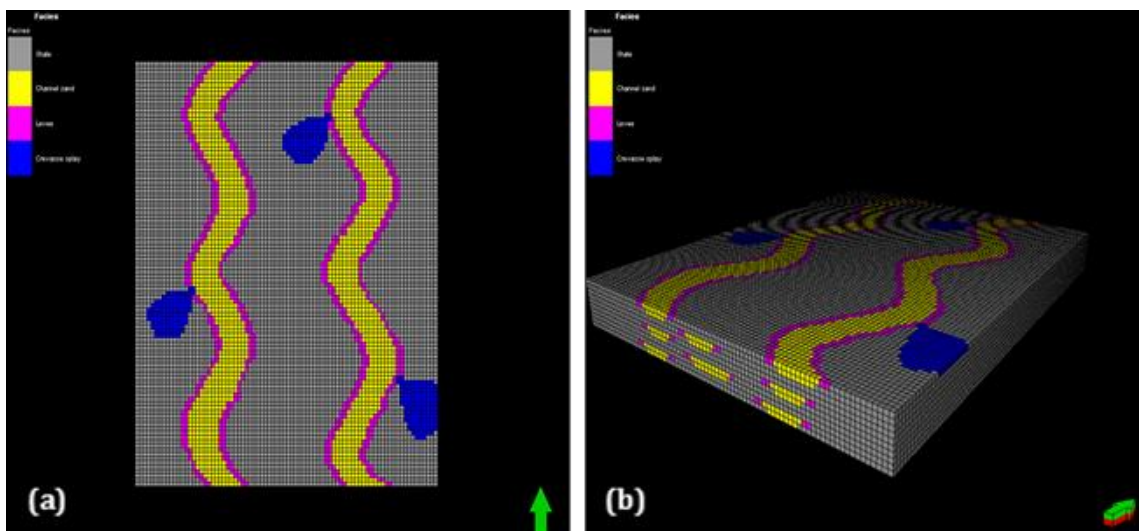


Figure 8. TI 4 – training image showing floodplain (grey), channel (yellow), levee (pink) and crevasse splay (blue): (a) map view, (b) oblique view

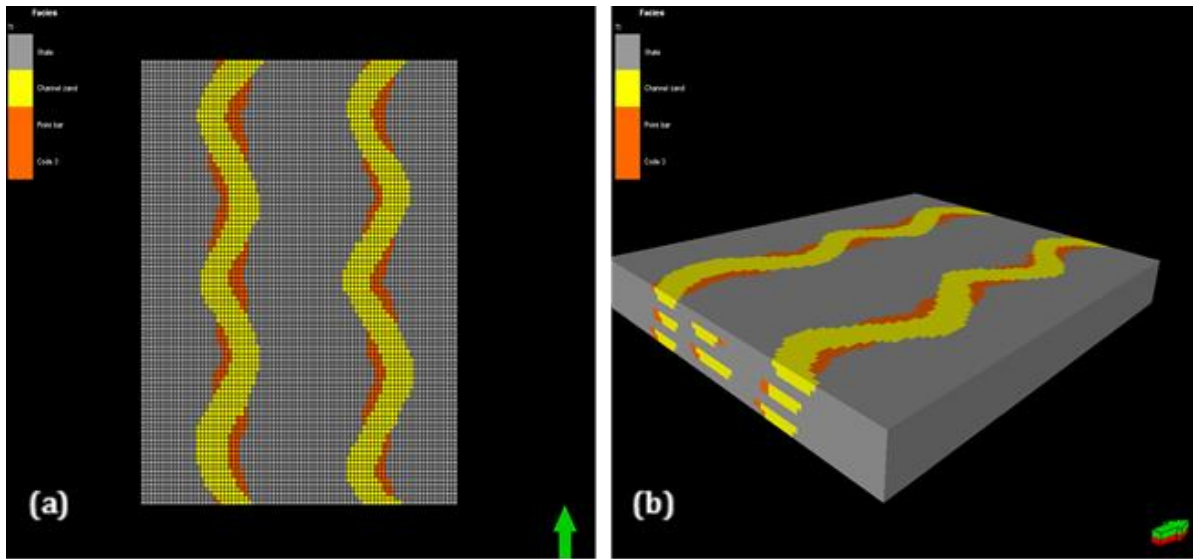


Figure 9. TI 5 – training image showing floodplain (grey), channel (yellow) and point bar (orange): (a) map view, (b) oblique view.

The interactive facies modelling technique also allows the user to directly trace the patterns on the satellite image onto the TI grid. Selected sections of satellite image can be imported into Petrel as bitmaps. Once imported, the limits of the bitmaps can be set to match the TI grid parameters (Figure 10a), so that the bitmap can fit onto the grid. The bitmap can be placed on the grid by setting its Z (depth) value to 0 (Figure 10b).

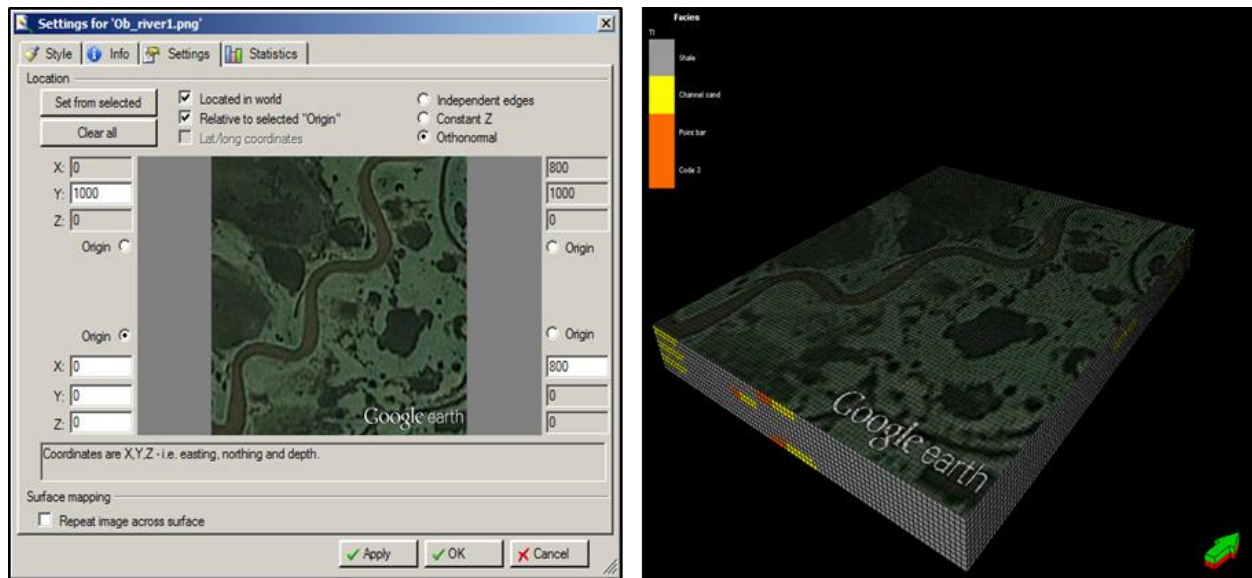


Figure 10. a. Limits of bitmap set to match TI grid parameters, b. Oblique view of bitmap placed on TI grid

The interactive facies modelling technique is especially suitable for patterns that cannot be modelled with the facies bodies available in object-based modelling, such as point bar and large meander loops with narrow necks (Figure 11). Such patterns are best created using interactive facies modelling.

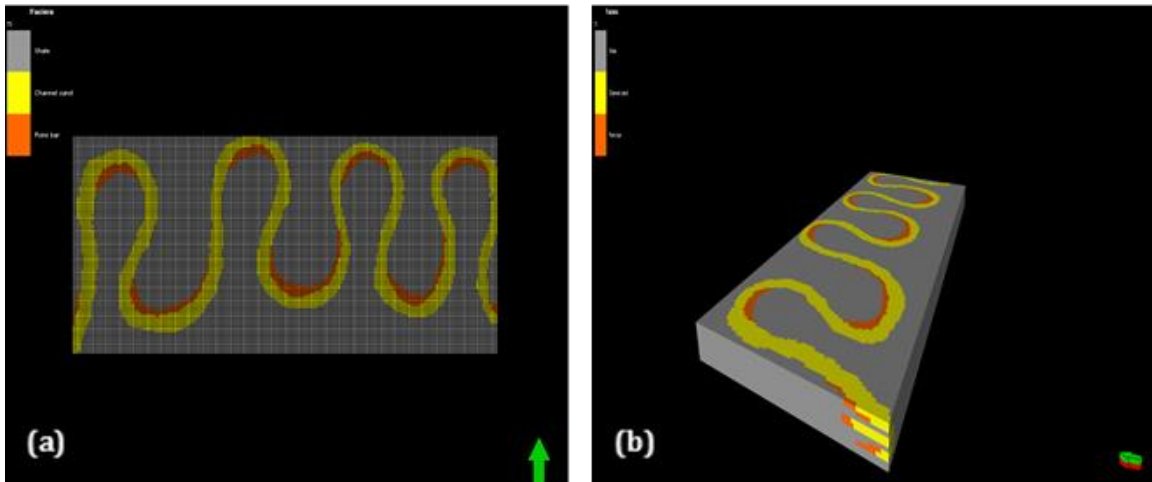


Figure 11. TI 6 – training image showing floodplain (grey), channel (yellow) and point bar (orange): (a) map view, (b) oblique view

#### 4.5. Multi-point facies patterns

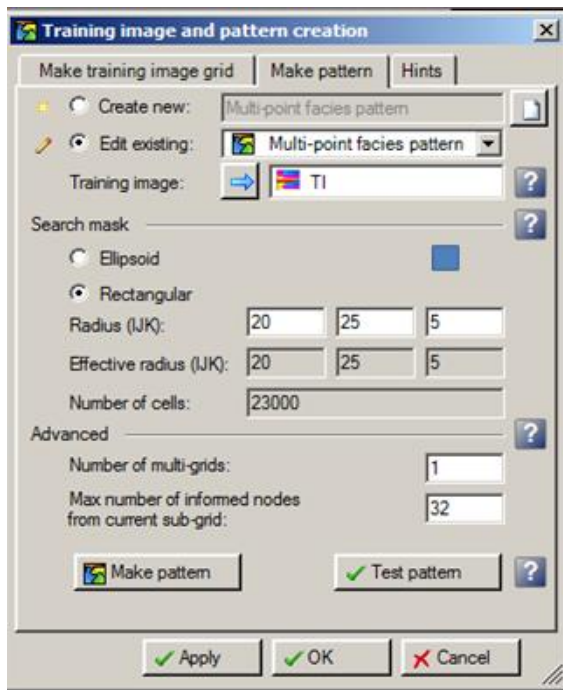


Figure 12. Training image and pattern creation dialog box

MPS utilizes patterns extracted from training images as its main input, which are reproduced during the stochastic simulation. Petrel® allows the user to create these patterns (Figure 12), which explain the neighborhood relationship of facies. This makes the process more intuitive, as the user is able to visualize the patterns to be reproduced prior to simulation.

It is important to consider the effects of the search mask and multi-grids on the patterns (figure 12). During multi-point facies pattern creation, the coarsest grid is populated first. The coarsest grid is given by  $2^{(m-1)}$ , where 'm' is the number of multi-grids. For example, if 2 is chosen as the number of multi-grids, the coarsest grid will be  $2^{(2-1)} = 2$ . This means that the second cell in every direction would be populated first, starting with the central cells. For 4 multi-grids, the coarsest grid will be  $2^{(4-1)} = 8$ , which means that the 8<sup>th</sup> cell in every direction would be populated first. This implies that the smaller the number of multi grids,

the better the patterns are reproduced, and the larger the search mask needed to cover the required area.

Figures 13 and 14 show the effect of ergodic fluctuations on the extracted patterns. The patterns appear broken in the direction of their largest continuity i.e. channels lengths (larger distance) as manifestations of this fluctuations. The extracted patterns (Figures 13 and 14) display these channel discontinuities because they are of the same size as the training images (Figures 5 and 9, respectively). This effect can be eliminated when building the reservoir model. To eliminate the effect, the training image size must be at least twice as large as the largest feature (channel length) reproduced in the reservoir model.

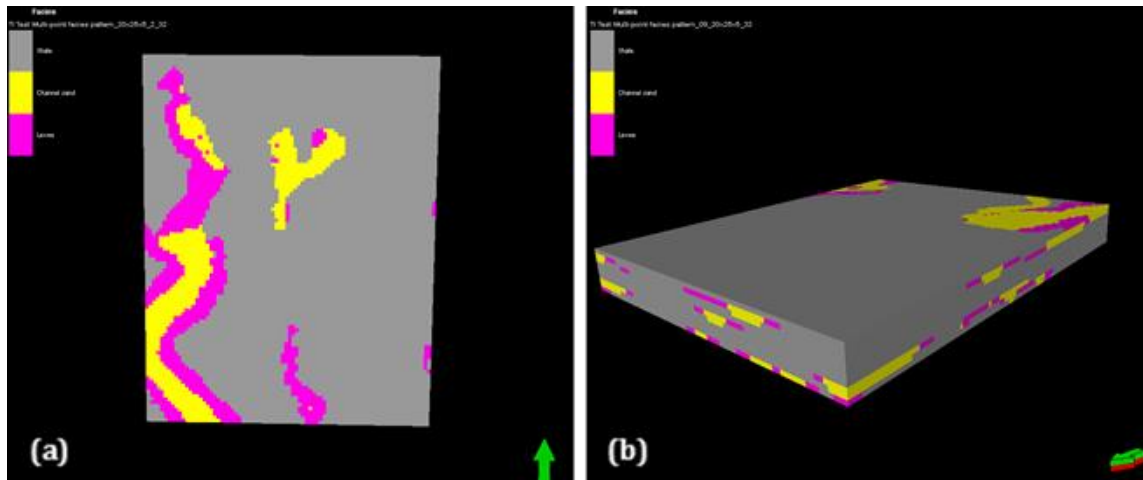
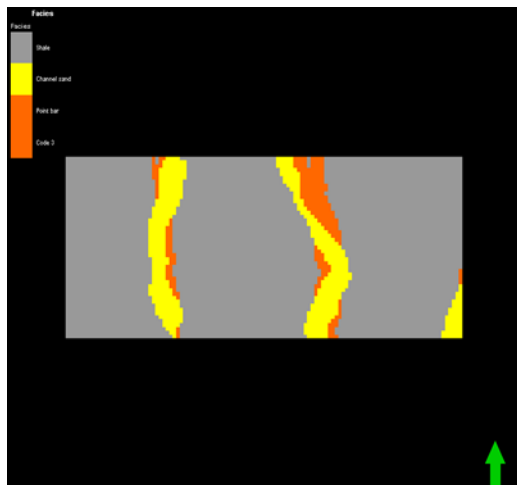


Figure 14. Multi-point facies pattern from TI 5 showing floodplain (grey), channel (yellow) and point bar (orange): (a) map view, (b) oblique view

#### 4.6. MPS Model



The pattern (Figure 14) extracted from TI 5 (Figure 9) was used to create a simple unconditional conceptual MPS model. The model was built to half the size of the training image in the direction of the channels lengths to prevent the manifestation of ergodic fluctuations. The channels are the largest features to be reproduced in the reservoir model hence the smaller size in the direction of their lengths. The pattern was reproduced during the stochastic simulation and the resulting model (Figure 15) shows complete and continuous channels across the floodplain.

Figure 15. Map view of a simple conceptual MPS reservoir model showing floodplain (grey), channel (yellow) and point bar (orange)



#### 5. Conclusions

Satellite images of modern fluvial depositional environments can serve as a library of analogues for meandering fluvial reservoirs, which can be used to create training images for multiple-point statistics. However, this goes with the caveat that they must be stationary. The principle of stationarity, which MPS relies upon to capture and reproduce the information contained in a training image, limits the analogues that can be used to create training images. Suitable satellite images, which satisfy the condition of stationarity can be directly used to create training images based on the object-based and/or the interactive facies modelling techniques following the workflow presented in this paper. The training image must be at least twice the size of the reservoir model in the direction of channels lengths to prevent the manifestation of ergodic fluctuations as channel discontinuities in the reservoir model.

## References

- [1] Strebelle S, Journel AG. Reservoir modeling using multiple-point statistics. The SPE Annual Technical Conference and Exhibition 2001. New Orleans, USA: SPE # 71324.
- [2] Strebelle S. Conditional simulation of complex geological structures using multiple-point statistics. *Mathematical Geology*, 2002; 34: 1-22.
- [3] Liu Y. Using the Snesim program for multiple-point statistical simulation. *Computers & Geoscience*, 2006; 23: 1544-1563.
- [4] Strebelle S, Levy M. Using multiple-point statistics to build geologically realistic reservoir models: the MPS/FDM workflow. *Geological Society London Special Publication*, 2008; 309 (1): 67-74.
- [4] Strebelle S, Zhang T. Non-stationary multiple-point geostatistical models. *In: Leuangthong O, Deutsch CV (Eds) Quantitative Geology and Geostatistics*, 2004; 14: 235-244.
- [5] Zhang T, McCormick D, Hurley N, Signer C. Applying multiple-point geostatistics to reservoir modelling – A practical perspective. *Petroleum Geostatistics 2007*. Cascais, Portugal.
- [6] Strebelle S. Multiple-point geostatistics: from theory to practice. 9<sup>th</sup> International Geostatistics Congress, June 11 – 15, 2012. Oslo, Norway.
- [7] Strebelle S. Sequential simulation drawing structure from training images. Stanford University, Stanford, CA, USA: PhD Thesis, 2000.
- [8] Okabe H. Pore-scale modeling of carbonates. Imperial College, London: PhD Thesis, 2004.
- [9] Zhang T. Incorporating geological conceptual models and interpretations into reservoir modelling using multiple-point geostatistics. *Earth Science Frontiers*, 2008; 15(1): 26-35.
- [10] Caers J, Zhang T. Multiple-point geostatistics: a quantitative vehicle for integrating geologic analogs into multiple reservoir models. *Computers & Geosciences*, 2002; 30: 741-751.
- [11] Harding A, Liu Y, Abriel W, Strebelle S. Multiple-point simulation integrating wells, three-dimensional seismic data and geology. *American Association of Petroleum Geologists Bulletin*, 2004; 88: 905-921.
- [12] Bridge JS. Fluvial facies models: Recent developments, *In: Posamentier HW, Walker RG (eds), Facies Models Revisited*. SEPM Special Publication, 2006; 84: 85-170.
- [13] Miall AD. *The geology of fluvial deposits: Sedimentary facies, Basin analysis and Petroleum geology*. Springer Berlin, 1996.

---

*To whom correspondence should be addressed: Buhari U. Ardo, Department of Geology, Modibbo Adama University of Technology, Yola, Nigeria*

## FUEL CHARACTERIZATION AND THERMAL DEGRADATION BEHAVIOUR OF OWUKPA COAL

*Bemgba B. Nyakuma*<sup>1\*</sup>, *Edo O. Ojoko*<sup>2</sup>, *Olagoke Oladokun*<sup>1</sup>, *Aliyu A. Bello*<sup>1</sup>,  
*Adakole B. Aboje*<sup>3</sup>, *Terstegha J-P. Ivase*<sup>4</sup>, *Ali H. Al-Shatri*<sup>1</sup>, *Habib Alkali*<sup>1</sup>

<sup>1</sup> Faculty of Engineering, School of Chemical and Energy Engineering, Universiti Teknologi Malaysia, 81310 Skudai, Johor Bahru, Malaysia

<sup>2</sup> Faculty of Engineering, School of Civil Engineering, Universiti Teknologi Malaysia, 81310 Skudai, Johor Bahru, Malaysia

<sup>3</sup> Ehinehi Nigeria Enterprises Limited, 11 Crescent, Flat 130 Kado Estates, Federal Capital Territory (FCT), Abuja, Nigeria

<sup>4</sup> Bio-Resource Development Centre (BIODEC), National Biotechnology Development Agency, Makurdi, Benue State, Nigeria

Received September 27, 2018; Accepted October 19, 2018

---

### Abstract

Coal is a fossil fuel and feedstock utilised globally for the production of chemicals, fertilisers and electricity. Intrinsically, coal is an integral part of the global energy mix and has significantly contributed to the socioeconomic growth and development of nations worldwide. With the second largest deposits in Africa, Nigeria is expected to invest in coal electricity in the future. However, limited data on the fuel characteristics, thermal degradation behaviour, and evolved pollutants profiles of Nigerian coals has hampered the establishment of coal power plants. Therefore, this study examined the physicochemical, mineralogical, and thermal properties of Owukpa (WKP) coal. The results showed that WKP contains high carbon, hydrogen, volatile matter, fixed carbon, ash and higher heating value but low nitrogen, sulphur, oxygen, and moisture. The mineral content was comprised of organic and inorganic mineral elements. The thermal analysis revealed significant mass loss (but low residual mass) for flash combustion (FCO) compared to low mass loss (high residual mass) for flash pyrolysis (FPY). The thermal decomposition of WKP under FCO and FPY occurred in two stages due to drying and devolatilization, although FCO was more thermally efficient than FPY. Consequently, WKP can be effectively utilised for energy recovery under either oxidative or non-oxidative conditions.

**Keywords:** Fuel Characterization; Thermal Degradation; Owukpa, Benue; Nigeria.

---

## 1. Introduction

Coal is an important fossil-based fuel and feedstock globally utilised for the production of chemicals, fertilisers and most importantly, electricity. As a result, coal remains an integral part of the global energy mix accounting for over 38% of global electricity generation [1]. Given its importance, analysts posit that coal will remain a crucial contributor to energy production and supply in the future. Accordingly, coal utilisation for energy production is expected to expand significantly in developing countries particularly India, China, and South Africa which have large deposits [2].

Likewise, the trend is expected to grow in Nigeria, which has the second largest deposits of coal in Africa [3]. Currently, it is estimated that Nigeria has 640 million tonnes of proven reserves along with 2.8 billion tonnes of inferred reserves. The distribution of Nigerian coal is comprised of 12% lignites, 49% subbituminous, and 39% bituminous [3]. Despite its huge potential, coal utilisation for electricity production in Nigeria remains insignificant [4]. As a result, Nigeria continues to experience severe power shortages resulting in an energy crisis that has stifled socio-economic growth and sustainable development.

---

The nation's inability to harness coal energy is attributed to numerous challenges which can be broadly categorised as socio-economic, environmental, and technological. Furthermore, the non-existence of coal in Nigeria's energy mix is due to the lack of comprehensive physicochemical, thermo-kinetic, and thermodynamic data on various Nigerian coals [5]. Current data on Nigerian coals is limited to its rheological [6], petrographic [7-8], geochemistry [9-10], and mineralogical [11-12] properties. Other studies have attempted to examine the power generation characteristics of selected coals in Nigeria [13-15].

However, there is limited data on the fuel characteristics, thermal degradation behaviour, evolved gas and pollutants profile of Nigerian coals along with its solid waste profiles after combustion. As a result, the design, operation, and maintenance of coal power plants in Nigeria remains plagued by such technical issues. Therefore, it is important to critically examine the fuel properties of various Nigerian coals such as Owukpa, which is a sub-bituminous coal from Benue state in Nigeria. Aptly termed the "food basket of the nation", Benue state produces large quantities of fresh agricultural produce annually. However, the lack of power supply has hampered the efficient storage, transportation, and conversion of the farm produce into finished products, thereby resulting in huge economic losses, waste disposal, and environmental challenges.

Therefore, the main objective of this study is to examine the fuel characteristics and thermal properties of Owukpa coal as a potential feedstock for future power generation in Nigeria. The study presents the physicochemical, microstructural, mineralogical and thermal properties of Owukpa (WKP) coal. It is envisaged that the findings will avail engineers, policy, and decision makers with comprehensive data on Owukpa coal required to implement technologically, economical and environmentally friendly strategies for future energy recovery in power plants.

## 2. Experimental

The Owukpa coal sample was supplied by Ehinehi Nigeria Enterprises Limited – a mining and prospecting company based in the Federal Capital Territory, Abuja, Nigeria. The rock sample was crushed, ground, and sieved to obtain homogeneous sized particles below 250  $\mu\text{m}$ . Next, the powdered Owukpa (WKP) was subjected to physicochemical analysis in which the sample was characterised by ultimate, proximate, and calorific analyses to examine its elemental, proximate and higher heating values (HHV). The elemental analysis was performed on the CHNS elemental analyser (Model: vario MACRO Cube, Germany) based on ASTM standard D5373-93.

The proximate analysis was performed by thermogravimetric analysis (TGA) based on the procedure described in the literature [16]. The higher heating value was determined by combustion calorimetry using an oxygen bomb calorimeter (Model: IKA C2000, USA) based on the isoperibolic measurement procedure described in ASTM standard D2015. The surface morphology, microstructure, and mineral composition of WKP were examined through Scanning Electron Microscopy (SEM). The SEM was fitted with an Energy Dispersive X-ray (EDX) detector (Model: JEOL-JSM IT 300 LV, Germany) and analysed based on procedures previously described in the literature [17].

Lastly, the thermal analysis of WKP was performed to examine its degradation behaviour and characteristic profile temperatures (TPC) under flash combustion and pyrolysis conditions. The non-isothermal thermogravimetric analysis (TGA) was performed by heating 10 mg of pulverised WKP in an alumina crucible at a heating rate of 50°C/min from room temperature (RT) to 900°C. For flash pyrolysis, ultra-pure nitrogen (flow rate 20 mL/min) was employed to flush the TG analyser whereas air (flow rate of 20 mL/min) was employed for flash combustion. The objective was to examine the thermal properties of WKP under conditions similar to pulverised coal combustion and pyrolysis. On completion, the raw data was retrieved and plotted as mass loss (TG, %) and derivative mass loss (DTG %/min) against temperature in degrees Celsius. Next, the temperature profile characteristics (TPC) of WKP were determined through the Shimadzu thermal analysis software (version: TA-50 Workstation) to examine its thermal degradation behaviour (TDB). The TPCs examined in this study were; onset or ignition ( $T_{on}$ ), midpoint ( $T_{mid}$ ), and maximum decomposition ( $T_{max}$ ), and burnout ( $T_{off}$ ) temperatures together with the mass loss ( $M_L$ , %) and residual mass ( $R_M$ , %) of WKP coal. The definition of the TPC terms is detailed in our previous study [17].

### 3. Results and discussion

#### 3.1. Physicochemical analyses

The physicochemical properties of Owukpa (WKP) coal was examined by ultimate, proximate, calorific analysis and the results presented in Table 1. The results were compared with the values of Owukpa reported in Chukwu *et al.*, [31].

Table 1. Physicochemical properties of Owukpa coal

Analysis	Element	Symbol (Unit)	This Study	Chukwu <i>et al.</i> , [31]
Ultimate	Carbon	C (wt.%)	65.40	67.82
	Hydrogen	H (wt.%)	5.23	5.88
	Nitrogen	N (wt.%)	1.60	1.43
	Sulphur	S (wt.%)	0.46	0.60
	Oxygen	O (wt.%)	27.32	9.47
Proximate	Moisture	MC (wt.%)	6.50	11.50
	Volatile matter	VM (wt.%)	31.49	39.10
	Fixed Carbon	FC (wt.%)	41.78	46.10
	Ash	AC (wt.%)	20.23	3.30
Calorific	Heating Value	HHV (MJ/kg)	26.67	26.51

The results in Table 1 indicate the elemental composition of WKP consists of high proportions of C and H but low N, S, and O content. The proximate composition of WKP indicates high volatiles (VM), fixed carbon (FC) and ash (AC) but low moisture (M) content. The calorific value was 26.68 MJ/kg, which according to ASTM D388 standard [18] categorises WKP as a subbituminous A, non-agglomerating low-rank coal (LRC). Furthermore, the HHV of WKP is significantly higher than other Nigerian coals from Garin Maiganga (23.74 MJ/kg) [19], Inyi (19.39 MJ/kg), and Ezimo (20.96 MJ/kg) [3], Ihioma (20.33 MJ/kg) and Ogboligbo (16.33 MJ/kg) [20]. However, it is in good agreement with the HHV of 26.51 MJ/kg reported for Owukpa in Chukwu *et al.*, [31]. In addition, the CHNS and proximate (MC, VM, FC) properties of WKP in this study are in fairly good agreement with Chukwu *et al.*, [31]. However, there are striking differences of 17.85 wt.% and 16.93 wt.% in the oxygen (O) and ash (A) content, respectively. This observation may be due to the methods of coal sampling, preparation, and characterisation techniques employed in both studies.

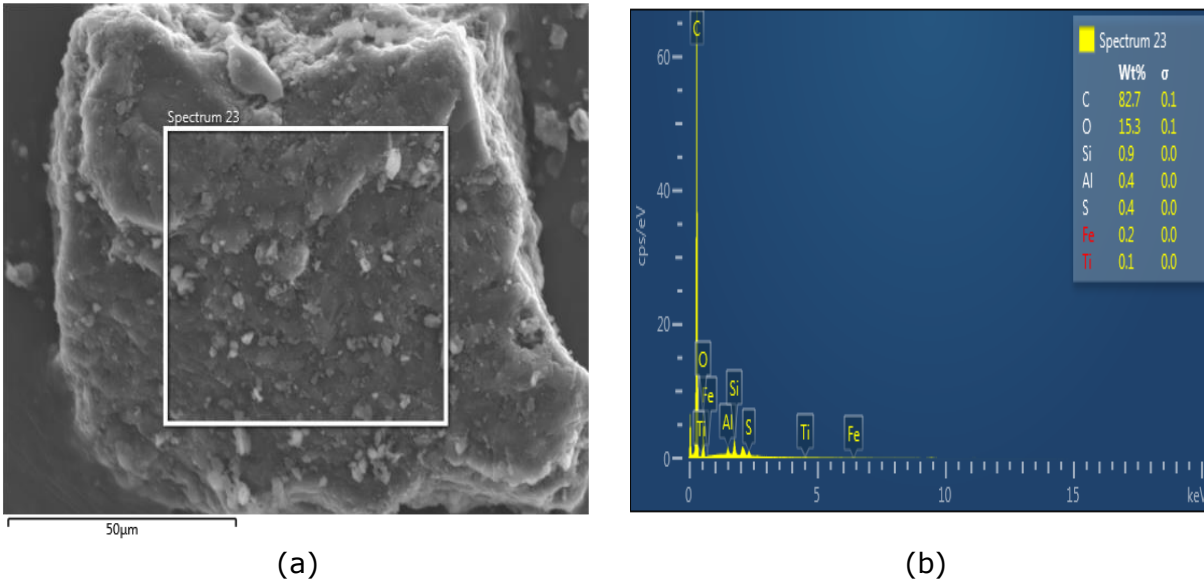
#### 3.2. Microstructure and mineralogical analyses

The SEM micrographs for Owukpa coal are presented in Figures 1 (a) and (b). As observed in Figure 1 (a), the micrograph reveals Owukpa coal consists of a heterogeneous mix of fine and coarse-grained particles characterised by a distinctive glossy appearance. This is due to the composition of metallic elements present in the complex structure of the coal. Therefore, the mineralogical composition of WKP was examined through Energy Dispersive X-ray (EDX) to determine its constituents. The EDX is presented in the electron micrograph in Figure 1(b).

As observed in Figure 1(a), the mineralogical composition of WKP is due to the elements C, O, Si, Al, S, Fe, and Ti (wt.%) in decreasing order of magnitude. The composition of each element in the WKP structure is presented in weight per cent (wt.%) in Table 2.

Table 2. Mineral composition of Owukpa coal

Coal element	Chemical symbol	Composition (wt.%)	Coal element	Chemical symbol	Composition (wt.%)
Carbon	C	82.74	Sulphur	S	0.40
Oxygen	O	15.29	Iron	Fe	0.18
Silicon	Si	0.90	Titanium	Ti	0.06
Aluminium	Al	0.43			



(a) (b)  
Figure 1. SEM/EDX micrographs for Owukpa coal

As observed in Table 2, the mineral composition of WKP is mainly carbon (C=82.7 wt.%), oxygen (O=15.3 wt.%), silicon (Si=0.90 wt.%) and aluminium (Al=0.43 wt.%) with trace amounts of iron (Fe=0.18 wt.%) and titanium (Ti=0.06 wt.%). The elements of silicon and aluminium indicate the presence of oxides of silicon (SiO<sub>2</sub>), aluminium (Al<sub>2</sub>O<sub>3</sub>), sulphur (SO<sub>3</sub>), iron (Fe<sub>2</sub>O<sub>3</sub>), and titanium (TiO<sub>2</sub>). In addition, the mineral composition may also contain silicates, sulphates, sulphides, and carbonate compounds.

In summary, the EDX results indicate that WKP coal has high mineral matter which may account for the high ash content reported in Table 1. The potential energy recovery from WKP particularly under oxidative conditions will potentially result in the deposition of high ash content rich in mineral matter. This could cause ash deposition and eventual operational challenges due to fouling, sintering, and agglomeration in equipment during coal conversion in power plants. Therefore, further tests are required to critically examine the ash and mineral matter content of WKP and its effects on thermal conversion.

### 3.3. Thermal analyses

The TG-DTG plots for the flash combustion (FCO) and flash pyrolysis (FPY) for Owukpa (WKP) are presented in Figures 2 and 3.

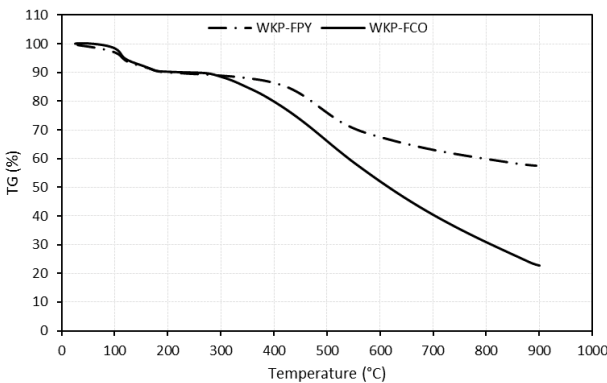


Figure 2. TG plots for flash combustion and pyrolysis of WKP

As observed in Figure 2, the thermal analysis of WKP under flash combustion and pyrolysis resulted in a progressive mass loss (M<sub>L</sub>) and ultimately a mass of residues (R<sub>M</sub>). The FCO process resulted in a more significant M<sub>L</sub> as evident in the curved plot in Figure 2. This may be due to the oxidative nature of the process resulting in the exothermic reactions that ensured significant thermal degradation of WKP coal constituents. However, the thermal degradation of WKP under FPY resulted in lower M<sub>L</sub> due to the non-oxidative and endothermic nature of the process.

As a result of the difference in operating conditions, it is expected that thermal degradation behaviour, thermal reactivity, and temperature profile characteristics (TPC) of WKP will vary distinctly. To examine the thermal degradation behaviour, the TPCs were deduced from the Shimadzu Thermal analysis software (version: TA-50 Workstation). The results of the TPCs deduced from the TG plots are presented in Table 3.

Table 3. TG-TPCS for Flash Pyrolysis and Combustion of Owukpa coal

Thermal analysis	Onset temperature ( $T_{ons}$ , °C)	Midpoint temperature ( $T_{mid}$ , °C)	Offset temperature ( $T_{off}$ , °C)	Mass loss ( $M_L$ , %)	Residual mass ( $R_M$ , %)
FPY	339.06	469.41	617.25	42.09	57.91
FCO	274.56	519.47	759.23	77.41	22.59

As can be observed in Table 3, the thermal degradation of WKP under FPY (flash pyrolysis) resulted in 42.1% mass loss ( $M_L$ ) compared to 77.4% during FCO (flash combustion). As a result, the residual mass ( $R_M$ ) for FPY and FCO were 57.9% and 22.6%, respectively. Based on the onset ( $T_{ons}$ ) and offset ( $T_{off}$ ) TG-TPC temperatures, the FPY occurred between 339.06°C and 617.25°C whereas the FCO occurred between 274.56°C and 759.23°C. This indicates that FCO occurred over the temperature range of 484.67°C compared to 278.19°C for FPY accounting for the higher  $M_L$  (and lower  $R_M$ ) in the former compared to the latter.

Next, the thermal degradation behaviour and decomposition pathway for the FPY and FCO of WKP coal were also examined by derivative thermogravimetric analysis (DTG). The DTG plots are presented in Figure 3.

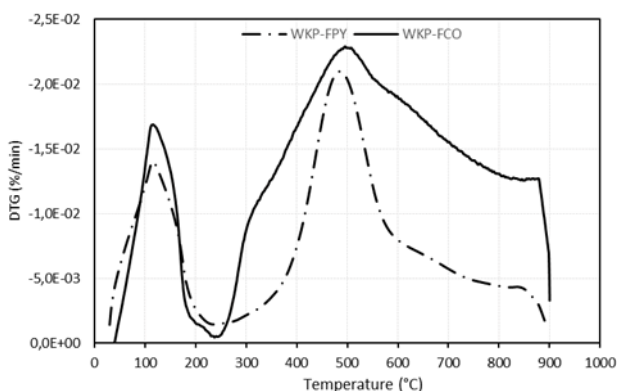


Figure 3. DTG plots for flash combustion and pyrolysis of WKP

As observed in Figure 3, the DTG plots for FPY and FCO are characterised by two predominant set of peaks in two distinct regions. The first region occurred between RT and 250°C whereas the second region was from 250°C to 900°C. Since the first region occurred below 250°C thereby resulting in mass loss below 10%, it can be ascribed to loss of moisture or drying of WKP during FPY and FCO. However, the mass loss in the second region was significantly higher than during drying and ascribed to the loss of volatile matter (or devolatilization) in WKP. The degree or rate of mass loss and the TPCs for drying and

devolatilization were examined as presented in Table 4.

Table 4 DTG-TPCS for Flash Pyrolysis and Combustion of Owukpa coal

Thermal Analysis	Peak drying temperature ( $D_{max}$ , °C)	$M_L$ rate (%/Min)	Peak devolatilization temperature ( $T_{max}$ , °C)	$M_L$ Rate (%/Min)
FPY	116.48	3.86	487.41	5.53
FCO	116.17	5.50	495.84	5.26

As observed in Table 4, the  $D_{max}$  (peak drying temperature) for FPY and FCO differ slightly during drying. Furthermore, the rate of  $M_L$  at  $D_{max}$  for FPY (3.9 %/min) is lower than that for FCO (5.5 %/min). Similarly, the devolatilization peak temperature ( $T_{max}$ ) for FPY and FCO

differed slightly during devolatilization. This indicates that the oxidative or non-oxidative nature of the process does not significantly influence the  $M_L$  rate or degradation pathways during the FPY and FCO of WKP under the conditions examined in this study.

#### 4. Conclusion

The paper examined the fuel characteristics and thermal degradation of Owukpa (WKP) coal from Benue state in Nigeria. The fuel characteristics of WKP were examined based on elemental, proximate, and calorific analyses. On the other hand, the thermal degradation behaviour was examined by non-isothermal thermogravimetric analysis under flash combustion (FCO) and flash pyrolysis (FPY) conditions. The results indicate Owukpa coal contains high proportions of combustible elements (C, H) but low pollutant elements (N, S) and O. The proximate properties revealed low moisture content but significantly high proportions of volatile matter, fixed carbon, ash and higher heating value. The mineralogical composition of WKP is due to C, O, Si, Al, S, Fe, and Ti elements in decreasing order. The thermal degradation of WKP revealed significant mass loss (but low residual mass,  $R_M$ ) for flash combustion (FCO) whereas the pyrolysis process (FPY) was characterised by low mass loss (but high residual mass,  $R_M$ ). This demonstrates that the FCO process is more thermally efficient compared to FPY. The DTG plots revealed WKP decomposes in two stages characterised by drying and devolatilization. Lastly, the TPCs indicated that the degradation pathways for FCO and FPY are similar as observed in the study. In general, the fuel characteristics and thermal properties of WKP confirmed it is a prospective fuel for energy recovery under either oxidative or non-oxidative conditions provided the high ash content can be addressed.

#### References

- [1] IEA, Market Series Report: IEA Coal 2017 2017; International Energy Agency: Paris, France. 1-8.
- [2] OECD Working Paper, The Global Value of Coal 2012.
- [3] Chukwu M, Folayan C, Pam G, and Obada D. Characterization of some Nigerian coals for power generation. *Journal of Combustion*, 2016; 2016.
- [4] WorldBank. Access to electricity (% of population) - The case of Nigeria. 2018; Available from: <https://bit.ly/2Ih1b8L>.
- [5] Nyakuma BB and Jauro A. Chemical and Pyrolytic Thermogravimetric Characterization of Nigerian Bituminous Coals. *GeoScience Engineering*, 2016; 62(3): 1-5.
- [6] Ryemshak SA and Jauro A. Proximate analysis, rheological properties and technological applications of some Nigerian coals. *International Journal of Industrial Chemistry*, 2013; 4(1): 7.
- [7] Odeh AO. Exploring the potential of petrographics in understanding coal pyrolysis. *Energy*, 2015; 87: 555-565.
- [8] Ayinla HA, Abdullah WH, Makeen YM, Abubakar M, Jauro A, Yandoka BMS, and Abidin NSZ. Petrographic and geochemical characterization of the Upper Cretaceous coal and mudstones of Gombe Formation, Gongola sub-basin, northern Benue trough Nigeria: Implication for organic matter preservation, paleodepositional environment and tectonic settings. *International Journal of Coal Geology*, 2017; 180: 67-82.
- [9] Jauro A, Obaje N, Agho M, Abubakar M, and Tukur A. Organic geochemistry of Cretaceous Lamza and Chikila coals, upper Benue trough, Nigeria. *Fuel*, 2007; 86(4): 520-532.
- [10] Ogala JE. The geochemistry of lignite from the neogene ogwashi-asaba formation, niger delta basin, southern nigeria. *Earth Sciences Research Journal*, 2012; 16(2): 151-164.
- [11] Ogala J, Siavalas G, and Christanis K. Coal petrography, mineralogy and geochemistry of lignite samples from the Ogwashi-Asaba Formation, Nigeria. *Journal of African Earth Sciences*, 2012; 66: 35-45.
- [12] Akinyemi S, Gitari W, Akinlua A, and Petrik L, Mineralogy and geochemistry of sub-bituminous coal and its combustion products from Mpumalanga Province, South Africa, in *Analytical Chemistry*. 2012; InTech.
- [13] Sonibare O, Ehinola O, Egashira R, and KeanGiap,L. An investigation into the thermal decomposition of Nigerian Coal. *Journal of Applied Sciences*, 2005; 5(1): 104-107.
- [14] Sambo A. Prospect of coal for power generation in Nigeria. in A paper presented at the International Workshop for the Promotion of Coal for Power Generation. 2009.

- [15] Oji J, Idusuyi, N, and Kareem, B. Coal power utilization as an energy mix option for Nigeria: a review. *American Academic & Scholarly Research Journal*, 2012; 4(4): 1.
- [16] Donahue CJ and Rais EA. Proximate Analysis of Coal. *Journal of Chemical Education*, 2009; 86(2): 222.
- [17] Nyakuma B, Jauro A, Oladokun O, Bello A, Alkali H, Modibo M, and Abba M. Physicochemical, Mineralogical, and Thermogravimetric Properties of Newly Discovered Nigerian Coals. *Petroleum & Coal*, 2018; 60(4): 641-649.
- [18] Speight JG. *The Chemistry and Technology of Coal*. Chemical Industries, 2012: 8.
- [19] Nyakuma BB and Jauro A. Physicochemical Characterization and Thermal Decomposition of Garin Maiganga Coal. *GeoScience Engineering*, 2016; 62(3): 6-11.
- [20] Nyakuma BB, Oladokun O, Jauro A, and Nyakuma DD. Evaluating the Energy Recovery Potential of Nigerian Coals under Non-Isothermal Thermogravimetry. *IOP Conference Series: Materials Science and Engineering*, 2017; 217(1): 012013.

---

*To whom correspondence should be addressed: Bemgba.B. Nyakuma (MSc), School of Chemical & Energy Engineering, Faculty of Engineering, Universiti Teknologi Malaysia, 81310 UTM Skudai, Johor Bahru, Malaysia*

## PRODUCTION OF BOILER AND FURNACE FUELS FROM DOMESTIC WASTES (POLYETHYLENE ITEMS)

*Andrey Grigorov, Aleksey Mardupenko, Irina Sinkevich, Alena Tulsakaya\*, Oleg Zelenskyi*

*National Technical University "Kharkiv Polytechnic Institute", Kharkiv, Ukraine*

Received July 17, 2018; Accepted October 19, 2018

---

### Abstract

The results of the thermal destruction of solid domestic waste (which are polyethylene items) were presented for batch-type laboratory equipment. According to the modern requirements of EU for the amount of sulphur in fuel and boiler fuels, polyethylene items are a valuable source for production of these fuels.

During atmospheric heating of the raw material in reactor the intensive destruction of polyethylene can be observed in the range of temperature 560–580 K. It has been defined the composition of products of polyethylene thermal destruction: 95 % (mass.) of liquid hydrocarbons, 4,5 % (mass.) of light hydrocarbon gases and 0,5 % (mass.) of coke. Fractionation of liquid hydrocarbons allows to separate 15 % (mass) of fraction 340-488 K, 14 % of fraction 406-518 K, 43 % of fraction 438-546 K and 27 % of residue (>623°C fractions).

Liquid products can be applied for production of boiler and furnace fuels independently and in a mixture with the petroleum processing products in different ratio.

**Keywords:** polyethylene items; thermal destruction; reactor; boiler fuel; fractionation, residue; aromatic hydrocarbons.

---

## 1. Introduction

In a condition of strong development of technosphere, we have a problem of accumulation of municipal, industrial and other waste. The territories which are considered to be applied for utilization of waste must be withdrawn from the agricultural fund for no less than 100 years. Nevertheless, technological processing of waste is an important income item in many countries of EU and can be applied for the production of electrical energy and different construction materials.

## 2. Publication analysis

Nowadays polyethylene items are the most common source of domestic waste in a world, and the most common way for their utilization are landfilling and burning with the production of electrical energy <sup>[1]</sup>. However, implementation of these ways doesn't solve the problem of environmental pollution because the burning of polymers leads to the formation of a huge amount of gaseous and solid waste.

The most common way of utilization is crushing and granulation of polyethylene waste for the further production of packet, film, etc. <sup>[2-3]</sup> and production of complex technical items through the die-casting <sup>[4]</sup>.

There is a way of production of synthetic fuel through the dissolving of solid polyethylene briquettes with the heating of solution up to 380-400 K with the further supply to the burners of an internal combustion system <sup>[5]</sup>. To increase the strength of briquettes, different authors propose to dissolve 8-14 % mass of polyethylene in the liquid hydrocarbon fraction with the further cooling and crystallization of the hardener <sup>[6]</sup>. Authors of <sup>[7]</sup> have performed the tech-

nology of production of composite solid fuel by the combined processing which includes briquetting of the mixture (5-10% (mass.) of polyethylene, 3-5% (mass.) of waste oil and up to 90% (mass.) of coal or coke dust. There is a technology of carbonization of solid domestic waste at 720 K in an ultrahigh-frequency microwave radiation field which is aimed at obtaining of 12.9 % (mass) gaseous products, 48.5 % (mass.) of fuel oil 38.6 % (mass.) of solid residue [8].

There is also a well-known way of processing of polymer materials through the catalytic thermal decomposition in the alkyl-benzene. Temperature is 540-700K and pressure is 6 MPa. The disadvantage of the process is the application of expensive rare-earth material for the catalyst [9].

There was proposed the catalytic destruction of polyethylene at 620–670K at atmospheric pressure. The hydrocarbon mixture that was obtained in this way can be applied as a raw material for the motor fuels or at petrochemical plants [10]. Due to the destruction of polyethylene in the presence of synthetic catalyst, we can obtain a fraction which is similar to gasoline [11]. Authors of [12] described the production of motor fuel components which contain a significant part of iso-structure hydrocarbons that increase the antidetonation properties of this fuel.

Boiler and furnace fuel are widely used along with the motor in the industry and domestic economy that's why the production of the boiler and furnace fuel should be carefully studied.

### 3. The purpose and goal of the research

Current trends in the EU according to the application of liquid boiler fuel with a low amount of sulfur, require the complete desulfurization of raw material. From the one side, it makes the application of condensing boils easier and decreases the harmful emission, from the other side – it makes the fuel more expensive. The most rational solution is the production of the boiler and furnace fuel which meet the EU standards and decrease the environmental impact of the accumulated waste.

### 4. Experimental part

Exhausted polyethylene items are processed for obtaining of liquid components of the boiler and furnace fuel at the laboratory unit (Fig. 1). Sorted and crushed polyethylene (size of particles is 2×2 mm) was uploaded into the reactor 1. The raw material was heated up by the electric oven 2. Pressure and temperature were controlled by pressure gauge 3 and two thermocouples 4.

The shut-off valve was installed to provide the high pressure if it is necessary. Thermal destruction products get to the condensing fridge 6 through the shut-off valve 5. Non-condensed gases can be removed from the unit through the condensing fridge 6.

If it is necessary to keep the temperature of the coolant (oil) in condensing fridge 6 between 546-566 K, the electrical heating can be provided. That's why oil is applied as a coolant in fridge 6 instead of water. Condensed liquid products get to the storage after thermal destruction.

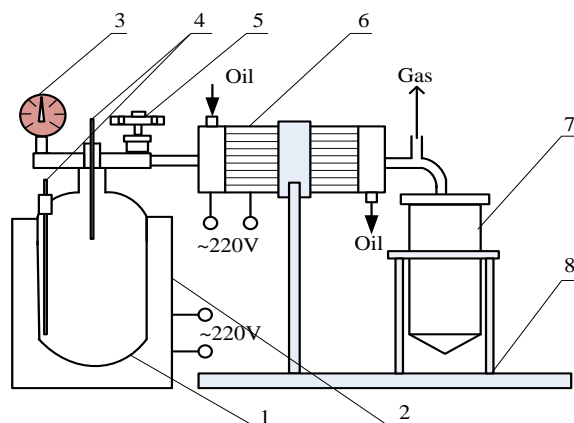


Fig 1. Laboratory unit for polyethylene destruction: 1 – reactor; 2 – oven; 3 – pressure gauge; 4 – thermocouples; 5 – shut-off valve; 6 – condensing fridge; 7 – storage for the liquid product; 8 – tray

During the atmospheric heating of polyethylene, the intensive thermal destruction of polyethylene is performed at 560-580 K (zone II). Before (zone I) and after (zone III) this area speed of thermal destruction is constant (Fig. 2)

The speed of thermal destruction (Fig. 3) has been also studied. The speed increases at 560 K, passes through the maximum at 578 K and rapidly decreases at 588 K which correlates to the zone of intensive thermal destruction.

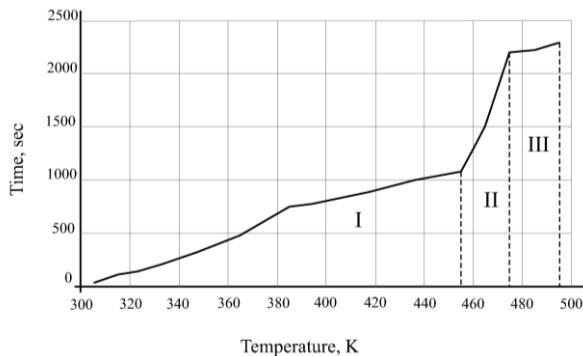


Fig.2. Temperature variation through time

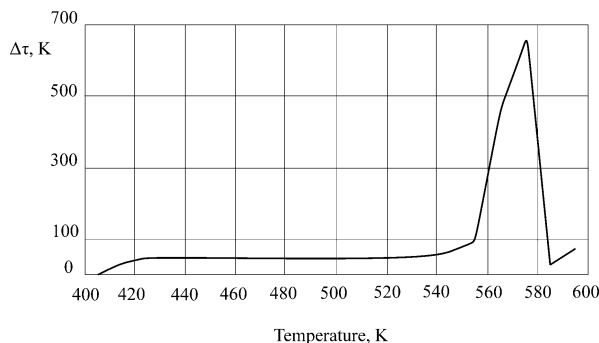


Fig 3. Research of thermal destruction speed

Liquid products of destruction were studied in the laboratory by the standardized methods for determining the physico-chemical quality indices. Gasoline and diesel fractions were studied by the chromatograph to determine their chemical composition. The liquid residue of thermal polyethylene destruction was studied by IR spectroscopy.

### 5. Results and discussion.

Fractional composition of thermal decomposition liquid products was studied according to the standard ASTM D86 (Fig. 4). Fraction №1 (conditionally gasoline) was taken at 453 K, fraction № 2 (conditionally kerosene)–453-513 K and fraction №3 (conditional diesel)–513-623 K.

Light hydrocarbon gases yield was about 4,5 % (mass.), coke yield – about 0,5% (mass.). Results of a laboratory study of narrow fractions have been performed in table 1. Results of a chromatographic study of gasoline and diesel fraction have been performed at fig. 5 and 6.

The summary content of aromatic hydrocarbons in gasoline fraction is 7.48 % (mass) and 0.84 % of benzene, which completely correlates to the current requirements. In diesel fraction high-molecular aromatic hydrocarbons that cause formation of soot in fire chambers and also cause the formation of harmful carcinogenic substances in the gaseous burning are completely absent.

The liquid residue of destructive polyethylene processing was studied by IR spectroscopy which has defined normal paraffin mainly (wave number 2851 – 2954 cm<sup>-1</sup>). The content of other aromatic hydrocarbons (wave number 1641 cm<sup>-1</sup>) is insignificant.

Table 1. Results of laboratory research of narrow fractions after the thermal destruction

№	Name of indices	Name of a narrow fraction		
		Gasoline	Kerosene	Diesel
1.	Density, kg per m <sup>3</sup>	732	789	807
2.	Fractional composition, yield, % (vol.) at temperature, °C	IBP – 67 10 – 80 50 – 118 90 – 187 FBP – 215	IBP – 133 25-195 FBP – 245	IBP – 165 50 – 268 96 – 331 FBP – 348
3.	Pour point, K	-	255	263
4.	Flash point, K	-	309	348
5.	Kinematic viscosity, mm <sup>2</sup> per second at 313 K	-	2.36	2.68
6.	Sulfur content, % (mass.)	0	0	0

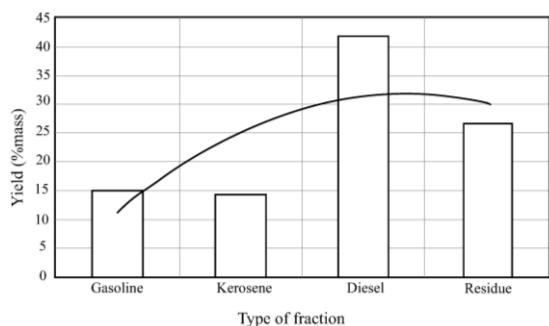


Fig. 4. Fractional composition of thermal decomposition liquid products

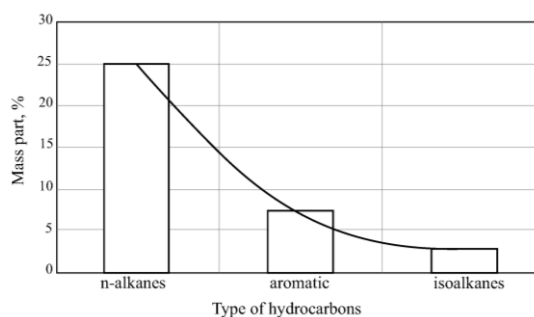


Fig. 5 The composition of the gasoline fraction

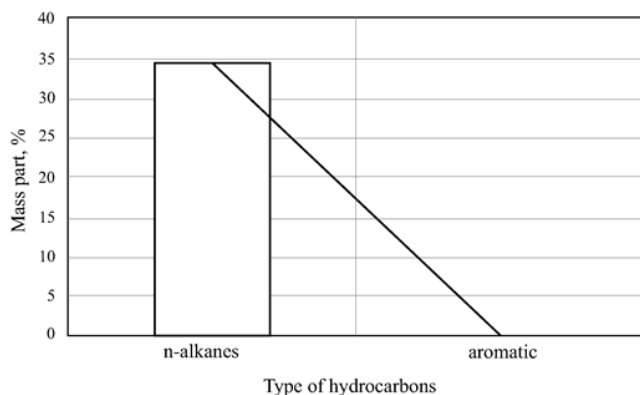


Fig. 6. The composition of diesel fraction

## 5. Conclusion

The provided research has shown the possibility of application of domestic polyethylene waste as a valuable source for production of liquid hydrocarbons by thermal destruction (total output of liquid products is 95% (mass.) of raw material). These products can be applied for production of boiler and furnace fuel both independently and in a mixture with the petroleum processing products. The components percentage is calculated according to the physical and chemical indices of fuel.

It should be mentioned that provided research is only the first step for the industrial implementation of thermal destruction of polyethylene and this process has to be studied in the direction of raw material preparation and compounding of commodity fuel according to the technical and ecological requirements.

## References

- [1] Denisenko TM. Doslidzhennya suchasnih tehnologiy pererobki plastikovih virobiv. Visnik chernigivskogo derzhavnogo tehnologichnogo universitetu. 2014; 1 (71): 55–64.
- [2] Kartovenko VM, Makarov YuV. Rus. Patent 2537916, 2011.
- [3] Ischenko VA. Doslidzhennya tsiklu utilizatsiyi plastikovih virobiv. Visnik natsionalnogo tehnichnogo universitetu Ukrayini «Kiyivskiy politehnichniy Institut». Seriya «Himichna Inzheneriya, ekologiya ta resursozberezhennya». 2012; 1: 77-79.
- [4] Mikulonok IO. Obladnannya i protsesi pererobki termoplastichnih materialiv z vikoristannyam vtorinnoyi sirovini: monografiya. IVTs "Vidavnitstvo «Politehnika". 2009; 265 p.
- [5] Gavrilyuk YuM. Analiz tehnologiyi vigotovlennya virobiv iz polietilenu metodom litva pid tiskom. Visnik KNU Imeni Mihayla Ostrogradskogo. 2010; 6 (65): 89-91.
- [6] Shleyfer AA, Shleyfer AA. Rus Patent 2035493, 1995.

- [7] Ramazanov KR. Kompozitnoe toplivo iz othodov. Novyy universitet. 2016; 1 (47): 9-11.
- [8] Gunich SV. Tehnologiya mikrovolnovoy karbonizatsii organicheskikh komponentov tverdyih byitovyyih othodov. Izvestiya VUZov. Prikladnaya himiya i biotekhnologiya. 2011; 1: 137-139.
- [9] Platonov VV. Rus. Patent 2110535, 1998.
- [10] Galiahmetov RN, Sudakova OM. Sposob polucheniya topliva iz othodov polietilena. Pererabotka uglevodorodnogo syriya, 2016; 2: 249 - 250.
- [11] Furda LV. Kataliticheskaya destruktsiya polietilena v prisutstvii sinteticheskikh alyumosilikat. Zhurnal prikladnoy himii. 2008; 81(9): 1555-1558.
- [12] Poluchenie motornogo topliva iz othodov polimerov. Uspehi himii i himicheskoy tekhnologii, 6: 44-49.
- [13] Sharma BK, Moser BR, Vermillion KE, Doll KM, Rajagopalan N. Production, characterization and fuel properties of alternative diesel fuel from pyrolysis of waste plastic grocery bags. Fuel Processing Technology, 2014; 122: 79-90.
- [14] Syamsiro M, Saptoadi H, Norsujianto T, Noviasri P, Cheng S, Alimuddin Z, Yoshikawa K. Fuel Oil Production from Municipal Plastic Wastes in Sequential Pyrolysis and Catalytic Reforming Reactors. Energy Procedia., 2014; 47: 180-188.

---

*To whom correspondence should be addressed: prof. Alena Tul'skaya, National Technical University "Kharkiv Polytechnic Institute", Kharkiv, Ukraine*

ON THE ASSESSMENT OF PSEUDO STEADY-STATE HORIZONTAL WELL PRODUCTIVITY: APPLICATION IN RECTANGULAR AND SQUARE DRAINAGE AREAS

Arash Kamari<sup>1</sup>, Alireza Bahadori<sup>\*2</sup> Amir H. Mohammadi<sup>\*\*3</sup>

<sup>1</sup> Department of Geology, Kansas State University, 108 Thompson Hall, Manhattan, KS, 66506, USA

<sup>2</sup> School of Environment, Science & Engineering, Southern Cross University, Lismore, NSW, Australia

<sup>3</sup> Discipline of Chemical Engineering, School of Engineering, University of KwaZulu-Natal, Howard College Campus, King George V Avenue, Durban 4041, South Africa

Received April 4, 2018; Accepted September 28, 2018

---

## Abstract

The productivity index is accounted as one of the main characteristics of well performance, and is of much importance in assessing the production amount/volume of liquids from wells. Furthermore, pseudo skin factor is an effective parameter in calculations related to the productivity index of producing oil/gas wells. In this study, an accurate and reliable method is proposed to estimate the pseudo skin factor as a function of dimensionless length and the ratio of horizontal well length over drainage area in both square and rectangular drainage areas. To measure the accuracy performance of the newly developed method, a smart technique called least square support vector machine algorithm was used as a comparative method. The result demonstrate that the developed method can estimate the pseudo skin factor data with lower average absolute relative deviation compared to the smart technique (9.2 against 11.4%).

**Keywords:** Productivity performance; Pseudo skin factor; LSSVM model; Drainage area; Horizontal well.

---

## 1. Introduction

As a matter of fact, the productivity index (PI) which plays a key role in evaluating the production amount/volume of liquids from wells, is accounted as one of the main characteristics of well performance [1]. In other words, productivity index is required for a large number of calculations related to production and reservoir engineering. As a definition with no considering the type of formation and wellbore, the PI is the amount/volume of possible daily production of reservoir fluids from a gas and/or oil well by 1 psi pressure drop [2]. As a result, several parameters (i.e. the reservoir permeability, geometry of drainage area, the length of horizontal wellbore, the properties of reservoir fluid, etc.) have influences on the value of PI for a drilled well particularly horizontal one. Nowadays, use of horizontal wells has gained considerable attention in petroleum industry because it can increase the production of oil/gas from reservoir, and the ability of injection to reservoirs for enhanced oil recovery (EOR) cases. Therefore, it is of great importance to assess the productivity performance of hydrocarbon reservoirs in case of horizontal wells.

Normally, the producing wells partially penetrates the formation of oil fields, so that if an oil and/or gas well is completed as partially penetrating, the streamline converges and the area for flowing the reservoir liquid reduces in the environs of the wellbore, which results in added resistance (pseudo skin factor) [3]. Subsequently, pseudo skin factor is recognized as an effective parameter in calculations related to the PI and performance evaluation of producing oil/gas wells. Therefore, it is needed to estimate the pseudo skin factor due to partial penetration through analytical and empirical methods. Babu and Odeh [4] proposed a complicated equation for estimating the PI of horizontal wells which needed that the drainage volume be approximately box-shaped, and all the boundaries of the drainage volume be sealed. Li et al. [5]

proposed a new method to evaluate the productivity performance of fractured reservoirs. They studied the influences of fracture properties on the PI of the wells. Fokker et al. [6] developed a new method for assessing the PI of complex wells. The results indicated that method proposed could be applied in the finite-conductivity wells, well interference, non-homogenous formations, and hydraulically fractured reservoirs. Bahadori et al. [7] developed an easy-to-utilize empirical correlation for the evaluation of pseudo steady-state PI of horizontal oil wells. To this end, pseudo skin factor was obtained by their new method. In the equation, they considered pseudo skin factor as a function of dimensionless length and the ratio of horizontal well length over drainage area side. Yu et al. [8] conducted a sensitivity analysis using the numerical simulation in order to find the effects of various geometries of multiple transverse hydraulic fractures on gas production.

The aim of present study was to develop a reliable, accurate and applicable method for the evaluation of oil horizontal well productivity through estimation of pseudo skin factor. To this end, the literature data of pseudo skin factor as a function of dimensionless length and the ratio of horizontal well length over drainage area side were collected. Furthermore, the results obtained by the newly proposed method were compared with least square support vector machine (LSSVM). Finally, the influences of dimensionless length and the ratio of horizontal well length over drainage area side on the pseudo skin factor estimated by the newly developed method were evaluated using a sensitivity study technique.

## 2. Proposing new method

As mentioned earlier, the reservoir properties, geometry of drainage area, the length of horizontal wellbore, and the properties of reservoir fluid, etc., have significant effects on predicting the fluid productivity of wells. Furthermore, pseudo skin factor is accounted as one of the most important parameters in calculations related to well-testing analysis and productivity index. Therefore, a simple method which could rapidly estimate the pseudo skin factor is needed to evaluate the productivity performance of producing wells. To develop such method, the data of pseudo skin factor or shape-related skin factor ( $S_{CAh}$ ) as a function of dimensionless length ( $L_D$ ) and the ratio of horizontal well length over drainage area side ( $U$  or  $L/2xe$ ) for square and rectangular shapes with ratios of sides 1, 2, and 5, was collected from literature [9-10]. The collected databank collected in this study covers a wide range of pseudo skin factor from 1.412 to 5.86. Additionally, dimensionless length and the ratio of horizontal well length over drainage area side range from 1 to 100 and 0.2 to 1, respectively.

Regarding issues discussed earlier, a simple method with two variables including dimensionless length and the ratio of horizontal well length over drainage area side should be proposed for the determination of pseudo skin factor or shape-related skin factor. During development of the method, average absolute relative deviation (AARD or  $E_a$ ) was considered as an error function to measure the accuracy of the newly proposed model. Final form of the method is as follow:

$$S_{CAh} = \frac{2U + L_D^{0.3767} + 2.6936}{Ln(2.752 L_D)} \quad (1)$$

where  $S_{CAh}$  stands for pseudo skin factor,  $L_D$  expresses dimensionless length, and  $U$  is the ratio of horizontal well length over drainage area side ( $L/2xe$ ). The equation for calculating dimensionless length has previously been reported as follow:

$$L_D = \frac{L}{2h} \sqrt{\frac{k_v}{k_h}} \quad (2)$$

where  $L$  denotes the horizontal well length (ft),  $h$  expresses the formation thickness (ft),  $k_v$  is vertical permeability (mD), and  $k_h$  stands for horizontal permeability (mD). Here, it should be noted that the method proposed (Eq. (1)) is applicable for both rectangular and square drainage areas.

### 3. Sensitivity study

To illustrate the relevancy of the selected variables (*i.e.* dimensionless length and the ratio of horizontal well length over drainage area side) for the estimation of pseudo skin factor, a sensitivity study was carried out in this study. To this end, the relevancy factor (*r*) approach [11] is employed to measure the influence degree of each variable applied in Eq. (1) for the determination of pseudo skin factor. In this approach, the positive or negative influence of input variables on the pseudo skin factor is however not determined by absolute value of *r*. The *r* values are calculated as follow [12]:

$$r(Inp_k, \mu_g) = \frac{\sum_{i=1}^n (Inp_{k,i} - \overline{Inp_k})(\mu_i - \bar{\mu})}{\sqrt{\sum_{i=1}^n (Inp_{k,i} - \overline{Inp_k})^2 \sum_{i=1}^n (\mu_i - \bar{\mu})^2}} \quad (3)$$

where:  $Inp_{k,i}$  stands for *i*th value of the *k*th input variables and  $Inp_k$  denotes the average value of the *k*th input variables,  $\mu_i$  indicates the *i*th value of the pseudo skin factor calculated by Eq. (1), and  $\bar{\mu}$  is the average value of the pseudo skin factor calculated by Eq. (1).

### 4. Results and discussion

As a consequence, the LSSVM approach has successfully been implemented for estimation of the different important properties in petroleum and chemical engineering [13-17]. Therefore, LSSVM methodology [18-19] as a smart predictive technique was used in this study for comparing the results obtained by the newly proposed method (Eq. (1)) for the estimation of pseudo skin factor. In the LSSVM algorithm has two tuning parameters including  $\sigma^2$  and  $\gamma$  which should be optimized through an optimization technique. Hence, the coupled simulated annealing (CSA) [20-22] as an adjusting strategy was applied in the current study. Using the CSA technique, the tuned values of  $\sigma^2$  and  $\gamma$  for the developed LSSVM model for estimation of the pseudo skin factor are reported as 0.002228 and 27288.14, respectively. Furthermore, some important error parameters are considered to measure the accuracy of methods developed in this study as shown in Table 1. Table 1 also reports the results obtained by both Eq. (1) and LSSVM model for the estimation of pseudo skin factor. As clear in the table, the average absolute relative deviation obtained for the newly developed method is less than LSSVM model. The AARD values reported for Eq. (1) and LSSVM model are 9.2 and 11.4%, respectively. This clearly shows that Eq. (1) is more accurate than LSSVM model for calculation of pseudo skin factor.

Table 1. Statistics error parameters of developed model for prediction of wax deposition rate

Performance	$E_a^a$ %	$E_r^b$ %	SD <sup>c</sup>	RMSE <sup>d</sup>	$R^2$ <sup>e</sup>
LSSVM approach	11.4	-2.7	0.14	0.354	0.90
New method (Eq. (2))	9.2	4.2	0.12	0.382	0.90

$$^a E_a \% = \frac{1}{n} \sum_{i=1}^n |E_i \%| \text{ where } E_i \% = \left[ \frac{X_{exp} - X_{rep./pred}}{X_{exp}} \right] \times 100 \Rightarrow i = 1, 2, 3, \dots, n$$

$$^b E_r \% = \frac{1}{n} \sum_{i=1}^n E_i \% \quad \quad \quad ^c SD = \sqrt{\frac{1}{n-1} \sum_{i=1}^n \left( \frac{X_{i exp} - X_{i rep./pred}}{X_{i exp}} \right)^2}$$

$$^d RMSE = \sqrt{\frac{1}{n} \sum_{i=1}^n (X_{i exp} - X_{i rep./pred})^2} \quad \quad \quad ^e R^2 = 1 - \frac{\sum_{i=1}^N (X_{(i) exp} - X_{(i) rep./pred})^2}{\sum_i (X_{(i) rep./pred} - average X_{(i) rep./pred})^2}$$

Figs. 1 and 2 illustrate the pseudo skin factor data calculated by Eq. (1) and LSSVM model in comparison with the literature reported records, respectively. Top vies of the two figures shows scatter diagram, and bottom view is considered for illustrating the distribution of relative error calculated for both Eq. (1) and LSSVM model.

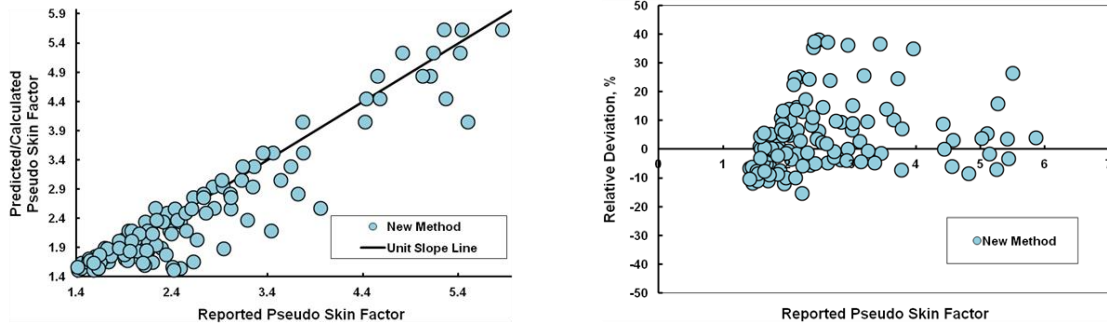


Fig. 1. Graphical error analysis for the proposed method. left: scatter diagram; right: relative error distribution plot

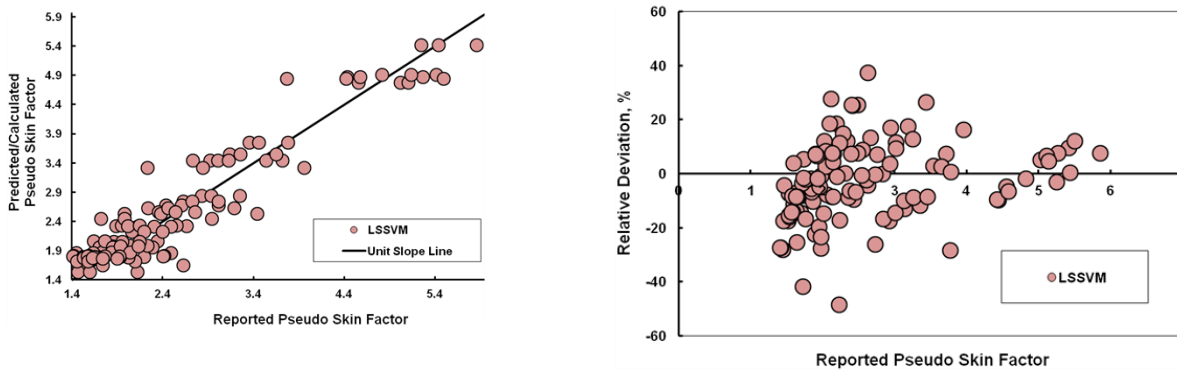


Fig. 2. Graphical error analysis for the developed LSSVM model. Left: scatter diagram; right: relative error distribution plot

As can be seen from the figures, the results obtained by Eq. (1) are in more agreement with the actual data of pseudo skin factor. Additionally, it is clear from the figures that the values obtained by LSSVM model have been more distributed around zero line compared to values calculated by Eq. (1). A further comparison between two methods is displayed in Fig. 3. Fig. 3 indicates the smooth performance of the both Eq. (1) and LSSVM model against actual data of pseudo skin factor. In other words, the figure illustrates the trend plot of pseudo skin factor estimated by Eq. (1) and LSSVM model versus dimensionless length at the ratio of horizontal well length over drainage area side equal to 0.2 ( $L/2x_e=0.2$ ). The figure confirms that the values estimated by Eq. (1) are more matched with the actual data of pseudo skin factor compared to the LSSVM model. This means that the Eq. (1) has an acceptable smoothness trend in estimating pseudo skin factor.

As already mentioned, a relevancy analysis is carried out to see the impacts of dimensionless length and the ratio of horizontal well length over drainage area side on the pseudo skin factor estimated by Eq. (1). Fig. 4 illustrates the results of such sensitivity analysis. This figure shows that the dimensionless length and the ratio of horizontal well length over drainage area side have positive and negative effects on the pseudo skin factor estimated by Eq. (1), respectively. The results obtained in this study demonstrate that the proposed method is capable and reliable for the estimation of pseudo skin factor. Additionally, the method proposed in this study could be applied in reservoir engineering soft wares to estimate the productivity perfor-

mance of horizontal oil wells with rectangular and square drainage areas. Finally. It is worthwhile to mention that the method proposed in this study is a small equation with few number of coefficients which can be re-optimized if more relevant data become available in future.

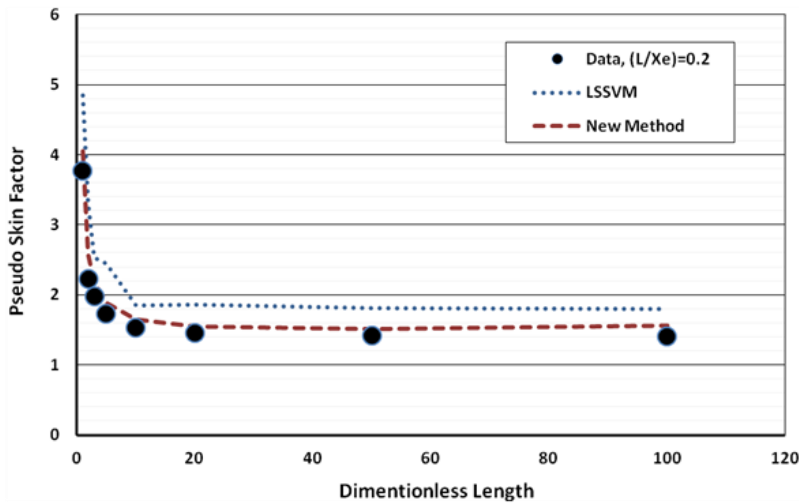


Fig. 3. Smooth performance of the proposed method and LSSVM model in estimating pseudo skin factor at the ratio of horizontal well length over drainage area side equal to 0.2 ( $L/2x_e=0.2$ )

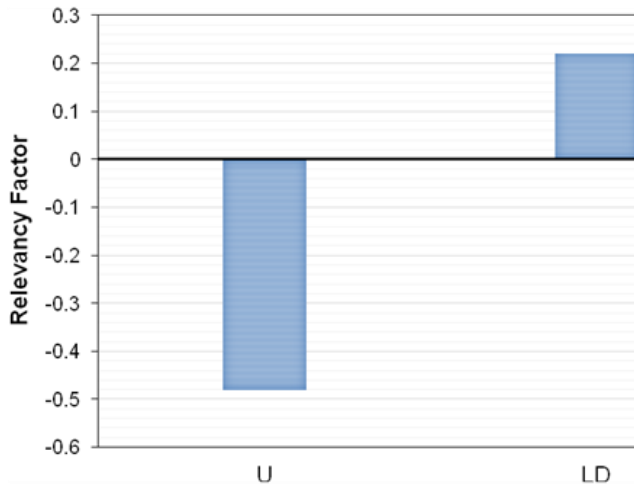


Fig. 4. The impact of variable used in Eq. (1) on pseudo skin factor

### 5. Conclusions

This study aimed to assess the productivity performance of horizontal oil wells in square and rectangular drainage areas. To this end, an accurate and reliable equation was proposed to estimate the pseudo skin factor. The equation is applicable in both square and rectangular drainage areas. To measure the accuracy performance of the newly developed method, a comparative study was graphically and statistically carried out. Therefore, a smart technique called least square support vector machine algorithm was used to see whether the proposed method is reliable. The result demonstrate that the developed method can estimate the pseudo skin factor data with lower average absolute relative deviation compared to the smart technique (9.2 against 11.4%). Finally, a sensitivity analysis was performed to observe the effects of variables applied in the proposed method. The results indicate that the dimensionless length and the ratio of horizontal well length over drainage area side have positive and

negative effects on the pseudo skin factor estimated by the newly proposed method, respectively.

### Nomenclature

<i>EOR</i>	<i>enhance oil recovery</i>
<i>PI</i>	<i>productivity index</i>
<i>LSSVM</i>	<i>least square support vector machine</i>
<i>CSA</i>	<i>coupled simulated annealing</i>
<i>AARD</i>	<i>average absolute relative deviation</i>
<i>R</i>	<i>relevancy factor</i>
<i>SC<sub>Ah</sub></i>	<i>pseudo skin factor</i>
<i>L<sub>D</sub></i>	<i>dimensionless length</i>
<i>U</i>	<i>ratio of horizontal well length over drainage area side (<math>L/2xe</math>)</i>
<i>L</i>	<i>horizontal well length, ft</i>
<i>h</i>	<i>formation thickness, ft</i>
<i>k<sub>v</sub></i>	<i>vertical permeability, mD</i>
<i>k<sub>h</sub></i>	<i>horizontal permeability, mD</i>

### References

- [1] Aulisa E, Ibragimov A, and Walton JR. A new method for evaluating the productivity index of nonlinear flows. *SPE J*, 2009; 14(4): 693-706.
- [2] Al Rbeawi S, and Tiab D, Predicting productivity index of hydraulically fractured formations. *Journal of Petroleum Science and Engineering*, 2013; 112: 185-197.
- [3] Lu J, and Tiab D. Pseudo-Steady-State Productivity Formula for a Partially Penetrating Vertical Well in a Box-Shaped Reservoir. *Mathematical Problems in Engineering*, 2010.
- [4] Babu D, and Odeh AS. Productivity of a Horizontal Well (includes associated papers 20306, 20307, 20394, 20403, 20799, 21307, 21610, 21611, 21623, 21624, 25295, 25408, 26262, 26281, 31025, and 31035). *SPE Reservoir Engineering*, 1989; 4(04): 417-421.
- [5] Li H, Jia Z, and Wei Z. A new method to predict performance of fractured horizontal wells, International three-day conference & trade show on horizontal well technology. 1996; pp. 179-185.
- [6] Fokker PA, Verga F, and Egberts P. 2005. New Semi-Analytic Technique to Determine Horizontal Well PI in Fractured Reservoirs. *SPE Reservoir Evaluation & Engineering*, 2005; 8(02): 123-131.
- [7] Bahadori A, Jamili A, and Zendehboudi S. 2013. Calculating pseudo-steady-state horizontal oil well productivity in rectangular drainage areas using a simple method. *Chemical Engineering Communications*, 2013; 200(2): 222-234.
- [8] Yu W, Luo Z, Javadpour F, Varavei A, and Sepehrnoori K. Sensitivity analysis of hydraulic fracture geometry in shale gas reservoirs. *Journal of Petroleum Science and Engineering*, 2014; 113: 1-7.
- [9] Chaudhry A. *Oil well testing handbook*. Elsevier 2004.
- [10] Mutalik P, Godbole S, and Joshi S. Effect of drainage area shapes on horizontal well productivity, *SPE 63rd Annual Technical Conference 1988*, Houston, Texas, October, pp. 2-5.
- [11] Chen G, Fu K, Liang ZZ, Idem R. The genetic algorithm based back propagation neural network for MMP prediction in CO<sub>2</sub>-EOR process. *Fuel*, 2014; 126: 202-212.
- [12] Hosseinzadeh M, and Hemmati-Sarapardeh A. Toward a predictive model for estimating viscosity of ternary mixtures containing ionic liquids. *Journal of Molecular Liquids*, 2014; 200: 340-348.
- [13] Kamari A, Bahadori A, and Mohammadi A. A Two-parameter Model for the Determination of Optimum Liquefied Petroleum Gasses (LPG) Storage Volume. *Petroleum Science and Technology*, 2015; 33(4): 494-501.
- [14] Kamari A, Bahadori A, Mohammadi AH, and Zendehboudi S. Evaluating the Unloading Gradient Pressure in Continuous Gas-lift Systems During Petroleum Production Operations. *Petroleum Science and Technology*, 2014; 32(24): 2961-2968.
- [15] Kamari A, Bahadori A, Mohammadi AH, and Zendehboudi S. New tools predict monoethylene glycol injection rate for natural gas hydrate inhibition. *Journal of Loss Prevention in the Process Industries*, 2015; 33: 222-231.

- [16] Kamari A, Mohammadi A, Bahadori A, and Zendejboudi S. A Reliable Model for Estimating the Wax Deposition Rate During Crude Oil Production and Processing. *Petroleum Science and Technology*, 2014; 32(23): 2837-2844.
- [17] Kamari A, Mohammad, AH, Bahadori A, and Zendejboudi S. Prediction of Air Specific Heat Ratios at Elevated Pressures Using a Novel Modeling Approach. *Chemical Engineering & Technology*, 2014; 37(12): 2047-2055.
- [18] Suykens JAK, and Vandewalle J. Least squares support vector machine classifiers. *Neural processing letters*, 1999; 9(3): 293-300.
- [19] Suykens JAK, van Gestel T, de Brabanter J, de Moor B, and Vandewalle J. *Least Squares Support Vector Machines*. World Scientific Publishing Company 2002.
- [20] Atiqullah MM, and Rao S. 1993. Reliability optimization of communication networks using simulated annealing. *Microelectronics Reliability*, 1993; 33(9): 1303-1319.
- [21] Fabian V. Simulated annealing simulated. *Computers & Mathematics with Applications*, 1997; 33(1): 81-94.
- [22] Vasan A, and Raju KS. 2009. Comparative analysis of simulated annealing, simulated quenching and genetic algorithms for optimal reservoir operation. *Applied Soft Computing*, 2009; 9(1): 274-281.

---

*To whom correspondence should be addressed: Dr. Alireza Bahadori, School of Environment, Science & Engineering, Southern Cross University, Lismore, NSW, Australia  
Prof. Amir H. Mohammadi, Discipline of Chemical Engineering, School of Engineering, University of KwaZulu-Natal, Howard College Campus, King George V Avenue, Durban 4041, South Africa*

## BIOMARKER DISTRIBUTIONS OF THE CAMPANO-MAASTRICHTIAN NKPORO GROUP OF ANAMBRA BASIN, SOUTHEASTERN NIGERIA

*K. C. Chiadikobi and O. I. Chiaghanam*

*Department of Geology, Chukwuemeka Odumegwu Ojukwu University, Uli, Anambra State, Nigeria*

Received July 17, 2018; Accepted September 3, 2018

---

### **Abstract**

Biomarkers are a group of compounds, primarily hydrocarbons, found in oils, rock extracts, recent sediment extracts, and soil extracts. The type/origin of the source rock, depositional environment/age and thermal maturity status of the organic matter contained in the samples were determined based on the distributions and abundance of aliphatic biomarkers in the shale extracts. From the biomarker analysis results, the *n*-Alkane in Nkporo and Enugu Formations ranges from C<sub>14</sub>- C<sub>35</sub> maximizing at C<sub>14</sub> and C<sub>20</sub>. This pattern of distribution indicates organic matter derived from marine organic sources. The pristane/phytane ratios of the Nkporo Formation samples range from 0.33-0.78 while that of Enugu Shale samples range from 0.65-0.75. These ratios indicate an anoxic depositional environment rich in marine organic matter. The resultant ratios of isoprenoids/*n*-alkanes (pristane/*n*-C<sub>17</sub> and phytane/*n*-C<sub>18</sub>) of Nkporo source rocks range from 0.19 to 2.47 and 0.08 to 1.25. While that of Enugu source rocks range from 0.24 to 0.43 and 0.07 to 0.14. These ratios reflect that most of the Cretaceous source rocks were derived from mixed organic sources, deposited under transitional environment and show a degree of maturation and no biodegradation. Also the nature of kerogen shows that the Nkporo and Enugu source rocks are of Type II/III. The CPI values of the Nkporo Formation range from 0.73 to 1.06 while that of the Enugu Shale range from 0.97 to 1.09 (Table 4.10) indicating that, these source rocks are mainly mature and most probably generated from marine organic sources (Bray and Evans, 1961). Also the plot of CPI against OEP and Pr/Ph against CPI shows that the Nkporo and Enugu source rocks are mature and deposited in a reducing environment respectively. The polycyclic hydrocarbon (triterpanes) distribution showed that the source rock is of marine organic source. The occurrence of oleanene isomers in Nkporo and Enugu samples indicates that it is of the Cretaceous or younger age. The presence of hopane, homohopane (C<sub>31</sub>-C<sub>35</sub>) and steranes in the samples showed that the Nkporo and Enugu samples are derived from marine organic sources and are of the early mature stage to generate hydrocarbon.

**Keywords:** GC-MS, Biomarkers; *n*-Alkanes; Isoprenoids; Triterpanes; Steranes.

---

### **1. Introduction**

Several authors have demonstrated the usefulness and organic petrologic methods of accessing the generative potential and characteristics of source rocks in the Anambra Basin [1-4]. The deposition of organic sediments in the Benue Trough was first reported by Murat [5] and examined in greater details by various workers [6-9]. The use of biomarkers as indicators of biogenic, paleoenvironmental, and geochemical processes on earth has been widely accepted [10-16]. Biomarkers are widely used in petroleum geochemical studies for source rock evaluation, oil-oil or oil-source rock correlations, basin evaluation and reservoir management [17]. The objective of this work is to determine the type/origin of the source rock, depositional environment/age and thermal maturity status of the organic matter contained in the samples of the Nkporo Group.

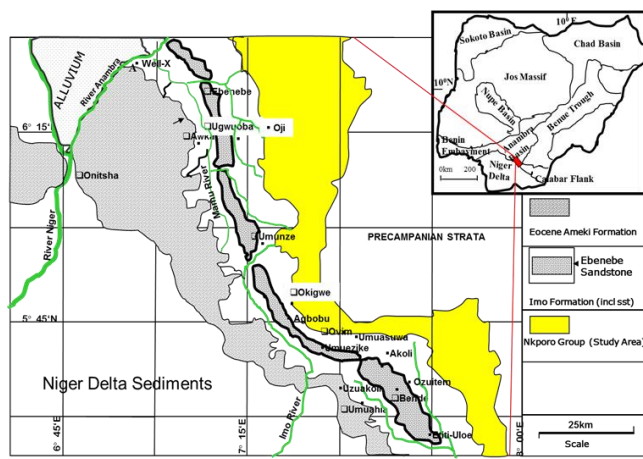


Fig. 1. Geologic map showing the study area

## 2. Methodology

The saturated hydrocarbon fractions were analyzed for biomarker using a gas chromatographic system coupled with a mass spectrometer (GC-MS). Compound separation was performed on an Agilent 6890 Series GC-instrument equipped with an injection system and a fused silica capillary column (SGE BPX5; 50m length, inner diameter = 0.22 mm, film thickness = 0.25  $\mu\text{m}$ ). Helium was used as carrier gas, and the temperature of the GC oven was programmed from 50°C (1 min) to 310°C at a rate of 3°C/min, followed by an isothermal phase of 10 min. The injector temperature was programmed from 52°C to 300°C at a rate of 12°C/sec. For compound identification, the gas chromatographic system was linked to a Finnigan MAT 95 XL mass spectrometer operating in the electron impact mode (70 eV). Full scan mass spectra were recorded from  $m/z$  50 to 650 at a scan rate of 1 s per decade and an interscan delay of 0.2 s, resulting in a scan cycle time of 1.3 s. The GC-MS analysis was performed at the University of Ibadan, Oyo State, Nigeria.

## 3. Results and discussion

The type/origin of the source rock, depositional environment/age and thermal maturity status of the organic matter contained in the samples were determined based on the distributions and abundance of aliphatic biomarkers in the shale extracts. This was achieved by using the Gas Chromatography- Mass Spectrometry (GC-MS). Ten (10) samples of the Campano-Maastrichtian Nkporo Group (Six samples from Nkporo Formation and four samples from Enugu Shale) were analyzed. These samples have high TOC,  $T_{\text{max}}$  and Vitrinite Reflectance values based on the results gotten from the source rock data. The Gas Chromatography- Mass Spectrometry (GC-MS) are calibrated into three major distributions; n-alkanes and Isoprenoid, Polycyclic Hydrocarbon (Triterpanes) and Steranes.

### 3.1. n-alkanes and isoprenoid distribution

The specific geochemical parameters, which have been assessed by the aid of  $C_{15}$  analysis, are: Normal alkanes, Isoprenoid (pristane/phytane ratio), isoprenoids/n-alkanes ratio and carbon preference index. These parameters can be used for interpreting some geochemical aspects of the studied source rocks such as origin, depositional environments, and biodegradation [18].

#### 3.1.1. Normal alkanes (n-Alkanes)

The distribution of normal alkanes in the saturated hydrocarbons sheds light on the genetic origin of source rock. [19]. It is known that the amorphous sapropelic organic matter is characterized by a maximum peak concentration of  $C_{14}$ – $C_{25}$ , reflecting marine organic sources [18].

Furthermore, the organic matters which were derived from the remains of higher vascular plants (terrestrial) are characterized by a maximum concentration of n-paraffins at n-C<sub>25</sub>-C<sub>29</sub> [19]

The n-alkane in Nkporo and Enugu Formations ranges from C<sub>14</sub>- C<sub>35</sub> maximizing at C<sub>14</sub> and C<sub>20</sub>. The gas chromatograms of the n-Alkane in Nkporo and Enugu Formations ranges from C<sub>14</sub>- C<sub>35</sub> and are characterized by the predominance of the maximum peak of C<sub>14</sub>. This pattern of distribution indicates organic matter derived from marine organic sources [17].

### 3.1.2. Isoprenoid

The most common isoprenoids which are used in this work have a pristane/phytane ratio. The pristane/phytane ratio has been used as an indicator of the depositional environment with a low specificity due to the interferences by thermal maturity and source inputs [17]. The pristane/phytane ratios of oil show some kind of correlation with the canonical variable (CV) values. They are found that the low pristane/phytane ratio (<1) and CV (<0.47) associates with carbonate oils, rich in marine organic matter and more than one of pristane/phytane ratio and CV (>0.47) indicates deltaic oils, derived from the contribution of terrestrial and detrital sediments.

The pristane/phytane ratios of the Nkporo Formation range from 0.33-0.78 while that of Enugu Shale ranges from 0.65-0.75 (Table 1). These ratios indicate an anoxic depositional environment rich in the marine organic matter [17].

Table 1. Source and depositional environment parameters computed from n-alkanes and isoprenoids distributions of Nkporo and Enugu Shale

Sample No.	C17	C18	Pr	Ph	Pr/Ph	Pr/nC17	Ph/nC18	CPI	CPI (1)	OEP	OEP (2)
NKP 03	26.857	30.605	27.06	30.605	0.77	0.19	0.08	1.06	0.98	0.48	0.94
NKP 07	26.842	30.304	27.046	30.574	0.55	0.22	0.09	0.84	0.63	0.43	0.73
NKP 08	26.839	30.295	27.035	30.565	0.57	0.34	0.12	1.06	0.87	0.50	0.91
NKP 12	26.835	30.300	27.025	30.596	0.33	2.47	1.25	0.87	0.81	0.87	0.81
NKP 16	26.836	30.296	27.027	30.575	0.78	0.22	0.06	0.85	0.39	0.27	0.60
NKP 17	26.840	30.301	27.032	30.571	0.72	0.25	0.07	0.73	0.58	0.36	0.72
ENU 20	26.832	30.300	27.031	30.572	0.75	0.24	0.07	0.97	0.75	0.44	0.85
ENU 21	26.842	30.299	27.023	30.560	0.65	0.30	0.08	0.98	0.48	0.27	0.72
ENU 24	26.845	30.305	27.113	30.571	0.76	0.43	0.14	1.09	0.91	0.55	0.96
ENU 25	26.846	30.309	27.040	30.584	0.68	0.27	0.11	0.99	0.85	0.50	0.87

Pr = Pristane Ph= Phytane CPI= Carbon Preference Index OEP= Odd-Even Preference  
 NKP- Nkporo Formation; ENU- Enugu Shale

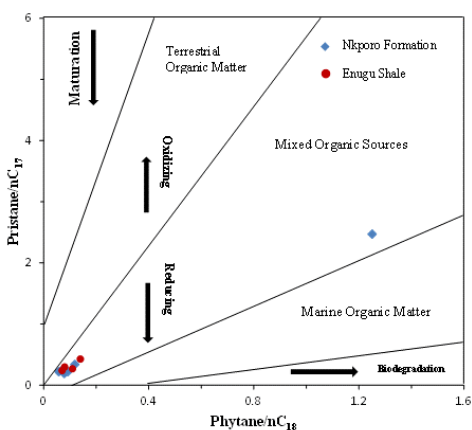


Fig. 2. Plots of Pr/nC17 against Ph/nC18 of showing the organic sources and maturation of Nkporo and Enugu Formation samples [20].

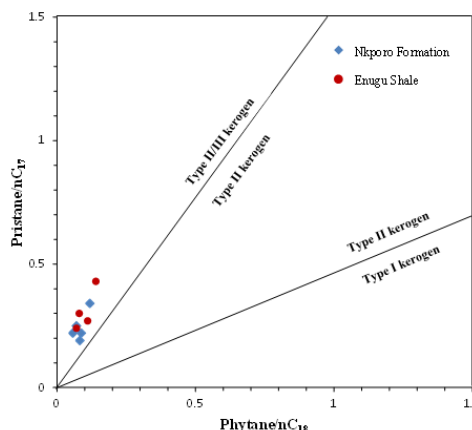


Fig. 3. Plots of Pr/nC17 against Ph/nC18 of showing the type of kerogen of Nkporo and Enugu samples [20]

### 3.1.3. Isoprenoids/n-Alkanes ratio

Pristane/n-C<sub>17</sub> and phytane/n-C<sub>18</sub> ratios have been used for oil-source rock correlation. These ratios are influenced by the nature of kerogen and extent of generation and maturation [17].

The resultant ratios of isoprenoids/n-alkanes (pristane/n-C<sub>17</sub> and phytane/n-C<sub>18</sub>) of Nkporo source rocks range from 0.19 to 2.47 and 0.08 to 1.25. While that of Enugu source rocks range from 0.24 to 0.43 and 0.07 to 0.14. (Table 1). These ratios reflect that most of the Cretaceous source rocks were derived from mixed organic sources, deposited under the transitional environment and show a degree of maturation and no biodegradation [20] (Fig. 2). Also, the nature of kerogen shows that the Nkporo and Enugu source rocks are of Type II/III kerogen (Fig. 3).

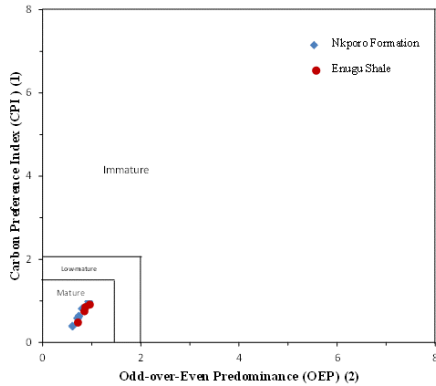


Fig. 4. Plots of CPI against OEP of Nkporo and Enugu samples [21]

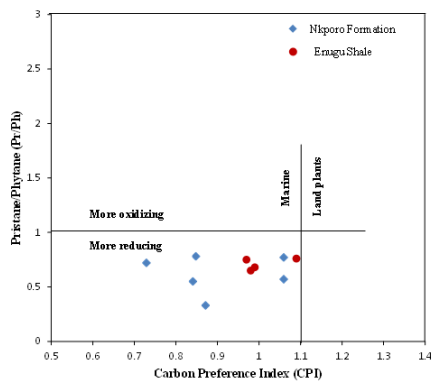


Fig. 5. Plots of Pr/Ph against CPI of Nkporo and Enugu Formation samples [21]

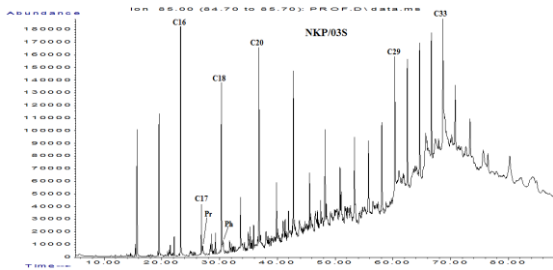


Fig. 6a. Gas chromatograms (m/z 85) of the saturated hydrocarbon fractions showing the distribution of n-Alkanes of Nkporo Formation (NKP/03)

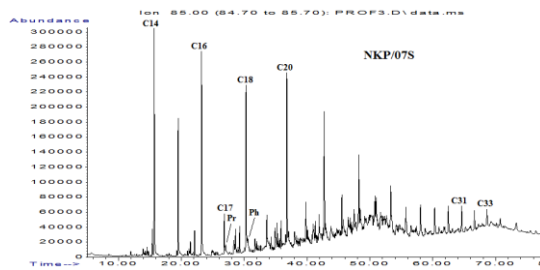


Fig. 6b. Gas chromatograms (m/z 85) of the saturated hydrocarbon fractions showing the distribution of n-Alkanes of Nkporo Formation (NKP/07)

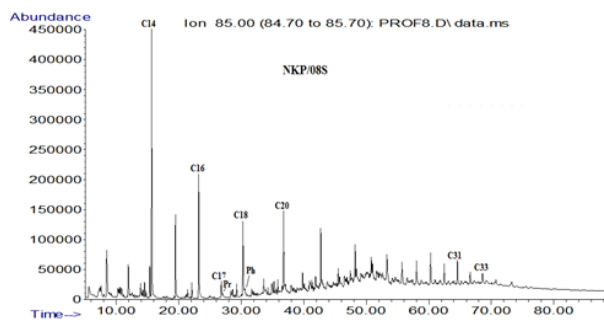


Fig. 6c. Gas chromatograms (m/z 85) of the saturated hydrocarbon fractions showing the distribution of n-Alkanes of Nkporo Formation (NKP/08)

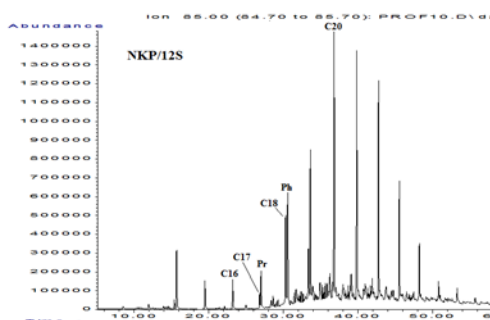


Fig. 6d. Gas chromatograms (m/z 85) of the saturated hydrocarbon fractions showing the distribution of n-Alkanes of Nkporo Formation (NKP/12)

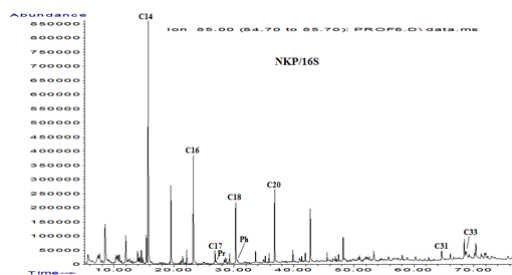


Fig. 6e. Gas chromatograms (m/z 85) of the saturated hydrocarbon fractions showing the distribution of n-Alkanes of Nkp/16S

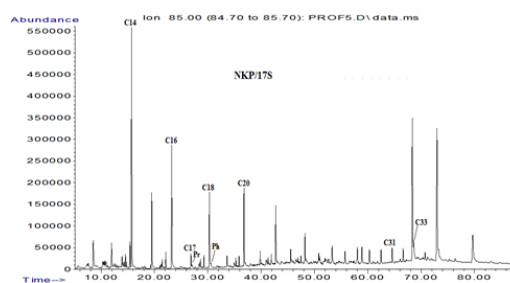


Fig. 6f. Gas chromatograms (m/z 85) of the saturated hydrocarbon fractions showing the distribution of n-Alkanes of Nkp/17S

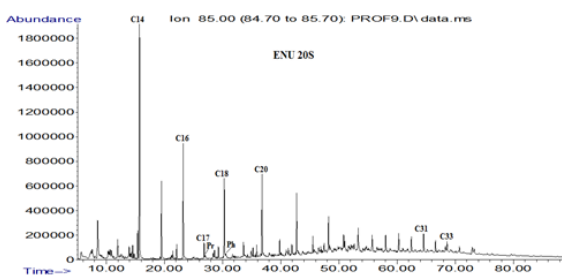


Fig. 6g. Gas chromatograms (m/z 85) of the saturated hydrocarbon fractions showing the distribution of n-Alkanes of Enugu Shale (ENU/20S)

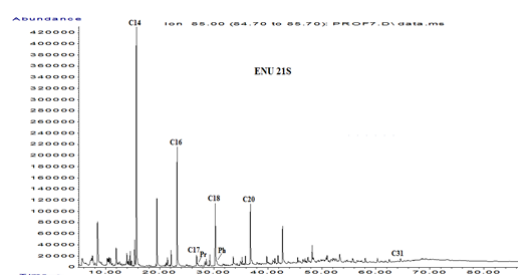


Fig. 6h. Gas chromatograms (m/z 85) of the saturated hydrocarbon fractions showing the distribution of n-Alkanes of Enugu Shale (ENU/21S)

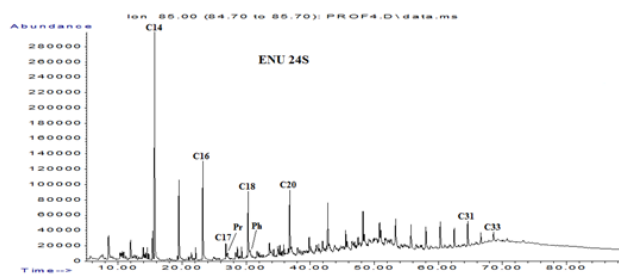


Fig. 6i. Gas chromatograms (m/z 85) of the saturated hydrocarbon fractions showing the distribution of n-Alkanes of Enugu Shale (ENU/24S)

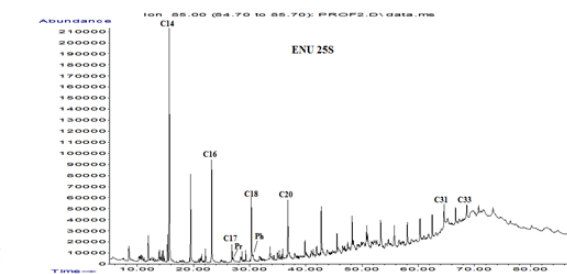


Fig. 6j. Gas chromatograms (m/z 85) of the saturated hydrocarbon fractions showing the distribution of n-Alkanes of Enugu Shale (ENU/25S)

### 3.2. Polycyclic-hydrocarbons

Polycyclic-hydrocarbon biomarkers (triterpenes) are also considered to be the most powerful tool for oil-source rock correlation due to their resistance to biodegradation [22]. The most common polycyclic biomarker compounds used in this work are tricyclic and tetracyclic terpanes, moretanes, gammacerane, oleanane, and pentacyclic extended hopane. These compounds represent an unusual organic input to the sediment and are abundant in many crude oils generated from lacustrine source rocks, often associated with the hypersaline environment [23].

#### 3.2.1. Tricyclic and tetracyclic terpanes

A series of tricyclic terpanes ranging from C19 to C29 are observed in Nkp/16S and Enugu Shale samples (Figs. 7 a,b,c,d,e,f,g,h,i and j). The source rocks have low percentages of C19-C26 tricyclic terpanes which indicate organic matter derived from marine origin [24]. The C24tetra/C26tri(R+S) ratios range between 0.63- 2.0 and 0.55- 1.54 for the Nkp/16S and Nkp/17S respectively, probably both reflecting marine organic matter input [25] (Table 2).

Various ratios of tricyclic terpanes have been used to distinguish marine carbonate, lacustrine, paralic, coal/resin and evaporitic source depositional environments [17,26-28]. The C<sub>22</sub>/C<sub>21</sub> tricyclic terpane ratio in the samples range from 0.25 to 1.47 for the Nkp/16S and

0.57 to 1.07 for the Enugu Shale, suggesting organic matter were both deposited in fluvial/deltaic to the marine depositional environment [17] (Table 2). C<sub>24</sub>tetra/C<sub>30</sub>hopane ratio has also been used to assess depositional environment of source rock [17]. C<sub>24</sub>tetra/C<sub>30</sub>hopane ratios in the sample range between 0.09 and 0.14 for Nkporo Formation, while that of Enugu Shale is between 0.07 and 0.08. These values also indicate organic matter deposited in the fluvial/deltaic-marine depositional environment [17] (Table 2).

Table 2. Source and depositional environment parameters from tri- and tetracyclic terpanes of Nkporo and Enugu Shale

Sample No.	%C19-C21 triterpane	%C23 triterpane	C24tetra/C26(R+S) tri	C24tetra/C30Hopane	C22/C21 triterpane
NKP/ 03	NIL	NIL	1.56	NIL	0.7
NKP/07	NIL	NIL	1.78	0.09	0.7
NKP/08	NIL	NIL	0.63	0.08	0.55
NKP/12	58.3	41.7	1.08	0.14	0.27
NKP/16	40.7	59.3	1.16	0.11	0.25
NKP/17	NIL	NIL	2	0.11	1.46
ENU/20	25.1	74.9	0.56	0.08	0.6
ENU/21	NIL	NIL	1.19	0.08	0.83
ENU/24	NIL	NIL	1.54	0.07	1.07
ENU/25	NIL	NIL	0.55	0.08	0.57

$C_{24}tetra/C_{30}hopane = C_{24}tetracyclic\ terpane/C_{30}hopane;$

$C_{24}tetra/C_{26}(R+S)tri = C_{24}tetracyclic\ terpane/C_{26}(R+S)tricyclic\ terpane;$

NKP- Nkporo Formation; ENU- Enugu Shale

### 3.2.2. Moretanes

High moretanes concentration seemed to be abundant in organic materials of terrestrial origin [29]. Also very low moretanes concentration seemed to be abundant in organic materials of marine origin (Figs. 7 a,b,c,d,e,f,g,h,i and j) shows that moretanes (peak MOR, see peak identification in Table 4) in the Nkporo and Enugu Shale extracts are has very low concentrations and slightly abundant, indicating contribution from marine sources [29]. Moretanes are less stable with an increase in maturity; this is because of their relatively low concentrations in oil samples [29] (Figs. 7 a,b,c,d,e,f,g,h,i and j).

### 3.2.3. Gammacerane

High gammacerane concentrations were originally considered to be markers for lacustrine facies. Gammacerane occurs in major or minor concentrations in many rocks that are definitely not of lacustrine origin as they are dominant in marine rocks [30]. The lacustrine environment had abundant gammacerane and considered also as a salinity marker [31]. Gammacerane (peak G, Figs. 7 a,b,c,d,e,f,g,h,i and j, see peak identification in Table 4) is only detected, in a relatively low amount, in the both Nkporo and Enugu source rock extract indicating input of marine organic matter in different saline environments.

### 3.2.4. Oleanane

Low or absent oleanane concentrations are originally considered to be markers for marine facies [32]. Also, high oleanane concentrations are originally considered to be markers for terrigenous facies [32]. Figs. 7 a,b,c,d,e,f,g,h,i and j shows that oleanane (peak OLE, see peak identification in Table 4) of the Nkporo and Enugu Shale extracts has very low concentrations, both indicating contribution from marine sources [29]. Oleananes are regarded as a reliable marker for angiosperm; being significant constituents of wood, roots, and bark in Cretaceous or younger effective source rocks in deltaic petroleum system [17,24,34-37]. There is the presence of oleananes in both Nkporo and Enugu Formations which is an indication of organic matter from higher land plants of Cretaceous or younger age.

### 3.2.5. Pentacyclic extended hopane

The unusually large amount of C<sub>35</sub> extended hopane seems to be associated with marine carbonates or evaporites [38]. High C<sub>35</sub>/C<sub>34</sub> ratios in the marine environment with a low redox potential rather than with lithology as not all carbonate rocks have high C<sub>35</sub> concentration [39]. The concentration of C<sub>35</sub> extended hopane

(Figs. 7 a,b,c,d,e,f,g,h,i and j, see peak identification in Table 4) is more abundant in Nkporo and Enugu Shale. Such results indicate the marine input of the Nkporo and Enugu source rocks [38].

### 3.3. Hopanes and homohopanes

C<sub>29</sub>/C<sub>30</sub> hopanes ratios are generally high (>1) in oils generated from organic rich carbonates and evaporate [40]. The majority studied source rock samples, having lower concentrations of C<sub>29</sub> than C<sub>30</sub> hopane, with low C<sub>29</sub>/C<sub>30</sub> hopane ratios, range from 0.71 to 0.82 of the Nkporo source rocks and 0.59 to 0.79 of Enugu source rocks (Table 4), These data illustrate that the shale samples might be sourced from source rocks rich in carbonaceous organic matters.

C<sub>29</sub> and C<sub>30</sub>αβ-hopane occur in an appreciable amount in all the Nkporo and Enugu shale samples, indicating a significant contribution of prokaryotic organisms (i.e., bacteria, cyanobacteria, and blue algae) to the source organic matter.

The regular steranes/17α(H)-hopanes ratio reflects the input of eukaryotic (mainly algae and higher plants) versus prokaryotic (bacteria) organisms to the source rock [41]. The sterane/hopane ratio is relatively high in the marine organic matter, with values generally approaching unity or even higher. In contrast, low steranes and sterane/hopane ratios are more indicative of terrigenous and/or microbially reworked organic matter [41].

The sterane/hopane ratio values range from 0.07-0.27 for the Nkporo Formation and 0.05-0.32 for the Enugu Shale (Table 3). This indicates that the studied source rock can be considered generated from terrigenous organic matter source. The ratio values (<0.6) according to [32,42-43,] indicative of the incorporation of the high level of bacterial inputs commonly associated with terrigenous organic matter in shales (non-marine organic matter). The appreciable quantity of homohopanes (C<sub>31</sub>-C<sub>35</sub>) in all the samples suggest that bacteriohopanetetrol and other polyfunctional C<sub>35</sub> hopanoids; bacteriohopanepolyols, aminopolyols, etc. [44], common in prokaryotic micro-organisms [45-46] were significant contributors to the biomass.

Table 3. Source, maturity and depositional environment parameters computed from the hopane and homohopane distributions of Nkporo and Enugu Formations

Sample No	Mor-tane/Hopane	Hop/Hop +Mortane	Ts/Ts+ Tm	Sterane/Hopane	C <sub>35</sub> /C <sub>30</sub> Hopane	C <sub>29</sub> /C <sub>30</sub> Hopane	Ts/Tm	C <sub>35</sub> /C <sub>34</sub> αβS Hopane	Homohopane
NKP/07	0.30	0.77	0.66	0.09	0.21	0.80	1.95	0.42	0.05
NKP/08	0.17	0.85	0.57	0.27	0.07	0.71	1.34	0.5	0.04
NKP/12	0.2	0.83	0.51	0.25	0.1	0.80	1.04	0.79	0.07
NKP/16	0.29	0.78	0.46	0.07	NIL	0.82	0.86	NIL	NIL
NKP/17	0.32	0.76	0.54	nil	NIL	0.74	1.19	NIL	NIL
ENU/20	0.19	0.84	0.50	0.32	0.1	0.59	1.00	0.61	0.06
ENU/21	0.50	0.67	0.58	0.05	NIL	0.79	1.39	NIL	NIL
ENU/24	0.41	0.71	0.48	0.07	NIL	0.71	0.94	NIL	NIL
ENU/25	0.30	0.77	0.51	0.15	0.18	0.63	1.02	0.38	0.05

Mor/Hop = Moretane/Hopane (C<sub>30</sub>); Hop/Hop + Mor = Hopane/Hopane + Moretane (C<sub>30</sub>)

C<sub>32</sub>HH = C<sub>32</sub>homohopane;

Sterane/Hopane=C<sub>27</sub>+C<sub>28</sub>+C<sub>29</sub>steranes/[(C<sub>29</sub>+C<sub>30</sub>)αβhopane+(C<sub>31</sub>+C<sub>32</sub>+C<sub>33</sub>)αβ(R+S)homohopane]

C<sub>35</sub>/C<sub>30</sub> = C<sub>35</sub>αβ(R+S) homohopane/ C<sub>30</sub>αβ hopane + C<sub>30</sub>βa moretane

Homohopane ratio ,C<sub>35</sub>/C<sub>34</sub> αβS = C<sub>35</sub>αβS/C<sub>34</sub>αβS homohopane

Homohopane index = C<sub>35</sub>/ (C<sub>31</sub>+C<sub>32</sub>+C<sub>33</sub>+C<sub>34</sub>+C<sub>35</sub>) αβ(R+S) homohopane

The C<sub>35</sub>/C<sub>30</sub> hopane ratio values range from 0.07 to 0.21 for the Nkporo Formation and 0.1 to 0.18 for Enugu Shale (Table 3), which reflects organic matter deposited in lacustrine environments [17]. The homohopane ratio (C<sub>35</sub>αβS/C<sub>34</sub>αβS) range from 0.42 to 0.79 for the

Nkpore Formation and 0.38 to 0.61 for the Enugu Shale. The homohopane index ( $C_{35}/C_{31} - C_{35}$ ) range from 0.04 to 0.07 for the Nkpore Formation and 0.05 to 0.06 for Enugu Shale and 0.15 to 0.92 (Table 3). The low homohopane index of the samples indicates oxic condition during organic matter deposition [17,39,47-48]. Hopanes with  $\alpha\beta$  epimers are more prominent in all the samples while no  $\beta\beta$ -epimer is detected. Homohopanes ranging from C31-C35 showed a notable predominance of the 22S over the 22R epimer. These observations reflect the high maturity status of the samples [17,49-50].

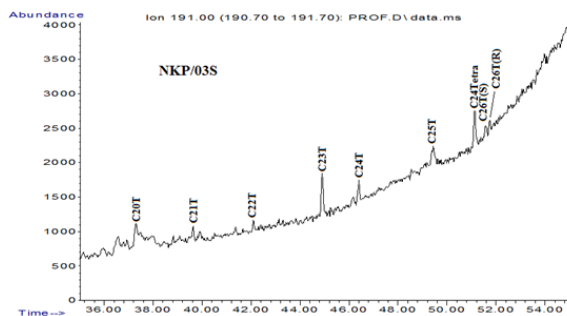


Figure 7a. Mass chromatograms (m/z 191) showing the distribution of polycyclic hydrocarbon, hopanes and homohopanes in the source rock extracts of Nkpore Formation (NKP/03)

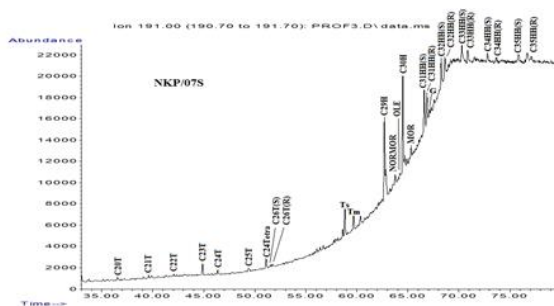


Figure 7b. Mass chromatograms (m/z 191) showing the distribution of polycyclic hydrocarbon, hopanes and homohopanes in the source rock extracts of Nkpore Formation (NKP/07)

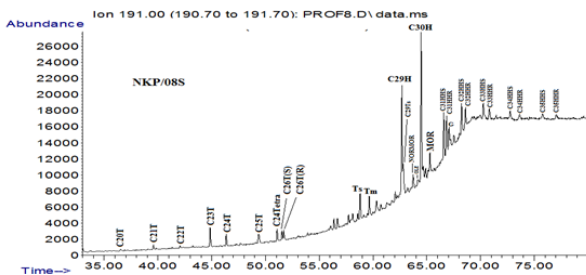


Figure 7c. Mass chromatograms (m/z 191) showing the distribution of polycyclic hydro-carbon, hopanes and homohopanes in the source rock extracts of Nkpore Formation (NKP/08)

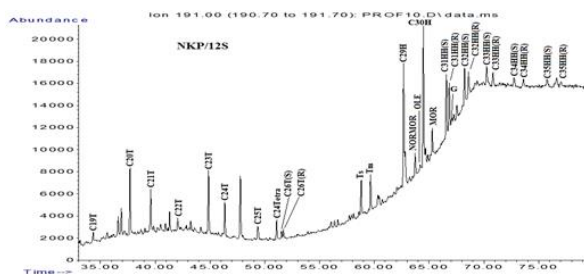


Figure 7d Mass chromatograms (m/z 191) showing the distribution of polycyclic hydro-carbon, hopanes and homohopanes in the source rock extracts of Nkpore Formation (NKP/12)

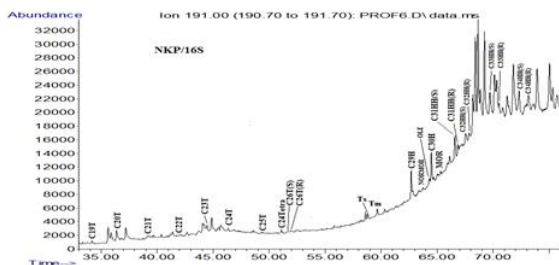


Figure 7e. Mass chromatograms (m/z 191) showing the distribution of polycyclic hydro-carbon, hopanes and homohopanes in the source rock extracts of Nkpore Formation (NKP/16)

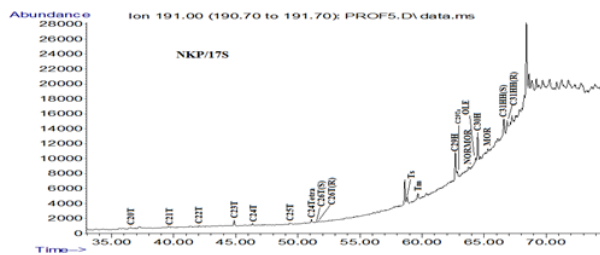


Figure 7f. Mass chromatograms (m/z 191) showing the distribution of polycyclic hydrocarbon, hopanes and homohopanes in the source rock extracts of Nkpore Formation (NKP/17)

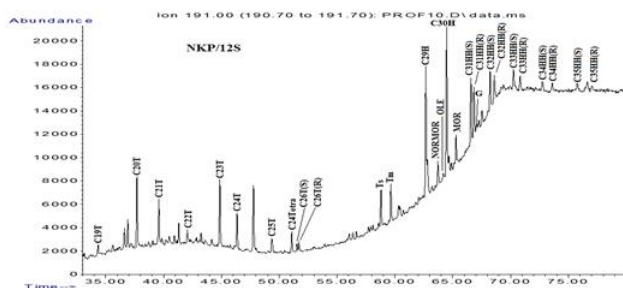


Figure 7g. Mass chromatograms (m/z 191) showing the distribution of polycyclic hydrocarbon, hopanes and homohopanes in the source rock extracts of Enugu Shale (ENU/20)

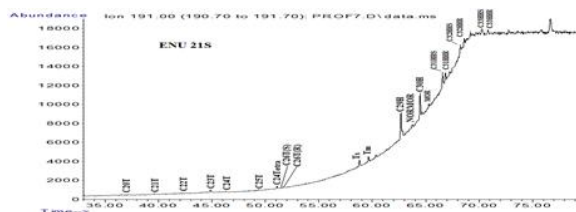


Figure 7h. Mass chromatograms (m/z 191) showing the distribution of polycyclic hydrocarbon, hopanes and homohopanes in the source rock extracts of Enugu Shale (ENU/21)

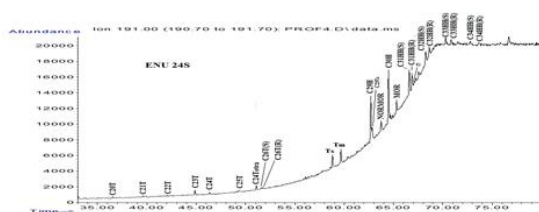


Figure 7i. Mass chromatograms (m/z 191) showing the distribution of polycyclic hydrocarbon, hopanes and homohopanes in the source rock extracts of Enugu Shale (ENU/24)

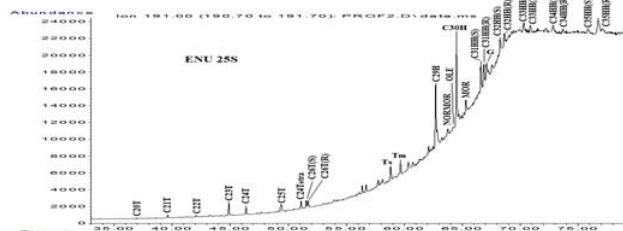


Figure 7j. Mass chromatograms (m/z 191) showing the distribution of polycyclic hydrocarbon, hopanes and homohopanes in the source rock extracts of Enugu Shale (ENU/25)

Table 4. Peak identification of triterpenes (m/z 191) fragmentograms

Peak	Compounds	Peak	Compounds
C19tri	C19 tricyclic terpanes	C30H	17 $\alpha$ (H), 21 $\beta$ (H)-hopane C <sub>30</sub>
C20tri	C20 tricyclic terpanes	MOR	Moretane
C21tri	C21 tricyclic terpanes	C31HHS	22S 17 $\alpha$ (H), 21 $\beta$ (H)- 30-homohopane C <sub>31</sub>
C22tri	C22 tricyclic terpanes	C31HHR	22R 17 $\alpha$ (H) ,21 $\beta$ (H)-30-homohopane C <sub>31</sub>
C23tri	C23 tricyclic terpanes	G	Gammacerane
C24tri	C24 tricyclic terpanes	C32HHS	22S 17 $\alpha$ (H) ,21 $\beta$ (H)-30,31-bishomohopane C <sub>32</sub>
C25tri	C25 tricyclic terpanes	C32HHR	22R 17 $\alpha$ (H), 21 $\beta$ (H)-30,31-bishomohopane C <sub>32</sub>
C24tetra	C24 tetracyclic terpanes	C33HHS	22S 17 $\alpha$ (H) 21 $\beta$ (H)-30,31,32-trishomohopane C <sub>33</sub>
C26tri	C26 tricyclic terpanes	C33HHR	22R 17 $\alpha$ (H),21 $\beta$ (H)-30,31,32-trishomohopane C <sub>33</sub>
Ts	18 $\alpha$ (H)-22,29,30-trisnorneohopane Ts, C <sub>29</sub>	C34HHS	22S 17 $\alpha$ (H) ,21 $\beta$ (H)-30,31-bishomohopane C <sub>34</sub>
Tm	17 $\alpha$ (H)-22,29,30 Trisnorhopane Tm, C <sub>27</sub>	C34HHR	22R 17 $\alpha$ (H), 21 $\beta$ (H)-30,31-bishomohopane C <sub>34</sub>
C29H	17 $\alpha$ (H), 21 $\beta$ (H)-30- norhopane C <sub>29</sub>	C35HHS	22S 17 $\alpha$ (H) 21 $\beta$ (H)-30,31,32-trishomohopane C <sub>35</sub>
NORMOR	Normoretane	C35HHR	22R 17 $\alpha$ (H),21 $\beta$ (H)-30,31,32-trishomohopane C <sub>35</sub>
OLE	Oleanane		

The ratio of Ts/Tm - Ts (trisnorneohopane) to Tm (trisnorhopane) more than (0.5) increases as the portion of shale in calcareous facies increases [22]. Also, this ratio was proved to be useful in paleofacies predictions, though not as decisive as mature parameters. Van Grass [56] stated that Ts/Tm ratios begin to decrease quite late during maturation, but Waples and Machihara [30] reported that Ts/Tm ratio does not appear to be appropriate for quantitative estimation of maturity. The Ts/Tm ratios range from 0.86 to 1.95 for the Nkporo source rock, while that of Enugu source rock range from 0.94 to 1.39 (Table 3). These relatively high ratios suggest that the studied source rocks were generated mainly from calcareous facies.

The Moretane/Hopane, Hopane/Hopane + Moretane and Ts/Ts + Tm, ratios for the Nkporo Formation range from 0.17 to 0.30; 0.77 to 0.85 and 0.51 to 0.66 respectively, while that of Enugu Shale ranges from 0.19 to 0.50, 0.67 to 0.84 and 0.48 to 0.58 respectively (Table 3). These values indicate samples that are within the early oil window [17,32,47]. The abundance of C<sub>35</sub> pentacyclic extended hopane seems to be associated with marine carbonates or evaporites [38]. However, Peters and Moldowan [39] prefer to correlate high C<sub>35</sub>/C<sub>34</sub> ratios in the marine environment with a low redox potential rather than with lithology as not all carbonate rocks have high C<sub>35</sub> concentration. The concentration of C<sub>35</sub> extended hopane (Fig. 4, see peak identification in Table 4) is more abundant in the Nkporo and Enugu Shale extracts. Such results indicate the marine input of the Nkporo and Enugu source rocks [38]. The C<sub>35</sub>/C<sub>30</sub> hopane ratio values range from 0.42 to 0.79 for the Nkporo source rock and 0.38 to 0.61 for Enugu source rock, which reflects organic matter deposited in marine environments [17] (Table 3). The *m/z* 191 showing the distributions of polycyclic hydrocarbons, hopanes and homohopanes in the samples are shown in Fig. 7 a,b,c,d,e,f,g,h,i and j of Nkporo and Enugu source rocks. Peak identities are listed in Table 4.

### 3.4. Steranes

The occurrence of C<sub>27</sub> to C<sub>29</sub> steranes was detected in Nkporo and Enugu Shale samples (Figs. 8 and 9). The sterane distributions for all the samples occur in the order of C<sub>29</sub>>C<sub>28</sub>>C<sub>27</sub> (Table 5).

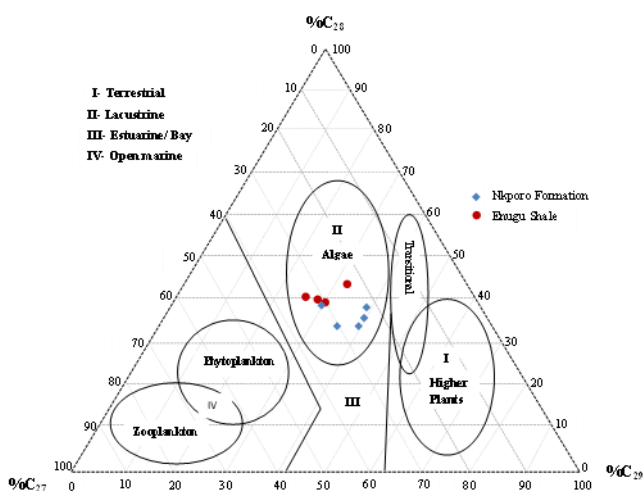


Fig. 8. Ternary plot of C<sub>27</sub>, C<sub>28</sub> and C<sub>29</sub> Steranes distribution showing the environment of deposition of Nkporo and Enugu Shale samples [17]

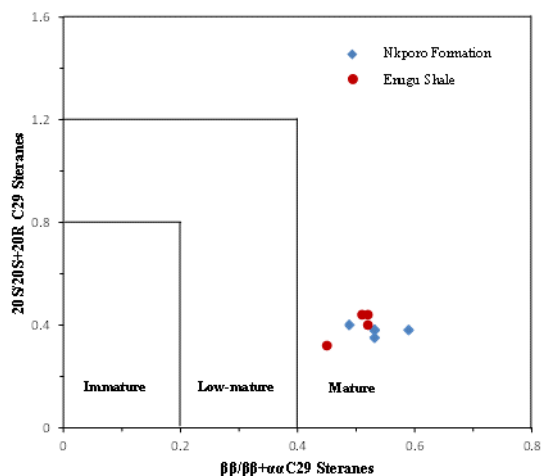


Fig. 9. Plot of 20S/20S+20R versus  $\beta\beta/\beta\beta+\alpha\alpha$  C<sub>29</sub> Steranes of the Nkporo and Enugu source rock samples

Table 5. Source, maturity and depositional environment parameters computed from the sterane distributions of Nkporo and Enugu Formations

Sample No	%C <sub>27</sub>	%C <sub>28</sub>	%C <sub>29</sub>	%Diasterane/ Sterane	20S/20S+20R C <sub>29</sub> Steranes	B $\beta$ /B $\beta$ + $\alpha\alpha$ C <sub>29</sub> Sterane
NKP/ 03	-	-	-	-	NIL	NIL
NKP/07	39.1	22.4	38.5	1.19	0.38	0.53
NKP/08	29.8	31.3	38.9	0.32	0.4	0.49
NKP/12	39	27.1	33.9	0.82	0.38	0.53
NKP/16	35.9	30.9	33.2	2.55	0.38	0.59
NKP/17	39.8	24.9	35.3	1.47	0.35	0.53
ENU/20	30.2	32.1	37.7	0.41	0.44	0.52
ENU/21	30	30.3	39.7	1.47	0.32	0.45
ENU/24	32.9	24.6	42.5	1.05	0.4	0.52
ENU/25	27.5	32.2	40.3	0.35	0.44	0.51

The predominance of C27 sterane over C29 sterane reflects a greater input of marine relative to terrestrial organic matter [17,47,51-53]. The ternary plots of sterane distribution in (Fig. 8) indicate organic matter derived from marine materials deposited in lacustrine settings [17,47,51,54]. This observation is supported by C27/C29 ratios (Table 4.7), which range from 0.77 to 1.13 for the Nkporo samples and 0.68 to 0.80 for the Enugu samples [17]. The dominance of C30 steranes over dinosterol in these samples reflects typical marine source rocks [17].

The 20S/20S+20R and  $\alpha\beta\beta/\alpha\beta\beta+\alpha\alpha\alpha$  C<sub>29</sub> ratios range from 0.35 to 0.38 and 0.49 to 0.59 for the Nkporo Formation, while that of Enugu Shale range from 0.32 to 0.44 and 0.45 to 0.52 respectively (Table 5). These values show that the samples are mature and are within the early oil generative window [17,47] (Fig. 9).

### 3.4.1 Ratio of sterane to Pr/Ph

Conditions of the paleodepositional environment of the source rock were evaluated using a graph of C<sub>27</sub>/ (C<sub>27</sub>+C<sub>29</sub>) sterane versus Pr/Ph (Fig. 10a and b).

The C<sub>27</sub>/ (C<sub>27</sub>+C<sub>29</sub>) sterane versus Pr/Ph ratios ranges from 0.43 to 0.53 and 0.33 to 0.78 for the Nkporo Formation which indicate that the organic matter was deposited in a pelagic and anoxic environment, while that of Enugu Shale ranges from 0.41 to 0.44 and 0.65 to 0.76 which indicate that the organic matter was deposited in a coastal and anoxic environment [55] (Fig. 4.57a and b).

The *m/z* 217 mass chromatograms showing the distribution of steranes and diasteranes in all the samples are shown in Figs. 11 a,b,c,d,e,f,g,h and i. Peak identities are listed in Table 6.

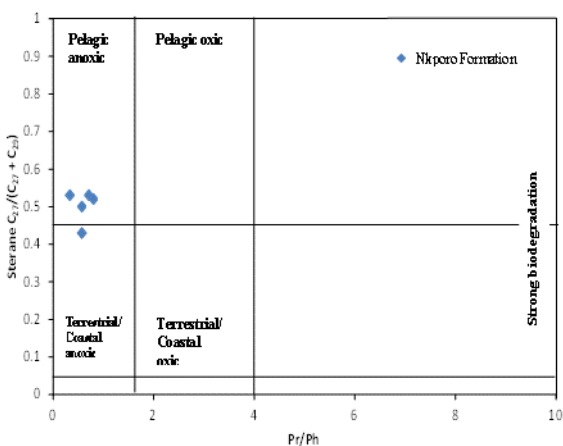


Fig. 10a. Plots of C<sub>27</sub>/ (C<sub>27</sub>+C<sub>29</sub>) versus pristane/phytane ratio of the Nkporo Formation samples [55]

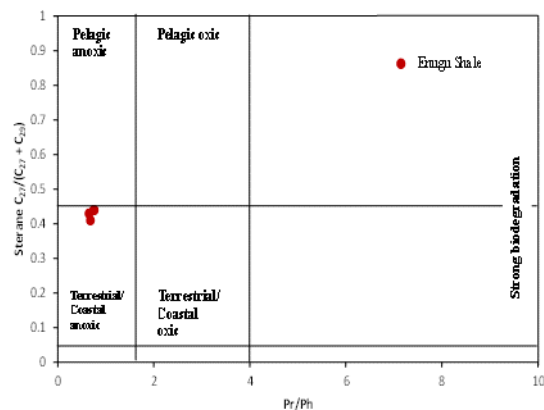


Fig. 10b. Plots of C<sub>27</sub>/ (C<sub>27</sub>+C<sub>29</sub>) versus pristane/phytane ratio of the Enugu Shale samples [55]

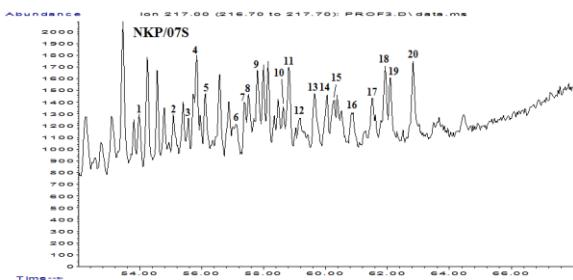


Figure 11a Mass chromatograms (*m/z* 217) showing the distribution of steranes in the source rock extracts of Nkporo Formation (NKP/07)

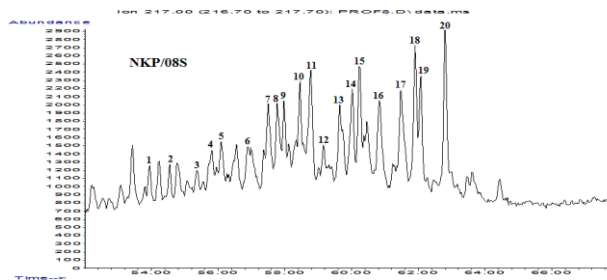


Figure 11b. Mass chromatograms (*m/z* 217) showing the distribution of steranes in the source rock extracts of Nkporo Formation (NKP/08)

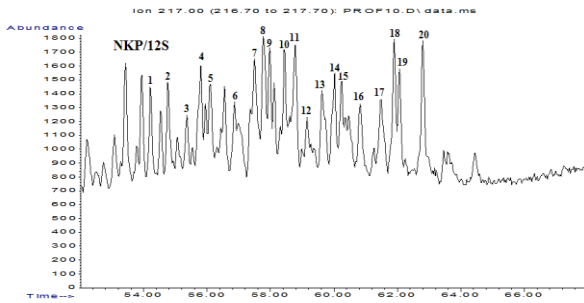


Figure 11c. Mass chromatograms (m/z 217) showing the distribution of steranes in the source rock extracts of Nkporo Formation (NKP/12)

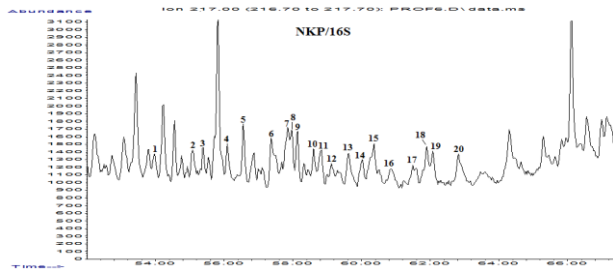


Figure 11d. Mass chromatograms (m/z 217) showing the distribution of steranes in the source rock extracts of Nkporo Formation (NKP/16)

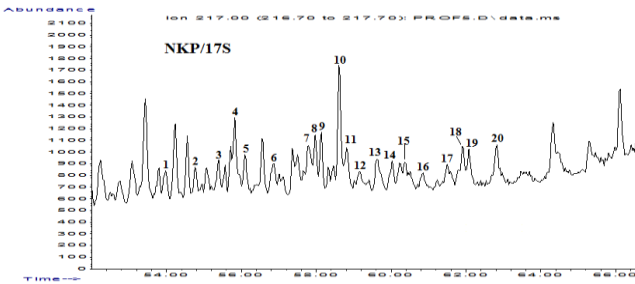


Figure 11e. Mass chromatograms (m/z 217) showing the distribution of steranes in the source rock extracts of Nkporo Formation (NKP/17)

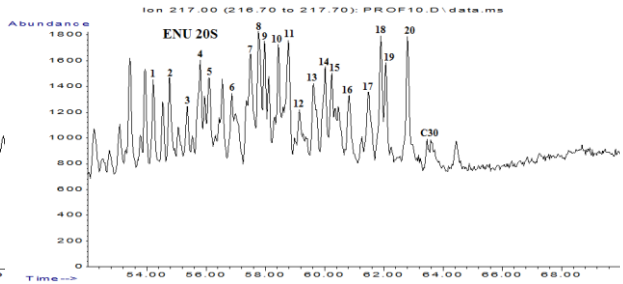


Figure 11f. Mass chromatograms (m/z 217) showing the distribution of steranes in the source rock extracts of Enugu Shale (ENU/20)

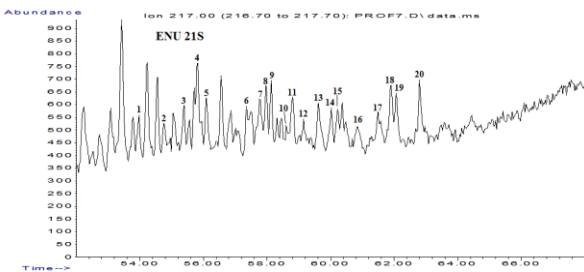


Figure 11g. Mass chromatograms (m/z 217) showing the distribution of steranes in the source rock extracts of Enugu Shale (ENU/21)

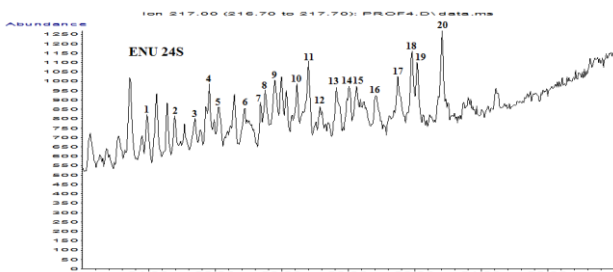


Figure 11h. Mass chromatograms (m/z 217) showing the distribution of steranes in the source rock extracts of Enugu Shale (ENU/24)

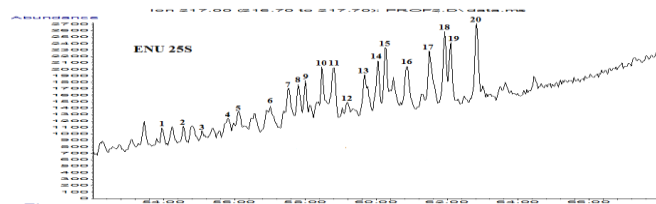


Figure 11i. Mass chromatograms (m/z 217) showing the distribution of steranes in the source rock extracts of Enugu Shale (ENU/25)

Table 6. Peak identification of Steranes and Diasteranes (m/z 217) fragmentograms

Peak	Compounds	Peak	Compounds
1	20S 13 $\beta$ , 17 $\alpha$ -diacholestane C <sub>27</sub>	12	20S 24-ethyl-13 $\alpha$ ,17 $\beta$ -diacholestane C <sub>29</sub>
2	20R 13 $\beta$ , 17 $\alpha$ -diacholestane C <sub>27</sub>	13	20S 24-methyl-14 $\alpha$ ,17 $\alpha$ -cholestane C <sub>28</sub>
3	20S 13 $\alpha$ ,17 $\beta$ -diacholestane C <sub>27</sub>	14	20R 24-methyl-14 $\beta$ ,17 $\beta$ -cholestane C <sub>28</sub>
4	20S 24-methyl-13 $\beta$ ,17 $\alpha$ -diacholestane C <sub>28</sub>	15	24-methyl-14 $\alpha$ ,17 $\alpha$ -cholestane C <sub>28</sub>
5	20R 24-methyl-13 $\beta$ ,17 $\alpha$ -diacholestane C <sub>28</sub>	16	20R 24-methyl-14 $\alpha$ ,17 $\alpha$ -cholestane C <sub>28</sub>
6	20R 24 methyl -13 $\beta$ ,17 $\alpha$ -diacholestane C <sub>28</sub>	17	20S 24-ethyl-14 $\alpha$ ,17 $\beta$ -cholestane C <sub>29</sub>
7	20R 24 methyl -13 $\alpha$ ,17 $\beta$ -diacholestane C <sub>28</sub> + 20S 14 $\alpha$ ,17 $\alpha$ cholestane C <sub>27</sub>	18	20R 24-ethyl-14 $\beta$ ,17 $\alpha$ -cholestane C <sub>29</sub>
8	20S 24 ethyl -13 $\beta$ ,17 $\alpha$ -diacholestane C <sub>29</sub> + 20R 14 $\beta$ ,17 $\beta$ cholestane C <sub>27</sub>	19	20S 24-ethyl-14 $\beta$ ,17 $\beta$ -cholestane C <sub>29</sub>
9	20R 24 methyl -13 $\alpha$ ,17 $\beta$ -diacholestane C <sub>28</sub> + 20S 14 $\beta$ ,17 $\beta$ cholestane C <sub>27</sub>	20	20R 24-ethyl-14 $\alpha$ ,17 $\alpha$ -cholestane C <sub>29</sub>
10	20R 14 $\alpha$ ,17 $\alpha$ -cholestane C <sub>27</sub>	C <sub>30</sub>	C <sub>30</sub> sterane
11	20R 24-ethyl-13 $\beta$ ,17 $\alpha$ -diacholestane C <sub>29</sub>		

## 5. Conclusion

The distributions of *n*-alkanes showed that Nkporo and Enugu samples were formed from organic matter derived from both mixed organic sources and deposited in transitional environments. The Pr/Ph ratios of samples from Nkporo and Enugu samples reflect organic matter deposition under anoxic conditions marine. The presence of hopane, homohopane (C<sub>31</sub>-C<sub>35</sub>) in all the samples showed that bacteriohopanetetrol and other polyfunctional C<sub>35</sub> hopanoids common in prokaryotic microorganisms have significant contributions to the organic matter. The occurrence of oleanene isomers in Nkporo and Enugu samples favoured marine organic matter deposited in lacustrine environment. In addition, the detection of gammacerane in Nkporo and Enugu samples represents marine water stratification during organic matter source deposition. The abundance of C<sub>29</sub> Steranes and diasteranes in the samples indicate marine input of the organic matter.

## References

- [1] Akande SO, Ojo OJ, Erdtmann BD, and Hetenyi M. Paleoenvironments, Source Rock Potential and Thermal Maturity of the Upper Benue Rift Basins, Nigeria: Implications for Hydrocarbon Exploration. *Organic Geochemistry*, 1998; 29: 531-542.
- [2] Baskin DR. Organic Geochemistry and Geological interpretations; *Journal of Geological Education*, 1972; 20: 221-234.
- [3] Petters SW. Mid-Cretaceous Paleoenvironment and Biostratigraphy of the Benue Trough, Nigeria. *Geol. Soc. America Bull.*, 1978; 89: 151-154.
- [4] Ojo OJ, and Akande SO. Petroleum Geochemical Evaluation of the Mid Cretaceous sequence in the Dadiya Syncline, Yola Basin, Northeastern Nigeria. *Journal of Mining and Geology*, 2002; 38: 35-42.
- [5] Murat RC. Stratigraphy and Paleogeography of the Cretaceous and Lower Tertiary in Southern Nigeria. In: Dessauvage, T.F.J. and Whiteman, A.J., (Eds.), *African Geology*. University of Ibadan press 1972: 251-266.
- [6] Petters SW. Stratigraphic Evolution of the Benue Trough and its Implication for the Upper Cretaceous Paleogeography of West Africa. *Journal of Geology*, 1982; 86: 311-322.
- [7] Petters SW, and Ekweozor CM. Petroleum Geology of Benue Trough and Southeastern Chad Basin, Nigeria. *AAPG Bull.*, 1982; 66: 1141-1149.
- [8] Akaegbobi MI, and Schmitt M. Organic facies, Hydrocarbon Source Potential and the Reconstruction of the Depositional Paleoenvironment of the Campano- Maastrichtian Nkporo Shale in the Cretaceous Anambra Basin, Nigerian. *Nigeria Association of petroleum explorationist*, 1998; 19: 1-19.
- [9] Ehinola O, Sonibare OO, Falode OA, and Awofala BO. Hydrocarbon Potential and Thermal Maturity of Nkporo Shale from Lower Benue Trough, Nigeria. *Journal of Applied Sciences*, 2005; 5: 207-216.

- [10] Mackenzi, AS, Brassell SC, Eglinton G, and Maxwell JR. Chemical fossils-the geological fate of steroids. *Science*, 1982; 217: 491-504.
- [11] Johns RB. Biological markers in sedimentary record. Elsevier Science Publisher, Amsterdam, 1986; 157-163.
- [12] Simoneit BRT, Grimalt JO, Wang TG, Cox RE, Hatcher PG, and Nissenbaum A. Cyclic terpenoids of contemporary resinous plant detritus and of fossil woods, amber and coal. *Organic Geochemistry*, 1986, 10: 877-889.
- [13] Brassell SC. Biomarkers in recent and ancient sediments: the importance of the diagenetic continuum. In: Whelan, J.K., Farrington, J.W., editors. *Organic matter-productivity, accumulation, and preservation in recent and ancient sediments*. New York: Columbia University Press, 1992; 339-367.
- [14] Imbus SW, and McKirdy DM. Organic geochemistry of Precambrian sedimentary rocks. In: Engel MH, Macko SA., editors. *Organic geochemistry*. New York: Pergamon Press, 1993; 657-684.
- [15] Mitterer RM. The diagenesis of proteins and amino acids in fossil shells. In: Engel, M.H., Macko, S.A., editors: *Organic geochemistry, principles and applications*. Plenum Press, New York, 1993; 739-753.
- [16] Simoneit BRT. Biomarker PAHs in the environment. In: Neilson, A., Hutzinger, O., editors. *The handbook of environmental chemistry*. Berlin: Springer Verlag, 1998, 175-221.
- [17] Peters KE, Walters CC, and Moldowan JM. *The Biomarker Guide: biomarkers and isotopes in petroleum systems and human history*, 2<sup>nd</sup> edition, Cambridge University Press, United Kingdom, 2005; 476.
- [18] Waples DW. 1985. *Geochemistry in Petroleum Exploration*. Inter. Human Resources and Develop. Co., Boston, 232.
- [20] Shanmugam G. Significance of coniferous rain forests and related organic matter in generating commercial quantities of oil, Gippsland Basin, Australia. *Am Assoc Pet Geol Bull.*, 1985; 69: 1241-1254.
- [21] Bray EE, and Evans ED. Distribution of n-paraffins as a clue to recognition of source beds. *Geochimica et Cosmochimica Acta*, 1961; 22: 2-15.
- [22] Hunt JM. *Petroleum Geochemistry and Geology*: Freeman, W.H., San Francisco, 1996; 617.
- [23] Zumberge JE. Organic geochemistry of Estancia Vieja Oils, Rio Negro Norte block, in: M.H. Engel, A.S. Macko (Eds.), *Organic Geochemistry Principles and Applications*, Plenum Press, New York, 1993; 461-470.
- [24] Ozcelik O, and Altunsoy M. Organic Geochemical Characteristics of Miocene Bituminous Units in the Bey pazari Basin, Central Anatolia, Turkey. *The Arabian Journal of Science and Engineering*, 2005;30 (2), 181-194.
- [25] Philp RP, and Gilbert TD. Biomarker distributions in Australian oils predominantly derived from terrigenous source material. *Organic Geochemistry*, 1986; 10: 73-84.
- [26] de Grande SMB, Aquino Neto FR, and Mello MR. Extended tricyclic terpanes in sediments and petroleum. *Organic Geochemistry*, 1993; 20: 1039-1047.
- [27] Tuo J, Wang X, and Chen J. Distribution and evolution of tricyclic terpanes in lacustrine carbonates. *Organic Geochemistry*, 1999; 30: 1429-1435.
- [29] Mann AL, Goodwin NS, Lowe S. Geochemical characteristics of lacustrine source rocks: a combined palynological/molecular study of a tertiary sequence from offshore China, *Proceedings of the Indonesian petroleum association, 60th Annual Convention*, 1, Indonesian Petroleum Association, Jakarta, 1987; 241-258.
- [30] Waples DW, and Machiara T. Application of Sterane and Triterpane Biomarkers in Petroleum Exploration. *Bulletin of Canadian Petroleum Geology*, 1991; 38: 357-380.
- [31] Fu Jiamo GY. Biological marker composition of typical source rocks and related crude oils of terrestrial origin in The People's Republic of China: a review *Applied. Geochem.*, 1989; 4 (1): 13-22.
- [32] Peters KE, and Moldowan JM. *The Biomarker Guide, Interpreting molecular fossils in petroleum and ancient sediments*, Prentice Hall, 1993; 363.
- [34] Moldowan JM, Peters KE, Carlson RMK, Schoell M, and Abu-Ali MA. Diverse applications of petroleum biomarker maturity parameters. *Arabian J. for Science and Engineering*, 1994; 19: 273-298.
- [35] Nytoft HP, Bojesen-Koefed JA, Christiansen FG, and Fowler MG. Oleanane or lupane? Reappraisal of the presence of oleanane in Cretaceous-Tertiary oils and sediments. *Organic Geochemistry*, 2002; 33: 1225-1240.

- [36] Otto A, Simoneit BRT, and Rember WC. Conifer and angiosperm biomarkers in clay sediments and fossil plants from the Miocene clarkia Formation, Idaho, USA. *Organic Geochemistry*, 2005; 36: 907-922.
- [37] Bechtel A, Woszczyk M, Reischenbacher D, Sachsenhofer RF, Gratzner R, Püttmann W, and Spychalski W. Biomarkers and geochemical indicators of Holocene environmental changes in coastal Lake Sarbsko (Poland). *Organic Geochemistry*, 2007; 38 (7): 1112-1131.
- [38] Riediger CL, Fowler MG, Brooks PW, and Snowdon LR. Triassic oils and potential Mesozoic source rocks, Peace River Arch area, Western Canada Basin. *Organic Geochemistry*, 1990; 16: 295-305
- [39] Peters KE, and Moldowan JM. Effects of source, thermal maturity and biodegradation on the distribution and isomerization of homohopanes in petroleum. *Organic Geochemistry*, 1991; 17: 47-61.
- [40] Connan J, Bouroullec J, Dessort D, and Albrecht P. The microbial input in carbonate-anhydrite facies of a sabkha palaeoenvironment from Guatemala: a molecular approach. *Organic Geochemistry*, 1986; 10: 29-50.
- [41] Noriyuki S, Masaru S, and Kuniaki T. Biomarker distributions in oils from the Akita and Niigata Basins, Japan, Alexander Chekhmakhchey. *Chemical geology*, 1996; 133: 1-14.
- [42] Tissot BP, and Welte DH. *Petroleum Formation and Occurrence*: New York, Springer-Verlag, 1984; 699.
- [43] Norgate CM, Boreham CJ, and Wilkens AJ. Changes in hydrocarbon maturity indices with coal rank and type, Buller Coalfield, New Zealand. *Organic Geochemistry*, 1999; 30: 985-1010.
- [44] Wang P, L, M, and Larter SR. Extended hopanes beyond C40 in crude oils and source rocks extracts from Liaohe Basin, N.E.China. *Organic Geochemistry*, 1996; 24 (5): 547-551.
- [45] Ourisson G, Albrecht P, and Rohmer M. Predictive microbial biochemistry from molecular fossil to prokaryotic membranes. *Trends in Biochemistry Sciences*, 1982; 7: 236-239.
- [46] Rohmer M. The hopanoids, prokaryotic triterpenoids and sterol surrogates. In: *Surface Structures of Microorganisms and their interactions with the Mammalian Host* (Edited by E. Schriener et al.). *Proceeding of Eighteen Workshop Conference. Hocchst, Schloss Ringberg*, 1987; 227-242.
- [47] Killips SD, and Killips VJ. *Introduction to organic geochemistry*. Second edition. U.K: Blackwell Publishing Limited. Kingston, D.R., Dishroon, C.P. and Williams, P.A. *Hydrocarbon Plays and Global Basin Classification. AAPG Bull.*, 1983, 67: 2175-2193.
- [48] Yangming Z, Huanxin W, Aiguo S, Digang L, and Dehua P. Geochemical characteristics of Tertiary saline lacustrine oils in the Western Qaidam Basin, Northwest China. *Applied Geochemistry*, 2005; 33: 1225-1240.
- [49] Miranda ACML, Loureiro MRB, and Cardoso JN. Aliphatic and Aromatic hydrocarbons in *Candidia* col samples: novel series of bicyclic compounds. *Organic Geochemistry*, 1999; 30: 1027-1028.
- [50] Tuo J, Ma W, Zhang M, and Wang X. Organic geochemistry of the Dongsheng sedimentary uranium ore deposits, China. *Applied Geochemistry*, 2007; 22: 1949-1969.
- [51] Huang WY, and Meinschein WG. Sterols as ecological indicators: *Geochimica et Cosmochimica Acta*, 1979; 43: 739-745.
- [52] Volkman JK. The biological marker compounds as indicators of the depositional environments of petroleum source rocks. In: Fleet, A.J., Kelts, K., Talbot, M.R. (Eds.), *Lacustrine Petroleum Source Rocks. Geological Society Special Publication*, 1988; 40: 103-122.
- [53] Kagya MLN. Geochemical characterization of Triassic petroleum source rock in the Mandawa basin, Tanzania. *Journal of African Earth Sciences*, 1996; 23 (1): 73-88.
- [54] Killips SD, and Killips VJ. *An Introduction to Organic Geochemistry*. UK: Longman Group Ltd, 1993; 221.
- [55] Hossain HZ, Sampei Y, and Roser BP. Characterization of organic matter and depositional environment of Tertiary mudstones from the Sylhet Basin, Bangladesh. *Org. Geochem.*, 2009; 40 (7): 743-754.
- [56] van Graas GW. Biomarker maturity parameters for high maturities: calibration of the working range up to the oil/condensate threshold. *Organic Geochemistry*, 1990; 16: 1025-1032.

*To whom correspondence should be addressed: K. C. Chiadikobi, Department of Geology, Chukwuemeka Odumegwu Ojukwu University, Uli, Anambra State, Nigeria, [kinsomino@yahoo.com](mailto:kinsomino@yahoo.com)*

## IMPACT OF FAILURE CRITERION CHOICE ON ONSET SANDING PREDICTION

*Fredrick Temitope Ogunkunle<sup>1</sup>, S. O. Isehunwa<sup>2</sup>, D. O. Orodu<sup>1</sup>*

<sup>1</sup> *Department of Petroleum Engineering, Covenant University, Ota, Nigeria*

<sup>2</sup> *Department of Petroleum Engineering, University of Ibadan, Ibadan, Nigeria*

Received June 13, 2018; Accepted September 27, 2018

---

### **Abstract**

Sand production is the migration of formation materials (sand grains) triggered by the flow of reservoir fluids. It is initiated when the failure of reservoir rock occurs around the perforation and/or cavity openings. Subsequently, fluid flow thrust the loose sand grains into the borehole causing problems ranging from reduced productivity to complete sanding up of the well. In this study, sanding potential of unconsolidated sandstone reservoirs was assessed using three sanding criteria developed by incorporating three well known failure criteria, i.e., Hoek-Brown, Murrell's Extension of Griffith and Mohr-Coulomb, into the general stability equation. Using these criteria, the condition for sanding was formulated to be a minimum well flowing pressure at which sanding is expected to occur. Therefore, sand production occurs if field well pressure is less than the predicted well pressure by these criteria. Results indicate that the three failure criteria give different estimates of sanding potential of the studied wells. Hoek-Brown failure criterion predicted the lowest well pressure for all the wells, while Mohr-Coulomb seems to be a bit conservative in terms of the estimated well pressures. Similar trend and close estimate were observed between Murrell's extension of Griffith and Hoek-Brown failure criterion.

**Keywords:** Sand Production; Failure Criterion; Minimum well Pressure; Well-logs.

---

## **1. Introduction**

Production of sand along with desired reservoir fluid is a common production challenge in weakly consolidated to unconsolidated sandstone reservoirs which play host to around 70 percent of global oil production [7]. Sand production is the migration of formation materials (sand grains) triggered by the flow of reservoir fluids. It is initiated when the failure of reservoir rock occurs around the perforation, and fluid flow thrust the loose sand grains into the borehole [3]. Depletion of reservoir pressures induces borehole stresses, when the maximum stress at the perforation or cavity opening exceeds the yield strength of the rock at the perforation or cavity opening, the formation rock fails in shear and sand production is initiated.

Associated problems with sand production include: plugging and eventual damage of production and completion equipment, plugging of sand control devices, pipe erosion, ground surface subsidence and environmental challenges of sand treatment and disposal [26]. Sanding is a two stage phenomenon: reservoir rock formation must first fail and followed by transport of formation materials by the flowing fluid.

The first stage is stress induced, and the flowing velocity caused the transportation of the detached sands [25]. Many techniques exist in the literature relating to sand production prediction, a number of which are effective and are still currently being used in the industry. They are based on parameters that indicate stress around an open cavity such as elastic and plastic models and also numerical models that are anchored on finite element methods. Of paramount importance is understanding and use of appropriate failure mechanism when developing a model for predicting sand production [15-16]. Numerous works has been done on sand production based on shear failure mechanism. Such works as Edwards, Sharma, and Charron [12];

Coates and Denoo [9]; Edwards, Joranson, and Spurlin [11] used elastic, brittle failure model to predict sand production, it is quite easy to implement, but does not offer a realistic description of the formation (friable and loose). Other researchers used an elastic plastic material model which gives a close description of the material behaviour. These models requires computational efforts [2,9,21-22].

In using a shear failure mechanism to model sand production, it is good to take note that the result of the model is largely dependent on the choice of failure criterion and yield envelope.

For instance, modeling could be based on Mohr-Coulomb [9,12,19] or Drucker-Prager yield envelope [4-6,11,19,21] and their failure criteria based on any of the following;

- Maximum plastic yield zone size
- Maximum plastic strain
- Maximum stress

Using any of these could lead to different results even though they are all based on the same triaxial test experimental data [20,24]. There exist other models based on tensile failure mechanism, these include; Bratli & Risne [8] and Risnes, Bratli & Horsrud [23], the authors used an assumed ideally plastic friction material to derive normalized pressure gradient. Javani, Aadnoy, Rastergarni, Nadimi, Aghighi & Maleki [17], evaluated the effect of failure criterion on solid production in an Iranian Carbonate reservoir rock by comparing estimated collapse pressure predicted using Mohr-Coulomb and Mogi-Coulomb failure criteria. The results show different estimations of the solid production potential of the studied reservoir. Therefore, it is imperative to assess sanding potential of unconsolidated reservoir rocks using different failure criteria when appropriate failure criterion cannot be assigned to a particular failure of reservoir rocks under study.

## 2. Sand prediction models

The onset of sand production is the failure of intact rock; thus, if this can be predicted and prevented, then sand production becomes no issue [13]. Therefore, the starting point for a most predictive tool for predicting sanding potentials in unconsolidated sandstones is identifying the stresses at the perforation cavity and failure prediction around the perforation cavity or open hole. The stepwise process in the model development is listed as follows:

1. Identifying the in-situ stress magnitude.
2. Assessing the stress state at the borehole wall or perforation tunnel, having in mind the orientation of the borehole.
3. Applying the appropriate failure criterion.

## 3. Failure Criteria

In this work, three well known failure criteria were used in estimating minimum well flowing pressure during production to evaluate the potential for sand production in a vertical wellbore drilled through a sandstone reservoir.

### 3.1. Hoek-Brown Failure Criterion

The Hoek-Brown failure criterion is an empirically derived failure criterion that describes the non-linear increase in peak strength of isotropic rock with increasing confining stress. The original non-linear Hoek Brown failure expression for intact was introduced in 1980 as;

$$\sigma_1 = \sigma_3 + \sqrt{mC_o\sigma_3 + SC_o^2} \quad (1)$$

where:  $\sigma_1$ -major principal stress;  $\sigma_3$ -minor principal stress;  $C_o$ - uniaxial compressive strength of intact rock,  $m$  and  $S$  are dimensionless empirical constants.

To account for reservoir rocks that are no longer intact, Hoek Brown criterion was updated in response to experience gained with its use and to address the practical limitation of friable rocks [14]. In achieving this, a generalized form of the criterion was reported in 1995 as follows;

$$\sigma_1' = \sigma_3' + C_o \left( M \frac{\sigma_3'}{C_o} + S \right)^{0.5} \quad (2)$$

where:  $M$  – a term introduced to account for broken rock;  $a$  – empirical constant to account for system's bias towards hard rock.

### 3.2. Murrell's extension of Griffith failure criterion

The original Griffith criterion is applicable to plane stress and plain strain cases both in tension and shear. The criterion is given as;

$$(\sigma_1' - \sigma_3')^2 = -8T_o(\sigma_1' + \sigma_3') \quad (3)$$

In 1963 Murrell extended the Griffith theory to a three-dimensional case and the result presented below:

$$(\sigma_1' - \sigma_3')^2 = C_o(2\sigma_1' + \sigma_3') \quad (4)$$

### 3.3. Mohr-Coulomb

The Mohr-Coulomb failure criterion is a common failure criterion used in most rock mechanics and formation engineering applications. The criterion is expressed as:

$$\sigma_1' = 2 \frac{S_o \cos \theta}{1 - \sin \theta} + \sigma_3' \frac{(1 + \sin \theta)}{(1 - \sin \theta)} \quad (5)$$

As earlier mentioned, sand production from shear dominated failure occurs when the maximum stress at the wellbore exceeds the yield strength of the formation. The two major stresses in the borehole environment as presented by [13] are the tangential stress and the radial stress given below;

$$\sigma_r' = (1 - \alpha)P_{wf} \quad (6)$$

$$\sigma_\theta' = 2\sigma_h - \alpha \frac{1 - 2\nu}{1 - \nu} \bar{P} - \left(1 + \alpha \frac{\nu}{1 - \nu}\right) P_{wf} \quad (7)$$

Considering a common case of borehole failure when  $\sigma_\theta \geq \sigma_v \geq \sigma_r$ , and taking tangential stress (Eq. 7) to be the maximum stress at the borehole wall, stability occur when the stress estimated by Eq. 7 is equal to the one estimated by each of the aforementioned failure criteria. i.e. Eq. 2, 4 & 5 written in cylindrical coordinates. That is;

#### For the Hoek-Brown failure criterion.

Substituting equation 6 for  $\sigma_r'$  in each of equations (8a) and solving for well pressure, the minimum well flowing pressure at failure is given below;

$$2\sigma_{h(t)} - \alpha \frac{1 - 2\nu}{1 - \nu} \bar{P} - \left(1 + \alpha \frac{\nu}{1 - \nu}\right) P_{wf} = \sigma_r' + C_o \left[ M \frac{\sigma_r'}{C_o} + S \right]^{0.5} \quad (8a)$$

If  $\frac{1 - 2\nu}{1 - \nu} = n$

$$(2 - \alpha n)^2 P_{wf}^2 - P_{wf} [MC_o(1 - \alpha) - 2(2 - \alpha n)(\alpha n \bar{P} - 2\sigma_h)] + (\alpha n \bar{P} - 2\sigma_h)^2 - SC_o^2 = 0$$

Using the general quadratic equation given as Eq. 9:

$$x = - \frac{b \pm \sqrt{b^2 - 4ac}}{2a} \quad (9)$$

$$a = (2 - \alpha n)^2$$

$$b = [MC_o(1 - \alpha) - 2(2 - \alpha n)(\alpha n \bar{P} - 2\sigma_h)]$$

$$c = (\alpha n \bar{P} - 2\sigma_h)^2 - SC_o^2$$

$$\text{Let } (2 - \alpha n) = R \quad (\alpha n \bar{P} - 2\sigma_h) = Y \quad (1 - \alpha) = U$$

Then;

$$a = R^2 \quad b = MC_o U - 2RY \quad c = Y^2 - SC_o^2$$

Therefore,  $P_{wf}$  is given as;

$$P_{wf} = \frac{-(MC_o U - 2RY) \pm \sqrt{(MC_o U - 2RY)^2 - 4R^2(Y^2 - SC_o^2)}}{2R^2} \quad (10)$$

Hoek-Brown material constant  $M$  and  $S$  were reported according to Hoek *et al.* [14] as

$$M = m_i \exp\left(\frac{GSI - 100}{24 - 14D}\right) \quad (11)$$

$$S = \exp\left(\frac{GSI - 100}{9 - 3D}\right) \quad (12)$$

**For Mohr-Coulomb failure criterion**

$$2\sigma_h - \alpha \frac{1-2\nu}{1-\nu} \bar{P} - \left(1 + \alpha \frac{\nu}{1-\nu}\right) P_{wf} = 2 \frac{S_o \cos\theta}{1 - \sin\theta} + \sigma_r' \frac{(1 + \sin\theta)}{(1 - \sin\theta)} \quad (8b)$$

Substituting equation 6 for  $\sigma_r'$  in each of equations (8b) and solving for well pressure, the minimum well flowing pressure at failure is given below;

$$\frac{2\sigma_h(1-\nu) - \alpha(1-2\nu)\bar{P} - C_o(1-\nu)}{1-\nu} = \left[ \frac{2-2\nu + 2\alpha\nu - \alpha(1 + \sin\theta)}{(1-\nu)(1 - \sin\theta)} \right] P_{wf} \quad (13)$$

$$P_{wf} = \frac{[2\sigma_h(1-\nu) - \alpha\bar{P}(1-2\nu) - C_o(1-\nu)][1 - \sin\theta]}{2[1-\nu + \alpha\nu] + \alpha(1 + \sin\theta)} \quad (14)$$

**For Murrell's Extension of Griffith failure criterion**

$$\begin{aligned} & \left(2\sigma_h - \alpha \frac{1-2\nu}{1-\nu} \bar{P} - \left(1 + \alpha \frac{\nu}{1-\nu}\right) P_{wf} - \sigma_r'\right)^2 \\ & = C_o \left[ 2 \left(2\sigma_h - \alpha \frac{1-2\nu}{1-\nu} \bar{P} - \left(1 + \alpha \frac{\nu}{1-\nu}\right) P_{wf}\right) + \sigma_r' \right] \quad (8c) \end{aligned}$$

Substituting equation 6 for  $\sigma_r'$  in each of equations (8c) and solving for well pressure, the minimum well flowing pressure at failure is given below;

$$\begin{aligned} & \left[ 2 - \frac{2\alpha}{1-\nu} + \alpha^2 + 5\alpha\nu(1-\nu) - \alpha\omega - \frac{\alpha^2\nu\omega}{1-\nu} \right] P_{wf}^2 - [(2-\alpha n)(4\sigma_h - 2\alpha n\bar{P}) + C_o(1+\alpha\beta)] P_{wf} \\ & + (\alpha n\bar{P} + 2\sigma_h)^2 - 2C_o(2\sigma_h - \alpha n\bar{P}) \quad (16) \end{aligned}$$

Applying the general quadratic equation

$$y = \frac{-b \pm \sqrt{b^2 - 4ac}}{2a} \quad \text{therefore, } P_{wf} = \frac{-b \pm \sqrt{b^2 - 4ac}}{2a}$$

where:

$$a = \left[ 2 - \frac{2\alpha}{1-\nu} + \alpha^2 + 5\alpha\nu(1-\nu) - \alpha\omega - \frac{\alpha^2\nu\omega}{1-\nu} \right]$$

$$b = [(2-\alpha n)(4\sigma_h - 2\alpha n\bar{P}) + C_o(1+\alpha\beta)]$$

$$c = (\alpha n\bar{P} + 2\sigma_h)^2 - 2C_o(2\sigma_h - \alpha n\bar{P})$$

**4. Estimate of input parameters**

To apply the developed models proposed in the methodology, estimates of in-situ stresses, minimum horizontal stress, average reservoir pressure, Poisson's ratio, poro elastic constant, uniaxial compressive strength together with the Hoek-Brown material constants are required. Generally, the parameters consist of elastic and strength characteristics of the rocks as well as the pore pressures. The details of the ideologies and correlations used in this work for estimates of the aforementioned parameters is presented in Khaksar, Taylor, Fang, Kayes, Salazar & Rahman [18] and the output results are corresponding to each wells were only presented.

**4.1. Case study**

Five hypothetical data from Almisned [1] was used to investigate the potential for solid production using different failure criteria. The data include different types of petrophysical logs such as density log and sonic compressive and shear travel time (Table 1). The initial reservoir pressure was given, and the field imposed well pressure was set at 2000 psi. From these logs, using correlations from Khaksar *et al.* [18], rock mechanical properties were estimated and presented in Figures 1 & 2, the results serve as input data for the developed sanding criteria models.

Table 1. Input data for the cases studied

Case A					Case B				
Depth (ft)	Initial Pressure (psia)	Log compressional time (mic.sec/ft)	Log shear time (mic.sec/ft)	Log bulk density (g/cm <sup>3</sup> )	Depth (ft)	Initial Pressure (psia)	Log compressional time (mic.sec/ft)	Log shear time (mic.sec/ft)	Log bulk density (g/cm <sup>3</sup> )
3000	2400	88	121	2.56	3000	2400	87	120	2.56
3250	2600	80	118	2.1	3250	2600	79	117	2.1
3500	2800	71	111	2	3500	2800	71	111	2
3750	3000	70	100	2.5	3750	3000	74	105	2.5
4000	3200	65	94	2.2	4000	3200	72	104	2.2

Case C					Case D				
Depth (ft)	Initial Pressure (psia)	Log compressional time (mic.sec/ft)	Log shear time (mic.sec/ft)	Log bulk density (g/cm <sup>3</sup> )	Depth (ft)	Initial Pressure (psia)	Log compressional time (mic.sec/ft)	Log shear time (mic.sec/ft)	Log bulk density (g/cm <sup>3</sup> )
3000	2400	85	121	2.56	3000	2400	85	125	2.56
3250	2600	84	111	2.1	3250	2600	92	128	2.1
3500	2800	75	110	2	3500	2800	85	130	2
3750	3000	78	107	2.5	3750	3000	90	124	2.5
4000	3200	72	100	2.2	4000	3200	80	115	2.2

Case C				
Depth (ft)	Initial Pressure (psia)	Log compressional time (mic.sec/ft)	Log shear time (mic.sec/ft)	Log bulk density (g/cm <sup>3</sup> )
3000	2400	90	134	2.56
3250	2600	100	130	2.1
3500	2800	85	131	2
3750	3000	90	127	2.5
3000	2400	90	134	2.56

## 6. Results and discussion

In investigating the potential for sand production for the cases presented, predicted minimum well pressures from the three (3) failure criteria were compared to the field-imposed well pressure since we assume that shear failure corresponds to the initiation of sand production. Figures 1a & b shows the stress profiles for cases A to E, including the pore pressure trends and the rock mechanical properties estimated.

From Figures 2a and b for cases A to E respectively, it can be observed that minimum well pressure predicted by Mohr-Coulomb failure criterion is higher than the minimum well pressures predicted by Hoek-Brown and Griffith failure criteria. This is in agreement with the reported work of Javani *et al.* [17], in which he reported the result of comparing critical collapse pressure predicted from Mohr-Coulomb with Mogi-Coulomb predicted. Generally, from the current study, the predicted minimum well pressure from Hoek-Brown and Murrell's extension of Griffith failure criterion compared favorably, even with field imposed well-pressure. They both showed consistency and similar trends for all the cases analyzed, while minimum well pressure predicted using the Mohr-Coulomb failure criterion is somewhat conservative in terms of predictive accuracy.

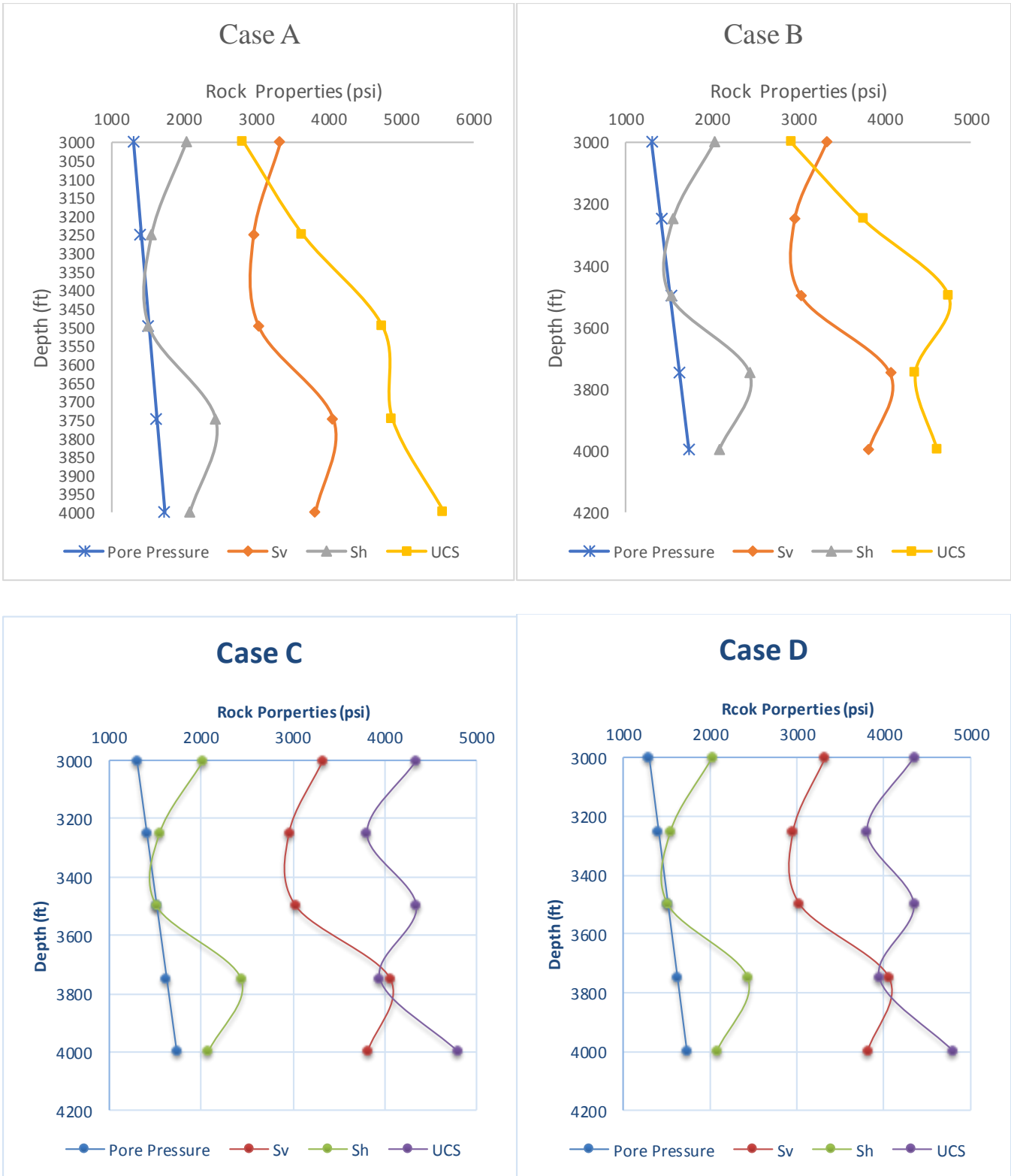


Figure 1a Estimated mechanical properties of the case studies, pore pressure and stress profile

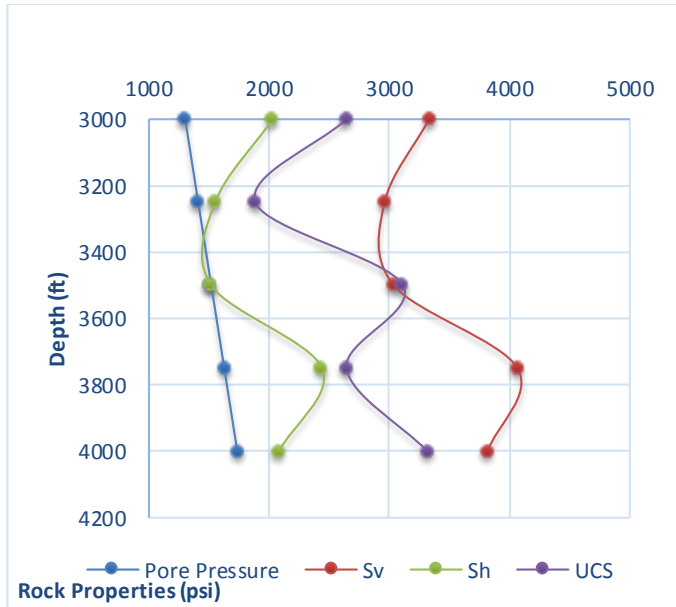


Figure 1b Estimated mechanical properties of the case E, pore pressure and stress profile

The choice of failure criterion depends on the ductility and brittleness of the reservoir rock under analysis. To understand a failure phenomenon, a specific and compatible criterion must be applied. While some rocks such as sandstone, fail in shear, others such as clay, fails as a result of plastic deformation. However, the understanding of the ductility and brittleness or the structural geology of such rock may not be available when determining the post drilling stability of reservoir rocks prior to completion.

Numerous empirical criteria have been established to predict reservoir rocks, and formation failure such are those employed in this study, but it is essential to understand the physical and practical interpretation of these criteria before they are been applied.

Mohr-Coulomb failure criterion offers a more conservative, easy to use and less complex correlation with input parameters that can be easily estimated.

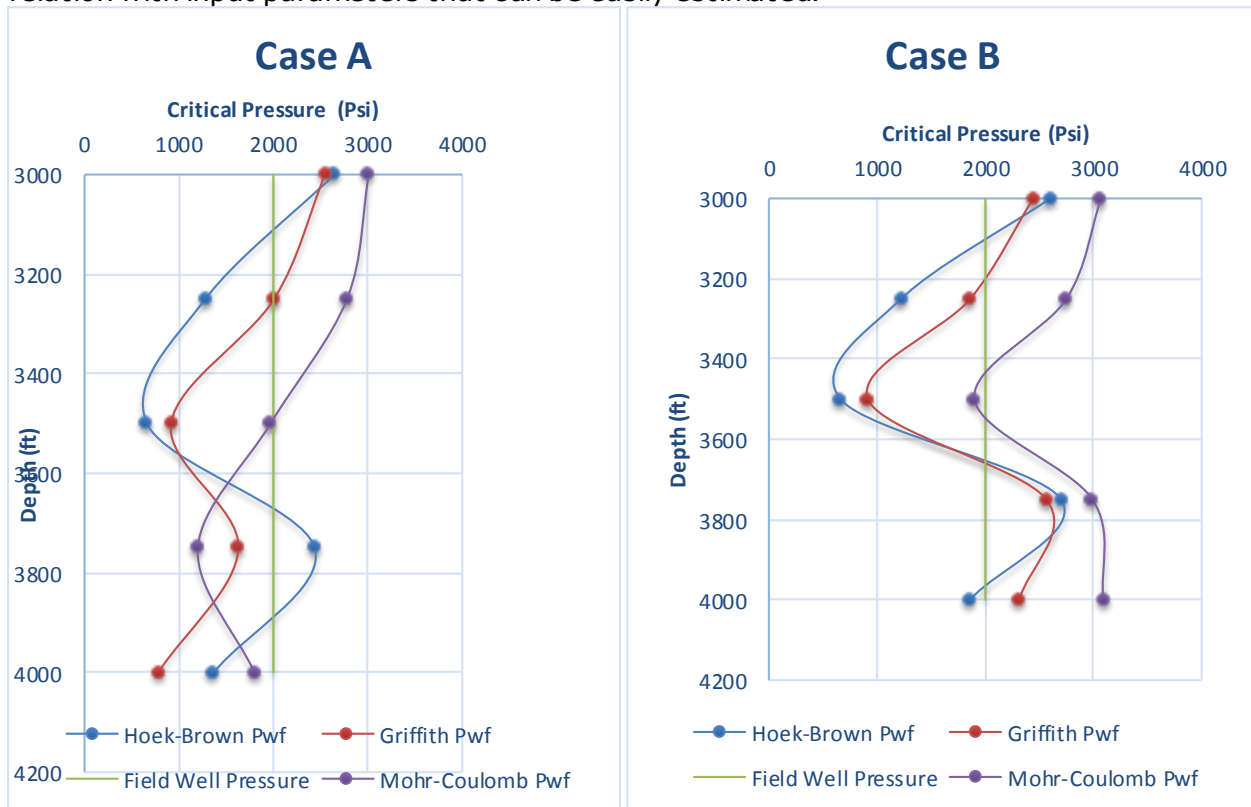


Figure 2a. Predicted minimum well pressure using different failure criteria for cases A and B

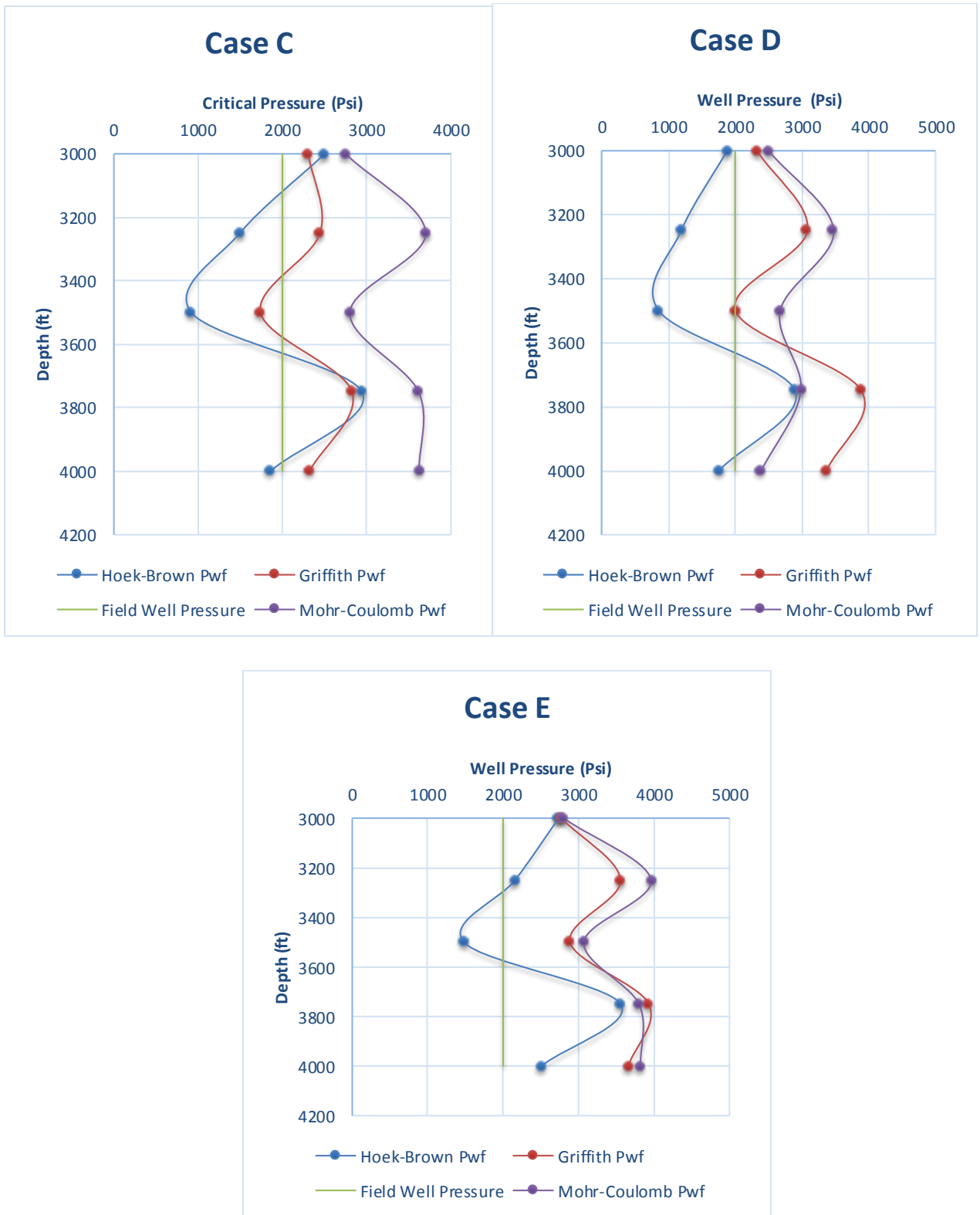


Figure 2b. Predicted minimum well pressure using different failure criteria for cases C, D and E

But can only be used to account for the failure of intact rocks, Hoek-Brown failure criterion can better describe the material quality of reservoir rocks at failure but with additional empirical constants that accurately estimating them may pose a serious question. Mogi-Coulomb introduced a third stress parameter in terms of the intermediate stress which was assumed to be negligible by the other two criteria but also introduced two new constants that make it application complex. In other words, since the results of sanding prediction with different failure criteria demonstrates different results, but generally show similar trends, it is proposed that when the brittleness and ductility cannot be ascertained, different sand onset prediction models should be used to predict sanding onset. This will allow the establishment of a stable margin of operation that will not induce sand failure.

## 7. Conclusions

In this study, sand production criteria assuming shear failure as the dominant failure mechanism was developed using three (3) well known failure criteria. These criteria were used to assess the potential for sand production in five hypothetical case studies. The condition for sand production was formulated to be minimum well pressure at/or below which sand is to be expected. From the results, minimum well pressures vary with the choice of failure criterion, Hoek-Brown and Murrell's extension of Griffith failure criteria showed consistency and similar trends while Mohr-Coulomb failure criterion predicted (conservative) higher minimum well pressure at failure than the two other criteria. For best practice, it is proposed that sanding onset predictive tools anchored on several failure criteria should be used to assess sand production potential when the ductility and brittleness of the reservoir rock under analysis is not known.

### Nomenclature

$m$  = material constant in Hoek – Brown criterion, dimensionless  
 $M$  = material constant in Hoek – Brown criterion, dimensionless  
 $m$  = material constant in Hoek – Brown criterion, dimensionless  
 $S$  = material constant in Hoek – Brown criterion, dimensionless  
 $C_0$  = Rock Strength = Uniaxial compressive strength,  $m/Lt^2$ , psi  
 $T_0$  = Rock Strength,  $m/Lt^2$ , psi  
 $UCS$  = Uniaxial compressive strength  $m/Lt^2$ , psi  
 $Pwf$  = bottom hole flowing pressure,  $m/Lt^2$ , psi  
 $n$  = constant, dimensionless  
 $P$  = average reservoir pressure,  $m/Lt^2$ , psi  
 $r$  = radial coordinate, L, ft  
 $x$  = coordinate, L, ft  
 $y$  = coordinate, L, ft  
 $z$  = coordinate, L, ft  
 $\alpha$  = Biot's constant, dimensionless  
 $\theta$  = angle, dimensionless, radian  
 $\nu$  = Poisson's ratio, dimensionless, fraction  
 $\rho_f$  = density of gas,  $m/L^3$ ,  $lbm/ft^3$   
 $\sigma$  = total normal stress,  $m/Lt^2$ , psi  
 $\sigma'$  = effective stress,  $m/Lt^2$ , psi  
 $\sigma_1$  = maximum principal stress,  $m/Lt^2$ , psi  
 $\sigma_2$  = intermediate principal stress,  $m/Lt^2$ , psi  
 $\sigma_3$  = minimum principal stress,  $m/Lt^2$ , psi  
 $\sigma_h$  = total minimum horizontal stress,  $m/Lt^2$ , psi  
 $\sigma'_h$  =  $Sh$  = effective minimum horizontal stress,  $m/Lt^2$ , psi  
 $\sigma_H$  = total maximum horizontal stress,  $m/Lt^2$ , psi  
 $\sigma'_H$  = effective maximum horizontal stress,  $m/Lt^2$ , psi  
 $\sigma_r$  = total radial stress,  $m/Lt^2$ , psi  
 $\sigma'_r$  = effective radial stress,  $m/Lt^2$ , psi  
 $\sigma'_v$  =  $Sv$  = effective vertical stress,  $m/Lt^2$ , psi  
 $\sigma_x$  = total normal stress in x direction,  $m/Lt^2$ , psi  
 $\sigma'_x$  = effective normal stress in x direction,  $m/Lt^2$ , psi

$\sigma_y$  = total normal stress in y direction,  $m/Lt^2$ , psi  
 $\sigma_z$  = total normal stress in z direction,  $m/Lt^2$ , psi  
 $\sigma'_z$  = effective normal stress in z direction,  $m/Lt^2$ , psi  
 $\sigma'_\theta$  = effective tangential stress,  $m/Lt^2$ , psi  
*a* = empirical constant to account for system's bias towards hard rock

## References

- [1] Almisned OA. A Model for Predicting Sand Production from well Logging Data. PhD Thesis, University of Oklahoma 1995.
- [2] Antheunis D, Vriezen PB, Schipper BA, van der Vlis AC. Perforation Collapse: Failure of perforated friable Sandstones. SPE 5750. European Spring Meetings. Amsterdam 1976: Society of Petroleum Engineers.
- [3] Araujo EF, Alzate GA, Arbelaez A, Clavijo SP, Ramirez AC, Naranjo A. Analytical Prediction Model of Sand Production Integrating Geomechanics for Open Hole and Cased-Perforated Wells 2014. SPE-171107-MS.
- [4] Asadi MS, Rahman K, Pham HV, Le Minh T, Butt A. Sand Production Assessment Considering the Reservoir Geomechanics and Water Breakthrough. The APPEA Journal, 2015; 5(01): 215 - 224.
- [5] Asadi MS, Khaksar A, Nguyen HQ, Manapov TF. Solids Production Prediction and Management in a High Porosity Carbonate Reservoir-A Case Study from Offshore Vietnam. In SPE/IATMI Asia Pacific Oil & Gas Conference and Exhibition 2017 October, Society of Petroleum Engineers.
- [6] Asadi MS, Khaksar A, Ring MJ, Saric D, Yin Yin M. Solids production prediction and management for oil producers in highly depleted reservoirs in a Mature Malaysian field. In SPE Annual Technical Conference and Exhibition. Society of Petroleum Engineers 2016.
- [7] Bianco LCB, and Halleck PM. Mechanisms of arch instability and sand production in two-phase saturated poorly consolidated sandstones. The SPE European Formation Damage Conference 2001. Hague, Netherlands: Society of Petroleum Engineers.
- [8] Bratli RK, and Risne R. Stability and Failure of Sand Arches. Society of Petroleum Engineers Journals, 1981; 236-248.
- [9] Coates DR, and Denoo SA. Mechanical Properties Program Using Borehole Analysis and Mohr's Circle. June 23- 26. SPWLA 22nd Annual Logging Symposium 1981, (pp. 1156 - 1158). Los Angeles.
- [10] Dusseault MB, Santarelli FJ. A conceptual model for massive solid production in poorly consolidated sandstones. ISRM-SPE Int. Symposium. Rock at great depth 1989, (pp. 789 - 797). Pau: SPE.
- [11] Edwards D, Joranson H, Spurlin J. Field normalization of formation mechanical properties for use in sand control management. SPWLA 29th Annual Logging Symposium 1988.
- [12] Edwards DP, Sharma Y, and Charron A. Zones of sand Production Identified by log-derived Mechanical Properties: Case study. SPWLA 8th European Formation Evaluation Symposium 1983. London.
- [13] Fjaer E, Holt RM, Horsrud P, Raaen AR, and Risnes R. Petroleum Related Rock Mechanics. Amsterdam 1992, The Netherlands: Elsevier Science Publishers.
- [14] Hoek E, Carranza-Toress CT, Corkum B. Hoek-Brown failure criterion. 5th North American Rock Mechanics Symposium (NARMS-TAC) 2002 (pp. 00. 267 - 273). University of Toronto, Canada: Toronto Press.
- [15] Isehunwa SO and Farotade A. (2010). Sand Failure Mechanism and Sanding Parameters for Niger/Delta Oil Reservoirs. International Journal of Engineering Science and Technology, 2010; 2(5): pp777-78.
- [16] Isehunwa SO, Ogunkunle TF, Onwuegbu SM, Akinsete OO. (2017). Prediction of sand production in gas and gas condensate wells. Journal of Petroleum and Gas Engineering, 2017; 8(4): 29-35.
- [17] Javani D, Aadnoy B, Rastegarnia M, Nadimi S, Aghigh, MA, Maleki B. (2017). Failure criterion effect on solid production prediction and selection of completion solution. Journal of Rock Mechanics and Geotechnical Engineering, 2017; 9(6): 1123-1130.2.
- [18] Khaksar A, Taylor PG, Fang Z, Kayes T, Salazar A, Rahman K. (2009). Rock Strength from Cores and Logs: Where We Stand and Ways to Go. SPE Europe C/EAGE Annual Conference and Exhibition 2009: (pp. 1- 16). Amsterdam: Society of Petroleum Engineers.
- [19] Nordgren R. Strength of well completions. 18th Symposium on Rock Mechanics 1977, (pp. 4A3-1 4A3-9). Keystone co.

- [20] McLean MR, and Addis MA. A Review of current methods of analysis and their field application. IADC/SPE Drilling Conference. Houston 1990: SPE.
- [21] Morita N, Whitfill DL, Massie I, Knudsen TW. (1989). Realistic Sand Prediction : Numerical Approach. SPE Production Engineering, Feb 1989: 15-25.
- [22] Peden JM, Yassin AAM. Determination of optimum Production and completion conditions for sand free oil production. SPE 15406. 61st Annual Technical Conference and Exhibition. New Orleans 1986: SPE.
- [23] Risnes R, Bratli RK, Horsrud P. Sand Stresses Around a Wellbore. Society of Petroleum Engineers Journal, 1982; 883-898.
- [24] Veeken CAM, Davies DR, Kenter CJ, Kooijman AP. Sand production prediction review: developing an integrated approach. In SPE annual technical conference and exhibition 1991. Society of Petroleum Engineers.
- [25] Venkitaraman A, Behrmann LA, Chow CV. Perforating requirements for sand control. SPE European Petroleum Conference 2000. (pp. 1-5), France: <https://doi.org/10.2118/65187-MS>.
- [26] Wan R, Wang J. Analysis of sand production in unconsolidated oil sand using a coupled erosional-stress-deformation model. Journal of Canadian Petroleum Technology, 2004; 43(2): 47-53.

---

*To whom correspondence should be addressed: Fredrik Temitope Ogunkunle, Department of Petroleum Engineering, Covenant University, Ota, Nigeria*

3D MODELING OF POROSITY IN SARVAK FORMATION VIA GAUSSIAN SIMULATION METHOD IN DEZFUL EMBAYMENT, A CASE STUDY

*Hossein Tabatabaei*

*Department of Petroleum Engineering, Gachsaran Branch, Islamic Azad University, Gachsaran, Iran*

Received July 27, 2018; Accepted November 12, 2018

---

## **Abstract**

Porosity is a petrophysical property used for reservoir 3D modeling and prediction of production scenarios for the purpose of economic decisions play an important role in field and reservoir management. In this study, drilling data (logs) from 7 wells and geostatistical method including sequential Gaussian simulation were used to predict porosity petrophysical property. Sequential Gaussian simulation is widely used for porosity model construction since it is easily applied and is flexible in real heterogeneous conditions. In this method, with the available data including values and coordinates values of the same parameter in unknown points can be predicted. In Sequential Gaussian method cells having certain values from petrophysical parameters are taken into account. After, constructing reservoir structural model and analyses of petrophysical data, simulations models for 5 reservoir units of Sarvak in the Kupal oil filed were established for porosity with high precision. The results of this study showed that the applied method is highly accurate and can be used based on computational methods to identify reservoir zones contains hydro-carbon. The results of this study indicate that the concentration of petroleum in the layers 4 and 5 of Sarvak is higher than other formations and is suggested for the initial production, this reservoir will be developed.

**Keywords:** *Petrophysical Properties; Porosity; Geostatistical method; sequential Gaussian simulation; Dezful Embayment.*

---

## **1. Introduction**

The oil and gas industry is one of the industries in which Geostatistics is rapidly becoming epidemic and has grown rapidly. One of the causes of this rapid growth is the nature of the reservoir data. Petrophysical data of the reservoirs, such as porosity and permeability, are those data that have a spatial correlation in the reservoir space and in the field of geostatic shows the spatial structure, and these are the same types of variables that the Geostatistics relates to. On the other hand, due to the low reservoirs data compared to reservoir volume, the reservoir engineers have always sought to find a method for estimating the spatial distribution of petrophysical parameters in the reservoir space [1]. Along with all the advantages of the Geostatistics estimation than the other statistical methods, Geostatistics estimations like the other methods of estimating, are based on the averaging method. This led engineers to find new methods. These methods express a quantitative spatial distribution of petrophysical parameters in a probable space. Thus, after gridding the reservoir, for each block, a range of data is created, and several probable facts are simulated for each petrophysical parameter [2].

The introduction of geostatistics has revolutionized the modeling of oil reservoirs. Many people have examined the use of geostatistics in reservoir modeling. George Matron is one of the pioneers in the use of geostatistics for modeling. The basis of his work is modeling based on variogram. Models based on variograms are divided into two categories [3].

The first category is definitive models that include estimation methods like consecutive Kriging and sequential Kriging. These estimation methods are geostatistical, which yields a model for each variogram, resulting in deterministic models due to estimation methods [4].

The second group is called probabilistic models. The basis of these models is simulation methods. In simulation methods, several models are obtained by using a variogram, for this reason, simulation models yield probabilistic models. Since the mid-1990s, simulation models have been developed in the petroleum industry. Simulated models have anomalous properties of petroleum reservoirs [3]. Since the mid-1990s, 3D seismic data has been used as a secondary parameter in estimating and simulating reservoir parameters [5]. Three-dimensional seismic data were obtained by means of sequential estimation or simulation methods. Until today, these methods provide an optimal model of the static parameters of the reservoir [6]. Over the past 30 years, the development of geostatistical methods and the development of various software, has led to changes in reservoir engineering and the estimation or simulation of reservoir parameters. In this study, the petrophysical parameter of porosity is estimated using a sequential Gaussian simulation method (a geostatistical method) in Kupal oil fields.

## 2. Geological settings

Sarvak formation has expanded in Fars, Khuzestan, and Lurestan [7]. In Bangestan Anticline (section type) Sarvak formation having a thickness of more than 830m has been noticed which consists of medium to thick layers and massive fossiliferous limestones. Kupal oil field is located in the Dezful embayment (Figure 1).

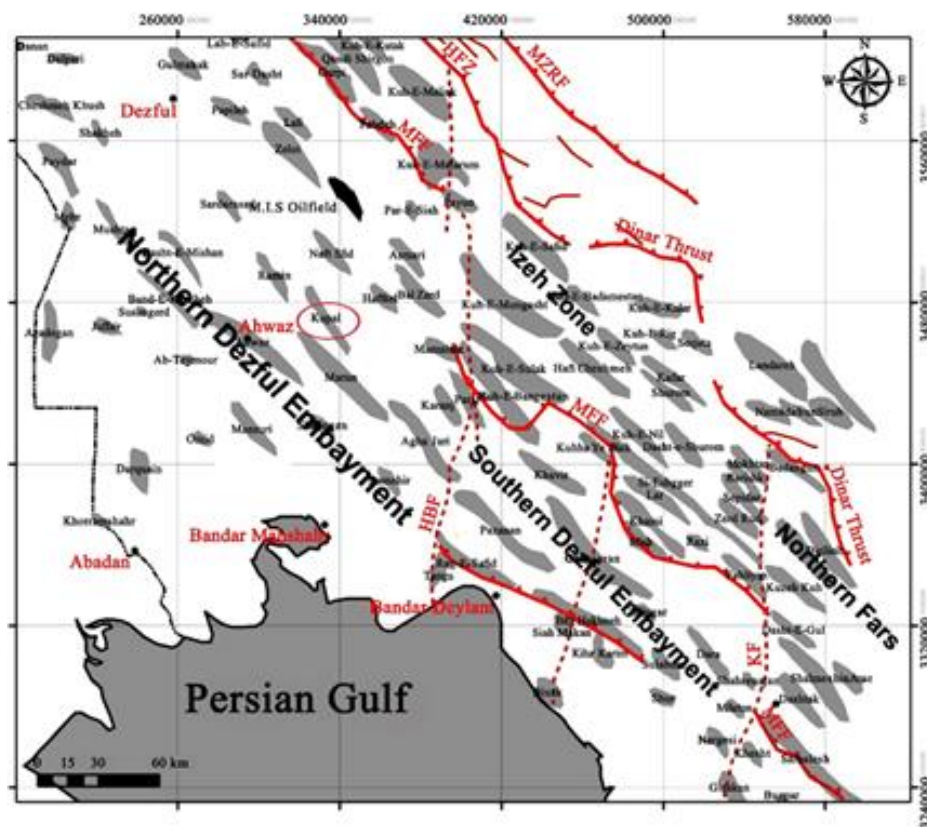


Figure 1. Located of Kupal oil field in Dezful embayment, Zagros, Iran

This oil field is located in Khuzestan provinces in the south west of Iran. Their lower limits (Albian-Cenomanian) are gradational and conformable from the Kazhdomi formation, and the upper limit has been distinguished from Ilam formation in Kupal oil field [8]. The boundary between Sarvak and Ilam Formation is the disconformities that determine some areas by

breccia or conglomerates [9]. Disconformities between Sarvak and overlies Formation indicates some part of middle Cretaceous epirogenic activities in the Zagros. Lithostratigraphical column of Sarvak Formation has been controlled by Austrian tectonic activities, but variation aggradations pattern of Sarvak Formation depends on the rate of subsidence in the sedimentary basin. Sarvak Formation was deposited on the passive margin which existed in the east of the Arabian craton throughout much of the Mesozoic [9]. This passive margin was generally covered by shallow waters. However, a number of deeper-water intra shelf basins had been formed during the Cretaceous [10]. The thickness of the Sarvak Formation in the studied oil field is including two major facies (Benthic and pelagic). The Benthic facies includes a massive limestone containing algae, echinoderms, rudists, Gastropods, and Orbitolina. The pelagic deposits contain abundant Oligostegina. Pelagic facies in Sarvak Formation changes to benthic facies, which relates to Austrian movement [11]. Lateral and vertical variations in stratigraphic thicknesses in Zagros area can be related to the presence of locale faults in the Zagros Basin that effect in rates of sedimentation with lower rates of deposition in the basin.

### 3. Material and methods

Data from well logs and seismic data in petroleum researches are considered as the primary data and main parameters. In this study, data of 7 wells and part of seismic data have been used. The location of the wells in relation to the position of the data is shown in Figure 2, In this study, by using multivariate statistics methods, neutron logs, and density, total porosity was obtained, and the resulting total porosity values are used as well parameter values for use in the correlations. The histogram obtained from the total porosity of the wells in the studied area is shown in Figure 3.

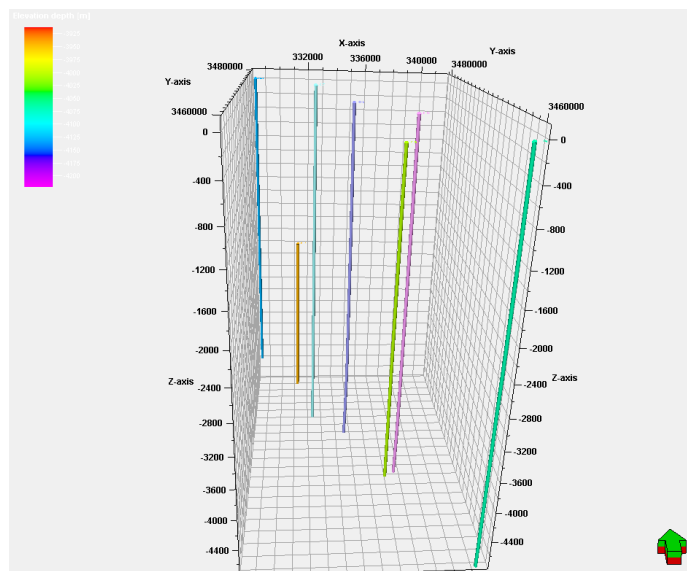


Figure 2. Position of wells No.3, 4, 25, 33, 37, 48 and 52, in the studied oil field

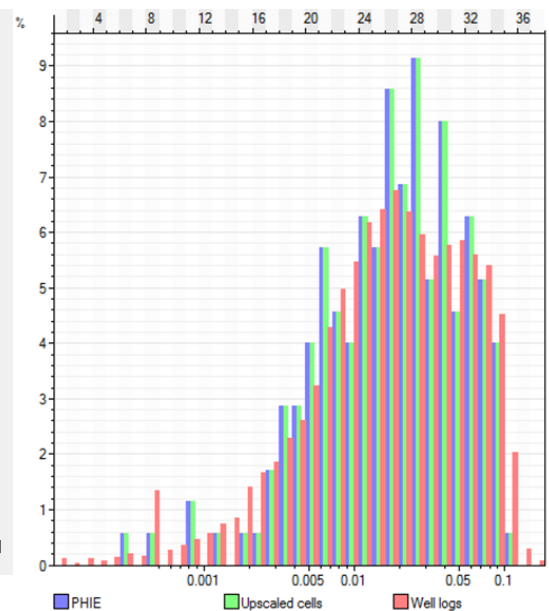


Figure 3. Cumulative histogram of porosity model derived from well logging data in Kupal oil field

### 4. Definition of reservoir geometry and gridding

After entering data and creating Ischore Map Logs, in the second stage, it is time to build a construction model. At this stage, a geocell network is created proportional to the dimensions of the field. This network as the main framework of the model allows for the simultaneous examination and integration of structural data and petrophysical properties for the creation of realistic models, and when making petrophysical modeling, it causes the defined petrophysical

parameters for each well, can be extended to the entire reservoir. At this stage, where the reservoir is divided into a cellular network in which all properties of each cell, including petrophysical and lithological properties are the same in whole volume, and according to the distance between the networks and the amount of data, the same properties in cells without data, can be estimated. The dimensions of the network are 500\*500, and the number of reservoir cells are 1620060, which are considered along X and Y directions. (Figures 4 and 5). After making the horizons at the time of layering, these blocks are separated in depth or Z direction.

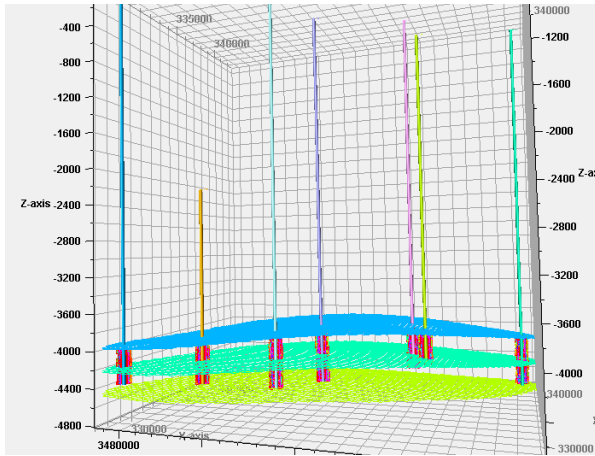


Figure 4. A view of created cellular network in Kupal oil field.

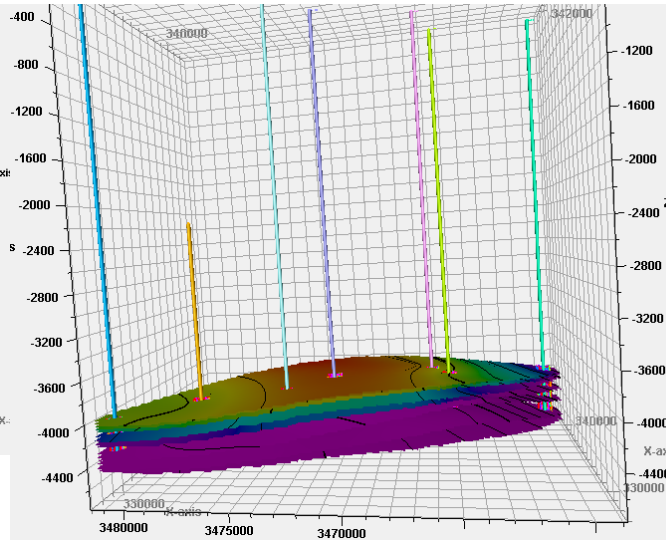


Figure 5. A view of the created horizons in the cellular network

### 5. Data analysis and variography

In the third step, the data obtained from petrophysical logs by scale up and analyzing data, Variography are ready to convert into a 3D model [12]. Scale up means attribution of logs recorded values to blocks of the three-dimensional network where its log information is available [13]. The Scale up the logs is necessary to distribute each one in each cell for use in modeling and generalizing these properties to the entire grid network. Given that, each cell can only have one value; the log values should be averaging. There are many techniques for averaging [14]. This is called the Scale up well logs. The data are processed in the variography stage, and the variograms are plotted (Figure 6). Property modeling is usually used for inherent properties of a parameter. A variogram is a tool for describing these inherent properties [15]. In other words, variogram is used as a method of analyzing and describing these spatial changes based on the principle that samples close together are more similar than samples far from each other [14].

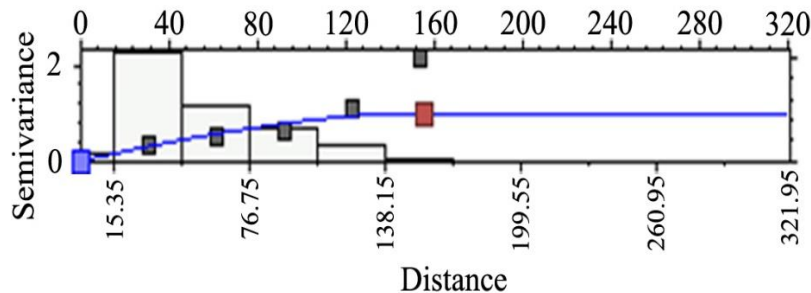


Figure 6. Variography model in the main-horizontal direction for porosity logs in zone 5

The modeling of reservoir porosity was carried out using the output of the variography stage by a consecutive Gaussian simulation method. Porosity values for different zones are given in Table (1).

Table.1 Average porosity for each zone of Sarvak formation, Kupal oil field.

Zone	Average porosity	Thickness (m)
1	5.5	65
2	4	243
3	4.5	132
4	6.5	140
5	7	70

### 6. Discussion and results

Due to its simplicity and flexibility in generating real heterogeneities, sequential Gaussian simulation is widely used for modeling. The steps of performing a sequential simulation include 5 steps. These steps include conversion of main data to a new space; variogram modeling in new space; determination of a stochastic route in order to visit all of the places lacking sample; estimation of places without a sample in an alternate way and finally reversed conversion of simulated values (Figure 7).

Geostatistical simulation is a technique for producing data compatible with a regional variable. The main feature of the simulation data is that it can create a histogram and modifying the real data space.

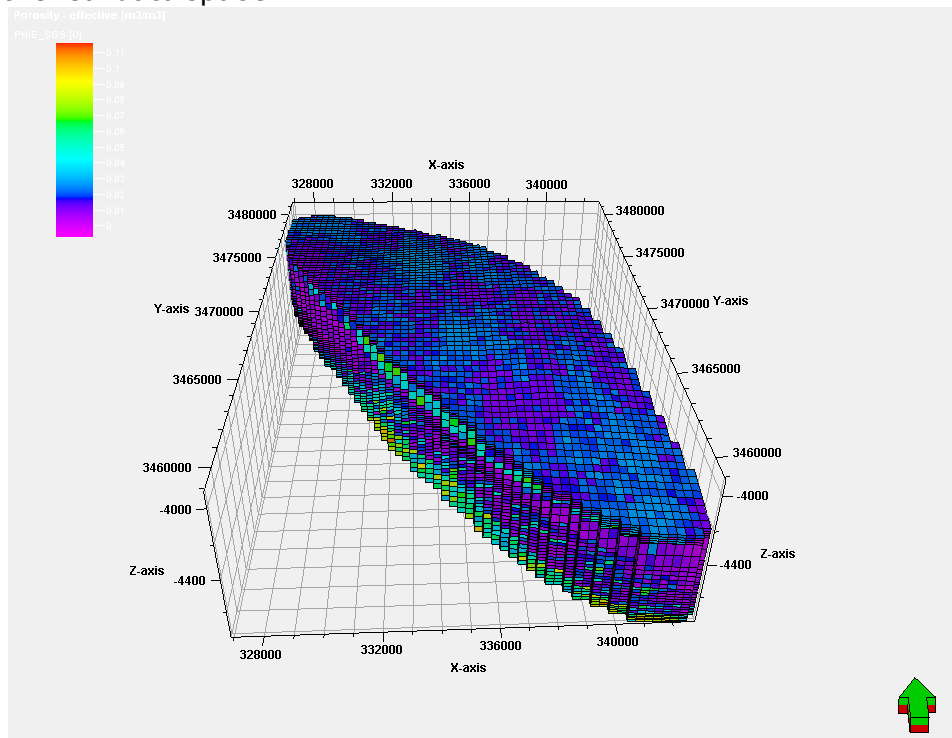


Figure 7. 3D modeling of porosity in Kupal oil field

### 7. Conclusion

The use of sequential Gaussian simulation (SGS) method is one of the common methods for determining petrophysical parameters. This method showed that simulation methods in cases where the initial data is less than the reservoir space are a suitable method for creating data in the space between the wells. In the simulation, decision-making is not based on a simulated model, but based on the sum of simulated values, the probability of occurrence of

each reality is determined. Of course, it should be noted that sometimes, the goal is to determine the operational risk in petroleum production planning. In these cases, it is necessary to select the best and worst of all simulated models, and in order to reduce the risk of operation, modeling of the reservoir is based on these two models. In this study, data of 7 wells have been used. For better modelling of reservoir properties, it is better to use more wells or to extend them in to the entire reservoir .The results of the porosity parameter for each zone are presented separately. According to these results, the concentration of petroleum in Layers 4 and 5 of Sarvak is higher than other zones, and it is suggested for the initial production, this reservoir will be developed

The average porosities are about 5.5% and for each zone is 5.5%, 4%, 4.5%, 6.5% and 7% in the Sarvak respectively.

### Acknowledgement

We would like to express our sincere thanks to the Department of Petroleum Engineering, Gachsaran Branch, Islamic Azad University, and all our colleagues for critical discussions and support. Thanks also to the anonymous referees for all their gracious and critical points.

### References

- [1] Zingano AC, Costa JFCL, Koppe JC. Simulation—an approach to risk Analysis in coal mining. *Exploration and Mining Geology*, 2000; 9: 1, 43-49.
- [2] Sahin A, and Al-Salem AA. Stochastic Modeling of Porosity Distribution in a Multi-Zonal Carbonate Reservoir. *SPE 68113.01*, 2001, DOI: 10.2118/68113-MS.
- [3] Dubrule O, (2003). Geostatistics for seismic data integration in earth model, Society of Exploration Geophysics (SEG), European Association of Geoscientists & Engineers, DISC No. 6.
- [4] Kaviyani Nezhad H, Tabatabaei H, (2017), Simulation of Petrophysical Parameters of Asmari Reservoir Using SGS Method in Mansuri Oil Field, Southwest of Iran, *Open Journal of Geology* 7: 1188-1199.
- [5] Amanipoor H, Ghafoori M. and Lashkaripour GR. The Application of Geostatistical Methods to Prepare the 3D Petrophysical Model of Oil Reservoir. *Open Journal of Geology*, 2013; 3: 7-18.
- [6] Kaufmman O, and Martin T. 3D Geological Modeling from Boreholes, Cross-Sections and Geological Maps, Application over Former Natural Gas Storages in Coal Mines. *Journal of Computers & Geosciences*, 2008; 34: 278-290.
- [7] Nadjafi M, Mahboubi A, Moosavi Harami R, Mirzaee Mahmoodabadi R. Depositional history and Sequence Stratigraphy of outcropping tertiary carbonates in the Jahrum and Asmari Formations, Shiraz (SW Iran). *Journal of Petroleum Geology*, 2004; 27:179-190.
- [8] Motiei H. *Geology of Iran. The stratigraphy of Zagros*. 5st ed. Tehran 1993, Iran: Geological Survey of Iran.
- [9] Asghari M, Adabi MH. Diagenesis and Geochemistry of the Sarvak Formation in Ahvaz oil field- Iran. *Geochemistry Journal*, 2014; 1:1-7.
- [10] Murriss R. Middle East: Stratigraphic evolution and Oil habitat, *American Association of Petroleum Geologists Bulletin*, 1980; 64: 597-618.
- [11] Afghah M, Dehghaniyan MS. Quantitative and qualitative Study of sarvak Formation microfacies in Kuh-e Khaneh kat and kuh- e shahneshin section in fars. *Journal of Applied Geology*, 2007; 1: 7-16.
- [12] Robinson A, Griffiths P, Price S, Hegre J, and Muggeridge A. The Future of Modelling in Hydrocarbon Development. Special Publication No:309. The Geological Society London, 2008, doi.org/10.1144/SP309.
- [13] Schumberger. *Petrel Introduction course*, Schumberger information solutions, 2006.
- [14] Schumberger. *Seismic- to- Simulation Software, Property Modeling Course*. p. 503, 2009.
- [15] Dean L. *Reservoir Engineering for Geologists, Part 3- Volumetric Estimation, Reservoir*, 2007;11, p. 20.
- [16] Holden L, Mostad P, Nielsen BF, Gjered J, Townsend C, and Ottesen S., (2003). Stochastic Structural Modeling. *Journal of Mathematical Geology*, 2003; 35: 899-914.

*To whom correspondence should be addressed: Dr. Hossein Tabatabaei, Department of Petroleum Engineering, Gachsaran Branch, Islamic Azad University, Gachsaran, Iran*

## DETERMINATION OF COMPRESSIBILITY FACTOR FOR NATURAL GASES USING ARTIFICIAL NEURAL NETWORK

Joseph C. Nwosu<sup>1</sup>, Stanley U. Ibeh<sup>\*2</sup>, Stanley I. Onwukwe<sup>1</sup>, Boniface O. Obah<sup>1</sup>

<sup>1</sup> Department of Petroleum Engineering, Federal University of Technology Owerri, Nigeria

<sup>\*2</sup> Department of Petroleum Engineering, Madonna University Akpugo, Enugu, Nigeria

Received July 19, 2018; Accepted October 19, 2018

---

### Abstract

This work proposes the use of data division and if statements in a programming language, as an effective classifier in Artificial Neural Network. The Standing and Katz chart was digitized to obtain input (pseudo reduced temperature and pressure) and output (gas compressibility factor) data points, which was used in developing the artificial neural network. A total of 114,120 input data points and 57,060 output data points were used. The dataset was divided into 4 groups, and each of the groups was assigned a neural network that corresponds to the value range of the grouped data using a Matlab nnet tool box.

**Keywords:** gas compressibility factor; artificial neural network; natural gas; gas correlation; Matlab.

---

## 1. Introduction

Fluid properties are determined from the laboratory using applicable experimental procedures, with the aim of analyzing samples to meet conditions of interest. The unavailability of these samples brings rise to the use of empirical correlations. The determination of accurate compressibility factor is of great importance in the industry. This parameter has been a tool in determining the deviation of real gas from ideal behaviour. A compressibility factor is a useful tool in various engineering applications, which include; designing pipelines, gas flow rates, the design of oil and gas separators, gas reserves estimation, etc. According to Cengel and Boles [1], the principle of corresponding states indicates that all gases, when compared at the same reduced pressure (Ppr) and reduced temperature (Tpr), have approximately the same compressibility factor. The development of the general EOS and the elaboration of general experimental charts expressed in terms of the reduced properties were based on this principle. Standing and Katz [2] developed a chart for the compressibility factor and pseudo reduced properties (temperature and pressure) which is an industry standard. Other correlations exist and each of which shows better prediction at specific ranges of pseudo reduced temperatures.

Katz *et al.* [3] developed a chart of compressibility factor in terms of pseudo reduced properties for natural gases at pressures of 10,000 to 20,000psia. The chart displays a high level of linearity, which makes prediction less complex without the need for multiple data points selection across the pseudo reduced temperature curves.

Kamyab *et al.* [4] worked on digitizing the Standing-Katz and Katz compressibility chart to obtain input and output data, in which artificial neural network was used as a tool in predicting the output of compressibility factor. In their project, a two-hidden-layer feed forward network was designed and trained with back-propagation supervised learning. They developed a methodology to obtain z-factors for Natural Hydrocarbon Gases using Artificial Neural Networks (ANN). Data obtained directly from the Standing-Katz and Katz compressibility charts were used to train several topologies of ANN. The input parameters in the ANN are the pseudo-reduced pressure and temperature, and the output is the z-factor. Two of the

successful networks have two hidden layers. The first ANN uses five neurons in each hidden layer and the second ANN uses ten neurons in each hidden layer (called 2-5-5-1 and 2-10-10-1 networks respectively). These topologies were trained with the data from the charts using a back-propagation training algorithm. This work had a limitation in understanding the level of accuracy of artificial neural networks as a predictive tool for complex datasets.

Beggs and Brill [5] developed a correlation for the determination of compressibility factor which is given below as:

$$Z = A + (1 - A)e^{-B} + CP_{pr}^D \tag{1}, \text{ where:}$$

$$A = 1.39 (T_{pr} - 0.92)^{0.5} - 0.36T_{pr} - 0.101 \tag{2}$$

$$B = (0.62 - 0.23T_{pr})P_{pr} + \left[ \left( \frac{0.066}{T_{pr} - 0.86} \right) - 0.037 \right] P_{pr}^2 + \left[ \frac{0.32}{10^9(T_{pr} - 1)} \right] P_{pr}^6 \tag{3}$$

$$C = (0.132 - 0.32 \log T_{pr}) \tag{4}$$

$$D = 10^{0.3106 - 0.49T_{pr} + 0.1824T_{pr}^2} \tag{5}$$

Dranchuk and Abou-Kassem [6] developed their equation for the determination of the compressibility factor as follows;

$$Z = 1 + C_1(T_{pr})\rho_{pr} + C_2(T_{pr})\rho_{pr}^2 - C_3(T_{pr})\rho_{pr}^5 + C_4(\rho_{pr}T_{pr}) \tag{6}, \text{ where:}$$

$$\rho_{pr} = 0.27 \frac{P_{pr}}{zT_{pr}} \tag{7}$$

$$C_1(T_{pr}) = A_1 + A_2T_{pr}^{-1} + A_3T_{pr}^{-3} + A_4T_{pr}^{-4} + A_5T_{pr}^{-5} \tag{8}$$

$$C_2(T_{pr}) = A_6 + A_7T_{pr} + A_8T_{pr}^{-2} \tag{9}$$

$$C_3(T_{pr}) = A_9[A_7T_{pr}^{-1} + A_8T_{pr}^{-2}] \tag{10}$$

$$C_4(\rho_{pr}T_{pr}) = A_{10}(1 + A_{11}\rho_{pr}^2)(\rho_{pr}^2T_{pr}^{-2}) \tag{11}$$

The constants A1 through A11 are as follows: A1 = 0.3265; A2 = -1.07; A3 = -0.5339; A4 = 0.01569; A5 = -0.05165; A6 = 0.5475; A7 = -0.7361; A8 = 0.1844; A9 = 0.1056; A10 = 0.6134; A11 = 0.721 They used Newton's method to determine the solution of the above equations.

## 2. Artificial neural network

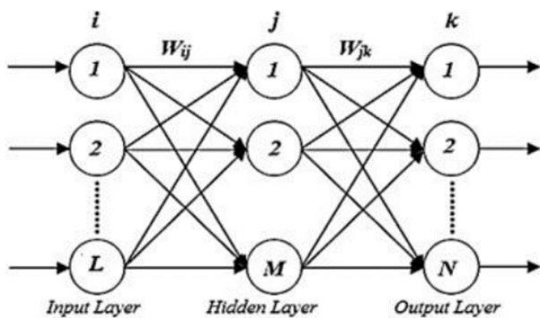


Fig. 1 Structure of an Artificial Neural Network

Artificial Neural Networks are simulators, which work on the basis of the human nervous system to carry out certain tasks like classification, pattern recognition, etc. The artificial neurons present in the network lies in constitutive layers of the network. Layers are linked to the next by specific weights ( $w$ ). One of the most practical structures of the Artificial Neural Network is Multi-Layer Perceptron (MLP) (Fig. 1) in which the input and output layers are connected to each other by an additional layer called hidden layer.

This structure was adapted in the course of this work. Each input is multiplied by its corresponding weights. Weights carry the information needed by the neural network to solve a problem and also represent the strength of the interconnection between neurons inside the neural network.

Activation functions are set to serve as a transfer function used to get the desired output. There are linear as well as the non-linear activation function. Some of the commonly used activation function is - binary, sigmoidal (linear) and tan hyperbolic sigmoidal functions (non-linear). The structure of an Artificial Neural Network is given in Fig. 3.

### 3. Proposed approach

The Standing and Katz chart data has been read directly from a scanned figure of the original plot drawn by Standing and Katz in 1951. The software used in digitizing the chart and obtaining the dataset was GraphClick. According to Rakap *et al.* [7], this software has been tested and qualified to be able to digitize charts. Each one of the pseudo-reduced temperature curves from Standing and Katz chart was been digitized [4], some curves needed more points (Fig. 4) to describe the curvature better while other curves are almost linear and fewer points (Fig. 5) were necessary to define the curve. It should also be noted the need for data uniformity in the distribution of data points, so as to enable the neural network to understand the data progression pattern.

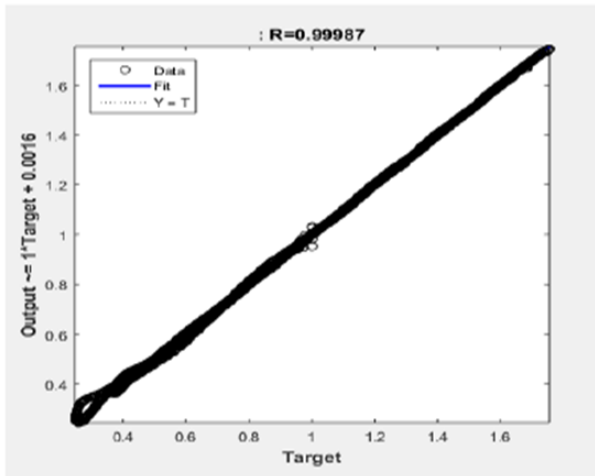


Fig 2. Regression plot for outputs derived from  $1.05 \leq T_{pr} \leq 1.2$

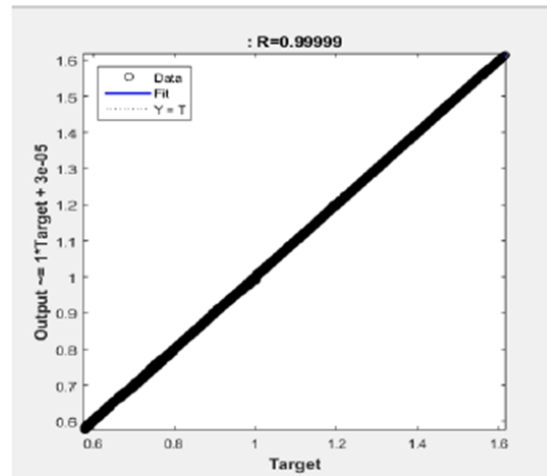


Fig 3. Regression plot for outputs derived from  $1.5 \leq T_{pr} \leq 2.0$

The human nervous system works as a transmitter of information which perceives, interprets and transmits information to target organs in the human body. A key fact that should be noted is that the information been perceived and interpreted are later classified (during the interpretation phase) before been transmitted to target organs, which optimizes the effectiveness of the nervous system in transmitting information. Classification in this context means allocating information to be transmitted to a particular target organ for execution depending on the information perceived. Artificial Neural Network works on this base principle, and the importance of data classification/grouping should always be noted especially when dealing with large datasets, as it increases the effectiveness in prediction.

This work made use of the Nnet toolbox in Matlab software to develop the needed Neural Networks using the back propagation algorithm. The Neural network assumed a total number of 30 hidden layers, using 99% data for training, 0.5% for Testing and 0.5% for validation. The dataset has 2 input data columns and 1 output data column, having a matrix of  $57,060 \times 2$  and  $57,060 \times 1$  respectively. The dataset was divided into 4 groups with the aim of developing a neural network for each group of dataset divided. The development of an individual neural network for each grouped data was to reduce the complexity in determining the output variables, in this case, the compressibility factor. Each of the Neural networks covered the ranges of pseudo reduced temperature values  $1.05 \leq T_{pr} \leq 1.2$ ,  $1.2 < T_{pr} \leq 1.5$ ,  $1.5 < T_{pr} \leq 2.0$  and  $2.0 < T_{pr} \leq 3.0$  respectively, at Pseudo, reduced pressures of  $0.5 \leq P_{pr} \leq 5.5$ .

This work proposes the use of "If Statements" in programming the desired neural network as a predictive tool for the compressibility factor when the Input data; Pseudo reduced pressure and temperature are provided. The results were compared with other existing correlations and showed an overall outstanding performance (Tables 1-5).

Table 1. Compressibility factors at different Tpr=1.2 using various correlations

Ppr	Standing and Katz	This approach	Kamyab <i>et al.</i> [4]	Beggs & Brill [5]	Dranchuk-Aboukassem [6]
0.5	0.8930	0.8960	0.8953923	0.9026461	0.8950631
1.5	0.657	0.6573	0.6607512	0.6758659	0.6532419
2.5	0.519	0.5196	0.5179963	0.4977865	0.5180675
3.5	0.565	0.5663	0.5676801	0.5605500	0.5631805
4.5	0.650	0.6499	0.6492856	0.6589953	0.6501377
5.5	0.741	0.7406	0.7424365	0.7567099	0.7453363

Table 2. Compressibility factors at different Tpr=1.3 using various correlations

Ppr	Standing and Katz	This approach	Kamyab <i>et al.</i> [4]	Beggs & Brill [5]	Dranchuk-Aboukassem [6]
0.5	0.916	0.9182	0.9196115	0.9266436	0.9203019
1.5	0.756	0.7584	0.7567070	0.7675523	0.7543694
2.5	0.638	0.6399	0.6394479	0.6526911	0.6377871
3.5	0.633	0.6329	0.6341957	0.6234648	0.6339351
4.5	0.684	0.6832	0.6857549	0.6921991	0.6898314
5.5	0.759	0.7604	0.7611212	0.7779095	0.7663247

Table 3. Compressibility factors at different Tpr=1.5 using various correlations

Ppr	Standing and Katz	This approach	Kamyab <i>et al.</i> [4]	Beggs & Brill [5]	Dranchuk-Aboukassem [6]
0.5	0.948	0.9493	0.9508509	0.9555248	0.9509373
1.5	0.859	0.8592	0.8607096	0.8618306	0.8593144
2.5	0.794	0.7974	0.7940885	0.7945385	0.7929993
3.5	0.770	0.7694	0.7685691	0.7691830	0.7710525
4.5	0.790	0.7910	0.7867923	0.7828753	0.7896224
5.5	0.836	0.8344	0.8323518	0.8248905	0.8331893

Table 4. Compressibility factors at different Tpr=2.0 using various correlations

Ppr	Standing and Katz	This approach	Kamyab <i>et al.</i> [4]	Beggs & Brill [5]	Dranchuk-Aboukassem [6]
0.5	0.982	0.9837	0.9839990	0.9853337	0.9824731
1.5	0.956	0.9575	0.9572277	0.9629020	0.9551087
2.5	0.941	0.9406	0.9414698	0.9471826	0.9400752
3.5	0.937	0.9365	0.9352303	0.9471826	0.9385273
4.5	0.945	0.9437	0.9453140	0.9404180	0.9497137
5.5	0.969	0.9686	0.9693022	0.9443010	0.9715388

Table 5. Compressibility factors at different Tpr=3.0 using various correlations

Ppr	Standing and Katz	This approach	Kamyab <i>et al.</i> [4]	Beggs & Brill [5]	Dranchuk-Aboukassem [6]
0.5	1.002	1.0036	1.0028553	1.0040392	0.9984498
1.5	1.009	1.0102	1.0095269	0.9514557	0.9995529
2.5	1.018	1.0187	1.0179196	0.7082371	1.0061111
3.5	1.029	1.0292	1.0286167	0.1399229	1.0176846
4.5	1.041	1.0412	1.0412701	-0.8897010	1.0336417
5.5	1.056	1.0570	1.0563968	-2.5178952	1.0532809

### 4. Results

The Matlab software produced 4 regression plots which contained the Mean Square error and Root Mean Square error of the individual Neural Network developed. The mean square error gives the squared mean deviation of the output data (actual value) from the target data (estimated value). The closer the mean square error value is to zero, the more accurate and the lesser the error of the estimated value. The root means square error measures how much error there is between two data sets, in other words, it compares an estimated value and the actual value. The R-squared value is an indicator of how well the model fits the data. An R-square close to 1 indicates that the model accounts for almost all the variability in the data. The first Neural Network for data group  $1.05 \leq Tpr \leq 1.2$  (Fig. 2), had a mean square error of 0.0016 and a root mean square error of 0.99987. The second Neural Network for data group  $1.2 < Tpr \leq 1.5$  (Fig.4) had a mean square error of 0.000081, and a root mean square error of 1.0000. The third Neural Network for data group of  $1.5 < Tpr \leq 2.0$  (Fig.3) had a mean square error of 0.00003, and a root mean square error of 0.99999 and the last Neural Network for data group  $2.0 < Tpr \leq 3.0$  (Fig. 5) had a mean square error of 0.000011 and a root mean square error of 1.0000.

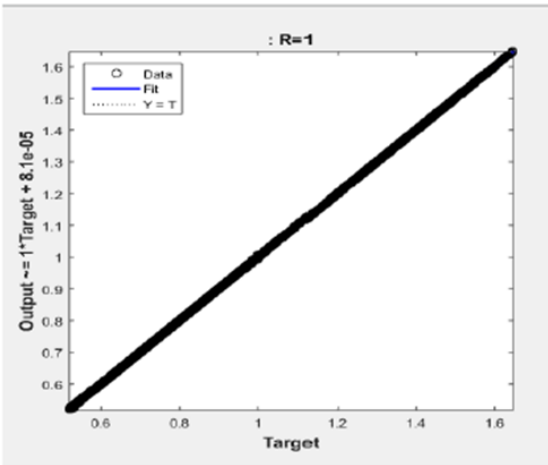


Fig 4. Regression plot for outputs derived from  $1.2 < Tpr \leq 1.5$

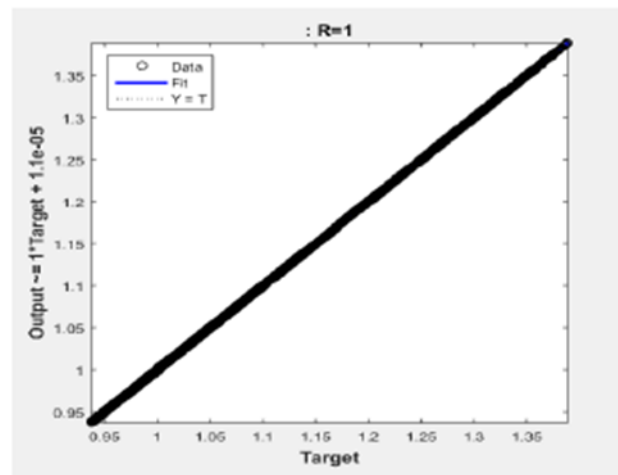


Fig 5. Regression plot outputs derived from  $2.0 < Tpr \leq 3.0$

The average absolute error (mean square error), was determined using the following formula

$$MAE = \frac{1}{n} \sum_i^n |V_e - V_a| \tag{12}$$

where:  $V_e$  = estimated value;  $V_a$  = actual value; MAE = mean absolute error.

The mean absolute error determination gives the deviation of the estimated output data from the actual output data. The lower the value of this error, the higher the precision. This was determined for all the correlations used in the comparison and proved this approach to have the least mean absolute error of about 0.00111. The value of the mean square error proves the precision of this approach to other methods and can be seen in Table 6.

Table 6. Average absolute errors

This approach	Kamayab <i>et al.</i> [4]	Beggs & Brill [5]	Dranchuk-Aboukassem [6]
0.00111	0.00281249	0.233375273	0.0033042

The data obtained from this method was compared with existing correlations like; Begs and Brill, Dranchuk-Aboukassem [6] and Kamyab *et al.* [4]. These correlations were proven by previous research to have a high degree of accuracy in the determination of the compressibility.

The test data used for this comparison was derived from previous literature that proved these correlations to have a high level of accuracy. The comparisons were made and given below in the table of values (Tables 1–5).

## 5. Conclusion

The values derived from this approach proved to be better than existing methods. This approach has justified the uniqueness and accuracy of Artificial Neural Network in data analysis and pattern recognition, especially in data division. The theory from this approach can be deployed in computer based applications to give precision in the determination of the compressibility factor.

## Nomenclature

$P$ - pressure, psia	$T$ - temperature, R
$P_c$ - critical pressure, psia	$T_c$ - critical temperature, R
$P_{pr}$ - pseudo-reduced pressure	$T_{pr}$ - pseudo-reduced temperature
$\rho_g$ - density of gas, lbm/ft <sup>3</sup>	$z$ - gas compressibility factor
$\rho_{pr}$ - pseudo-reduced density	

## Reference

- [1] Cengel YA, and Boles MA. Thermodynamics an Engineering Approach. 6<sup>th</sup> ed., Mc Graw-Hill Book Co. 2007.
- [2] Standing MB, Katz DL. 1942. Density of natural gases. Transactions of the AIME. 1942; 146 (1): 140-149. doi:10.2118/942140-G.
- [3] Katz DL, Cornell D, Kobayashi, R, Poettmann FH, Vary JA, Elenbaas JR, Weinaug CF. Handbook of Natural Gas Engineering. McGraw-Hill 1959, New York, p. 107.
- [4] Kamyab M, Sampaio JH, Qanbari F, Eustes AW 2010. Using artificial neural networks to estimate the z-factor for natural hydrocarbon gases. Journal of Petroleum Science and Engineering, 2010; 73 (3-4): 248-257.
- [5] Beggs H, and Brill J. 1978. Two-phase flow in pipes, Tulsa 1978, University of Tulsa.
- [6] Dranchuk PM, and Abou-Kassem H. 1975. Calculation of Z factors for natural gases using equations of state. *Journal of Canadian Petroleum Technology*, 1975; 14 (3): 34-36.
- [7] Rakap S, Evran D, Cig O. 2016. Comparative evaluation of the reliability and validity of three data extraction programs: UnGraph, GraphClick, and DigitizeIt. Computers in Human Behavior, 2016; 55 (A): 159-166.

---

*To whom correspondence should be addressed: Stanley U. Ibeh, Department of Petroleum Engineering, Madonna University Akpugo, Enugu, Nigeria*

THE SELECTION OF RAW MATERIALS FOR THE PRODUCTION OF ROAD BITUMEN MODIFIED BY PHENOL-CRESOL-FORMALDEHYDE RESINS

*Volodymyr Gunka, Yuriy Demchuk, Serhiy Pyshyev, Starovoit Anatolii, Yurii Lypko*

*Department of Chemical Technology of Oil and Gas Processing, Lviv Polytechnic National University, Bandery str. 12, Lviv 79013, Ukraine*

Received May 22, 2018; Accepted August 27, 2018

---

## Abstract

Resins obtained from the phenolic fraction of coal tar have been synthesized by the method of formaldehyde condensation polymerization. The phenol-cresol-formaldehyde resins have been derived from the following types of starting materials: a wide phenolic fraction, narrow fractions sampled before and after 185 °C (fraction: IBP – 185 and 185 – EBP °C) coupled with the so called raw (technical) phenols that had been separated from these fractions.

The capability of utilizing resins obtained as a modifier of distilled (residual) and oxidized petroleum road bitumens has been determined. It has been shown that adding these resins increases the softening point and essentially boosts the adhesion of petroleum-based bitumens for roads.

**Keywords:** bitumen; phenol; cresol; formaldehyde; bitumen modifier.

---

## 1. Introduction

Data in 2011 [1] say that yearly about 102 million tons of bitumen are consumed worldwide. Nearly 85 % of all the bitumen is used as a binder in various types of paving asphalt: pavements for pedestrians and roads, airports, etc. [1-2]. Thus, more than 90 % of 5.2 million km of European motorways are estimated [3] to be covered with the asphalt whose main binder while produced is petroleum-derived bitumen for roads.

While utilizing road bitumens, a number of problems arise. However, the most acute problem is insufficiently high stiffness and adhesive properties of finished bitumens (even if they achieve high standards of regulations) [1-2].

One of the most promising directions in raising the quality of binders as to produce road surfaces with good performances is their modification with polymeric materials [1, 2, 4].

For the modification of road bitumens, thermoplastic elastomers (primarily, block copolymers of the SBS type styrene) account for the largest use due to their ability not only to increase bitumen strength, but also to make a polymer-bitumen blend more elastic, including at low temperatures, as well as increase the adhesion of bitumen to the mineral material. The content of such polymers in modified bitumen may reach 3-10 % by weight [1-5].

The main drawback that reduces the growth rate of the production of bitumens modified by thermoplastic elastomers is their high costs (1.5 – 2.5 times higher than the cost of unmodified bitumens) [1-2]. Therefore, it is important to search for inexpensive substances that would improve bitumen performance – foremost, adhesive properties.

In the past years there have been studies into the development of relatively cheap and effective modifiers of petroleum-derived bitumens from liquid products of the coal carbonization at the Department of Chemical Technology of Oil and Gas Processing of Lviv National Polytechnic University [2, 6-9].

Phenol-formaldehyde resins are known [1, 2, 10, 11] to be quite effective modifiers of petroleum bitumens. But these pure phenol resins were not widely used as polymer modifiers and this also relates, primarily, to their high cost. On the other hand, one of the products of coking

---

plants is a phenolic fraction of coal tar with a core portion of phenols and cresols (approximately 65 %) concentrated in it and that are formed during the carbonization process. The price of the phenolic fraction of coal tar, which normally contains more than 30 % by phenol weight and its derivatives, is 35-40 times lower than the cost of synthetic phenol [12].

In this regard, this paper aims to open up the possibility for developing phenol-cresol-formaldehyde resins from the wide phenolic fraction (WPhF), narrow fractions sampled before and after 185°C (fraction: IBP – 185°C and 185 – EBP°C) and raw phenol separated from these fractions. Besides, the paper seeks to determine whether modifying residual and oxidized petroleum bitumens for roads that are derived from phenol-cresol-formaldehyde resins is appropriate.

## 2. Experimental

The wide phenolic fraction (WPhF) was sampled at Zaporizhkojs PJSC for investigations. The WPhF characteristic is given in Table 1. For the purpose of concentration (separation) of phenol and cresols, the WPhF was divided into two fractions, an initial boiling point (IBP – ~ 92°C) – 185 and 185 and end boiling point (EBP ~ 211°C)°C (the boiling point of phenol is 182°C, of cresols – 191-202°C). Table 1 lists the characteristic of fractions derived. The mass balance of distillation is shown in Table 2.

Table 1. Characteristics of a starting material

Indexes	wide phenolic fraction (WPhF)	Values		Procedure*
		Fraction IBP – 185°C	Fraction 185 – EBP°C	
Distillation (oC):				
Initial boiling point	105	92	172	GOST 2177
10 % distilled at the temperature	164	147	177	
20 % distilled at the temperature	172	156	179	
30 % distilled at the temperature	174	161	181	
40 % distilled at the temperature	177	166	183	
50 % distilled at the temperature	179	169	184	
60 % distilled at the temperature	182	172	187	
70 % distilled at the temperature	185	174	190	
80 % distilled at the temperature	197	181	200	
90 % distilled at the temperature	202	184	206	
95 % distilled at the temperature	208	189	211	
Molecular weight	136	108	167	-
Bromine number (g Br <sub>2</sub> /100 g product)	81.64	81.28	75.84	GOST 8997-89

\*GOST – Ukrainian national standards

Table 2. Mass balance of the WPhF distillation.

Article	Yield by weight, %
Fraction IBP – 185 °C (phenol concentrate)	50.60
Fraction 185 – EBP °C (cresols concentrate)	46.77
Distillation residue	2.63
Total	100.00

Phenol and its derivatives hereinafter called raw (technical) phenols – RPh1, RPh2 and RPh3 – were separated from the WPhF, the fraction IBP – 185 and the fraction 185 – EBP°C by using a 20% NaOH solution. The removal of phenols with the solution of NaOH was based on the fact that phenol and its derivatives form water-soluble phenolates. The latter were made into phenols by using the concentrated hydrochloric acid. The yield of raw phenols with the WPhF, the fraction IBP – 185 and the fraction 185 – EBP°C accounted for 32.3, 32.0 and 35.1 % wt, respectively.

The resins were derived from initial fractions and those raw phenols that were obtained from them by the method of formaldehyde condensation polymerization.

The scheme of the research is given in Figure 1.

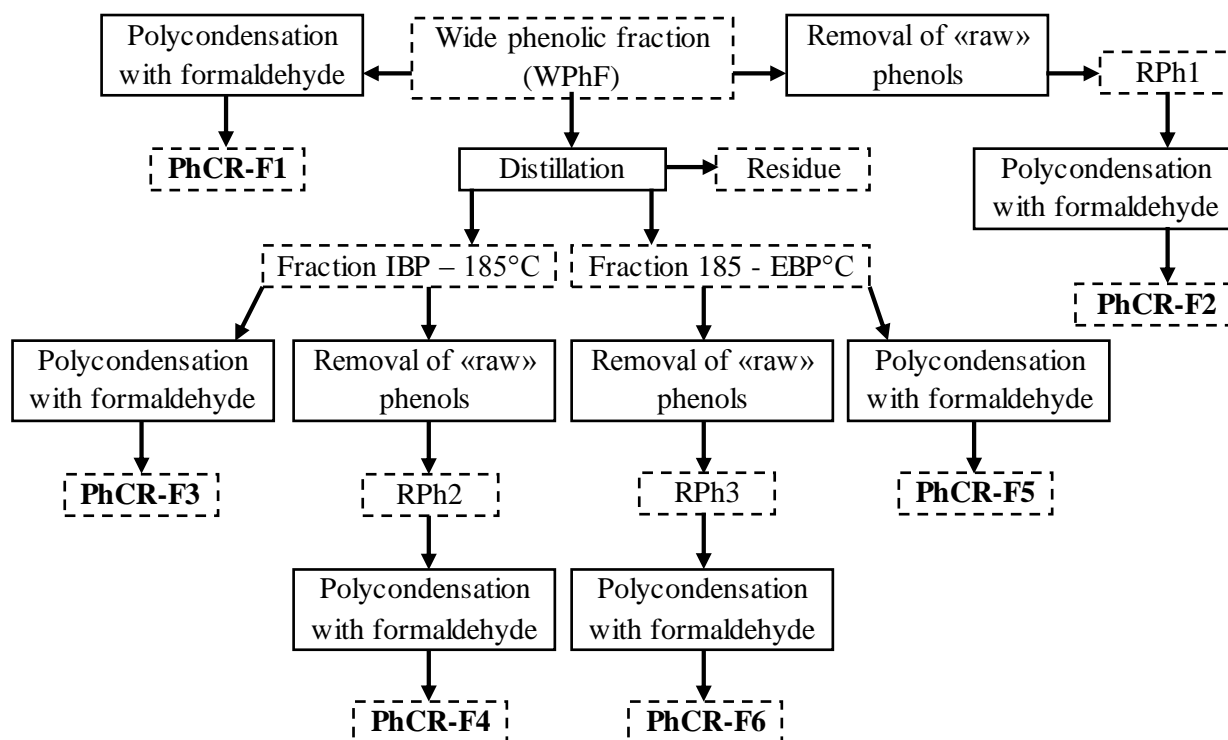


Figure 1. Scheme of the research: PhCR-F - phenol-cresol-formaldehyde resin; RPh - raw (technical) phenols

The process of formaldehyde condensation polymerization of phenols was carried out on the laboratory facility for synthesis that is depicted in Figure 2. The raw material was placed in a three-pipe reactor and heated while stirring at 100°C in a thermostat. Then, a necessary amount of formalin (a weight content of formaldehyde in formalin equaled 37 %) was added along with a concentrated hydrochloric acid (catalyst), followed by recording the start of the process that was done for 60 s. As the synthesis is over, a hot reaction mixture, obtained from raw phenols, was poured into a glass. After cooling the mixture, an aqueous phase was drained and the resin was exposed to the 3-hour drying in a vacuum dryer at 100°C. When the WPhF was used as the starting material, the fraction IBP - 185 and the fraction 185 - EBP°C, at first there was the distillation of water and unreacted constituents carried out under vacuum. After that the resulting resin was dried some more in the vacuum dryer for 3 hours at 100°C. The yield of the resins obtained was determined by the weighing of the starting material and the phenol-cresol-formaldehyde resins (PhCR-F).

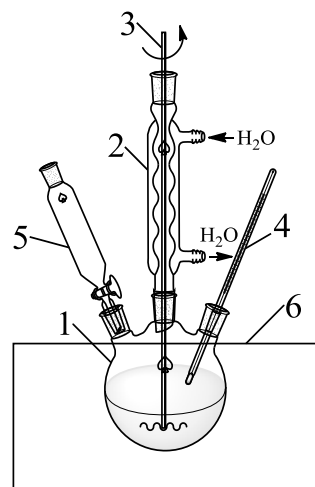


Figure 2. Laboratory facility for the synthesis of phenol-cresol-formaldehyde resins: 1 - three-pipe reactor; 2 - refrigerator; 3 - mixer; 4 - thermometer; 5 - separation funnel; 6 - thermostat

In order to obtain PMBs, the distillate (residual) petroleum-derived bitumen for roads of the BD 60/90 grade and the BND 60/90 oxidized petroleum-derived bitumen for roads were utilized. The BD 60/90 distillate (residual) petroleum road bitumen was selected at the road maintenance department of Frankivsk region (Lviv city) with its main characteristics given in Table 3.

Table 3. Main characteristics of the BD 60/90 distillate road bitumen

Index	BD 60/90	Standard for BD 60/90**	Procedure*
Penetration at 25°C (m×10 <sup>-4</sup> )	80	61-90	GOST 11501
Softening point (ball & ring method) (°C)	43	44-52	GOST 11506
Ductility at 25°C (m×10 <sup>-2</sup> )	>100	>100	GOST 11505
Adhesion to glass (%)	60	>20	DSTU B V.2.7 – 81 with supplement according to point 8.6 DSTU 4044-2001

\*DSTU and GOST – Ukrainian national standards

\*\* bitumen according to SOU 45.2-00018112-069:2011

The oxidized petroleum-derived road bitumen of the BND 60/90 grade was sampled at *Ukratnafta* PJSC (the city of Kremechuk) with its main characteristics shown in Table 4.

Table 4. Main characteristics of the BND 60/90 oxidized road bitumen

Index	BD 60/90	Standard for BD 60/90**	Procedure*
Penetration at 25°C (m×10 <sup>-4</sup> )	70	61-90	GOST 11501
Softening point (ball & ring method) (°C)	46	47-53	GOST 11506
Ductility at 25°C (m×10 <sup>-2</sup> )	63	>55	GOST 11505
Adhesion to glass (%)	47	non standardized	DSTU B V.2.7 – 81 with supplement according to point 8.6 DSTU 4044-2001

\*DSTU and GOST – Ukrainian national standards

\*\* bitumen according to SOU 45.2-00018112-069:2011

The PMB has been prepared by virtue of mixing in the following sequence: a necessary amount of bitumen was heated while stirring (Re = 1200) to the temperature of modification. Then with a required amount of the modifier added, it was sustained for 1 hour.

### 3. Results and discussion

Novolac phenol-cresol-formaldehyde resins were obtained according to the scheme given in Figure 1 by the method of formaldehyde condensation polymerization with the WPhF, the fraction IBP – 185 C and the fraction 185 – EBP°C and from the raw phenols extracted from these fractions. Synthesis conditions for the resins were set out on the basis of [13] and are shown in Table 5. As recommended by [13], the obtaining of novolac phenol-formaldehyde resins requires maintaining the mole ratio of phenol to formaldehyde at 1.12 – 1.42, while for novolac cresol-formaldehyde resins it should equal 2.27. Considering that the raw phenols that were derived from the phenolic fraction of coal tar contain both phenols and cresols at various ratios, the syntheses were done at the mole ratio of raw phenols to formaldehydes at the value of 1.42. For calculations of reactor loading, it was assumed that the molar mass of the resulting raw phenols was 94.1 g/mole, which is equal to the molecular weight of pure

phenol. The effect of the ratio of reaction constituents on the production of resin will be looked into in further studies.

Table 5. Synthesis conditions for PhCR-F

Parameter	Value
*Mole ratio of raw phenols to formaldehyde	1.42
Weight ratio of raw phenols to formalin (formaldehyde content in formalin – 37% wt)	1.78
Catalyst weight content (concentrated HCl), % by raw phenols	1.0
Temperature, °C	100
Process duration, min	60

\*The molar mass of raw phenols was proposed to be 94.1 g/mol.

The mass balance for the obtaining of phenol-cresol-formaldehyde resins is given in Table 6.

Table 6. Mass balances involved in syntheses for the obtaining of PhCR-F

Article	PhCR-F1	PhCR-F2	PhCR-F3	PhCR-F4	PhCR-F5	PhCR-F6
<b>Loaded</b>						
1. Starting material	WPhF	RPh1	fr. IBP-185 °C	RPh2	fr. 185-EBP °C	RPh3
g	100.00	32.30	50.60	16.19	46.80	16.43
% wt to be loaded	84.42	63.64	84.54	63.64	83.30	63.64
wt for a frond-end fraction	10.00 <sup>1</sup>	32.30 <sup>1</sup>	100.00 <sup>2</sup>	32.00 <sup>2</sup>	100.00 <sup>3</sup>	35.10 <sup>3</sup>
% wt for WPhF	100.00	32.30	50.60	16.19	46.80	16.43
2. Formalin						
g	18.13	18.13	9.09	9.09	9.22	9.22
% wt to be loaded	15.31	35.72	15.19	35.72	16.41	35.72
% wt for a frond-end fraction	18.13 <sup>1</sup>	18.13 <sup>1</sup>	17.96 <sup>2</sup>	17.96 <sup>2</sup>	19.70 <sup>3</sup>	19.70 <sup>3</sup>
% wt for WPhF	18.13	18.13	9.09	9.09	9.22	9.22
3. Concentrated HCl						
g	0.32	0.32	0.16	0.16	0.16	0.16
% wt to be loaded	0.27	0.64	0.27	0.64	0.29	0.64
% wt for a frond-end fraction	0.32 <sup>1</sup>	0.32 <sup>1</sup>	0.32 <sup>2</sup>	0.32 <sup>2</sup>	0.35 <sup>3</sup>	0.35 <sup>3</sup>
% wt for WPhF	0.32	0.32	0.16	0.16	0.16	0.16
Total, g	118.45	50.75	59.85	25.44	56.18	25.81
<b>Results</b>						
1. Tar						
g	18.20	29.65	8.20	13.20	9.03	14.39
% wt to be loaded	15.36	58.42	13.70	51.87	16.08	55.75
% wt for a front-end fraction	18.20 <sup>1</sup>	29.65 <sup>1</sup>	16.20 <sup>2</sup>	26.08 <sup>2</sup>	19.30 <sup>3</sup>	30.75 <sup>3</sup>
% wt for WPhF	18.20	29.65	8.20	13.20	9.03	14.39
2. Water and unreacted components						
g	100.25	21.10	51.65	12.25	47.15	11.42
% wt to be loaded	84.64	41.58	86.30	48.13	83.92	44.25
% wt for a front-end fraction	100.25 <sup>1</sup>	2.10 <sup>1</sup>	102.08 <sup>2</sup>	24.20 <sup>2</sup>	100.75 <sup>3</sup>	24.40 <sup>3</sup>
% wt for WPhF	100.25	21.10	51.65	12.25	47.15	11.42
Total, g	118.45	50.75	59.85	25.44	56.18	25.81

<sup>1</sup>for the wide phenolic fraction (WPhF); <sup>2</sup>for the fraction IBP – 185°C; <sup>3</sup>for the fraction 185 – EBP°C

When the concentrated phenols (raw phenols) are used in the act of synthesis, the yield is observed to be higher while loading the reactor (almost fourfold increase: 51.9 – 58.4% wt against 13.7 – 16.1% wt) and for the initial fraction (nearly 2 times higher: 26.1– 30.8% wt against 16.2– 18.2% wt). So, for the obtaining of effective modifiers of petroleum bitumens,

it is mostly appropriate to carry out the synthesis not with the use of the coal tar phenolic fraction but with the raw phenols being separated from this tar.

Additionally, it is counterproductive to break up the WPhF with two narrower fractions. This is explained by that using RPh1 as the starting material produces 29.65% of the resin yield (calculated per WPhF) whereas the total resin yield if two raw phenols – RPh2 and RPh3 – are used appears to be lower:  $13.20 + 14.39 = 27.59\%$ .

From then on, in order to specify a temperature for bitumen modification, the BD 60/90 residual bitumen was modified with PhCR-F3 and PhCR-F4 resins derived directly from IBP – 185°C and RPh2 raw phenol, respectively, at 110°C and 190 °C temperatures. It can be stated that mechanical mixing of bitumen components occurs at 110°C while at 190°C physical and chemical interactions between them are likely to be. Characteristics of bitumen-polymer blends obtained are given in Table 7.

Table 7. Preparation conditions and main characteristics of obtained PMBs

Index	BD 60/90	Modification temperature, °C (modifier content in PMB – 2.4 % wt)			
		PhCR-F3		PhCR-F4	
		110	190	110	190
Penetration at 25 °C ( $m \times 10^{-4}$ )	80	78	75	–	62
Penetration decline, %	–	2.5	6.3	–	22.5
Softening point (ball & ring method) (°C)	43	44	46	–	47
Softening point increase, %	–	2.3	7.0	–	9.3
Ductility at 25 °C ( $m \times 10^{-2}$ )	>100	>100	>100	–	>100
Adhesion to glass (%)	60	83	82	–	88
Increase in adhesion to glass, %	–	38.3	36.7	–	46.7
Homogeneity	non standard-ized	homogeneous	homogeneous	not homogeneous	homogeneous

Based on the data of Table 7, it can be suggested that the addition of synthesized PhCR-F3 and PhCR-F4 (except for the case of 110°C and PhCR-F4) into bitumen leads to an increase in the softening point and, especially, in the adhesion of residual petroleum bitumen. The modification of petroleum bitumen with PhCR-F3 can be done at both 110°C and 190°C. In comparison, with PhCR-F4 – at 190°C as 110°C produces modified bitumen that does not meet requirements of homogeneity. Mixing at 190°C makes it possible to increase the softening point to a greater extent. It follows from mentioned above that further modification of petroleum-based bitumens with phenol-cresol-formaldehyde resins that were obtained from the coal tar phenolic fraction was decided to be made at 190°C.

A comparison of main characteristics of obtained bitumen-polymer blends is shown in Table 8. Table 8 shows that adding all the obtained resins essentially improves the adhesive properties of bitumen. The data outlined in Table 8 indicate that the addition of the BD 60/90 resins synthesized from raw phenol (PhCR-F2, PhCR-F4 and PhCR-F6) gives rise to a larger increase in the softening point and adhesion compared to the ones synthesized from the WPhF, fraction IBP – 185, 185 – EBP°C (PhCR-F1, PhCR-F3 and PhCR-F5), but more increasingly reduces the plasticity (penetration) of the BD 60/90 residual bitumen.

With an increased content of cresols in the starting material (PhCR-F5 and PhCR-F6) compared to PhCR-F3 and PhCR-F4, the obtained modified bitumen possesses better adhesive properties (95 – 96 % against 82– 88 %, see Table 8). Nevertheless, the use of raw phenols produced from the WPhF allows almost the same adhesive properties to be obtained and the softening point to be raised as when PhCR-F5 and PhCR-F6 are used.

Table 8. Preparation conditions and main characteristics of obtained PMBs

Index	BD 60/90	Modified bitumen at 190°C (modifier content in PMB – 2.4 % wt)					
		PhCR-F1	PhCR-F2	PhCR-F3	PhCR-F4	PhCR-F5	PhCR-F6
Penetration at 25°C (m×10 <sup>-4</sup> )	80	75	65	75	62	74	70
Penetration decline, %	–	6.3	18.8	6.3	22.5	7.5	12.5
Softening point (ball & ring method) (°C)	43	44	46	46	47	45	46
Softening point increase, %	–	2.3	7.0	7.0	9.3	4.7	7.0
Ductility at 25 °C (m×10 <sup>-2</sup> )	>100	>100	>100	>100	>100	>100	>100
Adhesion to glass (%)	60	87	94	82	88	95	96
Increase in adhesion to glass, %	–	45.0	56.7	36.7	46.7	58.3	60.0
Homogeneity	non standardized	homogeneous	homogeneous	homogeneous	homogeneous	homogeneous	homogeneous

Consequently, this results in:

- higher yield of resin if raw phenols are used for its synthesis;
- slightly better characteristics of resin-modified bitumens, which contain more cresols (PhCR-F2, PhCR-F5 and PhCR-F6);
- lack of appropriateness to break up the WPhF with two narrow fractions.
- distilled road bitumens should be preferably modified with PhCR-F2.

To confirm the possibility of modifying the resulting resins as well as the oxidized bitumens coupled with the ability to compare the effectiveness of modifying the oxidized and residual bitumens, Table 9 shows the main characteristics of these PhCR-F2 modified bitumens.

Table 9. Comparison of main characteristics between residual and oxidized PhCR-F2 modified bitumens

Index	BD 60/90	BD 60/90 + PhCR-F2 (2,4 % wt)	BND 60/90	BND 60/90 + PhCR-F2 (2,4 % wt)
Penetration at 25°C (m×10 <sup>-4</sup> )	80	65	70	60
Penetration decline, %	–	18.8	–	14.3
Softening point (ball & ring method) (°C)	43	46	46	49
Softening point increase, %	–	7.0	–	6.5
Ductility at 25°C (m×10 <sup>-2</sup> )	>100	>100	63	25
Adhesion to glass (%)	60	94	47	97
Increase in adhesion to glass, %	–	56.7	–	106.4
Homogeneity	non standardized	homogeneous	non standardized	homogeneous

Supported by data given in Table 9, it may be argued that the modification with PhCR-F2 resin raises the softening point of both distilled and oxidized road bitumens by 3°C. For the distilled bitumen, the adhesive properties of PMBs are increased by 56.7% (from 60 to 94 ), while the oxidized one exhibits an increase of 106.4% (from 47 to 97%). This indicates that the resin obtained can also be utilized as adhesive additives in particular for the oxidized bitumens.

#### 4. Conclusions

1. By the distillation method, the wide phenolic fraction of coal tar sampled at Zaporizhkoks PJSC was separated into two ones, IBP (the initial boiling point – ~92°C) – 185 and 185 – EBP°C (the end boiling point ~ 211°C). From the wide phenolic fraction and narrow fractions

- that were derived by using 20% NaOH solution, raw phenols were extracted, yielding 32.3% wt, 32.0% wt and 35.1% wt, respectively, for the initial and narrow fractions.
2. Novolac phenol-cresol-formaldehyde resins were produced by the method of formaldehyde condensation polymerization and from the wide phenolic fraction, fraction IBP – 185 and 185 – EBP°C and from the raw phenols extracted from these fractions. The results achieved show that the use of raw phenols as the starting material is the most advisable for the synthesis of resins as this allows the resin yield to be increased nearly fourfold while loading the reactor (from 13.7 – 16.1% wt to 51.9 – 58.4% wt, respectively).
  3. Modification of petroleum-derived road bitumens should be performed with phenol-cresol-formaldehyde resin that was obtained from raw phenols, extracted from the wide phenolic fraction of coal tar. It is counterproductive for the obtaining of resin to break up the wide phenolic fraction with phenol concentrate (fraction IBP – 185°C) and concentrate of cresols (185 – EBP°C).
  4. It has been observed that with a content of 2.4% by weight of phenol-cresol-formaldehyde resins in distilled (residual) and oxidized petroleum-derived road bitumens, there is an increase of 3°C in the softening point and adhesive properties for the distilled bitumen by 56.7% (from 60 to 94%), for the oxidized one – by 106, 4 (from 47 to 97 ).

### References

- [1] Zhu J, Birgisson B and Kringos N., *European Polymer Journal*, 2014; 54: 18-38
- [2] Pyshyev S, Gunka V, Grytsenko Y and Bratychak M., *Chemistry and Chemical Technology*, 2016; 10 (4s): 631-636.
- [3] Kowalski KJ, Krol J, Radziszewski P, Casado R, Blanco V, Perez D, Vinas VM, Brijse Y, Frosch V, Le DM and Wayman M., *Transportation Research Procedia*, 2016; 14: 3582-3591.
- [4] Schaur A, Unterberger S and Lackner R., *European Polymer Journal*, 2017; 96: 256-265.
- [5] Kishchynskiy SV., *Vestn. HNADU*, 2008; 40: 28-32.
- [6] Pyshyev S, Gunka V, Grytsenko Y, Shved M and Kochubei V., *International Journal of Pavement Research and Technology*, 2017; 10 (4): 289-296.
- [7] Pyshyev S, Grytsenko Y, Bilushchak H, Pyshyeva R and Danyliv N., *Pet Coal*, 2015; 57 (4): 303-314.
- [8] Pyshyev S, Hrytsenko Y, Khlibyshyn Y, Strap H and Koval T., *East-European Journal of Enterprise Technologies*, 2014; 2/11 (68): 4-8.
- [9] Pyshyev S, Hrytsenko Y, Nikulyshyn I and Hnativ Z., *Coal Chemistry Journal (Ukhlekhimicheskii Zhurnal)*, 2014; 5: 41-48.
- [10] Strap G, Astakhova O, Lazorko O, Shyshchak O and Bratychak M., *Chemistry and Chemical Technology*, 2013; 7 (3): 279-287.
- [11] Çubuk M, Gürü M, Çubuk M and Arslan D., *Journal of Materials in Civil Engineering*, 2014, 26 (6): 4014-4015.
- [12] Pavlovich LB and Solovyova NY, *Bulletin of the Siberian State Industrial University*, 2016, 1 (15): 35-39.
- [13] Toroptseva AM, Belogorodskaya KM and Bondarenko VM., *Laboratory session on chemistry and technology of high-molecular compounds; Chemistry: L.*, 1972, p. 416.

*To whom correspondence should be addressed: Dr Volodymyr Gunka, Department of Chemical Technology of Oil and Gas Processing, Lviv Polytechnic National University, Bandery str. 12, Lviv 79013, Ukraine*

## PHYSICOCHEMICAL AND OXIDATIVE THERMAL ANALYSIS OF NIGERIAN LIGNITE COALS

Bemgba Bevan Nyakuma<sup>1\*</sup>, Olagoke Oladokun<sup>1</sup>, Edo Oga Ojoko<sup>2</sup>, Bruno Lot Tanko<sup>3</sup>, Aliyu Jauro<sup>4</sup>

<sup>1</sup> Faculty of Engineering, School of Chemical and Energy Engineering, Universiti Teknologi Malaysia, 81310 Skudai, Johor Bahru, Malaysia;

<sup>2</sup> School of Environmental Studies, Federal Polytechnic Nasarawa, P.M.B. 001, Nasarawa, Nasarawa State, Nigeria

<sup>3</sup> Faculty of Built Environment, Universiti Teknologi Malaysia, 81310 Skudai Campus, Johor Bahru, Malaysia

<sup>4</sup> National Centre for Petroleum Research and Development (NCPRD), Abubakar Tafawa Balewa University, P.M.B 0248, Bauchi State, Nigeria

Received July 19, 2018; Accepted October 19, 2018

---

### Abstract

This paper presents the physicochemical and oxidative thermal properties of new lignite coals from Obomkpa (BMK), Ihioma (IHM), and Ogboligbo (OGB) in Nigeria. Furthermore, the microstructural and mineralogical properties of the coals were examined in the study. The results revealed high compositions of carbon (C), hydrogen (H), oxygen (O) and sulphur (S) but low nitrogen (N) for all samples. The highest values of C (50.4 wt.%), H (5.62 wt.%), HHV (19.66 MJ/kg) and the lowest O (42.45 wt.%) were observed in BMK. However, IHM exhibited the highest volatile matter (69.5 wt.%) and lowest fixed carbon (23.3 wt.%); whereas the lowest ash (1.03 wt.%) and moisture (3.12 wt.%) were observed in OGB. The microstructure analysis revealed Al, C, Ca, Fe, K, O, S, Si, and Ti although K and Ca were undetected in IHM and OGB. Thermal analysis revealed a mass loss of 75.7% for BMK, and 79.4% for IHM, and 56.2% for OGB. The DTG plots revealed two distinct regions for drying and devolatilization during coal thermal degradation. The temperature profile characteristics (TPC) revealed IHM is the most reactive compared to BMK and OGB. Overall, the results indicated that IHM is suited for gasification, BMK for combustion, and OGB for pyrolysis.

**Keywords:** Fuel Characterization; Combustion Characteristics; Lignite; Coal; Nigeria.

---

## 1. Introduction

Coal is one of the most abundant and accessible fossil-based fuels worldwide [1]. Currently, coal accounts for over 35% of global electricity generation and by extension the world's energy mix. Over the years, this widely distributed resource has contributed significantly to socio-economic growth and development as witnessed in India and China. Against this backdrop, many analysts posit that coal has the potential to supply most of the world's growing energy demand particularly in developing countries with large deposits. In recent years, various studies have reported on the discovery of large deposits and the potential of various low-rank coals (LRC) in Nigeria [2-6]. The findings indicate that despite growing attention, coal mining in Nigeria has dwindled from its peak of 925,000 tonnes in 1958 to below 20,000 tonnes today [3]. Furthermore, the studies report that Nigeria holds 640 million tonnes of proven reserves and 2.8 billion tonnes of provisional reserves located across the nation's sedimentary basin [7]. The rank classification of Nigerian coals consists of 39% bituminous, 49% subbituminous, and 12% lignite [5], currently utilized in cement, iron and steel manufacturing.

However, the contribution of coal to Nigeria's electricity generation remains insignificant [3]. As a result, Nigeria's drive for industrialisation has been stunted by the current energy crises

and inability to exploit the large coal deposits for electricity generation [5-6]. This is partly due to limited data on the thermochemical fuel characteristics of lignites as required for the design and operation of coal-fired power plants. Even so, various studies have examined the geological [8-10], petrographic [11-13], and mineralogical [14-16] properties of selected Nigerian coals. However, the reviewed literature is limited to the geochemical and mineralogical properties of Nigerian coals and its potential environmental impacts. Other studies including Sonibare *et al.*, [17], Ryemshak and Jauro [2], and Chukwu *et al.* [5], have examined the thermal and power generation properties of sub-bituminous and bituminous Nigerian coals. However, there are limited studies on the thermal, kinetic, thermodynamic and rheological fuel properties of lignites, typically utilised for electricity generation through pulverised coal combustion [18]. This shows there is an urgent need to examine and highlight the fuel properties of Nigeria's abundant lignite reserves for future power generation.

Therefore, this study will present an in-depth analysis on the physicochemical, microstructural, mineralogical, and thermal properties of Obomkpa (BMK), Ihioma (IHM), and Ogboligbo (OGB) lignites from Delta, Imo, and Kogi States, respectively. It is envisaged that the findings will avail engineers and policymakers with empirical data for power generation, greenhouse gas (GHG) emissions and life cycle analyses.

## 2. Experimental

The lignite coals examined in this study were acquired in rock form from Obomkpa in Aniocha-North, Ihioma in Orlu, and Ogboligbo in Igalamela-Odolu located in Delta, Imo, and Kogi States of Nigeria, respectively. The samples were subsequently labelled; BMK (Obomkpa), IHM (Ihioma) and OGB (Ogboligbo) before pulverisation and sieving into 250  $\mu\text{m}$  sized particles for characterisation. The coal preparation procedures are described in our previous study [19]. Next, the fuel characteristics of the pulverised coals were characterised by physicochemical, functional group, microstructural, mineralogical, and thermal analyses.

The physicochemical analyses were performed to determine the elemental, proximate, and calorific properties of the coals. The elemental analysis was performed using the CHNS elemental analyser (Model: vario MICRO Cube, Germany) according to the ASTM standard D5291-16. The proximate analysis was performed by thermogravimetric analysis (TGA) according to the procedures described in the literature [20]. Lastly, the calorific analysis was determined by bomb calorimetry based on the procedures described in ASTM D2015 for the IKA C2000 (Bomb calorimeter, USA).

The functional group compositions of the samples were determined by Fourier transform infrared-attenuated transform reflectance (FTIR-ATR) spectroscopy (Model: Shimadzu Prestige 21, Japan). During each test, a small amount of each coal sample was placed in the ZnSe prism plate and scanned with the detector to acquire FTIR spectra from 4000 – 600  $\text{cm}^{-1}$  based on Happ-Genzel Apodization. Each sample was subjected to 20 scans at 8  $\text{cm}^{-1}$  resolution for a total runtime of five (5) seconds. After the analysis was completed, ATR correction was applied to the spectra before plotting the raw data in transmittance (T %).

The microstructural and mineralogical analyses were performed by SEM/EDX (scanning electron microscopy-energy dispersive x-ray) microscopy. The SEM microscope (Model: JEOL-JSM IT 300 LV, Germany) equipped with an EDX detector was used to examine the microstructure and mineral composition of the coals. Before each test, the samples were sputter coated with platinum using the Quorum Q150R S apparatus. Next, the samples were placed in the SEM/EDX analyser operating at 20 kV, the working distance of 5 mm, and magnification of  $\times 1000$ . The SEM images were subsequently examined on the AZTEC EDX software (Oxford Instruments, UK) and the mineral composition determined by point ID and mapping. The resulting mineral compositions were reported in weight per cent (wt.%).

The thermal analysis was determined by thermogravimetric analysis (TGA) under non-isothermal oxidative conditions. The TG runs involved heating approximately 18 mg of sample in an alumina crucible from 30°C to 900°C by employing a dynamic heating rate of 50°C/min to simulate flash combustion. During each test, the TG analyser (Model: Shimadzu TG-50, Japan) was

purged with air at a flow rate of 20 mL/min to ensure an oxidative atmosphere. At the end of the process, the raw (.tad) data was retrieved and analysed to determine the mass loss (%) and derivative mass loss (%/min) for the samples which were plotted as TG and DTG, respectively.

Based on the TG-DTG data, the temperature profile characteristics (TPC) for the flash combustion of the coals were examined. The examined TPCs were onset or ignition ( $T_{ons}$ ), midpoint ( $T_{mid}$ ), maximum decomposition ( $T_{max}$ ), and burnout ( $T_{off}$ ) temperatures, along with the mass loss ( $M_L$ , %), mass loss rate ( $M_{LR}$ , %/min) and residual mass ( $R_M$ , %). The descriptions of the TPC and the procedures for determining the terms are presented in our previous study [6].

### 3. Results and discussion

This section presents the physicochemical properties, functional group analysis (FTIR), microstructural and mineralogical properties (SEM/EDX), thermal degradation properties (TGA-DTG), and temperature profile characteristics (TPCs) of the coal samples.

#### 3.1. Physicochemical fuel properties

Table 1 presents the physicochemical fuel properties of the coals based on ultimate, proximate and calorific analyses. As observed, the ultimate (elemental) analysis revealed high compositions of C, H, O and S but low N content. BMK exhibited the highest composition of C, and H but the lowest O whereas OGB exhibited the lowest composition of C and H. The proximate analysis revealed high compositions of VM and FC but low M and ash as observed in Table 1. The highest and lowest compositions of VM was observed in IHM and OGB, respectively. However, OGB contained the highest FC and the lowest was observed in IHM. The highest ash content was observed in BMK and the lowest in OGB.

Table 1. Physicochemical properties of BMK, IHM, and OGB

Analyses	Element	Symbol	BMK	IHM	OGB
Ultimate	Carbon	C (wt. %)	50.38	46.80	37.48
	Hydrogen	H (wt. %)	5.62	5.39	3.51
	Nitrogen	N (wt. %)	0.59	0.64	0.80
	Sulphur	S (wt. %)	0.96	1.52	2.33
	Oxygen	O (wt. %)	42.45	45.64	55.88
Proximate	Moisture	M (wt. %)	3.63	4.75	3.12
	Volatiles	VM (wt. %)	58.05	69.52	51.43
	Ash	A (wt. %)	11.73	2.43	1.03
Heating Value	Fixed Carbon	FC (wt. %)	26.61	23.30	44.41
	Higher Value	HHV (MJ/kg)	19.66	19.40	15.55

Lastly, the calorific analysis revealed BMK has the highest energy content based on the HHV of 19.66 MJ/kg compared to 19.40 MJ/kg for IHM and 15.55 MJ/kg of OGB. The HHV variation is due to the high compositions of C, H and low O in the BMK coal compared to the other samples. The findings also indicate that BMK has the highest energy recovery potential compared to IHM and OGB coals. Hence, the coals can be classified as brown or lignite, low ranked coals (LRC) with potential for electric power generation or cement manufacture.

#### 3.2. Functional group properties

The functional group composition of the coal samples was determined by FTIR-ATR spectroscopy as presented in the spectra in Figure 1. As observed, the spectra revealed several peaks for stretching vibrational intensities which ranged from 4000 – 600  $\text{cm}^{-1}$  during the analyses. The results reveal that the largest stretching vibrations were in the high-frequency region (4000 – 1450  $\text{cm}^{-1}$ ), compared to the fingerprint region (1450 – 600  $\text{cm}^{-1}$ ). Based on the spectra, the stretching vibrations in the region 4000 – 3800  $\text{cm}^{-1}$  can be ascribed to the rotational vibrations of O–H groups present in water vapour. This confirms the presence of moisture in the structure of the coals examined in this study. However, the sharp peaks observed in the region

3800 – 3500  $\text{cm}^{-1}$  and the medium to weak peaks in the regions 1300 – 1400  $\text{cm}^{-1}$  and 1200 – 1000  $\text{cm}^{-1}$  are either due to free or H bonded O–H groups.

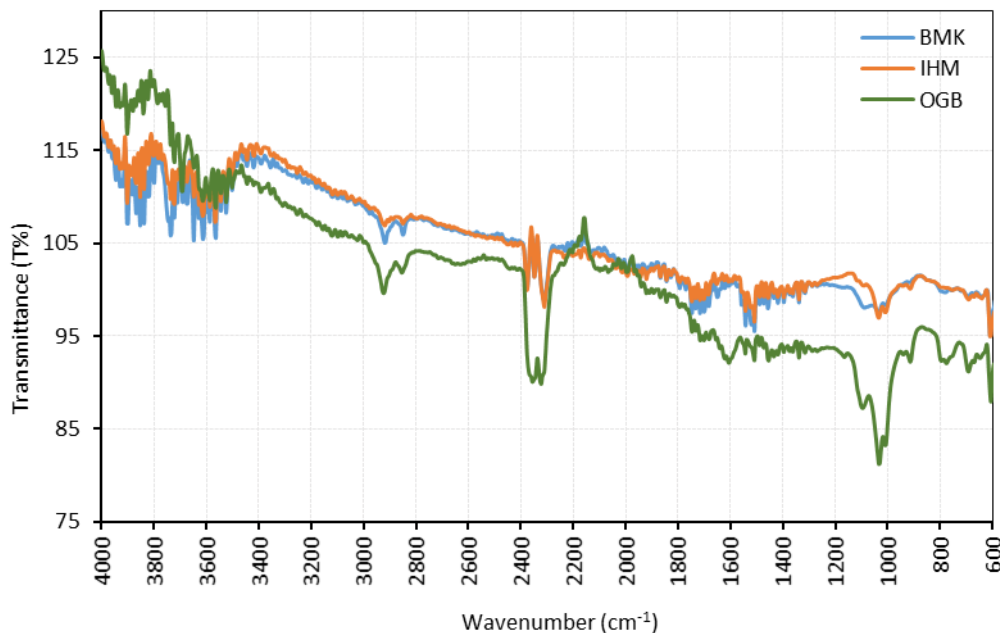


Figure 1. FTIR spectra of Nigerian lignite coals

Furthermore, the pair of medium to weak peaks the region 3000 – 2800  $\text{cm}^{-1}$  are due to the deformation or rocking effects of  $-\text{CH}_3$ ,  $-\text{CH}_2$  and C–H aliphatic groups of alkanes. However, the strong peaks in the range 2300 – 2200  $\text{cm}^{-1}$  can be due to the  $-\text{C}\equiv\text{C}-$  or  $-\text{C}\equiv\text{N}-$  groups in alkynes. However, the medium peaks in the same region may be due to  $-\text{N}=\text{C}=\text{O}$ ,  $-\text{N}=\text{C}=\text{S}$  or  $\text{N}=\text{C}=\text{N}$  groups. The medium to strong peaks at 1500  $\text{cm}^{-1}$  and 1600  $\text{cm}^{-1}$  could be due to  $-\text{C}=\text{C}-$  groups found in arenes.

In general, the FTIR-ATR results indicate OGB coal has the most intense peaks followed by IHM and BMK. Lastly, the findings indicate that the chemical structure of the coals is complex and could be due to the presence of alkane, alkene, arene, and aromatic functional groups. However, further analyses are required to elucidate the chemical structure of the coals.

### 3.3. Microstructural and mineralogical properties

The microstructural and mineralogical properties of the coals were determined by SEM/EDX analyses, as presented in Figures 2-4(a) and 2-4(b), respectively.

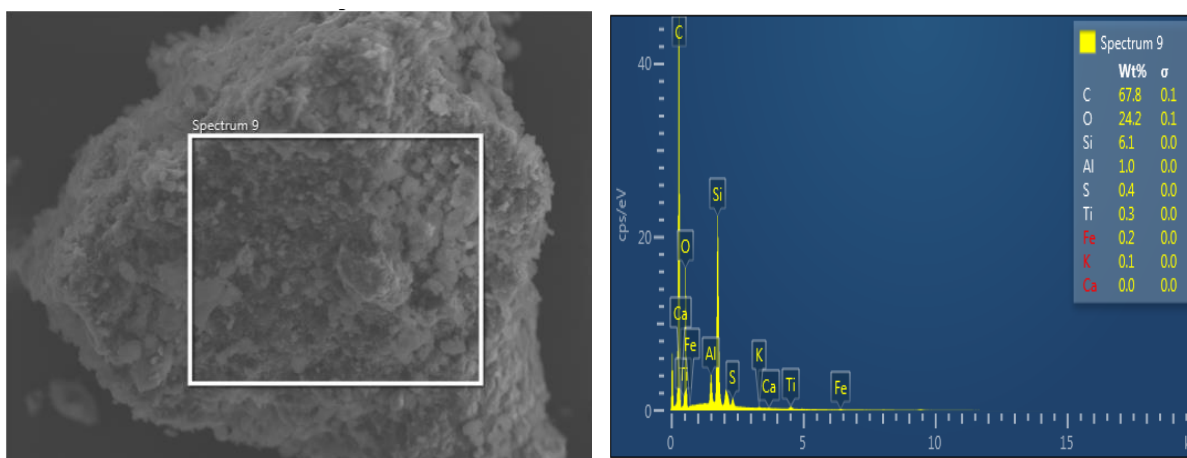


Figure 2 (a) (b). SEM/EDX Spectra for BMK

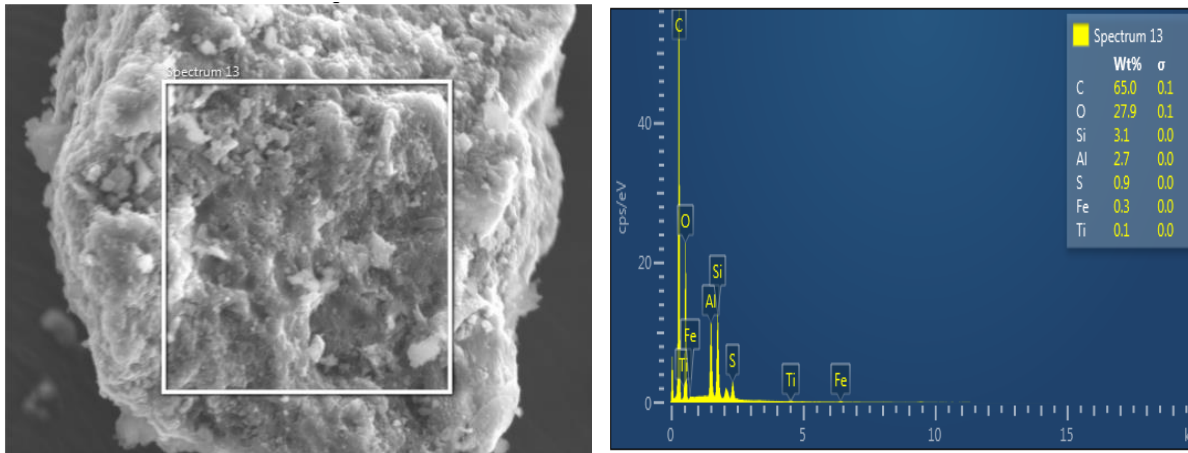


Figure 3 (a) (b). SEM/EDX Spectra for IHM

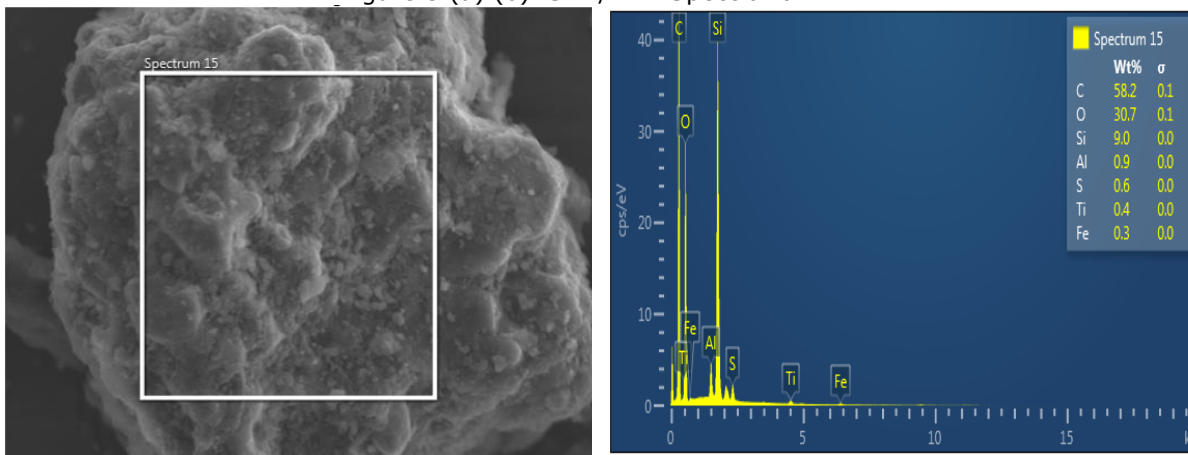


Figure 4 (a) (b). SEM/EDX Spectra for OGB

The results indicate that BMK, IHM, and OGB contain a range of fine to coarse-grained particles in their microstructures. In particular, the morphology of BMK is characterised by small-sized particles which appear scattered in clusters or agglomerates on the sample surface. However, OGB is characterised by layers of small particles in its microstructure. Lastly, IHM is comprised of coarse-grained particles characterised by a distinct lustre which may be due to the metal elements present in its structure. To verify this, the mineral composition of the coals was examined by EDX as presented in weight percentages (wt.%) in Table 2.

Table 2. Mineral composition of Nigerian lignite coals BMK, IHM, and OGB

Element	Symbol	BMK (wt. %)	IHM (wt. %)	OGB (wt. %)
Carbon	C	67.79	65.01	58.15
Oxygen	O	24.17	27.88	30.66
Aluminium	Al	0.97	2.73	0.88
Silicon	Si	6.10	3.08	9.01
Sulphur	S	0.38	0.88	0.60
Potassium	K	0.07	ND	ND
Calcium	Ca	0.04	ND	ND
Titanium	Ti	0.30	0.13	0.36
Iron	Fe	0.18	0.28	0.34

As observed in Table 2, the coal samples examined in this study contain both metal and non-metal elements; C, O, Al, Si, S, K, Ca, Ti, and Fe, although K and Ca were not detected (ND)

in IHM and OGB. In comparison, the most abundant elements present in the coals were C, O, Si whereas the least abundant elements were Ti and Fe. Based on the results, the highest C was observed in BMK, followed by IHM and OGB. However, the presence of O was in the order  $BMK < IHM < OGB$  which accounts for the higher heating value (HHV) of BMK compared to IHM and OGB as presented in Table 1. The Si was in the order  $IHM < BMK < OGB$ . The presence of Si typically in free crystalline form is indicative of the presence of  $SiO_2$  (quartz) in the structure of the coals. Lastly, the elements S and Al are also present in the coals with the highest compositions in IHM.

### 3.4. Thermal and degradation behaviour

The thermal degradation behaviour and temperature profile characteristics (TPCs) of the coals were also examined as presented in the TG-DTG plots in Figures 5 and 6.

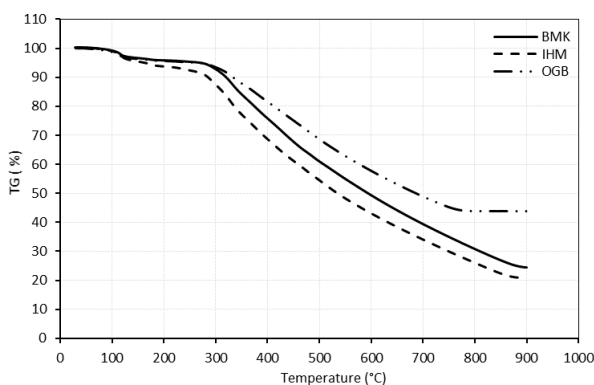


Figure 5. TG Plots for flash combustion of BMK, IHM, OGB

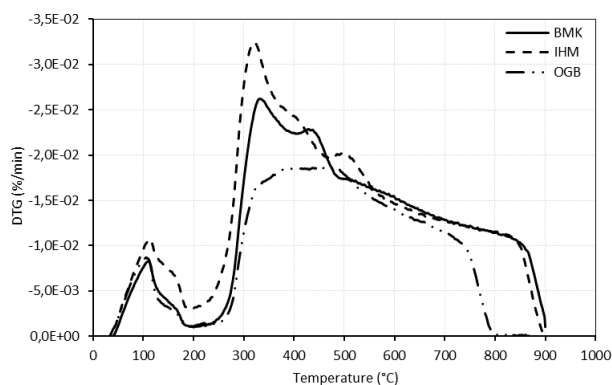


Figure 6. DTG Plots for flash combustion of BMK, IHM, OGB

As observed in Figure 5, the thermal analysis resulted in a significant mass loss or thermal degradation as evident in the downward sloping plots in Figure 5. Furthermore, the TG plots revealed that the highest degradation occurred in IHM compared to BMK and OGB. Hence, IHM is more reactive compared to BMK and OGB, under the conditions examined in this study. However, the lowest thermal reactivity or degradation was observed for OGB as evident in its TG plot which plateaus at 43.80%. The high reactivity of IHM may be ascribed to its higher volatiles (VM) and fixed carbon (FC) contents compared to OGB as reported in Table 1. Therefore, the VM and FC are responsible for the temperature profile characteristics (TPC) and thermal reactivity during TGA. To further examine this, the TPCs were deduced from the TG-DTG plots using the Shimadzu TA-60 Workstation, as presented in Tables 3 and 4.

The degradation mechanism for the flash combustion of the coals was further examined from the DTG plots in Figure 6. As observed, the TG analysis resulted in two distinct regions of thermal degradation. The first region, characterised by the small peaks observed below 200°C, can be ascribed to the loss of moisture and low molecular weight volatile compounds. However, the second region occurred at 200°C – 750°C for OGB and 200°C – 850°C for both BMK and IHM during TG analysis. The mass loss ( $M_L$ , %) in this stage can be ascribed to the loss of high molecular weight or volatile compounds resulting in ash formation due to the oxidative nature of the process. As a result, the final or residual mass ( $R_M$ , %) of the process are representative of the ash that could potentially result from the flash combustion of BMK, IHM, and OGB under flash conditions. The resulting values for  $M_L$ , % and the  $R_M$ , % for each coal is presented in Table 3.

### 3.5. Temperature profile characteristics (TPC)

The TPCs for the TG is presented in Table 3, and Table 4 presents the TPCs from the DTG plots. The TPCs examined in this study are; onset or ignition ( $T_{ons}$ ), midpoint ( $T_{mid}$ ), burnout ( $T_{off}$ ) temperatures, along with the mass loss ( $M_L$ , %) and residual mass ( $R_M$ , %). The results

revealed that the ignition ( $T_{ons}$ ) temperatures ranged from 246.18°C (IHM) to 269.69°C (BMK) or an average of 256.68°C. This indicates that IHM undergoes thermal degradation or devolatilization earlier than BMK and OGB (254.16°C). This is due to the high VM content of IHM (69.52 wt.%) compared to BMK (58.05 wt.%) and OGB (51.43 wt.%).

Table 3. TG Temperature Profiles Characteristics of BMK, IHM, OGB

Coal Sample	Onset temperature ( $T_{ons}$ , °C)	Midpoint temperature ( $T_{mid}$ , °C)	Burnout temperature ( $T_{off}$ , °C)	Mass loss ( $M_L$ , %)	Residual mass ( $R_M$ , %)
BMK	269.69	479.68	614.35	75.67	24.33
IHM	246.18	453.98	587.86	79.37	20.63
OGB	254.16	474.17	689.14	56.19	43.81

The midpoint ( $T_{mid}$ ) temperatures ranged from 453.98°C to 479.68°C for IHM and BMK, respectively. However, the burnout ( $T_{off}$ ) temperatures were between 587.86°C and 689.14°C for IHM and OGB, respectively. Lastly, the mass loss ( $M_L$ , %) and residual mass ( $R_M$ , %) for the coals were examined. The mass loss ( $M_L$ , %) was between 56.19% and 79.37% for OGB and IHM. Therefore, OGB experienced the lowest mass loss whereas the highest (and most reactive) was IHM. However, the residual mass was from 20.63% to 43.81% for IHM and OGB, respectively. This indicates that OGB is thermally stable during TG compared to IHM and BMK.

The TPCs for the DTG plots are; the drying peak ( $D_{max}$ ), maximum decomposition ( $T_{max}$ ), and mass loss rates ( $M_{LR}$ , %/min) at  $D_{max}$  and  $T_{max}$  were examined as presented in Table 4.

Table 4. DTG temperature profiles characteristics of BMK, IHM, OGB

Coal Sample	Maximum drying peak temperature ( $D_{max}$ , °C)	Rate (%/min)	Maximum decomposition peak temperature ( $T_{max}$ , °C)	Rate (%/min)
BMK	109.29	2.82	330.03	7.25
IHM	113.65	3.09	322.00	8.56
OGB	105.82	2.88	452.94	3.28

As observed, the maximum drying peak ( $D_{max}$ ) temperatures ranged from 105.82°C (OGB) to 113.65°C (IHM). However, the maximum decomposition ( $T_{max}$ ) temperatures occurred between 322.00°C (IHM) and 452.94°C (OGB). Further examination of the  $M_{LR}$  (%) at  $D_{max}$  showed that the lowest and the highest mass values were observed for BMK (2.82 %/min) and IHM (3.09 %/min). Conversely, the lowest and the highest  $M_{LR}$  (%) at  $T_{max}$  was from 3.28 %/min (OGB) to 8.56 %/min (IHM). In summary, the temperatures  $D_{max}$ ,  $T_{max}$  and mass loss rates ( $M_{LR}$ , %) confirm that IHM is more reactive than BMK and OGB.

#### 4. Conclusion

The study examined physicochemical and oxidative thermal analysis of newly discovered brown coals from Obomkpa (BMK) in Aniocha-North, Ihioma (IHM) in Orlu, and Ogboligbo (OGB) in Igalamela-Odolu in Nigeria. The study investigated the elemental, proximate, calorific and functional group properties of the coals. Furthermore, the study examined the microstructural, mineralogical and thermal analyses. The results revealed high compositions of C, H, O and S but low N. BMK exhibited the highest composition of C, and H but the lowest O whereas the lowest values were observed in OGB. The highest and lowest compositions of VM was observed in IHM and OGB, respectively. The calorific analysis revealed an HHV of 19.7 MJ/kg for BMK, 19.4 MJ/kg for IHM and 15.6 MJ/kg for OGB.

The functional group analysis revealed the complex coal structure is due to the presence of alkane, alkene, arene, and aromatic functional groups. The microstructure analysis also revealed fine to coarse-grained particles characterised by metal and non-metal elements such as C, O, Al, Si, S, K, Ca, Ti, and Fe. The thermal analysis revealed the highest degradation

occurred in IHM which is more reactive than BMK and OGB. The DTG plots revealed two distinct regions of thermal degradation ascribed to drying and devolatilization. The TPC analysis of ignition ( $T_{ons}$ ), midpoint ( $T_{mid}$ ), burnout ( $T_{off}$ ) temperatures, and the mass loss ( $M_L$ , %) and residual mass ( $R_M$ , %) revealed IHM is the most reactive coal compared to BMK and OGB.

### Acknowledgement

The financial and technical support of the following institutions; Universiti Teknologi Malaysia (UTM, Skudai Campus) and the National Centre for Petroleum Research and Development (NCPRD) at Abubakar Tafawa Balewa University (ATBU) Nigeria are gratefully acknowledged.

### References

- [1] Coal Industry Advisory Board, The Global Value of Coal. 2012; IEA Headquarters: Paris, France.
- [2] Ryemshak SA and Jauro A. Proximate analysis, rheological properties and technological applications of some Nigerian coals. *International Journal of Industrial Chemistry*, 2013; 4(1): 7.
- [3] Ohimain EI. Can Nigeria generate 30% of her electricity from coal. *International Journal of Energy and Power Engineering*, 2014; 3(1): 28-37.
- [4] Nyakuma BB. Physicochemical Characterization and Thermal Analysis of newly discovered Nigerian coals. *Bulgarian Chemical Communications*, 2016; 48: 4.
- [5] Chukwu M, Folayan C, Pam G, and Obada D. Characterization of some Nigerian coals for power generation. *Journal of Combustion*, 2016; 2016.
- [6] Nyakuma BB, Jauro A, Oladokun O, Bello A, Alkali H, Modibo M, and Abba M. Physicochemical, Mineralogical, and Thermogravimetric Properties of Newly Discovered Nigerian Coals. *Petroleum & Coal*, 2018; 60(4): 641-649.
- [7] Sonibare O, Jacob D, and Foley S. Quantitative Estimation of Major and Trace Elements in Coals of the Benue Trough, Nigeria. *Energy Sources, Part A: Recovery, Utilization, and Environmental Effects*, 2013; 35(8): 753-761.
- [8] Obaje N, Moumouni A, Goki N, and Chaanda M. Stratigraphy, paleogeography and Hydrocarbon resource potentials of the Bida Basin in North-Central Nigeria. *Journal of Mining and Geology*, 2011; 47(2): 97-114.
- [9] Ogala JE. The geochemistry of lignite from the neogene Ogwashi-Asaba formation, Niger Delta basin, Southern Nigeria. *Earth Sciences Research Journal*, 2012; 16(2): 151-164.
- [10] Whiteman, AJ. Nigeria: Its petroleum geology, resources and potential. 2012; 1.
- [11] Ogala J, Siavalas G, and Christanis K. Coal petrography, mineralogy and geochemistry of lignite samples from the Ogwashi-Asaba Formation, Nigeria. *Journal of African Earth Sciences*, 2012; 66: 35-45.
- [12] Odeh AO. Exploring the potential of petrographics in understanding coal pyrolysis. *Energy*, 2015; 87: 555-565.
- [13] Ayinla HA, Abdullah WH, Makeen YM, Abubakar M, Jauro A, Yandoka BMS, and Abidin NSZ. Petrographic and geochemical characterization of the Upper Cretaceous coal and mudstones of Gombe Formation, Gongola sub-basin, northern Benue trough Nigeria: Implication for organic matter preservation, paleodepositional environment and tectonic settings. *International Journal of Coal Geology*, 2017; 180: 67-82.
- [14] Adedosu T, Sonibare O, Tuo J, and Ekundayo O. Aromatic hydrocarbons distribution in Nigerian coal and their geochemical significance. *Energy Sources, Part A: Recovery, Utilization, and Environmental Effects*, 2010; 33(2): 145-155.
- [15] Akinyemi S, Gitari W, Akinlua A, and Petrik L. Mineralogy and geochemistry of sub-bituminous coal and its combustion products from Mpumalanga Province, South Africa, in *Analytical Chemistry*. 2012; InTech Publishers, USA.
- [16] Wuyep EO, and Obaje NG. Petrographic evaluation of the ranks and technological applications of some coal deposits in the Anambra Basin and Middle Benue Trough of Nigeria. *J. Earth Sci. Eng*, 2012; 2(4): 220-234.
- [17] Sonibare O, Ehinola O, Egashira R, and KeanGiap L. An investigation into the thermal decomposition of Nigerian Coal. *Journal of Applied Sciences*, 2005; 5(1): 104-107.
- [18] Speight JG. *The Chemistry and Technology of Coal*. Chemical Industries, 2012: CRC Press, USA.
- [19] Nyakuma BB, Oladokun O, Jauro A, and Nyakuma DD. Evaluating the Energy Recovery Potential of Nigerian Coals under Non-Isothermal Thermogravimetry. *IOP Conference Series: Materials Science and Engineering*, 2017; 217(1): 012013.

- [20] Donahue CJ, and Rais EA. Proximate Analysis of Coal. *Journal of Chemical Education*, 2009; 86(2): 222.

---

*To whom correspondence should be addressed: Bemgba Bevan Nyakuma, Faculty of Engineering, School of Chemical and Energy Engineering, Universiti Teknologi Malaysia, 81310 Skudai, Johor Bahru, Malaysia*

OCCURRENCE, DISTRIBUTION, AND ORIGIN OF SHALLOW BIOGENIC GAS IN LATE QUATERNARY UN-CONSOLIDATED SAND DEPOSIT OF SHAHBAZPUR STRUCTURE, SOUTHERN BANGLADESH

*Morshedur Rahman<sup>1</sup>, S.M. Mainul Kabir<sup>1</sup>, Badrul Imam<sup>1</sup>, AKM Eahsanul Haque<sup>2\*</sup>, Md. Al Amin<sup>1</sup>*

<sup>1</sup> *Department of Geology, Faculty of Earth & Environmental Sciences, University of Dhaka, Dhaka-1000, Bangladesh*

<sup>2</sup> *Department of Physical and Geological Sciences, Universiti Brunei Darussalam, Gadong BE1410, Brunei Darussalam*

Received July 20, 2018; Accepted October 19, 2018

---

## Abstract

Gas occurrences at shallow depths have been a common feature noticed in alluvial plain in shallow water well drillings in the southeastern part of Bangladesh. The gas occurs in recent (< 2 Mya) alluvial sediments at shallow depths and flows in a range of few hours to several days before being exhausted. The only exception is the shallow gas occurrence in Bhola Island, which flows from almost similar depth but have been consistently flowing for more than ten years. This shallow gas occurs within the recent deposit of Holocene age of Shahbazpur structure at a depth of 260m to 290m. These recent deposits are composed of unconsolidated sand with thin clay layers. The individual shallow gas pools are discontinuous and indicate that the shallow reservoir sand bodies have frequent facies change, which implies their lateral extensions are limited. Field data collected all over the Bhola island shows that the shallow gas accumulation is only located in Burhanuddin upozila. Entirely composed of methane, very high methane-ethane (+) (>1000) ratio and high dryness value (>0.99) of shallow gas is suggestive of its biogenic origin.

**Keywords:** *Shallow Gas; Biogenic origin; Shahbazpur structure; Southern Bangladesh.*

---

## 1. Introduction

Shallow gas is a well-known phenomenon, being accumulations of gas located in the upper sediments, close to the surface. It is trapped typically in shallow and immature sediments, indicating their formation in swamps, paddy fields, anoxic freshwater lakes, and sub littoral-marine bays, as well as glacial drifts and marine sediments beneath the anaerobic sulfate-reducing zone [1-2]. Though shallow gas is often known as drilling hazards, it has been used as commercial production of gas in some countries of the world and it's utilization is increasing day by day. Some countries recognized shallow gas as a natural resource such as Canada, Russia, and China [3-5]. A large accumulation of biogenic gas is known to occur in shallow (<1000) Cretaceous reservoirs of the Northern Great Plains (mainly Montana), USA and southeastern Alberta and southwestern Saskatchewan, Canada [6-7]. Such gas in shallow depths are typically rich in methane and are not associated with oils. Methane is the only hydrocarbon actually generated in significant volumes during the biogenic stage [1-8]. Occurrences of shallow gas during drilling of water well reported for many years in Bangladesh plain land. In recent years, the occurrences of shallow gas are more widely reported in Bangladesh because of the increasing number of tube Wells having sunk. The reported depths of biogenic gas occurrence ranges in different depths from 10 meters to 100 meters below the surface, but most of these occur at depths more than 30 meters [9]. All of these have been proved to be non-commercial and record gas flow for short intervals of a few days to a few weeks. However, the occurrence

of shallow gas in Bhola district in southern Bangladesh is the only exception in the sense that gas seepages have been continuing for as much as 10 years.

The shallow gas occurs in Quaternary sediments in Bhola Island at depth ranges from 200 to 300m meaning a deeper habitat compared to all other known Quaternary shallow gas in Bangladesh. Use of these shallow gas by local people through make shift crude technology (rubber tube and drum) have made the gas sub commercial. Although the subject have been reported in the news media for several years, no in-depth geological evaluation and research has been carried out on the gas seepages of Bhola. The present research aims at geological evaluation of the occurrences, distribution and origin of the shallow gas in the Bhola Island based on field studies and laboratory analyses. A comparison has also been made between the shallow gas as mentioned above and the deep reservoir gas of the Shahbazpur gas field that occurs in Miocene sediments at depth range in excess of 2500m [10].

## 2. Geological setting

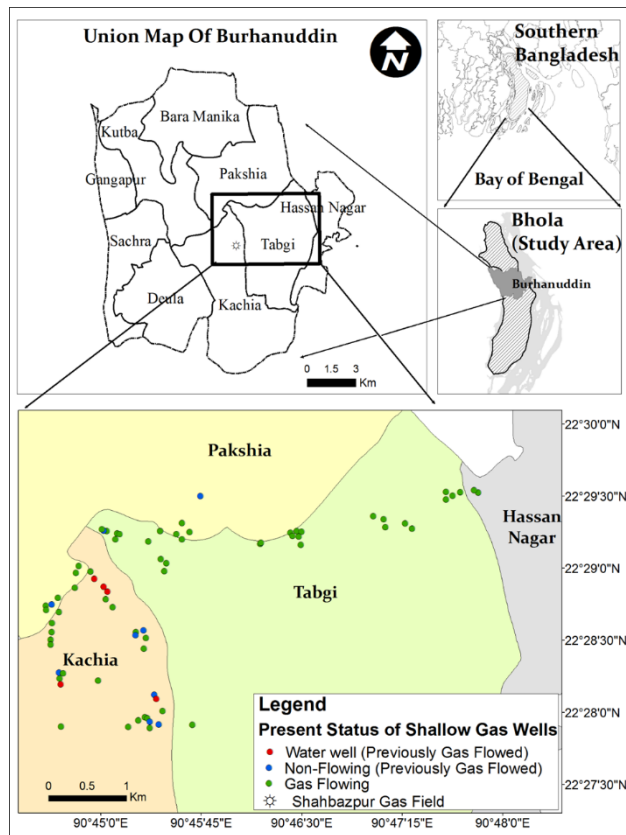


Fig.1. Location map of the study area and present status of shallow gas wells

## 3. Stratigraphic sequence

The stratigraphy of Foredeep area of Bengal basin is characterized by an enormous thickness of Tertiary sedimentary succession. This succession is thicker in the southern part of the regions in the Faridpur and Hatia Troughs, but the stratigraphy is little known there [12]. The stratigraphy of the Shahbazpur area was established with the help of systematic lithological description of the drilled section, log data and from seismic data, and from correlation with neighboring well and is summarized in Table 1. It ranges from Miocene to Recent in age, although the base is not seen. The Shahbazpur-1 succession is divided into four sequences named Shahbazpur (SB) sequence -I, -II, -III and -IV [13]. These sequences have been assigned

Bhola, an island district of Bangladesh is located in Foredeep area of Bengal basin or can be said more precisely in the Hatia trough. The Foredeep part of the Bengal is at the west of eastern fold belt. Here the intensely folded sedimentary layers gradually become strata of mild folding or no folding at all. Therefore, the sedimentary layers are generally horizontal to sub horizontal and are free from major tectonic deformation in the Foredeep area. This unit covers the central part of the basin and is represented by river to delta plain topography at the surface [11]. The Shahbazpur structure is a subsurface anticlinal structure situated in the middle of the Bhola Island. There is no surface expression of the Shahbazpur subsurface anticline rather the surface is floored with recent alluvial plain deposits. Field survey has been carried out in almost all parts Bhola district. However, the shallow gas wells are found to be located only in Burhanuddin upozila. It covers the longitude range from  $90^{\circ} 43'E$  to  $90^{\circ} 50'E$  and latitude range from  $22^{\circ} 24'N$  to  $22^{\circ} 32'N$  (Fig. 1).

to the traditional stratigraphic succession of Bangladesh, i.e. the Surma Group (SB sequence 3 and 4), the Tipam Group (SB sequence 2) and the Dupi Tila Group (SB sequence 1) [14].

Table 1. Stratigraphy and lithology in the Shahbazpur area [Modified after 13, 14].

Depth (m)	Age	Group	Sequence (m)	Lithology	Depositional Environment
0-480	Recent		Alluvium (480)	Loose unconsolidated sand with occasional clay	Fluvial Plain
480-1505	Pleistocene (?)	Dupi Tila (Tentative assignment)	SB sequence I(1025)	Shale with occasional occurrence of interbedded sandstone and calcareous siltstone	Deltaic to Fluvial plain
1505-2010	Pleistocene-Pliocene	Tipam	SB sequence II(505)	Shale and sandstone	
2010-2750	Plio-Miocene	Surma	SB sequence III (740)	Sandstone and shale	Deep sea to shallow marine
2750-3631	Miocene		SB sequence IV (881)	Sandstone and shale	

#### 4. Materials and methods

##### 4.1. Field Procedure and sampling

Field survey in the study area carried out twice during this study. First, a reconnaissance survey performed in winter (January 2015) to observe the status of the shallow gas wells. To get the general overview of the well location, suggestion of the local people taken. A hand held GPS was used to note down the well location. Another field visit was done in the beginning of rainy season (April 2015) to observe whether the flowing status of well are changed or not. At second visit period, gas samples were collected from several locations. Gas samples (Table 2) were collected by the water displacement method from each gas well. These samples immediately kept in glass bottles at the sampling sites and the bottles opened just before analysis in laboratory.

Table 2. Location of sampling wells

Area	Well	Depth (m)	Coordinates	
			Latitude (N)	Longitude (E)
Kachia	K-1	262	22°27'58.80"	90°45'19.93"
Kachia	K-22	259	22°28'31.26"	90°44'37.92"
Tabgi	T-15	259	22°28'59.70"	90°45'28.92"
Tabgi	T-23	290	22°29'17.52"	90°47'8.04"
Tabgi	T-26	262	22°29'15.30"	90°46'25.44"
Pakshia	P-2	259	22°29'15.90"	90°45'40.32"
Hassan Nagar	H-2	290	22°29'32.76"	90°47'47.76"

##### 4.2. Analytical procedures

Hydrocarbon compositions of natural gases were analyzed by a gas chromatograph. The gas samples have been analyzed by Bruker 450 gas chromatograph fitted with a Hayesep 6'x 1/8" column in parallel with a Molsieve 13X 4'x 1/8" column, both connected to Thermal Conductivity Detector (TCD) and a CP-Sil 5CB 60m \* 0.25mm capillary column connected to Flame Ionization Detector (FID). Gas samples are passed through a 14-port valve to fill three individual loop of 250 µL and then it is injected to three columns separately by programmed valve switching. Temperature program was kept at 45° C for 6.5 min, then raised at a rate of

20° C/min up to 200° C and hold for 3.75 min. Helium was used as carrier gas. Hydrogen and oxygen (air) for FID. Presence of hydrogen sulfide (H<sub>2</sub>S) in gas was tested with lead acetate.

**5. Results and discussion**

**5.1. Subsurface occurrence and distribution of shallow gas**

**5.1.1. Occurrences: depth wise**

A generalized stratigraphy established from the well tops information, which shows the position of the gas zones in stratigraphic sequence (Fig. 2a).

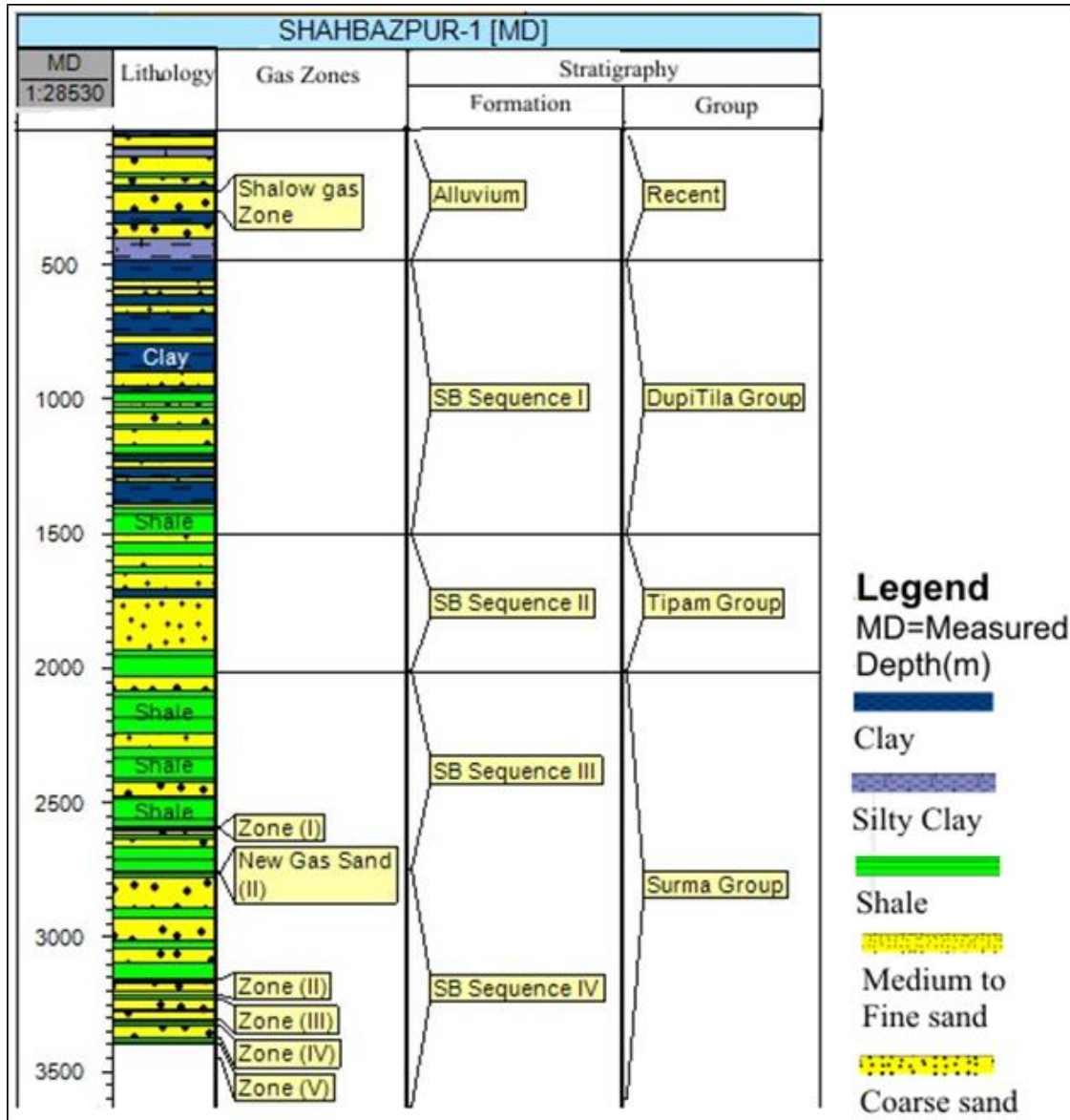


Fig. 2a. Occurrence of shallow gas in generalized stratigraphy (modified after [13])

From the figure, it can be noticed that the shallow gas zones occur in alluvial deposit of recent age where deep gas zone occurred in Surma group of Miocene-Pliocene age. A correlation has also been made between seismic stratigraphy of Shahbazpur gas field and Litholog made from Shah-bazpur-1 well (Fig. 2b) which shows that shallow gas zone occurred as delta top deposit of Megasequence 3, where most deep gas zones occurred as deep sea to shallow

marine deposits of Megasequence 1. Two deep gas zones occurred at the base of the incised valley fills of Megasequence 2 [15].

A cross-section (A-B) has been constructed along the shallow gas wells taking in reference Pakshia-1 well, which Litholog were made from available borehole data. From the Litholog it can be observed that the dominant lithology is unconsolidated sand with several thin to thick clay layers. A well correlation established along the cross-section based on top of the shallow gas zone where the base of the shallow gas zone was not known yet (Fig. 3). From the correlation of shallow gas wells, it can be found that the depth range of the top of the shallow gas zone is about 260m-290m.

A detail relation of seismic line with shallow gas wells shown in (Fig. 4). The relation between gas wells and seismic lines give a relationship between the occurrence of shallow gas wells and deep gas wells. The maximum distance from the seismic line to well is taken as 1000m that is, the wells that fall within this 1000m radius will show in the seismic line. It has been observed that the shallow gas wells have TWT (milliseconds) is about less than 500ms where the Shahbazpur gas wells have TWT is about 2500ms. The shallow gas wells clustered in the north of the Shahbazpur gas wells and there are no shallow gas wells in the south of Shahbazpur gas wells.

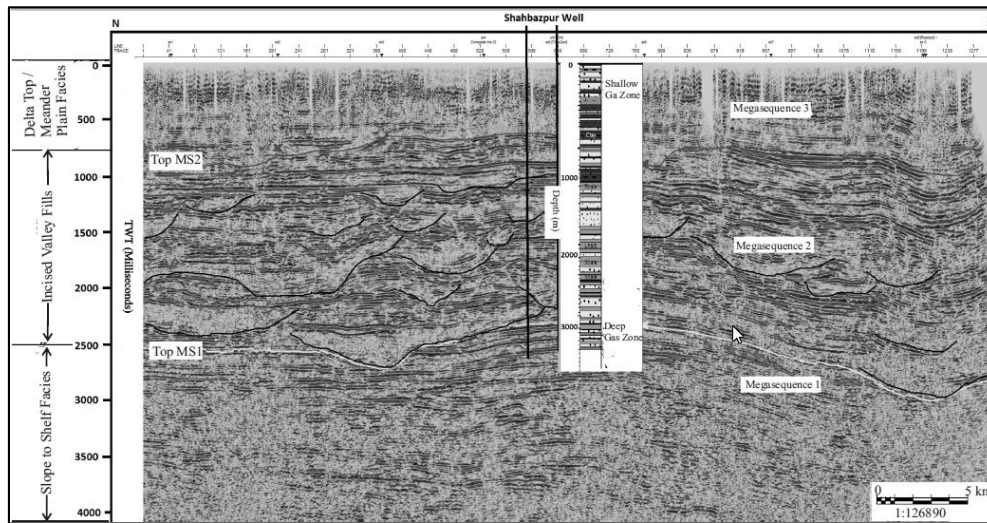


Fig. 2b. Occurrence of shallow gas in seismic stratigraphy (modified after [15])



Fig. 3. Well correlation of shallow gas wells

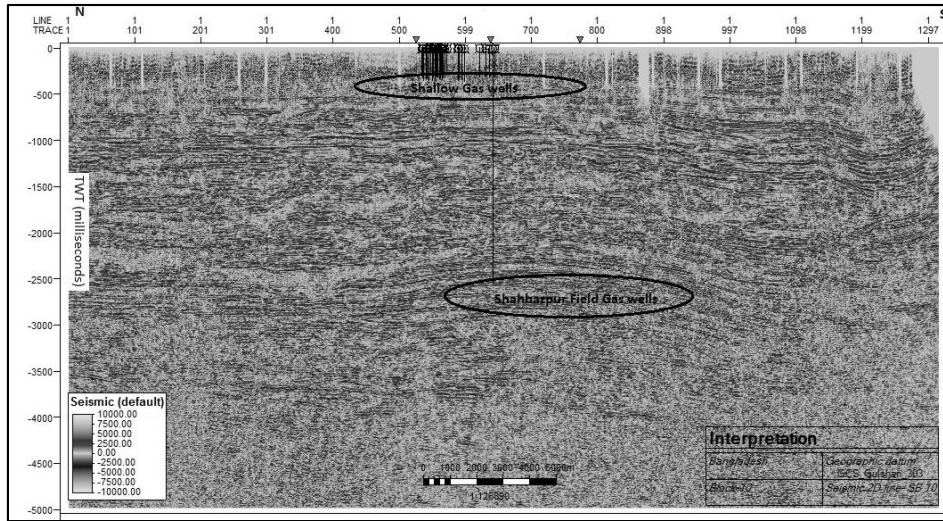


Fig. 4. Distribution of shallow gas wells in Shahbazpur seismic line

**5.1.2. Distributions: area wise**

Field survey has been carried out in all part of Bhola island, after that it has been confirmed that the shallow gas wells are located only in Burhanuddin upozila out of 7 upozila of Bhola district. The shallow gas wells are only present in four union of the upozila they are Kachia, Tabgi, and Pakshia and Hassan Nagar union (Fig. 1). No other union has reported of having such shallow gas wells. Most of the shallow gas wells are located in Kachia union, and they have a clustered distribution. The shallow gas wells located from Kachia to Tabgi to Hassan Nagar and some of the wells found in the bank of the Meghna River. According to local people, so many wells lost into the Meghna River. The shallow gas wells found from the north of the Shahbazpur gas field and no shallow gas wells found in the south of the Shahbazpur gas field. Some of the shallow wells are now used as water well; some are just abandoned because they are not flowing water or gas and most of them are still flowing gas, and new shallow gas wells are also exploited (Fig. 1). The pressure of the flowing gradually decreased with increasing age of wells. It has been observed that some wells stopped flowing or has lower flow rate gas during winter whether the rainy season they have full flow.

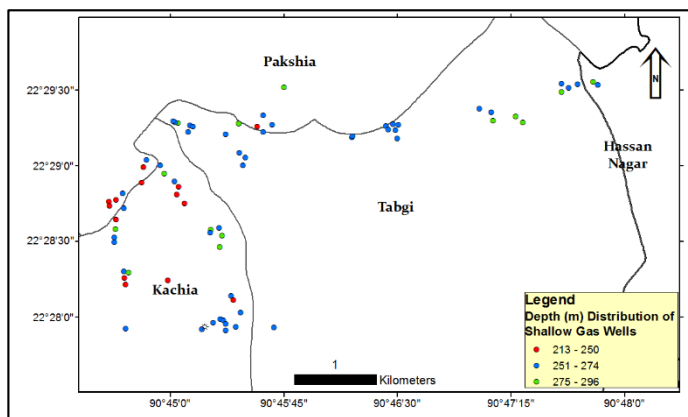


Fig. 5a. Depth distribution of shallow gas wells

The shallow gas wells in Kachia have higher flow rate than wells in Tabgi. When collecting gas samples, the less time required to fill the sample bottle in Kachia union than other unions. A depth distribution map was also made based on the depth information of shallow gas wells in the study area (Fig. 5a). The very shallow gas wells (213m-244m) are located in the west and North-west of the study area. All of the wells that are located in the in the northeastern part of the study area having depth range 250m-

290m. When collecting data in the field, it has been observed that the average depth of shallow gas wells in Tabgi union is higher than the average depth of shallow gas wells in Kachia union. It has also been observed that the shallow gas wells are not clustered to the closure rather than they also distributed towards flanks of the structure (Fig. 5b).

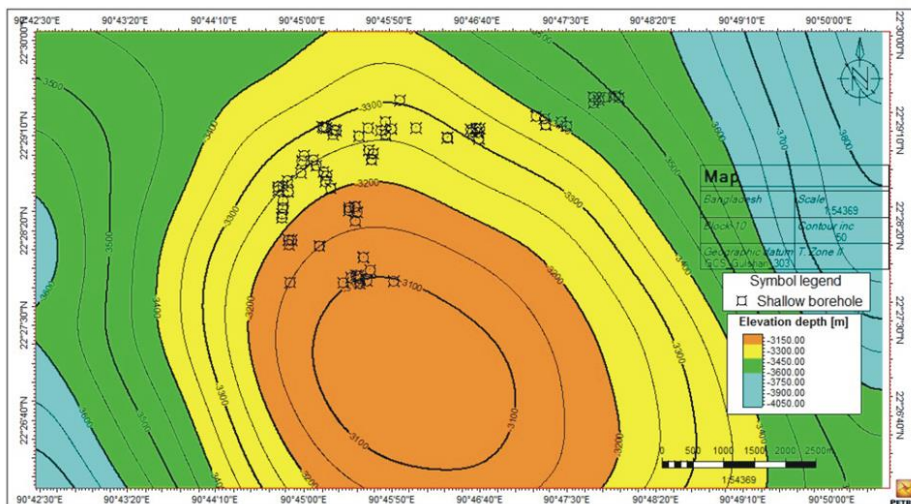


Fig. 5b. Showing distribution of shallow gas wells in Shahbazpur structure

### 5.2. The chemical composition of the shallow gas

Seven gas samples were analyzed for chemical composition. The analyses show that the samples are dominated by methane (as much as 90%), with minor C<sub>2+</sub> hydrocarbons (<0.2%), N<sub>2</sub>, and CO<sub>2</sub>. The gas compositions of the shallow gas samples are shown in Table 3.

Table 3. Molecular composition of analyzed natural gases

Well	Molecular Composition (vol %)									
	CH <sub>4</sub>	C <sub>2</sub> H <sub>6</sub>	C <sub>3</sub> H <sub>8</sub>	i-C <sub>4</sub>	n-C <sub>4</sub>	i-C <sub>5</sub>	n-C <sub>5</sub>	N <sub>2</sub>	CO <sub>2</sub>	H <sub>2</sub> S
K-1	96.86	0.07	nd	nd	nd	nd	nd	2.51	0.56	nd
K-22	97.29	0.05	nd	nd	nd	nd	nd	2.18	0.48	nd
T-15	98.26	0.07	nd	nd	nd	nd	nd	0.83	0.84	nd
T-23	97.73	0.05	nd	nd	nd	nd	nd	1.11	1.11	nd
T-26	98.02	0.03	nd	nd	nd	nd	nd	0.94	1.01	nd
P-2	96.40	0.05	nd	nd	nd	nd	nd	2.72	0.83	nd
H-2	97.15	0.08	nd	nd	nd	nd	nd	1.89	0.89	nd

\*nd=not detected

For the gas samples collected from Kachia union, the ranges of hydrocarbon compositions are CH<sub>4</sub>: 96.86 - 97.29%, C<sub>2</sub>H<sub>6</sub>: 0.05 - 0.07%, CO<sub>2</sub>: 0.48 - 0.56% and N<sub>2</sub>: 2.18-2.51%. For the gas samples collected from Tabgi union, the ranges of hydrocarbon compositions are CH<sub>4</sub>: 97.73 - 98.26%, C<sub>2</sub>H<sub>6</sub>: 0.03 - 0.07%, CO<sub>2</sub>: 0.84 - 1.11% and N<sub>2</sub>: 0.83 - 1.11%. For the gas, samples collected from Pakshia union the hydrocarbon compositions are CH<sub>4</sub>: 96.40%, C<sub>2</sub>H<sub>6</sub>: 0.05%, CO<sub>2</sub>: 0.83% and N<sub>2</sub>: 2.72%. For the gas, samples collected from Hassan Nagar union the hydrocarbon compositions are CH<sub>4</sub>: 97.15%, C<sub>2</sub>H<sub>6</sub>: 0.08%, CO<sub>2</sub>: 0.89% and N<sub>2</sub>: 1.89%. From the above observation, it can be said that the range of hydrocarbon compositions of shallow gas is CH<sub>4</sub>: 96 - 98 %, C<sub>2</sub>H<sub>6</sub>: 0.03 - 0.08 %, CO<sub>2</sub>: 0.5 - 1% and N<sub>2</sub>: 1- 3%. The higher hydrocarbon constituent (>C<sub>2+</sub>) were not present in the gas samples. It should be mentioned that the smell of hydrogen sulphide (H<sub>2</sub>S) was found during collecting gas samples but was not found during lead acetate test in the laboratory.

### 5.3. Comparison of shallow gas with deep thermogenic gas

Comparison of two gases can be made by chemical and isotopic composition. As there is no facility available for isotope analysis in the country, only chemical analysis results by gas chromatography are used for comparison. For the deep thermogenic gases (>2 500m) of

Shahbazpur gas field the ranges of hydrocarbon compositions are CH<sub>4</sub>: 89.82 - 94.9%, C<sub>2</sub>H<sub>6</sub>: 3.00 - 4.090%, C<sub>3</sub>H<sub>8</sub>: 0.55 - 1.12%, i-C<sub>4</sub>: 0.15 -0.25%, n-C<sub>4</sub>: 0.06 -0.11%, i-C<sub>5</sub>: 0.02 - 0.08%, n-C<sub>5</sub>: 0.01 -0.05%, CO<sub>2</sub>: 0.6 -0.9% and N<sub>2</sub>: 0.4- 3.0%. Hydrogen sulphide was not present in the deep thermogenic gas.

The shallow gas does not have any higher hydrocarbon constituent (>C<sub>2</sub>), it can be possible if the shallow gas were produced by bacterial biodegradation. However, a small amount of ethane can be present in the bacterial gas because ethane has high bacterial resistance [16]. Where the deep gas has higher hydrocarbon like propane, butane, pentane, and hexane. Therefore, from the composition of the shallow gas and deep gas, it can be said that the shallow gas is different from deep reservoir gas.

#### 5.4. Origin of the shallow gas

To understand the resource-base, it is necessary to determine whether a gas accumulation is microbial, thermal or mixed. This is accomplished through an analysis of both molecular and isotope composition. However, isotope composition gives better result about the origin of the gas, but the molecular composition of the analysis can also give an indication of the origin of the gas. The values of C<sub>1</sub>/C<sub>2+</sub> greater than 1,000 indicated biogenic sources, whereas values less than 50 signaled thermogenic sources [17]. From the gas analysis of shallow gas and deep gas, it can be observed that the shallow gas have the range for C<sub>1</sub>/C<sub>2+</sub> ratio is about 1200-3500 where the deep gas has the range for C<sub>1</sub>/C<sub>2+</sub> ratio is about 20-35 (Fig. 6a).

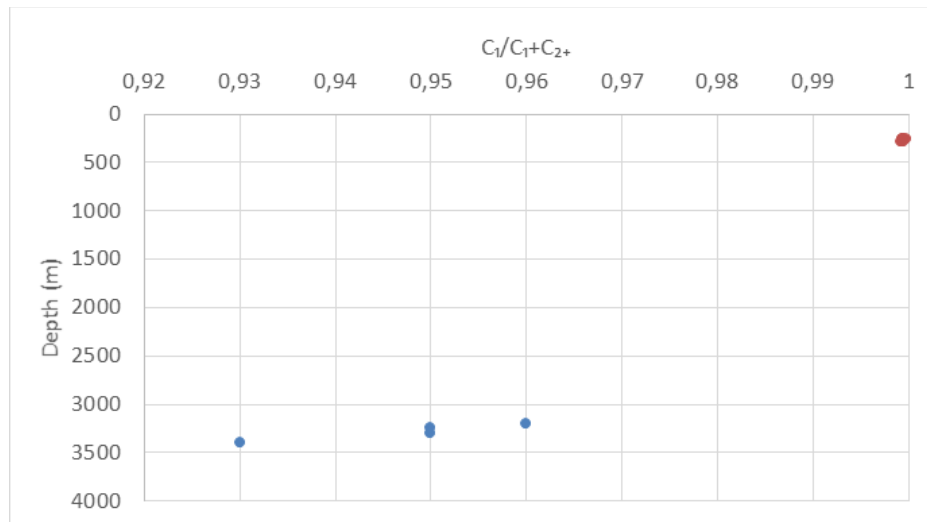


Fig. 6a. Dryness value of the shallow gas and deep gas

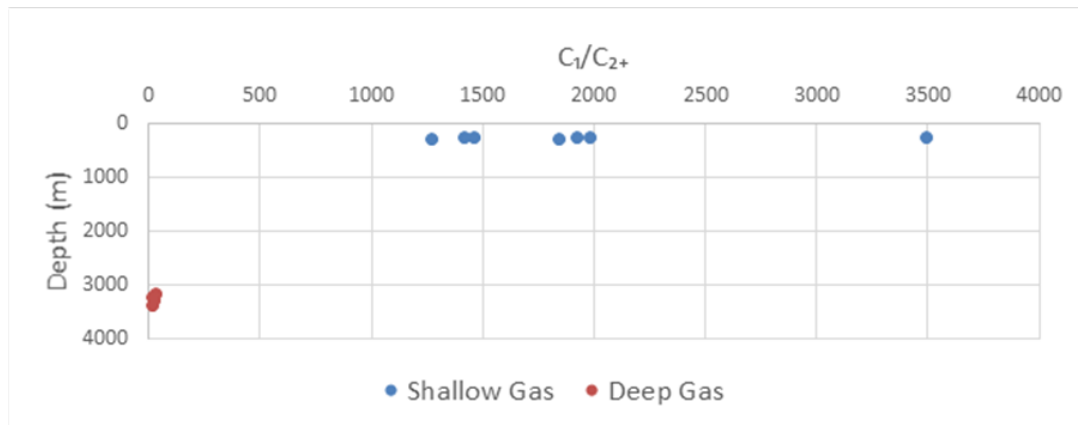


Fig. 6b. Showing the value of C<sub>1</sub>/C<sub>2+</sub> ratio in shallow gas and deep gas

Biogenic gases characteristically are composed almost entirely of methane ( $C_1/(C_1+C_{2+}) > 0.98$ ) [5]. In other words, it can be said that the gas is very dry due to the dryness of methane. Generally, microbial gas is typically considered dry (i.e., depleted in  $C_{2+}$  components), but there is clear evidence that ethane and possibly propane may also form through microbial processes [16]. From the analyzed gas samples, the shallow gas has the range of the  $C_1/(C_1+C_{2+})$  value is about 0.9992-0.9997 where the deep gas have the range of the  $C_1/(C_1+C_{2+})$  value is about 0.93-0.96 (Fig. 6b).

Therefore, from the above observation discussed above it can be concluded that the shallow gas is quite different from conventional reservoir gas. The  $> 1000 C_1/C_{2+}$  ratio value and  $> 0.98 C_1/(C_1+C_{2+})$  value suggest the biogenic origin of the shallow gas, where the  $< 50 C_1/C_{2+}$  ratio value and  $< 0.98 C_1/(C_1+C_{2+})$  value proved the thermogenic origin of the deep gas. Therefore, it can be summarized that the shallow reservoir gas in the study area is biogenic in origin though isotope analysis is needed for further confirmation.

### 5.5. Prospect of the shallow gas

During the field survey, it was observed that water is continuously drawing out from the tube well. The local people use a filter, which separates the water at the base and gas at the top (Fig. 7). The local people said that they are using this gas for about 30 years.

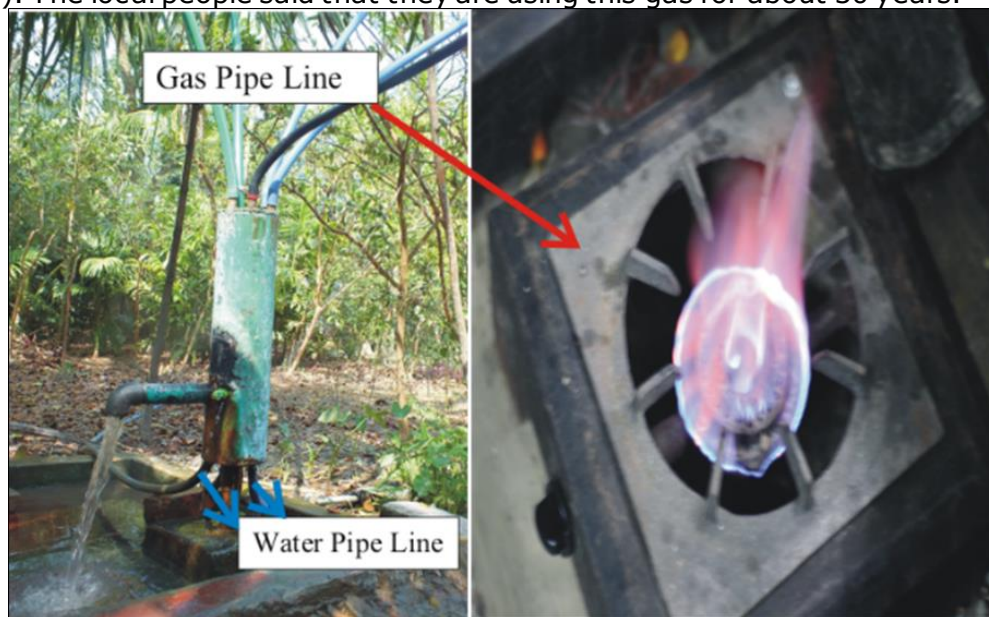


Fig. 7. Local filtering method for separating gas and using it for cooking purpose

It is true that all of the gas wells were not continually flowed from the beginning. Some of the gas wells flowed for 1 (one) year, some are for 5 (five) years, and some are still flowing (Fig. 8). There are some wells, which are flowed for more than 16 years, and there are two wells one in kachia and another in Pakshia, which flowed more than 30 years and they are still flowing.

There are on average 2-7 connections per well. Most of the gas wells having no connection with consumers are located in Kachia. The lack of connectivity is due to the absence of flow, but they flow previously. They had the connection like present flowing well when they flowed, but it is difficult to get the information on how many connections they had because no one has a clear idea about the connections. From the presently flowing gas wells, the wells from Tabgi and Hassan nagar union has more connection (Fig. 9).

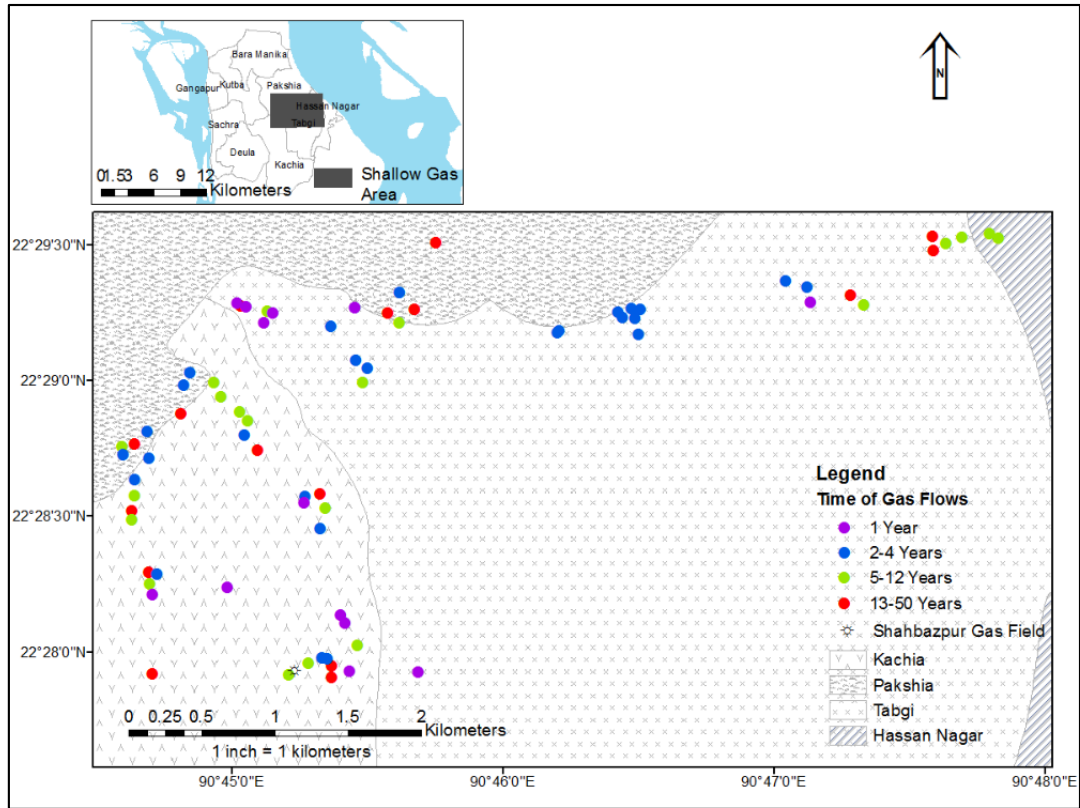


Fig. 8. Period of gas flow from shallow gas wells

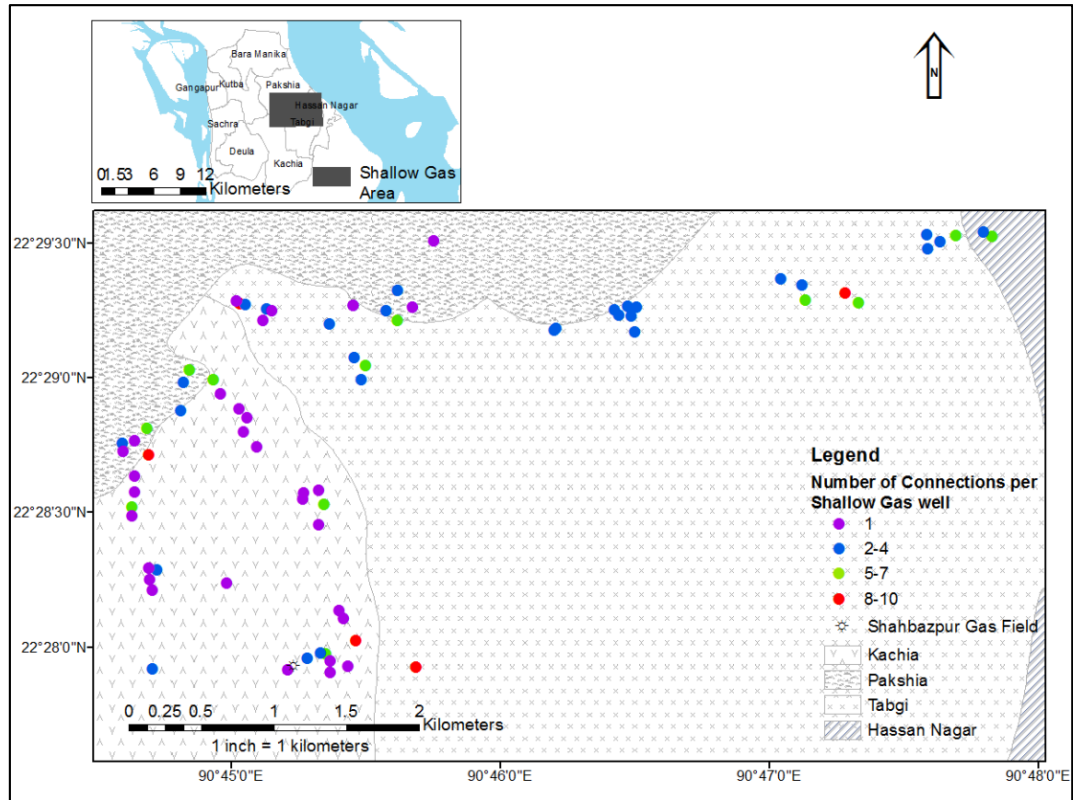


Fig. 9. Number of connections per shallow gas well

Therefore, from the above observation it cannot be said that the shallow gas has no prospect or no value, rather it can be marked that the gas has a moderate prospect or sub-commercial value, which is proved by its extreme utilization of local people.

## 6. Conclusions

The occurrence of shallow gas is restricted only to the Burhanuddin upozila in the central part of Bhola Island. The potential map has been produced to summarize the distribution of shallow gas wells. From that, it can be concluded that the shallow gas wells are only distributed within the four unions of Burhanuddin upozila. The other parts of the Burhanuddin upozila, as well as Bhola Island, do not have the shallow gas occurrence.

The shallow gas reservoir zones are consisted of fine to coarse sand which has an average porosity of 35%. The occurrence depth of the shallow gas reservoir is increasing towards the eastern part of the area. The shallow gas reservoir is sealed by a clay layer at the top. From the distribution of the shallow gas occurrence, it can be concluded that a localized stratigraphic trap exists in the area. The organic rich clay and shale that lie below the reservoir are the possible source of the shallow gas.

The chemical composition of shallow gas consists of entirely methane with less than 0.2% methane where the deep thermogenic gas consists of ethane as well as higher hydrocarbon like ethane, propane, butane, etc. The shallow gas has high methane-ethane (+) ratio (>1000) where the deep gas low methane-ethane (+) ratio (<50) and shallow gas has dryness value >0.99 (close to 1) where deep gas has dryness value >0.93.

The shallow gas is genetically different from the deep gas in being biogenic origin while the deep gas is the thermogenic origin. These two have a different generation, migration and accumulation pattern in their respective pools. Further study is needed including stable isotope geochemistry to conclude the origin of the gas.

Finally, it can be concluded that the shallow gas at recent deposit has a sub-commercial value which has been proved by the long term use of this gas in the community. Shallow gas is currently of little economic interest due to low-pressure drive to recovery at the surface. But it is of better potential for commercial interest in the future with the development of new and better technologies associated with biogenic gas. A country like Bangladesh that suffers from the long term energy crisis, the energy of this type can genuinely provide an aid to overcome the future energy crisis.

## Acknowledgments

The authors are thankful to Managing Director of BAPEX for his support and permission of the research for the MS degree in Geology of University of Dhaka. The authors also want to express thanks to Mr. Md. Abul Kashem, Mr. Mohammad Asif Eqram Khan, Mr. Md. Masud Khan, Mr. Saman Uddin Ahmed, Ms. Rokshana Pervin and Mr. S.M. Mahtab-Ul-Alam for their support during the research work.

## References

- [1] Rice DD, Claypool GE. Generation, Accumulation, and Resource Potential of Biogenic Gas. American Association of Petroleum Geologists Bulletin, 1981; 65: 5–25.
- [2] Lin CM, Gu LX, Li GY, Zha YY, Jiang WS. Geology and formation mechanism of late Quaternary shallow biogenic gas reservoirs in the Hangzhou Bay area, eastern China. American Association of Petroleum Geologists Bulletin, 2004; 88: 613–625.
- [3] Hu Y, Li H, Xu J. Shallow gas accumulation in a small estuary and its implications: A case history from in and around Xiamen Bay. Geophysical Research Letters, 2012; 39.
- [4] Lin CM, Li YL, Zhuo HC, Shurr GW, Ridgley JL, Zhang ZP, Xue T. Features and sealing mechanism of shallow biogenic gas in incised valley fills (the Qiantang River, eastern China): A case study. Marine and Petroleum Geology, 2010; 27: 909–922.
- [5] Milkov AV. Methanogenic biodegradation of petroleum in the West Siberian Basin (Russia): Significance for formation of giant Cenomanian gas pools. American Association of Petroleum Geologists Bulletin, 2010; 94(10): 1485–1541.

- [6] Ridgley JL, Hester TC, Condon SM, Cook T, Anna LO, Lillis PG, Rowan EL, Snyder GT. Assessment of Shallow Biogenic Gas Resources in Montana: CSPG Special Publications 2001. <https://serc.carleton.edu/resources/13146.html>
- [7] Ridgley J. Regional Geochemical Study of the Upper Cretaceous Shallow Biogenic Gas System in Saskatchewan, Alberta, and Montana - Application of Isotope and Compositional Systematics to Understanding the Distribution of Gas Resources. Saskatchewan Geological Survey 2002; 143-150.
- [8] Floodgate GD, Judd AG. The origin of Shallow Gas. Continental Shelf Research. 1992; 12: 1145-1156.
- [9] Ahmed KM, Hoque M, Hasan MK, Ravenscroft P, Chowdhury LR. Occurrence and Origin of Water Well Methane Gas in Bangladesh. Journal of Geological Society of India, 1998; 51: 697-708, 0016-7622/198-51-5-697.
- [10] Rahman M. Occurrence and Distribution of Shallow Gas in Southern Bangladesh: A Case Study on Bhola Island. M.S. Department of Geology, University of Dhaka, Ramna, Dhaka. August, 2015.
- [11] Imam B. Energy resources of Bangladesh: natural gas, oil, coal: Dhaka, University Grants Commission of Bangladesh, 2nd ed.; University Grants Commission of Bangladesh, Dhaka, Bangladesh, 2013; 16-113, 984-809-020-1.
- [12] Alam M, Alam MM, Curray JR, Chowdhury MR, Gani MR. An overview of the sedimentary geology of the Bengal Basin in relation to the regional tectonic framework and basin-fill history. Sedimentary Geology, 2003; 155: 179-208.
- [13] Mondal D, Islam M, Islam A. Electrofacies Analysis of Neogene Sequence in the Well Shahbazpur-1, Bhola, Bengal Basin. The IUP Journal of Earth Sciences, 2009; 5: 57-74.
- [14] Roy DK, Roser B. Geochemistry of Tertiary Sequence in Shahbazpur-1 Well, Hatia Trough, Bengal Basin, Bangladesh: Provenance, Source Weathering and Province Affinity. Journal of Life and Earth Science, 2012; 7: 1-13.
- [15] Najman Y, Allen R, Willett EAF, Carter A, Barfod D, Garzanti E, Wijbrans J, Bickle MJ, Vezzoli G, Ando S, Oliver G, Uddin MJ. The record of Himalayan erosion preserved in the sedimentary rocks of the Hatia Trough of the Bengal Basin and the Chittagong Hill Tracts, Bangladesh. Basin Research, 2012; 24: 499-519.
- [16] Katz BJ. Microbial Processes and Natural Gas Accumulations. The Open Geology Journal, 2011; 5: 75-83.
- [17] Bernard B, Brooks J, Sackett W. Natural gas seepage in the Gulf of Mexico. Earth and Planetary Science Letters, 1976; 31: 48-54.

---

*To whom correspondence should be addressed: AKM Eahsanul Haque, Department of Physical and Geological Sciences, Universiti Brunei Darussalam, Gadong BE1410, Brunei Darussalam*

## EVALUATION OF SOURCE ROCKS OF THE CAMPANO-MAASTRICHTIAN NKPORO GROUP OF ANAMBRA BASIN, SOUTHEASTERN NIGERIA

*K. C. Chiadikobi and O. I. Chiaghanam*

*Department of Geology, Faculty of Physical Sciences, Chukwuemeka Odumegwu Ojukwu University, Uli, Anambra State, Nigeria*

Received August 16, 2018; Accepted October 19, 2018

---

### **Abstract**

The Nkporo Group of the Anambra Basin consists mostly of dark-grey to black shales, mudstones, sandstone and siltstone. The aim of this study is to evaluate the source rocks and paleoenvironments of the Nkporo Group in the Anambra Basin. The objectives are to: determine the organic richness of the source rock and the type of organic matter (kerogen type), determine their thermal maturity and evaluate the hydrocarbon generation potentials of the source rocks of the Nkporo Group (Nkporo Formation and Enugu Shale). The study was undertaken in three stages: desk work, field and laboratory studies. Twenty-five samples from the Nkporo Formation and Enugu Shale were analyzed using Leco CS 125 and HAWK pyrolyser for the organic geochemical parameters. This parameter was used to assess the source rock quantity and quality, type of organic matter, maturity and generating potential of the source rocks (shales). From the results of the geochemical analysis, the Total Organic Carbon (TOC) contents of the Nkporo Formation and Enugu Shale varied from 0.41 to 2.42wt.% and 0.53 to 3.15 wt.% respectively. This shows that Nkporo Formation and Enugu Shale has fair to very good organic matter contents. The organic matter richness varies from 0.08 to 4.40mgHC/g for the Nkporo Formation and 0.36 to 3.97mgHC/g for the Enugu Shale. Hydrogen Index versus Oxygen Index plots and visual kerogen shows that the Nkporo Formation was of Type III/IV while Enugu Shale was of Type II/III kerogen. The Thermal maturity index (Tmax) of the Nkporo Formation and Enugu Shale varies from 418 to 443°C and 430 to 443°C respectively. These suggest that the Nkporo Formation is marginally mature to mature while Enugu Shale is mature. The results of this study has shown that the source rocks of the Nkporo Formation is immature and has not generated hydrocarbon while that of the Enugu Shale is mature and has generated hydrocarbon.

**Keywords:** *Nkporo Formation; HAWK Pyrolysis; Kerogen; Organic Matter; Hydrocarbon.*

---

### **1. Introduction**

Anambra Basin has a total sediment thickness of about 9km and presents an economically viable hydrocarbon Province [1]. It is characterized by enormous lithologic heterogeneity in both lateral and vertical extension [1]. The search for commercial deposit of hydrocarbon in the Anambra Basin has been on the drawing board especially to oil companies and research groups. Initial efforts were unrewarding, and this leads to the neglect of this basin in favour of the Niger Delta Basin [2-3]. The increasing global energy demand, the advent of improved exploration tools, integrated basin analytical methods, the need to circumvent the pending energy crises, and ultimately the allocation of concession blocks in Anambra Basin, oil/gas exploration and prospecting activities have provided the impetus for sustained exploration in the basin. It is against this background that this research focuses on providing necessary information to optimize development in exploration and exploitation of petroleum in the Anambra

Basin. The maturity of organic matters is one of the most important processes in the evaluation of sources rock [4] (Fig. 1). Rock-eval pyrolysis and vitrinite reflectance are the most commonly used methods in the assessment of the maturity of organic matter.

Unomah [5] evaluated the quality of organic matter in the Cretaceous shales of the Lower Benue Trough as the basis of the reconstruction of the factors influencing organic sedimentation. He deduced that the organic matter and shales were deposited under a low rate of deposition. Specific reference to the organic richness, quality and thermal maturity in the Mamu Formation and Nkporo Shale has been reported by Unomah and Ekweozor [6]. Akaegbobi and Schmitt [7], Obaje *et al.* [8], Akaegbobi [1] and Ekweozor [9] reported that the sediments are organic rich but of immature status.

Anozie *et al.* [10] carried out research on thermal maturation of the rock of Campanian Enugu Shale in Anambra Basin, and concluded that the hydrogen index (HI) and generation potential (GP) of the shale attained values required for a quality source rock, suggesting that the shale has to gas generative potential and belong to type III kerogen with few records of type IV kerogen. The degree of thermal maturation obtained from the Rock-Eval data suggests that the shale sediments are thermally immature to generate petroleum. The objectives of this study sought to determine the organic richness of the source rock, determine the thermal maturity and the type of organic matter and evaluate the hydrocarbon generation and expulsion potentials of the source rock.

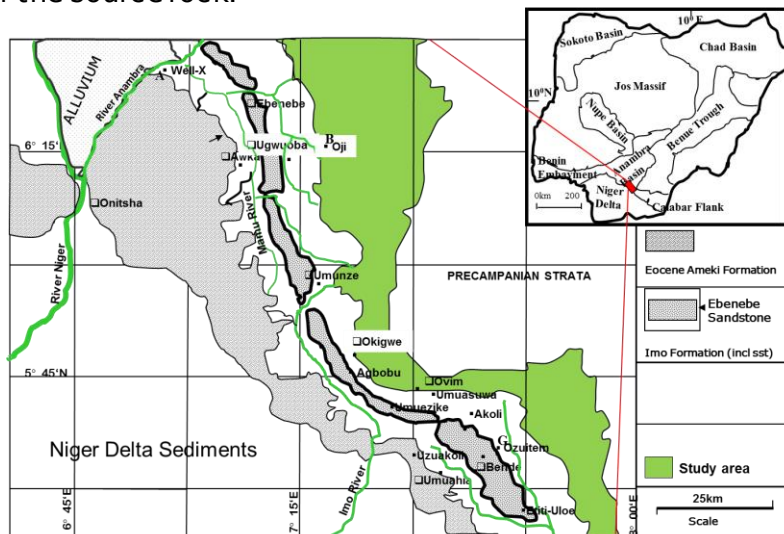


Fig. 1. Geologic Map showing the study area

## 2. Geologic setting

The oldest succession in the Anambra Basin is Nkporo Group [11]. It was deposited in Late Campanian [12-13]. The Nkporo Group comprises of Nkporo Formation, Enugu Shale and Owelli Sandstone which is lateral equivalent to each other. Nkporo Group is overlain by Mamu Formation (Fig 2). It was deposited in Early Maastrichtian [14-15]. It comprises a succession of siltstone, shale coal seam and sandstone [14]. The Ajali Sandstone (Maastrichtian) overlies the Mamu Formation [11-12], which consists mainly of unconsolidated coarse-fine grained poorly cemented sand stone and siltstone [14]. The Ajali Sandstone is overlain by dichronous Nsukka Formation (Maastrichtian - Danian) which is also known as upper coal measure [15] (Fig. 2).

### 2.1. Nkporo Formation

The Formation has its type locality at the Nkporo Town in Ohafia Local Government Area of Abia State. The Nkporo Shale is the basal sedimentary unit that was deposited following the Santonian folding in Southeastern Nigeria and indicates a Late Campanian, based on the pres-

ence of *Afrobolivina afra* [12]. The Nkporo Formation encountered in the study area is subdivisible into two lithostratigraphic units, namely, a lower sandstone and an overlying carbonaceous mud rock and shale unit. The basal sandstone unit is composed of ferruginized, poorly-sorted, coarse-medium grained and pebbly sandstone that rests unconformably on the tilted Coniacian- Turonian Formations. In boreholes at the proximal Alade and Nzam localities the unit is up to 150 m thick, while in the more basinal Ogbaku and Leru sections where the unit oversteps the Pre-Campanian Formations, the thickness decreases to less than 10 m. The overlying carbonaceous mud rock unit is better developed in the more basinal area south of Awgu, where it begins with grey, bioturbated mudstone that is characterized by concretionary pyritic layers 5-10 cm in thickness. The interval passes upward into nodular, fossiliferous black carbonaceous, fissile shale inter-bedded with grey, to milky-white, sharp-based beds of limestone and very fine grained sandstone/siltstone [15-18]. The best exposure of the Nkporo Shale is at Leru, along the Enugu – Port Harcourt express road. It is also exposed in Abia and Akanu in Arochukwu LGA; Nkporo, Item, Amaiyi in Ohafia LGA all in Abia State; Owutu, Nguzu-Edda, Ekoji and Eburnwana in Afikpo South LGA of Ebonyi State.

### 2.2. Enugu Shale

The Enugu Shale, a lateral equivalent of the Nkporo Formation, consists of grey, blue or dark shale, occasional white sandstones and striped sandy shale beds [19]. The Formation has its type locality at the Enugu Municipality, with an area coverage that stretches north to Ikem-Ihandiagu area, and southwards to Awgu area [19]. It underlies the Cross-River Plains east of the Enugu Cuesta and largely overlies the Awgu Shale. The formation consists mainly of shales, with two distinguishable sandstone bodies- the Otobi and the Okpaya Sandstones- which are regarded as members of the Formation [19]. Most of the territory underlain by the formation is low ground except for a few laterites- capped mounds or ridges considered to be erosional resistors left behind as the Cuesta scarp retreated westwards. Relatively consolidated siltstones and/or fine sandstones underlie some of these isolated topographic prominences [19]. The best exposure of the Enugu Shale is along the Enugu – Port Harcourt express road, Enugu- Onitsha express road and River Emene all at Enugu State [19].

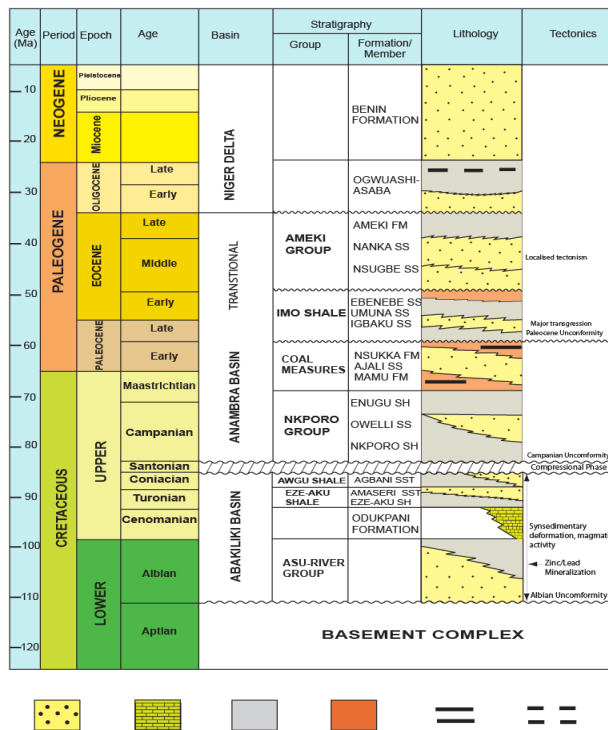


Fig. 2. Stratigraphic succession of Southeastern Nigeria showing the study area [20]

### 3. Methodology

#### 3.1. Total Organic Carbon (TOC) analysis

The total organic carbon (TOC) analysis was performed by means of the LECO CS 125 carbon analyzer according to the following procedure. About 200mg of the pre-clean shale was crushed and accurately weighed into dean LECO crucibles. The rocks were de-mineralised by hot 10% HCl and afterwards washed repeatedly with distilled water. After drying at 60°C, the crucibles were automatically introduced into the furnace for combustion and measurement of the organic carbon content.

#### 3.2. HAWK pyrolysis

An advanced pyrolysis instrument was used to identify the type and maturity of organic matter and to detect petroleum potential in sediments. This instrument is known as Hydrocarbon Analyzer with Kinetics (HAWK). HAWK pyrolysis is done using the Wildcat Technologies, HAWK™ Plus TOC module at Geomark Research Laboratories, Humble, TX. USA. The HAWK instrument measures all the classical pyrolysis parameters (S1, S2, S3, and Tmax) and TOC (Total Organic Carbon) using only about 100 milligrams of 60 mesh size ground rock sample. In addition, HAWK pyrolysis measures inorganic carbon and therefore gives you the carbonate carbon content of your rock samples. Acid preparation of samples for TOC analysis on the HAWK is not required. Utilizing the HAWK-eye software, interpretive results such as Oil Saturation, Hydrogen Index and Maturity can be obtained in near real-time to facilitate geosteering.

HAWK is ideal for analysis of not only conventional samples but also unconventional ones for which, the rock formation's generative and non-generative organic carbon contents can be determined while any generated, expelled or retained hydrocarbons can be quantified. The HAWK's maximum oven temperature is 850°C which insures complete pyrolysis of difficult to break-down Type III kerogen and also assures you that the complete decomposition of carbonates such as calcite and dolomite will occur. The HAWK also provides the capability for processing kinetics data using software such as GeoIsochem's Kinetics05. HAWK's kinetics data output can be configured to suit your needs. Whenever desired, analyses on the HAWK can continue overnight with no operator attention because it has a fully electronic, high precision autoloader with removable and interchangeable trays holding up to 126 samples. HAWK's PyroSmart panel displays real-time instrument status without the need of an external PC. All the critical parameters including gas flows are stored within the sample file so when you review your data, you can go into the data base and look into both the instrument and sample run parameters. HAWK's data file captures all real-time data associated with individual runs. In addition, HAWK can be used for designation of formation tops and geosteering while drilling. The HAWK instrument was designed with laboratory and well-site in mind. Samples chosen to be measured on the HAWK instrument are usually subsampled from the freeze-dried material previously crushed for analyses on the coulometer and CNS.

The HAWK pyrolysis method consists of a programmed temperature heating (in a pyrolysis oven) in an inert atmosphere (helium) of a small sample (~100 mg) to quantitatively and selectively determine (1) the free hydrocarbons contained in the sample and (2) the hydrocarbon- and oxygen-containing compounds (CO<sub>2</sub>) that are volatilized during the cracking of the unextractable organic matter in the sample (kerogen). The analysis process involved the transfer of each sample into the furnace where it was heated initially at 300°C for three minutes in an atmosphere of helium to release the free hydrocarbons (S1). Pyrolysis of the bound hydrocarbons to give the S2 peak followed immediacy as the oven temperature was ramped up rapidly to 550°C at the rate of 25°C/min. both the S1 and S2 hydrocarbon peaks were measured using a flame ionization detector (FID). A splitting arrangement permitted the measurement of the S3 peak (carbon dioxide) by means of a thermal conductivity detector (TCD). The instrument automatically recorded the temperature corresponding to the maximum of the S2 peak. i.e. Tmax. An in-built computer processed the raw data afford the values corresponding to the respective rock-Eval indices.

In summary, the four basic parameters obtained by pyrolysis (Table 1) are as follows:

Table 1. Rock-Eval parameters [21]

Sample	Formula	Description
S <sub>1</sub> (mgHC/g sample)	-	
S <sub>1</sub> (mgHC/g sample)	-	
S <sub>1</sub> (mgHC/g sample)	-	
S <sub>1</sub> (mgHC/g sample)	-	
T <sub>max</sub> (°C)	-	
PI	S <sub>1</sub> /S <sub>1</sub> +S <sub>2</sub>	Production index
PC(%)	0.1[0.83(S <sub>1</sub> +S <sub>2</sub> )+0.273S <sub>3</sub> +0.429(S <sub>3</sub> CO+0.53S <sub>3</sub> CO)]	Pyrolysable organic carbon
TOC(%)	PC+RC	Total organic carbon
BI (mg HC/g TOC)	100S <sub>1</sub> /TOC	Bitumen index
HI (mg HC/g TOC)	100S <sub>2</sub> /TOC	Hydrogen index
OI (mg CO <sub>2</sub> /g TOC)	100S <sub>3</sub> /TOC	Oxygen index
RC (%)	RC CO+ RC CO <sub>2</sub>	Residual organic carbon

## 4. Results and discussion

In order to evaluate the organic carbon content and source rock maturity different factors including organic matter richness, generating potentialities, type of organic matter and thermal maturation. Twenty-five (25) shale samples of part of the Nkporo Group (Nkporo Formation and Enugu Shale) were discussed based on Hydrocarbon Analyzer with Kinetics (HAWK) pyrolysis data and Total organic carbon (Toc) (Table 2a and 2b).

### 4.1. Organic matter richness

The quantity of organic matter expressed as total organic carbon is a measure of the organic richness of sedimentary rocks [22] i.e quantity of organic matter presented in rock and expressed as TOC in weight percent of the dry rock. The organic carbon richness of the rock samples (TOC %), is important in the evaluation of source rock for hydrocarbon. Tissot and Welte [4], Peters and Cassa, [23] and Peters [24] presented a scale for the assessment of source rocks potentiality, based on the TOC% and HAWK pyrolysis data (Table 2a and b).

The Total organic carbon (TOC) of the shale samples of the Nkporo Formation ranges from 0.41-3.54 wt% with an average of 1.53 wt% which indicates a good source rock. The Enugu Shale samples range from 0.53-3.39 wt%, with an average of 2.03 wt% (Table 2a and b). This average value indicates a very good source rock [23,25-27]. Total organic carbon (TOC) value of 0.5wt% is the threshold value required for a potential sources rock to generate hydrocarbon. The number of free hydrocarbons (gas and oil) in the sample, S<sub>1</sub> and the number of hydrocarbons generated through thermal cracking of nonvolatile organic matter, S<sub>2</sub> for Nkporo Formation is poor which has an average of 0.07 and 0.05 respectively (Table 2a). The average value of S<sub>1</sub>, and S<sub>2</sub> of Enugu Shale samples, are 0.09 and 1.92 respectively. These values indicate that Enugu Shale is a poor quality source rock for generation of hydrocarbon (Table 2b). This conclusion is confirmed by the result of the plot of S<sub>2</sub> versus TOC (wt %) (Fig. 3) [27-28].

### 4.2. Generation potential

The generation potential (GP) is the sum of the values S<sub>1</sub> and S<sub>2</sub>. According to Hunt [26], source rocks with a GP < 2, from 2 to 5, from 5 to 10 and >10 are considered poor, fair, good and very good generation potential, respectively. The relationship between (S<sub>1</sub>+S<sub>2</sub>) and TOC (wt%) [27,29] shows that the Nkporo Formation and the Enugu Shale samples are considered as poor to fair source potential (Fig. 4). The average generation potential for Nkporo Formation is 1.22mg/g which indicates a poor source potential, while that of Enugu Shale has an average generation potential of 2.01mg/g which indicates a fair source potential. The hydrocarbon yield is derived from the plot of genetic potential, GP against calculated vitrinite reflectance,

%Ro which shows that the two samples from Nkporo Formation (NKP/03 and NKP/06) and Enugu Shale (ENU/24 and ENU/25) indicates oil; eight samples from Nkporo Formation (NKP/01, NKP/08, NKP/15, NKP/16/002, NKP/16/004, NKP/16/008, NKP/17/001, NKP/17/001 and NKP/17/003) and three samples from (ENU/22, ENU/23 and ENU/27) indicates gas; another eight samples from Nkporo Formation (NKP/02, NKP/04, NKP/06, NKP/09, NKP/10, NKP/12, and NKP/13) and one sample from Enugu Shale (ENU/21) indicates gas potential; one sample from Enugu Shale (ENU/20) indicates oil potential (Fig. 5).

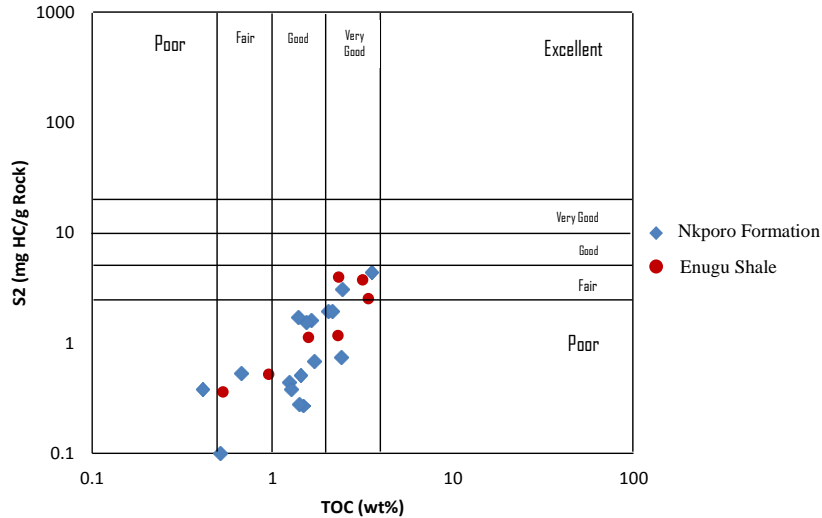
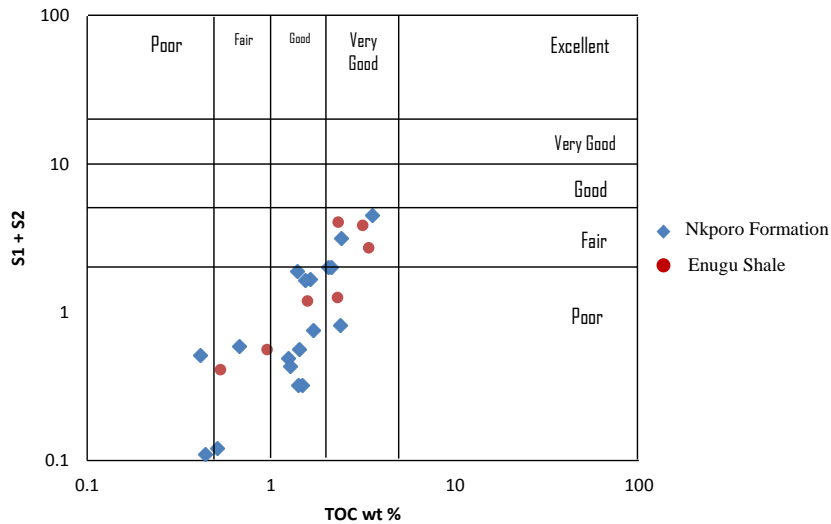


Fig. 3. Plot of S2 versus TOC (wt%) demonstrate the quality and quantity of hydrocarbon of Nkporo and Enugu Formations [28]



capable of generating mixed gas and oil. Hydrogen indices between 300 and 600 mg HC/g contain a substantial amount of type II kerogen and thus are considered to have good source potential for generating oil in the marine environment. Hydrogen indices >600 mg/g usually consist of type I kerogen and thus have excellent potential to generate oil in the lacustrine environment.

In this study, Langford and Blanc-Valleron kerogen type diagram were used to represents the plot of S2 versus TOC (Fig. 6). This diagram shows that the studied samples for Nkporo Formation are characterized by kerogen of type III and type IV having mostly an atomic H/C of <0.7, while that of Enugu Shale is characterized mostly by type III which have an atomic H/C between 0.7 and 1.0.

Based on pyrolysis data, kerogen classification diagrams were constructed using the Hydrogen Index (HI) versus Oxygen Index (OI), which is used to determine the kerogen type (Fig. 7). The results show that the analyzed Nkporo Formation samples are of type III and IV kerogen which is predominantly inert, while the analyzed Nkporo Shale samples are of type III kerogen which is gas prone. Hydrogen Index, HI for Nkporo Formation and Enugu Shale have an average value of 65.72mg HC/g TOC and 87.2972mg HC/g TOC respectively which indicates gas prone.

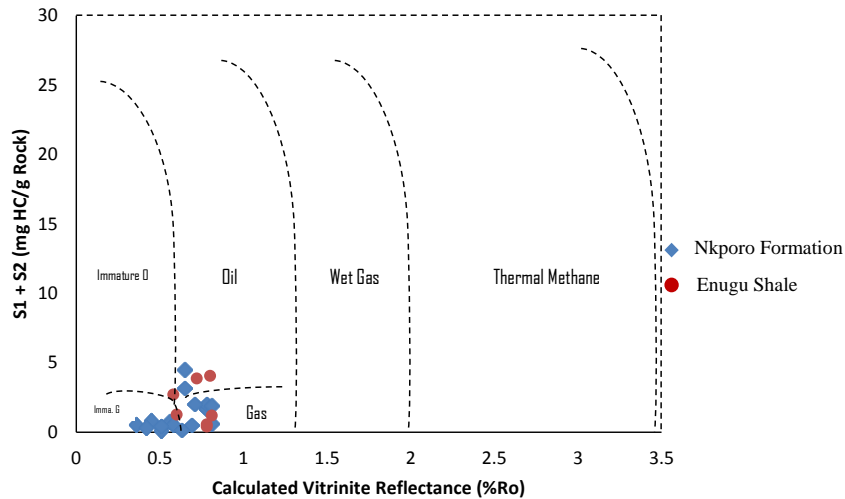


Fig. 5. Plot of GP (S1 + S2) versus Calc. %Ro of the Nkporo and Enugu Formations

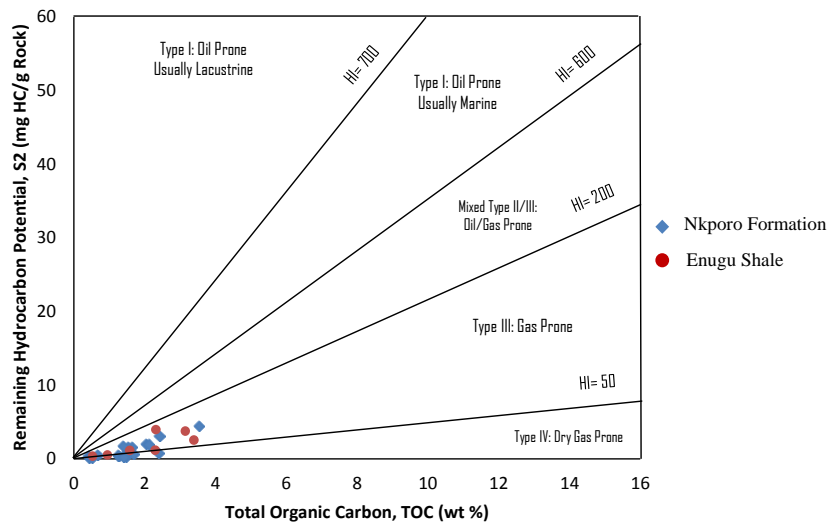


Fig. 6. Plot of S2 versus TOC (wt%) to identify the kerogen quality/ type of hydrocarbon produced from the source rock of the Nkporo Formation [30]

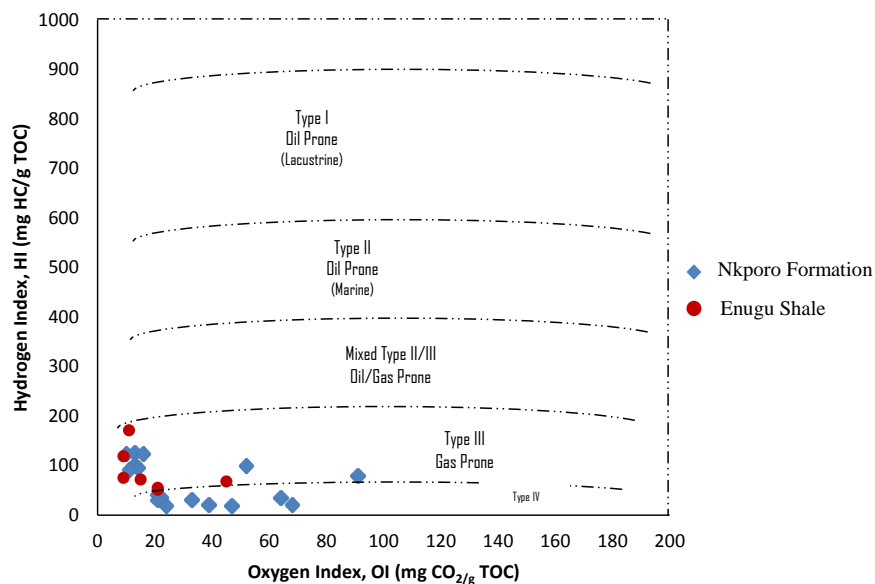


Fig. 7. Plot of Hydrogen Index (HI) versus Oxygen Index (OI) indicating the type of kerogen available in the source rock of Nkporo Formation samples [28]

#### 4.4. Thermal maturity of organic matter

The generation of petroleum from the organic matter during its burial history is a part of the overall process of thermal metamorphism of organic matter [4]. The concentration and distribution of hydrocarbons contained in a particular source depend on both the type of organic matter and its degree of thermal alteration [4,27,30]. In the present study, the thermal maturity level of the source rocks has been determined by the study of the geochemical parameters as Rock-Eval temperature pyrolysis "Tmax", production index "PI" [23,26,28]. Peters and Cassa, [23] reported that oil generation from source rocks began at Tmax between 435–470°C, and production index "PI" between 0.10 to > 0.25, the organic matters are in immature stage when "Tmax" has a value less than 435°C, and "PI" less than 0.10 and the gas generation from source rocks began at "Tmax" greater than 470°C. Results of Hydrogen Index, HI, Tmax and Production Index, PI for Nkporo Formation and Enugu Shale samples are shown in Table 2.

Based on pyrolysis data, kerogen classification diagrams were constructed using the Hydrogen Index, HI versus Tmax plot and Hydrogen Index, HI versus calculated vitrinite reflectance was carried out by Espitalie *et al.*, [28]. These plots were used to determine the kerogen type and maturity. The plot of Hydrogen Index, HI versus Tmax shows that the analyzed Nkporo Formation samples are ranges from the immature to mature zone of type III and IV kerogen, while the analyzed Enugu Shale samples of the studied area are at the mature stage of oil window and also of type III kerogen (Fig. 8).

The plot of Hydrogen Index, HI versus calculated vitrinite reflectance shows that the Nkporo Formation samples consist of kerogen which ranges from type III and IV. Some of the samples within the type III kerogen fell into the oil window, while the analyzed Enugu Shale samples of the studied area mostly within the type III kerogen also falls into the oil window (Fig. 9).

The plot of Production Index, PI versus Tmax diagram [24,29] shows that most of the Nkporo Formation samples are immature source rocks, while the Enugu Shale samples are mature source rocks except that of sample location ENU/20 and ENU/21 which are marginally mature (Fig. 10). The plot of Production Index, PI versus calculated vitrinite reflectance, %Ro shows that studied Nkporo Formation samples range from immature to the oil window, while most of the samples gotten from the Enugu Shale are within the oil window (Fig. 11).

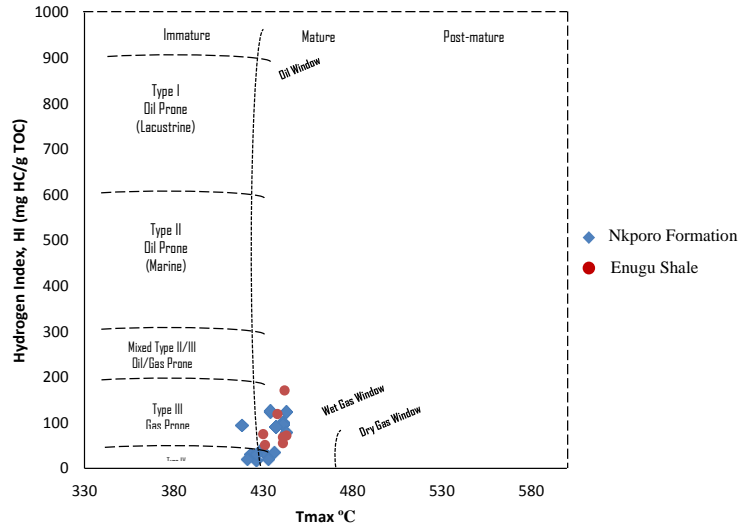


Fig. 8. Plot of Hydrogen Index (HI) versus Tmax showing the type and maturity of the Nkporo Formation samples [28]

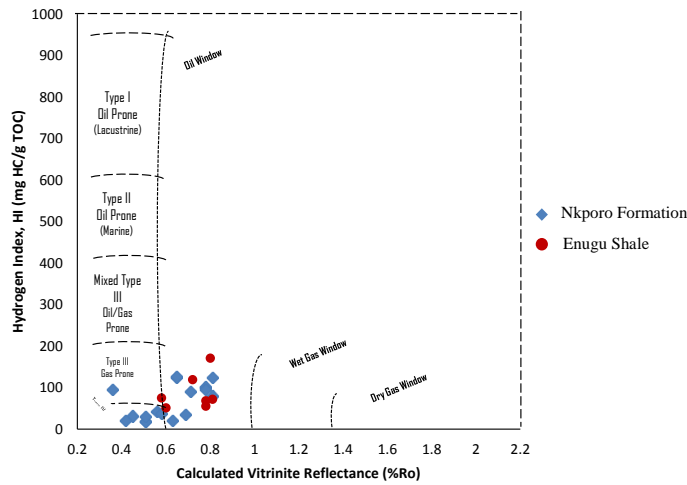


Fig. 9. Plot of Hydrogen Index (HI) versus Calculated Vitrinite Reflectance (%Ro) showing the type and maturity of the Nkporo Formation samples [28]

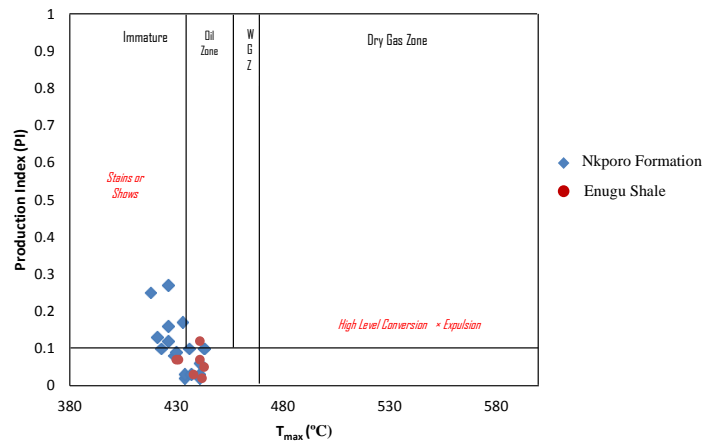


Fig. 10. Plot of Hydrogen Index (HI) versus Calculated Vitrinite Reflectance (%Ro) showing the type and maturity of the Enugu Shale samples [28]

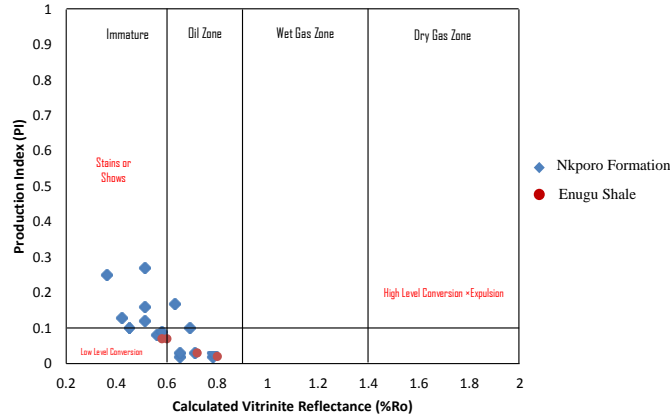


Fig. 11. Plot of Production Index (PI) versus calculated Vitrinite Reflectance (%Ro) showing the maturity of the Enugu Shale samples (Peters [24])

The average value of T<sub>max</sub> for Nkporo Formation is 432.33°C which indicates an immature stage for thermal maturity for oil (Table 4.9a), while that of Enugu Shale has an average value of 438 °C which indicates an early mature stage for thermal maturity for oil (Table 2). The average value of Production Index, PI, for Nkporo Formation is 0.10 which indicates an early maturity stage for oil, while that of Enugu Shale has an average value of 0.06 which indicates an immature stage for thermal maturity for oil. The cross-plot of T<sub>max</sub> and Calculated Vitrinite Reflectance (%Ro) can be used to further understand the thermal maturity of the source rock (Fig. 12a and b). This figure shows a positive correlation between both indices, and indicates mostly thermally mature source rock except seven shale samples which indicate thermally immature source rock in Nkporo Formation, while that of Enugu Shale indicates thermally mature source rocks.

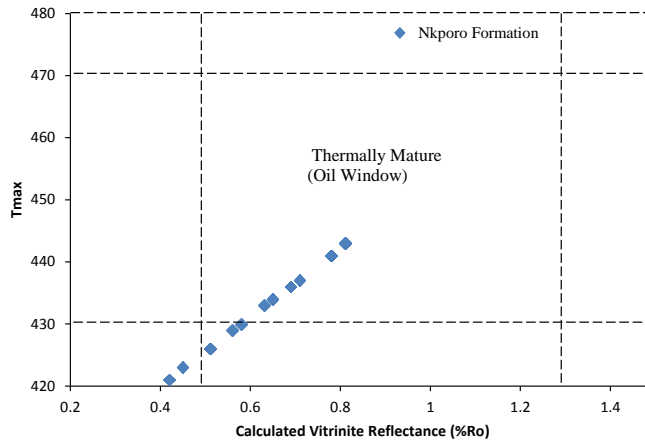


Fig. 12a. Plot of T<sub>max</sub> versus Calculated Vitrinite Reflectance (%Ro) to indicate source rock thermal maturity of Nkporo Formation samples (Qadri et al. [31])

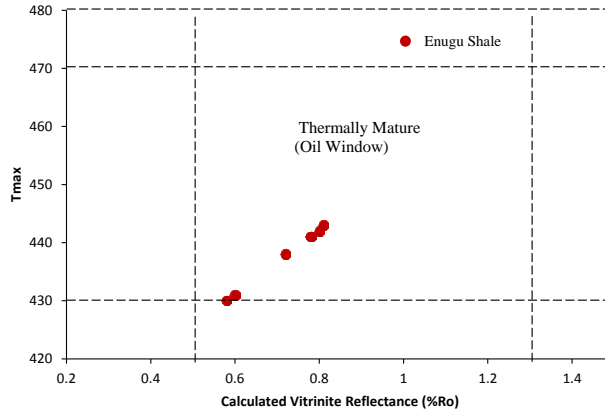


Fig. 12b. Plot of Tmax versus Calculated Vitrinite Reflectance (%Ro) to indicate source rock thermal maturity of Enugu Shale samples (Qadri et al. [31])

The summary of the interpreted result of HAWK pyrolysis on shale samples of the Campanian Nkporo Group shows that the Total Organic Carbon (TOC) content of Nkporo Shale ranges from poor to very good source rock which is mostly thermally immature and the percent of maturity is about 33.33%. The Total Organic Carbon (TOC) content of Enugu Shale ranges from fair to very good source rock which is mostly thermally mature and can yield mostly gas and little oil. The percentage maturity of Enugu Shale is about 71.47 (Table 3).

The correlation of various maturation indices and zone of petroleum generation and destruction shows that the vitrinite reflectance of Nporo Formation ranges from 0.36 to 0.81 %Ro while that of Enugu Shale ranges from 0.60 to 0.81% (Fig. 13). The Tmax of Nkporo Shale ranges from 418 to 441°C while that of Enugu Shale ranges from 430 to 443°C. You may recall that the Vitrinite Reflectance and Tmax are indicators in the maturity of organic matter and has a benchmark of 0.60%Ro and 435°C respectively which reflects the early maturity stage in the generation of hydrocarbon.

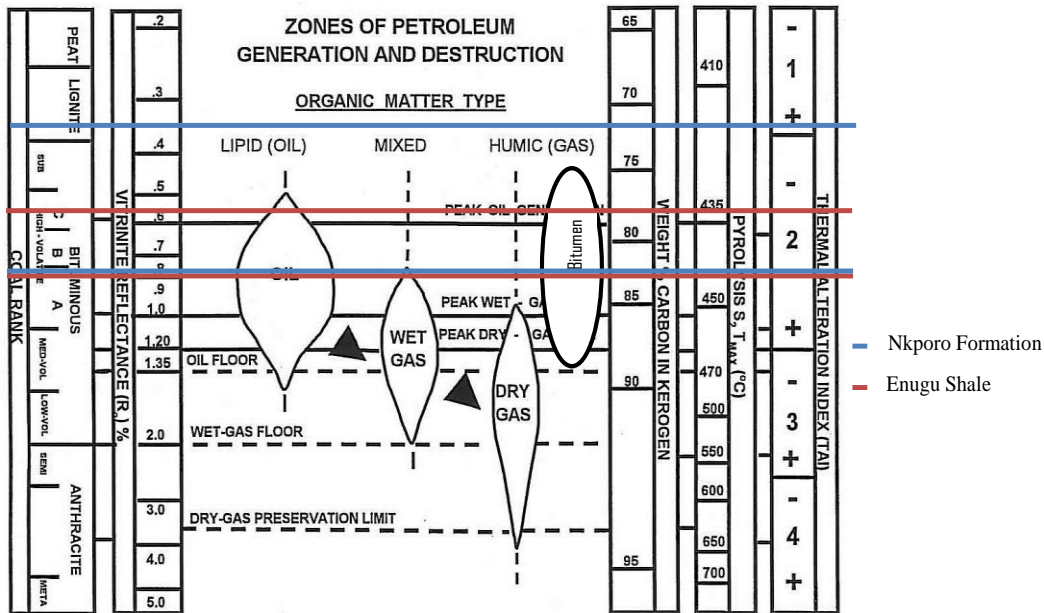


Fig. 13. Correlation of various maturation indices and zone of petroleum generation and destruction of the Nkporo and Enugu Formations (Jarvie [21])

## 5. Conclusion

From the results of the geochemical analysis, The Total Organic Carbon (TOC) contents of the Nkporo Formation and Enugu Shale varied from 0.41 to 2.42wt. % and 0.53 to 3.15 wt.% respectively. This showed that Nkporo Formation and Enugu Shale had fair to very good organic matter contents. The organic matter richness varied from 0.08 to 4.40mgHC/g for the Nkporo Formation and 0.36 to 3.97mgHC/g for the Enugu Shale. Hydrogen Index versus Oxygen Index plots and visual kerogen showed that the Nkporo Formation was of Type III/IV while Enugu Shale was of Type III kerogen. The Thermal maturity index (Tmax) of the Nkporo Formation and Enugu Shale varied from 418 to 443°C and 430 to 443°C respectively. These suggested that the Nkporo Formation was marginally mature to mature while Enugu Shale was mature. The results of this study has shown that the source rocks of the Nkporo Formation is immature and has not generated hydrocarbon while that of the Enugu Shale is mature and has generated hydrocarbon.

## References

- [1] Akaegbobi MI. Sequence Stratigraphy of Anambra Basin. *Journal of African Earth Sciences*, 2005; 42: 394-406.
- [2] Reijers TJA. Selected Chapters in Geology, Sedimentary Geology and Sequence Stratigraphy in Nigeria and Three Case Studies and a Field Guide. SPDC of Nig. Corporate Reprographic Services, Warri, 1996; 197.
- [3] Nexant I. National oil and gas policy: A draft report prepared for the Bureau of Public Enterprises (Nigeria) by Nexant, Griffin House, In: Obaje, Wehner H, Scheeder G, Abubakar MB, Jauro A Hydrocarbon prospectivity of Nigeria's inland basins: From the viewpoint of organic geochemistry and organic petrology. *Am. Assoc. Petrol. Geol. Bull.*, 2003; 88 (3): 326-327.
- [4] Tissot BP, and Welte DH. *Petroleum Formation and Occurrence*: New York, Springer-Verlag, 1984; 699.
- [5] Unomah GI. Petroleum evaluation of Upper Cretaceous Shales in Lower Benue Trough, Nigeria, Unpublished Ph. D. Thesis, Univ. of Ibadan, Ibadan Nigeria, 1989; 164
- [6] Unomah GI, and Ekweozor CM. Petroleum Source Rock Assessment of the Campanian Nkporo Shale, Lower Benue Trough, Nigeria. *Nigeria Association of Petroleum Explorationist Bulletin*. 1993; 8: 172-186.
- [7] Akaegbobi MI, and Schmitt M. Organic facies, Hydrocarbon Source Potential and the Reconstruction of the Depositional Paleoenvironment of the Campano- Maastrichtian Nkporo Shale in the Cretaceous Anambra Basin, Nigerian. *Nigeria Association of petroleum explorationist*, 1998; 19: 1-19.
- [8] Obaje NG, Wehner H, Scheeder O, Abubakar MB, Jauro H. Hydrocarbon prospectivity of Nigeria's inland basins: from the view point of organic geochemistry and organic petrology. *AAPG Bull.* 2004; 87: 325-353.
- [9] Ekweozor CM. Investigation of Geohistory of Anambra Basin, part 5 case history 3," in *Basic Geochemistry*, Lecture Presented at the Oil and Gas Academy, Port Harcourt, 2006; 210-215.
- [10] Anozie HC, Chiaghanam OI, and Chiadikobi KC Source Rock and Thermal Maturation of Campanian Enugu Shale in Anambra Basin, Southeastern Nigerian. *Intl. Journal of Geol., Earth and Environmental science*, 2014; 4 (3): 296-307.
- [11] Nwajide CS. Cretaceous Sedimentation and Paleogeography of the Central Benue Trough. In Ofoegbu, C.O; (Ed.), *The Benue Structure and Evolution*. International monograph series, Branschweig, 1990; 19-38.
- [12] Reyment RA. *Aspects of the geology of Nigeria: The stratigraphy of the Cretaceous and Cenozoic Deposits*. University of Ibadan press, Nigeria, 1965; 145.
- [13] Obi GC. Okogbue CO, and Nwajide CS. Evolution of the Enugu cuesta: A tectonically driven erosion process: *Global journal of pure and Applied science*, 2001; 7: 321-330.
- [14] Kogbe CA. The Cretaceous and Polygene Sediments of southern Nigeria: In: Kogbe C.A. (Ed.) *Geology of Nigeria*. Elizabeth publ., Lagos, Nigeria, 1989; 273-286.
- [15] Obi GC. Depositional model for the Campanian-Maastrichtian succession, Anambra Basin, Southeastern Nigeria. Unpublished Ph.D thesis, University of Nigeria, Nsukka, Nigeria, 2000; 291.
- [16] Arua I. Borings and shell damage in Eocene Gastropoda: Southeastern Nigeria, *Paleoclimatology and Paleoecology*, 1988; 13: 120-126.

- [17] Okoro AU. Depositional History of the Sandstone Facies of the Nkporo Formation (Campanian-Maastrichtian) in Leru Area, Southeastern Nigeria, *Journal of Mining Geology*, 1995; 31 (2): 105-586.
- [18] Zaborski P. Stratigraphy and Structure of the Cretaceous Gongola Basin, Northeast Nigeria. *Bulletin du Centre de Recherches Elf Exploration Production*, 1983, 21 (1): 153-185.
- [19] Nwajide CS. Geology of Nigeria's sedimentary Basin. *CSS Bookshops*, 2013; 277-518.
- [20] Ekwenye OC, and Nichols G. Depositional Facies and Ichnology of a Tidally Influenced Coastal Plain Deposit: The Ogwashi Formation, Niger Delta Basin. *Arabian Journal of Geosciences*, 2016; 9: 1-27.
- [21] Jarvie DM. Shale Resource Systems for Oil and Gas: In: Breyer, J. A., *Shale Reservoirs Giant Resources for the 21st Century: AAPG Memoir*, 2012; 97: 69 – 87.
- [22] Jarvie DM. Total Organic Carbon (TOC) analysis. In: Merrill, R.K., (ed.), *Treatise of petroleum geology. Handbook of Petroleum geology, source and migration processes and evolution techniques*. AAPG Bulletin, 1991; 113-118.
- [23] Peters KE, and Cassa MR. Applied source rock Geochemistry. In: *the petroleum system from source to trap*. Magoon, L.B. and Dow, W.G. (editors). AAPG memoir, 1994; 60: 93-117.
- [24] Peters KE. Guidelines for Evaluating Petroleum Source Rocks using programmed Analysis. *AAPG Bulletin*, 1986; 70: 318-329.
- [25] Hedberg DM, and Moody JO. Petroleum Prospects of Deep Offshore. *AAPG Bulletin*, 1979; 63: 286-300.
- [26] Hunt JM. 1996. *Petroleum Geochemistry and Geology*: Freeman, W.H., San Francisco, 617.
- [27] El Nady MM, Ramadan FS, Hammad MM and Lotfy NM. Evaluation of organic matters, hydrocarbon potential and thermal maturity of source rocks based on geochemical and statistical methods: Case study of source rocks in Ras Gharib oilfield, central Gulf of Suez, Egypt. *Egypt. J. Pet.*, 2015; 24 (2): 203-211.
- [28] Espitalie J. Deroo G, and Marquis F. Rock-Eval Pyrolysis and its Application, *Inst. Fr. Petrol.*, 1985; 72.
- [29] Waples DW. *Geochemistry in Petroleum Exploration*. Inter. Human Resources and Develop. Co., Boston, 1985; 232.
- [30] Longford FF, and Blanc-Valleron MM. Interpreting Rock-Eval Pyrolysis Data using Graphs of Pyrolyzable Hydrocarbons vs. Total Organic Carbon, *AAPG Bull.*, 1990; 74: 799-804.
- [31] Qadri ST, Shalaby MR, Islam MA, and Hoon LL. Source rock characterization and hydrocarbon generation modeling of the Middle to Late Eocene Mangahewa Formation in Taranaki Basin, New Zealand. *Arabian J. Geosci.* 2016; 9 (10): 8-9.

---

*To whom correspondence should be addressed: K. C. Chiadikobi, Department of Geology, Faculty of Physical Sciences, Chukwuemeka Odumegwu Ojukwu University, Uli, Anambra State, Nigeria, [kinsomino@yahoo.com](mailto:kinsomino@yahoo.com)*

SIGNIFICANCE OF SPECTROSCOPIC CHARACTERIZATION FOR DETERMINING DEPOSITIONAL ENVIRONMENT OF ORGANIC MATTER IN SOME DEVONIAN SHALE

*Syed Muhammad Ibad, Eswaran Padmanabhan*

*Department of Geosciences, Faculty of Geoscience and Petroleum Engineering, Universiti Teknologi PETRONAS, Bandar Seri Iskandar, 31750 Tronoh, Perak, Malaysia*

Received July 20, 2018; Accepted November 12, 2018

---

## Abstract

The aim of this paper is to show the possibilities of applying the quick FTIR molecular vibrational spectroscopy with ATR technique and UV-Vis spectroscopy to determine the depositional environment of organic matter in shale with its infrared and ultraviolet spectra. The technique is employed for 20 shale rock samples of the Timah Tasoh (TT) formation (Lower Devonian), which was collected from the Sanai Hill A located at Kampung Guar Jentik, Beseri District, Perlis, Malaysia. Spectroscopic characterization was carried out to explore the hydrocarbon distribution and type of humic substances present in these shales. The FTIR spectra of the shale samples from TT formation are divided into three zones, -OH groups stretching vibration, Alkyne C-H bending bands in aliphatic hydrocarbons and the absorption spectrum of aromatic OPCH stretching and aromatic IPCH stretching bands. In this paper, particular attention is devoted to the OPCH bending vibrations between 690 and 900  $\text{cm}^{-1}$ . The absorbance values of aromatic OPCH, in shale of TT formation, is in the range of 0.11-0.19. In terms of the E4/E6 ratio which was treated with methanol and DCM, TT formation shows the dominance of humic acid within the samples. The E4/E6 ratio treated with methanol and DCM in TT Formation ranges from 0.78 to 1.31 and 0.98 to 1.67 respectively. Alkyl naphthalenes have found in all samples of FTIR spectra at 690  $\text{cm}^{-1}$ (w), 775  $\text{cm}^{-1}$ (s), 795  $\text{cm}^{-1}$ (s) and 832  $\text{cm}^{-1}$  (w) bands in OPCH bending vibrations, suggesting their sourcing mainly from terrestrial organic matter. Humic acid presence in TT formation shale supports the FTIR results and indicates that the organic matter in these shales contains plant derived hydrophilic minerals i.e. terrestrial in origin.

**Keywords:** *Spectroscopy; Depositional environment; Organic matter; Shale; Humic acid.*

---

## 1. Introduction

FTIR spectroscopy is a frequently used technique capable of differentiating the hydrocarbon functional group in shale or coal [1]. The functional groups of aromatic and aliphatic hydrocarbons can be determined. This can be done through the vibrational characteristics of their structural, chemical bonds. The use of ATR accessories, by those using very hard crystals (like germanium, silica, zinc selenide and diamond) characterized by their range of hardness values and optical properties, has further advanced the use of FTIR in soils, shale, and coal [2]. Dilution with KBr is no longer necessary, reproducibility is increased, and the nondestructive nature of this analysis allows the sample to be re-used for other analyses. Like FTIR, UV-Vis is increasingly employed for in-field applications [3-5] for laboratory studies of crude oils and in determining the type of humic substance [6-7]. For the organic chemist, UV-Vis is mostly concerned in conjugated systems with electronic transitions; the intensities and positions of the absorption band largely depend on the specific system under consideration [8].

Alkyl naphthalenes are widespread constituents of geological and geochemical materials. They are commonly found in oils and various types of sedimentary rocks such as shales and coals [9-12]. It has been suggested that alkyl naphthalenes are derived mainly from the de-functionalization of terpenoids, so they have the potential to provide information about their

precursor, as well as depositional environment [9-15]. However, the presence of the alkyl naphthalenes by using FTIR spectra in shale rocks has not been commonly carried out. In the present study, shales were collected from the Timah Tasoh (TT) Formation located at Sanai Hill. There is a lack of data available on literature that focused on the spectroscopic characterization of the shales in the TT formation. Furthermore, spectroscopic methods such as UV-Vis and ATR-FTIR have been used in the evaluation of liquid petroleum yield of hydrocarbon source rocks [16-18]. However, the spectroscopic analysis used for the origin of organic matter in the source or reservoir rocks have received very little attention to date. Therefore, the objective of the present study is to use spectroscopic analysis and obtain the hydrocarbon distribution and humic substance type, which will determine the source depositional environment of organic matter in shale.

## 2. Study area

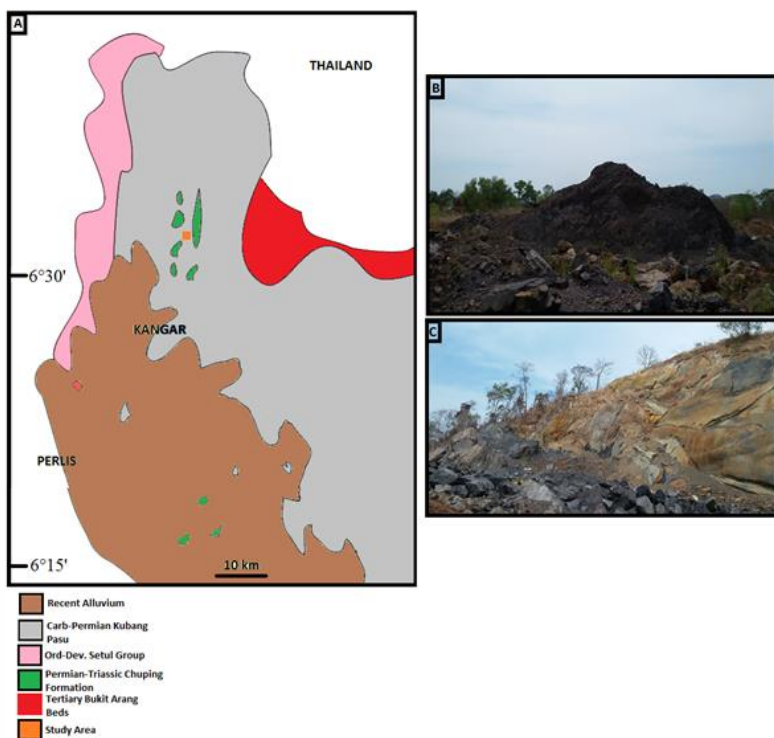


Figure 1. Study area. (A) General Geological Map of Perlis. (B,C) Timah Tasoh Shale beds from Kampung Guar Jentik outcrops

The Timah Tasoh Formation conformably overlies pelagic limestone of the Silurian Mempelam Limestone and ranges between 5 to 40 m in thickness. It comprises dark to mudstone, with occasional cherts. The Timah Tasoh Formation exposed at Sa-nai Hill A, B and C, Hutani Aji and Pulau Langgun, Langkawi [19-20]. In the present study shale from Timah, Tasoh formation has been collected from Sanai Hill A (Figure 1). At the North East of Hutani Lipur Bukit Ayer in Kampung Guar Jentik, Berseri District, Perlis of Peninsular Malaysia, just south of Timah Tasoh Dam, the study area is located. It is about 16 km north of Kangar. The samples were collected from the outcrop which is located at the coordinates of 6°33'18.00"N 100°12'24.00"E (Fig. 1).

## 3. Samples and methods

At the Timah Tasoh formation, 20 samples of shale were handpicked through channel sampling by using the method mentioned in [21] from exposures that were not weathered. All samples were ensured that weathered exposures are removed by eliminating the surface material. The rock samples were all air dried to remove any moisture present in the sample. Colors of shale are varying from medium light gray to dark. All samples were crushed into fine grains (2mm). Coning and quartering sub-sampling method were used to homogenize all of the samples; this is to ensure that the samples are homogenized and reduce bias results as well as increased the accuracy of the data [22]. These samples were then used to carry out spectroscopic characterization by using Attenuated total reflectance (ATR) Fourier transform infrared spectroscopy (FTIR) and Ultraviolet-Visible Spectroscopy (UV-Vis).

Infrared measurements were made using a Cary 660 Series FTIR Spectrometer equipped with PIKE MIRACLE diamond attenuated total reflectance spectroscopy (ATR). Data collection

was done using the Resolutions Pro software package which was also used for background and automatic baseline correction of all spectra. Spectra were acquired at transmittance mode from 16 coadded scans between 4000 and 400  $\text{cm}^{-1}$  at a resolution of 4  $\text{cm}^{-1}$ , then area normalized prior to further analysis. The limit of detection of the instrument is 0.08%. Background scans were collected using the same settings as the sample analyses. Replicate spectra collected on selected samples showed consistent peak positions and absorbance intensities. The data collected was further analyzed using the software called Essential FTIR. The area percentage of hydrocarbon functional groups was calculated by summing the absorbance intensities between the respected wavelength [23].

The ultraviolet-visible (UV-Vis) is used in analytical chemistry. The main purpose for UV-Vis is mainly to study the E4/E6 ratio. E4 is determined at the absorption frequency of 465 nm, and E6 is determined at the absorption frequency of 665 nm. For identifying the type of humic substance dichloromethane and dichloromethane: methanol was used as a solvent. Both chemical reagents and solvents had a high degree of purity and were used without prior purification. The spectra in the UV-VIs were obtained according to procedures described in Cunha *et al.* [24]. This study evaluated the nature of humic material by determining the E4/E6 ratio. The U.S. EPA method 3550 was used. 2.0g of each sample was weighed and treated with 8ml of methanol each. Later, 3 minutes of ultrasonic stirring was carried out followed by 5 minutes of centrifugation. The extraction of each of the 10 samples was analyzed using Shimadzu UV-3150 UV Vis Spectrophotometer by placing the liquid samples in quartz cells. The range of the scanning wavelength was 400 nm- 700 nm.

## 4. Results

### 4.1. Ultraviolet-Visible spectroscopy

It is suggested that the values of the relationship E4/E6 for humic acid are smaller than 5.0 and between 6.0 and 8.0 for fulvic acids [24]. In term of the E4/E6 ratio which was treated with methanol and DCM, TT Formation shows the dominance of humic acid within the samples (Table 1). The value of E4 and E6 that are treated with methanol and DCM are range from 0.05 to 2.91, 0.04 to 2.73 and 0.08 to 1.98, 0.06 to 2.22 respectively. Almost equal values of E4 and E6 also indicate the presence of humic acid in TT Formation. The E4/E6 ratio treated with methanol and DCM in TT Formation ranges from 0.78 to 1.31 and 0.98 to 1.67 respectively (Table 1).

Table 1. UV-Vis results of shale from TT Formation treated with methanol and DCM

Sample	Absorbance in methanol			Absorbance in DCM			Sample	Absorbance in methanol			Absorbance in DCM		
	E4	E6	E4/E6	E4	E6	E4/E6		E4	E6	E4/E6	E4	E6	E4/E6
TT-1	2.91	2.73	1.07	0.12	0.11	1.11	TT-11	1.87	1.66	1.13	0.24	0.22	1.08
TT-2	0.14	0.11	1.26	0.22	0.13	1.67	TT-12	2.64	2.47	1.07	0.21	0.21	0.98
TT-3	0.50	0.46	1.08	0.21	0.14	1.51	TT-13	0.39	0.32	1.23	0.21	0.17	1.20
TT-4	0.10	0.08	1.21	0.23	0.23	0.97	TT-14	0.27	0.23	1.14	0.79	0.78	1.01
TT-5	0.81	0.73	1.11	0.15	0.14	1.05	TT-15	0.05	0.04	1.26	0.15	0.12	1.24
TT-6	1.12	1.02	1.09	1.58	1.50	1.05	TT-16	0.05	0.04	1.31	0.13	0.11	1.23
TT-7	2.38	2.09	1.14	0.68	0.80	0.85	TT-17	0.04	0.03	1.23	0.13	0.11	1.24
TT-8	0.40	0.33	1.21	1.98	2.22	0.89	TT-18	0.04	0.06	0.78	0.14	0.11	1.22
TT-9	0.76	0.62	1.23	0.72	0.74	0.98	TT-19	0.11	0.09	1.19	0.08	0.07	1.26
TT-10	1.62	1.50	1.08	0.10	0.07	1.46	TT-20	0.95	0.91	1.04	0.08	0.06	1.29

### 4.2. Fourier transform infrared spectroscopy

The ATR-FTIR analysis was conducted to characterize the functional groups in the shale. The FTIR spectra of the shale samples from TT Formation is divided into three zones, -OH groups stretching vibration, Alkyne Aliphatic =C-H bending in Aliphatic hydrocarbons and the absorption spectrum of Aromatic In plane C-H (IPCH) bending and Aromatic out-of-plane C-H (OPCH) bending (Table 2 and Figure 2).

Table 2. Functional groups identified through FTIR spectra of the shale in the TT formation

Samples	Alkyne APH 700–600 =C–H bend- ing Absorbance	Aromatic bending 900–690 Out-of-plane C–H bending Absorbance	Aromatic bending 1275–1000 In-plane C–H bending Absorbance	Aromatic C=C stretch- ing 1430-1650 Absorbance	-OH Stretching 3600-3000 Absorbance
TT-1	0.069	0.112	0.159	0.011	0.015
TT-2	0.098	0.153	0.225	0.013	0.020
TT-3	0.150	0.182	0.266	0.016	0.023
TT-4	0.134	0.173	0.247	0.010	0.016
TT-5	0.097	0.129	0.195	0.007	0.014
TT-6	0.145	0.191	0.268	0.013	0.018
TT-7	0.133	0.171	0.253	0.020	0.015
TT-8	0.142	0.177	0.251	0.016	0.018
TT-9	0.141	0.162	0.234	0.017	0.018
TT-10	0.155	0.197	0.280	0.020	0.023
TT-11	0.162	0.195	0.274	0.021	0.024
TT-12	0.134	0.144	0.210	0.018	0.021
TT-13	0.147	0.179	0.252	0.020	0.018
TT-14	0.119	0.127	0.202	0.023	0.015
TT-15	0.089	0.158	0.225	0.037	0.020
TT-16	0.104	0.191	0.266	0.034	0.021
TT-17	0.069	0.131	0.302	0.120	
TT-18	0.098	0.125	0.262	0.133	
TT-19	0.150	0.158		0.037	
TT-20	0.134	0.191		0.034	

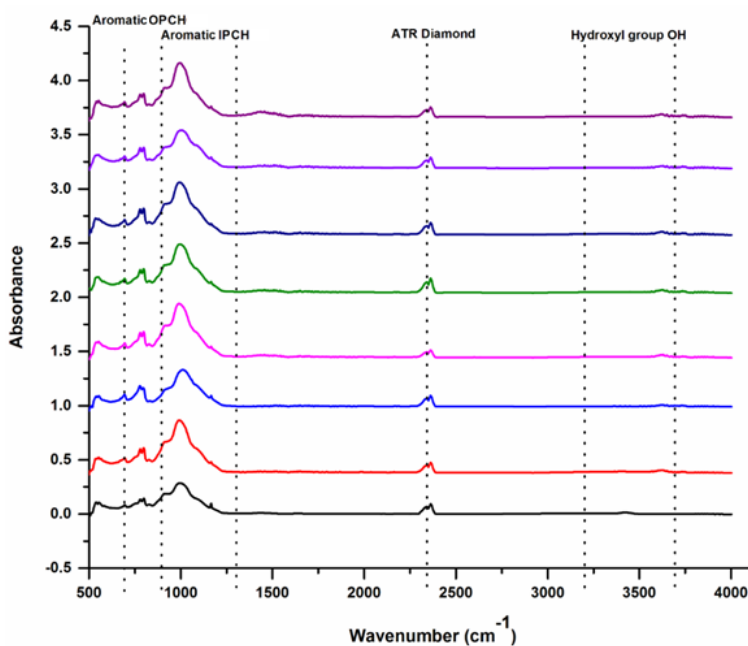


Figure 2. FTIR spectra of few shale samples from the TT Formations in the wavenumber 4000-500  $\text{cm}^{-1}$ , showing the Aromatic OPCH bending bands, Aromatic IPCH bending bands, ATR Diamond and -OH stretching bands



The critical region of the infrared spectrum for assessing alkyne C-H bending bands in aliphatic hydrocarbon is 600-700  $\text{cm}^{-1}$ . Aromatic OPCH bending appears in the regions 900–690  $\text{cm}^{-1}$  and Aromatic in plane C-H bending observed in the region of 900-1250  $\text{cm}^{-1}$ . Intensity peak of free OH-compounds is detected in the region of 3700–3200  $\text{cm}^{-1}$  [25-28]. All samples of shale in TT Formation contains alkyne C-H bending bands, aromatic in plane C-H bending and Aromatic OPCH bending (Figure 2). The absorbance values of aromatic OPCH, aromatic IPCH and aromatic C=C stretching in shale of TT Formation are in the range of 0.11-0.19, 0.15-

0.30 and 0.007-0.133 respectively (Table 2). Only one aliphatic hydrocarbon functional group (Alkyne APH) has identified through FTIR spectra. The absorbance values of Alkyne APH in shale of TT Formation is in the range of 0.069-0.162 (Table 2). This study is focused on aromatic hydrocarbons to determine the source depositional environment of organic matter. Therefore, particular attention is given to Aromatic OPCH bending bands.

## 5. Discussion

### 5.1. Humic acid and its relation to the source of organic matter

Humic acid is one of the organic constituents of oil shale. It has been considered to be a major kerogen precursor, which in turn can be a major petroleum precursor [29]. Humic acid deposited in shale as the death of thick growth of vegetation, it accumulated in large piles, and as geological time passed, it was buried from rock and mudflows and deposits of sand and silt. The weight of the overflow compacted or compressed out all the moisture, and what remains today is a deposit of dried, prehistoric plant derivatives. Therefore, the presence of humic acid in TT formation shale indicates that these shales contain plant derived hydrophilic minerals which are very small in size compared to metallic minerals which come from the ground up rocks and soil. It is suggested that a higher degree of aromaticity of humic acid in shale was evidenced by lower E4/E6 ratio [24]. Therefore, we predicted that four samples (TT-15-18) of TT formation, which shows relatively low absorbance values of E4/E6 (Table 2), indicating the degree of aromaticity is much higher in these samples as compared to other samples.

### 5.2. Alkyl Naphthalenes and its relation to the source of organic matter

Some of the aromatic compounds found in crude oils and sediments are believed to have been derived from a modification of biologically produced compounds such as steroids and terpenoids. Steroids give rise to substituted phenanthrenes, and terpenoids appear to produce alkylnaphthalenes. The processes by which higher plant triterpenoids in sediments are converted into aromatic hydrocarbons have been proposed to commence with loss of the C-3 oxygen functionality, followed by sequential aromatisation from the A ring through to the E ring the ultimate products of this process would, therefore, be tetracyclic and pentacyclic aromatic hydrocarbons [30]. Alkyl naphthalenes are derived from various precursor compounds and their composition change with increasing thermal maturity. However, alkyl naphthalenes are often abundant in oils and sedimentary organic matter which have undergone biodegradation or thermal cracking. Alkyl naphthalenes generally occur in terrestrial oils and rocks in higher concentrations than in marine oils and rocks, suggesting their sourcing mainly from terrestrial organic matter [31].

### 5.3. The 700-900 $\text{cm}^{-1}$ region

Usually, aromatic hydrocarbons are dominated by the OPCH ( $700\text{-}900\text{ cm}^{-1}$ ) bend vibrations [32-33]. Correlations for substituted benzene rings may be applied to polynuclear aromatic compounds, but the known absorption regions for the OPCH bending vibrations must be broadened. The ranges are as follows: 4 adjacent hydrogens--( $720\text{-}780\text{ cm}^{-1}$ ), 3 adjacent hydrogens--( $780\text{-}800\text{ cm}^{-1}$ ), 2 adjacent hydrogens--( $800\text{-}910\text{ cm}^{-1}$ ), 1 hydrogen--( $860\text{-}910\text{ cm}^{-1}$ ). Although the pattern is fairly complex, these bands can be identified as the strongest in this region. Weak and medium bands are no indication as to the type of substitution. The absorption bands of the studied shale in this region are listed in Table 3 [34].

Naphthalenes substituted in the 1-position showed a doublet at  $800$  and  $780\text{ cm}^{-1}$  which can be attributed to three and four adjacent hydrogen atom vibrations. When substituents are in the 2-position, the expected band at  $900\text{ cm}^{-1}$  for a single hydrogen atom is weak. The  $900\text{ cm}^{-1}$  band varies in strength with the number of single hydrogen atoms present and is very strong when they are in the 9,10-position [35].

Table 3. Distribution of aromatic out of plane banding bonds in TT shale samples

Sample	Data	Aromatic out of plane banding			
		Pentylnaphthalene (C <sub>15</sub> H <sub>18</sub> )			
TT-1	Wavenumber (cm <sup>-1</sup> )	694.74	778.97	798.11	827.52
	Absorbance	0.08	0.14	0.14	0.09
TT-2	Wavenumber (cm <sup>-1</sup> )	694.39	778.82	797.80	827.17
	Absorbance	0.11	0.19	0.20	0.12
TT-3	Wavenumber (cm <sup>-1</sup> )	694.46	778.78	797.39	827.17
	Absorbance	0.13	0.23	0.25	0.14
TT-4	Wavenumber (cm <sup>-1</sup> )	694.07	778.70	797.23	827.37
	Absorbance	0.14	0.22	0.23	0.12
TT-5	Wavenumber (cm <sup>-1</sup> )	693.24	777.24	795.42	829.69
	Absorbance	0.11	0.19	0.17	0.05
TT-6	Wavenumber (cm <sup>-1</sup> )	694.19	778.17	797.04	827.80
	Absorbance	0.15	0.25	0.26	0.13
TT-7	Wavenumber (cm <sup>-1</sup> )	74.06	58.53	57.34	80.05
	Absorbance	0.13	0.23	0.24	0.10
TT-8	Wavenumber (cm <sup>-1</sup> )	694.35	778.17	796.96	827.72
	Absorbance	0.13	0.23	0.24	0.12
TT-9	Wavenumber (cm <sup>-1</sup> )	694.07	778.10	796.92	827.83
	Absorbance	0.13	0.21	0.22	0.11
TT-10	Wavenumber (cm <sup>-1</sup> )	694.23	778.74	797.31	827.68
	Absorbance	0.15	0.25	0.26	0.14
TT-11	Wavenumber (cm <sup>-1</sup> )	694.23	778.66	797.23	827.52
	Absorbance	0.15	0.24	0.26	0.14
TT-12	Wavenumber (cm <sup>-1</sup> )	694.07	778.74	797.43	827.48
	Absorbance	0.11	0.18	0.19	0.10
TT-13	Wavenumber (cm <sup>-1</sup> )	694.19	777.98	796.92	828.11
	Absorbance	0.14	0.24	0.24	0.12
TT-14	Wavenumber (cm <sup>-1</sup> )	694.07	778.06	797.04	828.26
	Absorbance	0.11	0.19	0.19	0.08
TT-15	Wavenumber (cm <sup>-1</sup> )		779.01	798.54	830.76
	Absorbance		0.07	0.08	0.07
TT-16	Wavenumber (cm <sup>-1</sup> )		778.97	798.62	831.15
	Absorbance		0.08	0.09	0.08
TT-17	Wavenumber (cm <sup>-1</sup> )		777.90	797.88	830.15
	Absorbance		0.11	0.11	0.08
TT-18	Wavenumber (cm <sup>-1</sup> )		778.54	798.03	831.23
	Absorbance		0.09	0.10	0.07
TT-19	Wavenumber (cm <sup>-1</sup> )	693.96	778.58	796.88	826.37
	Absorbance	0.14	0.21	0.22	0.12
TT-20	Wavenumber (cm <sup>-1</sup> )	694.31	777.94	796.81	827.80
	Absorbance	0.16	0.27	0.29	0.14

In the present study, alkyl naphthalenes (pentylnaphthalenes) confirms by the presence of two strong and two weak bands in the OPCH (700-900 cm<sup>-1</sup>) bend vibration region [34]. These are 690 cm<sup>-1</sup> (w), 775 cm<sup>-1</sup> (s), 795 cm<sup>-1</sup> (s) and 832 cm<sup>-1</sup> (w). The absorbance range of strong bands, i.e. 795 and 775 cm<sup>-1</sup> bands in TT shales between the range of 0.29-0.08 and 0.27-0.07 respectively. Weak bands of pentylnaphthalenes at 695 and 832 cm<sup>-1</sup> between the range of 0.16-0.08 and 0.14-0.05 respectively (Table 2, Fig. 3). 690 cm<sup>-1</sup> bands were absented in TT15-18 samples only (Table 2, Fig. 3). However, 710 cm<sup>-1</sup> band can be seen in these samples which show, might be 690cm<sup>-1</sup> bands were shifted due to the actual frequency shift of a single absorption band or alternatively by the relative intensity changes of overlapped bands [36]. It has also observed that the absorbance values of pentylnaphthalenes in these four samples are relatively very low as compared to all other samples (Table 2).

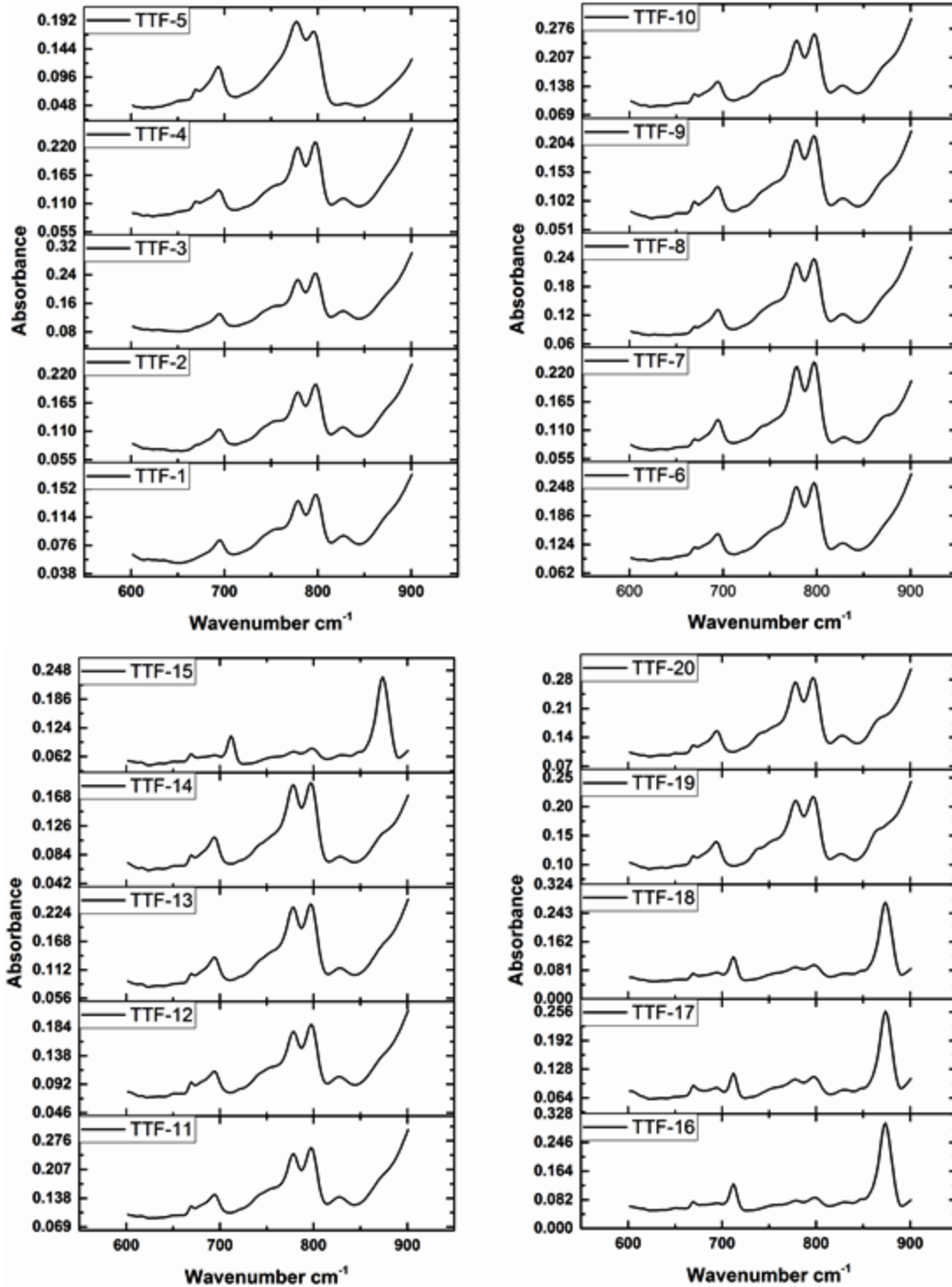


Figure 3. FTIR spectra of TT shale showing Aromatic OPCH region

## 6. Conclusions

The study showed the significance of spectroscopic techniques to determine the source depositional environments of organic matter in shale. Three divisions have been made in FTIR spectra of the shale samples from TT Formation: -OH groups stretching vibration, Alkyne C-H bending bands in Aliphatic hydrocarbons and the absorption spectrum of Aromatic OPCH and

Aromatic IPCH. Alkyl naphthalenes have found in all the samples of FTIR spectra at  $695\text{ cm}^{-1}$  (w),  $775\text{ cm}^{-1}$ (s) and  $795\text{ cm}^{-1}$ (s) and  $832\text{ cm}^{-1}$  (w) bands in OPCH bending vibrations, suggesting the terrestrial origin of organic matter. The E4/E6 ratio treated with methanol and DCM in TT Formation shows the dominance of humic acid. Presence of humic acid also indicates that the organic matter in these shales is terrestrial in origin. Only four samples (TT-15-18) show relatively low absorbance values of both humic acid and pentylnaphthalenes in FTIR and UV-Vis spectra.

### Acknowledgment

This work was supported by the PETRONAS Research Fund (PRF) grant awarded to E. Padmanabhan

### Reference

- [1] Ramer G, Lendl B. Encyclopedia of Analytical Chemistry. In: Meyers R. A. (Ed.), Encyclopedia of Analytical Chemistry, John Wiley & Sons Ltd 2006, Chichester.
- [2] Artz RRE, and Chapman SJ. FTIR spectroscopy can be used as a screening tool for organic matter quality in regenerating cutover peatlands. *Soil Biology & Biochemistry*, 2008; 40: 515–527.
- [3] Crombie A, Halford F, Hashem M, McNeil R, Thomas EC, Melbourne G, and Mullins OC. Innovations in Wireline fluid sampling. *Oilfield Review*, 1998; 10(3): 26-41.
- [4] Andrews RJ, Beck G, Castelijns K, Chen A, Cribbs ME, Fadnes FH, Irvine-Fortescue J, Williams S, Hashem M, Jamaluddin A(J), Kurkjian A, Sass B, Mullins OC, Rylander E, and Van Dusen A. Quantifying contamination using color of crude and condensate. *Oilfield Review*, 2001; 13(3): 24.
- [5] Yokota T, Scriven F, Montgomery DS, and Strausz OP. Absorption and emission spectra of Athabasca asphaltene in the visible and near ultraviolet regions. *Fuel*, 1986; 65, 1142-1149.
- [6] Strausz OP, Peng P, and Murgich J. About the colloidal nature of asphaltenes and the MW of covalent monomeric units. *Energy Fuels*, 2002; 16(4): 809-822.
- [7] Evdokimov IN, and Losev AP. Potential of UV-visible absorption spectroscopy for characterizing crude petroleum oils. *Oil and Gas Business*, 2007; 1–21.
- [8] Eglinton G. Applications of Infrared Spectroscopy to Organic Chemistry, in *An Introduction to Spectroscopic Methods for the Identification of Organic Compounds*. Volume 2. ISBN: 9781483280776.
- [9] Radke M, Willsch H, Leythaeuser D. Aromatic components of coal: relation of distribution pattern to rank. *Geochim. Cosmochim. Acta*, 1982; 46: 1831–1848.
- [10] Radke M, Leythaeuser D, Teichmuller M. Relationship between rank and composition of aromatic hydrocarbons for coals of different origins. *Org. Geochem.*, 1984; 6: 423–430.
- [11] Radke M, Welte DH, Willsch H. Maturity parameters based on aromatic hydrocarbons: influence of the organic matter type. *Org. Geochem.*, 1986; 10: 51–63.
- [12] Radke M, Rulkötter J, Vriend SP. Distribution of naphthalenes in crude oils from the Java Sea: source and maturation effects. *Geochim. Cosmochim. Acta*, 1994; 58: 3675–3689.
- [13] Bastow TP, Alexander, R., Fisher, S.J., Singh, R.K., van Aarssen, B.G.K., Kagi, R.I. Geosynthesis of organic compounds. Part V – methylation of alkylnaphthalenes. *Org. Geochem.*, 2000; 31: 523–534.
- [14] Hossain MdA, Suzuki N, Matsumoto K, Sakamoto R. (2014). In-reservoir fractionation and the accumulation of oil and condensates in the Surma Basin, NE Bangladesh. *J. Pet. Geol.*, 2014; 37: 269–286.
- [15] Sun Y, Püttmann W, Kalkreuth W, Horsfield B. Petrologic and geochemical characteristics of Seam 9-3 and 2, Xingtai Coalfield, Northern China. *Int. J. Coal Geol.*, 2002; 49: 251–262.
- [16] Maciel GE, Bartuska VJ, and Miknis FP. Correlation between oil yields of oil shale and  $^{13}\text{C}$  nuclear magnetic resonance spectra. *Fuel*, 1978; 57: 505–506.
- [17] Solomon PR, and Miknis FP. Use of Fourier transform infrared spectroscopy for determining oil shale properties. *Fuel*, 1980; 59: 893–896.
- [18] Evdokimov IN, Eliseev NYu, and Akhmetov BR. Assembly of Asphaltene Molecular Aggregates as Studied by Near-UV/Visible Spectroscopy. II. Concentration Dependencies of Absorptivities. *J. Pet. Sci. Eng.*, 2003; 37(3-4): 145-152.
- [19] Hassan MHA, Aung AK, Becker RT, Rahman NAA, Ng TF, Ghani AA, Shuib MK. Stratigraphy and palaeoenvironmental evolution of the mid- to upper Palaeozoic succession in Northwest Peninsular Malaysia. *Journal of Asian Earth Sciences*. 2014; 83: 60-79.

- [20] Hutchison CS, Tan DNK. Geology of Peninsular Malaysia. University of Malaya 2009, ISBN: 978-983-44296-9.
- [21] Coe AL. Geological Field Techniques. John Wiley & Sons 2010, ISBN 978-1-4443-3061-8,.
- [22] Gerlach RW, Dobb D, Raab GA, Nocerino JM. Gy sampling theory in environmental studies. 1. Assessing soil splitting protocols. Journal of Chemometrics. 2002; 16(7): 321-328.
- [23] Washburn KE, and Birdwell JE. Multivariate analysis of ATR-FTIR spectra for assessment of oil shale organic geochemical properties. Organic Geochemistry. 2013; 63: 1-7.
- [24] Cunha JF, Novotny EH, Madari BE, Martin-Neto L, de O Rezende MO, Canelas LP, de M Benites V. Spectroscopy Characterization of Humic Acids Isolated from Amazonian Dark Earth Soils (Terra Preta De Índio), in Amazonian Dark Earths: Wim Sombroek's Vision, W.I. Woods, et al. Springer Netherlands: Dordrecht. p. 363-372.
- [25] Mahmoodi I, Padmanabhan E. Exploring the relationship between hydrocarbons with total carbon and organic carbon in black shale from Perak, Malaysia. Pet Coal, 2017; 59(6): 933-943.
- [26] Mahmoodi SMI, and Padmanabhan E. Hydrocarbon Bond Variation in Some Shales from Batu Gajah, Malaysia, in ICIPPEG: Proceedings of the International Conference on Integrated Petroleum Engineering and Geosciences 2016, M. Awang, et al., Editors. 2017, Springer Singapore: Singapore. p. 363-371.
- [27] Stuart BH, George B, McIntyre P. Modern Infrared Spectroscopy, John Wiley & Sons Ltd 1996, Chichester, United Kingdom, ISBN10 0471959170.
- [28] Coates J. Interpretation of Infrared Spectra, A Practical Approach, in Encyclopedia of Analytical Chemistry. John Wiley & Sons, Ltd., 2006, <https://doi.org/10.1002/9780470027318.a5606>
- [29] Khalili, F (1990). Isolation and characterization of humic acid from Jordanian oil shale. Fuel. 69(2): p. 151-156.
- [30] Strachan MG, Alexander R, Kagi RI. Trimethylnaphthalenes in crude oils and sediments Effects of source and maturity, Geochimica et Cosmochimica Acta, 1988; 52(5): 1255-1264.
- [31] Asahina K, Suzuki N. Alkyl naphthalenes and tetralins as indicators of source and source rock lithology – Pyrolysis of a cadinane-type sesquiterpene in the presence and absence of montmorillonite. Journal of Petroleum Science and Engineering, 2016; 145. 657–667.
- [32] Colthup NB, Daly LH, Wiberley SE. Introduction to Infrared and Raman Spectroscopy, 3rd Ed. Academic Press 1990, San Diego.
- [33] Cataldo F, Garcia-Hernandez DA, Manchado A. Far- and mid-infrared spectroscopy of complex organic matter of astrochemical interest: coal, heavy petroleum fractions, and asphaltenes, Monthly Notices of the Royal Astronomical Society, 2013; 429(4): 11.
- [34] Wiberley SE, and Gonzalez RD. Infrared Spectra of Polynuclear Aromatic Compounds in the C-H Stretching and Out-of-Plane Bending Regions, Applied spectroscopy, 1961; 15(6): 174-177.
- [35] Cannob CG, and Sutherland GBBB. The infra-red absorption spectra of some aromatic compounds, Spectrochimica Acta, 1951; 4(5): 353-495.
- [36] Ryu SR, Noda I, Jung YM. Positional Fluctuation of IR Absorption Peaks: Frequency Shift of a Single Band or Relative Intensity Changes of Overlapped Bands. American laboratory, 2011; 43(4):40-43.

*To whom correspondence should be addressed: Syed Muhammad Ibad, Department of Geosciences, Faculty of Geoscience and Petroleum Engineering, Universiti Teknologi PETRONAS, Bandar Seri Iskandar, 31750 Tronoh, Perak, Malaysia*

EVALUATION OF WATER SATURATION MODELS IN SHALY LIMESTONE ZONE OF ASMARI FORMATION, KUPAL OIL FIELD, SW OF IRAN

*Hossein Tabatabaei*

*Department of Petroleum Engineering, Gachsaran Branch, Islamic Azad University, Gachsaran, Iran*

Received October 1, 2018; Accepted November 12, 2018

## Abstract

Fluid saturation is one of the most important parameters that is used to determine the properties of oil reservoirs. In clean formations, water saturation is calculated by Archie's relation. However, in shaly zones, Archie's formula should change, or a new model should be generated that connect saturation with petrophysical parameters of the reservoirs such as the volume of shale, effective porosity and specific resistance. This practical study has used actual well logging data from the field of South West of Iran to evaluate and compare the most popular fore shaly limestone models for calculating water saturation. In this study, water saturation was calculated by Indonesia, Waxman-Smiths, Simandoux models and CEC on Asmari reservoirs in one of the wells of Kupal oil field. The results show that shale volume models calculate the rate of water saturation more than CEC models. In smaller reservoirs zones, the use of CEC models brings results that are more realistic. Asmari formation is the main hydrocarbon reservoir in the South-West of Iran.

**Keywords:** *Petrophysics, Water saturation, CEC model, Asmari formation, Kupal oil field.*

## 1. Introduction

Porosity and saturation of fluid are important parameters that are used to determine the properties of oil and gas reservoirs [1]. One of the most important goals of the analyst is to determine a fraction of vacancies filled with hydrocarbons. The saturation is equal to the ratio of saturated vacancies volume of the fluid ( $V_h, V_w$ ) to the total volume of vacancies ( $V_t$ ). Saturation is used for water ( $S_w$ ) and hydrocarbon ( $S_h$ ) (relations 1 and 2).

$$S_w = V_w/V_t \quad (1)$$

$$S_h = V_h/V_t \quad (2)$$

Shale is the most important components of the rocks in the analyzer and have an important effect in the permeability and porosity. They have an important effect on the electrical properties of the rock due to certain electrical properties and influence the saturation.

In the clean formations (without shale), water saturation is calculated by Archie's relation [2]. In shaly formations, the negative ions of clays freely move within the formation and create conductivity. The use of Archie model [2] in determining the saturation in the shaly formation shows the amount of saturation more than the actual amount [3]. The Archie formula relates the specific resistance of the formation and saturation to each other. Assuming that only the electrolyte, which presents in the vacant spaces can have flow conductivity, and other parts of the rock are nonconductive [4], in the presence of the shale, the Archie formula should change, or should be considered under the influence of shale or there should be a new model that provides for saturation and special resistance in shaly formations.

## 2. Geological setting

The Kupal oil field is located at 66km NE of the Ahwaz City and in the middle of Dezful Embayment. This oil field is asymmetry and between Haftkel in the north, Marun in south and Ahwaz in the west. This anticline is an asymmetrical structure with NE-SW trend, and southern



percentage of lithology with respect to the distance of the point from the background lines [7]. Most of the points are in the limestone and dolomite range. Gamma ray point on the dolomite and limestone lines indicate the presence of shale, but the amount of shale has decreased in the sandstone line. This indicates an increase for shale in the lime to dolomite of Asmari formation (Figure 2).

### 4.2. Volume of shale

Different equations and models of the saturation of shaly formations are divided into two groups. These are models that are based on the percentage of shale volume and note that the effect of shale depends on the amount of shale volume in the reservoir without being associated with clay minerals. This model is not scientifically accurate because shale's volume is only used to justify the saturation [8]. The advantage of this model is that all of the necessary parameters can be obtained from the data of the graph such as total shale, Juhas, Simandoux, and Indonesia.

#### 4.2.1. Simandoux model

In 1963, Simandoux obtained this model by testing on a dry mixture of the sand and montmorillonite [9].

$$S_w = \sqrt[n]{\left[\frac{aR_w}{\phi^m}\right] \times \left[\frac{1}{R_t} - \frac{V_{sh}}{R_{sh}}\right]} \tag{3}$$

In relation 3,  $S_w$  is water saturation,  $\phi$  is total porosity,  $R_t$  is the resistance of formation,  $V_{sh}$  is shale resistance,  $R_{sh}$  is the volume of shale,  $R_w$  is specific the resistance of water,  $m$  is saturation power,  $n$  is the coefficient of cementing and  $a$  is winding factor. The percentage of water saturation frequency is 4-96 present in this model.

#### 4.2.2. Indonesia model

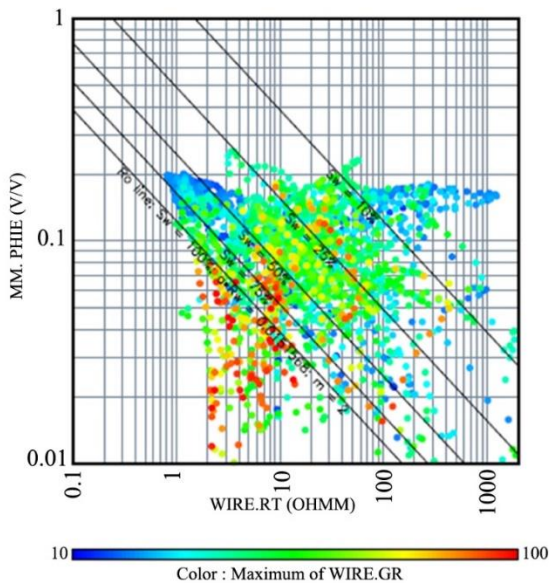


Figure 3. Water saturation ( $S_w$ ) of Asmari formation for well No.54, based on PHIE to RT

Indonesia model was presented by Poupon and Leveaux in 1971 [10] that known as Indonesia. It was presented to use in Indonesia because the presence of sweet formation water and high shale percentage caused the inefficiency of other formulas in the country. This formula states that  $V_{sh}$  has a power that is a function of  $V_{sh}$  itself.

$$S_w = \sqrt[n]{R_t \frac{1}{FR_w + 2 \sqrt{\frac{V_{sh}^{(2-V_{sh})}}{FR_w R_{sh}} + \frac{V_{sh}^{(2V_{sh})}}{R_{sh}}}}} \tag{4}$$

In (4) relation,  $S_w$  is water saturation,  $R_t$  the resistance of formation,  $V_{sh}$  shale resistance,  $R_{sh}$  shale volume,  $n$  the confidant of cementing,  $R_w$  specific resistance of water and  $F$  is formation resistance factor. The percentage of water saturation frequency has been given as 7-93 percent in Indonesia model.

In figure 3, identified the  $S_w$  of Asmari formation for well No.54, based on Indonesia model and data from PHIE, RT, and GR log.

### 4.3. CEC models

Clay minerals consist of a tetrahedral and octahedral structure of silica and aluminum. Due to the placement of cations with a low positive charge in clay sheets, a negative charge is generated in the clay. In order to neutralize this negative charge, ions with a positive charge (cations or exchange ions) accumulate at the surface of clay minerals [11]. The ability of clay mineral to form a dual electric layer is called Cation exchange capacity (CEC). To measure this property, the sample containing clay is first saturated with salty water, and then the barium solution passes from the sample. Sodium is substituted by Barium, and the amount of substitution is measurable. The amount of positive charge on the clay surface is called Cation exchange capacity (CEC). The CEC value should be measured in the laboratory and using a core. Although the CEC measurement is simple and is considered as a titration, but in the absence of core and not calculating it from the graph the use of CEC based formulation is limited. The effect of clay on the characteristics of the reservoir and Charts depends on the clay mineral in formation. According to this crossover chart and the plotted points in this formation, the type of Asmari clay minerals are mostly Illite and Montmorillonite with different percentages. Figure 4 shows the specification of the type of clay minerals in Asmari formation (Well No.54) using Th/K chart.

The use of two-layer ionic is not simple because  $Q_v$  value shows a different value in different laboratories [12].  $Q_v$  is the amount of ions that interact with shale.  $Q_v$  value is calculated according to relation (5).

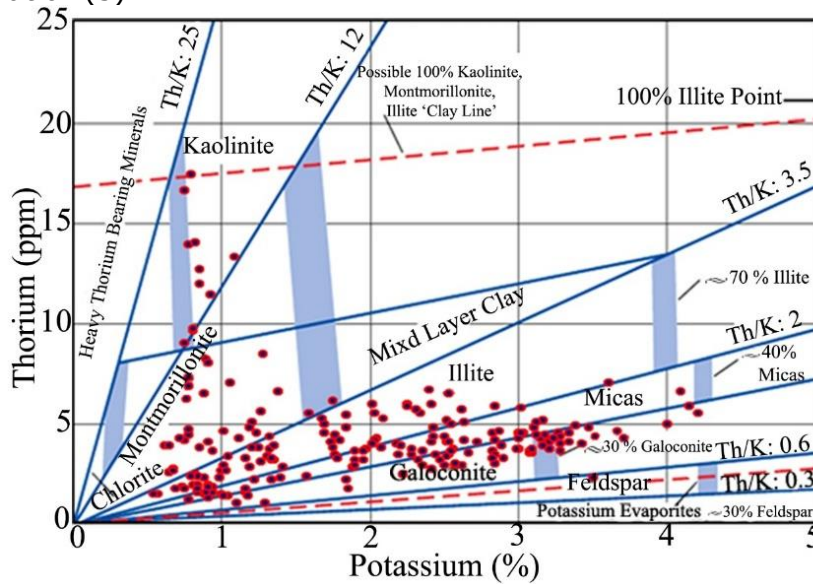


Figure 4. Identify the type of clay minerals for well No.54 in the Kupal oil field

$$Q_v = CEC(1 - \phi) \cdot \rho_{ma} \phi - 1 \tag{5}$$

In relation 5, CEC is cation exchange capacity,  $\phi$  is porosity and  $\rho_{ma}$  is the density of matrix. The values of porosity and density of the matrix are obtained from well logging, but CEC value is calculated based on the core samples, and its value is different in different wells. The result of a well cannot be generalized to other wells of the same field. This relation has many problems. For example, changing the size of the grains and the amount of cementation, the porosity value also changes [13].

This model is scientifically more acceptable. To use this model, it is necessary to calibrate the shale- dependent parameters against some petrophysical quantities of the graph such as Waxman- Smiths and dual – water models. The examination of the formation with each of these formulas may lead to a result, which is not similar to other formulas.

#### 4.4. Waxman – Smiths model

Waxman and Smiths [14] proposed an equation for the relationship between saturation and the specific resistance of the shaly formations. In this equation, additional conductivity in the rock is related to the CEC.

$$S_w^2 + BQ_v R_w S_w - \frac{aR_w}{\phi^m R_t} = 0 \quad (6)$$

In equation (6),  $S_w$  is water saturation,  $F$  is formation factor associated with the related porosity,  $B$  is equivalent to the conductivity of clay cations that contain sodium,  $\phi$  is total porosity,  $m$  is saturation power,  $a$  is winding factor,  $R_t$  is the resistance of formation,  $R_w$  is the specific resistance of water and  $Q_v$  represents CEC per unit volume of vacancies.

Parameter  $B$  in Waxman – Smiths formula is the equivalent conductivity of NaCl and is a function of temperature and concentration of the salts.

$$B = \frac{-1.28 + 0.225T - 0.0004059T^2}{1 + (0.045T - 0.27)R_w^{1.23}} \quad (7)$$

In relation (7),  $T$  is the temperature in Celsius degree, and  $R_w$  is the specific resistance of water.

Parameter  $Q_v$  is related to CEC according to relation (8).

$$Q_v = \frac{CEC \times \rho_b (1 - \phi)}{\phi} \quad (8)$$

In relation (8),  $\rho$  is total density and  $\phi$  is total porosity that can be obtained from the graphs. One of the main drawbacks of this model is that it does not take into account the absorbing properties of the clays [14]. This model calculated the percentage of water saturation frequency between 18-82 percent.

#### 4.5. Dual Water model

Clavier, Coates, and Dumenaoir presented initial dual water model in 1977, and the latest version was completed in 1984 [15]. This model is based on 3 principles:

1. the conductivity of the clay results from CEC,
2. the CEC value of the pure clay is proportional to the specific surface of the clay mineral,
3. Clay is considered as an agent clinging to the water of crystalline clay.

The mineral clay alone is insulated. The electrical conductivity of the clay minerals is due to the water clinging to them and is not related to the type of clay mineral, and is a function of temperature and salinity of the formation water [15]. According to the above three principles, the relation of dual- water is as follows.

$$S_w = \left[ \frac{(S_{wt} - S_{wb})}{(1 - S_{wb})} \right] \quad (9)$$

In relation (9),  $S_w$  is water saturation  $S_{wt}$ , is total saturation and  $S_{wb}$  is the saturated water clinging to the clays. The percentage of water saturation frequency has been calculated to be 27 to 73 percent.

#### 4.6. The comparison of water saturation models

The mean water saturation in the models of shale volume is higher than the mean water saturation in CEC models. Therefore, shale volume models show higher water saturation (Figure 5). On the other hand, in reservoir areas with low content of water and oil, the minimum water saturation in CEC models is more than shale volume models because the volume of shale is low in small reservoir areas, water saturation is measured by low shale volume models that these models don't show accurate results in small reservoir areas. In small reservoir areas, CEC models show the amount of actual water saturation because they measure this amount based on the cation exchange capacity of the clays (Figure 6).

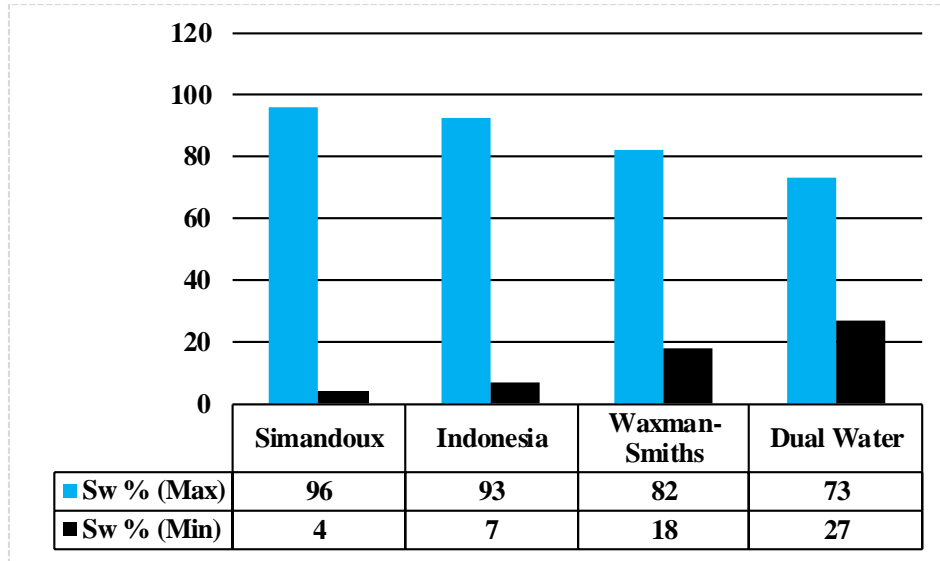


Figure 5. Water saturation percentage in fore models of water saturation

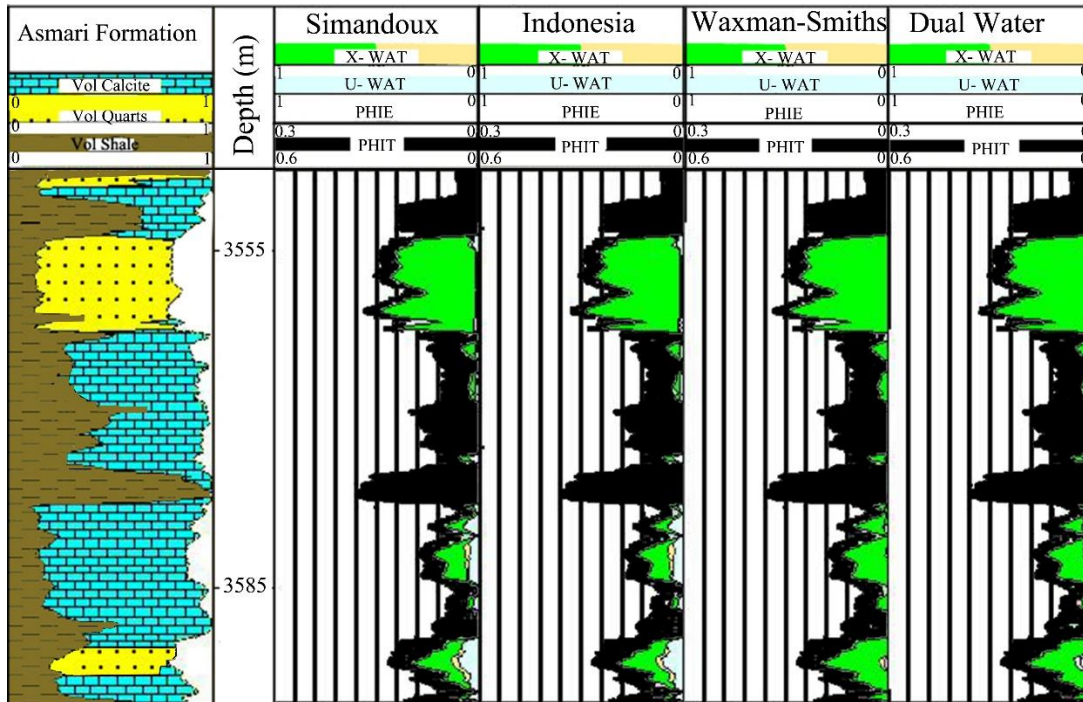


Figure 6. The mixed graph of water saturation models in Kupal oil field, well No.54.

### 5. Conclusions

The minimum and maximum percentage of water saturation frequency in Simandoux, Indonesia, Waxman-Smiths and dual- water is measured as 4-96, 7-93, 18-82 and 27-73 respectively. The mean of water saturation in shale volume models is higher than the mean of water saturation in CEC models. In reservoirs areas with low content of water and oil, shale volume models calculate the amount of water saturation higher than CEC models. In smaller reservoir areas, the results of water saturation of CEC models are closer to reality.

## References

- [1] Timur A. An Investigation of Permeability, Porosity, and Residual Water Saturation Relationships. SPWLA 9th Ann. Log. Symp. 1968, Paper SPWLA-1968-J.
- [2] Archie GE. The Electrical Resistivity as an Aid in Determining Some Reservoir Characteristics. Trans. Am. Inst. Min. Metall. Engrs., 1942; 146: 54-62.
- [3] Shazly TF, Ramadan MAM. 2011, Well logs application in determining the impact of mineral types and proportions on the reservoir performance of Bahariya formation of Bassel-1x well, western desert, Egypt, Journal of American Science, 2011; 7(1): 498-505.
- [4] El-khatib N. A fast and accurate method for parameter estimation of Archie saturation equation, Middle east oil show, Berlin 1997, SPE 37744.
- [5] Tiab D, Donaldson CE. Petrophysics, theory and practice of measuring reservoir rock and fluid transport properties, Gulf professional publishing 2044, Second edition, ISBN: 9780750677110.
- [6] Aghanabati SA. Geology of Iran, Geological survey and mineral exploration of Iran, (2003) p 586, (in Persian).
- [7] Hearst JR, Nelson PH, and Paillet FL. well logging for physical properties, John Wiley & Sons Ltd, Chichester 2000, 483p.
- [8] Rezaee M, and Chehrazi A. Principles of interpolating and interpreting of well logging graphs, Tehran University Press 2006, p 699.
- [9] Simandoux P. Mesures diélectriques en milieu poreux, application a mesure des saturations en eau, Etude du Comportment des massifs Argileux. Supplementary Issue 1963, Revue de l'Institut Français du Pétrole.
- [10] Poupon A, Leveau J. Evaluation of Water saturation in Shaly Formation, SPWLA 12th Annual Symposium 1971.
- [11] Carroll D. Ion exchange in clays and other minerals. Geological Society of America Bulletin, 1959; 70 (6): 749-780pp.
- [12] Ipek G. Log-derived Cation exchange capacity of shaly sands: application to hydrocarbon detection and drilling optimization, Ph.D. Thesis, Louisiana State University and Agricultural and Mechanical College 2002, 167p.
- [13] Fertl D, Welker W. Method for in situ determination of the cation exchange capacity of subsurface formations, U.S patent 4263509.
- [14] Waxman MH, Smits LJ. Electrical conductivities in oil bearing shaly sands, SPE-1863-A. 1968; 8(2): <http://dx.doi.org/10.2118/1863-A>.
- [15] Clavier C, Coates GR, and Dumanoir JL. Theoretical and experimental bases for the dual-water model for the interpretation of shaly sand, Society of Petroleum Geology Journal, 1984; 24(2): 153-168.

---

*To whom correspondence should be addressed: Dr. Hossein Tabatabaei, Department of Petroleum Engineering, Gachsaran Branch, Islamic Azad University, Gachsaran, Iran*

## CHARACTERIZATION OF ORGANIC MATTER IN PROCESS WATER ORIGINATING FROM CRUDE DISTILLATION UNITS OF LUKOIL NEFTOHIM BURGAS REFINERY

*Antoaneta Pavlova\**, *Dicho Stratiev*, *Ivelina Shishkova*, *Angel Nedelchev*

*LUKOIL Neftohim Burgas JSC, 8104 Burgas, Bulgaria*

Received August 14, 2018; Accepted October 19, 2018

---

### Abstract

The distribution of organic matter in process waters originating from crude distillation units of LUKOIL Neftohim Burgas refinery were determined. The organic matter was identified by gas chromatography-mass spectrometry as the oxygen-containing compounds (naphthenic acids and phenols) and the sulfur-containing species mainly cyclic polysulfides. The levels of phenol compounds and naphthenic acids species were ranged between 0.05 to 24.4 mg/L and 0.05 to 3000 mg/L, respectively. This study showed that the sulphur species were varied between <0.05 to 24.6 mg/L. The result of this research can be generalizable as the deeper understanding of the substance composition in process wastewater and a theoretical basis for their control and reused. The identification of corrosion substances in refinery effluent will be useful for the protection of the technological equipment.

**Keywords:** *naphthenic acid species (alicyclic carboxylic acids); phenolic compounds; polysulphur components; refinery process waters; gas chromatography-mass spectrometry.*

---

## 1. Introduction

During the refining process, large volumes of wastewater are generated, as their quality varies widely, and usually, their volume is up to 1.6 times the volume of the oil being processed [1]. In recent decades, due to the growing importance of crude oil for industrial development, efforts have been made to improve the management of process waters from petrochemical facilities [2-3]. In this aspect of efforts, engineers continue to seek solutions for the characterization of production waters due to the occurrence of corrosive problems related to the technological equipment in the refineries. Studying the polar compounds that raise environmental and toxic issues in the petroleum refinery business, is a major challenge to a nalytical practice and analytical control.

Wastewater from oil refineries has a significant impact on the pollution of surface water systems because they contain different amounts of hazardous pollutants [4-5]. Among the polar components of petroleum, which contain heteroatoms, are naphthenic acids and phenolic compounds - the most common oxygen-containing classes of compounds. Additionally, naphthenic acids and phenolic components have been reported as one of the corrosive substances in the refinery [6-7]. The presence of naphthenic acids and sulfur compounds significantly increase the corrosion in high temperature process parts during the distillation of petroleum [6]. Corrosive problems in refinery equipment arise during the treatment of highly acidic types of oil. Corrosion mainly affects transmission pipelines between preheating furnaces and atmospheric and vacuum distillation units. Naphthenic acids may cause corrosion problems at temperatures between 220°C and 350°C in production equipment, storage, and transport facilities [8]. In the refining process, even the presence of small quantities of naphthenic acids in crude oil can cause operational problems such as foam formation in different production units. Traditionally, naphthenic acids are defined as mono carboxylic acids, which comprise one or more saturated cyclic ring structures in their molecule. In addition, linear carboxylic acids often refer to the

naphthenic acid class [9]. One of the most important environmental pollutants is phenol and alkyl phenol derivatives. The concentration range of phenolic compounds, naturally occurring organic chemicals, in the process water worldwide ranges from 0.6 to 23 mg/L [10]. They also have their presence in wastewater from the petrochemical industry and oil refineries [11-17]. In addition to its highly corrosive property, the phenol is also a serious agent in the poisoning of the nervous system of the living organism. Phenol causes harmful side effects such as acidity in the mouth, diarrhea, disturbed vision, etc. It is a highly toxic and dangerous agent for aquatic fauna [18]. Naphthenic acids are highly toxic for a number of organisms. Low molecular weight naphthenic acids, in petroleum sands, are the most significant ecological and toxic pollutants [19-20,44].

Sulfur compounds are the most discussed and undesirable components of petroleum products during technological refining processes. In general, sulfur occurs in the form of hydrogen sulphide, organic sulphides, disulfides, polysulfides, benzothiophene, dibenzothiophene and their derivatives [21]. These compounds cause corrosion in refinery process equipment at temperatures of 230°C to 425°C [22]. Heterocyclic polysulfide species are found in petroleum wastewater, with concentrations of these substances reaching 41 mg/L [23-24].

In each case, identification of corrosion substances in refinery effluent is required and an assessment of the degree of their negative environmental and technological impact. To this end, it is necessary to identify low molecular weight naphthenic acids, phenolic, and cyclic polysulfide compounds in order to select appropriate measures for the protection of the technological equipment against possible corrosive processes and for the protection of the environment.

The characterization and structural determination of naphthenic acids from various sources have been investigated using a wide range of diverse analytical techniques and tools. The apparatus used is exclusively based on chromatographic separation by gas chromatography (GC) or high performance liquid chromatography (HPLC) methods, followed by detection by electron impact (EI) or electrospray ionization mass spectrometry (ESI) [5,26-27]. The ionization technique used depends on its compatibility with chromatographic eluates and assembled detectors, which may be high or low resolution mass spectrometers. Alternative ionization techniques for the analysis of naphthenic acids include fast atom bombardment (FAB-MS, which is used to a minor extent) or, more commonly, atmospheric chemical ionization (APCI) or photoionization (APPI) [8-15]. Many approaches for characterization of naphthenic acids include liquid extraction and reprocessing or fractionation of naphthenic acids prior to analysis, methods such as solid phase extraction (SPE), silver ion chromatography (Ag-Ion) or ion exchange chromatography (IE). Most steps include preparative gas chromatography and supercritical fluid extraction (SFE). Modern chromatographic techniques include multiple gas chromatography-mass spectrometry (GC×GC-MS), gas chromatography coupled with Fourier transformation-ionic cyclotron resonance mass spectrometry (e.g., GC-APCI FT-ICR MS and GC-TQ FT-ICR MS), liquid chromatography (HPLC) or supercritical liquid chromatography (SFC) ion-trap mass spectrometry (HPLC-or SFC-Orbitrap MS). The wide range of techniques including basic mass spectrometry is summarized in the numerous reviews and reports published over the past decade [9,25,28-34,43].

Numerous studies have demonstrated the application of gas chromatography-mass spectrometry and high performance liquid chromatography for the analysis of phenolic compounds in wastewater [8-12].

A number of publications describe applications of the gas chromatography method with the various selective detectors-mass selective detector, sulfur-selective detector, a flame-photometric detector for the analysis of a number of organic sulfur compounds [28-30].

Many of the different methods for identifying and characterizing naphthenic acids, phenolic, and cyclic polysulfide compounds have respective advantages and disadvantages, but there is currently no universal method covering both quantitative and qualitative study of these polar components. Various information about them from various sources related to various extrac-

tion and preparation procedures, derivatization methods, ionization techniques, chromatographic conditions, mass spectral parameters, and even data representation are all factors that affect the actual and final composition of naphthenic acids, phenolic and cyclic polysulfide compounds in refinery effluent [31-40].

In this project, gas chromatography-mass spectrometry is applied in the chemical characterization of organic matter in process waters originating from crude distillation units of LUKOIL Neftohim Burgas refinery. These organic matters are identified as the oxygen-containing compound (naphthenic acids and phenols), and the sulfur-containing species mainly cyclic polysulfides. The objective of the current study was also to determine the organic matter contents. The distribution of organic compounds in the process waters indicates a possible health risk to aquatic organisms. Our work will provide a deeper understanding of the substance composition in process wastewater and a theoretical basis for their control and reused.

## 2. Experimental

### 2.1. Materials, extraction

Analytical grade standard of the phenol is obtained from Merck (Bulgaria). Commercial naphthenic acids technical grade (a mixture of alkylated cyclopentane carboxylic acids) is obtained from Sigma Aldrich (Buchs, Switzerland). Dichloromethane is purchased from Merck and is Uvasol grade solvent. The extraction procedure is described in details previously [36-37].

### 2.2. Wastewater samples

Wastewater samples are gathered from the technological facilities of atmospheric-vacuum distillation unit of LUKOIL Neftohim Burgas AD (LNB), Bulgaria. Three-distillation process facilities operate in LNB: AD-4- an atmospheric distillation of crude oil, AVD-1 integrated atmospheric and vacuum distillation of crude oil and VDM-2-vacuum distillation of atmospheric residue. The wastewaters from these units generally have different origins.

### 2.3. Instrumentation

The gas chromatography-mass spectrometry (GC-MS) analyses are performed in an Agilent Technologies 7890A model gas chromatograph connected to a 5975C Inert XL EI/CI Agilent Technologies mass selective detector (Agilent Technologies, Inc., USA). GC-MS system equipped with HP PONA 50 length  $m \times 0.2$  mm id  $\times 0.5$   $\mu$ m film thickness capillary column. The helium carrier gas is kept at a constant flow rate of 0.8 mL/min, and a 1.0  $\mu$ L extract was injected into a split/splitless injector at typically temperature 300°C. Temperature programming of the column oven: 80°C and ramp with 6°C min<sup>-1</sup> to 250°C. The ion source and transfer line temperatures are 225°C and 250°C, respectively. An ionization energy 70 eV is employed with mass scanning from  $m/z$  15 to  $m/z$  450.

The components identification is based on comparisons of the retention times and by interpretation of the mass spectra obtained from the NBS/NIST library (NIST Mass Spectral Library, 2002).

## 3. Results and discussion

The main quantities of process waters are generated during technological processes of crude oil preparation (desalting and dewatering) and rectification with water steam for stripping. Small quantities of wastewater are generated by the residual amount of water remaining in the crude oil after desalting. In accordance with the best refinery practices, the wash water rate vs. crude oil feed flow-rate varies between 3% and 7% depending on the quality of the processed oil [38]. Higher salt content supposes higher wash water rates in order to remove salts effectively. Effluent wastewater stream from desalting and dewatering section (E-109) goes to the water treatment facilities.

The other main source of wastewater from straight-run distillation units is processed condensates that are generated from the overhead streams of the rectification towers (atmospheric and vacuum). In LNB, these are the preflash tower (K-101), the main fractionators of the

atmospheric distillation units (K-102), and vacuum towers from the vacuum distillation units (K-1 in the vacuum section in AVD-1 and K-101 in VDM-2). Often these water streams are called sour water condensates because of its lower pH and hydrogen sulphide content. The process condensate from the preflash tower is formed only by the residual amount of water remaining in the crude oil after desalting section.

The process condensate from the main fractionator is formed predominantly from the water steam, which is injected to the bottom of the tower and side strippers for extracting middle distillates in order to reduce the partial pressure of the hydrocarbons and to improve the separation processes. Depending on the throughput of the unit, stripping steam flow-rate could vary, but the rate vs. crude oil remains about 2.5%.

Process condensates in VDM-2 unit have the same origin such as the condensates from the main fractionators–stripping water steam. At this vacuum distillation process unit, water steam is injected not only for stripping but also as a turbulizer in the furnace passes. Both streams leave the system such as a process condensate from the overhead condensers drum.

The organic matter in process waters originating from crude distillation units depends on the crude oil composition and the process of oil production. Generally, extracts obtained from the wastewater samples have chemical compositions that differ significantly from one another. The extracts investigated are exhibited a relative wide molecule weight range compounds. They are arranged according to their dominant contents in the samples. Identification of the corresponding compounds is summarized in Table 1.

Table 1. Concentration of organic matter in process waters originating from crude distillation units of LUKOIL Neftohim Burgas refinery

	Molecular formula	Concentration, mg/L								
		AVD-1			AD-4			VDM-1	VDM-2	
		E-101	E-102	E-109	E-101	E-102	E-109	E-3	E-103	
Phenol	C <sub>6</sub> H <sub>6</sub> O	3.5	2.8	7.1	0.6	3.6	3.4	1.2	7.1	
Phenol, 2-methyl-	C <sub>7</sub> H <sub>8</sub> O	< 0.05	5.8	2.5	0.5	5.8	4.4	5.7	17.1	
Phenol, 4-methyl-	C <sub>7</sub> H <sub>8</sub> O	4.0	6.8	3.2	0.6	9.1	5.6	6.3	24.4	
Phenol, 2,4-dimethyl-	C <sub>8</sub> H <sub>10</sub> O	0.6	0.9	0.8	0.1	0.9	1.6	0.5	1.9	
Phenol, 2,5-dimethyl-	C <sub>8</sub> H <sub>10</sub> O	1.9	0.8	0.4	0.1	1.0	0.9	1.7	4.9	
Phenol, 2,3-dimethyl-	C <sub>8</sub> H <sub>10</sub> O	0.9	1.8	0.9	< 0.05	3.0	1.5	7.5	12.0	
Phenol, 3,4-dimethyl-	C <sub>8</sub> H <sub>10</sub> O	0.6	0.6	0.7	< 0.05	1.2	2.0	3.7	11.0	
Phenol, 2,6-dimethyl-	C <sub>8</sub> H <sub>10</sub> O	0.7	0.8	0.6	< 0.05	2.0	2.6	5.2	3.8	
Phenol, 4-ethyl-	C <sub>8</sub> H <sub>10</sub> O	0.5	< 0.05	0.3	< 0.05	0.9	1.7	2.1	3.2	
3-Isopropylphenol	C <sub>9</sub> H <sub>12</sub> O	0.2	< 0.05	0.5	< 0.05	0.4	1.4	2.5	3.4	
3-n-Propylphenol	C <sub>9</sub> H <sub>12</sub> O	0.8	< 0.05	1.2	< 0.05	0.1	1.7	1.2	3.0	
Phenol, 2-ethyl-6-methyl-	C <sub>9</sub> H <sub>12</sub> O	0.4	< 0.05	1.4	< 0.05	< 0.05	3.0	1.9	2.1	
Phenol, 2,4,6-trimethyl-	C <sub>9</sub> H <sub>12</sub> O	0.4	< 0.05	0.9	< 0.05	< 0.05	2.2	2.2	1.5	
Phenol, 3,4,5-trimethyl-	C <sub>9</sub> H <sub>12</sub> O	0.12	< 0.05	1.1	< 0.05	< 0.05	3.5	5.0	3.7	
Formic acid	CH <sub>2</sub> O <sub>2</sub>	100	50	1000	13.0	2.0	6.0	< 0.05	< 0.05	
Acetic acid	C <sub>2</sub> H <sub>4</sub> O <sub>2</sub>	240	310	1500	14.0	1.8	12.0	< 0.05	< 0.05	
Propanoic acid	C <sub>3</sub> H <sub>6</sub> O <sub>2</sub>	25	47	2500	8.5	5.0	7.5	< 0.05	< 0.05	
Butanoic acid	C <sub>4</sub> H <sub>8</sub> O <sub>2</sub>	10	12	3000	1.8	< 0.05	3.4	< 0.05	< 0.05	
Acetic acid, phenylthio-	C <sub>8</sub> H <sub>8</sub> O <sub>2</sub> S	0.2	< 0.05	0.7	0.1	0.2	0.5	1.8	2.0	
Propanoic acid, 3-phenylthio-	C <sub>9</sub> H <sub>10</sub> O <sub>2</sub> S	0.4	1.9	1.1	< 0.05	2.8	0.5	1.8	0.8	
Methylene bis-thioglycolic acid	C <sub>5</sub> H <sub>8</sub> O <sub>4</sub> S <sub>2</sub>	< 0.05	2.1	1.6	< 0.05	2.2	5.6	< 0.05	1.3	
4,4'-Dithiobis-butanoic acid	C <sub>8</sub> H <sub>14</sub> O <sub>4</sub> S <sub>2</sub>	< 0.05	0.2	0.2	< 0.05	0.3	< 0.05	< 0.05	< 0.05	
1,2,4-Trithiolane	C <sub>2</sub> H <sub>4</sub> S <sub>3</sub>	8.9	0.7	1.0	< 0.05	0.7	0.5	< 0.05	< 0.05	
1,3,5-Trithiane <sup>[40]</sup>	C <sub>3</sub> H <sub>6</sub> S <sub>3</sub>	3.2	3.6	0.6	0.3	0.4	3.1	1.0	< 0.05	
2,4,5-Trithiohexane	C <sub>3</sub> H <sub>6</sub> S <sub>3</sub>	6.6	< 0.05	0.5	< 0.05	< 0.05	< 0.05	< 0.05	< 0.05	
1,2,4,5-Tetrathiane	C <sub>2</sub> H <sub>4</sub> S <sub>4</sub>	1.7	0.7	0.7	0.1	< 0.05	< 0.05	1.7	< 0.05	
1,2,4,6-Tetrathiepane	C <sub>3</sub> H <sub>6</sub> S <sub>4</sub>	0.2	< 0.05	< 0.05	< 0.05	0.7	1.2	1.1	< 0.05	
1,2,5,6-Tetrathiocane	C <sub>4</sub> H <sub>8</sub> S <sub>4</sub>	0.6	< 0.05	1.7	< 0.05	< 0.05	0.6	< 0.05	< 0.05	
1,3,5,7,9-Pentathiepane	C <sub>5</sub> H <sub>10</sub> S <sub>5</sub>	3.0	< 0.05	< 0.05	0.1	0.1	2.0	2.1	< 0.05	
Lenthionine	C <sub>2</sub> H <sub>4</sub> S <sub>5</sub>	0.4	< 0.05	3.2	0.2	< 0.05	2.2	4.0	< 0.05	

In the tested samples, numerous methyl-, dimethyl- and trimethyl-phenol isomers are identified. The spectra of phenol and methyl-phenols are assigned from the strong molecular ions  $m/z$  94 and  $m/z$  108, while the spectra of dimethyl and trimethyl-phenol isomers are characterized by ions of  $m/z$  107 and  $m/z$  121 connected with the loss of the methyl group. 2,4-Dimethyl-phenol is considered as the compound responsible for carcinogenic influence [41]. In this research, only four phenolic compounds are determined in all of the sampling sites (Table 1) while the other compounds are with different concentration even they were below detectable limits. The levels of individual phenolic compounds in the wastewater of AVD-1, AD-4, VDM-1, and VDM-2 samples range from detection limits to 7.1 mg/L, detection limits to 9.1 mg/L, from 0.5 to 7.5 mg/L and from 1.5 to 24.4 mg/L, respectively. The results indicate maximum content 24.4 mg/L of 4-methyl-phenol in the wastewater sample collected from E-103, VDM-2. The wastewater sample of VDM-2 shows higher total phenol content (99.1 mg/L) than wastewater sample of VDM-1 (46.7 mg/L) and wastewater sample of E-102, AD-4 (28.8 mg/L). Compared with the data in the literature, the contents of total phenol compounds are higher than the ones observed in the previous studies [42].

Naphthenic acid species analysis in all wastewater samples indicate a generally most abundant. Examination of the quantitative data confirms the more abundant presence of the naphthenic acid species in the AVD-1 wastewater compared to the other tested wastewater samples (Table I). The data show the level of individual naphthenic acid species is ranged between below detection limits to 3000 mg/L. The levels of naphthenic acid species are in agreement with earlier report data [42,45]. The highest concentrations of naphthenic acid species measured are in the E-109, AVD-1 wastewater.

S-containing hydroxy acids are also present of oil sands process water [9,28]. Analysis of the mass spectrum of acetic acid, phenylthio- reveals significant ions at  $m/z$  123 (loss of carboxylic group),  $m/z$  168 (molecule ion) and a smaller ion at  $m/z$  45 (carboxylic group). The mass spectrum of propanoic acid, 3-phenylthio- also has significant ions at  $m/z$  123,  $m/z$  182 (molecule ion) and  $m/z$  45. Analysis of the mass spectrum of methylene bis-thioglycolic acid reveal to have an ion  $M^{+}$  at  $m/z$  196, and other significant ions are confirming the cleavage of the main chain ( $m/z$  77 sulphur-carboxylic group cleavage). The formation of the fragment ion  $m/z$  105 is associated with  $\beta$ -cleavage with respect to the sulphur atom. The abundance of  $m/z$  137 results from the loss of methyl-carboxylic groups, cleaved from the thioglycolic acid main chain. Analysis of the mass spectrum of 4,4'-dithiobis-butanoic acid reveals that the significant ions exist at  $m/z$  45 (carboxylic group) and  $m/z$  87 (loss of the carboxylic group and hydrocarbon main chain). The presence of the fragment ion at  $m/z$  134 indicates that the Sulphur atoms are present in the alkyl main chain of the 4,4'-dithiobis-butanoic acid. Total naphthenic acid contents and S-containing hydroxy acids the values range from 3.6 mg/L to 8000 mg/L.

High sulphur content in crude oils results in the significant generation of sulphur species, which are major environmental pollutants. In the present investigation, the spectrum of the 1,3,5-trithiane is characterized by abundant molecular ion  $m/z$  138 and dominated ions by a peak ion of  $m/z$  46,  $m/z$  45 and  $m/z$  92 due to heterocycle cleavage of the cyclic trimer and in losses of a C-S group. 1,2,4-trithiolane is identified by interpretation of the mass spectrum. Major fragment ion is  $m/z$  45, and large fragment ions are  $m/z$  78,  $m/z$  46 and  $m/z$  124. The result of the sulphur analysis indicates a generally high level of sulphur species in wastewaters. Table I summarizes the mean concentrations of sulphur species in the wastewater samples. The most abundant is 1,2,4-trithiolane in the wastewater of E-101, AVD-1 with a concentration of 8.9 mg/L, accounting for 36.2% of the total sulphur species. Interestingly, sulphur species in the wastewater E-103, VDM-2 sample are not detected. The levels of total sulphur species content vary between a minimum of detection limits and maximum 24.6 mg/L, and this the value is less in previous studies reported [23]. In comparison, the results obtained of the different sulphur species in the wastewater sample of E-101, AVD-1 are higher than those of the other wastewater samples investigated.

One way to display the similarities or differences between phase distributions of organic matter in process wastewaters is to construct certain types of plots, such as plots of the percentage concentration of different classes of compounds. The distribution of single compounds varied among different wastewater samples. As can be seen from Figure 1 naphthenic species (4.0–99.6%) are predominant in the wastewaters investigated, and this may be attributed to their higher solubility. It is clear that the proportion of phenolic species in the wastewater is found to range from 0.3 to 96.9%. The proportion of sulphur species is in the range 0.1 to 12.0%.

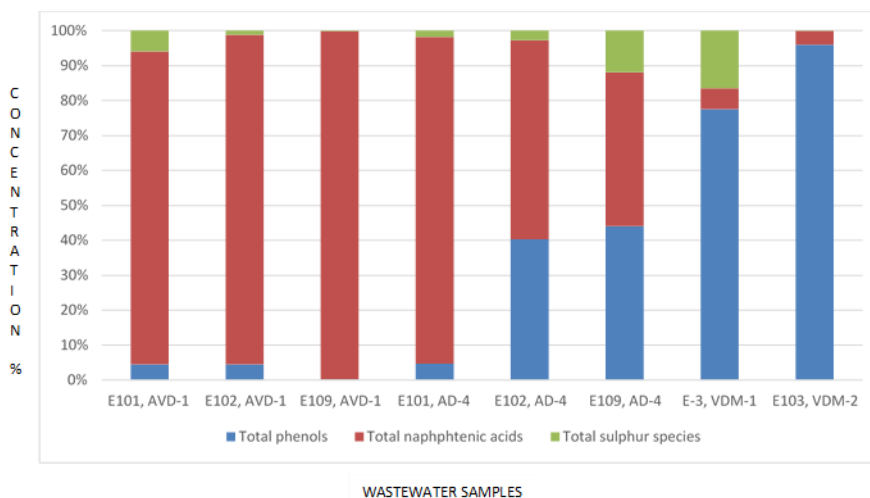


Figure 1. Composition of organic matter in process waters, originating from crude distillation units

#### 4. Conclusion

By the use of gas chromatography-mass spectrometry the organic matter in process waters originating from crude distillation units are identified. The study herein shows the most abundant content of naphthenic acid species (alicyclic carboxylic acids) followed by phenolic compounds and polysulphur components.

By specifying organic matter contents, users can intake to describe the routing of water through the refinery or water can be additionally used before being assigned to one of the effluent streams.

#### References

- [1] Coelho A, Castro AV, Dezotti M, Sant' Anna GLJr. Treatment of petroleum refinery sour water by advanced oxidation processes. *J. Hazard. Mater.*, 2006, 137: 178–184.
- [2] Saïen J, Nejati H. Enhanced photocatalytic degradation of pollutants in petroleum refinery wastewater under mild conditions. *J. Hazard. Mater.*, 2007, 148: 491–495.
- [3] Wang B, Wan Y, Gao Y, Zheng G, Yang M, Wu S, Hu J. Occurrences and behaviors of naphthenic acids in a petroleum refinery wastewater treatment plant. *Environ. Sci. Technol.*, 2015, 49: 5796–5804.
- [4] Yang M, Zeng SK. Pollutant removal-oriented yeast biomass production from high-organic-strength industrial wastewater: A review. *Biomass Bioenergy*, 2014, 64: 356–362.
- [5] Clemente JS, Fedorak PM. A review of the occurrence, analyses, toxicity, and biodegradation of naphthenic acids. *Chemosphere*, 2005, 60: 585–600.
- [6] James G. Speight *Fouling in Refineries*, Gulf Professional Publishing is an imprint of Elsevier 225 Wyman Street, Waltham, MA 02451, USA, The Boulevard, Langford Lane, Kidlington, Oxford, OX5 1GB, UK 2015 Elsevier Inc. 2015; Chapter 17; p. 413.
- [7] Foroulis ZA. Prevention of corrosion using heterocyclic nitrogen compounds. U.S Patent 3 553 101, 1971.

- [8] Bota G M, Qu D, Nestic S. Naphthenic acid corrosion of mild steel in the presence of sulfide scales formed in crude oil fractions at high temperature. Presented at the NACE International Conference & Expo, San Antonio, USA, March 2010.
- [9] Headley JV, Peru KM, Mohamed MH, Frank RA, Martin JW, Hazewinkel RRO, Humphries D, Gurprasad NP, Hewitt LM, Muir DCG, Lindeman D, Strub R, Young RF, Grewer DM, Whittal RM, Fedorak PM, Birkholz DA, Hindle R, Reisdorph R, Wang X, Kasperski KL, Hamilton C, Woudneh M, Wang G, Loescher B, Farwell A, Dixon DG, Ross M, Pereira ADS, King E, Barrow MP, Fahlman B, Bailey J, McMartin DW, Borchers CH, Ryan CH, Toor NS, Gillis HM, Zuin L, Bickerton G, McMaster M, Sverko E, Shang D, Wilson LD, Wrona FJ. Chemical fingerprinting of naphthenic acids and oil sands process waters—a review of analytical methods for environmental samples. *Journal of Environmental Science and Health, Part A*. 2013b, 48: 1145-1163.
- [10] Neff JM. Bioaccumulation in marine organisms. Effect of contaminants from oil well produced water, Elsevier Ltd., The Boulevard Langford Lane. Kidlington, Oxford OX5 1GB, UK, 2002.
- [11] Silva CA, Madureira LAS. Application of headspace solid-phase microextraction and gas chromatography-mass spectrometry (HS-SPME-GC/MS) on the evaluation of degradation efficiency of phenolic compounds and identification of by-products from produced water. *J. Braz. Chem. Soc.*, 2015, 26 (4): 676-686.
- [12] Sun J, Tao H. Determination of phenols in wastewater by dispersive liquid-liquid microextraction coupled to capillary gas chromatography. Presented at the International Conference on Chemical, Material and Food Engineering (CMFE-2015). Kunming, Yunnan, China, July 2015, ISBN: 978-1-5108-0982-6, pp364.
- [13] Jiangyong H, Huan W, Ling X. Determination of phenols in alkaline wastewater from oil refinery by high-performance liquid chromatography and gas chromatography-mass spectrometry. *Guangdong Chemical Industry*, 2013, 08.
- [14] Guangqing S, Hongbo X, Ling P, Shuling L, Yuexi Z, Jie L. Analysis of organic pollutants in refinery wastewater by gas chromatography. *Petrochemical Technology*. 2012, 04.
- [15] Ballesteros O, Zafra A, Navalón A, Vílchez JL. Sensitive gas chromatographic-mass spectrometric method for the determination of phthalate esters, alkylphenols, bisphenol A and their chlorinated derivatives in wastewater samples. *Journal of Chromatography A*, 2006, 1121(2): 154-162.
- [16] Pérez AIN. Analysis and improvement proposal of a wastewater treatment plant in a Mexican refinery. Master's thesis. Chalmers University of Technology Gothenburg, Sweden, 2015.
- [17] Singh A, Kumar V, Jn S. Assessment of bioremediation of oil and phenol contents in refinery waste water via bacterial consortium. *J Petroleum & Environmental Biotechnology*. 2013, 4 (3): 1-4.
- [18] Moschella PS, Laane RPWM., Back S, Behrendt H, Bendoricchio G. et al. Group report: Methodologies to support implementation of the water framework directive. *Managing European Coasts Environmental Science Springer Berlin Heidelberg*, 2005; p. 137.
- [19] Headley JV, McMartin DW. A review of the occurrence and fate of naphthenic acids in aquatic environments. *J. Environ. Sci. Health, Part A: Toxic/Hazardous Substances & Environ. Eng.* 2004, A39 (8): 1989 -2010.
- [20] Rogers VV, Wickstrom M, Liber K, MacKinnon MD. Acute and subchronic mammalian toxicity of naphthenic acids from oil sands tailings. *Toxicol. Sci.*, 2002, 66: 347-355.
- [21] Speight JG. *Oil and Gas Corrosion Prevention*. Gulf Professional Publishing, Elsevier, Oxford, 2014.
- [22] Rebak RB. Sulfidic corrosion in refineries – a review. *Corrosion Reviews*, 2011, 29 (3-4): 123-133.
- [23] Witter AE, Jones AD. Chemical characterization of organic constituents from sulfide-rich produced water using gas chromatography/mass spectrometry. *Environmental Toxicology and Chemistry*, 1999, 18 (9): 1920-1926.
- [24] Headley JV, Peru KM, Fahlman B, McMartin DW, Mapolelo MM, Rodgers RP, Lobodin VV, Marshall AG. Comparison of the levels of chloride ions to the characterization of oil sands polar organics in natural waters by use of Fourier transform ion cyclotron resonance mass spectrometry. *Energy&Fuel*, 2012, 26: 2585-2590.
- [25] Dzidic I, Somerville AC, Raia JC, Hart HV. Determination of naphthenic acids in California crudes and refinery wastewaters by fluoride ion chemical ionization mass spectrometry. *Anal. Chem.*, 1988, 60: 1318-1323.
- [26] Grewer DM, Young RF, Whittal RM, Fedorak PM. Naphthenic acids and other acid-extractables in water samples from Alberta: what is being measured? *Science of the Total Environment*, 2010, 408: 5997-6010.

- [27] Holowenko FM, MacKinnon MD, Fedorak PM. Characterization of naphthenic acids in oil sands wastewaters by gas chromatography-mass spectrometry. *Water Research*, 2002, 36: 2843-2855.
- [28] Kohnen MEL, Sinninghe Damsté JS, Ten Haven HL, Kock-van Dalen AC, Schouten S, De Leeuw JW. Identification and geochemical significance of cyclic di- and trisulphides with linear and acyclic isoprenoid carbon skeletons in immature sediments. *Geochimica et Cosmochimica Acta*, 1991, 55: 3689-3695.
- [29] Sun J, Hu S, Sharma KR, Keller-Lehmann B, Yuan Z. An efficient method for measuring dissolved VOCs in wastewater using GC-SCD with static headspace technique. *Water Research*, 2014, 52: 208-217.
- [30] Sheng Y, Chen F, Wang X, Sheng G, Fu J. Odorous Volatile Organic Sulfides in Wastewater Treatment Plants in Guangzhou, China. *Water Environment Research*, 2008, 80: 324-330.
- [31] Headley JV, Peru KM, Barrow MP. Mass spectrometric characterization of naphthenic acids in environmental samples: A review. *Mass Spectrometry Reviews*, 2009, 28: 121-134.
- [32] Headley JV, Peru KM, Barrow MP. Advances in mass spectrometric characterization of naphthenic acids fraction compounds in oil sands environmental samples and crude oil—a review. *Mass Spectrometry Reviews*. 2015, 35: 311-328.
- [33] Zhao B, Currie R, Mian H. Catalogue of analytical methods for naphthenic acids related to oil sands operations. Oil sands research and information network, University of Alberta, School of Energy and the Environment, Edmonton, Alberta. OSRIN Report No. TR-21, 2012.
- [34] Brown LD, Ulrich AC. Oil sands naphthenic acids: A review of properties, measurement, and treatment. *Chemosphere*. 2015, 127: 276-290.
- [35] Barrow MP, Headley JV, Peru KM, Derrick PJ. Data visualization for the characterization of naphthenic acids within petroleum samples. *Energy & Fuels*, 2009, 23: 2592-2599.
- [36] Stratiev D, Yankov V, Petrov I, Shishkova I, Pavlova A, Ivanova P, Surleva A, Hristov K, Todorova E, Obryvalina A, Telyashev R. Study on the origin of sediment formation in a high pressure near zero sulfur diesel hydrotreater. *Fuel Processing Technology*, 2014, 126: 332-342.
- [37] Pavlova A, Stratiev D, Dinkov R, Sharafutdinov I, Shishkova I, Chakarov P, Mitkova M. Determination of organic nitrogen and phenolic compounds in sour wastewater from ebullated bed hydrocracking unit. *Pet Coal*, 2016, 58 (3): 339-348.
- [38] Pruneda E, Escobedo E, Vázquez J. Optimum Temperature in the Electrostatic Desalting of Maya Crude Oil. *J. Mex. Chem. Soc.* 2005, 49(1): 14-19.
- [39] Dalmaschio GP, Malacarne MM, de Almeida VMDL, Pereira TMC, Gomes A O, de Castro EVR, Greco SJ, Vaz BG, Romão W. Characterization of polar compounds in a true boiling point distillation system using electrospray ionization FT-ICR mass spectrometry. *Fuel*, 2014, 115: 190-202.
- [40] da Silva<sup>1</sup> CB, Dalarmi L, Dias JFG, Zanin SMW, Rech KS, Kulik JD, Kerber VA, Simionatto E, Ré-Poppi N, Gebara SS, Miguel OG, Miguel MD. Effects of volatile oils of the *Microlobius foetidus* on trypsin, chymotrypsin and acetylcholinesterase activities in *Aedes aegypti* (Diptera: Culicidae), *African Journal of Pharmacy and Pharmacology*, 2014, 8(5): 148-156.
- [41] Kharayat Y, Verma ShVKSh, Kumar B, Sharma CS. Phenols&phenolic compounds, Central Pollution Control Board, Ministry of Environment, Forests & Climate Change, PariveshBhawan, East Arjun Nagar, Delhi-110032, [www.cpcb.nic.in](http://www.cpcb.nic.in) August, 2016.
- [42] Neff JM, Lee K, De Blois EM. Produced water: overview of composition, fates and effects. *Produced water*. 2011, 1-51.
- [43] Wilde MJ. On the bicyclic acids of petroleum. A thesis submitted to Plymouth University in partial fulfillment for the degree of Doctor of Philosophy in School of Geography, Earth and Environmental Sciences, Plymouth, England, December 2015.
- [44] West CE, Scarlett AG, Tonkin A, O'Carroll-Fitzpatrick D, Pureveen J, Tegelaar E, Gieleciakc R, Hager D, Petersen K, Tollefsen K-E, Rowland SJ. Diaromatic sulphur-containing "naphthenic" acids in process waters, *Water Research*, 2014, 51: 206-215.
- [45] Jones D. Synthesis, fractionation, characterization and toxicity of naphthenic acids from complex mixtures. A thesis submitted to Plymouth University in partial fulfillment for the degree of Doctor of Philosophy in School of Geography, Earth and Environmental Sciences, Plymouth, England, April 2013.

To whom correspondence should be addressed: Dr. Antoaneta Pavlova, LUKOIL Neftohim Burgas JSC, 8104 Burgas, Bulgaria, [Pavlova.Antoaneta.I@neftochim.bg](mailto:Pavlova.Antoaneta.I@neftochim.bg)

STUDIES ON THE RHEOLOGICAL AND TRIBOLOGICAL PROPERTIES OF ACYLATED DERIVATIVES OF CASTOR OIL AND THEIR APPLICATION AS BIO-LUBRICANTS

*Hamdy S. Abdel-Hameed*<sup>1\*</sup>, *Nehal S. Ahmed*<sup>1</sup>, *Amal M. Nassar*<sup>1</sup>, *Shymaa M. El-Saeed*<sup>1</sup>, *Ahmed F. El-Kafrawy*<sup>2</sup>, and *Ahmed I. Hashem*<sup>2</sup>

<sup>1</sup> *Department of Petroleum Applications, Egyptian Petroleum Research Institute, Nasr City, Cairo, Egypt*

<sup>2</sup> *Chemistry Department, Faculty of Science, Ain Shams University, Abbasiya, Cairo, Egypt*

Received August 8, 2018; Accepted October 19, 2018

---

## Abstract

Castor oil was used as a starting material for obtaining bio-lubricants via some chemical transformations. Thus the oil was firstly epoxidized by peroxy formic acid, prepared in situ, in the presence of ambrolite as a catalyst. The epoxide obtained was subjected to base-catalyzed transesterification with methanol/NaOH followed by ring opening with alcohol (2-ethyl-1-hexanol) to give the corresponding diol. Finally, the latter diol was acylated using acetic anhydride in pyridine, whereby the acylated product was isolated.

The structures of the products of the different steps were illustrated from their spectral data (FT-IR) and (<sup>1</sup>H-NMR). The rheological and tribological properties of the compounds obtained were evaluated to confirm their suitability as bio-lubricants.

**Keywords:** *Castor oil; Bio-Lubricants; Transesterification; Spectral data; Rheological and Tribological properties.*

---

## 1. Introduction

Lubricants used globally are commonly made from petroleum, coals or natural gases [1-2]. Due to their wide utilization, there is the need to search for alternative sources for producing lubricants. As a result of the long-term pollution effects associated with mineral oil-based lubricants on the environment, and the expected depletion of petroleum reservoirs all over the world in the future there is a need for cheap and renewable feedstock for the production of biodegradable lubricants [3].

There are many alternatives to petroleum based lubricant, such as synthetic or animal fat lubricants. However, lubricants derived from vegetable oils have received greater attention due to their favourable and acceptable physical properties. Among the advantages of bio-based lubricants is their high lubricity, as well as, much lower coefficient of friction compared with petrobased lubricants. Furthermore, bio-based lubricants have high flash points, which make them effective in high temperature environment to impede evaporation or dissipation [4-6].

Bio-lubricants also have relatively stable viscosity indexes, so that they are useful over a large range of temperatures. In addition, bio-based lubricants are generally derived from vegetable oils, and its processing involves a clean and pollution free method, as well as, being renewable. Finally, the non-toxic and biodegradable nature of bio-based lubricants ensures easy disposal in the environment, unlike petroleum based lubricant. These properties make bio-based lubricants an attractive alternative to petroleum based lubricants [7].

Vegetable non-edible oils have some undesired characteristics, particularly a poor resistance to high temperatures and limited use in low temperatures range because of solidification, which prevents their use, in their natural state, in many areas of lubrication. Also, Vegetable oils are prone to oxidation, i.e. have low oxidation stabilities due to the presence of allylic hydrogens in their alkyl chains. Various techniques have been applied to overcome the potential problems produced by vegetable oil, such as blending with other diluents such as (1)

polyalphaolefins, (2) chemical modification such as esterification, transesterification, (3) epoxidation.

The objective of this work is to shed light on the potential of vegetable non-edible oil in the automotive sector [8-9].

Better performances are instead obtained from esters produced by epoxidation reaction, in which a peracid is used for oxygen transfer to the double bonds in the fatty acid chains [10-11]. The peracid is usually formed in situ from hydrogen peroxide and acetic or formic acid, addressing almost all of the above-mentioned principles of green chemistry. Furthermore, fewer coloured epoxidation products are obtained which is indicative of the mild process conditions [12-14]. Fatty acids (with long chain), derived from oils, and mono-functional or poly-functional bio-based alcohols. The performance of esters depends on their chemical structure and, as a result of using alcohols and/or fatty acids which differ in their molecular weights and/or functionality (di, tri, tetra), the synthesis can be directed to obtain products with characteristics oriented to different performances (viscosity, viscosity index, pour point). For this reason, research on these products continues, and new syntheses are continually proposed both in open and patent literature [15].

In the present work epoxidation of castor oil in the presence of mixed catalyst Amberlite/HCOOH/H<sub>2</sub>O<sub>2</sub>, followed by transesterification of the product using methanol was performed. Ring opening of the products obtained by 2-ethyl-1-hexanol then finally acylation of the product using acetic anhydride afforded acylated castor oil derivatives. The structures of the prepared compounds were confirmed using Fourier transform infrared spectroscopy (FT-IR), proton nuclear magnetic resonance (<sup>1</sup>H-NMR). Finally, the rheological and tribological properties of the products by modular compact rheometry (MCR) were carried out.

Evaluation of the prepared acylated castor oil derivatives as bio-lubricants was performed by measuring the viscosities and pour points of the prepared compounds.

## 2. Experimental

### 2.1 Epoxidation of castor oil

The reaction was carried out in three necked-round bottomed flask equipped with a mechanical stirrer, efficient condenser, and thermometer. Epoxide was derived by in-situ epoxidation reaction using H<sub>2</sub>O<sub>2</sub> as oxygen donor and HCOOH as an active oxygen carrier in the presence of ion exchange resin (Amberlite IR 120). The experiment was designed at the following molar ratio castor oil: formic acid (88%): H<sub>2</sub>O<sub>2</sub> (30%) was (1:0.5:1.5) and ion exchange resin Amberlite IR 120 weight percentage (15%). The reaction was maintained with vigorous stirring (1000+ rpm) at 60°C for 15 hrs. Finally, the solvent and trace water were distilled by rotary evaporator to yield the product (EC<sub>1</sub>), with designation shown in Table 1.

### 2.2. Transesterification of the product obtained

Transesterification of the epoxidized non-edible oils with methanol can be carried out using both homogeneous (acid or base). Methanol is used due to their low cost and physical and chemical advantages. The transesterification reaction occurs between alcohol adsorbed on catalyst and ester of the reactant. Homogeneous catalysts such as sodium hydroxide, potassium hydroxide, and sodium methoxide formed an alkoxide group on reaction with alcohol. The transesterification reaction was thereafter carried out by using methanol to oil molar ratio (8:1), at 60°C for 4 hrs to yield of product (EC<sub>2</sub>) with designation shown in Table 1.

### 2.3. Ring opening of the obtained products

Epoxides are highly reactive towards acids and alcohols to give diols and polyols products. So 35 gm of the product (EC<sub>2</sub>) was treated with 1.630 mL of H<sub>2</sub>SO<sub>4</sub> as catalyst and toluene as solvent and 9.604 ml of 2-ethyl-1-hexanol over 4 hrs at 110°C. The reaction was left overnight then the product was washed with brine water and dried over Na<sub>2</sub>SO<sub>4</sub> [16-17]. The excess solvent was removed with a rotary evaporator to give the product (EC<sub>3</sub>) with designation shown in Table 1.

Table 1. The designation of prepared compounds

Abbreviation	Prepared compounds	Abbreviation	Prepared compounds
EC1	Epoxidized castor oil	EC3	The diol
EC2	Transesterified EC1	EC4	Acylated pproduct

## 2.4. Acylation of the obtained products:

To a stirred solution (0.09 mol) of product (EC<sub>3</sub>), acetic anhydride (0.36 mol) was added, 4-dimethylaminopyridine (0.87 mol) and 150 mL of xylene were added. The obtained suspension was stirred and heated to 140-150°C for 8 h. Then, the product was distilled at 140-160°C to eliminate solvent then the product was extracted by ethylacetate. The product was washed with brine and dried over aqueous Na<sub>2</sub>SO<sub>4</sub> overnight, and finally, the solvent was removed by rotary evaporator to yield the target product (EC<sub>4</sub>) with designation shown in Table 1.

## 3. Characterization of the prepared compounds

The prepared compounds were characterized by using FT-IR, Model Type 'Nicolet iS10 FT-IR Spectrometer. The sample prepared as a disk. Room temperature, DTGS detector, 4 cm<sup>-1</sup> spectral resolutions. Maximum speed: 40 spectra per second at 16 cm<sup>-1</sup> resolution [18]. The prepared compounds were characterized by <sup>1</sup>H-NMR spectroscopy. Using <sup>1</sup>H-NMR type [300 M.Hs. spectrophotometer W-P-300, Bruker].

### 3.1. Evaluation of the prepared products as bio lubricant

Viscosity indices (VI) of the products were measured according to ASTM D2270-87. The kinematic viscosities of the tested compounds which were determined at 40°C and 100°C.

The pour points of the prepared compounds were measured according to the ASTM-9787. The instrument used for measuring the pour points was the Cold Filter Plugging Point Automatic Tester (CFPPA-T), model 1st CPP97-2 (France).

The flash points of the prepared compounds were determined using a Cleaveland open cup tester conforming to ASTM D92-12b.

TGA experiments were carried out using Simultaneous Q- 600 DSC/TGA (USA). The experiments use a 0.01 g polymer sample, at a heating rate of 10°C min<sup>-1</sup> from 25°C to 600°C and under a flowing (25 ml min<sup>-1</sup>) nitrogen atmosphere.

### 3.2. Measuring rheological and tribological properties by modular compact rheometry (MCR)

Different rheological and tribological tests were employed for the prepared compounds as illustrated in Figs. 8, 9. These tests were performed using a ball-on-three-plates tribometer (tribology measurement cell, Rheometer MCR502, Anton-Paar GmbH, Stuttgart, Germany [19]) Fig. 1 and 0.9 ml of each sample. Each measurement started with a conditioning run followed by the measurement of Stribeck curves at temperatures (80°C) and loads (10 N). Stribeck curves generally describe the friction coefficients of lubricated systems as a function of sliding velocity, contact pressure, or viscosity.

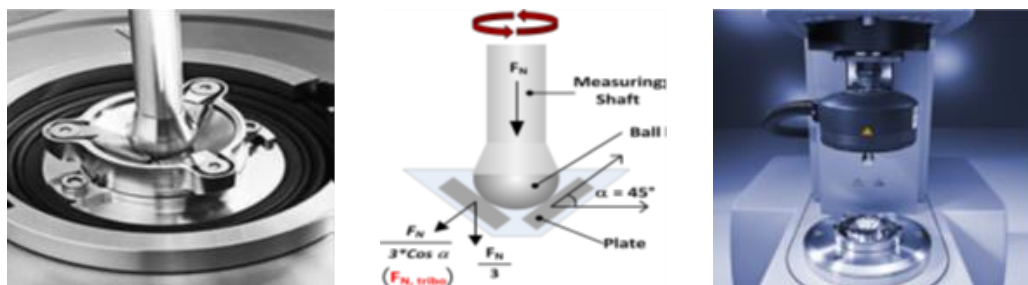
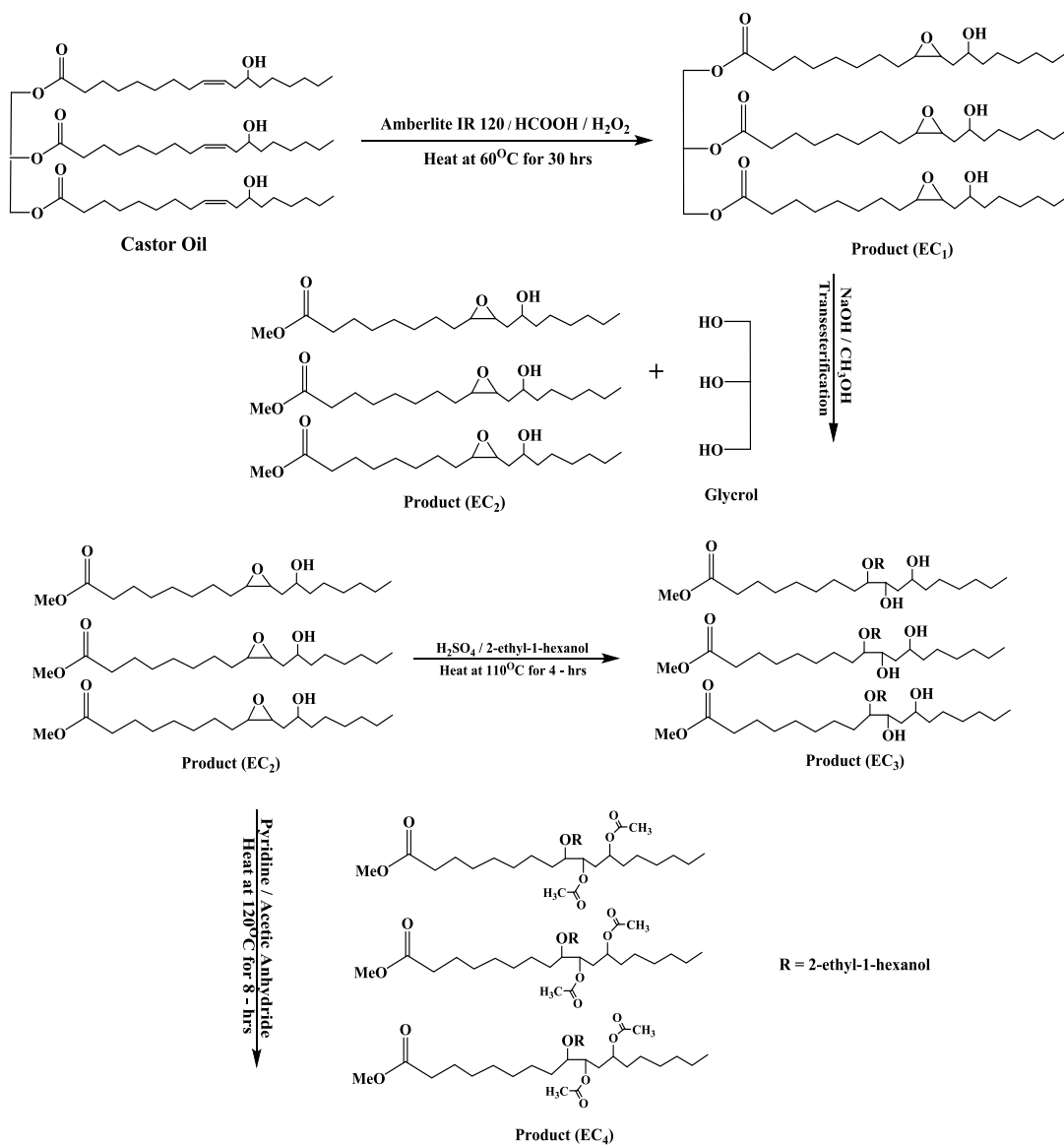


Fig. 1. Rheometer MCR502 component

#### 4. Results and discussion

In the last decades, there is an increasing concern in finding substitutes for petroleum refinery products. This is due to two reasons: first, the expected depletion of petroleum reservoirs in the future; second, petroleum products and their wastes, being non-biodegradable represent environmental petroleum due to the toxicity of most of their components. Vegetable oils, being renewable and biodegradable sources, represent suitable candidates for this purpose. Although vegetable oils suffer from the disadvantages of being susceptible to oxidation due to the presence of allylic hydrogen in their backbone, this problem could be overcome by using suitable doses of antioxidant additives.

It is hoped that this investigation will be a contribution to this trend. Thus castor oil was used as a starting material to obtain some bio-lubricants via the chemical transformations illustrated by scheme (1).



Scheme (1)

The products obtained were characterized by spectral tools (FTIR and  $^1\text{H-NMR}$ ). Evaluation of the rheological and tribological characteristics of these compounds was also performed.

#### 4.1. Spectral characterization

##### 4.1.1. The infrared spectra (FT-IR)

The infrared spectrum of castor oil is given in Fig. 2, showed the following: The hydroxyl (OH) bands appear clearly near to  $3436\text{ cm}^{-1}$  as broad bands. C-H of alkanes in the range of  $2855\text{ cm}^{-1}$  and  $2925\text{ cm}^{-1}$ . C=O appears at  $1744\text{ cm}^{-1}$ . C-O appears at  $1166\text{ cm}^{-1}$ . CH of  $\text{CH}_3$  group appears at  $1462\text{ cm}^{-1}$  and  $1362\text{ cm}^{-1}$ . CH of  $\text{CH}_2$  group appears at  $1462\text{ cm}^{-1}$  and  $1376\text{ cm}^{-1}$ . C=C of alkene appears at  $1650\text{ cm}^{-1}$ . =CH appears at  $3008\text{ cm}^{-1}$ . C=O of ester appears at  $1744\text{ cm}^{-1}$ .

The infrared spectrum of product ( $\text{EC}_1$ ) is given in Fig. 3, showed the following: The disappearance of C=C of alkene and also for =CH band, and appearance of epoxide band at  $859\text{ cm}^{-1}$ . C=O appears at  $1741\text{ cm}^{-1}$ . The hydroxyl (OH) bands appear clearly near to  $3453\text{ cm}^{-1}$  as broad bands, C-H of alkanes in the range of  $2855\text{ cm}^{-1}$  and  $2928\text{ cm}^{-1}$ . C-O appears at  $1173\text{ cm}^{-1}$ . CH of  $\text{CH}_2$  group appears at  $1462\text{ cm}^{-1}$  and  $1438\text{ cm}^{-1}$ .

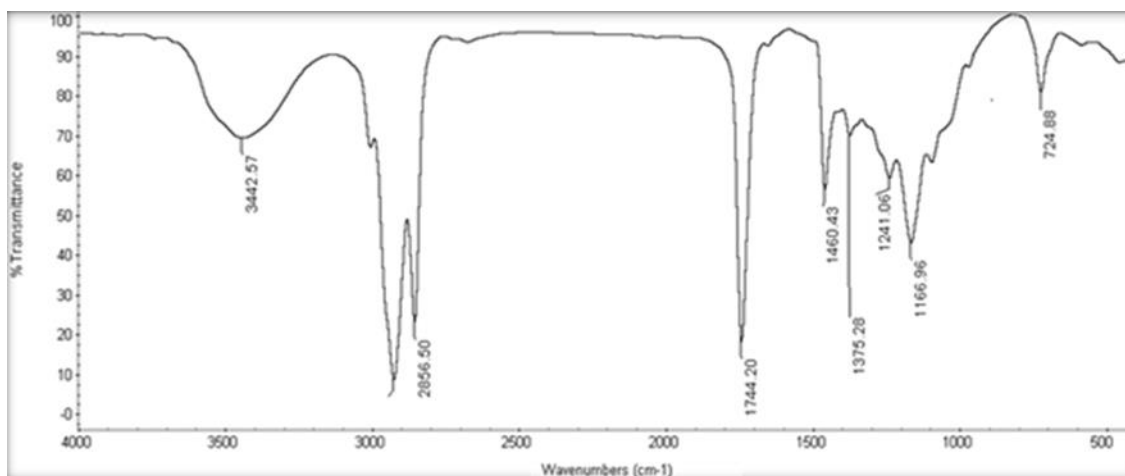


Fig. 2. The infrared spectrum of castor oil

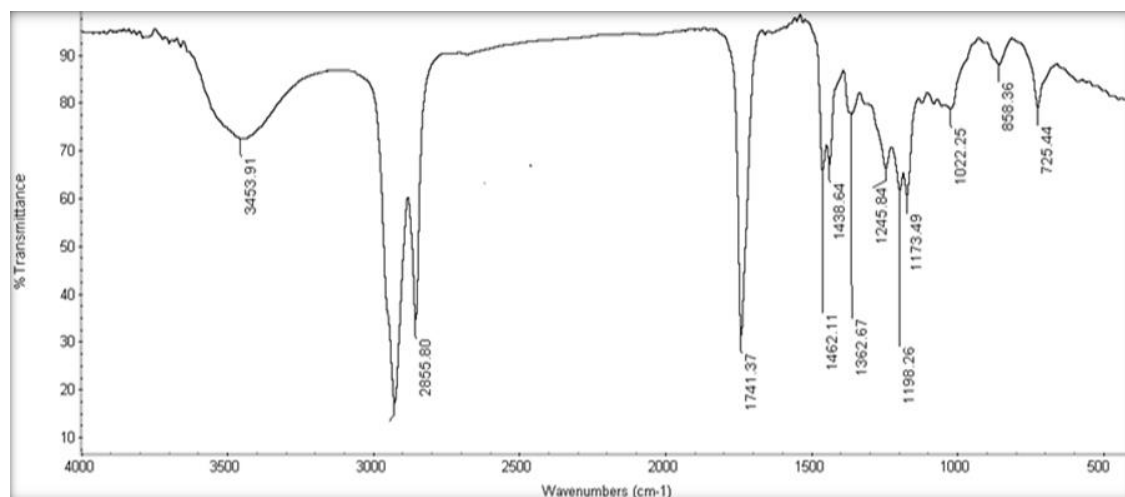


Fig. 3. The infrared spectrum of compound ( $\text{EC}_1$ )

The infrared spectrum of product ( $\text{EC}_3$ ) is given in Fig. 4, indicates the following: The disappearance of epoxide band, and appearance of hydroxyl (OH) bands appears clearly near to

3456  $\text{cm}^{-1}$ . C=O appears at 1741  $\text{cm}^{-1}$ . C-H of alkanes in the range of 2856  $\text{cm}^{-1}$  and 2928  $\text{cm}^{-1}$ . C-O appears at 1172  $\text{cm}^{-1}$ . CH of  $\text{CH}_2$  group appears at 1438  $\text{cm}^{-1}$  and 1372  $\text{cm}^{-1}$ .

The infrared spectrum of product ( $\text{EC}_4$ ) is given in Fig. 5, showed the following: There is no band for hydroxyl (OH) nearly due to acylation reaction. C=O appears with at 1740  $\text{cm}^{-1}$ . C-H of alkanes in the range of 2856  $\text{cm}^{-1}$  and 2928  $\text{cm}^{-1}$ . CH of  $\text{CH}_2$  group appears at 1462  $\text{cm}^{-1}$  and 1373  $\text{cm}^{-1}$ .

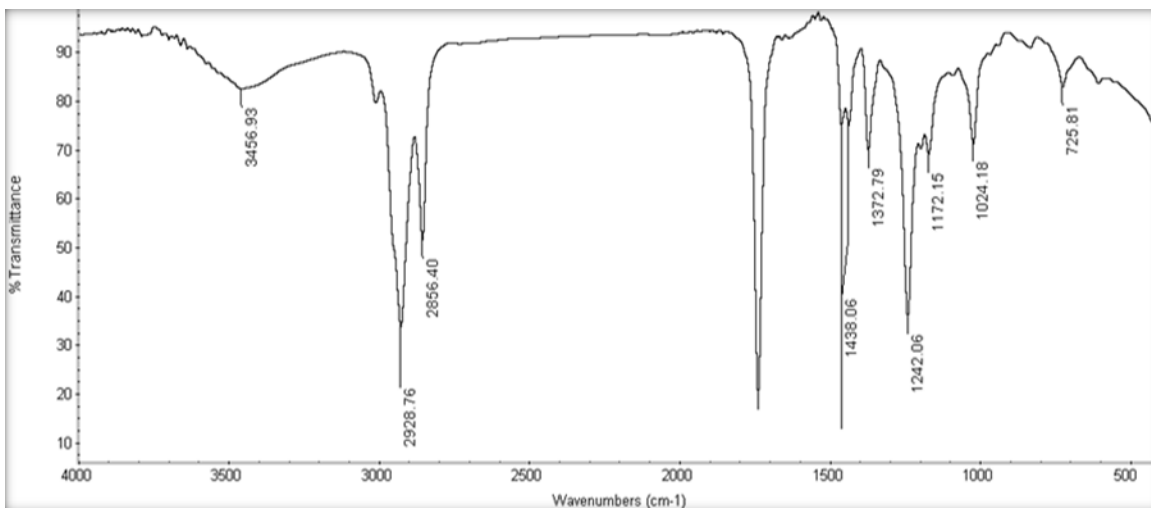


Fig. 4. The infrared spectrum of compound ( $\text{EC}_3$ )

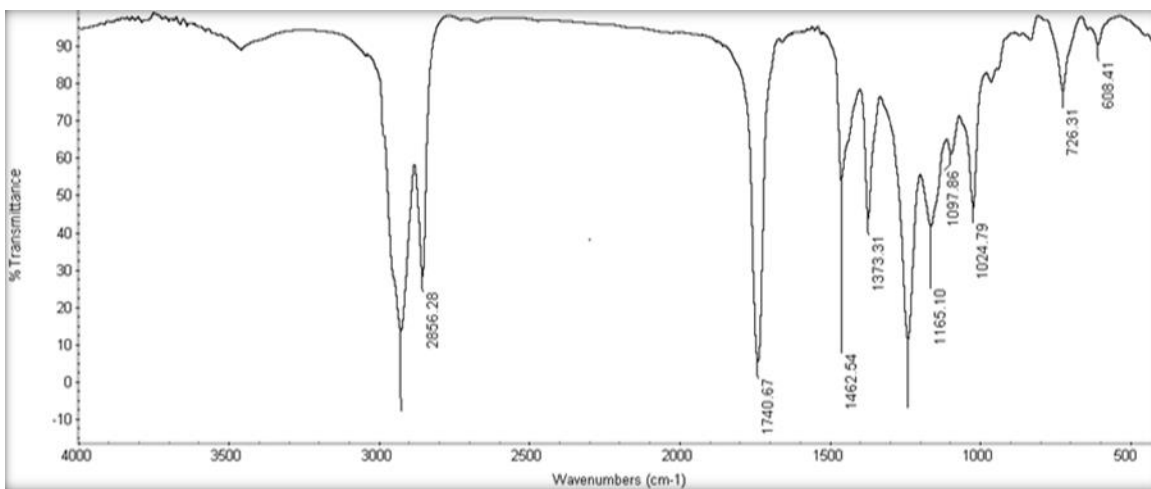


Fig. 5. The infrared spectrum of compound ( $\text{EC}_4$ )

#### 4.1.2. The nuclear magnetic resonance spectra ( $^1\text{H-NMR}$ )

The  $^1\text{H-NMR}$  spectra of products ( $\text{EC}_1 - \text{EC}_4$ ) are illustrated: The  $^1\text{H-NMR}$  spectrum of castor oil which illustrates the appearance of the  $\text{CH}_3$  terminal at  $\delta$ -0.96 ppm, -CH-OH protons at  $\delta$ -3.5 ppm, =C-H protons at  $\delta$ -5.5 ppm and methylene ( $\text{CH}_2$ ) protons at  $\delta$ -1.3 ppm.

The  $^1\text{H-NMR}$  spectrum of product ( $\text{EC}_1$ ) which illustrates the appearance of the  $\text{CH}_3$  terminal at  $\delta$ -0.96 ppm, -CH-OH protons at  $\delta$ -3.5 ppm, epoxy protons at  $\delta$ -3.2 ppm, methylene ( $\text{CH}_2$ ) protons at  $\delta$ -1.3 ppm and disappearance of =C-H protons at  $\delta$ -5.5 ppm.

The  $^1\text{H-NMR}$  spectrum of product ( $\text{EC}_4$ ) which shows the appearance of the  $\text{CH}_3$  terminal at  $\delta$ -0.96 ppm, the disappearance of -CH-OH protons at  $\delta$ -3.5 ppm and disappearance epoxy protons at  $\delta$ -3.2 ppm.

## 4.2. Evaluation of the prepared compounds

From comparison of the viscosity index value of castor oil with that synthesized compounds shown in Table 2, it is evident that the viscosity index for castor oil (221) is lower than acylated transester of treated castor oil (EC<sub>4</sub>) with value (232) which implies that the synthesized compounds show better bio-lubricant properties compared with castor oil.

Low temperature studies showed that most vegetable oils undergo poor flow and solidification at -18°C as they have a tendency to form microcrystalline structure at low temperature. The pour point should be low enough to ensure that the bio-lubricant is pump-able when the equipment is started at extremely low temperatures. So, comparing pour points of the synthesized compounds with the value of castor oil it was found that there is a clear pour point improvement for the product (EC<sub>4</sub>) with value -27°C.

Table 2. Physicochemical properties of synthesized castor oil and its acylated derivatives

Properties	Standard ASTM	Castor Oil	Prod (EC <sub>1</sub> )	Prod (EC <sub>2</sub> )	Prod (EC <sub>3</sub> )	Prod (EC <sub>4</sub> )
Viscosity index	D2270	221	175	187	193	232
Flash Point , °C	D 92	255	240	267	282	300
Pour Point , °C	D 97	-18	-9	-15	-21	-27

Flash point is useful in determination the volatility and fire resistance of a bio-lubricant and also for determination of transportation and storage temperature. So, it must be high enough to allow for safe operation at maximum operating temperature. From the results, it is evident that the product (EC<sub>4</sub>) has a value of 300°C which is necessary for most demanding applications.

The thermal stability of the prepared compounds was investigated, Figs. 6, 7, both integral is shown. It was found that the primary degradation occurs at 300°C, while the complete degradation occurs at 500°C. This confirms the suitability of the prepared compounds as bio-lubricants.

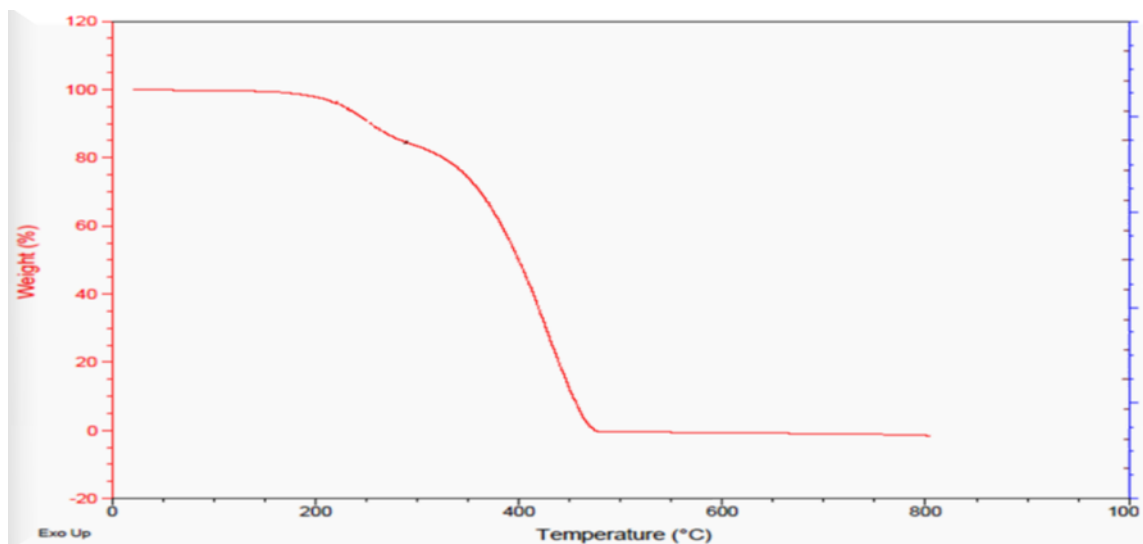


Fig. 6. TGA Curve of compound (EC<sub>3</sub>)

The most important rheological parameters for lubricants is viscosity as it also affects the tribological properties like friction between interacting surfaces and wears. In the steady-shear test, shear rates from 0 to 120 s<sup>-1</sup> at Fig. 8 were applied to the bio-lubricant. It was found that castor oil and its derivatives exhibit a Newtonian flow and by increasing shear rate, dynamic viscosity is nearly constant which is an advantage.

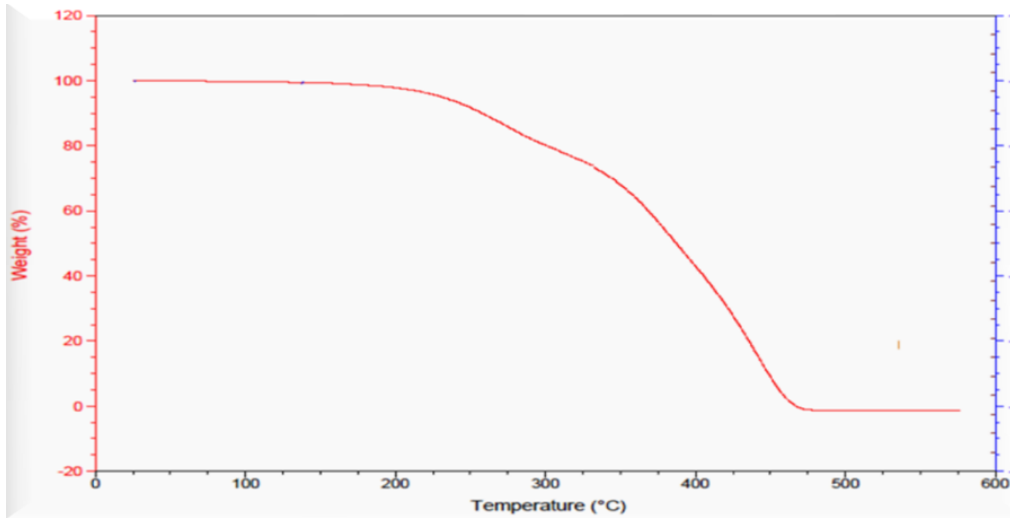


Fig. 7. TGA Curve of compound (EC4)

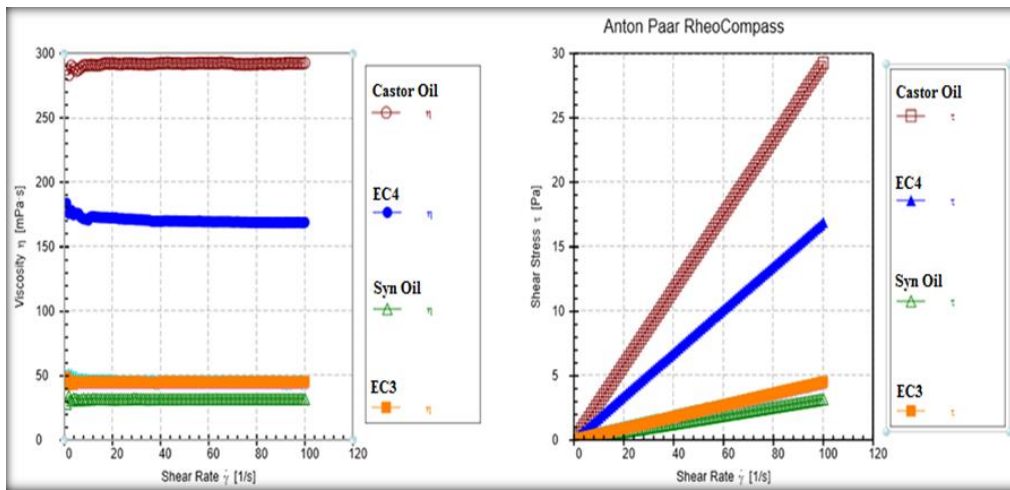


Fig. 8. Shear rate versus shear stress for castor oil, product (EC<sub>3</sub>), product (EC<sub>4</sub>) and conventional synthetic oil

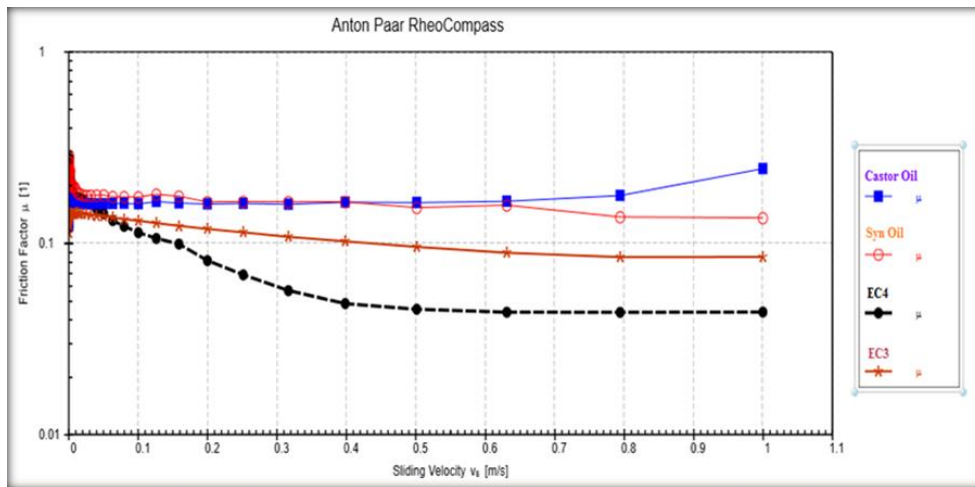


Fig. 9. Coefficient of friction (COF) versus sliding velocity for castor oil, product (EC<sub>3</sub>), product (EC<sub>4</sub>) and conventional synthetic oil

Stribeck curve shown in Fig. 9 has three types of lubricant conditions which are a boundary, mixed and hydrodynamic lubricant [20]. In the middle between mixed and hydrodynamic lubricant condition, there was an elastohydrodynamic lubricant which is the friction coefficient decreasing during the increasing of the parameter. Acylated castor oil showed low friction coefficient at 80°C compared with castor oil and conventional synthetic oils.

## 5. Conclusion

Castor oil can be used, after some chemical transformations, as a suitable candidate for obtaining environmental friendly bio-lubricants. Saturation of double bonds of castor oil gives products less susceptible to oxidation than the oil itself, i.e. having more oxidation stabilities.

Chemically modified castor oil products were given excellent results as rheological and tribological properties. Being a non-edible oil, castor oil can be used as a source for obtaining bio-lubricants without causing any nutritional problems

## References

- [1] Quinchia LA, Delgado MA, Reddyhoff T, Gallegos C, Spikes HA. Tribological studies of potential vegetable oil-based lubricants containing environmentally friendly viscosity modifiers. *Tribology International*. 2014; 69:110-117.
- [2] Tewari DD. A historical policy review of success of castor revolution in Gujarat. India. *Journal of Human Ecology*. 2012; 38(3):213-222.
- [3] Severino LS, Auld DL, Baldanzi M, Cândido MJD, Chen G, Crosby W, Tan D, He X, Lakshamma P, Lavanya C, Machado OLT, Mielke T, Milani M, Miller TD, Morris JB, Morse SA, Navan AA, Soares DJ, Sofiatti V, Wang ML, Zanotto MD, and Zieler H.A review on the challenges for increased production of castor. *Agronomy Journal*. 2012; 104(4):853-880.
- [4] Panwar NL, Shrirame HY, Rathore NS, Jindal S, Kurchania AK. Performance evaluation of a diesel engine fueled with methyl ester of castor seed oil. *Journal of Applied Thermal Engineering*. 2010; 30(2-3):245-249.
- [5] Sonalee D, Priyanka P, Smita M, Sanjay KN. Influence of NCO/OH and transesterified castor oil on the structure and properties of polyurethane: Synthesis and characterization. *Journal of Material Express*. 2015; 5(5):377-389.
- [6] Amit S, Sarviya RM, Rehman A, Khaira HK. Experimental study of castor oil based lubricant for automotive applications. *Journal of Engineering Research and Applications*. 2014; 4(1):104-107.
- [7] Aidan MD, Talib MA, Ammar SA, Ziad TA. Biodiesel production by esterification of oleic acid over zeolite Y prepared from kaolin. *Journal of Renewable Energy*. 2016; 97:19-23.
- [8] Ebtisam KH, Mamdouh SE, Salah A K, Naser ME. Manufacturing of environment friendly bio-lubricants from vegetable oils. *Egyptian Journal of Petroleum*. 2017; 26:53-59.
- [9] El-Magly IA, Nagib HK, Mokhtar WM. Aspects of the behavior of some pentaerythritol ester base synlubers for turbo-engines. *Egyptian Journal of Petroleum*. 2013; 22:169-177.
- [10] Venu BB, Vaibhav VG. Improved thermos-oxidative stability of structurally modified waste cooking oil methyl esters for bio-lubricant application. *Journal of Cleaner Production*. 2016; 112:4515-4524.
- [11] Talib N, Nasir RM, Rahim EA. Tribological behaviour of modified jatropha oil by mixing hexagonal boron nitride nanoparticles as a bio-based lubricant for machining processes. *Journal of Cleaner Production*. 2017; 147:360-378.
- [12] Isbell TA, Lowery BA, DeKeyser SS, Winchell ML, Cermak SC. Physical properties of triglyceride estolides from lesquerella and castor oils. *Journal of Industrial Crops and Products*. 2006; 23:256-263.
- [13] Geethanjali G, Sony MK, Padmaja KP, Karuna MSK, Prasad RBP. Novel acyl derivatives from karanja oil: alternative renewable lubricant base stocks. *Journal of Industrial & Engineering Chemistry Research*. 2014; 53:8685-8693.
- [14] Garcia-Zapateiro LA, Franco JM, Valencia C, Delgado MC, Gallegos C. Viscous thermal and tribological characterization of oleic and ricinoleic acids-derived and their blends with vegetable oils. *Journal of Industrial and Engineering Chemistry*. 2013; 19:1289-1298.
- [15] Satya BP, Venkata PK, Venkata SKRB, Saravanan K, Badari NPR. Castor oil fatty acid based estolide esters and their derivatives as potential lubricant base stocks. US Patent. Council of Scientific and Industrial Research (CSIR). 2014; 8742150 B2.

- [16] Nassar AM, Ahmed NS, Kamal RS. Study the Efficiency of Some Esters as Synthetic Lubricating Oil. *Journal of Pet Coal*. 2018; 60(3):520-541.
- [17] Kamal RS, Ahmed NS, Nassar AM. Synthesis and Characterization of Mixed Esters as Synthetic Lubricants. *Journal of Pet Coal*. 2018; 59(6):736-746.
- [18] Nassar AM, Ahmed NS, Abdel-Hameed HS, El-Kafrawy AF. Synthesis and utilization of non metallic detergent / dispersant and antioxidant additives for lubricating engine oil. *Journal of Tribology International*. 2016; 93(Part A):297-305.
- [19] Tobias Z, Jhina HM, Raimund J, Somphong P. Wear mechanisms and abrasion rates in selective laser sintering materials. *Journal of Polymer Testing*. 2018; 67:545–550.
- [20] Eder SJ, Bianchi D, Neacsu IA, Vorlaufer G. An experimental and signal analysis workflow for detecting cold-induced noise emissions (cold squealing) from porous journal bearings. *Journal of Mechanical Systems and Signal Processing*. 2019; 115:60–69.

---

*To whom correspondence should be addressed: Dr. Hamdy S. Abdel-Hameed, Department of Petroleum Applications, Egyptian Petroleum Research Institute, Nasr City, Cairo, Egypt, [dr\\_hamdy5@yahoo.com](mailto:dr_hamdy5@yahoo.com)*

## DIAGENETIC UNDERSTANDINGS BASED ON QUANTITATIVE DATA, MIOCENE CARBONATE BUILDUP, OFFSHORE SARAWAK, MALAYSIA

Syed Haroon Ali<sup>1</sup>, Michael C. Poppelreiter<sup>1</sup>, Mumtaz M. Shah<sup>2</sup>, Saw Bing Bing<sup>1</sup>, Markus Schlaich<sup>1</sup>

<sup>1</sup> South East Asia Carbonate Research Laboratory (SEACARL), Department of Geosciences, Faculty of Geosciences and Petroleum Engineering, Universiti Teknologi PETRONAS, 31750 Tronoh, Perak, Malaysia

<sup>2</sup> Department of Earth Sciences, Quaid-i-Azam University, 45320, Islamabad, Pakistan

Received August 3, 2018; Accepted October 19, 2018

---

### Abstract

The Central Luconia is one of the major carbonate province formed by 200 carbonate buildups with gas reserves of 63 Tcf. Structurally, the Central Luconia represents an area of low degree of structural deformation. It is located between areas of compression in south and subsidence in north. Carbonate sediments, were mainly deposited during the Upper Miocene (locally referred to as cycles IV and V). The reservoir quality of the carbonate sequence is largely controlled by diagenesis. Hence, understanding of diagenetic process and products (pore types/cements) is of prime importance for predicting reservoir quality in the subsurface. In this study, about 1150 feet of core and 160 thin sections from well X are used to calculate the qualitative and quantitative description. The platform is grain dominated (32%), dominant components are corals and foraminifera (53%). The dominant porosity type is mouldic (30%), carbonates are poorly cemented with blocky equant calcite cement (35%) having as dominant cement. However, diagenesis has altered these original minerals HMC (High Mg Calcite)/aragonite into LMC (Low Mg Calcite) and dolomite. Based on our observations, we can conclude that the platform was near to clastic source, highly dolomitized, porosity secondary in nature and coral facies are more diagenetically altered. Paragenetic sequence comprises of micritization, dissolution, dolomitization, cementation, mechanical compaction and stylolitization.

**Keywords:** Central Luconia; diagenesis; reservoir; Offshore Sarawak.

---

## 1. Introduction

The carbonate build-up in the Central Luconia provides an excellent opportunity to reveal diagenetic pattern that largely controls the reservoir properties (Figure 1). This province presents, 200 platforms distributed over 40,000 km<sup>2</sup> covered by high resolution 3D seismic, 15km core, +300 wells and 40 years of production (Figure 1).

The carbonate deposition in Central Luconia started in Upper Miocene (mainly after cycle III), on structure highs developed during the Upper Eocene to Lower Miocene [1-3]. The carbonate petrography and diagenesis were discussed by [2-5] and provides a starting point for diagenetic workflow.

There is a lack of 3D genetic model(s) explaining the pore/cement type distribution in Central Luconia and isolated platforms in general. Porosity and permeability association with diagenetic body geometries are poorly understood. Although there have been studies on sedimentology and stratigraphy of Central Luconia, only few have addressed the question of distribution of limestone diagenetic features and the dolomitization process [2].

Following are few examples of studies done on diagenesis and sedimentology of Central Luconia carbonates [2,3,6-12], however, interpretations are often not clear as the data is only

available in subsurface, with no outcrop analogues [7-10, 12].

The primary objective of this study is to produce a predictive model for limestone diagenesis based on an understanding of patterns of pore/cements type distribution and inferred processes.

1. To designate various microfacies, cements and pore types.
2. To do qualitative and quantitative description of each diagenetic phase present.
3. To propose preliminary diagenetic sequence.

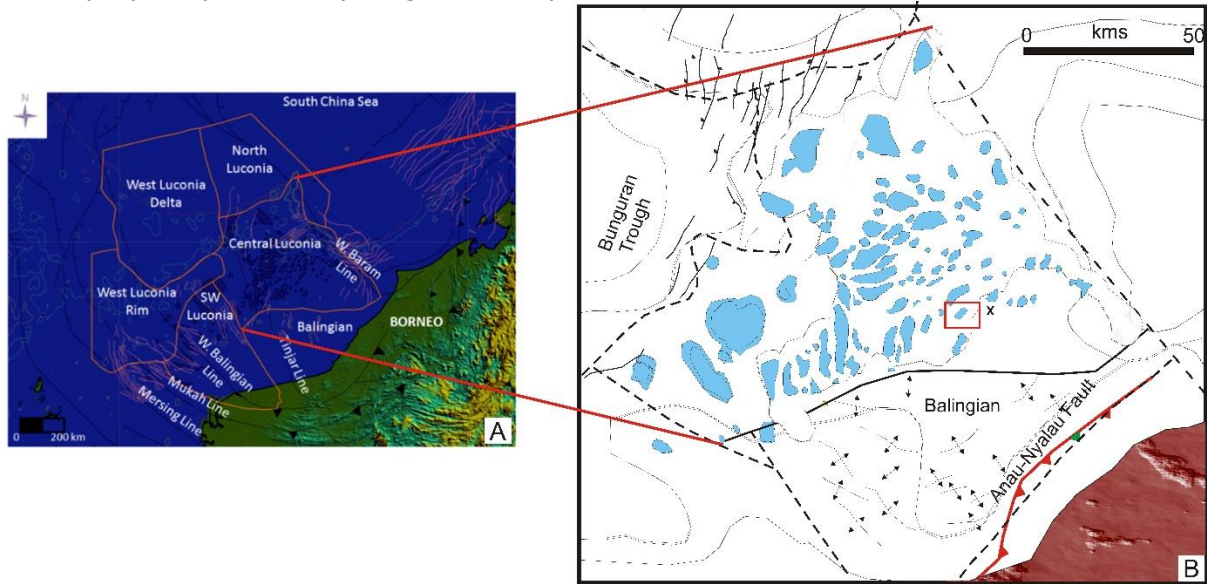


Figure 1. A) Location map of Central Luconia province with adjacent provinces, Offshore Sarawak Basin, Malaysia [3,6], B) Location of X buildup

## 2. Methods and datasets

A total of 1150ft (350.52m) of core and about 160 thin sections were used in this study representing, cycle IV and V carbonates. The methodology includes the description and digitization of the core sheet using WellCad software package, of well X-2 in Central Luconia. Main importance was given to semi-quantitative description of the platform based on lithology, facies, cement, pore, Dunham classification and components. The thin sections were described using sketches and Jmicrovision© software for point counting.

Conventional microscope (Olympus digital BX 43, with DP 72 Camera) was used for petrographic part and cement phases were established using cathodoluminescence microscopy of about 100 samples using Relion inst. CL device with vacuum below 60  $\mu$ torr with voltage 12 to 15 kV and current around 250A [13,14].

## 3. Results and discussions

### 3.1. Lithostratigraphy

The platform is divided into five stratigraphic sequences based on six flooding surfaces [15], mostly marked by argillaceous limestones (Figure 2). The sequence starts with the SS1. The lowermost part of the platform is dominated by shale dominated facies (Figure 3A), middle of the sequence is dominated by platy coral dominated facies with rare land plants. The upper part by interlayering of foraminiferal dominated wackestone and platy coral rudstone facies (Figure 3D & 3F).

SS2 marks the onset of carbonate buildup growth. This sequence is dominated by branching and massive coral float/rudstone facies (Figure 3C). It is dolomitic limestone to dolomite. SS3 is made up of dolomite and limestone lithologies, with branching and massive corals rudstone/floatstone facies and moderate red algal wackestone facies. The dominant depositional

environment of the sequence is shallow lagoon. SS4 majorly, composed of limestone with large variety of grain types e.g. red algae, foraminifera, mollusc and corals. The dominance of foraminiferal packstone to wackestone facies indicate that this sequence was deposited in deep lagoon. The final SS5 is dominated by a variety of lithologies ranging from limestone, dolomitic limestone and dolomite (Figure 3D). The top of this sequence marks the final drowning (?) of the platform. The dominant grain types are red algae and minor foraminifera in middle part of the sequence. The depositional environment of this sequence is shallow lagoon same as SS3.

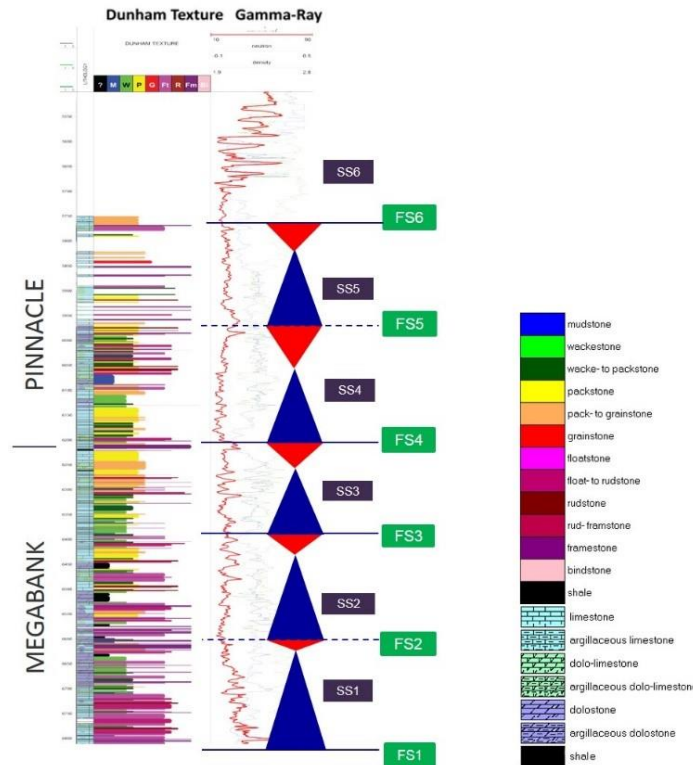


Figure 2. Vertical stratigraphic distribution of various facies in Well X-2, sequences and signatures of flooding surfaces on the Gamma ray log as well.

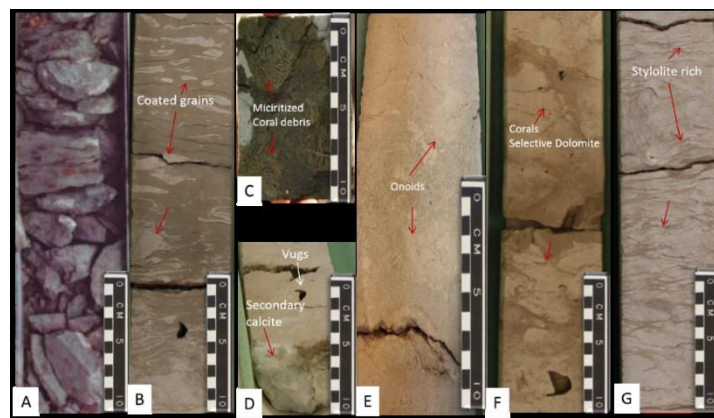


Figure 3. Key diagenetic features on core, A-Basal mixed carbonate-siliciclastic facies (cycle III-cycle IV boundary), B- Coated grain packstone facies with coral debris, C-Coral(massive) lime-packstone facies, D- Skeletal lime/dolomitic packstone facies, open vugs normally result of dissolution and closed vugs filled by secondary calcite cements, E-Oncolite lime grain dominated packstone, F-Coral(platy) lime mud dominated packstone facies, F- Coral (branching) lime dominated pack-grainstone facies.

Table1. Example of data-set resulting from microfacies, dominant cement and pores types from X-2 well

Depth core, (ft)	Microfacies	Cement types	Pore type
6200	Rhodolith floatstone-bindstone MF-7	Micritic	Minor fracture pores
6210	Amphistegina packstone-wackestone MF-3	Micritic/Equant	Micropores
6215	Amphistegina packstone-wackestone MF-3	Micritic/Equant	Mouldic
6225	Cycloclypeus-lepidocyclinids rudstone-floatstone MF-2	Blocky/equant	Mouldic
6235	Soritids(miliolid)-encrusting packstone-wackestone MF-4	Blocky/equant	Mouldic
6245	Amphistegina packstone-wackestone MF-3	Micritic	Mouldic
6255	Miogyopsina bryozoan packstone-grainstone MF-1	blocky/micrite	Mouldic/intraparticle
6265	Austrorillina mudstone-wackestone MF-5	Equant/blocky	Mouldic
6270	Rhodolith floatstone-bindstone MF-7	Sucrosic dolo./microdolomite	Intercrystalline/vugs
6285	Miogyopsina bryozoan packstone-grainstone MF-1	Micrite/equant	Mouldic
6295	Coral framestone/floatstone MF-8	Blocky/equant	Mouldic/micropores
6315	Operculinid packstone- grainstone MF-6	Equant/blocky	Mouldic
6330	Echinoid packstone- grainstone MF-10	Equant	Mouldic/micropores
6340	Soritids(miliolid)-encrusting packstone-wackestone MF-4	Equant/blocky	Mouldic/vugs
6350	Operculinid packstone- grainstone MF-6	Micrite/equant	Mouldic
6380	Soritids(miliolid)-encrusting packstone-wackestone MF-4	Equant/blocky	Mouldic/micropores
6390	Miogyopsina bryozoan packstone-grainstone MF-1	Micrite/equant	Micropores
6400	Amphistegina packstone-wackestone MF-3	Equant/blocky	Micropres

### 3.2. Core-based and petrographic description

The platform consists of 55% limestone, 20% dolomitic limestone, 15% dolomite and 10% argillaceous limestone (Figure 2). The texture of the X field is grain rich throughout, with mud-dominated packstone is forming the muddiest portions. Packstone composes 45%, grainstone 38%, rudstone 13% and mudstone 4% of the cored intervals (Figure 3&4). The grains are moderately to poorly sorted. The grain size varies from fine sand to coarse gravel, mud is virtually absent.

The 12 reported microfacies of the X-buildup based on lithological composition, components and other diagenetic features, some important microfacies are discussed here. Foraminiferal pack-wackestone microfacies, the microfacies has a mud to grain supported texture in a micritic matrix (36%) (Figure 4A). The majority of allochems are larger foraminifera (12%), corals (10%), echinoids (4%), red algae (1%) and broken mollusc shells (rare). Dolomitized massive/branching coral framestone microfacies, components are corals (39%), red algae (1%), miliolids (1%) bivalves (traces) and brachiopods (traces) (Figure 4B). Foraminiferal (miliolid) wacke- to mudstone, the microfacies have a mud supported texture in a micritic matrix of about 39% (Figure 4C) The majority of allochems are miliolid (10%) echinoids (8%), and planktonic foraminifera (2%). Sucrosic dolo-mudstone microfacies, in terms of petrographic observations this facies is characterized by fine to coarsely crystalline (60-100 µm) crystals that are loosely cemented (Figure 4D). The majority of allochems are red algae (4%) and unidentified skeletal debris (2%).

The dominant components (Figure 5) are corals (37%), foraminifera's (28%), red algae (21%), echinoderms (6%), molluscs (5%), brachiopods (<1%), bryozoans (<1%) and green algae (<1%). The depositional sub-environments of the atoll as interpreted in core are: coral debris dominate facies represents shallow lagoon and foraminifera dominate facies signifies deep lagoon.

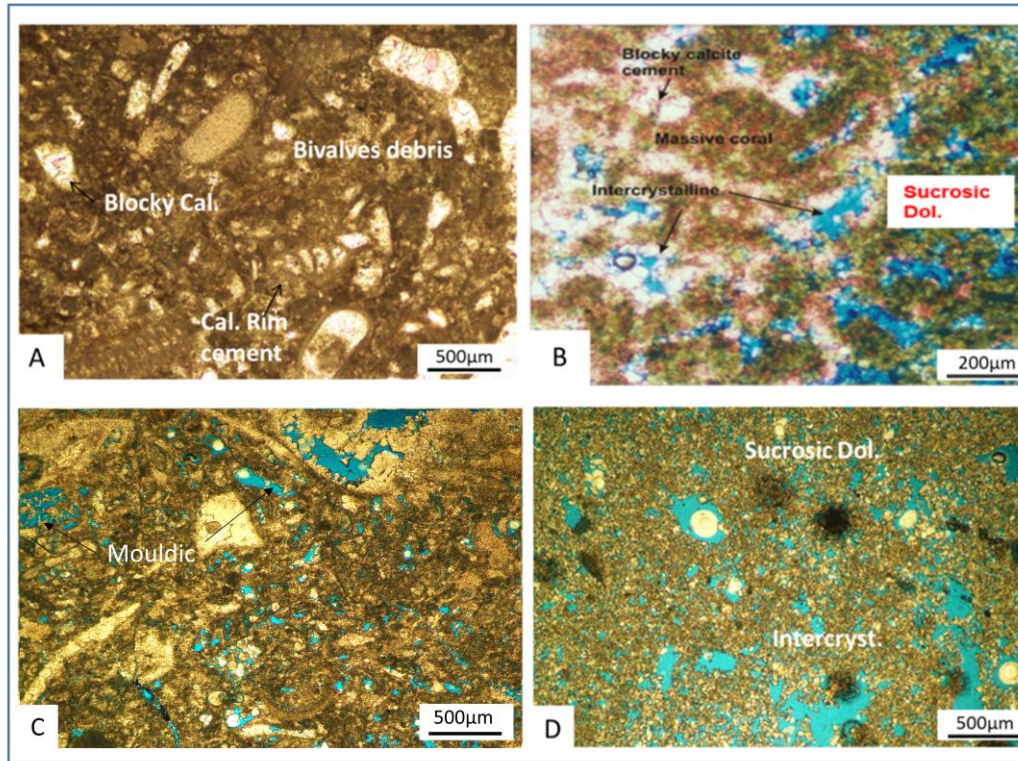


Figure 4. (A) Foraminiferal pack-wackestone microfacies with total porosity (1%), (B) Dolomitized massive/branching coral framestone, total porosity (13%), intragranular (8%) and intercrystalline (5%), (C) Miliolid wacke-mudstone microfacies, total (25%), mouldic (20%) and vuggy (5%). (D) Sucrosic dolomudstone microfacies, total porosity (30%), intercrystalline (13%), vuggy (13%) and microporosity (4%)

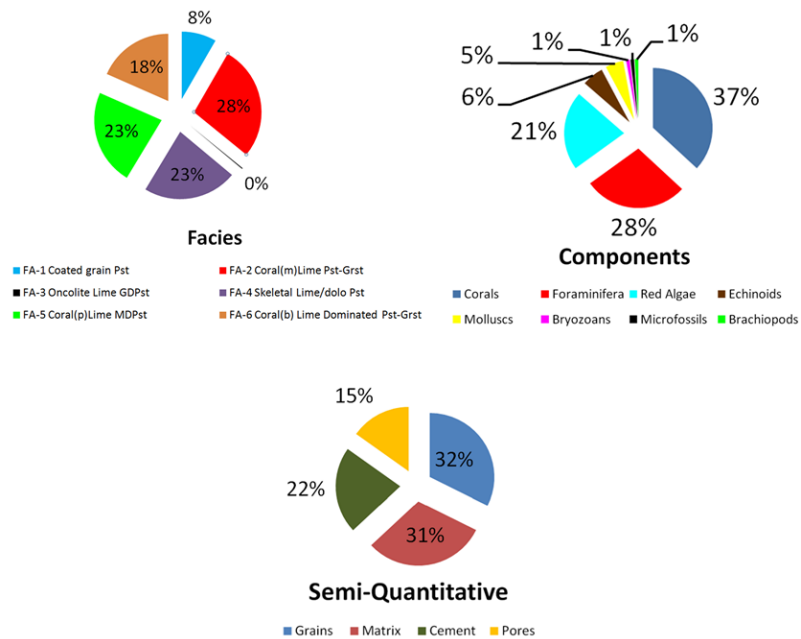


Figure 5. Quantitative description of X-Field, based on facies, components and semi-quantitative

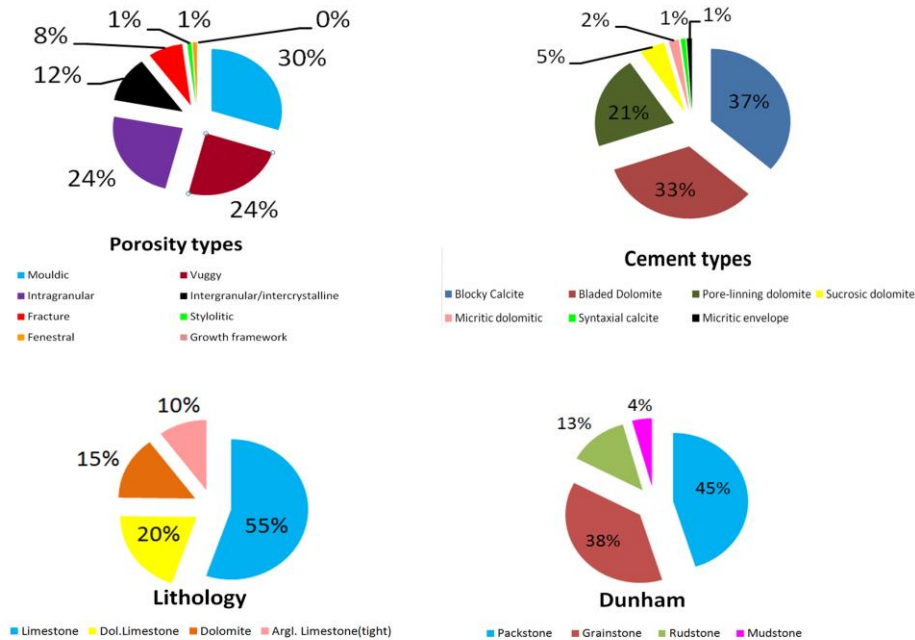


Figure 6. Quantitative Description of X-Field, based on porosity types, cement types, lithology and Dunham’s name

The original mineralogy can be inferred from the observed grains, e.g., 29% LMC (foraminifera, brachiopods) are mostly preserved, 43% aragonite (corals, molluscs, bryozoans) are largely re-crystallized, whereas 27% HMC (red algae, echinoderms) are mostly well preserved (Figure 5). Diagenesis has altered these original minerals into Low-Mg calcite and dolomite.

The main types of cements (by shape -Figure 6) are: 35% blocky equant calcite cement, 32% bladed calcite cement, 20% pore lining, blocky hypidiomorphic dolomite cement, 5% sucrosic dolomite cement, 5% micro-crystalline dolomite cement, 2% micritic/micro-sparitic calcite cement and <1% syntaxial/rim calcite cement (Figure 6)

### 3.3. Sequence stratigraphy

Carbonate sequence in buildup X represents three petrophysically distinct sections:

- *Flooding*: Argillaceous limestone (Figure 2 & 3F) mostly in mudstone facies, few skeletal fragments and high abundant bioturbations. These are characterized by poor reservoir quality and high values on gamma ray logs.
- *Aggradation and progradation*: The aggradation starts with foram-red algal wacke- mudstone facies that leads. The upper half of the sequence sees full development of coral debris facies association. The upper part of the sequence has excellent reservoir potential (Figure 7).
- *Exposure*: The karst indicates large gaps having lateral infill. Good reservoir facies exist below the karst surface, with vuggy pores, that indicate intense leaching (Figure 7).

### 3.4. Cement stratigraphy and paragenetic sequence

Paragenetic sequence includes early and burial diagenetic features (Figure 8): The 3 generations of dolomitization. The diagenetic changes vary stratigraphically within the X platform: The first stage of dissolution and leaching took place before the early calcite cementation (that destroyed all the generated pore spaces). Later dissolution and corrosion occurred after the dolomitization event and are related to burial diagenesis.

Based on cathodoluminescence observations the buildup is comprised of four stages of calcite (Figure 8A), three dolomites (Figure 8B), and one pyrite cementation stage.

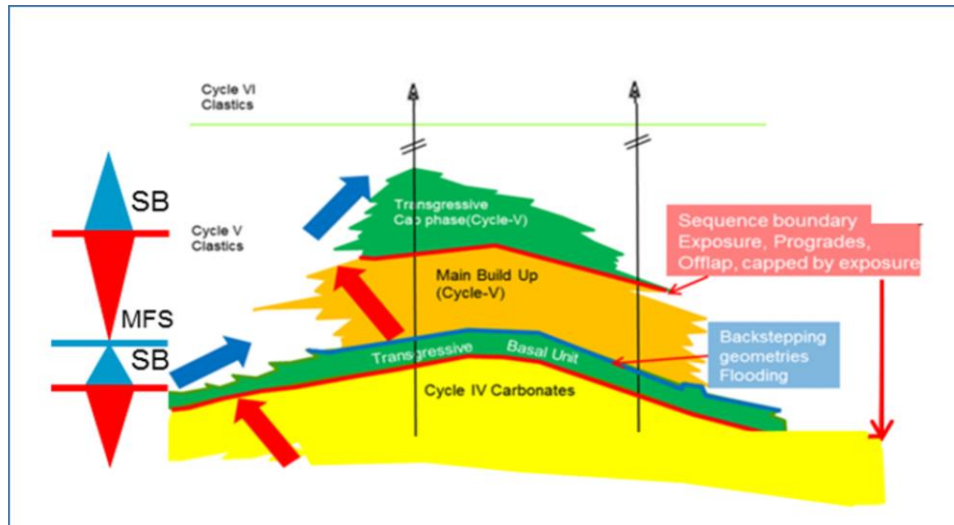


Figure 7. A typical growth pattern of a Central Luconia carbonates buildup[3], the sequence boundaries present more dolomitization, while the Maximum Flooding Surfaces (MFS) are more cemented in the reservoir

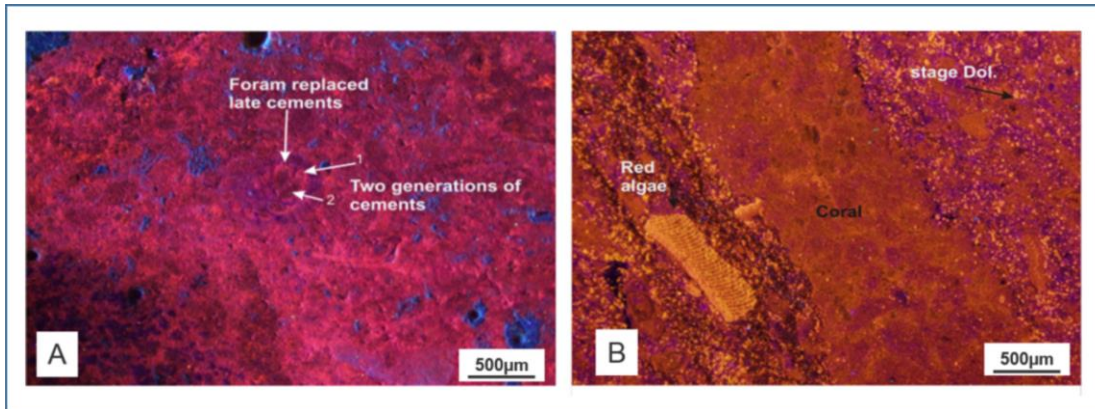


Figure 8. (A)Complex zonation in Foraminifera (Foram-Pack-Wackestone), (B) Calcite cement filling an intraparticle pores in coral with fabric destructive replacement dolomite (stage Dol-1)

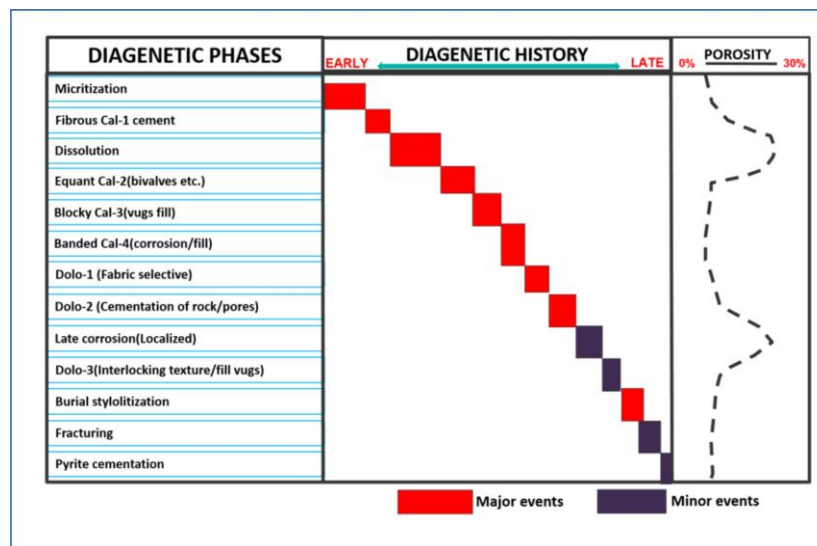


Figure 9. Paragenetic sequence within the X-Field

#### 4. Conclusions

Based on the quantitative information from the core and thin sections, buildup X, is located close to a clastic source.

- Platform is partially dolomitized (dolomitic limestone 20%; dolomite 15%). Strongest alterations are observed in coral-rich facies (reefal debris/shallow lagoon).
- Diagenesis occurs cyclically and corresponds to seismically detectable buildup geomorphology. The paragenetic sequence generated includes micritization, dissolution, dolomitization, cementation, mechanical compaction and stylolitization.
- Burial diagenesis moderately alters the pore structure in certain parts of the buildup.

#### Acknowledgments

We gratefully acknowledge the support by Department of Geosciences, University Technology Petronas, PETRONAS, Geo-Sample Center (PGSC).

#### References

- [1] Ali MY. Carbonate cement stratigraphy and timing of diagenesis in a Miocene mixed carbonate-clastic sequence, offshore Sabah, Malaysia: constraints from cathodoluminescence, geochemistry, and isotope studies. *Sediment. Geol.*, 1995; 99(3-4):191-214.
- [2] Rulliyansyah. Dolomitization In Miocene Carbonate Platforms Of Central Luconia, Sarawak: Character, Origin, And Impact On Reservoir Properties, Universiti Teknologi Petronas, 2011.
- [3] Epting M. Sedimentology of Miocene Carbonate Buildups, Central Luconia, Offshore Sarawak, *Geol. Soc. Malaysia, Bull.*, 1980; 12:17-30.
- [4] Hutchison C. S. Is there a satisfactory classification for Southeast Asian Tertiary basins?, *Pap. Present. Offshore South East Asia Conf. South East Asia Pet. Explor. Soc.*, 1984:1:6664-6676.
- [5] Janjuhah HT, Salim AMA, Ghosh DP, Wahid A. Diagenetic processes and their effect on reservoir quality in Miocene Carbonate Reservoir, Offshore Sarawak, Malaysia, *ICIPEG*, 2016; 545-558.
- [6] Ali MY, and Abolins P. Central Luconia Province, in *The Petroleum Geology and Resources of Malaysia*, in Petronas, K. L. (ed.), 1999; 371-392.
- [7] Wilson MEJ, and Evans MJ. Sedimentology and diagenesis of Tertiary carbonates on the Mangkalihat Peninsula, Borneo: Implications for subsurface reservoir quality, *Marine and Petroleum Geology*, 2002; 19(7): 873-900.
- [8] Madden RHC and Wilson MEJ. Diagenesis of Neogene Delta-Front Patch Reefs: Alteration of Coastal, Siliciclastic-Influenced Carbonates from Humid Equatorial Regions, *Journal of Sedimentary Research*, 2012; 82(11): 871-888.
- [9] Madden RHC and Wilson MEJ. Diagenesis of a SE Asian Cenozoic carbonate platform margin and its adjacent basinal deposits, *Sedimentary Geology*. 2013; pp. 20-38.
- [10] Madden RHC, Wilson MEJ and O'Shea M. Modern fringing reef carbonates from equatorial SE Asia: An integrated environmental, sediment and satellite characterisation study', *Marine Geology*, 2013; 344: 163-185.
- [11] Vahrenkamp VC, David F, Buijndam P, Newall M, Crevello P. Growth Architecture, Faulting, and Karstification of a Middle Miocene Carbonate Platform, Luconia Province, Offshore Sarawak, Malaysia', in. 2004; *AAPG Memoir* 81:329-350.
- [12] Janjuhah HT, Gamez Vintaned JA, Salim AMA, Faye I, Ghosh DP. Microfacies and Depositional Environments of Miocene Isolated Carbonate Platforms from Central Luconia, Offshore Sarawak, Malaysia', *Acta Geologica Sinica*, 2017; 91(5): 1778-1796.
- [13] Shah MM, Ahmed W, Ahsan N, Lisa M (2016) 'Fault-controlled, bedding-parallel dolomite in the middle Jurassic Samana Suk Formation in Margalla Hill Ranges, Khanpur area (North Pakistan): petrography, geochemistry, and petrophysical characteristics', *Arabian Journal of Geosciences*, 2016; 9(5): 405.
- [14] Swennen R, Dewit J, Fierens E, Muchez P, Shah MM, Nader F, Hunts D. Multiple dolomitization events along the Pozalagua Fault (Pozalagua Quarry, Basque-Cantabrian Basin, Northern Spain), *Sedimentology*, 2012; 59(4): 1345-1374.
- [15] Ali SH, Poppelreiter MC. Quantitative Diagenesis of a Miocene Carbonate Platform, Malaysia, in *Asia Petroleum Geoscience Conference and Exhibition (APGCE)*, 2017; 1-5.

*To whom correspondence should be addressed: Syed Haroon Ali, South East Asia Carbonate Research Laboratory (SEACARL), Department of Geosciences, Faculty of Geosciences and Petroleum Engineering, Universiti Teknologi PETRONAS, 31750 Tronoh, Perak, Malaysia*

## MODELLING OF REGENERATION PROCESS OF ZEOLITE-CONTAINING CRACKING CATALYSTS

Galina Y. Nazarova\*, Tatiana A. Shafran, Elena N. Ivashkina, Irena O. Dolganova

Fuel Engineering and Chemical Cybernetics Department, Tomsk Polytechnic University, Russia

Received August 1, 2018; Accepted October 19, 2018

---

### Abstract

The research aimed at discovering the patterns of the zeolite-containing cracking catalysts regeneration, which are required for the mathematical model development, is presented. This model takes into account the physicochemical and kinetic patterns of the of coke oxidation reactions in the air. The numerical calculations using the model allowed to predict of the regeneration temperature, the coke amount on the regenerated catalyst and the combustion gas composition depending on the process conditions of the reactor-regenerator unit and the coke amount on the dead catalyst.

**Keywords:** catalytic cracking; zeolite-containing catalyst; coke, regeneration; mathematical modeling.

---

## 1. Introduction

The catalytic cracking is the most important producer of the high-octane gasoline components and feedstock for the petrochemical industry all over the world and contributes to the oil refining deepening. The catalytic cracking capacity exceeds 35% of the oil refining volume in the US, 15% in Western Europe and less than 10% in Russia. Currently, the total global capacity of the catalytic cracking is about 700 million tons of feedstock per year [1]. The catalytic cracking efficiency is determined by the activity, the selectivity and the stability of the microspheric zeolite-containing catalysts primarily. However, the deterioration of these indicators during the operation is observed due to the catalysts deactivation by coke and heavy metals, abrasion, sintering, etc.

The catalysts deactivation by coke is a reversible process. In industrial conditions, the catalyst undergoes regeneration in order to restore the activity. During this process, the coke oxidation using the oxygen-containing mixtures and partial reduction of the catalytic properties occur, and the catalysts operation becomes cyclical as "operation-regeneration" process [2-3].

The oxidation rate of a coke can be intensified by increasing the oxygen amount in the supplied air to regeneration, and by introducing the oxidation promoters into the catalysts, which do not have a noticeable effect on the activity and selectivity of the catalysts.

At high oxidation rates, a sharp increase in the regeneration zone temperature occurs. This fact can become the main reason for the irreversible catalyst deactivation as a result of sintering the pore structure [4-7]. The problem of deactivation due to overheating is so the most important for regenerated catalysts, and it is required to reduce the oxidation rates instead of intensifying the coke oxidation.

Also, the heat released during the coke oxidation is used to conduct the process in the reactor. Heat transfer is carried out by heating the catalyst flow in the regenerator.

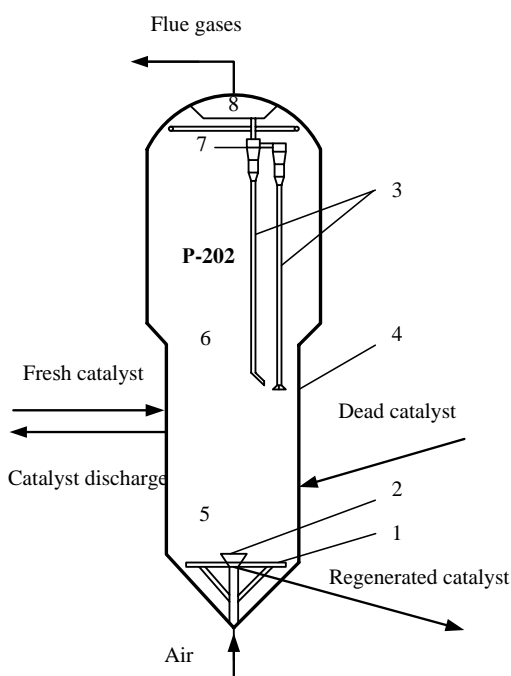
Thus, the oxidative regeneration efficiency has a significant effect on the economics of the catalytic processes, and it determines the competitiveness of various design options for catalytic cracking.

The development and application of mathematical model taking into account the physicochemical and kinetic patterns of the coke oxidation reactions with the air [8-17] allow to predict not only the residual coke amount on the catalyst and the composition of the flue gases of regeneration, but also the regeneration zone temperature depending on the process conditions of the reactor-regenerator block taking into account the amount of coke formed on the catalyst surface in the reactor.

The research aims to develop the mathematical model of the regeneration of zeolite-containing catalysts in catalytic cracking to forecast the oxidized coke amount on the catalyst, the regeneration temperature, and the flue gas composition.

## 2. Object and methods of research

The object of research is the oxidative regeneration process of the catalytic cracking unit (section S-200), which is a part of KT-1/1 combined unit for deep processing of fuel oil. A microspheric zeolite-containing catalyst with an average particle size of 90  $\mu\text{m}$  bulk and an apparent density of 840 and 1400  $\text{kg}/\text{m}^3$  is circulated between the reactor and the regenerator at the catalytic cracking unit.



Along with the target and by-products (unstable gasoline, rich gas, 195-510°C fraction, 310-420°C fraction, 420+°C fraction), the coke deposition on the zeolite-containing catalyst surface occurs during operation. The oxidative regeneration in the fluidized catalyst bed is carried out in order to partially catalyst reduction on the KT-1/1 unit. The regenerator capacity for oxidized coke is 13600  $\text{kg}/\text{h}$ . The regenerator is a cylindrical apparatus with internal diameters of 9 and 11 m and a height of 27.6 m. The effective regenerator volume is 1800  $\text{m}^3$  with an average height of the fluidized catalyst bed of 4 m (Fig. 1).

Fig. 1. The regenerator scheme of the KT-1/1 unit: 1-boxes and manifolds; 2-funnel; 3-2-stage cyclones; 4- regenerator shell; 5 - fluidized bed of the catalyst; 6-zone of the dilute-phase fluidized bed of the catalyst; 7- sedimentation zone; 8 - collecting chamber

After the oxidative regeneration stage, the regenerated catalyst from the regenerator P-202 is gravity feed to the reactor for the compounding with the feedstock. The main process conditions of the reactor-regenerator block are given below (Tab.1). The material balance of the KT-1/1 regenerator is given below (Tab.2).

The following methods were used during the modeling the oxidative regeneration of cracking catalysts and the studying the characteristics of cracking catalysts at the "operation-regeneration" cycle:

1. Granulometric analysis for determining the particle diameter distribution at catalyst sample using HORIBA LA-300 laser meter (detection limit 0.1 to 600  $\mu\text{m}$  in diameter using a laser diode, a maximum error of 0.6%).
2. A mathematical modeling method for the mathematical description of the regeneration of zeolite-containing cracking catalysts in order to forecast the residual coke on the regenerated catalyst, the regeneration temperature, and the flue gas composition.

Table 1. Operating factors and process conditions of the reactor-regenerator block of the KT-1/1 unit

Operating factors and process conditions	Value
Feedstock flowrate to reactor, tons per day	6686.2
Catalyst circulation ratio, $\text{ton}_{\text{cat}}/\text{ton}_{\text{feed}}$	7.95
Mass of the catalyst in the regenerator, ton	150–200
Coke amount on the coked catalyst, % wt	0.47
Residual coke amount on the catalyst, % wt	0.045
Catalyst flow temperature at the regenerator inlet, K	808.7
Air consumption in regenerator, $\text{m}^3/\text{h}$ at standard conditions.	167 522.2
Air temperature at the regenerator inlet, K	410.6
Regeneration zone temperature, K	903–1003
Air pressure at the regenerator inlet, MPa	0.42
Pressure in the regenerator sedimentation zone, MPa	0.17
Amount in flue gases of regeneration, % vol:	
– CO/CO <sub>2</sub>	0.0009/11.86
– O <sub>2</sub> /N <sub>2</sub>	4.94/83.19

Table 2. The material balance of the KT-1/1 regenerator (calculation)

Flow	Value tons per day	%
<b>Input:</b>		
– catalyst	53 219.8	95.84
– coke after reactor	251.3	0.45
– air	2 060.9	3.71
total	55 532.0	100.00
<b>Output:</b>		
– catalyst	53 219.8	95.83
– coke after regenerator	54.3	0.098
– flue gases	2 236.7	4.03
total	55 510.8	99.96

### 3. Development of regeneration model of zeolite-containing cracking catalysts

The main stages for the modeling the oxidative regeneration of zeolite-containing cracking catalysts are the following:

- conducting the thermodynamic analysis of all possible reactions in the regenerator;
- determination of the hydrodynamic mode of the regenerator in the fluidized bed of the catalyst;
- establishing the probable scheme for coke oxidation on the surface of the cracking catalyst;
- development of a kinetic and mathematical model of the regeneration;
- verification of the mathematical model.

#### 3.1. Thermodynamic analysis of the oxidative regeneration reactions

A calculation of the thermodynamic functions changing of the model reactions at the temperature range from 808 to 1003 K and a pressure of 1 bar was made in order to estimate and forecast the reactions probability and the carbon transformations products formation [18]. This temperature range corresponds to the regenerator process conditions. As it is known, the coke compounds on the surface of the catalyst are characterized by a complicated structure, and the thermochemical information for such compounds is limited in the literature. Therefore, it was accepted to investigate the coke structures reactions on the example of the combustible component – carbon in the oxygen atmosphere of air and water vapor (Tab.3).

Table 3. The dependence of the thermodynamic functions changing of model reactions at a temperature  $T = 808 \div 1003$  K and pressure 1 bar

Reaction	kJ/(mol·K)		kJ/mol	
	$\Delta_r S_T^0$	$\Delta_r H_T^0$	$\Delta_r G_T^0$	
$2C_{\text{coke}} + O_2 = 2CO$	$0.169 \div 0.166$	$-(226.35 \div 229.10)$	$-(362.97 \div 395.19)$	
$2CO + O_2 = 2CO_2$	$-(0.167 \div 0.165)$	$-(562.76 \div 561.20)$	$-(427.60 \div 395.36)$	
$C_{\text{coke}} + O_2 = CO_2$	$0.001 \div 0.000$	$-(394.56 \div 395.15)$	$-(395.28 \div 395.27)$	
$C_{\text{coke}} + H_2O_{\text{vapor}} = CO + H_2$	$0.127 \div 0.124$	$127.81 \div 125.71$	$25.00 \div 0.90$	
$C_{\text{coke}} + CO_2 = 2CO$	$0.168 \div 0.165$	$168.20 \div 166.05$	$32.31 \div 0.09$	

The thermodynamic analysis results of model reactions showed that the exothermic reactions (1) – (3) ( $\Delta_r G_T^0 < 0$ ) predominate and the endothermic reactions (4)–(5) are improbable ( $\Delta_r G_T^0 > 0$ ) under regenerator process.

### 3.2. Determination of the hydrodynamic mode of the regenerator

Hydrodynamic calculations [19-20] showed that the catalyst bed in the regenerator passes into the fluidization state at the flue gas velocity of 0.0014 m/s (calculated on the free area by (1)):

$$\omega_{if} = 0,005 \cdot \varepsilon^3 \cdot \frac{d^2 \cdot (\gamma_k - \gamma_a)}{\mu \cdot (1 - \varepsilon)}, \tag{1}$$

$$\omega_{sv} = \sqrt{\frac{4}{3} \cdot \frac{g \cdot d \cdot (\gamma_k - \gamma_a)}{C \cdot \gamma_a}}, \tag{2}$$

The destruction of the fluidized catalyst bed, which is characterized by the elutriation of the solid particles from a fluidized bed, occurs when the velocity is above than the suspension velocity of 0.23 m/s (2):

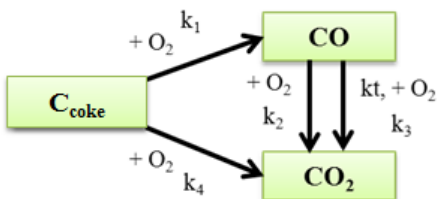
The actual velocity of the regeneration flue gas (3) is 0.69 m/s (3):

$$\omega_{av} = \frac{CF \cdot Q_t \cdot P_s \cdot (T_b + T_f)}{(P_b + P_f) \cdot T_b \cdot 3600 \cdot A_t} \tag{3}$$

here  $d$  – the average (effective) diameter of the catalyst particle, m;  $\gamma_k$  – the apparent density of the catalyst, kg/m<sup>3</sup>;  $\gamma_a$  and  $\mu$  – the density (kg/m<sup>3</sup>) and the dynamic viscosity (kgf/m<sup>2</sup>) of the fluidizing agent;  $g$  – the intensity of gravity, m/s<sup>2</sup>;  $c$  – the resistance coefficient;  $CF$  – the coke accounting constant in the regenerator (1,035);  $Q_t$  – the total air flow to regenerator, m<sup>3</sup>/h at standard conditions;  $P_s$  – the atmospheric pressure, kgf/cm<sup>2</sup>;  $T_b$  – the standard temperature (273.15) K;  $T_f$  – the temperature in the regeneration zone, K;  $P_b$  – barometric pressure, kgf/cm<sup>2</sup>;  $P_f$  – the average absolute pressure in the catalyst bed, kgf/cm<sup>2</sup>;  $A_t$  – sectional area of the regenerator (89.88 m<sup>2</sup>).

It can be considered that the fluidized bed is an approximation to the plug-flow reactor because the actual velocity of regeneration flue gases exceeds the value of the suspension velocity ( $\omega_{if} \ll \omega_{sv} \ll \omega_{av}$ ).

### 3.3. The development of the kinetic model of the oxidative regeneration of zeolite-containing cracking catalysts



The results of the thermodynamic analysis of all possible reactions in the regenerator at the temperature range 808- 1003 K allow suggesting a conversion scheme during the regeneration (Fig. 2).

Fig. 2. The scheme of coke oxidation on the catalytic cracking catalyst

By the coke oxidation scheme on the cracking catalysts surface, the mathematical model of the oxidative regeneration in the fluidized catalyst bed in steady state conditions of the plug-flow reactor was developed (4) (the assumption of quasi-homogeneity of the components was adopted):

$$\left\{ \begin{aligned} \frac{dC_{C_{\text{coke}}}}{d\tau} &= -2 \cdot k_1 \cdot \left( \frac{\rho_{fb} \cdot X_{\text{coke}}^{\text{deadcat}}}{MM_{\text{coke}}} \right)^2 \cdot c_{O_2} - k_4 \cdot \left( \frac{\rho_{fb} \cdot X_{\text{coke}}^{\text{deadcat}}}{MM_{\text{coke}}} \right)^2 \cdot c_{O_2}; \\ \frac{dC_{O_2}}{d\tau} &= -k_1 \cdot \left( \frac{\rho_{fb} \cdot X_{\text{coke}}^{\text{deadcat}}}{MM_{\text{coke}}} \right)^2 \cdot c_{O_2} - k_2 \cdot c_{CO}^2 \cdot c_{O_2} - k_3 \cdot c_{CO}^2 \cdot c_{O_2} - k_4 \cdot \left( \frac{\rho_{fb} \cdot X_{\text{coke}}^{\text{deadcat}}}{MM_{\text{coke}}} \right)^2 \cdot c_{O_2}; \\ \frac{dC_{CO}}{d\tau} &= 2 \cdot k_1 \cdot \left( \frac{\rho_{fb} \cdot X_{\text{coke}}^{\text{deadcat}}}{MM_{\text{coke}}} \right)^2 \cdot c_{O_2} - 2 \cdot k_2 \cdot c_{CO}^2 \cdot c_{O_2} - 2 \cdot k_3 \cdot c_{CO}^2 \cdot c_{O_2}; \\ \frac{dC_{CO_2}}{d\tau} &= 2 \cdot k_2 \cdot c_{CO}^2 \cdot c_{O_2} + 2 \cdot k_3 \cdot c_{CO}^2 \cdot c_{O_2} + k_4 \cdot \left( \frac{\rho_{fb} \cdot X_{\text{coke}}^{\text{deadcat}}}{MM_{\text{coke}}} \right)^2 \cdot c_{O_2}; \\ \frac{dT}{d\tau} &= \frac{k_1 \cdot \left( \frac{\rho_{fb} \cdot X_{\text{coke}}^{\text{deadcat}}}{MM_{\text{coke}}} \right)^2 \cdot c_{O_2} \cdot \Delta H_1 + k_2 \cdot c_{CO}^2 \cdot c_{O_2} \cdot \Delta H_2 + k_3 \cdot c_{CO}^2 \cdot c_{O_2} \cdot \Delta H_3 + k_4 \cdot \left( \frac{\rho_{fb} \cdot X_{\text{coke}}^{\text{deadcat}}}{MM_{\text{coke}}} \right)^2 \cdot c_{O_2} \cdot \Delta H_4}{\rho^f \cdot c_p^f} \end{aligned} \right. \quad (4)$$

here  $dC_i/d\tau$  – change in the concentration of the i-th reaction reagent by contact time, mol/(m<sup>3</sup>·s);  $k_i$  – the rate constant of the i-th reaction according to the Arrhenius equation, c<sup>-1</sup>;  $\rho_{fb}$  – the density of the fluidized bed of the catalyst, kg/m<sup>3</sup>;  $X_{\text{coke}}^{\text{deadcat}}$  – coke quantity on the coked catalyst;  $X_{\text{coke}}^{\text{deadcat}} = 0 \dots 1$ ;  $MM_{\text{coke}}$  – the molecular weight of coke, kg/mol;  $c_i$  – the current concentration of the i-th reaction reagent, mol/m<sup>3</sup>;  $\rho^f$  – the density of the reaction mixture, kg/m<sup>3</sup>;  $c_p^f$  – the specific heat of the reaction mixture, kJ/(kg·K);  $dT/d\tau$  – the temperature change in the regenerator by contact time, K/s;  $\Delta H_j$  – the thermal effect of the corresponding reactions, kJ/mol; the initial conditions:  $\tau=0$ ;  $C_{\text{coke}}=C_{\text{coke},0}$ ;  $C_{O_2}=C_{O_2,0}$ ;  $C_{CO}=0$ ;  $C_{CO_2}=0$ ;  $T=T_0$ .

The contact time in the volume of the is calculated according to (5):

$$\tau = \frac{V_{fb}}{V_{\text{coke}} + V_{\text{air}}}, \quad (5)$$

here  $V_{fb}$  – the volume of the fluidized bed of the catalyst, m<sup>3</sup>;  $V_{\text{coke}}$  – the coke amount on the catalyst surface from the reactor, m<sup>3</sup>/s;  $V_{\text{air}}$  – the total air flow for regeneration, m<sup>3</sup>/s.

The software implementation of the model is carried out using the PascalABC.NET integrated programming software.

The kinetic parameters of the oxidative regeneration reactions of the zeolite-containing cracking catalysts presented below were determined by solving the inverse kinetic problem using the experimental data from the industrial catalytic cracking unit for a long period of its operation. The activation energy values of the reactions are taken according to the literature data review [21].

Also, at the stage of the kinetic parameters establishing, it is important to estimate the pore-diffusion resistances presence for determining the kinetic region boundaries. Also, in accordance with [22], the regeneration of the microspherical cracking catalysts in the fluidized bed is characterized by the kinetic region at temperatures up to 923 K, by the transition region at 923–943K and by the diffusion region at temperatures above 943 K.

Estimation of the pore-diffusion resistances presence by the Thiele modulus (6) and the effectiveness factor (7) values for an average particle size of 90 μm showed that the pore-

diffusion resistances of the regeneration reactions on the zeolite-containing cracking catalysts are absent.

$$\psi = L \sqrt{\frac{kC_0^{n-1}}{D_{eff}}} \tag{6}$$

$$\eta = \frac{3}{\psi} \cdot \left( \frac{e^\psi + e^{-\psi}}{e^\psi - e^{-\psi}} - \frac{1}{\psi} \right), \tag{7}$$

here  $L$  – the catalyst grain size equal to the volume to the outer surface ratio,  $m$ ,  $k$  – the reaction rate constant,  $n$  – the reaction order,  $C_0$ – the reagent concentration, mol/l,  $D_{eff}$ – effective diffusion factor,  $m^2/s$ .

It is connected with the Thiele modulus value does not exceed  $\psi \leq 1$  for first-order reactions, and the effectiveness factor of the catalyst grain use is  $\sim 1$  (Tab.4).

The developed model of the regenerator allows forecasting the coke amount on the regenerated catalyst, the flue gases composition, the regeneration temperature.

Table 4. The kinetic parameters of regeneration at  $T = 945$  K and  $P = 0.17$  MPa

Reaction	$k_0, s^{-1}$	$E_a, kJ/mol$	$k(T), s^{-1}$	Thiele modulus	Effectiveness factor
$2C_{coke} + O_2 = 2CO$	$7.92 \cdot 10^5$	99.1	2.62	0.10	0.999
$2CO + O_2 = 2CO_2$	$6.52 \cdot 10^3$	50.4	10.65	0.21	0.997
$2CO + O_2 = 2CO_2$ (catalytic)	$8.38 \cdot 10^5$	90.8	7.98	0.18	0.998
$C_{coke} + O_2 = CO_2$	$2.90 \cdot 10^5$	65.2	71.90	0.54	0.981

### 3.4. Verification of the mathematical model

Calculated and experimental data comparison from the industrial catalytic cracking unit showed that the mathematical model describes the process with high accuracy (Fig. 3, 4), this model takes into account the physico-chemical and kinetic patterns of the coke oxidation reaction with the air.

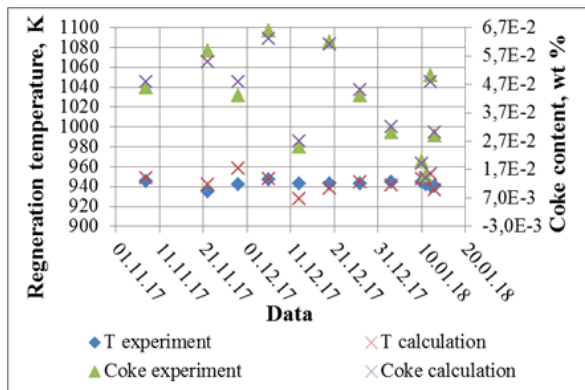


Fig. 3. Comparison of calculated and experimental data in the residual coke amount and the regeneration temperature

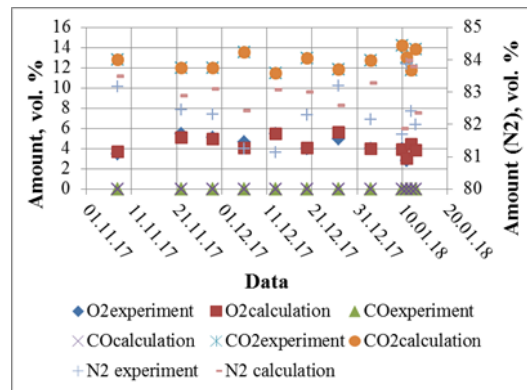


Fig. 4. Comparison of calculated and experimental data in the flue gases of regeneration ( $O_2$ ,  $CO$ ,  $CO_2$ ,  $N_2$ )

The average relative errors are 5.6% at the calculation of the coke amount on the regenerated catalyst, 5.3, 4.8%, 4.9 %, 0.9% at calculations of  $O_2$ ,  $CO$ ,  $CO_2$ , the  $N_2$  amount in the flue gas of regeneration relatively.

In addition, a different dynamics of coke oxidation is observed depending on the various initial conditions (temperature and air consumption, initial coke concentration and catalyst

temperature from the reactor outlet). The use of the developed model will ensure accounting of these factors at optimization of the reactor and regenerator process conditions.

#### 4. Conclusions

The thermodynamic and kinetic patterns of the oxidative regeneration of zeolite-containing cracking catalysts were discovered by the proposed coke oxidation scheme. It was determined that the coke oxidation reactions with the carbon dioxide formation ( $\Delta G_{av} = -395.28$  kJ/mol,  $k = 71.90$  s<sup>-1</sup>) and the afterburning of carbon monoxide in the gas phase ( $\Delta G_{av} = -411.48$  kJ/mol,  $k = 10.65$  s-1kJ/mol) are characterized by the greatest thermodynamic probability and the highest reaction rates. Also, the least intensive reaction under process conditions is the coke oxidation reaction with carbon monoxide formation ( $\Delta G_{av} = -395.19$  kJ/mol,  $k = 2.62$  s<sup>-1</sup>).

The adequate mathematical model of the oxidative regeneration of zeolite-containing cracking catalysts with justification the plug-flow reactor mode was developed (the maximum relative error is 5.6%).

The mathematical model allows forecasting the coke amount on the regenerated catalyst, the flue gases composition and the regeneration temperature depending on the process conditions of the catalytic cracking reactor and regenerator.

The application of the mathematical model allows to optimize the reactor and the regenerator process conditions, to prevent the irreversible deactivation of the catalyst (thermal deactivation), to forecast the residual coke and the catalyst activity, and to estimate the amorphism degree of coke regarding C/H ratio.

#### Acknowledgments

The work was performed within the framework of the state task №10.13268.2018/8.9 and the Grant of the President of Russia MD-4620.2018.8

#### References

- [1] Khavkin VA, Kapustin VM, Gerzeliev IM. The ways of catalytic cracking process development. World of Oil Products. The Oil Companies' Bulletin, 2016; 10: 4-9.
- [2] Jarullah AT, Awad NA, Mujtaba IM. Optimal design and operation of an industrial fluidized catalytic cracking reactor. Fuel, 2017; 206: 657-674.
- [3] Dagde KK, Puyate YT. Modelling and Simulation Of Industrial FCC Unit: Analysis Based On Five-Lump Kinetic Scheme For Gas-Oil Cracking. International Journal of Engineering Research and Applications (IJERA), 2012; 2(5): 698-714.
- [4] Bartholomew CH. Mechanisms of catalyst deactivation. Appl. Catal., A. 2001; 212(1-2): 17-60.
- [5] Boskovic G, Baerns M. Catalyst deactivation. Springer Ser. Chem. Phys., 2004; 75: 477-503.
- [6] Duda P, Felkowski Ł, Cyklis P. Identification of overheating of an industrial fluidized catalytic cracking regenerator. Appl. Therm. Eng., 2018; 129: 1466-1477.
- [7] Iyoki K, Yamaguchi Y, Endo A, Yonezawa Y, Umeda T, Yamada H, Yanaba Y, Yoshikawa T, Ohara K, Yoshida K, Sasaki Y, Okubo T, Wakihara T. Formation of a dense non-crystalline layer on the surface of zeolite Y crystals under high-temperature steaming conditions. Microporous Mesoporous Mater., 2018; 268: 77-83.
- [8] Zhang Y, Yao M, Sun G, Gao S, Xu G. Characteristics and kinetics of coked catalyst regeneration via steam gasification in a micro fluidized bed. Industrial and Engineering Chemistry Research., 2014; 53 (15): 6316-6324.
- [9] Tang G, Silaen AK, Wu B, Fu D, Agnello-Dean D, Wilson J, Meng Q, Khanna S, Zhou CQ. Numerical simulation and optimization of an industrial fluid catalytic cracking regenerator. Appl. Therm. Eng., 2017; 112: 750-760.
- [10] John YM, Patel R, Mujtaba IM. Modelling and simulation of an industrial riser in fluid catalytic cracking process. Comput. Chem. Eng., 2017; 106: 730-743.
- [1] Berrouk AS, Huang AL, Bale S, Thampi P, Nandakumar K. Numerical simulation of a commercial FCC regenerator using Multiphase Particle-in-Cell methodology (MP-PIC). Advanced Powder Technology., 2017; 28(11): 2947-2960.
- [12] Affum HA, Adu PS, Dagadu CPK., Addo MA, Mumuni II, Appiah GK, Coleman A, Adzaklo SY. Modeling Conversion in a Fluid Catalytic Cracking Regenerator in Petroleum Refining. Research Journal of Applied Sciences, Engineering and Technology, 2011; 3(6): 533-539.

- [13] Penteado JC, Negrão COR, Rossib LFS. Numerical approaches for a mathematical model of an FCCU regenerator. *Engenharia Térmica (Thermal Engineering)*, 2008; 7(01): 71-86.
- [14] Dolganova I, Dolganov I, Ivanchina E. Ivashkina E. Alkylaromatics in Detergents Manufacture: Modeling and Optimizing Linear Alkylbenzene Sulfonation. *Journal of Surfactants and Detergents*, 2018; 21(1): 175-184.
- [15] Belinskaya NS, Frantsina EV, Ivanchina ED. Mathematical modelling of "reactor – stabilizer column" system in catalytic dewaxing of straight run and heavy gasoils. *Chemical Engineering Journal*, 2017; 329: 283-294.
- [16] Ivanchina E, Ivashkina E, Nazarova G. Mathematical modelling of catalytic cracking riser reactor. *Chemical Engineering Journal*, 2017; 329: 262-274.
- [17] Belinskaya NS, Frantsina EV, Ivanchina ED, Bedareva EK, Borissov A. Estimation of technological parameters influence on the cold flow properties and yield of diesel fuel in the process of catalytic dewaxing. *Pet Coal*, 2018; 60(1): 7-13.
- [18] Stull DR, Westrum E., Sinke GC. *The Chemical Thermodynamics of Organic Compounds*; New York: J. Wiley, 1969; p. 865.
- [19] Galimov ZHF, Gazizov MH. *Raschety reaktorov i regenerátorov ustanovok kataliticheskogo krekkinga*, 2nd ed.; Ufa: Izd-vo Ufim. gos. neftyanogo tekhn. un-ta, 2003; p. 51.
- [20] Razumov IM. *Psevdoozhizhenie i pnevmotransport sypuchih materialov*; M: Himiya, 1972, p.240.
- [21] Saitgalina AD, Yunusov AA, Gubajdullin IM, Ahmetov IV. Conference materials; *Scientific Services and Internet: Supercomputing Centers and Applications*, September 2010; - M.: Izd-vo MGU, 2010 p. 694.
- [22] Hadzhiev SN. *Kreking neftyanyh frakcij na ceolitsoderzhashchih katalizatorah*; M: Himiya, 1982, p. 280.

---

*To whom correspondence should be addressed: Dr. Galina Y. Nazarova, Fuel Engineering and Chemical Cybernetics Department, Tomsk Polytechnic University, Russia*

## SENSITIVITY ANALYSIS OF THE PARAMETERS AFFECTING TEMPERATURE AND PRESSURE PROFILES ALONG THE WELLBORE

Babak Moradi<sup>1,2\*</sup>, Mohammed Ayoub<sup>2</sup>, Mahmood Bataee<sup>3</sup>

<sup>1</sup> LEAP Energy, Suite 14.08, Level 14, G Tower, 199, Jalan Tun Razak, 50400, Kuala Lumpur, Malaysia

<sup>2</sup> Petroleum Engineering Department, Universiti Teknologi PETRONAS, Bandar Seri Iskandar, 31750, Tronoh, Perak, Malaysia

<sup>3</sup> Petroleum Engineering Department, Asia Pacific University, Taman Teknologi Malaysia, 57000, Kuala Lumpur, Malaysia

Received July 20, 2018; Accepted October 19, 2018

---

### Abstract

An appropriate injection well completion design requires a knowledge of pressure and temperature profiles along the depth of the well. The results of sensitivity analysis can be used for preliminary design calculations of injection wells to find the optimum injection surface parameters and wellbore completion. In this study, the surface injection parameters and wellbore geometry are varied to examine the sensitivity of the results for various parameters by using the numerical model during water and gas injections. The results revealed that the temperature profile can be calculated for a single phase with a small error in absence of the pressure profile, the error is less than 3 %. It is found that the contribution of the acceleration term is too weak for building pressure and temperature profiles (less than 0.001%). Further, those comparisons of the results showed that except near the critical point, the pressure profile is not sensitive to the wellhead injection temperature (less than 1 %).

**Keywords:** Energy balance; momentum balance; radiation heat transfer; wellbore design.

---

## 1. Introduction

It has been one of the perennial objectives of the oil industry to increase the oil recovery factor for a given reservoir at the minimum possible cost. This goal has led to the development of numerous improved oil recovery (IOR) techniques [1-3]. Gas (methane, CH<sub>4</sub>, and carbon dioxide, CO<sub>2</sub>) and water injections are among the most common IOR methods used in industry. An Injection well is needed to implement those IOR techniques. An appropriate injection well completion design requires a knowledge of pressure and temperature profiles along the depth of the well [4-9]. The results of sensitivity analysis can be used for preliminary design calculations of injection wells to find optimum injection surface parameters and wellbore completion (e.g. diameter of casing). It will further direct us to parameters which can also influence the pressure and temperature profiles.

## 2. Methodology

In this study, the surface injection parameters and wellbore geometry are varied to examine the sensitivity of results for various parameters by using the numerical model developed Moradi *et al.* [6]. Fig. 1 represents flowchart of the calculation procedure of the numerical model. This numerical model has been selected for conducting the comparison due to it considers:

1. Joule Thompson effect in the wellbore.
2. Variable thermodynamic properties and overall heat transfer coefficient along the well depth.
3. Contribution of kinetic term in the energy balance equation.
4. Contribution of friction and acceleration terms in the momentum balance equation.

Sensitivity studies start with a base case that uses the typical wellbore parameters. Table 1 shows input values used for the base case. Then one parameter at a time is changed to discover the corresponding changes of the wellbore behaviour. This work conducts sensitivity analyses to study effects of wellhead injection temperature, wellhead injection pressure, injection mass flow rate, tubing size, overall heat transfer coefficient, radiation heat transfer, and contribution of different parameters for momentum balance and energy balance.

Table 1. Input parameters as the base case

Parameter	Value	Unit
Depth of the well	914.4	m
Deviation of wellbore from horizontal level	90	degree
Diameter of the wellbore	0.384	m
External diameter of the casing	0.128	m
External diameter of the tubing	0.07424	m
Geothermal temperature gradient	0.0364	°C/m
Injection mass flow rate	1.8	kg/s
Injection temperature at the wellhead	25	°C
Injection time	100	Day
Internal diameter of the casing	0.1152	m
Internal diameter of the tubing	0.064	m
Mean temperature of the surface	21.1111	°C
Thermal conductivity of the cement	0.3462	W/(m.°C)
Thermal conductivity of the earth	2.4234	W/(m.°C)
Thermal diffusivity of the earth	0.00372	m <sup>2</sup> /s

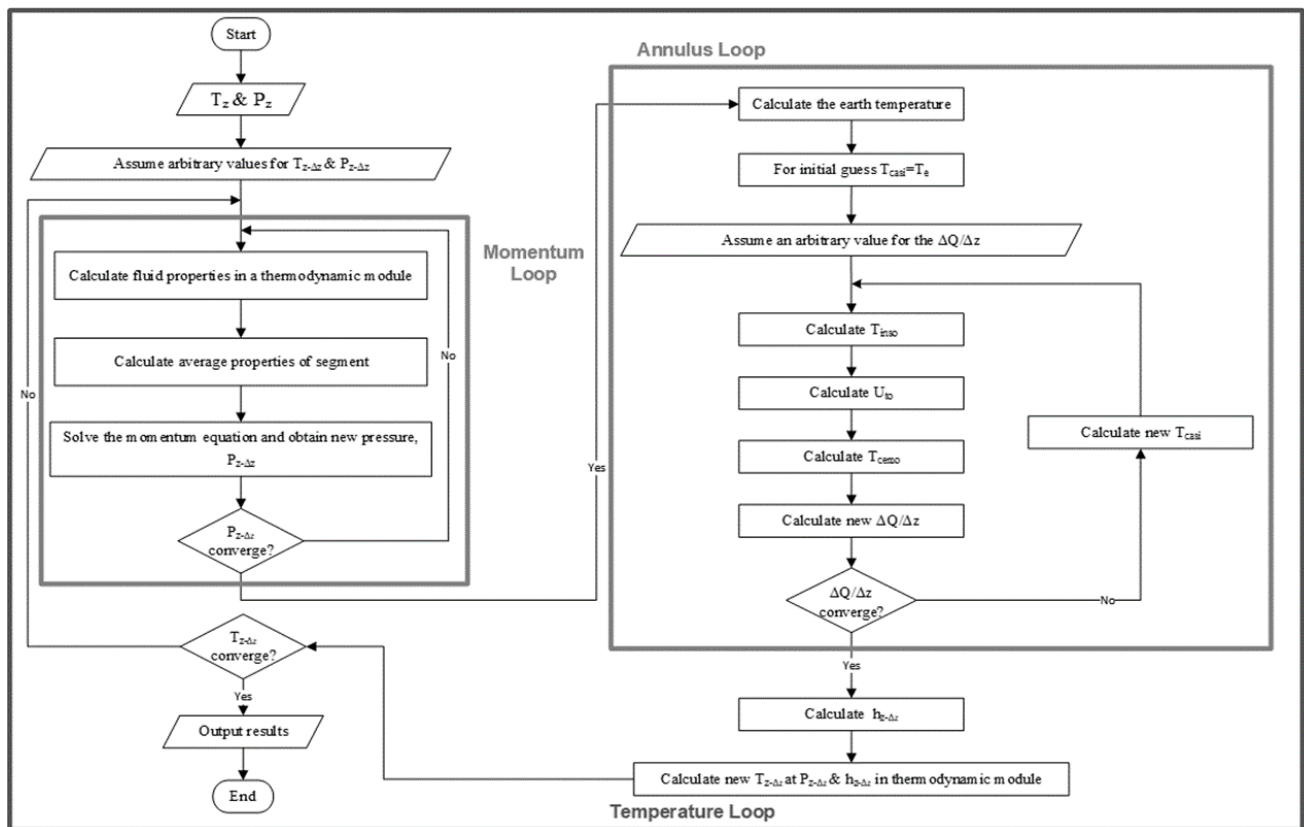


Fig 1. The procedure for calculating the pressure and temperature profiles along the borehole [6]

### 3. Effect of wellhead injection temperature

Fig. 2 represents temperature profiles of the fluid flow in the tubing versus depth at different wellhead injection temperatures (25°C, 65°C, and 105°C) during water, CO<sub>2</sub>, and CH<sub>4</sub> injection processes respectively. Comparisons of the results illustrate that the temperature change of water between the wellhead and bottomhole is less than CO<sub>2</sub> and CH<sub>4</sub>; due to the fact that the heat capacity of water is larger than CO<sub>2</sub> and CH<sub>4</sub> at temperature of 25°C, 65°C, and 105°C [10].

In addition, the results show that the fluid flow temperature inside the tubing during hot fluid injection is much higher than the earth temperature. This fact should be considered during well completion and surface facilities design.

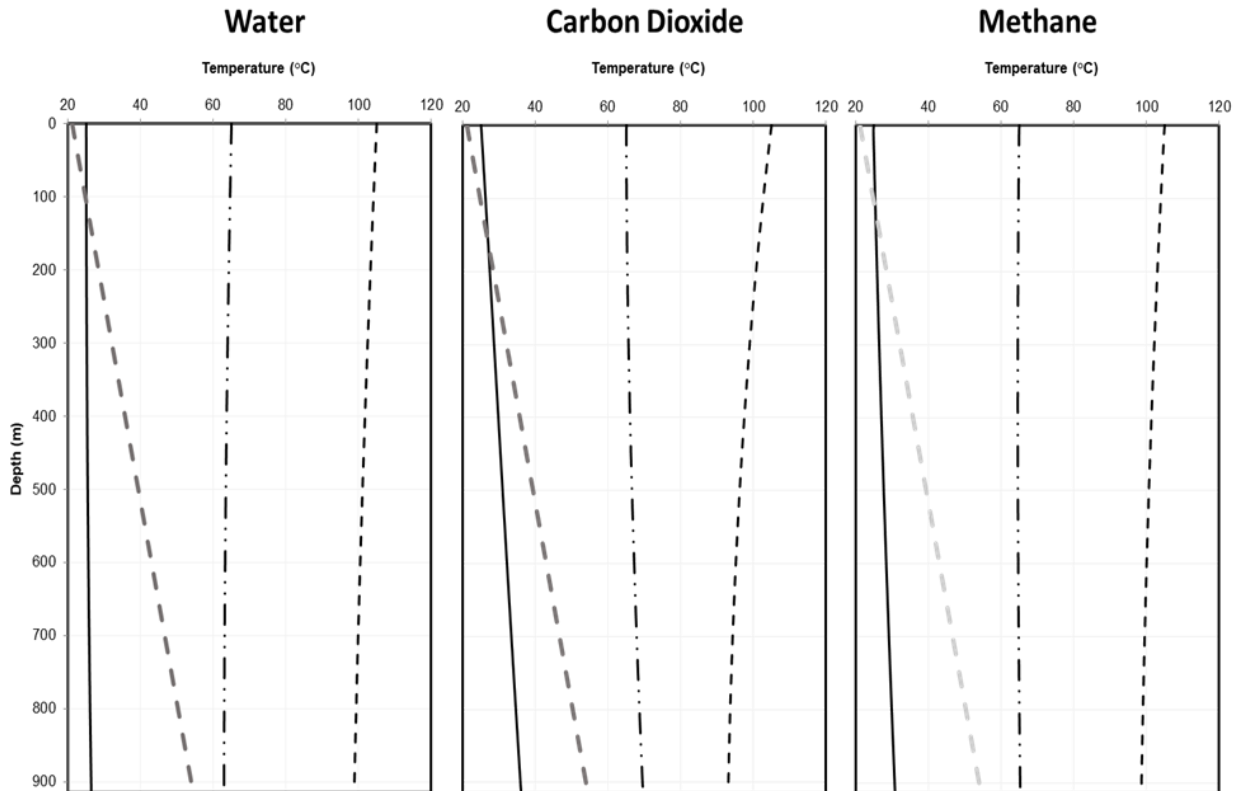


Fig. 2. Temperature profile during water, carbon dioxide, and methane injection at different wellhead injection temperature (—)  $T_{inj}$ : 25 (°C); (-·-·-)  $T_{inj}$ : 65 (°C); (---)  $T_{inj}$ : 105 (°C); (·····) Geothermal temperature

Fig. 3 illustrates pressure profiles of the fluid flow in the tubing versus depth at different wellhead injection temperatures during water, CO<sub>2</sub>, and CH<sub>4</sub> injection processes respectively. Comparisons of the results illustrate that, except near the critical point, the pressure profile is not sensitive to the wellhead injection temperature during water, supercritical CO<sub>2</sub>, and CH<sub>4</sub> injection cases (less than 0.2 MPa), due to the fact that density changes are negligible in a small range of temperature changes at a specific phase. For CO<sub>2</sub> injection case, there is a large temperature profile change between  $T_{inj} = 25^\circ\text{C}$  and  $T_{inj} = 65^\circ\text{C}$  &  $105^\circ\text{C}$  due to phase change. CO<sub>2</sub> exists in liquid phase and near its critical point at  $T_{inj} = 25^\circ\text{C}$  and it is a dense phase at this temperature but CO<sub>2</sub> changes to supercritical phase at  $T = 65^\circ\text{C}$  &  $105^\circ\text{C}$  as it has low density in supercritical condition [11-12], since the build up of the pressure at  $T_{inj} = 25^\circ\text{C}$  is larger than  $T_{inj} = 65^\circ\text{C}$  &  $105^\circ\text{C}$ .

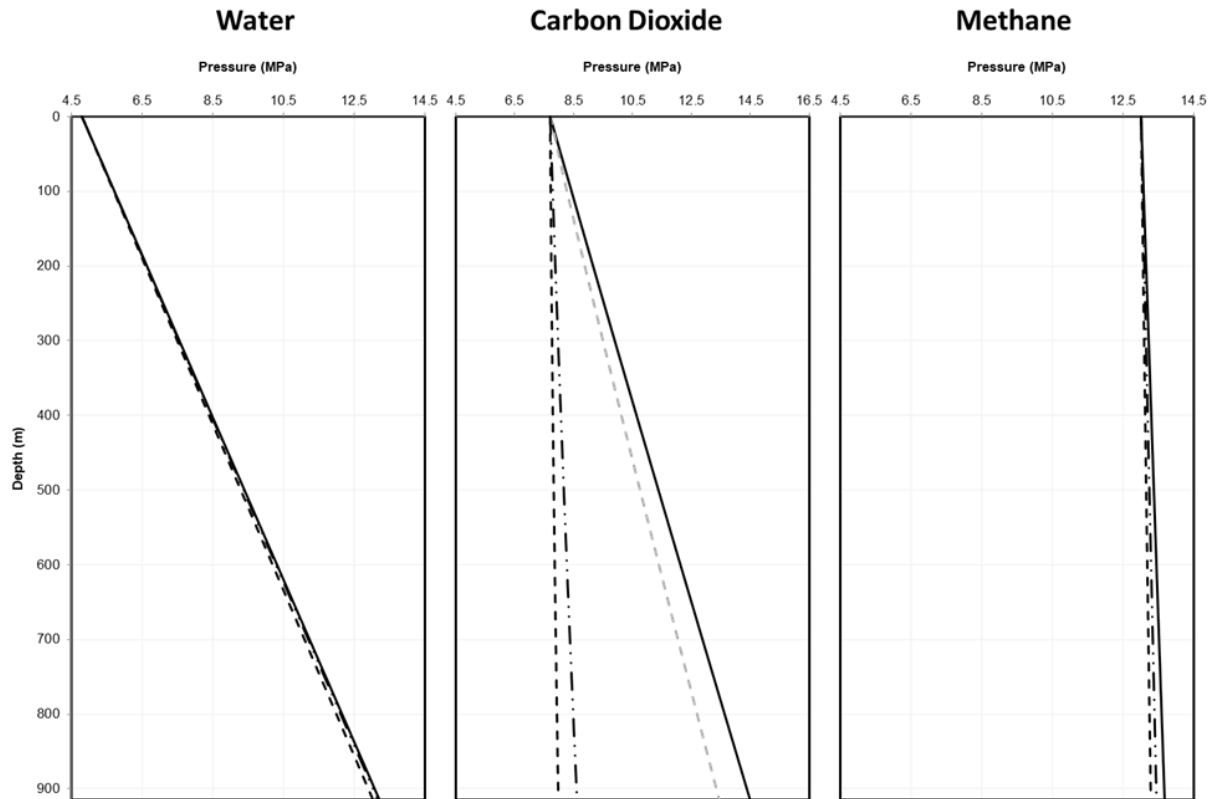


Fig. 3. Pressure profile during water, carbon dioxide, and methane injection at different wellhead injection temperature. (—)  $T_{inj}$ : 25 (°C); (---)  $T_{inj}$ : 31.1 (°C) [Critical temperature of  $CO_2$ ]; (-·-·-)  $T_{inj}$ : 65 (°C); (·····)  $T_{inj}$ : 105 (°C)

#### 4. Effect of wellhead injection pressure

Fig. 4 represents temperature profiles of the fluid flow in the tubing versus depth at different wellhead injection pressures (4.8 MPa and 6.8 MPa) during water,  $CO_2$ , and  $CH_4$  injection processes respectively. Comparisons of the results illustrate that the temperature profile is not sensitive to the wellhead injection pressure and the difference is less than 1.5°C. Fig. 5 shows pressure profiles of the fluid flow in the tubing versus depth at different wellhead injection pressures during water,  $CO_2$ , and  $CH_4$  injection processes respectively. Pressure gradient for water case is larger than  $CO_2$  and  $CH_4$  cases because water has larger density [10-11].

#### 5. Effect of injection mass flow rate

Injection mass flow rate determines the fluid production rate and thus, it is a significant variable [13]. Fig. 6 represents temperatures profiles of the fluid flow in the tubing versus depth at different injection mass flow rates of 0.8, 1.8, 2.8, and 3.8 kg/s for water,  $CO_2$ , and  $CH_4$  injection processes respectively. Comparisons of the results illustrate that temperature differences between the bottomhole and wellhead decreases by increasing the mass injection rate. This is due to the fact higher injection mass flow rate equals higher velocity, therefore the wellbore flow has less time for the heat transfer with the surrounding. The wellbore flow temperature during  $CH_4$  injection case is more sensitive to injection mass flow rate due to its small density and consequently higher velocity.

Injection mass flow rate strongly affects pressure changes during flow as shown in Fig. 9 during water,  $CO_2$ , and  $CH_4$  injection processes respectively. As one would expect, the bottomhole pressure decreases with an increase in injection mass flow rate due to increasing the velocity and subsequently increasing the friction term.

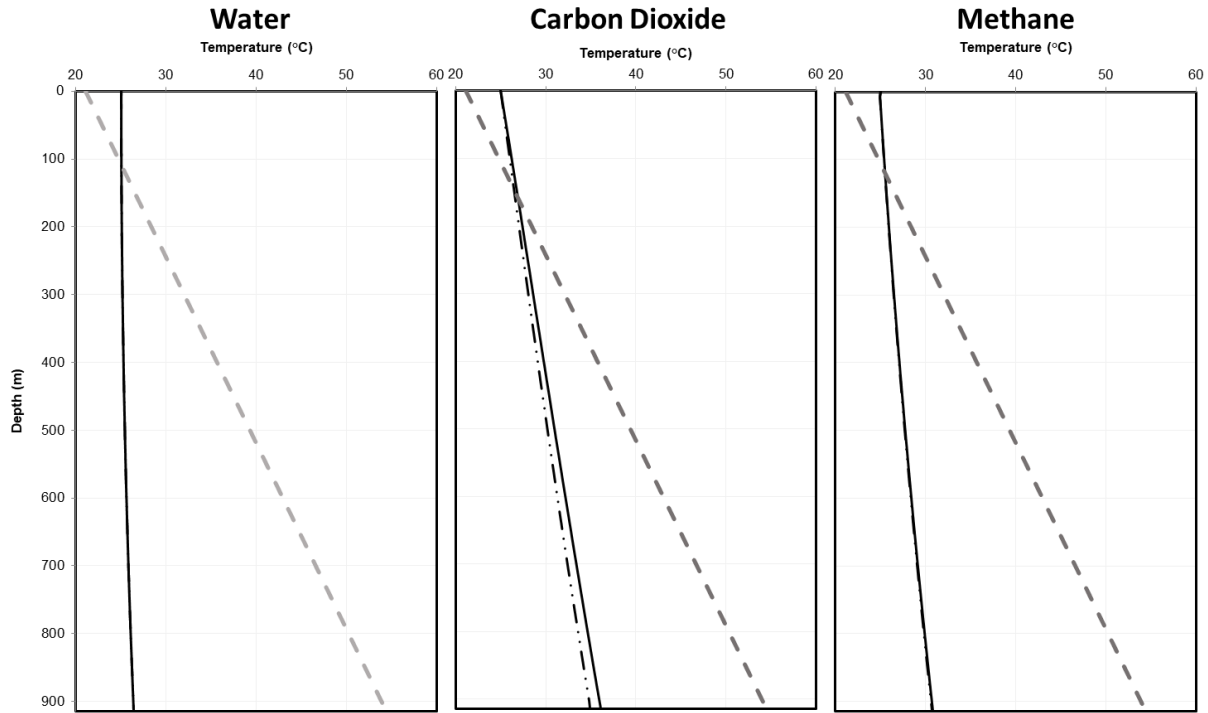


Fig. 4. Temperature profile during water, carbon dioxide, and methane injection at different wellhead injection pressure. (—)  $P_{inj}$ : 4.8 (MPa); (---)  $P_{inj}$ : 6.8 (MPa); (.....) Geothermal temperature

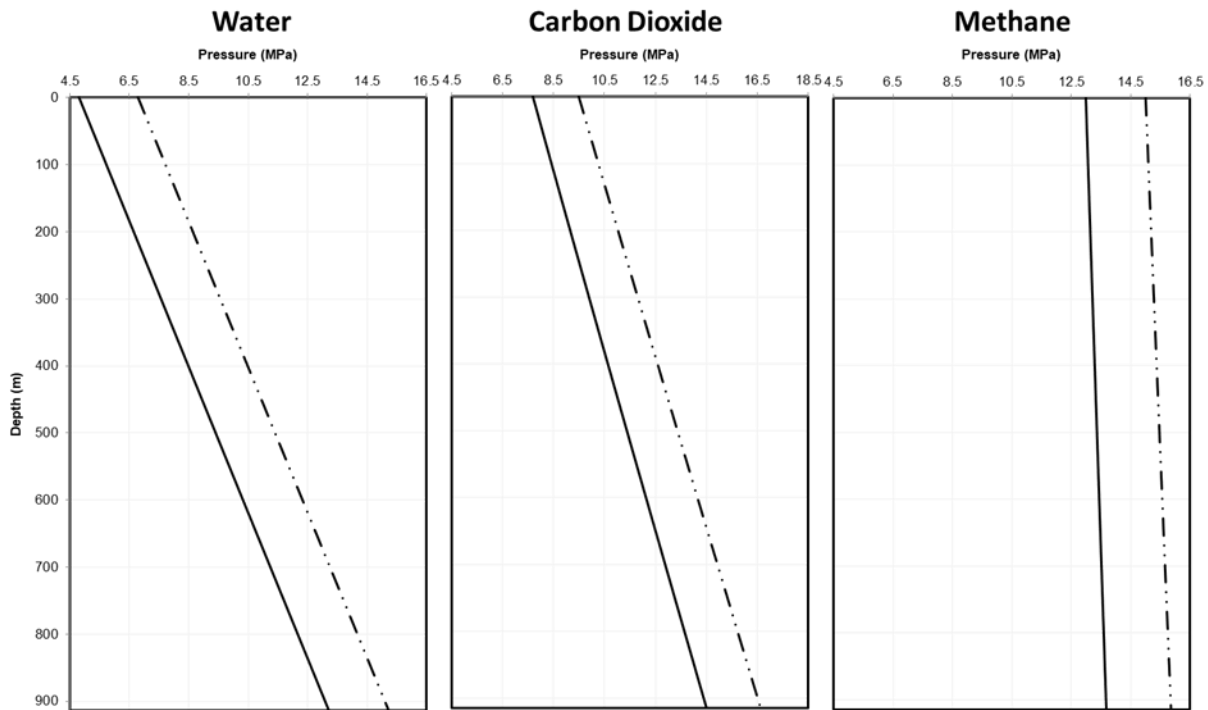


Fig. 5. Pressure profile during water, carbon dioxide, and methane injection at different wellhead injection pressure. (—)  $P_{inj}$ : 4.8 (MPa); (---)  $P_{inj}$ : 6.8 (MPa); (.....) Geothermal temperature

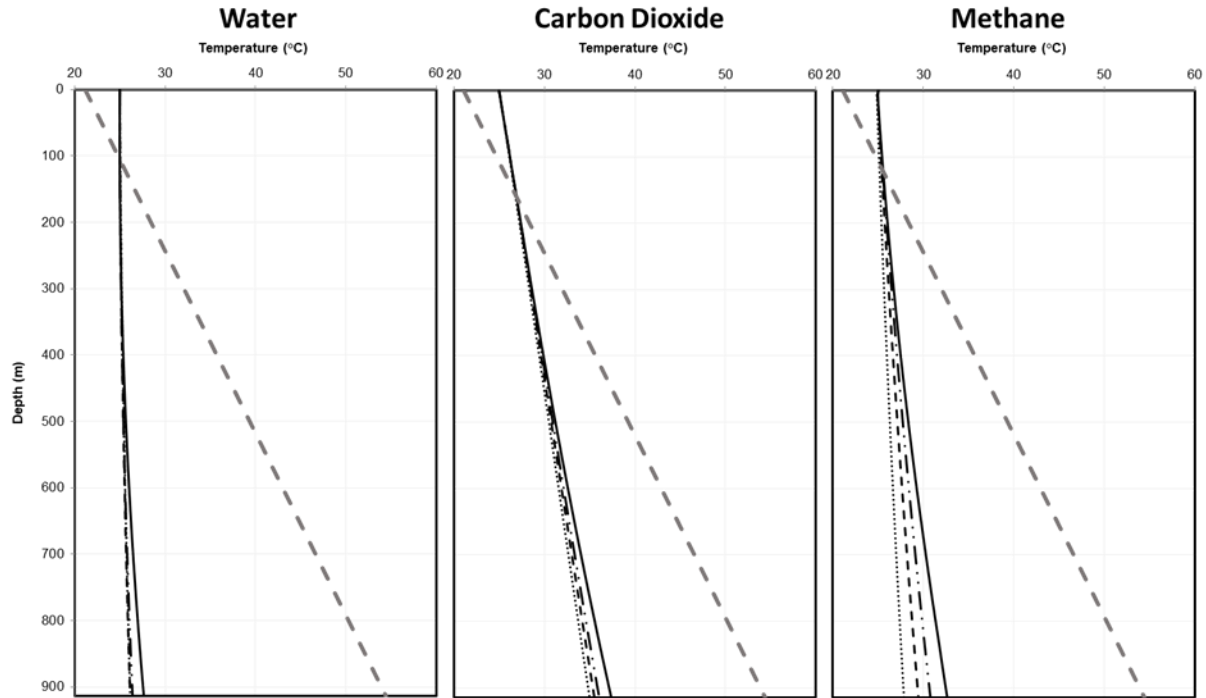


Fig. 6. Temperature profile during water, carbon dioxide, and methane injection at different injection mass rate. (—)  $Mass_{inj}$ : 0.8 (kg/s); (-·-·-)  $Mass_{inj}$ : 1.8 (kg/s); (·-·-·)  $Mass_{inj}$ : 2.8 (kg/s); (·-·-·)  $Mass_{inj}$ : 3.8 (kg/s); (---) Geothermal temperature

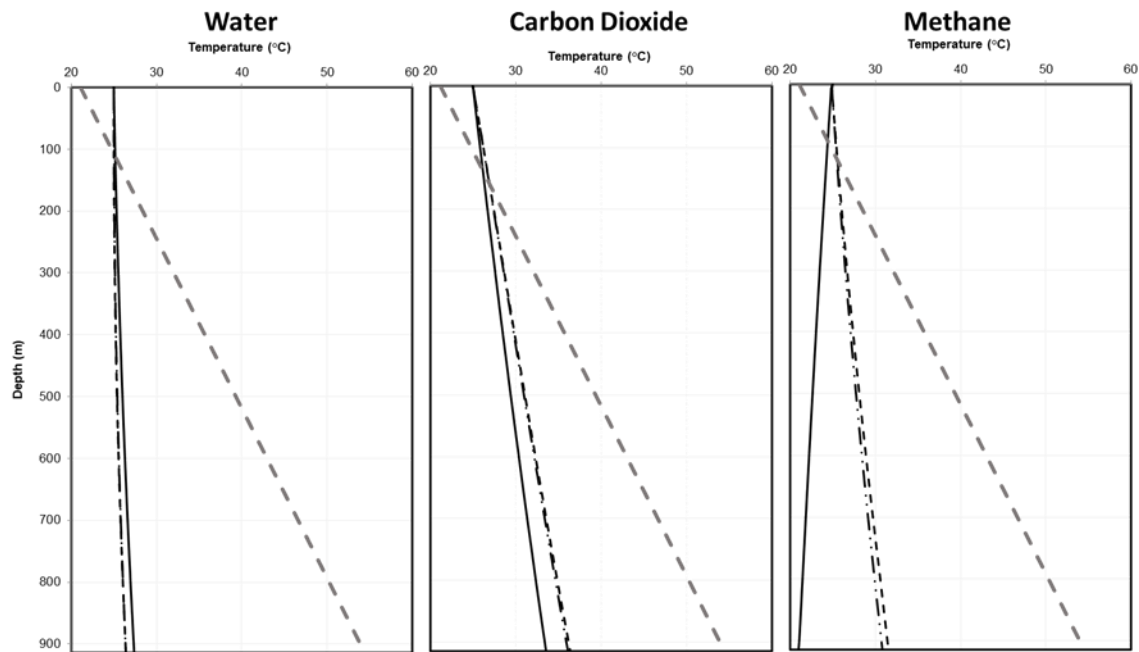


Fig. 7. Temperature profile during water, carbon dioxide, and methane injection at different tubing size. (—)  $R_{tub}$ : 0.01905 (m); (-·-·-)  $R_{tub}$ : 0.03175 (m); (·-·-·)  $R_{tub}$ : 0.0508 (m); (---) Geothermal temperature

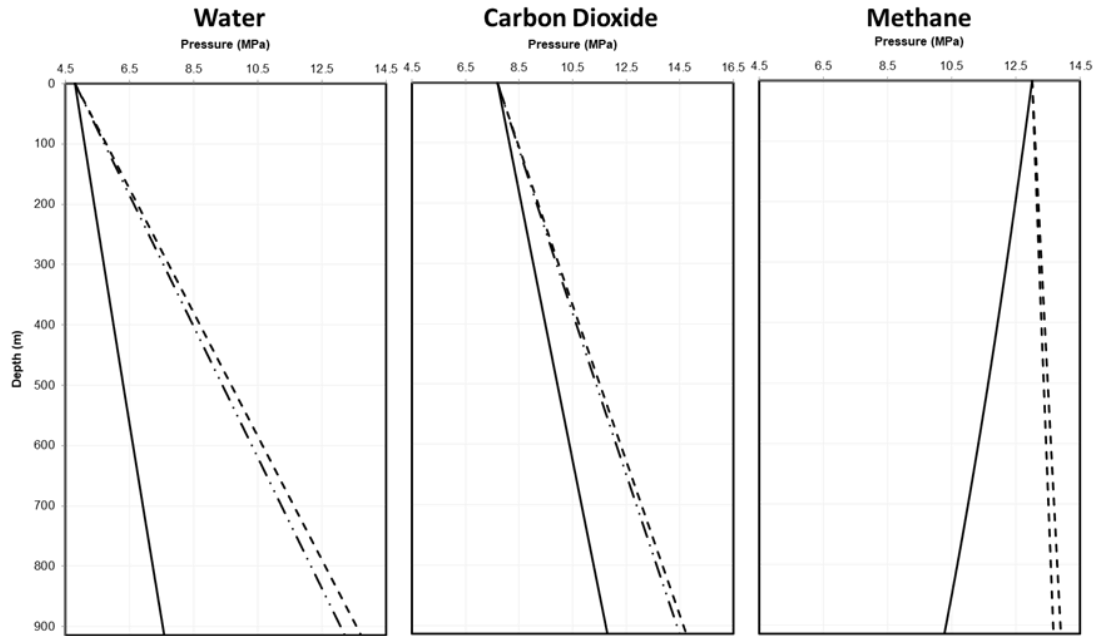


Fig. 8. Pressure profile during water, carbon dioxide, and methane injection at different tubing size. (—)  $R_{tub}$ : 0.01905 (m); (---)  $R_{tub}$ : 0.03175 (m); (.....)  $R_{tub}$ : 0.0508 (m)

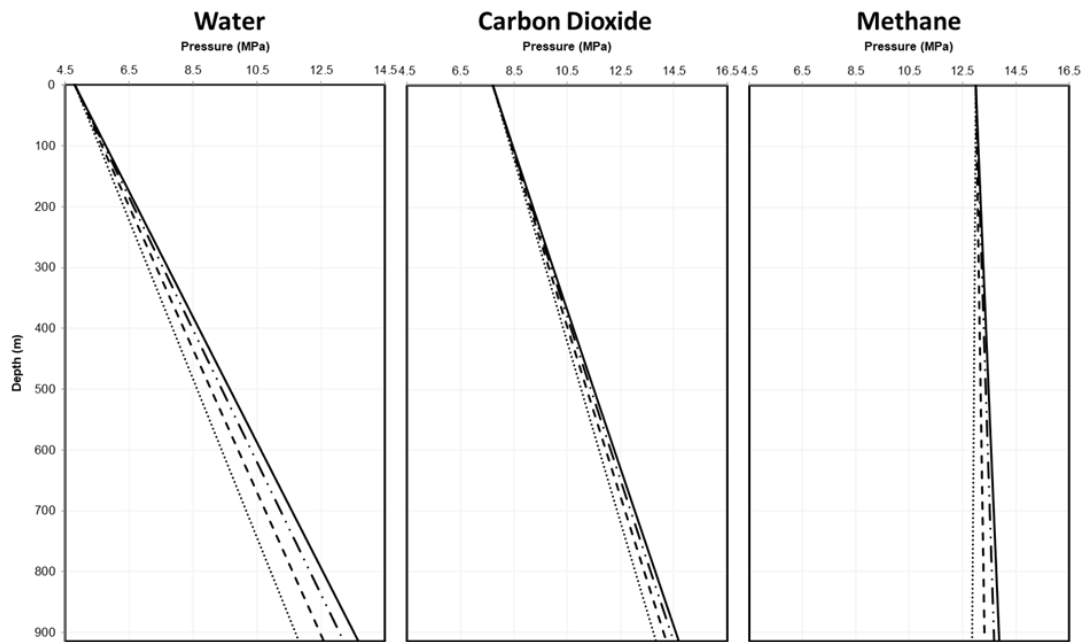


Fig. 9. Pressure profile during water, carbon dioxide, and methane injection at different injection mass rate. (—)  $Mass_{inj}$ : 0.8 (kg/s); (---)  $Mass_{inj}$ : 1.8 (kg/s); (.....)  $Mass_{inj}$ : 2.8 (kg/s); (-.-.-)  $Mass_{inj}$ : 3.8 (kg/s)

### 6. Effect of tubing size

The tubing radii of 0.01905, 0.03175, and 0.508 m were considered in this work to study the effects of the tubing radius on the temperature and pressure profiles. Fig. 7 represents temperature profiles of the fluid flow in the tubing versus depth at different tubing radius sizes

during water, CO<sub>2</sub>, and CH<sub>4</sub> injection processes respectively. Comparison of the results illustrates difference in temperatures between the bottomhole and wellhead decreases by decreasing the tubing radius size. It is because radiation heat transfer between tubing and casing is the predominant heat transfer mechanism for the wellbore and the radiation heat transfer rate is inversely proportional to radii difference of the tubing and casing. Therefore, by decreasing the tubing radius (for a constant casing size), heat transfer rate also decreases. In addition to that, higher fluid flow velocity occurs in the thinner pipe since the wellbore flow has less time for heat transfer with the surrounding in smaller tubing sizes. The wellbore flow temperature during CH<sub>4</sub> injection case is more sensitive to the tubing radius size due to its low density and consequently higher velocity. Fig 8 illustrates pressure profiles of the fluid flow in the tubing versus depth at different tubing radii during water, CO<sub>2</sub>, and CH<sub>4</sub> injection processes respectively. As one would expect, the pressure at the bottomhole decreases with a decrease in the tubing radius due to increasing the velocity and consequently increasing the friction term. There is higher pressure drop for CH<sub>4</sub> injection than water and CO<sub>2</sub> by decreasing the tubing radius because of its low density and consequently higher velocity. The bottomhole pressure decreases more than 5 MPa for a small tubing radius.

### 7. Effect of overall heat transfer coefficient

Overall heat transfer coefficient ( $U_{to}$ ) present thermal conductivity of the wellbore assembly [10]. The thermal resistivity of the wellbore assembly increases by decreasing overall heat transfer coefficient and the heat transfer rate is a linear function of overall heat transfer coefficient [6].

Fig. 10 presents temperature profile of the fluid flow in the tubing versus depth at wellhead injection temperature of 105°C and different overall heat transfer coefficients and injection times during water, CO<sub>2</sub>, and CH<sub>4</sub> injection processes respectively. Comparisons of results for small overall heat transfer coefficient show that the difference of temperature profile in the early and long times is negligible due to lower heat transfer rate between the wellbore flow and wellbore assembly. The difference of bottomhole temperatures are less than 1°C. However, heat transfer rate increases by increasing overall heat transfer coefficient since there is higher temperature drop in long times. Fig. 11 illustrates pressure profile of the fluid flow in the tubing versus depth at wellhead injection temperature of 105°C for different overall heat transfer coefficients and injection times during water, CO<sub>2</sub>, and CH<sub>4</sub> injection processes respectively. Comparisons of the results show that the pressure profile is not sensitive to the overall heat transfer coefficient. The difference in bottomhole pressures is less than 0.4 MPa.

### 8. Effect of radiation heat transfer mechanism

Some commercial software packages [14-15] fail to consider radiation heat transfer mechanism in calculating the wellbore flow temperature. The contribution of the radiation heat transfer mechanism in building the temperature profile is studied in this section. Temperature profile versus depth during water, CO<sub>2</sub>, and CH<sub>4</sub> injection processes at different wellhead injection temperatures with and without consideration of the radiation heat transfer mechanism is presented in Fig. 12. Comparisons of the results show that the consideration of the radiation heat transfer mechanism is not important at low temperature injection (difference in bottomhole temperatures is less than 1°C with and without consideration of the radiation heat transfer mechanism); but by increasing the difference between the wellbore flow temperature and the formation temperature especially during hot fluid injection, it becomes an effective mechanism in heat transfer and it must be considered in temperature profile computations.

Fig. 13 illustrates pressure profiles of the fluid flow in the tubing versus depth at different wellhead injection temperatures during water, CO<sub>2</sub>, and CH<sub>4</sub> injection processes respectively. Comparisons of the results that show the pressure profile is not sensitive to the temperature profile and radiation heat transfer mechanism. The difference of the bottomhole pressures with and with consideration of radiation heat transfer is less than 0.2 MPa.

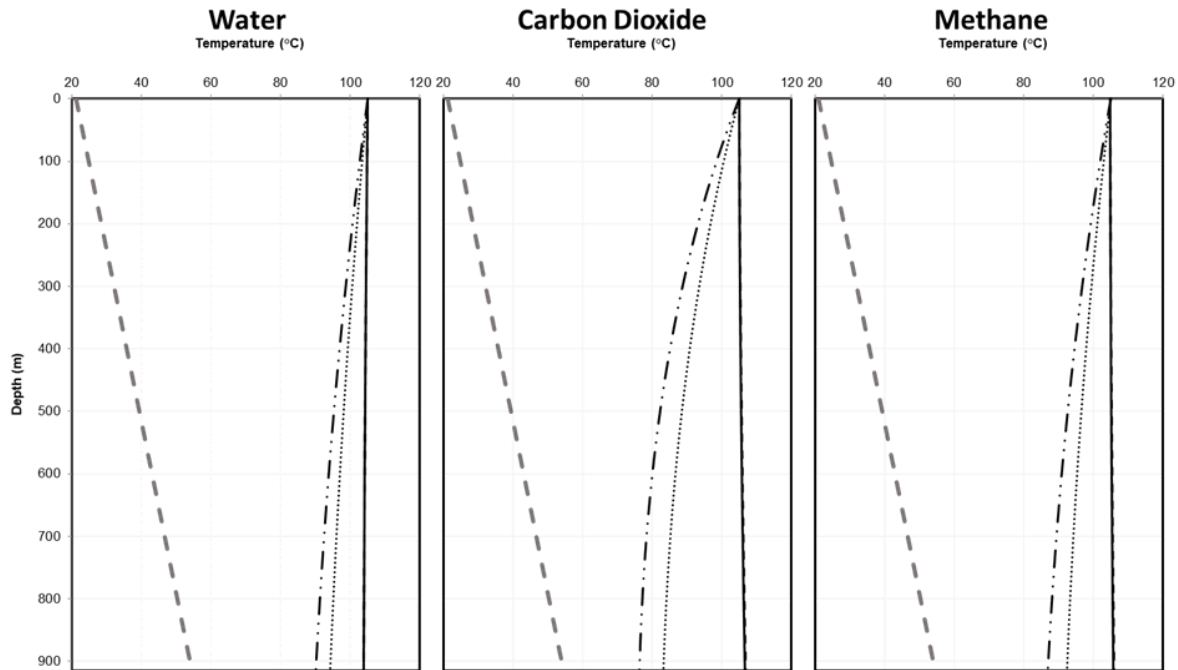


Fig. 10. Temperature profile versus depth during water, carbon dioxide, and methane injection for different overall heat transfer coefficients and injection times at the wellhead injection temperature of 105°C. (—)  $U_{tot}$ : 1 ( $W.m^{-2}.^{\circ}C^{-1}$ ) &  $t$ : 1 (hr); (---)  $U_{tot}$ : 10 ( $W.m^{-2}.^{\circ}C^{-1}$ ) &  $t$ : 1 (hr); (.....)  $U_{tot}$ : 1 ( $W.m^{-2}.^{\circ}C^{-1}$ ) &  $t$ : 2400 (hr); (-.-.-)  $U_{tot}$ : 10 ( $W.m^{-2}.^{\circ}C^{-1}$ ) &  $t$ : 2400 (hr); (.....) Geothermal temperature

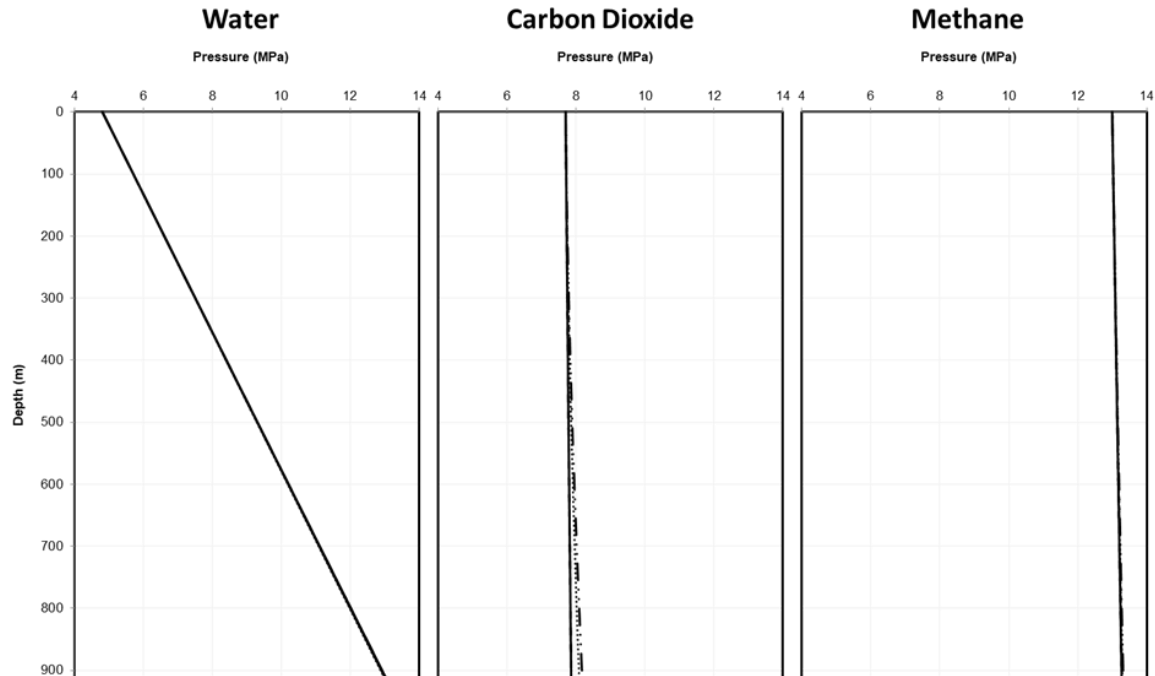


Fig. 11. Pressure profile versus depth during water, carbon dioxide, and methane injection for different overall heat transfer coefficients and injection times at the wellhead injection temperature of 105°C. (—)  $U_{tot}$ : 1 ( $W.m^{-2}.^{\circ}C^{-1}$ ) &  $t$ : 1 (hr); (---)  $U_{tot}$ : 10 ( $W.m^{-2}.^{\circ}C^{-1}$ ) &  $t$ : 1 (hr); (.....)  $U_{tot}$ : 1 ( $W.m^{-2}.^{\circ}C^{-1}$ ) &  $t$ : 2400 (hr); (-.-.-)  $U_{tot}$ : 10 ( $W.m^{-2}.^{\circ}C^{-1}$ ) &  $t$ : 2400 (hr)

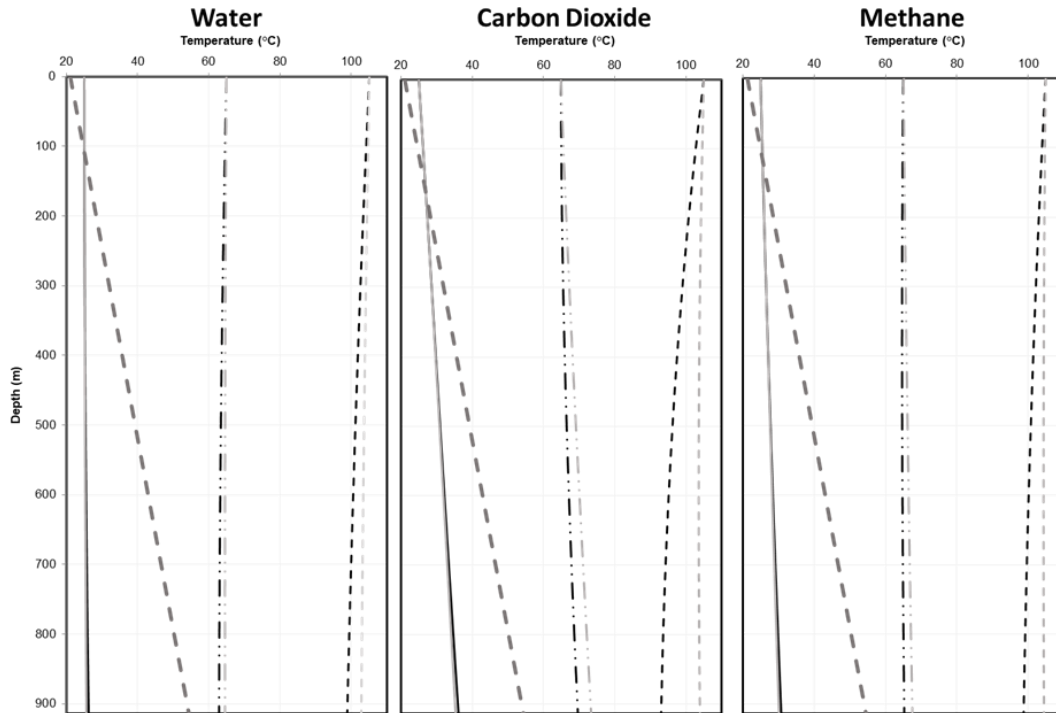


Fig. 12. Effect of the radiation heat transfer mechanism on the temperature profile along the wellbore. (——)  $T_{inj}$ : 25 (°C) [Considered]; (—)  $T_{inj}$ : 25 (°C) [Without consideration]; (— · — · —)  $T_{inj}$ : 65 (°C) [Considered]; (— · —)  $T_{inj}$ : 65 (°C) [Without consideration]; (— · — · —)  $T_{inj}$ : 105 (°C) [Considered] ; (— · — · —)  $T_{inj}$ : 105 (°C) [Without consideration]; (— · — · —) Geothermal temperature

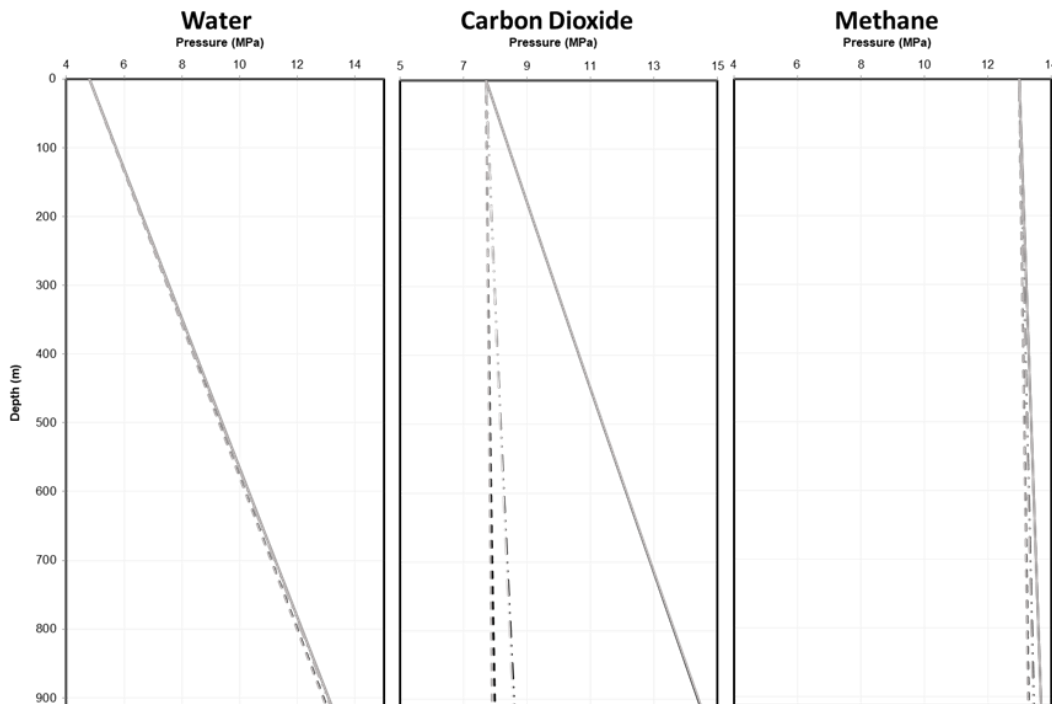


Fig. 13. Effect of the radiation heat transfer mechanism on the pressure profile along the wellbore. (——)  $T_{inj}$ : 25 (°C) [Considered]; (—)  $T_{inj}$ : 25 (°C) [Without consideration]; (— · — · —)  $T_{inj}$ : 65 (°C) [Considered]; (— · —)  $T_{inj}$ : 65 (°C) [Without consideration]; (— · — · —)  $T_{inj}$ : 105 (°C) [Considered] ; (— · — · —)  $T_{inj}$ : 105 (°C) [Without consideration]

### 9. Effective parameters for momentum balance

The total pressure gradient is the sum of the hydrostatic gradient, acceleration gradient, and frictional gradient [16]. Fig. 14 represents the hydrostatic, acceleration, and frictional terms versus depth respectively. Comparisons of the results [6] show that the contribution of the acceleration term is so weak to build a pressure profile (less than 0.0001 MPa) therefore it can be ignored to conduct faster calculations. The gravity term is the predominant term for building the pressure profile for dense fluid flow (e.g. liquid or near critical point phase) but its contribution reduces in gas phase flow as shown in Fig. 14.

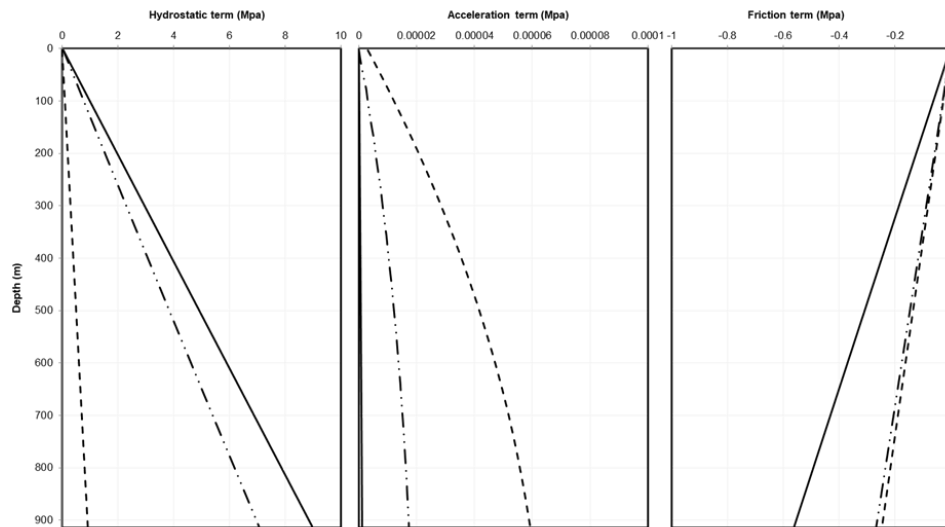


Fig. 14. Contribution of the hydrostatic, acceleration, and friction terms for building the pressure profile. (—) Water; (---) Carbon dioxide; (-----) Methane

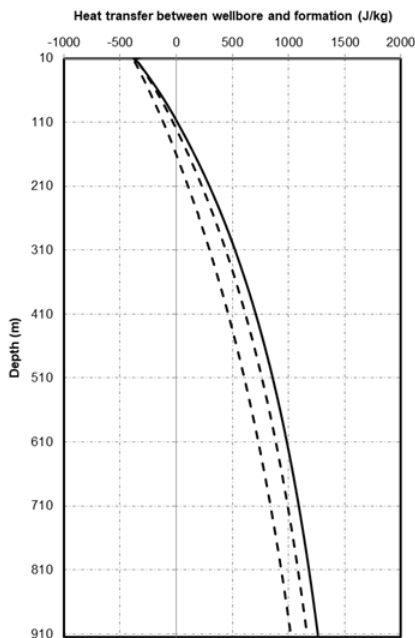


Fig. 15. Contribution of heat transfer between the wellbore and formation term for building temperature profile

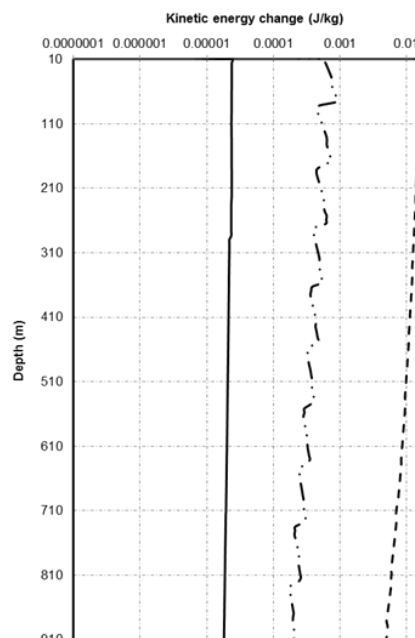


Fig. 16. Contribution of changing the kinetic energy term for building temperature profile

## 10. Effective parameters for energy balance

The energy balance equation includes the change in kinetic energy, potential energy per unit mass, and heat transfer rate between wellbore and formation. The potential energy per unit mass ( $gdz$ ) is constant along the wellbore depth and its contribution depends on the length of the wellbore.

Fig. 15 represents heat transfer at the wellbore/formation interface and Fig 16 shows change in kinetic energy along the wellbore depth calculated by the new procedure. Comparison of Figures 15 & 16 reveals that the kinetic energy change is negligible (less than 0.02 kJ/kg) and therefore, ignoring the kinetic energy term in energy balance equation is a reliable assumption to increase the speed of calculations.

## 11. Conclusions

In this study, the surface injection parameters and wellbore geometry are varied to examine the sensitivity of results for various parameters by using the numerical model developed Moradi *et al.* [6]. The main findings are summarized below:

- During the hot fluid injection, radiation becomes an effective mechanism in heat transfer and it must be considered in temperature profile computations.
- For single phase, the temperature profile can be calculated with a small error in the absence of the pressure profile, (the error is less than 3 %).
- The contribution of acceleration term is so weak for building pressure and temperature profiles (less than 0.001%).
- The pressure profile is a strong function of the tubing size. The bottomhole pressure decreases more than 30 % for a small tubing radius than a large radius.
- Except near the critical point, the pressure profile is not sensitive to the wellhead injection temperature (less than 1 %).

### Nomenclature

$CH_4$	Methane
$CO_2$	Carbon dioxide
$Mass_{inj}$	Injection mass flow rate (kg/s)
$P_{inj}$	Wellhead injection pressure (MPa)
$t$	time (hr)
$T_{inj}$	Wellhead injection temperature ( $^{\circ}C$ )
$U_{tot}$	Overall heat transfer coefficient ( $W.m^{-2}.^{\circ}C^{-1}$ )

### References

- [1] Latil M. Enhanced Oil Recovery. Éditions Technip, 1980.
- [2] Lake LW. Enhanced Oil Recovery. Prentice Hall, 1989.
- [3] Green DW, Willhite GP. Enhanced oil recovery, Society of Petroleum Engineers, 1998. 6th of SPE textbook series.
- [4] Aadnoy BS. Modern Well Design, CRC Press, 2010.
- [5] Leutwyler K. Casing Temperature Studies in Steam Injection Wells, Journal of Petroleum Technology, 1966; 18: 1–157.
- [6] Moradi B, Awang MB, Shoushtari MA. Pressure Drop Prediction in Deep Gas Wells, SPE Asia Pacific Oil and Gas Conference and Exhibition, Jakarta, Indonesia, Society of Petroleum Engineers, 2011.
- [7] Placido JCR, Ademar PJr, Paulo LABF, Pasqualino IP, Estefen SF. Stress-Analysis of Casing String Submitted to Cyclic Steam Injection. Latin American and Caribbean Petroleum Engineering Conference, Rio de Janeiro, Brazil, Society of Petroleum Engineers, 1997.
- [8] Rodriguez-Prada H. Improved Calculation of Casing Strains and Stresses in a Steam Injector Well Simulator. SPE Latin America Petroleum Engineering Conference, Janeiro, Brazil, Society of Petroleum Engineers, 1990.
- [9] Wu J, Gonzalez ME, Hosn NA. Steam-Injection Casing Design. SPE Western Regional Meeting, Irvine, California, Society of Petroleum Engineers, 2005.
- [10] Kreith F, Manglik R, Bohn M. Principles of Heat Transfer. Cengage Learning, 2010.

- [11] Span R, Wagner W. A New Equation of State for Carbon Dioxide Covering the Fluid Region from the Triple-Point Temperature to 1100 K at Pressures up to 800 MPa. *Journal of Physical and Chemical Reference Data*, 1996; 25: 1509–1596.
- [12] National Institute of Standards and Technology, 2011, Available at: <http://webbook.nist.gov/chemistry/fluid/>.
- [13] Ali SMF. A Comprehensive Wellbore Stream/Water Flow Model for Steam Injection and Geothermal Applications. *Society of Petroleum Engineers Journal*, 1981; 21: 527–534.
- [14] Wellflo, 3.6d, Weatherford, 2001.
- [15] VFPi, 2011.2, Schlumberger, 2011.
- [16] Moradi B. A Thermal Study of Fluid Flow Characteristics in Injection Wells. LAP LAMBERT Academic Publishing, 2013.

---

*To whom correspondence should be addressed: Babak Moradi, LEAP Energy, Suite 14.08, Level 14, G Tower, 199, Jalan Tun Razak, 50400, Kuala Lumpur, Malaysia. Email: moradireservoir@gmail.com*

## DEPLOYING MATHEMATICAL MODELS FOR MONITORING THE QUALITY OF BIODIESEL PRODUCTS IN BIODIESEL PROCESSING PLANTS

Vincent E. Efevbokhan<sup>1\*</sup>, Comfort Eboigbe<sup>1</sup>, Temitayo E. Oladimeji<sup>1</sup>, Olatunde S. Dahunsi<sup>2</sup>

<sup>1</sup> Department of Chemical Engineering, Covenant University, Ota, Nigeria

<sup>2</sup> Department of Biological Sciences, Landmark University, Omu-Aran, Nigeria

Received May 23, 2018; Accepted October 19, 2018

---

### Abstract

This research was carried out to produce biodiesel from waste vegetable oil using homogenous and heterogeneous catalysis and hence obtain a good basis for effective comparison of the two processes. The percentage conversion of the waste vegetable oil to biodiesel and its fatty acid methyl ester (FAME) content were determined using established correlations. Potassium hydroxide (KOH) and calcium oxide (CaO) were respectively used for the homogenous and heterogeneous catalysis. From the results obtained, the highest conversion obtained from the homogeneous catalysis was 85.63% while 88.51% conversion was obtained from the heterogeneous process. FAME contents of the biodiesel produced from the homogenous and heterogeneous processes gave 94.19% and 97.87% respectively. The yield of biodiesel obtained from the homogenous process was 89% while the yield from the heterogeneous process was 75.1%. The average densities were 0.874g/mL and 0.892 g/mL of biodiesel produced using homogenous and heterogeneous catalysis respectively. The average viscosity was 4.59 cSt at 65°C at 150 minutes reaction time for biodiesel produced using a homogenous process and 4.23cSt at 150 minutes reaction time for biodiesel produced using the heterogeneous process.

**Keywords:** Biodiesel; quality; monitoring; models; processing.

---

## 1. Introduction

Biodiesel is one of the many energy alternatives that can help in reducing the over dependence on fuels from fossil origin [1-3]. It is derived from renewable sources such as vegetable oil or animal fats which can complement the conventional petroleum diesel fuel [1]. The increasing use of fossil fuels has caused several social and environmental challenges over the years such as high levels of land, air and water pollutions, global warming through the release of greenhouse gases (GHG) (CO<sub>2</sub>, CH<sub>4</sub>), coupled with increasing cost of production leading to high energy and transportation costs [4]. In comparison to fossil fuel, greenhouse gases emissions are reduced by about 41% during production and combustion of biodiesel [5], e.g. B20 reduces CO<sub>2</sub> by 15%. Thus, biodiesel is increasingly becoming the most attractive alternative energy source to petroleum diesel [2, 6-7]. It can be produced based on need with less pollution problems [8].

Generally, though, biofuels only offer a partial solution to many of the problems associated with fossil fuel usage. Hence there is the need to encourage more stakeholders' involvement in the full development of biodiesel production in order to mitigate the associated problems with fossil fuel usage. At the moment, there are a few hundreds of persons, industries, and agencies that are into biodiesel production using diverse processes such as homogeneous alkali-catalysed trans-esterification, acid esterification followed by base catalysed trans-esterification of vegetable oils or animal fats, heterogeneous catalysis (solid acid catalyst) or enzymatic process [9-16]. Biodiesel is the end product of all these processes.

The major reaction taking place is that between the vegetable oil and alcohol in the presence of a catalyst to form esters and glycerol [17]. Thus, the quality of biodiesel obtained from these varied processes is expected to vary considerably. Amongst the factors affecting biodiesel quality are, fatty acid content [6], the processing methods, conditions of processing (temperature, catalyst type, and dosage, agitation speed and time), water content, the type and quality of raw materials [9, 18]. Any change in the feed source especially that of vegetable oils, the composition of the biodiesel and consequently the properties of the biodiesel also change [9]. ASTM D6751 and EN 14214 are two specification types for standardizing the properties of biodiesel products and some of these properties include: viscosity, cold flow, flash point, cetane number, oxidative stability, iodine value, density, acid value, Free and total glycerol, Na, K, Mg, Ca, P, S, water and sediment, sulphated ash, carbon residue [2, 19].

More often than not, monitoring, testing and setting biodiesel standards require very sophisticated machines such as the nuclear magnetic resonance (NMR) spectrometer, high performance liquid chromatograph (HPLC), gas chromatograph-mass spectrometer, flame ionization detector (FID) or electron capture detector (ECD), Fourier Transform Infrared Spectrometer (FTIR) and a host of others, which are cost prohibitive and inaccessible to most biodiesel producers in developing countries. Mostly affected are the rural farmers who cannot afford this very expensive analytical equipment. It has been shown that when biodiesel is well processed, its quality and efficiency become more significantly better than petro diesel [9].

For predicting the properties of biodiesel, various models have been developed using various feed oils and their blends to determine the quality of biodiesel [9, 20]. Each model is used for the prediction of a given property of the biodiesel [10]. Literature reveals that there is a great volume of work done in the process design and manufacturing of biodiesel from various vegetable oils and a few prediction models for the very important properties of biodiesel [10]. The acid value (AV) is one of the analytical parameters usually employed to evaluate the quality of biodiesel [21]. Quality control of biodiesel fuel based on an acid value is very important in the determination of the rate and extent of conversion of the vegetable oil or fat to biodiesel.

Biodiesel is essentially composed of fatty acid methyl (or ethyl) ester (FAME or FAEE) depending on the alcohol (methanol or ethanol) used during the trans-esterification process and varying amounts of fatty acids. The fatty acid content is usually quantified or quoted as an acid number [22]. The acid-number limit for biodiesel, ASTM D 6751, has been set at 0.5. As the acid value (AV) of the biodiesel/oil system decreases, the percentage conversion of the oil to biodiesel increases. It is advantageous to have an acid value that is as low as possible signifying a high level of conversion of the triglycerides to biodiesel. The acid number of biodiesel fuel is measured according to JIS, ASTM D 664 or ISO standards either by potentiometric or volumetric titration [21-22]. Regulating bodies have established specifications for AV obtained from biodiesel analyses so as to set the quality of biodiesel obtained from the numerous production techniques used by biodiesel producers [21, 23]. The high acid value is an indication of the presence of unreacted vegetable oil in the biodiesel product which invariably affects the overall quality or properties (viscosity, cetane number, cold flow, pour point, flash point, density, etc.) of the biodiesel. Thus, with a single quality parameter (acid value), the percentage conversion of vegetable oil to biodiesel can be estimated using proven mathematical models. Consequently, during in-process checks in biodiesel processing plants, progressive monitoring of the acid number of biodiesel will give an indication of the level of completeness or extent of the trans-esterification reaction. This approach can then be popularized and used by many biodiesel producers especially with the rural populace who cannot afford the expensive and most times sophisticated biodiesel testing machines. In this study, the acid values of biodiesel formed were monitored against the reaction time and the values obtained were used to calculate the corresponding percentage conversion of waste frying oil (WFO) using Wang's correlation [24] and FAME content using Felizardo's correlation [25]. Both the homogenous and heterogeneous catalytic processes were employed at different reaction temperatures and times.

## 2. Materials and method

### 2.1. Materials

The waste frying oil used in this study was sourced from the Covenant University cafeteria, Ota, Nigeria. Reagents such as methanol (technical grade), potassium hydroxide pellets (85.0 % minimum assay, Qualikems), anhydrous calcium oxide (Sigma-Aldrich, >99.99% purity), were obtained from authorized manufacturers. Hot plate magnetic stirrer (JENWAY 1000 ST15 0SA, UK), weighing balance (Scout Pro SPU2001, China), Petroleum products kinematic viscosity tester (SYD-265D-1), stopwatch (Samsung tab clock), Mercury-in-glass 0-360° thermometer (UNISCOPE), reflux condenser. All glassware was J-SIL Borosilicate glass.

### 2.2. Experimental procedures

#### 2.2.1. Pre-treatment of waste frying oil

1 litre of the waste frying oil (WFO), was filtered using sieve cloth to remove bits of food residues and 500 mL of it was then heated at 115° C to a constant weight to remove its water/moisture content.

#### 2.2.2. Catalyst preparation (homogenous catalyst)

Potassium hydroxide pellets (1.1g of 0.8 w/w of WFO) were placed in a conical flask containing 144.4g of methanol. The conical flask was stoppered and agitated to ensure complete dissolution of the pellets in the methanol.

#### 2.2.3. Trans-esterification of oil using a homogenous catalyst

The method earlier described [\[26-27\]](#) was used for the trans-esterification reaction in this study. In doing this, a fixed amount of freshly prepared and well stirred KOH–methanol mixture was first added into the reactor (3-necked flat-bottom flask) equipped with a reflux condenser, a quick fit thermometer and a port for charging of the feed and then preheated to 40° C. The measured pre-treated WFO which was also pre-heated to the same temperature in a beaker on a hot plate was then carefully charged into the reactor under constant agitation and heating until the reaction temperature was achieved. The time of reaction started when the reaction reached the required temperature (40, 50, 55, 60, 65° C). The reaction was stopped after the present reaction times of between 30 to 150 minutes were respectively achieved.

#### 2.2.4. Transesterification of oil using a heterogeneous catalyst

The same experimental set up as in section 2.2.3 was used. Except that instead of KOH - ethanol mixture, a fixed amount of freshly prepared well stirred CaO–methanol mixture was used at a ratio of 9:1 methanol to oil. The best reaction temperature obtained from the homogeneous process (60° C) was used here but at a varied reaction time of between 30 and 150 minutes.

#### 2.2.5. Separation of biodiesel and glycerol phases

The products of reaction from the above sections were transferred to a separating funnel and allowed to settle for between 6 to 12 h to give two distinct phases of biodiesel on top and glycerol or aqueous phase at the bottom. The glycerol was then carefully drained out into a container while the biodiesel was left in the separating funnel for the washing stage.

#### 2.2.6. Biodiesel washing and drying

The biodiesel phase obtained was then washed with warm deionized water several times until the washing water became very clear. Water was then drained out from the separating funnel while the washed biodiesel was drained into a beaker for drying. The washed biodiesel was dried by heating to 115° C until a constant weight was obtained.

### 2.2.7. Determination of acid value of biodiesel

Methanol was neutralized with 0.1N NaOH using phenolphthalein as indicator. Ten (10) g of the biodiesel was weighed into a beaker. Then 50 ml each of benzene and the neutral alcohol were poured into the beaker containing the biodiesel sample. The mixture was stirred vigorously to ensure proper mixing and was then titrated with 0.1M KOH which was previously prepared using 3-4 drops of phenolphthalein indicator until a colour change (pink) was persistently observed for 15 s. The steps were repeated, and the average values were calculated. The acid value was calculated using equation 1 shown below;

$$\text{Acid value} = \frac{Q \times 56.1 \times M}{W} \quad (1)$$

where: W = weight of sample; M = strength of KOH; Q = average titre value.

### 2.2.8. Determination of percentage conversion of WFO to biodiesel

The determination of the percentage conversion of WFO to biodiesel was based on Yong's correlation [24] as given in equation 2:

$$\% \text{ conversion} = \left(1 - \frac{AV_{\text{biodiesel}}}{AV_{\text{WFO}}}\right) \times 100\% \quad (2)$$

where:  $AV_{\text{WFO}}$  is acid the value of the waste frying oil (WFO);  $AV_{\text{biodiesel}}$  is acid value of the biodiesel.

### 2.2.9. Specific gravity/density

A dry cleaned empty 50 ml density bottle was weighed and the mass recorded as M, it was then filled up with distilled water and subsequently with the sample with their weights taken as  $M_1$  and  $M_2$  respectively. The densities of the distilled water and biodiesel were then calculated from equation 2. Hence, the specific gravity was evaluated as shown below:

$$\text{Density}(g/cm^3) = \frac{\text{weight of (density bottle and content)} - \text{weight of empty bottle}}{\text{weight of equal volume}} \quad (3)$$

### 2.2.10. Cloud and pour points

A sample of the biodiesel was placed in a test jar to a mark and then placed inside a cooling bath. The temperature at the bottom of the test jar which is the temperature at which the biodiesel starts to form cloud was taken as the cloud point while the lowest temperature at which the fuel continues to flow was recorded as the pour point.

### 2.2.11. Kinematic viscosity

A viscometer was inserted into a water bath with a set temperature and left for 30 min. The sample was added to the viscometer and allowed to remain in the bath to equilibrate or attain the test temperature. The sample was then allowed to flow freely and the time required for the lower meniscus of the biodiesel sample to pass from the first to the second mark was taken using a stop watch. The procedure was repeated a number of times and the average time values were recorded. The kinematic viscosity of each sample was then calculated from equation 4.

$$\text{Kinematic viscosity} = t \times K \quad (4)$$

where K is 0.4959, the viscometer calibration factor.

### 2.2.12. Estimation of the FAME content of biodiesel

The Felizardo's correlation [25] (equation 4) was used to estimate the percentage FAME content of the biodiesel samples produced.

$$\text{FAME}\% = -45.055 \ln \mu + 162.85 \quad (5)$$

where  $\mu$  is the viscosity of the biodiesel sample produced [25].

### 3. Results and discussion

#### 3.1. Effect of variation in temperature and time on yield for biodiesel produced using homogenous and heterogeneous catalysis

From Table 1, the free fatty acid content of the WFO gave 1.74%. The value was far less than 5% and hence the choice of a single step trans-esterification process using KOH as the catalyst.

Table 1. Physiochemical properties of waste frying oil used for the production of biodiesel

Property	Value	Property	Value
Colour	Dark brown	Molecular weight of FA(g/mol)	263.92
Density (g/cm <sup>3</sup> )	0.91	Pour point (°c)	-3
Specific gravity	0.911	Cloud point(°c)	20
FFA value (%)	1.74	Acid value (mg KOH/g)	3.48
Saponification value	148.7	Kinematic viscosity (cSt) at 40°c	54

The research was designed so as to compare the extent of conversion of WFO to bio-diesel between two catalytic processes - heterogeneous and homogenous catalysis. Potassium hydroxide was used as the homogeneous catalyst while CaO was used as the heterogeneous catalyst. From Table 2, varied reaction temperatures and times were investigated principally to decide the overall best optimal reaction conditions in the trans-esterification of WFO to its corresponding biodiesel using the homogeneous catalytic process. The highest yield of 89% was obtained at 60°C. Hence it was this condition that was imposed on the heterogeneous trans-esterification of the WFO to its bio-diesel, (see Table 3).

Table 2. Results for biodiesel produced using a homogenous catalyst

Sample	Temp. (°C)	Time of reaction (min)	Yield (%)	Conversion (%)	Density (g/cm <sup>3</sup> )	FAME	Pour point (°C)	Cloud point (°C)
A1	40	30	78.87	24.14	0.878	74.73	2	11
A2		60	79.9	37.07	0.878	75.63	3	11
A3		90	83.5	50.00	0.876	77.35	3	12
A4		120	82.6	66.09	0.872	78.31	3	12
A5		150	83	74.14	0.870	78.93	5	12
B1	50	30	71.1	31.90	0.882	76.42	3	11
B2		60	77.5	45.11	0.882	76.88	5	11
B3		90	79.1	56.61	0.874	78.45	5	12
B4		120	76.6	67.82	0.880	80.43	5	12
B5		150	75.9	79.02	0.884	81.08	5	12
C1	55	30	72	40.23	0.872	84.51	3	11
C2		60	78.5	54.89	0.878	85.96	4	12
C3		90	85.2	74.14	0.882	78.45	4	13
C4		120	82.8	77.30	0.882	80.43	4	13
C5		150	83.7	83.91	0.884	81.08	5	13
D1	60	30	72.6	53.16	0.876	85.96	1	11
D2		60	76.1	72.70	0.878	86.70	2	12
D3		90	89	77.30	0.878	87.20	3	12
D4		120	87.5	80.75	0.882	90.70	3	13
D5		150	88.1	83.91	0.884	92.84	4	13
E1	65	30	70.9	67.82	0.864	87.54	1	11
E2		60	74.00	75.86	0.868	89.36	2	11
E3		90	76.50	80.75	0.870	91.90	4	12
E4		120	75.20	83.91	0.876	93.03	4	12
E5		150	75.70	85.63	0.884	94.19	5	13

Table 3. Results for biodiesel produced using a heterogeneous catalyst

S/N	Temp. (°C)	Time of reaction (min)	Yield (%)	Conversion (%)	Density (g/cm <sup>3</sup> )	FAME	Pour point (°C)	Cloud point (°C)
F1	60	30	67.6	69.25	0.9	85.07	2	11
F2		60	67.9	77.30	0.900	89.09	2	11
F3		90	69.2	87.07	0.902	91.16	2	11
F4		120	71.3	88.51	0.900	94.39	2	12
F5		150	75.1	77.30	0.882	97.87	3	12

From Table 2, the trend shows an appreciable rise in biodiesel yield from between 30 and 100 minutes getting to their maxima in about 90 minutes before they began to decline after that. The drop in yield after 90 minutes could be adduced to possible soap formation and backward reaction that may have been triggered after the residence time was exceeded [28]. It was observed that there was no well-defined trend of yield versus temperature. The highest yields were obtained at 60° C this agrees with a similar study done by Mathiyazhagan *et al.* [29] while the lowest yields were obtained at 65° C (the boiling point of methanol). The low yield at this temperature may be attributed to the continuous evaporation and condensation of methanol in the reaction medium leading to (i) equilibrium shift to the left (ii) imbalance in the methanol-oil molar ratio (iii) reduced contact time between the methanol and oil. It is this cumulative effect that gave rise to the reduced yield in biodiesel. In comparison (Table 2), the homogeneous catalysis produced the highest biodiesel yield (89.5%) in 90 minutes than the heterogeneous catalysis (75% in 150 minutes) at the same temperature (60° C) as shown in Table 3. The trend for biodiesel produced using heterogeneous catalyst agrees with the work of Bourney *et al.* [30].

### 3.2. Effect of variation in temperature and time on the physico-chemical properties of biodiesel produced using homogenous and heterogeneous catalysis

#### 3.2.1. Density

Table 2 and 3 shows the densities obtained at 60° C in response to temperature and time variations for both homogeneous and heterogeneous catalysis. The densities obtained from the heterogeneous catalysis were generally higher and remained practically the same at an average value of 0.90g/ml between 30 and 120 minutes but with a sharp fall to 0.882g/ml. While for homogeneous catalysis the densities rose steadily from 0.876 to 0.882 g/ml within the reaction time of 30 to 150 minutes. From Table 2 and 3, it was observed that temperature variations had only a little or no effect on densities of biodiesel produced. However, the densities of all of the biodiesel produced fell within EN 14214 standards (0.86-0.90) g/cm<sup>3</sup>.

#### 3.2.2. Viscosity

From Figure 1, it was observed that as reaction temperature and time increased there was the corresponding drop in the viscosity values of the biodiesel obtained. The results correspond to the work reported by Demirbas [3]. At 40° C, when compared with the kinematic viscosity (54cSt) of the waste frying oil, there was a significant drop in kinematic viscosity of the biodiesel obtained from the homogeneous catalysis within the reaction time considered. This may be attributed to the fact that the fatty acid bonds in the triglyceride structure have been broken and reacted with the methoxide to produce three moles of biodiesel. It is the formation of the biodiesel that leads to the viscosity drop as shown in Figure 1. Viscosity is a very important parameter in the production of fuels because it determines the burning efficiency, lubricity, and atomization of the fuel. From Figure 1, the viscosity (4.502) of biodiesel produced in 150 minutes and at 65° C gave the best. It falls within ASTM D6751 standards (1.9-6.0) cSt and EN 14214 standards (3.5-5.0) cSt. From Figure 2, it was observed that biodiesel produced with heterogeneous catalyst (CaO) at 60° C was less viscous (4.23cSt) than the viscosity (4.55cSt) biodiesel produced using a homogenous catalyst (KOH) at the same temperature.

Both viscosities, however, falls within ASTM D6751 standards (1.9-6.0) cSt and EN 14214 standards (3.5-5.0) cSt.

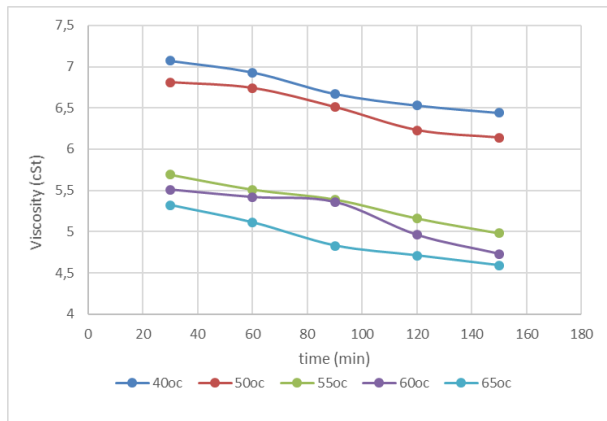


Figure 1. Variation in temperature and time on the density of biodiesel produced using a homogenous catalyst

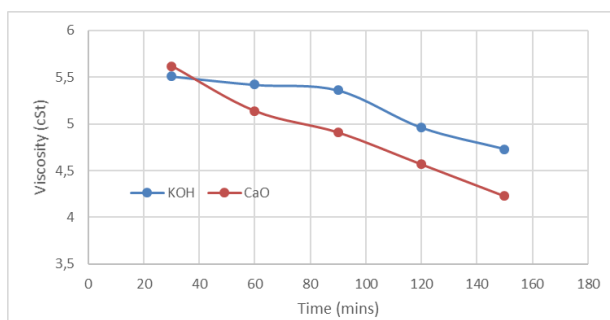


Figure 2. Variation in time on the viscosity of bio-diesel produced using homogenous catalyst and heterogeneous catalyst at 60°C

### 3.2.3. The effect of reaction time and temperature on the acid value of biodiesel

Table 4 respectively describe the effect of reaction time and temperature on the acid values of biodiesel. From Table 4, the effect of temperature was most vividly portrayed at different times horizontally across the table. As the temperature increased from 40 to 65°C while holding each time constant, the acid values reduced. This may be due to the fact that the rate of reaction generally increases as reaction temperature increases. This agreed with the work of other researchers [29, 31].

Table 4. The effect of temperature and time on the acid value of bio-diesel using homogenous and heterogeneous catalysts

Time (min)	Homogeneous catalysis					Heterogeneous catalysis
	40°C	50°C	55°C	60°C	65°C	60°C
Acid value, (mg KOH/g)						
30	2.64	2.37	2.08	1.63	1.12	1.07
60	2.19	1.91	1.57	0.95	0.84	0.79
90	1.74	1.51	0.90	0.79	0.67	0.45
120	1.18	1.12	0.79	0.67	0.56	0.40
150	0.90	0.73	0.56	0.56	0.50	0.40

Increased reaction rate means conversion of more of the oil into biodiesel and ultimate reduction in its acid number. The effect of reaction time (30 to 150 minutes) on the acid number of biodiesel followed the same decreasing trend for all the trans-esterification reactions at a constant temperature. All the acid numbers tended to lower values at higher reaction time. It was observed from Table 4, that lower acid values and hence higher conversions were obtained using heterogeneous catalysis than homogeneous catalysis at 60°C.

The acid values of biodiesel produced at 40°C and 50°C within the reaction time of 30 – 150 minutes did not meet the acceptable standard of ASTM D6751 (<0.8) while the acid values of biodiesel produced at 60°C and 65°C within 90 to 120 minutes met the acceptable standard of ASTM D6751. Also, the acid values of biodiesel produced from the heterogeneous catalysis using calcium oxide at 60°C and between 60 – 150 minutes fell within an acceptable standard of ASTM D6751.

### 3.2.4. Effect of variation in temperature and time on conversion of biodiesel produced using a homogenous catalyst

The conversion was calculated by determining the amount of fatty acid that was converted and comparing it to the amount of fatty acid initially present in the waste frying oil that was used. The acid values of the biodiesel obtained were calculated using equation 1. From Table 4 it was observed that the acid value of biodiesel was inversely proportional to its percentage conversion (see Tables 3 and 4). With increasing reaction time, all acid values (Table 4) of the biodiesel assumed decreasing trends while the percentage conversion of the corresponding biodiesel assumed increasing trends (Table 2 and 3). The lower the acid values of the biodiesel produced the higher is its corresponding percentage conversion. This observation corresponds to the work of of Pinto *et al.* [32]. From Table 2 and 3, it was observed that conversion of oil to biodiesel using the heterogeneous catalysis (CaO) was higher than that of the homogeneous catalysis (KOH) at 60° C and within the reaction time of 30 – 120 minutes. This finding agrees with the work of other researchers [33]. From Table 5 the qualities of two of the best biodiesel samples E5 and F5 are compared. They had 85.63 and 88.5% percentage conversions respectively. On comparing E5 and F5 with biodiesel standards of ASTM D6751 and EN 14214, the conformity level of the various parameters was high to pass for biodiesel. The relatively low % conversion (85.63% for E5 and 88.5% for F5) only indicates that there is room for improvement and optimization of the biodiesel batch processes used for the trans-esterification reactions. The attention and target would be at obtaining greater than 95% oils conversion to their corresponding biodiesel, which should automatically translate to better and improved biodiesel properties.

Table 5. Comparison of biodiesel samples with biodiesel standards

Properties	Petro-diesel ASTM D0975	Biodiesel ASTM D6751	Biodiesel EN 14214	Biodiesel Sample E5	Biodiesel Sample F5
Density at 30°C (g/cm <sup>3</sup> )	0.876	0.875-0.90	0.86-0.90	0.884	0.9
Viscosity at 40°C (cSt)	1.9-4.1	1.9-6.0	3.5-5.0	4.59	4.57
Pour point °C	-35 to -15	-15 to 16	-	5	3
Cloud point °C	-15 to 5	-3 to 12	-	13	12
Acid value (mg KOH/g)	0.35	<0.8	<0.5	0.5	0.4
FAME content (%)	-	-	-	94.19	97.87
Conversion (%)	-	-	-	85.63	88.51

### 3.2.5. Effect of variation in temperature and time on FAME content of biodiesel produced using a homogenous catalyst

From Table 2 and 3, it was observed that the FAME contents represented by the different curves assumed increasing trend with increasing reaction time and temperature. The effect of time and temperature were more pronounced at increasing time and temperature. The set of values represent the two lowest temperatures of 40 and 50° C (after about 150 minutes of reaction) gave 79 and 81% FAME contents respectively. The implication of this is that the impurity level or unconverted WFO is still very high and may thus not be suited for use as biodiesel. At the same reaction time of 150 minutes, the FAME contents obtained at 55, 60 and 65°C were 90.3, 93 and 94.2% respectively. Table 2 and 3 helps us to compare the FAME contents of biodiesel obtained from heterogeneous and homogeneous catalysis at 60° C. From the reaction time of 40 to 150 minutes, the percentage FAME contents of biodiesel samples obtained at 60° C were all higher than the corresponding biodiesel samples obtained from the homogeneous catalysis under the same set of temperature and time. At 60, 90, 120 and 150 minutes, the percentage FAME contents were 89, 91, 94 and 98% respectively for biodiesel

samples obtained from heterogeneous catalysis while they were 86.6, 87.3, 91 and 93% respectively for biodiesel samples obtained from homogenous catalysis.

#### 4. Conclusion

The study of the production of biodiesel using homogeneous and heterogeneous catalysis at varied temperature and time revealed that:

- Temperature and time were two critical factors to obtaining good quality biodiesel.
- Higher percentage conversions of WFO to biodiesel were obtained at higher temperatures of 55, 60 and 65°C than at 40 and 50°C.
- At 60°C, heterogeneous performed better than homogeneous catalysis in the conversion of WFO to biodiesel. The percentage conversion and FAME content of biodiesel from the heterogeneous catalysis were higher than that of homogeneous catalysis.
- Quality of biodiesel may be determined per time by monitoring the change in acid value as the trans-esterification reaction progresses.
- The acid value of biodiesel is inversely proportional to the % conversion of oils to biodiesel. The lower the acid value of biodiesel sample the higher is its % conversion.
- Well formulated mathematical models that relate acid value or number to oil conversion to biodiesel can be deployed to monitoring and obtaining the progress of trans-esterification reactions. At higher % conversion, conformity of the quality of the biodiesel products is assured.

#### Acknowledgement

The authors acknowledge with thanks the Management of Covenant University for their support in undertaking and publishing this research work.

#### References

- [1] Kumar V, and Kumar J. Kinetics of *Jatropha Curcas* transesterification in batch reactor. in Proceedings of the World Congress on Engineering and Computer Science. WCECS 2008, October 22 - 24, 2008, San Francisco, USA, ISBN: 978-988-98671-0-2.
- [2] Saini RD. Conversion of Waste Cooking Oil to Biodiesel. *International Journal of Petroleum Science and Technology*, 2017. 11(1): 9-21.
- [3] Demirbas A. Biodiesel from waste cooking oil via base-catalytic and supercritical methanol transesterification. *Energy Conversion and Management*, 2009. 50(4): 923-927.
- [4] Dahunsi SO, Oranusi S, and Efevbokhan VE. Cleaner energy for cleaner production: Modeling and optimization of biogas generation from *Carica papayas* (Pawpaw) fruit peels. *Journal of cleaner production*, 2017; 156: 19-29.
- [5] Hill J, Nelson E, Tilman D, Polasky S, Tiffany D. Environmental, economic, and energetic costs and benefits of biodiesel and ethanol biofuels. in Proceedings of the National Academy of Science of the United States of America (PNAS), 2006; 103(30): 11206-11210.
- [6] Lamaisri C, Punsuvon V, Champrame S, Liangsakul P. Relationship between fatty acid composition and biodiesel quality for nine commercial palm oils. *Songklanakarin Journal of Science & Technology*, 2015. 37(4) 389-395.
- [7] Ved K, and Padam K. Study of physical and chemical properties of biodiesel from sorghum oil. *Research Journal of Chemical Sciences*, 2013; 3(9): p. 64-68.
- [8] Tschakert P, Huber-Sannwald E, Ojima DS, Raupmn MR. Holistic, adaptive management of the terrestrial carbon cycle at local and regional scales, in *Glob. Environ. Change.*, 2008; 18(1):128-141.
- [9] Saxena P, Jawale S, and Joshipura MH. A review on prediction of properties of biodiesel and blends of biodiesel. *Procedia Engineering*, 2013; 51: 395-402.
- [10] Puspa Asri N, Budikarjono K, and Roesyadi A. Kinetics of Palm Oil Transesterification Using Double Promoted Catalyst CaO/KI/ $\gamma$ -Al<sub>2</sub>O<sub>3</sub>. *Journal of Engineering & Technological Sciences*, 2015; 47(4): 353-363.
- [11] Borges M, and Díaz L. Recent developments on heterogeneous catalysts for biodiesel production by oil esterification and transesterification reactions: a review. *Renewable and Sustainable Energy Reviews*, 2012; 16(5): 2839-2849.
- [12] Chouhan AS, and Sarma A. Modern heterogeneous catalysts for biodiesel production: A comprehensive review. *Renewable and Sustainable Energy Reviews*, 2011; 15(9): 4378-4399.

- [13] Ramírez-Ortiz J, Medina-Valtierra J, and Rosales MM. Used frying oil for biodiesel production over kaolinite as catalyst. *Engineering and Technology*, 2011; 80: 977-980.
- [14] Lam MK, Lee KT, and Mohamed AR. Homogeneous, heterogeneous and enzymatic catalysis for transesterification of high free fatty acid oil (waste cooking oil) to biodiesel: a review. *Biotechnology advances*, 2010; 28(4): 500-518.
- [15] Ghaly AE, Dave D, Books MS, Budge S. Production of biodiesel by enzymatic transesterification. *Am J Biochem Biotechnol*, 2010; 6(2): 54-76.
- [16] Chai F, Cao F, Zhai F, Chen Y, Wang X, Su Zh. Transesterification of vegetable oil to biodiesel using a heteropolyacid solid catalyst. *Advanced Synthesis & Catalysis*, 2007; 349(7): 1057-1065.
- [17] Okullo A, Temu A, and Ntalikwa J. Transesterification Reaction Kinetics of Jatropha Oil for Biodiesel Production. in *Second International Conference on Advances in Engineering and Technology*. 2011: 221-227.
- [18] Corral Bobadilla M, Lorza RL, Garcia RE, Gomez FS, González EPV. An Improvement in Biodiesel Production from Waste Cooking Oil by Applying Thought Multi-Response Surface Methodology Using Desirability Functions. *Energies*, 2017; 10(1): 130.
- [19] Knothe G. "Designer" biodiesel: optimizing fatty ester composition to improve fuel properties. *Energy & Fuels*, 2008; 22(2): 1358-1364.
- [20] Ruiz-Méndez M, Marmasat S, Liotta S, Doberganés MC. Analysis of used frying fats for biodiesel production. *Grasas y aceites*, 2008. 59(1): 45-50.
- [21] Gonzaga FB, and Sobral SP. A new method for determining the acid number of biodiesel based on coulometric titration. *Talanta*, 2012; 97: 199-203.
- [22] Mahajan S, and Konar SK. Determining the acid number of biodiesel. *Journal of the American Oil Chemists' Society*, 2006; 83(6): 567-570.
- [23] Standard Specification for Biodiesel Fuel Blend Stock (B100) for Middle Distillate Fuels. 2012: ASTM International.
- [24] Wang Y, Zhao M, Ma S, Kuang L, Han X, Tang S. Preparation of biodiesel from waste cooking oil via two-step catalyzed process. *Energy conversion and management*, 2007; 48(1): 184-188.
- [25] Felizardo P, Correia MJ, Raposo I, Mendes JF, Berkemeier R, Bordado JM. Production of biodiesel from waste frying oils. *Waste management*, 2006; 26(5): 487-494.
- [26] Efevbokhan VE, Ayoola A, Anawe PAL, Oteri O. The effects of trans-esterification of castor seed oil using ethanol, methanol and their blends on the properties and yields of biodiesel. *International Journal of Engineering and Technology*, 2012; 2(10): 1734-1742.
- [27] Enontiemonria EV, Abiodun OJ, and Eric KE. Extraction and Use of Potassium Hydroxide from Ripe Plantain Peels Ash for Biodiesel Production. *Journal of Biobased Materials and Bioenergy*, 2016; 10(1): 1-9.
- [28] Anitha A, and Dawn S. Performance characteristics of biodiesel produced from waste groundnut oil using supported heteropolyacids. *International journal of chemical engineering and applications*, 2010; 1(3): 261.
- [29] Mathiyazhagan M, Ganapathi A, Jaganath B, Benganayaki N, Sasireka N. Production of biodiesel from non-edible plant oils having high FFA content. *International Journal of Chemical and Environmental Engineering*, 2011; 2(2) 119-122.
- [30] Bournay L, Casanave D, Delfort B, Hillio G. New heterogeneous process for biodiesel production: a way to improve the quality and the value of the crude glycerin produced by biodiesel plants. *Catalysis Today*, 2005; 106(1-4): 190-192.
- [31] Jagadale S, and Jugulkar L. Review of various reaction parameters and other factors affecting on production of chicken fat based biodiesel. *International Journal of Modern Engineering Research*, 2012; 2(2): 407-411.
- [32] Pinto AC, Guarieiro LLN, Rezende MJC, Ribeiro NM, Torres EA, Lopes WA, Pereira PAP, de Andrade JB. Biodiesel: an overview. *Journal of the Brazilian Chemical Society*, 2005; 16(6B): 1313-1330.
- [33] Kim H.-J, Kang BS, Kim MJ, Park YM, Kim DK, Lee JS, Lee KY. Transesterification of vegetable oil to biodiesel using heterogeneous base catalyst. *Catalysis Today*, 2004; 93: 315-320.

*To whom correspondence should be addressed: Prof. Dr. Vincent E. Efevbokhan, Department of Chemical Engineering, Covenant University, Ota, Nigeria*

## PERFORMANCE OF HYPERBRANCHED DENDRITIC POLYESTERPOLYOLS ORGANIC COATINGS

*Abdel Azim A Abdel Azim<sup>1</sup> and Reem K. Farag\**

*Egyptian Petroleum Research Institute, Application department, Nasr City, 11727 Cairo, Egypt*

Received July 4, 2018; Accepted October 19, 2018

---

### **Abstract**

The present article depended on designation of four branched unsaturated resins in two steps. The first step includes the preparation of eight hydroxy branched groups based on pentaerythritol as a core molecule and dimethylolpropionic acid as monomer. In the second step polycondensation reactions of 1 mole prepared eight hydroxy terminated sample with four different molar ratios of maleic & phthalic anhydride namely 10:90, 30:70, 50:50 & 90:10 respectively assigned as H1, H2, H3 and H4. The chemical structures of the prepared polymers are confirmed using FTIR and <sup>1</sup>HNMR spectroscopic techniques. The particle sizes & molecular weights of the synthesized resins are determined. Four high reactive functional groups cross linked networks water based coating films are performed to improve their chemical and mechanical resistance.

**Keywords:** *Hyperbranched polymers; water based organic coatings; unsaturated polyester; nanoparticle resins; dimethylolpropionic acid.*

---

### **1. Introduction**

The creations and investigation of new polymeric architectures have a great attention among polymer scientists over the last eras [1]. Dendritic polymers are attractive for industrial needed because they have high functionality, high solubility and sole rheological manners. Dendritic polymers divided into two different classes: the monodisperse dendrimers and the polydisperse hyperbranched polymers [2]. Dendrimers have regular star-like structure and need various steps for preparation which certainly lead to a relative high cost price, and limit their use in applications.

Hyperbranched polymers have irregular structures tree-like macromolecules ended with a great numbers of reactive functional groups prepared in one and simple step method [1-10]. Properties of branched macromolecules do not only attract the academic research through their simplicity and synthetic experiment [2], but they also get more and more attention in industrialized research applications [11-15]. Because of the sole behaviors, multifunctional terminal groups, narrow polydispersity and low cost with easy synthesis, hyperbranched polymers can to be used as coating resins [2, 16, 17].

On the other hand, the traditional unsaturated polyester resins (UP) prepared previously in literatures suffer from various problems such as rigidity, low acid & alkali resistances and low adhesion with steel when cured with vinyl monomers [18-24]. To solve these badly-behaved polymers, low cost hyperbranched resins with small particle size ended by various reactive functional groups with high surface area containing different chain lengths are synthesized in the present research. In this respect, the present paper aims to design four branched unsaturated polyester resins using simple method with various chain lengths and different nanosizes for coating stability based on pentaerythritol (PEL) as a core molecule and dimethylolpropionic acid (DMPA) as monomers.

## 2. Experimental

### 2.1. Materials and methods

#### 2.1.1. Chemicals

Pentaerythritol (PEL), dimethylolpropionic acid (DMPA), Phthalic anhydride, adipic acid, lauric acid and stearic acid, maleic anhydride, styrene, para-toluene sulphonic acid (p-TSA) was added as catalyst, 10% HCl and 5% NaOH aqueous solutions, methyl ethyle keton peroxide (MEKP) as initiators, cobalt octoate as accelerator. Dichloromethane ( $\text{CH}_2\text{Cl}_2$ ) and distilled water are used for purification. The Fluka chemical company supplied all chemical.

#### 2.1.2 Synthesis of hyperbranched polyester

Equimolar ratio of pentaerythritol (PEL) as a core and dimethylolpropionic acid (DMPA) as monomers is placed in a 250 round flask equipped with a mechanical stirrer, thermometer, and condenser. 1wt% of p-toluenesulfonic acid (p-TSA) is added as catalyst. The temperature is adjusted to be constant between 140 and 160°C in the end of the reaction, eight hydroxyls terminated hyperbranched polyester is yielded and named (HB)-(OH)8 after evaporating the small amount of water produced [25-28].

#### 2.1.3. Synthesis of unsaturated hyperbranched polyester nanoparticles resin

The reaction system is evacuated using  $\text{N}_2$  gas for 30 min before the beginning of the reaction. One mole of eight hydroxyl ended hyperbranched polyester (HB)-(OH)8 is reacted with four different molar ratios of maleic & phthalic anhydride namely 10:90, 30:70, 50:50 & 90:10 respectively assigned as H1, H2, H3 and H4 in presence of 1wt% p-TSA of total weight reactants as catalyst at 160°C. The prepared resin was purified using  $\text{CH}_2\text{Cl}_2$ , and distilled water. After the solvent was evaporated, the polyester nanoparticles were mixed with large amounts of styrene vinyl monomer to yield 60% solution of the polyester. The schematic presentation of the synthesis is shown in Figure 1.

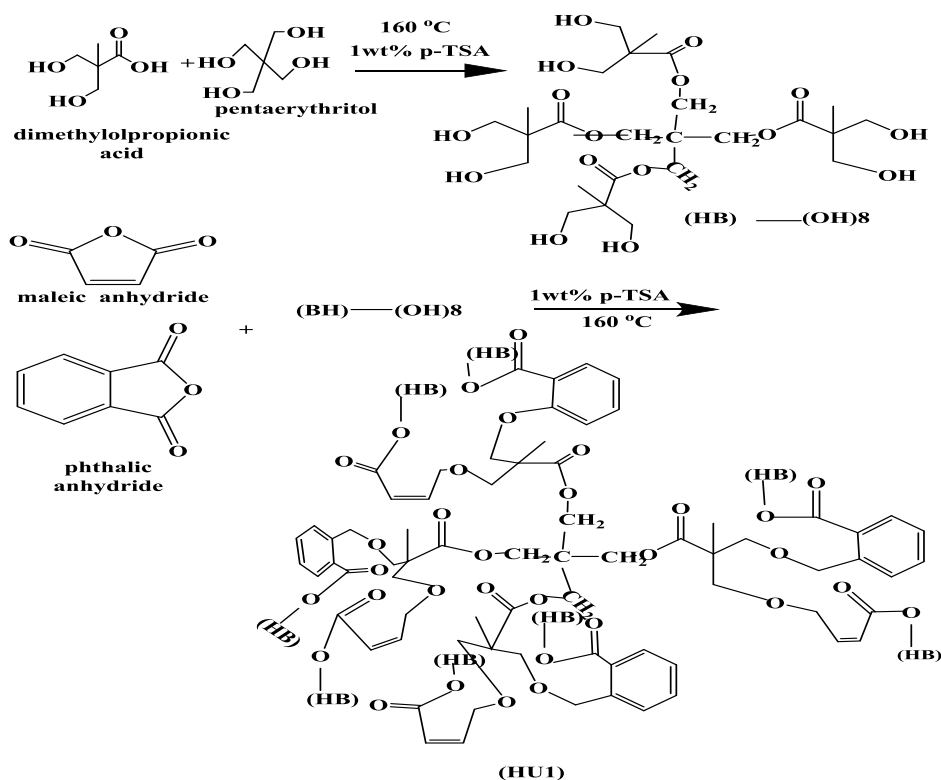


Figure 1. The schematic presentation of the synthesis of unsaturated hyperbranched nanoparticles

#### 2.1.4. Dynamic light scattering (DLS)

DSL is a technique in physics that can be used to determine the size distribution profile of small particles in suspension or polymers in solution. In the present study, the samples were dispersed in high dilution methanol and 2% diluted distilled water.

Gel permeation chromatography (GPC) was performed at 40°C using GPC-Water 2410, with a refractive index detector using 4 columns styragel HR tetrahydrofuran (THF) 7.8 x 300 mm, equipped with a water 515 HPLC pump. tetrahydrofuran and water were used as a mobile phase with a flow rate of 1 mL/min. Aliquots (1 ml) of each sample were diluted with an appropriate amount of THF or water and shaken vigorously. Afterwards, the samples were passed through a filter and injected into the GPC for analysis.

#### 2.2. Testing of the coatings

Steel panels of (10 x 15 cm) are used to evaluate the behaviors of coatings. The panels are coated with tested polymers by using methylethyl ketone peroxide as initiators and cobalt octoate as accelerator. Then the panels are tested to evaluate their mechanical properties (adhesion strength, pencil hardness test, impact resistance and T-bend test) and their durability.

Chemical resistance of organic coatings was evaluated from water resistance, acid & Alkali resistance and Solvent & fuel resistance according to ASTM D870-69, ASTM D1647-89, and ASTM D 870-92 respectively. The acid and alkali resistances of coated panels were determined after immersion in 10% of HCl aqueous solutions using distilled water. The duration of the test was 90 days at 38 °C. The degree of adhesion and visual inspection of blister and cracks were tested for the coated panels.

#### 2.3. Surface morphology studies

The scanning electron microscopy (SEM) of model type JEOL 5410, JEOL, Japan are used to detect the surface morphology of the coated and uncoated panel samples after immersion in 10% of HCl and 5% of NaOH aqueous solutions for 90 days at 38 °C.

### 3. Results and discussion

#### 3.1. Characterizations of the synthesized hyperbranched polyester

The FTIR spectrum of prepared hyperbranched polyester with 8 hydroxyl reactive ended groups (HB)-(OH)<sub>8</sub> which is represents in Figure 2(a) shows the following characteristic peaks:- Absorption bands at 3500 cm<sup>-1</sup> assigned for OH stretching band, the appearance of beak at 2900 cm<sup>-1</sup> assigned for stretching vibration of the aliphatic CH bond and the appearance of beak at 1730 cm<sup>-1</sup> assigned for C=O group indicate the completion of esterification reactions. The appearance of beak at 1105 cm<sup>-1</sup> assigned for stretching vibration of the C-O, 1450 cm<sup>-1</sup> assigned for stretching CH<sub>2</sub> and 1375 cm<sup>-1</sup> assigned for CH<sub>3</sub> peak.

Moreover Figure 3 shows <sup>1</sup>HNMR chart Protons of (HB)-(OH)<sub>8</sub> polymer. Hydroxyl terminated protons appears at the peaks of (4.8–5.2 ppm), CH<sub>3</sub> protons at (1.00 –1.10 ppm), CH<sub>2</sub>-O-C=O protons at (4.00–4.22 ppm) and CH<sub>2</sub>-OH protons at (3.35–3.56 ppm), the peak at about 2.5 ppm is certified to the remaining hydrogen protons of the solvent (DMSO). All the above peaks approve the construction of hyperbranched polymer.

On the other hand the constituents of the four performed hyperbranched unsaturated polyesters show the same FTIR charts. Figure 2(b) represents FTIR bands for H1 as representative sample, the spectrum shows absorption bands at 2982 cm<sup>-1</sup> (assigned for stretching vibration of the aliphatic CH bond). The appearance of peak at 1620 cm<sup>-1</sup> (assigned for stretching vibration of the (C=C) indicate the presence of unsaturation, 1450 cm<sup>-1</sup> (assigned for stretching CH<sub>2</sub>), 1375 assigned for CH<sub>3</sub> peak and the appearance of beak at 1730 cm<sup>-1</sup> assigned for C=O group. The appearance of hydroxyl and protons confirm hyper branched polymers terminated performance. Furthermore the synthesized unsaturated hyperbranched polymers have a more complex structure, and more types of repeating units so it may be difficult

to elucidate the exacted chemical structure using <sup>1</sup>HNMR spectroscopy technique accordingly the signals overlapped with each other so no definite peaks appears [15].

The size and distribution of the performed nano particle resins are estimated as shown in Table 1. Figure 5 give an example for DLS chart for H4 resin. It is clear from the data of particle size that, the particle size increase in order of H1>H2>H3>H4 this means that, the size of prepared resins increase by increasing terminal aliphatic chains (maleic moiety) .This may be attributed that, as the terminated ended chains increase the regular structure (ordering structure) may be formed with large surface area and small particle size [15].

The molecular weights of the synthesized hyperbranched resins decrease by increasing maleic anhydride moiety and all samples have polydispersity more than one as shown in Table1. This result may be attributed to the disordering of the arrangement of branched molecules by decreasing ended chain length as mentioned in our previous work [15].

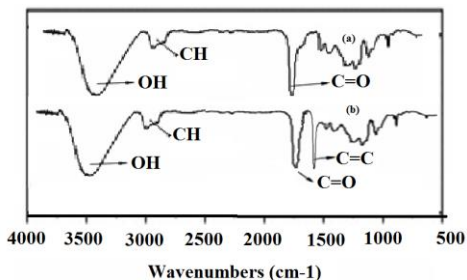


Figure 2. FTIR spectrum of (a) HB-(OH)8 and (b) H1 respectively

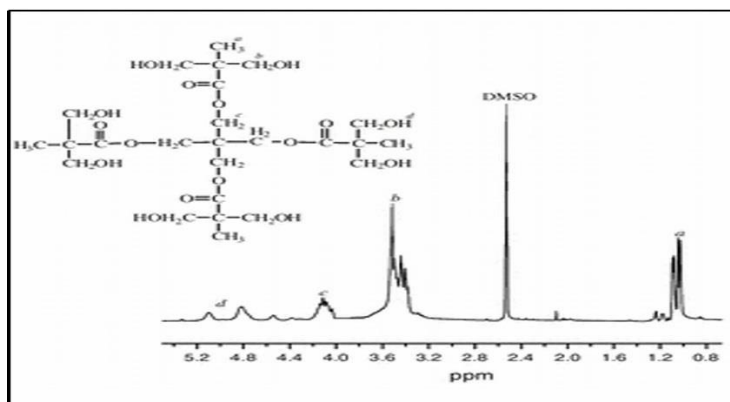


Figure 3. <sup>1</sup>HNMR spectrum of HB-(OH)8

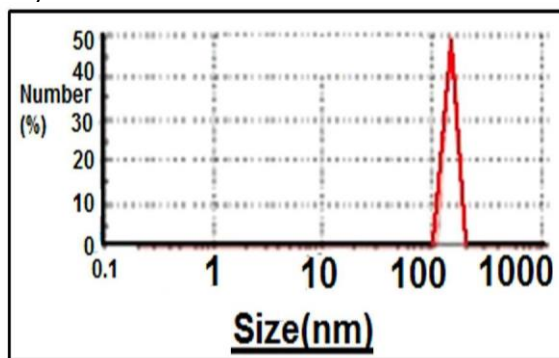


Figure 4. DLS Image of H4

Table 1. Molecular weights and diameter of the synthesized hyperbranched unsaturated nano particles polyester resin

Sample	Molecular weight (g/mol)	Polydispersity	Diameter (nm)
H1	9 760	1.3	350
H2	9 850	1.3	350
H3	12 564	1.2	200
H4		1.2	150

### 3.2. Evaluation of synthesized unsaturated polyester resins for coating applications

Hyperbranched polyolesters can be prepared using simple and low cost method. They have greatly branched strength and huge functional hydroxyl groups, which gives entree to a large

number of reactive groups. Their construction makes them excellent in water based organic coatings.

### 3.3. Chemical resistances

The effects of surrounding solutions are very important especially on durability. In this respect, four panels coated with the prepared resins and immersed to alkali, acid, solvent (acetone test) solutions to study the stability of coats at three months. The initial change of the panels was affected by the environmental conditions. With contact to the surrounding media, the appearance of all the panels changed to show color variations and roasting. The observations at 3 months are summarized in Table 2. It is obvious from the results that the four coated panels with the performed nanoparticle polymers stable and not affected by acid, alkali, water or solvent for 90 days but in case of coated panel with H1 stable for 60 days only and after that, the coated samples affected by acid and alkali solutions this may be attributed to its hardness which disappointed the stability of samples.

### 3.4. Surface morphology studies

Figure 5 shows the image of uncoated steel and four tested coated panel after immersion in 10% of HCl for 90 days. It is clear from the images that, the uncoated panel surface is highly corroded. Whereas smoother surface is seen for H2, H3 and H4 attributed huge functionality on the surface area with high moiety of maleic anhydride as aliphatic polymers. These results indicated that, the constituents of aliphatic chains molecules inhibit the cracking of the coated protective film on the steel surface after long time of immersion in hard environmental conditions [29-31]. But in case of H1 sample after 90 days cracking on coated film surface is occurred this is may be attributed to the rigidity of H1 sample due to the high content of phthalic acid moiety.

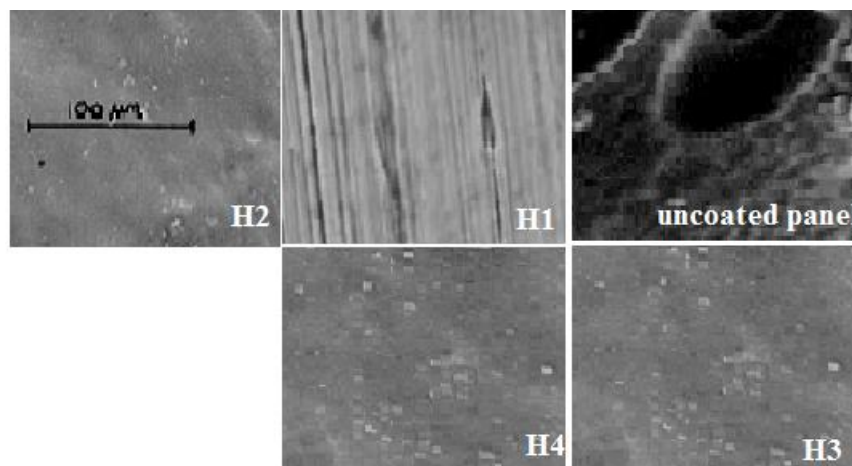


Figure 5. SEM images of uncoated panel, coated panel with H1, H2, H3 and H4 sample after immersion in immersion in 10% of HCl for 90days.

Table 2. Chemical resistance tests of the performed hyperbranched unsaturated polyester cured with styrene

Sample	Acid resistance (days)	Alkali resistance (days)	Water resistance	Solvent re- sistance
H1	60	60	+	+
H2	90	90	+	+
H3	90	90	+	+
H4	90	90	+	+

+ pass; - fail

### 3.5. Mechanical tests

The mechanical properties of the performed hyperbranched resins have been tested by determining the impact, T-bend, adhesion and hardness according to (ASTM D2794-04) (ASTM D 522/1999) (ASTM D 4541/20002) (ASTM D 3363/2000) respectively. The synthesized unsaturated hyperbranched polyester is transparent viscous liquid at room temperature it turn into solid state (cured) when adding 2g methyl ethyl keton peroxide initiator (MEKP) & 0.2g cobalt octoate activator to 100g of each tested resin containing 60% of styrene for 8-10 minutes for forming four cross linked networks coating films. In this respect, the tests for measuring the mechanical characteristics were evaluated after post-curing at 105°C for 24 h and standing for another 24 h at ambient temperature (25°C). The data of mechanical properties (adhesion, impact, and T-bending) for cured resins based are tabulated in Table 3. It is clear from the table that, the adhesion, impact at measured at 5.5&7.5J/mm and T-bond for the four unsaturated nanoparticles resins are all positive. This means that the prepared hyperbranched particles forming stable networks film with panels and having a good mechanical resistance. This may attributed to the nano size of the prepared polymers giving large surface area with stable networks which endorsed each to acts as excellent organic coatings. It is also obvious from the hardness results that the hardness decreases in the order of H4 < H3 < H2 < H1. This may be owing to, increasing aliphatic and huge reactive functional ended segments chain length donate the flexibility to the coatings compounds. So the mechanical brittleness is effectively by stability and flexibility of hyperbranched crosslinked films forming coating. The data reported on adhesion indicates that the tested branched resins have superior adhesion network properties with steel. This can be attributed to the high functionality of resins which have beneficial effects on adhesion. It is obvious from hardness results that, H1sample is the hardest polymer. This behavior is according to the high crosslinking density networks formation. The reasons for hard& dense network formed for H1 attributed to high contents of aromatic phthalic moiety.

Table 3 Coating tests of hyperbranched unsaturated polyester cured with styrene

Sample	Adhesion	Impact (5.5 or 7.5 J/mm)	T-bond	Hardness
HU1	+	+	+	H
HU2	+	+	+	HB
HU3	+	+	+	HB
HU4	+	+	+	HB

+ *pass*; - *fail*

### 3.6. Abrasion resistance test

This method test the resistance of organic coatings to abrasion produced by the Taber Abraser on coatings applied to a plane, rigid surface, such as a metal panel according to (ASTM D 4060 – 95) using abrasion test instrument. Abrasion resistance is calculated as loss in weight at identified number of abrasion cycles, as loss in weight per cycle, or as number of cycles required to remove a unit amount of coating thickness. A result in Table 4 represents mass loss of tested samples. It is clear from abrasion test that, the mass loss of the synthesized resins is slightly decrease in the order of H1>H2>H3>H4, as for example the final mass loss of H1 was 0.95 g<sub>m</sub> and H4 sample was 0.44g<sub>m</sub>. These results relate to the slightly decrease of particle size and the stability of high functional reactive groups coated samples which give high surface area to resist the conditions such as loads and scratching material. These results also indicates that, H4 is most efficient due its highest flexibility according to high contents of aliphatic moiety, functionality of the surface of coating and its small particle size with regular hyperbranched structure which gives height surface area for coating resistance conditions.

Table 4. Abrasion resistance of hyperbranched unsaturated polyester cured with styrene

	Wight of coated panel before the test (g <sub>m.</sub> )	Wight of coated panel after the test (g <sub>m</sub> )	Wight loss of coated panel after the test (g <sub>m</sub> )	Wight loss % of coated panel after the test
H1	80,23	79,29	0,95	1,20
H2	80,77	80,02	0,75	0,93
H3	81,79	81,12	0,66	0,81
H4	81,35	80,90	0,44	0,50

### 3.7 Mandrel bending test

Mandrel test performed according to ASTM D522 which contains two test methods used to determine the flexibility and resistance to cracking of organic coatings on substrates of sheet metal. Coatings attached to substrates are elongated when the substrates are bent during the manufacture of articles or when the articles are abused in service. These test methods used to examine the ability of coatings to attack cracking when stretched out. In this respect Figure 6 shows the four unsaturated nanoparticles coated panels when elongated with Mandrel bending tester. It is clear from this images that when aliphatic chains increase the panel become totally flexible and no cracks appear in order of H4>H3>H2>H1. This may be attributed to high contents of aliphatic moiety which decrease the hardness of coated samples.



Figure 6. Mandrel bend testing panel of HU1, HU2, HU3 and HU4 sample

## 4. Conclusions

Four samples of unsaturated hyperbranched polyester polyols resins are performed. The particle size of the synthesized resins decreases by increasing the molecular weights and by increasing maleic anhydride contents. The coated films showed excellent water, alkali, acid and acetone resistance. The prepared high functional reactive water based organic coatings have good adhesive and mechanical properties. H4 with high surface area and small particle size is the most stable sample with good chemical, mechanical, abrasion resistance. Moreover H4 is the best flexible sample and resistance to the cracking of organic coatings.

## References

- [1] Tomalia DA, Naylor AM, Goddard III WA. Starburst dendrimers: molecular-level control of size, shape, surface chemistry, topology, and flexibility from atoms to macroscopic matter. *Angew. Chem. Int. Ed.*, 1990; 29: 138–175.
- [2] Frechet JM. Functional polymers and dendrimers: reactivity, molecular architecture, and interfacial energy. *Science*, 1994; 263: 1710–1715.
- [3] Caminade AM, Maraval V, Laurent R, Majoral JP. Organometallic derivatives of phosphorus-containing dendrimers. Synthesis, properties and applications in catalysis. *Curr. Org. Chem.*, 2002; 6: 739–774.
- [4] Stiriba SE, Frey H, Haag R. Dendritic polymers in biomedical applications: from potential to clinical use in diagnostics and therapy, *Angew. Chem. Int.*, 2002; 41: 1329–1334.
- [5] Twyman LJ, King ASH, Martin IK. Catalysis inside dendrimers, *Chem. Soc. Rev.*, 2002; 31: 69–82.

- [6] Kabel KI, Abdelghaffar AM, Farag RK, Maysour NE, Zahran MAH. Synthesis and evaluation of PAMAM dendrimer and PDPF-b-POP block copolymer as asphaltene inhibitor/dispersant, Research on Chemical Intermediates, 2015; 41(1): 457-474.
- [7] Morikawa A. Comparison of properties among dendritic and hyperbranched poly(ether ether ketone)s and linear poly(ether ketone)s. Molecules, 2016; 21(2): 219-231.
- [8] Jagtap RN, and Chimankar YT. Synthesis of dumbbell shape hyperbranched polymer: Based on diethylene triamine and acryloyl chloride used as rheology modifier for water based paints. Advances in Applied Science Research, 2013; 4(2): 228-237.
- [9] Gao C, Yan D. Hyperbranched polymers: from synthesis to applications. Prog. Polym. Sci., 2004; 29: 183-275.
- [10] Romagnoli B, Hayes W. Chiral dendrimers—from architecturally interesting hyper-branched macromolecules to functional materials. J. Mater. Chem., 2002; 12: 767-799.
- [11] Chattopadhyay DK, Raju KVS. Structural engineering of polyurethane coatings for high performance applications, Prog. Polym. Sci., 2007; 32: 352-418.
- [12] Žagar E, Žigon M. Aliphatic hyperbranched polyesters based on 2,2-bis(methylol)propionic acid—Determination of structure, solution and bulk properties. Prog. Polym. Sci., 2011; 36: 53-88.
- [13] Zhang X. Modifications and applications of hyperbranched aliphatic polyesters based on dimethylolpropionic acid. Polym. Int., 2011; 60: 153-166
- [14] Kolhe P, Misra E, Kannan RM, Kannan S, Lieh-Lai M. Drug complexation, in vitro release and cellular entry of dendrimers and hyperbranched polymers. Int. J. Pharm., 2003; 259: 143-160.
- [15] Labena A, Kabel KI, Farag RK. One-pot synthesis of dendritic hyperbranched PA-MAM and assessment as a broad spectrum antimicrobial agent and anti-biofilm. Materials Science and Engineering: 2016; C 58: 1150-1159.
- [16] van Bentem RATM. (Rolf) Novel hyperbranched resins for coating applications. Progress in Organic Coatings, 2000; 40: 203-214.
- [17] Gurunathan T, Mohanty S, Nayak SK. Hyperbranched Polymers for Coating Applications: A Review. Polymer-Plastics Technology and Engineering, 2016; 55(1): 92-117.
- [18] Abdel-Azim AA, Milad R, El-Ghazawy R, Farag RK. Corrosion inhibition efficiency of water soluble ethoxylated trimethylol propane by gravimetric analysis. Egyptian Journal of Petroleum, 2014; 23(1): 15-20.
- [19] Atta AM, El-Saeed SM, Farag RK. New Vinyl Ester Resins Based on Rosin for Coating Applications. Reactive & Functional Polymers, 2006; 66: 1596-1608.
- [20] Atta AM, El-Saeed AM, Farag RK, El-Saeed SM. Synthesis of unsaturated polyester resins based on rosin acrylic acid adduct for coating applications. Reactive & Functional Polymers, 2007; 67: 549-563.
- [21] Sinha Ray S, Kundu AK, Ghosh M, Maiti S. A new route to synthesize polyamideimide from rosin. Eur. Polym. J., 1985; 21: 131-33.
- [22] Sinha Ray S, Kundu AK, Ghosh M, Maiti S. Polymers from renewable resources-13. Polymers from rosin acrylic acid adduct. Eur Polym J., 1990; 26: 471-74.
- [23] Hussein MA, Tay GS, Rozman HD. Real-Time Cure Monitoring of Unsaturated Polyester Resin from Ultra-Violet Curing. Journal of Research Updates in Polymer Science, 2012; 1: 32-42.
- [24] Paluvai NR, Mohanty S, Nayak SK. Synthesis and Modifications of Epoxy Resins and Their Composites: A Review. Polymer-Plastics Technology and Engineering, 2014; 53(16): 1723-1758.
- [25] Lin X, Zhang S, Qian J. Synthesis and properties of a novel UV-curable waterborne hyperbranched polyurethane. J. Coat. Technol. Res., 2014; 11(3): 319-328.
- [26] Du YY, Chen QL, Shen L, Xing YJ, Dai JJ. Synthesis and Application of Long-Chain Alkyl Quaternary Ammonium- Functionalized Hyperbranched Polyester. J. Appl. Polym. Sci., 2011; 121: 2927-2935.
- [27] Zhang XL. Synthesis and Characterization of Hyperbranched Polyesters Based on Isophthalic Acid and Trimethylolpropane. J. Macromol. Sci. A, 2011; 48: 128-134
- [28] Murillo EA, Cardona A, Lopez BL. Rheological Behavior in the Molten State and Solution of Hyperbranched Polyester of Fourth and Fifth Generation. J. Appl. Polym. Sci., 2011; 119: 929-935.
- [29] Noor El-Din MR, Farag RK, Elazbawy OE. Utilization of new anionic polymeric surfactants for corrosion inhibition enhancement in petroleum industries. Int. J. Electrochem. Sci., 2016; 11: 815 - 835
- [31] Hinder SJ, Lowe C, Maxted JT, Watts JF. The morphology and topography of polymer surfaces and interfaces exposed by ultra-low-angle microtomy. Journal of Materials Science, 2005; 40: 285-293.

- [31] Beck RCR, Lionzo MIZ, Costa TMH, Benvenuti EV, Ré MI, Gallas MR, Pohlmannand AR, Guterres SS. Surface morphology of spray-dried nanoparticle-coated microparticles designed as an oral drug delivery system , Brazilian Journal of Chemical Engineering, 2008; 25(2): 389–398.

---

*To whom correspondence should be addressed: Prof. Dr. Reem K. Farag, Egyptian Petroleum Research Institute, Application department, Nasr City, 11727 Cairo, Egypt*

## COMPOSITIONAL SIGNIFICANCE OF PHENANTHRENES FOR GEOCHEMICAL CORRELATION OF TWO COMMINGLED NIGER DELTA CRUDE OILS

Nwannedi C. Okoroh, Mark O. Onyema, and Leo C. Osuji

*Petroleum and Environmental Geochemistry Research Group, Department of Pure and Industrial Chemistry, University of Port Harcourt, P.M.B 5323 Choba, Port Harcourt, Rivers State, Nigeria*

Received August 21, 2018; Accepted November 19, 2018

### Abstract

This research focuses on the geochemical correlation of phenanthrenes peculiar to commingled crude oils for the purpose of deconvolution studies. Two crude oils collected from different parts of Nigeria's Niger Delta were mixed at different proportions of 4:1, 3:2, 2:3 and 1:4 respectively. All the samples were deasphalted, fractionated and the aromatic component analyzed by gas chromatography-mass spectrometry (GC-MS) for C<sub>0</sub>-C<sub>4</sub> phenanthrenes. Abundance values of 45 peaks selected for correlation of the samples did not show relationship indicating the abundance of the phenanthrenes did not mix linearly. The correlation coefficient of determination (R<sup>2</sup>) for plots of the abundance of some phenanthrenes; Ph, 2Ph, 3Ph, 6Ph<sub>2</sub>, 8Ph<sub>2</sub>, 20Ph<sub>3</sub>, 27Ph<sub>3</sub>, 31Ph<sub>4</sub> and 34Ph<sub>4</sub>, were low, from 0.022 to 0.285, and for composition were high, from 0.644 to 0.864. The results indicate negligible to weak correlation for the abundance of phenanthrenes and strong to very strong correlation for composition. Ratios of phenanthrene groups (P, P<sub>1</sub>, P<sub>2</sub>, P<sub>3</sub>, and P<sub>4</sub>) were plotted against all the samples. Plots of P/P<sub>3</sub>, P<sub>1</sub>/P<sub>3</sub> and P<sub>2</sub>/P<sub>3</sub> as well as double ratio plots of P/P<sub>2</sub> vs P<sub>2</sub>/P<sub>3</sub> and P/P<sub>2</sub> vs P<sub>1</sub>/P<sub>3</sub> had high R<sup>2</sup> values of 0.823 to 0.929 and 0.934 to 0.989 respectively indicating a very strong correlation between the oil samples which could account for 82 to 98% of the mixing pattern of the end member oils in their commingled oils. These results reveal that the composition of these phenanthrenes will better explain the pattern of mixing of the studied Niger Delta crude oils than their abundance.

**Keywords:** Phenanthrene; Commingling; Correlation; Crude Oil; Niger Delta; GC-MS.

## 1. Introduction

The compounds found in crude oils originate from the chemical and geological transformation of organic matter deposited during sedimentary processes [1]. Petroleum geochemistry utilizes geochemical compounds in crude oils for assessing oil type, depositional environment, maturation level, reservoir compartmentalization and continuity as well as a role in basin development [2-5]. Geochemical compounds typically reviewed in crude oils include polycyclic aromatic hydrocarbons (PAHs), light hydrocarbons (LHs), *n*-alkanes, isoprenoids, terpene, and sterane biomarkers [6-11].

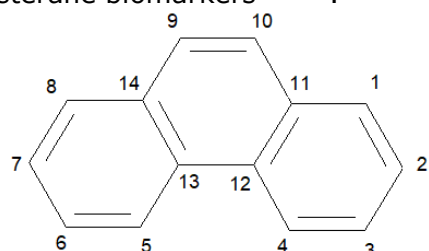


Figure 1. Structure of phenanthrene

Phenanthrene is a PAH composed of 3 benzene (C<sub>6</sub>H<sub>6</sub>) rings fused together (Fig. 1). Hydrocarbons based on the structure of phenanthrene occur in crude oil, and they include phenanthrene, methyl phenanthrenes, trimethyl phenanthrenes, and tetramethyl phenanthrenes, e.g. 9-methyl phenanthrene, 3-ethyl phenanthrene, and 2,6-dimethyl phenanthrene [12].

The phenanthrenes are relatively stable, highly degradation resistant and source-specific [13]. For light crude oils with similar compositions, characterization of phenanthrenes are essential for source identification, correlation and or differentiation [14].

Crude oil is the mainstay of the Nigerian economy. The operations of the oil industry in Nigeria are not isolated from global industrial practices, which include commingling of crude oils. Commingling is a terminology used in the oil and gas sector to refer to the mixing of two or more crude oils from different producing zones, wells or fields [15-16]. The commingling of crude oils is a common practice for sharing facilities and equipment to reduce cost. Adequate assessment of individual field contribution is essential for establishing sales value or tax liability and in effectively managing reservoirs and production operations [17]. According to the 2014 audit report of the Nigerian Extractive Industry Transparency Initiative (NEITI), \$4.1bn was lost because of non-existent and inadequate metering systems in the crude oil-producing Niger Delta region [18].

In a bid to restore accuracy, equity, fairness and conformity with international best practices, this research focuses on the development of a flexible, tiered geochemical analytical approach to facilitate the detailed compositional analysis of the phenanthrenes by gas chromatography-mass spectrometry (GC-MS). The distribution of the phenanthrenes would be correlated to identify those peculiar to the mixing of crude oils from the Niger Delta region for the purpose of deconvolution.

## **2. Materials and method**

### **2.1. Samples**

Crude oil samples used for this study were collected from Rivers State (Sample A) and Delta State (Sample F) both in the Niger Delta region of southern Nigeria. The samples were collected from producing oil wells by field technicians with the permission of the department of petroleum resources (DPR). The two crude oil samples (A and F) were mixed at different proportions of 4:1, 3:2, 2:3 and 1:4 to give samples B, C, D, and E respectively.

### **2.2. Crude oil fractionation**

50 mg of each crude oil sample was weighed into labeled centrifuge tubes and excess pentane added to precipitate the asphaltenes. The samples were allowed to stand for four hours and transferred into a fisher centrifuge set at 1,500 rpm for thirty minutes. The pentane soluble fraction was decanted, concentrated and introduced into a glass chromatographic column (30 cm x 1 cm) stuffed with glass wool at the bottom and packed with activated silica gel. Different compound classes were eluted with different solvents. Saturates were eluted with *n*-hexane, aromatics eluted with dichloromethane and resins eluted with dichloromethane/methanol (1:1) mixture. All solvents were evaporated in a water bath and then to dryness with nitrogen.

### **2.3. Gas chromatography-mass spectrometry (GC-MS) analysis**

Detailed analysis of the phenanthrenes was facilitated by Agilent 7820A gas chromatography (GC) system fitted to a fused silica capillary column (30m x 0.25µm) and equipped with an Agilent 5975 series mass selective detector (MSD). One microlitre (1µL) of the aromatic component of each fractionated oil sample was injected into the capillary column of the GC-MS system with the aid of automatic liquid sampler (ALS) using a split ratio mode of 100:1. The GC-MS fragmentation ion was set for phenanthrene (C<sub>0</sub>) at m/z 178, methyl phenanthrenes (C<sub>1</sub>) at m/z 192, ethyl-/dimethylphenanthrenes (C<sub>2</sub>) at m/z 206, trimethyl phenanthrenes (C<sub>3</sub>) at m/z 220 and tetramethyl phenanthrenes (C<sub>4</sub>) at m/z 234. Peak identification was by comparison with related literature. Quantification was acquired by area integration of each peak which was processed by Chemstation OPEN LAB CDS software.

### 3. Results and discussions

#### 3.1. Distribution of phenanthrenes

GC-MS analysis of the aromatic component of the studied oil samples identified phenanthrenes at ions ( $m/z$ ) 178, 192, 206, 220 and 234, which were well resolved (Fig. 2). A total of 45 phenanthrene peaks were selected for geochemical correlation of the two end-member crude oils, from Niger Delta (samples A and F) and their commingled oils (samples B, C, D, and E). One peak was selected for parent phenanthrene ( $C_0$ ) at  $m/z$  178, 4 peaks for methyl phenanthrenes ( $C_1$ ) at  $m/z$  192, 11 peaks for ethyl- and dimethyl phenanthrenes ( $C_2$ ) at  $m/z$  206, 12 peaks for trimethyl phenanthrenes ( $C_3$ ) at  $m/z$  220 and 17 peaks for tetramethyl phenanthrenes ( $C_4$ ) at  $m/z$  234.

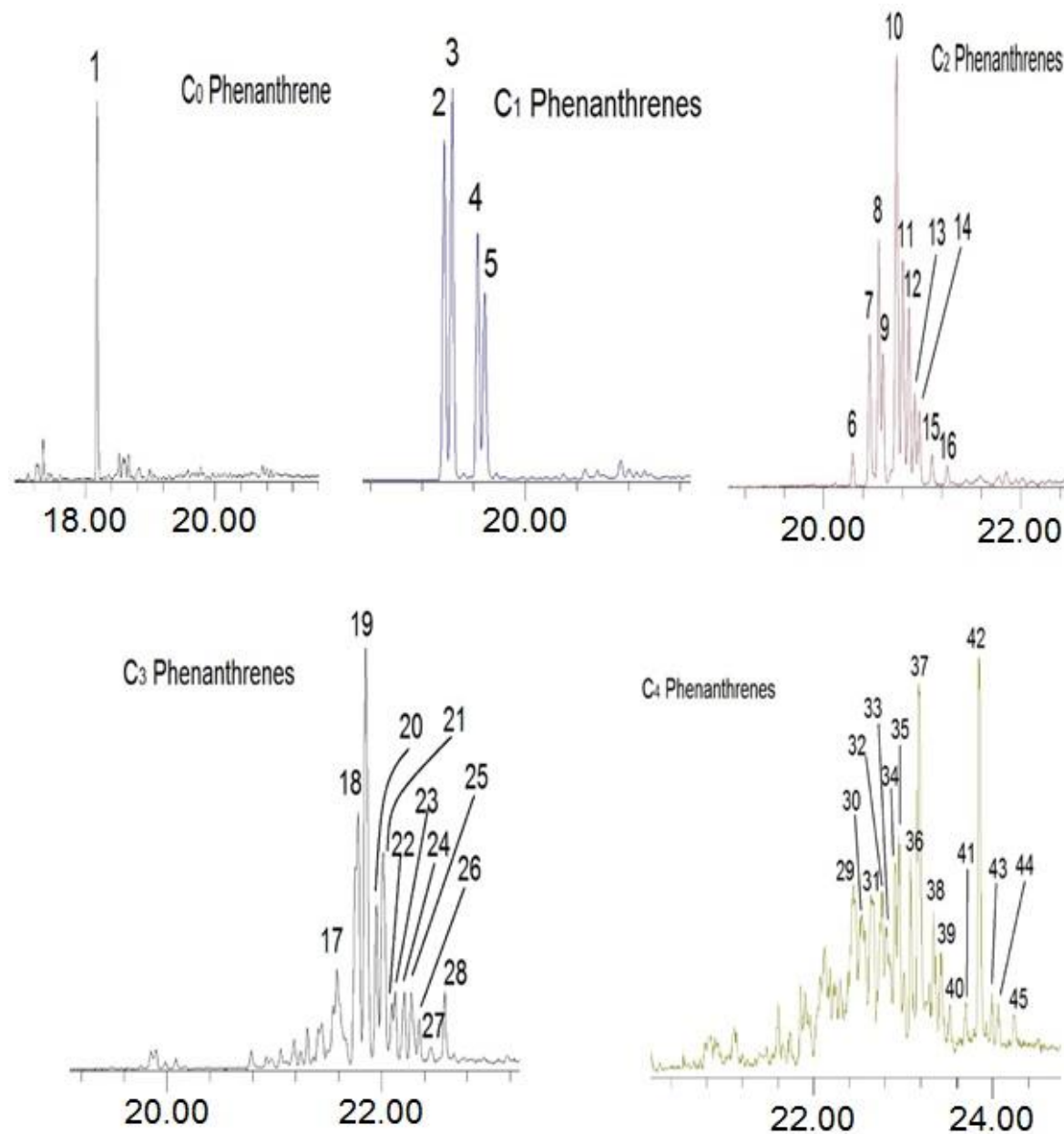


Figure 2. Representative GC-MS fragmentogram of  $C_0$ - $C_4$  phenanthrenes at ions ( $m/z$ ) 178, 192, 206, 220 and 234 showing the selected peak distributions in crude oil (sample B)

Area integration of each selected peak calculated by the GC-MS system gives the abundance of that peak. The abundances of the 45 selected phenanthrene peaks (C<sub>0</sub>-C<sub>4</sub>) for the end-member and commingled crude oils used for the study are presented in table 1.

Geochemical correlation of crude oils is based on similarities and/or dissimilarities of features which are usually established on the relative distribution patterns of certain compounds [16]. From Table 1, the abundance values of the phenanthrenes in the end-member oils (samples A and F) and their commingled oils (samples B, C, D, and E) did not show the relationship. This indicates that the abundance of the phenanthrenes did not mix linearly.

### 3.2. Correlation of phenanthrenes

In a bid to identify particular phenanthrenes which will attempt to explain the pattern of mixing and give the highest chance of allocation, the abundance, and composition of the forty-five selected peaks were plotted against all the studied oil samples. A relationship was observed between the two end-member and their commingled crude oils for some C<sub>0</sub>-C<sub>2</sub> phenanthrenes (Fig. 3) and C<sub>3</sub>-C<sub>4</sub> phenanthrenes (Fig. 4).

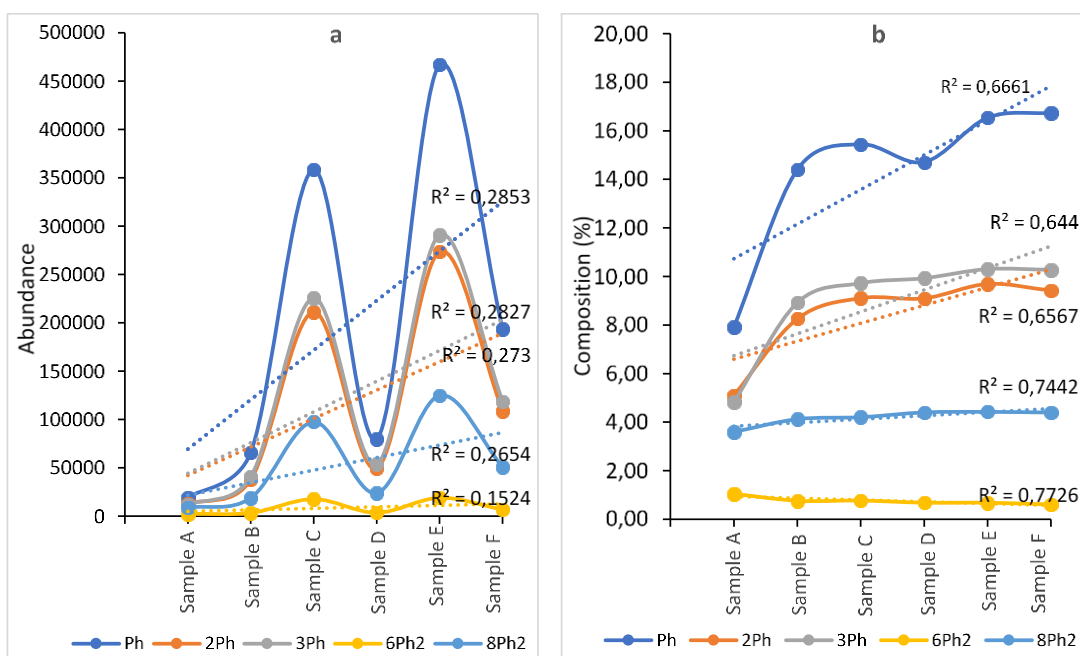


Figure 3. Plot of some C<sub>0</sub>-C<sub>2</sub> phenanthrenes (Ph, 2Ph, 3Ph, 6Ph2 and 8Ph2) against all the studied oil samples showing the level of correlation a. abundance b. composition

From Fig 3, the correlation coefficient ( $R^2$ ) of Ph, 2Ph, 3Ph, 6Ph2 and 8Ph2 (C<sub>0</sub>-C<sub>2</sub> phenanthrenes) for abundance range from 0.152 to 0.285 and for composition from 0.644 to 0.773. The  $R^2$  values of 20Ph3, 27Ph3, 31Ph4 and 34Ph4 (C<sub>3</sub>-C<sub>4</sub> phenanthrenes) for abundance range from 0.022 to 0.168 and for composition from 0.760 to 0.864. The correlation coefficient ( $R^2$ ) is a statistical tool used to indicate the strength of a linear relationship between variables. The closer the  $R^2$  value is to one (1) the closer the relationship between the variable and consequently deducing the trend.  $R^2$  values for abundance were low indicating the poor linear relationship of the variable (phenanthrenes) between the end-member and commingled oils (samples A to F). For composition, the  $R^2$  values were higher than that of abundance and indicated considerably linearity of the variable between the end-member oils and commingled oils. The  $R^2$  values from Figs. 3 and 4 reveal that the composition of some phenanthrenes will better explain the pattern of mixing of the studied Niger Delta crude oils than their abundance. Furthermore, from the forty-five phenanthrene peaks selected, peaks Ph, 2Ph, 3Ph, 6Ph2, 8Ph2, 20Ph3, 27Ph3, 31Ph4 and 34Ph4 showed better correlation and a good chance of being used

to evaluate contributions from the respective end-member oils to their commingled oil because their  $R^2$  values were high ( $> 0.6$ )

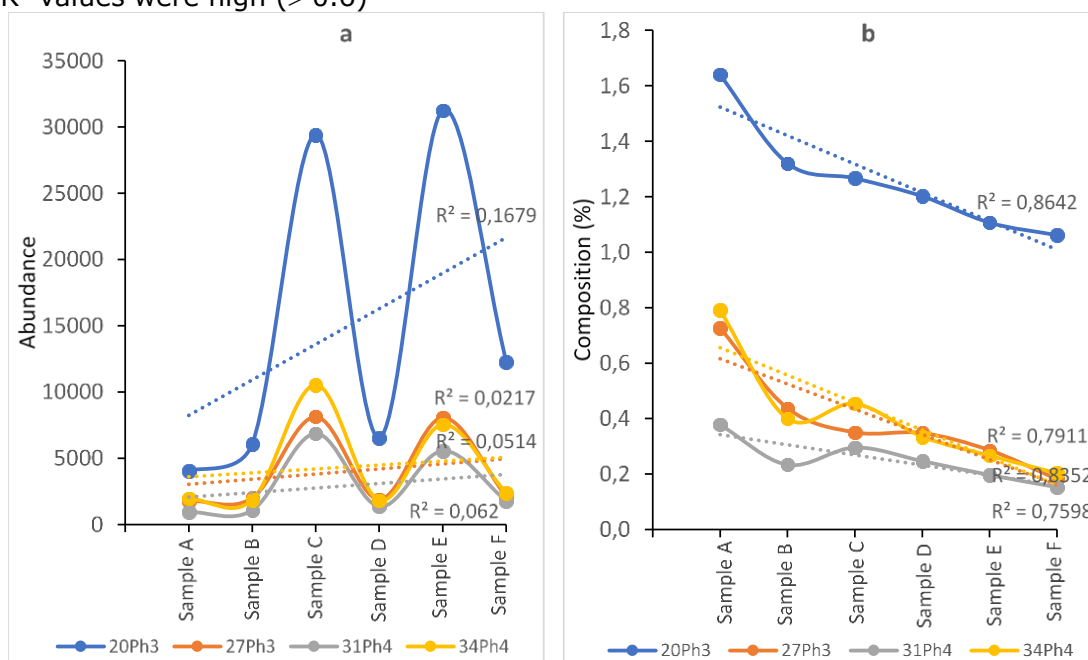


Figure 4. Plot of some C<sub>3</sub>-C<sub>4</sub> Phenanthrenes (20Ph3, 27Ph3, 31Ph4, and 34Ph4) against all the studied oil samples showing the level of correlation a. abundance b. composition

### 3.3. Ratios of the phenanthrenes

The abundance of individual phenanthrenes showed poor correlation and did not mix linearly (Table 1, Figs. 3 and 4). The relative composition of the phenanthrene types in the studied oil samples was used to evaluate the end-member and commingled crude oil samples. The abundance of phenanthrene types ( $\Sigma C_0 = P$ ,  $\Sigma C_1 = P_1$ ,  $\Sigma C_2 = P_2$ ,  $\Sigma C_3 = P_3$  and  $\Sigma C_4 = P_4$ ) are shown in table 1 and ratios calculated from it are presented in Table 2.

Table 2. Calculated ratios of phenanthrene types all the studied crude oil samples

	P/P1	P/P2	P/P3	P/P4	P1/P2	P1/P3	P1/P4	P2/P3	P2/P4	P3/P4
Sample A	0.42	0.21	0.31	0.84	0.50	0.74	2.03	1.49	4.06	2.73
Sample B	0.50	0.43	0.81	2.52	0.87	1.63	5.07	1.88	5.84	3.10
Sample C	0.50	0.50	0.94	2.59	1.00	1.89	5.20	1.89	5.21	2.75
Sample D	0.47	0.44	0.91	3.15	0.95	1.95	6.73	2.06	7.11	3.45
Sample E	0.51	0.51	1.13	4.30	1.00	2.23	8.43	2.24	8.47	3.79
Sample F	0.52	0.52	1.21	3.18	0.99	2.30	6.07	2.32	6.13	2.64

Ten ratios were calculated and plotted against the end-member and commingled oil samples. The plots of P/P<sub>3</sub>, P<sub>1</sub>/P<sub>3</sub>, and P<sub>2</sub>/P<sub>3</sub> ratios had the highest  $R^2$  values of 0.830, 0.823 and 0.929 respectively (figs. V, VI and VII).

$R^2$  value shows the relationship between variables and explains the percentage variation (y-axis) of the independent variables (x-axis). Values of  $R^2$  range from 0 to 1. A value of 1 indicates a perfect relationship which explains all the variability of the data, while a value of 0 indicates no relationship and explains no variation. The  $R^2$  values from the plots indicate a very strong relationship of P/P<sub>3</sub>, P<sub>1</sub>/P<sub>3</sub>, and P<sub>2</sub>/P<sub>3</sub> ratios within the end member and commingled oil samples and that these ratios can account for 83%, 82% and 93% of the mixing pattern

of the end member oils in their commingled oils respectively. This reveals a high significance of  $P/P_3$ ,  $P_1/P_3$ , and  $P_2/P_3$  ratios as correlational tools for allocation of commingled crude oils.

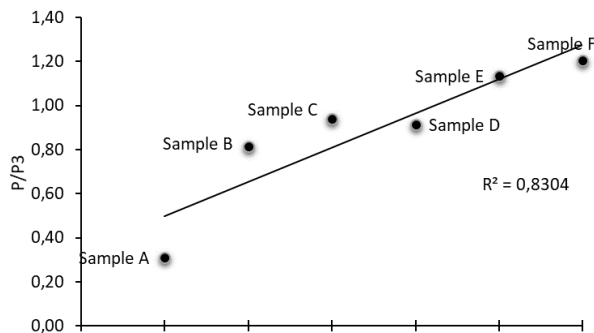


Figure 5. Plot of  $P/P_3$  phenanthrenes for the two end-member Niger Delta crude oils (samples A and F) and their commingled oils (B, C, D, and E)

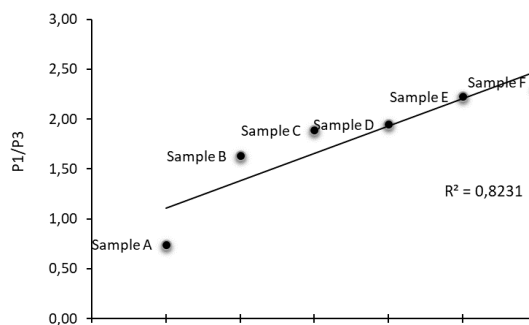


Figure 6. Plot of  $P_1/P_3$  phenanthrenes for the two end-member Niger Delta crude oils (samples A and F) and their commingled oils (B, C, D, and E)

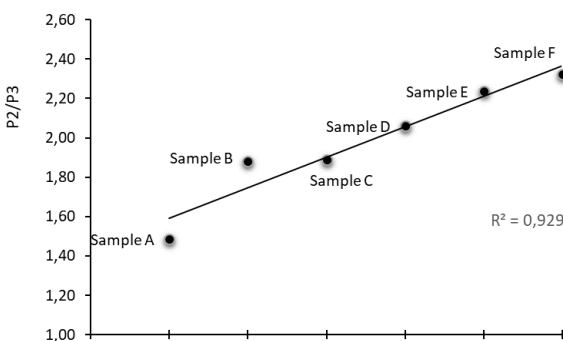


Figure 7. Plot of  $P_2/P_3$  phenanthrenes for the two end-member Niger Delta crude oils (samples A and F) and their commingled oils (B, C, D and E)

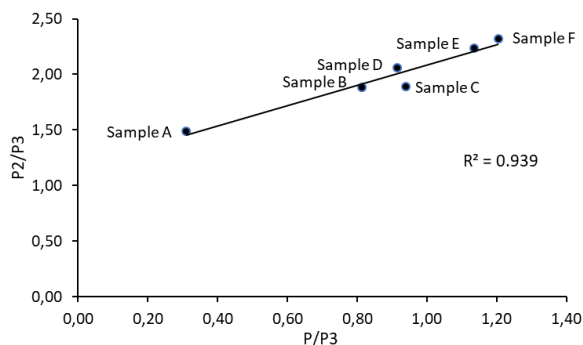


Figure 8. Plot of  $P/P_3$  vs.  $P_2/P_3$  phenanthrenes for the two end-member Niger Delta crude oils (samples A and F) and their commingled oils (B, C, D, and E)

Double ratio plots of  $P/P_2$  vs.  $P_2/P_3$  and  $P/P_2$  vs.  $P_1/P_3$  are shown in Figs. 8 and 9. The  $R^2$  values of these double ratio plots are 0.934 and 0.989 respectively. This  $R^2$  values indicate a very strong relationship of the double ratios with the oil samples and can account for 93% and 98% of the mixing pattern of the end member oils in their commingled oils respectively.

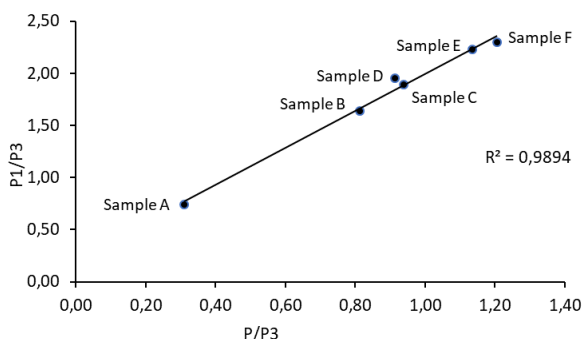


Figure 9. Plot of  $P/P_3$  vs.  $P_1/P_3$  phenanthrenes for the two end-member Niger Delta crude oils (samples A and F) and their commingled oils (B, C, D, and E)

From the  $R^2$  values of Figs. 8 and 9, the double ratio plots of  $P/P_2$  vs.  $P_2/P_3$  and  $P/P_2$  vs.  $P_1/P_3$  exhibited a high significance in the correlation of the phenanthrenes for allocation of the composition of the end member Niger Delta crude oils in their commingled oils. The extrapolation of these ratio values for a hypothetical mixture of two end member Niger Delta crude oils from the y-axis and down to the x-axis can estimate (93 to 98%) the contributions of the different end member oils to their commingled stream.

#### 4. Conclusion

GC-MS was used to analyze for C<sub>0</sub>-C<sub>4</sub> phenanthrenes in two Niger Delta crude oils (samples A and F) and their commingled oils (samples B, C, D, and E). Forty-five (45) phenanthrene peaks were selected for geochemical correlation of the oil samples. Abundance plots of some C<sub>0</sub>-C<sub>4</sub> phenanthrenes; Ph, 2Ph, 3Ph, 6Ph<sub>2</sub>, 8Ph<sub>2</sub>, 20Ph<sub>3</sub>, 27Ph<sub>3</sub>, 31Ph<sub>4</sub> and 34Ph<sub>4</sub>, gave low R<sup>2</sup> values which indicate negligible to the weak correlation of these phenanthrenes with the oil samples, while composition plots gave high R<sup>2</sup> values which indicate strong to a very strong correlation. R<sup>2</sup> values from plots of P/P<sub>3</sub>, P<sub>1</sub>/P<sub>3</sub> and P<sub>2</sub>/P<sub>3</sub> ratios, as well as double ratio plots of P/P<sub>2</sub> vs P<sub>2</sub>/P<sub>3</sub> and P/P<sub>2</sub> vs P<sub>1</sub>/P<sub>3</sub>, indicate a very strong correlation between the end member and commingled oils which could account for 82 to 98% of the mixing pattern. The results show the significance of phenanthrenes in Niger Delta crude oils for geochemical correlation and allocation of the composition of end member crude oils in their commingled oils. This method will be of advantage over the metering system as it measures the relative contributions of the end member crude oils production stream (instead of water + oil) and effective reservoir management in the Nigerian oil industry which has suffered from absence/inaccurate metering systems.

#### References

- [1] Tissot BP and Welte DH Petroleum Formation and Occurrence. Springer-Verlag Berlin Heidelberg New York, 1984.
- [2] Hunt JM. Petroleum Geochemistry and Geology, 2nd Ed.; W. H. Freeman and Company, U.S.A, 1996.
- [3] Peters KE, Fraser TH, Amris W, Rustanto B, Hermanto E. Geochemistry of Crude Oils from Eastern Indonesia. American Association of Petroleum Geologists Bulletin. 1999; 83: 1927-1942.
- [4] Hwang RJ, Baskin DK, Teerman SC. Allocation of Commingled Pipeline Oils to Field Production. Organic Geochemistry, 2000; 31: 1463-1474.
- [5] Ekweozor CM. Source Rocks of Giant Hydrocarbon Deposits in Deep Offshore, Niger delta. Abstract of Paper; Nigerian Association of Petroleum Explorationists and American Association of Petroleum Geologists Regional West Africa Deepwater Conference, Abuja, Nigeria; 2004.
- [6] Eneogwe CI, Ekundayo O, Patterson BA. Source-Derived Oleanenes Identified in Niger Delta Oils. Journal of Petroleum Geology, 2002; 25: 83-95.
- [7] Eneogwe CI. The Distribution of Light Hydrocarbons in Western Niger Delta Oils. Journal of Petroleum Geology, 2003; 26: 479-488.
- [8] De Luca G, Furesi A, Leardi R, Micera G, Panzanelli A, Piu PC, Sanna G. Polycyclic Aromatic Hydrocarbons Assessment in the Sediments of the Porto Torres Harbor (Northern Sardinia, Italy). Marine Chemistry, 2004; 86: 15-32.
- [9] Osuji LC and Antia BS. Geochemical Implications of Some Chemical Fossils as Indicators of Petroleum Source Rocks. J. Appl. Sci. Environ. Mgt., 2005; 9(1): 45-49.
- [10] Onyema MO and Manilla PN Light Hydrocarbon Correlation of Niger Delta Crude Oils. Journal of American Science, 2010; 6(6): 82-88.
- [11] Sosrowidjojo IB. Organic Geochemistry: Geographic Location of Crude Oil Based on Biomarker Composition of the Sundr-Asri Basins, Indonesia. Int. J. Phys. Sci., 2011; 6(31): 7291-7301.
- [12] Volk H, George SC, Middleton H, Schofield S. Geochemical Comparison of Fluid Inclusion and Present-day Oil Accumulations in the Papuan Forland – Evidence for Previously Unrecognised Petroleum Source Rocks. Organic Geochemistry, 2004; 36: 29-51.
- [13] Antle PM, Ziegler CD, Wilton NM, Robbat A. A More Accurate Analysis of Alkylated PAH and PASH and its Implications in Environmental Forensics. Intern. J. Environ. Anal. Chem., 2014; 94(4): 332-347.
- [14] Ali FM, Al-Khadrawi RM, Perzanowski H, Halpern HJ. Central Saudi Arabia crude oil: A Geochemical Investigation. J. Petrol. Sci. and Tech., 2002; 20: 633-654.
- [15] Hwang RJ, Ahmed AS, and Moldowan JM. Oil Composition Variation and Reservoir Continuity: Unity Field, Sudan. Organic Geochemistry, 1994; 21(2): 171-188.
- [16] Kaufman RL, Ahmed AS, and Hemphkins WB. A New Technique for the Analysis of Commingled Oils and its Application to Production Allocation Calculations. Presented at IPA 16th Annual Indonesian Petro. Assoc. Indonesia, 1987; 247-268.

- [17] Abivin P, Toribio MM, and Indo K. Methods for Allocating Commingled Oil Production. US Patent US2010/0307740 AI, 2010.
- [18] Nigeria Extractive Industries Transparency Initiative. Oil and Gas Industry Audit Report. Abuja, Nigeria, 2014.

---

*To whom correspondence should be addressed: Dr. Nwannedi C. Okoroh, Petroleum and Environmental Geochemistry Research Group, Department of Pure and Industrial Chemistry, University of Port Harcourt, P.M.B 5323 Choba, Port Harcourt, Rivers State, Nigeria*

## ESTIMATION OF HEAT FLOW FROM SPECTRAL ANALYSIS OF HIGH RESOLUTION AIRBORNE MAGNETIC DATA IN ILESHA AND ITS ENVIRONS, SOUTHWEST NIGERIA

O. T. Olurin<sup>1\*</sup>, S. A. Ganiyu<sup>1</sup>, O. S.Hammed<sup>2</sup>, A. A. Alabi<sup>1</sup>, M. O.Awoyemi<sup>3</sup>, and J. O. Coker<sup>4</sup>

<sup>1</sup> Department of Physics, Federal University of Agriculture Abeokuta, Ogun State, Nigeria

<sup>2</sup> Department of Physics, Federal University Oye – Ekiti, Nigeria

<sup>3</sup> Department of Physics, Obafemi Awolowo University Ile-Ife, Nigeria

<sup>4</sup> Department of Physics, Olabisi Onabanjo University, Ago Iwoye, Ogun State, Nigeria

Received August 21, 2018; Accepted November 19, 2018

---

### Abstract

This study presents an analysis of High-Resolution Airborne Magnetic Data (HRAMD) over Ilesha and its environs situated on geographic latitude 7°30'N to 8°00'N and geographic longitude 4°30'E to 5°00'E. The work presents the structural and quantitative interpretation of airborne magnetic data (Sheet No.243), which was acquired from the archive of Nigerian Geological Survey Agency (NGSA). The study is aimed at determination of Curie Isotherm region in Ilesha south-west Nigeria using filtering of source spreading of magnetic sources and spectral analysis (matched filtering) of aeromagnetic data. The magnetic data were subjected to Fast Fourier Transform which transforms HRAMD from its space domain to wave number domain. The HRAMD were divided into 25 equal overlap blocks. The finding outcome reveals that the depth to the bottom of magnetic anomaly sources (DBMS) varies between 16.48 km and 41.47 km. Subsequently, the variation of geothermal gradient ranged between 13.98°C/km and 35.20°C/km, while estimated values of the resulting heat flow in the study area vary between 34.96 W/m and 87.99 W/m. However, this study is crucial for structural thoughtful of the geo-processes and rheological parameters in delineating geothermal regime within the under study because the thermal structure of the earth's crust is one of the leading parameters scheming geodynamic methods.

**Keywords:** Aeromagnetic; Airborne, Geothermal; Magnetics; Regional and Spectral.

---

## 1. Introduction

High-Resolution Airborne Magnetic (HRAM) survey is the collection of magnetic data over a large expanse of the area by small aircraft and interpreting the data using several interpretational techniques [1]. HRAM surveys have a resolution in the nanotesla scale such that in addition to adequately mapping magnetic rocks which can be adopted to map intra-sedimentary faults segment with elevated magnetic minerals deposit concentration that generates small variation in the anomalies [2-3]. The magnetometer measured logged tiny variations in the intensity of the ambient magnetic field due to the effect of temporal constantly varying solar and spatial variations in the earth's magnetic field as the aircraft flies. This is due to both the regional magnetic field, and the local effect of magnetic minerals in the earth crust. The correction done by subtracting the solar and regional effects, the resulting airborne magnetic map shows the spatial circulation and comparative great quantity of magnetic minerals in the upper levels of the crust. Airborne magnetic surveys offer a nippy means of geological mapping. The magnetic data give information about geological patterns at depth about the metamorphic basement on which younger sedimentary rock lies, and channel light on the presence of major structures which could have influenced its development. Surveys of the spatial changes in the strength of the magnetic field over the surface of the earth have been used as a method for geophysical exploration for many decades [4]. The magnetic method has come into

use for identifying and locating masses of igneous rocks that have a relatively high concentration of magnetic minerals (magnetite). Magnetite is the most common ferromagnetic mineral, and in most cases, the magnetic permeability is determined by the amounts of magnetite and related minerals available in the rock.

Subsequently, adequate information of the earth's interior thermal configuration is significant in geodynamic and geothermal inquiries [5-6]. Direct crustal temperature measurements are not substantial for regional studies; hence the depth to Curie-temperature avails for estimating the temperature at depth [6-8] which match up to the temperature at which magnetic minerals lose their ferromagnetic properties, and for regional-scale studies which it occurs can be inferred as the Curie Isotherm depth. Several researchers [6, 9-27] have presented the Depth to the Bottom of Magnetic Sources (DBMS), which could also be considered as the Curie-point depth (CPD) and can be probably estimated from the analysis of regional magnetic data where various rocks lose their ferromagnetic natures (properties) due to an increase in temperature variation in the crust which will aid the heat flow [8,19].

The DBMS is an imperative factor in understanding the temperature distribution in the crust and the rheology of the Earth's lithosphere [25]. The main objective of heat flow measurements is to estimate the amount of heat energy being lost by natural process. The loss of high heat anomalies usually coincides with the trend of the structural geological features or extents with high thermal manifestations regime [3].

An assessment of DBMS in gridded blocks in the area would meaningfully compliment the available geophysical information and also add value to the thoughtful of the geothermal regime, crustal depiction, and geodynamic evaluation processes in Ilesha and its environs. The main objective of heat flow measurements is to estimate the amount of heat energy being lost by natural process. High heat loss anomalies usually coincide with the geological structural trend or areas with high thermal manifestations [3].

The present study is an attempt towards analyzing High-Resolution Airborne of Ilesha to estimate Depths to the Bottom of Magnetic Sources (DBMS) and ensuing geothermal parameters in order to infer geothermal regime within different blocks.

## **2. Description and geology of the study area**

Ilesha and its environ is situated in Osun State, Southwestern Nigeria. Ilesha is bounded in North by Kwara, in the south by Ondo, in the east by Ekiti and west by partly Oyo state. The area is located within geographic latitude 7°30'N to 8°00'N and geographic longitude 4°30'E to 5°00'E covering an area of about 3025 km<sup>2</sup>. Ilesha lies within the tropical climate marked by wet and dry seasons with an average elevation of 391m above sea level. The average daily temperature varies between about 20°C for a very cold day to about 35°C for a very hot day [28].

Ilesha is situated within the Nigeria Basement Complex of south-western Nigeria. The Ilesha and its surroundings lie in the Basement Complex of the Southwest Nigerian [29]. The formation is a pre-drift sequence of continental sands, grits, and silts (Figure 1). In 1953 and 1957, [30-31] proposed that the Nigerian Basement Complex rock is Polycyclic. In 1970 Hurley confirmed the rock ages using radiometric approach. The main rock associate Ilesha and its environ made up of a fragment of the Proterozoic schist straps in Nigeria. The geological formation of Ilesha and its environs comprise of Precambrian rocks that are typical for the basement complex of Nigeria [32]. Regarding the structural geological features, lithology, and mineralization, the schist belts of Nigeria display considerable resemblances to the Achaean Green Stone Belts [32-33].

## **3. Methodology**

### **3.1. Data acquisition**

In August 2009, a nationwide regional High-Resolution Airborne Magnetic (HRAM) data were acquired in Nigeria by Fugro Airborne Survey Limited United State of America for the Geological Survey Agency of Nigeria. This acquisition, processing, and compilation of the new data sets were jointly sponsored by the Federal Government of Nigeria and the World Bank as part of the Sustainable Management for Mineral Resources Project (SMMRP). The airborne

magnetic surveys, using 3x Scintrex CS3 cesium vapour magnetometers (resolution of 0.1 nT) with a data recording interval of 0.1 seconds, were done by means of Fixed-wing aircrafts flown at mean terrain clearance of 80m with 500 m line spacing and nominal tie-line spacing of 5000 m along series of NE-SW. The flight line and tie-line trends were 135 and 45 degrees respectively.

The average magnetic inclination, magnetic declination, and magnetic field strength across the survey were  $14.02^{\circ}$ ,  $3.83^{\circ}$  and  $32,446.006$  nT respectively. Map of the study area under consideration is published on a scale of 1:10000 (that is 1 cm = 1 km on the ground). The topographical detail of the map was based on 1: 100000 topographical series of Federal Surveys of Nigeria.

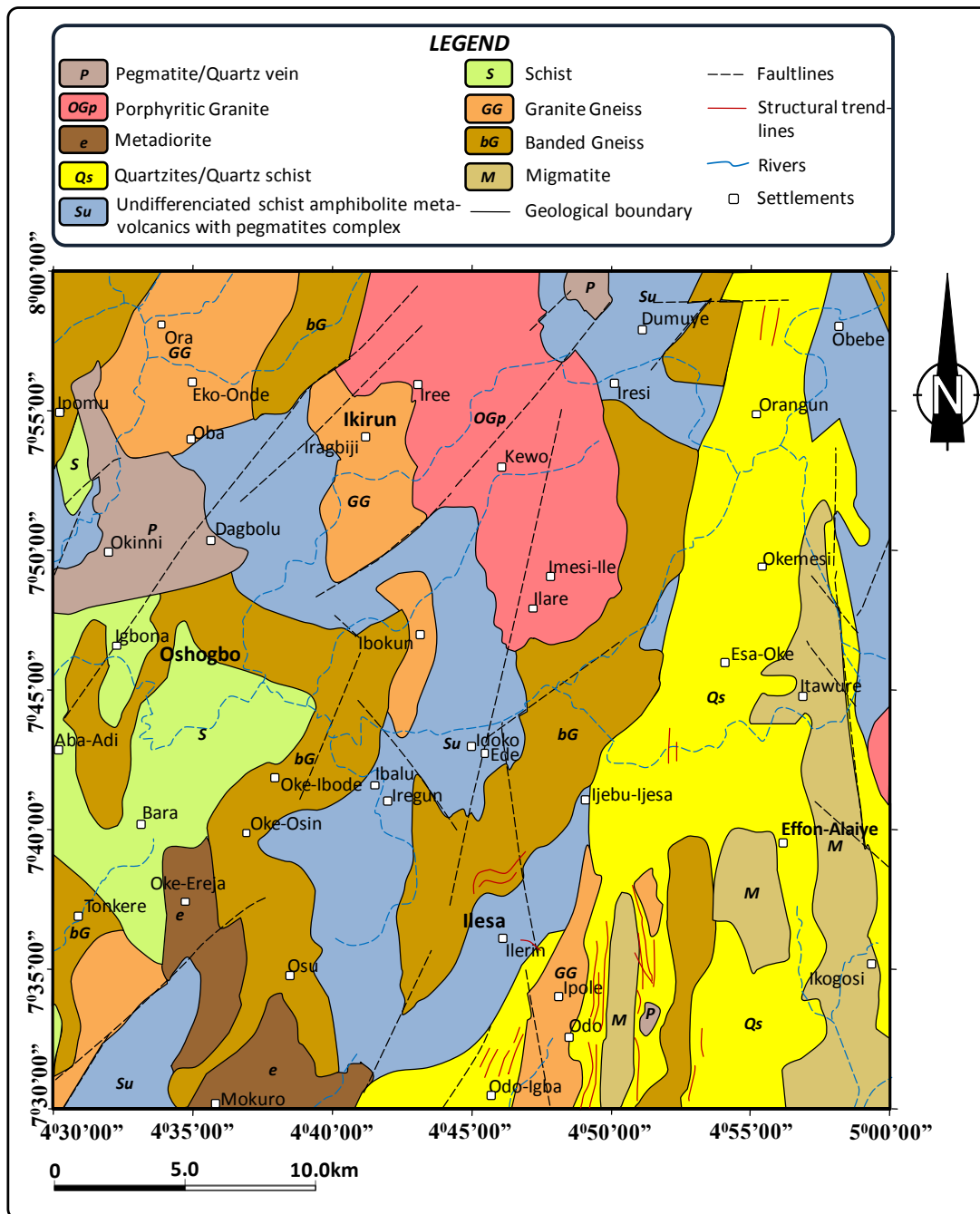


Figure 1. Geological Map of Ilesha and its Environs (Adapted from NGSA 2009)

### 3.2. Estimation of depth to the bottom of magnetic sources (DBMS)

Power Spectrum analysis of potential field data has been in used over the years to estimate the depth of definite geological features, such as magnetic basement [9,15,34-37]. Two-dimensional (2-D) spectral analyses of the potential field data have been used extremely over the past Four (4) decades to estimate the depth of target sources of anomaly [9,33]. Spectral depth analysis is based on the principle that a magnetic field measured at the surface can be considered as the integral of magnetic signatures from all depths [38]. The power spectrum of the apparent field can also be used to evaluate the average depth of anomalies source ensembles.

Several robust approaches have been employed in the estimation of DBMS [8-9,11,16,18,21,25]. The modified centroid method recently developed by [8] was adopted in this presented study. The adoption of conservative centroid method to evaluate DBMS is built on the spectral analysis of the target anomalies of the magnetic field [14,19]. Application of spectral analysis technique to infer magnetic anomalies have been expansively described by [9-11,37]. They validated that contributions from the source parameters; depth, width and thickness of a magnetic source ensemble could disturb the shape of the power spectrum. The principal term, which pedals the spectral shape, is known as the depth factor. The power spectral density (P(k)) and DTMS (Zt) are related by the expression proposed by [9,19].

The Discrete Fourier Transform is the mathematical tool for spectral analysis and applied to regularly spaced data such as the aeromagnetic data is given by Equation 1.

$$g(x) = h_0 + \sum_{n=1}^{\infty} \left( h_n \cos \frac{n\pi x}{J} + i_n \sin \frac{n\pi x}{J} \right) \quad (1)$$

In 1995, Blakely [16] introduced the power density spectra of the total field anomaly  $\Phi_{\Delta T}$ .

$$\Phi_{\Delta T}(K_x, K_y) = \Phi_M(K_x, K_y)F(K_x, K_y) \quad (2)$$

$$F(K_x, K_y) = 4\pi^2 C_m^2 |\theta_T|^2 |\theta_G|^2 e^{-2|k|Z_t} (1 - e^{-|k|(Z_b - Z_t)})^2 \quad (3)$$

where  $\Phi_M$  is the spectra power density of the magnetization,  $C_m$  is a proportionality constant, and  $\theta_T$  and  $\theta_G$  are factors of the direction of the magnetization and geomagnetic field direction, respectively.

Equation 3 can be simplified noting all terms, except  $|\theta_T|^2$  and  $|\theta_G|^2$ , which are radially symmetric. Moreover, the radial averages  $\theta_T$  and  $\theta_G$  are constant. If  $M(x, y)$  is downright random and uncorrelated,  $\Phi_M(K_x, K_y)$  is a fixed constant. Hence, the radial average of  $\Phi_{\Delta T}$  is given by equation 4,

$$\Phi_{\Delta T}(|k|) = Ae^{-2|k|Z_t} (1 - e^{-|k|(Z_b - Z_t)})^2 \quad (4)$$

where  $A$  is constant.

In the case where wavelength less than about twice the thickness of the layer, Eq. (4) becomes:

$$\ln \left[ \Phi_{\Delta T}(|k|)^{\frac{1}{2}} \right] = \ln B - |k|Z_t \quad (5)$$

where  $B$  is a constant.

The top bound of a target magnetic source could be evaluated from the slope of the power spectrum of the total field anomaly graph plotted against the wavenumber. Thus, Equation 5 can be written as:

$$\Phi_{\Delta T}(|k|)^{1/2} = Ce^{-|k|Z_0} (e^{-|k|(Z_t - Z_0)} - e^{-|k|(Z_b - Z_0)}) \quad (6)$$

where  $C$  is a constant. At long wavelengths, Eq. (6) is:

$$\begin{aligned} \Phi_{\Delta T}(|k|)^{1/2} &= Ce^{-|k|Z_0} (e^{-|k|(-d)} - e^{-|k|(d)}) \\ &\approx Ce^{-|k|Z_0} 2|k|d, \end{aligned} \quad (7)$$

where  $2d$  is the wideness of the magnetic anomaly source. From Eq. (7)

$$\ln \left\{ \left[ \Phi_{\Delta T}(|k|)^{1/2} \right] / |k| \right\} = \ln D - |k|Z_0 \quad (8)$$

where  $D$  is a constant, the top bound as well as the centroid of the magnetic source could be evaluated by fit a straight line through the high wavenumber and low wavenumber portions of the averaged radially spectrum of  $\ln \left[ \Phi_{\Delta T}(|k|)^{\frac{1}{2}} \right]$  and  $\ln \left\{ \left[ \Phi_{\Delta T}(|k|)^{1/2} \right] / |k| \right\}$  from Equation 5 and 8 respectively.

A plot of the power spectrum versus wavenumber usually shows straight-line segment which related to decreasing in gradient with increasing wavenumber, and the gradient of the sections provide give estimates of the depths to the magnetic sources causing the magnetic anomaly is calculated using equation 9

$$Z_t = \frac{\ln \Phi_{\Delta T}(k_{i+1}) - \ln \Phi_{\Delta T}(k_i)}{2(k_{i+1} - k_i)} \tag{9}$$

Relationships from the outspread wavenumber curves, where  $\Phi_{\Delta T}$  is the magnitude of the power spectrum of the filtered magnetic data (RTP),  $k$  is the angular frequency and  $Z$  is the depth of the anomaly target sources.

Then, Curie point depth ( $Z_b$ ) of the target magnetic sources in the area under consideration evaluated using equation 10 proposed by [11,14] and the graphs of the Logarithms of the Power spectral density for blocks using potential field package [39] as presented in Table 1.

$$Z_b = 2Z_0 - Z_t \tag{10}$$

Table 1. Estimate of Curie point depth and succeeding geothermal parameters

Block	D1(Residual)	D2 (Regional)	Zb(m)	q(Heat Flow)	dT/dZ
1	1.164863	1.329567	1.329567	1090.58	436.2322
2	1.166454	1.300923	1.300923	1114.593	445.8373
3	1.000955	1.902451	1.902451	762.1748	304.8699
4	0.905474	1.421069	1.421069	1020.358	408.1433
5	1.000955	1.7831	1.7831	813.1905	325.2762
6	1.028008	1.591343	1.591343	911.18	364.472
7	0.936505	1.591343	1.591343	911.18	364.472
8	0.926	1.421069	1.421069	1020.358	408.1433
9	0.926957	1.421069	1.265913	1145.418	458.1672
10	1.089274	1.459262	1.459262	993.6532	397.4613
11	1.097231	1.578612	1.578612	918.5282	367.4113
12	0.506525	2.248568	2.248568	644.8549	257.942
13	0.826703	1.46324	1.46324	990.9516	396.3806
14	0.932527	1.989179	1.989179	728.944	291.5776
15	1.144971	1.674093	1.674093	866.1407	346.4563
16	1.10837	1.344685	1.344685	1078.32	431.3278
17	0.821133	1.275461	1.275461	1136.843	454.7374
18	0.795672	1.530076	1.530076	947.6651	379.066
19	0.971515	1.736155	1.736155	835.1787	334.0715
20	0.760582	1.764799	1.764799	821.6231	328.6492
21	0.663033	1.193507	1.193507	1214.907	485.9627
22	0.82909	1.637492	1.637492	885.5005	354.2002
23	0.783259	1.856302	1.856302	781.123	312.4492
24	0.962763	2.188097	2.188097	662.6764	265.0705
25	1.363781	1063.221	1.363781	425.2882	142.8101

### 3.3. Calculation of the geothermal gradient and heat flow

In order to obtain geothermal gradient and heat flows, simple relation for conductive heat transport (Fourier's law) [6,19-42] was adopted. In the case of 1-dimensional using the assumptions that the variation in temperature direction is vertical and the gradient temperature is constant, the law takes the form as presented in Equation 11

$$q = -K \frac{dT}{dz} \tag{11}$$

where  $k$  and  $q$  is the coefficient of thermal conductivity and heat flux magnitude respectively

According to Tanaka *et al.* [19], the Curie temperature ( $T_c$ ) can be obtained from the Curie point depth  $Z_b$ , and the thermal gradient is given as Equation 12,

$$T_c = \frac{dT}{dz} Z_b \tag{12}$$

Substituting Equation 12 into Equation 11, it gives equation 13,

$$Z_b = -K \frac{T_c}{q} \tag{13}$$

In 1999, Tanaka *et al.* [19] revealed that the thermal isotherm is inversely proportional to heat flow, where  $q$  is the heat flow at any certain depth. Equation 11 indicates regions of high heat flow are associated with shallower isotherms; however regions of lower heat flow are associated with deeper isotherms [6]. Mean shallow heat flow value will compute using Equation 11 and will be based on possible Curie point temperature of 580°C using a thermal conductivity of 2.978 Wm<sup>-1</sup>°C<sup>-1</sup>, given by [43] and adopted as the [19,40-41] average for igneous rocks.

The results of the plot of the logarithm of the Power spectrum against wavenumber. Evaluating the slopes of the graphs, the average depths to the magnetic basement for each of the 25 blocks were calculated using Equation 9, and the results are presented in Table 1.

#### 4. Result and discussion

The quantitative interpretation was adopted for the interpretation of airborne magnetic in Ilesha, and its environ with the aim of estimating Depths to the Bottom of Magnetic Sources (DBMS) and ensuing geothermal parameters in order to inferred geothermal regime within the different block. Generally, the variations in the earth's magnetic field intensity magnitude are presented in Figure 2.

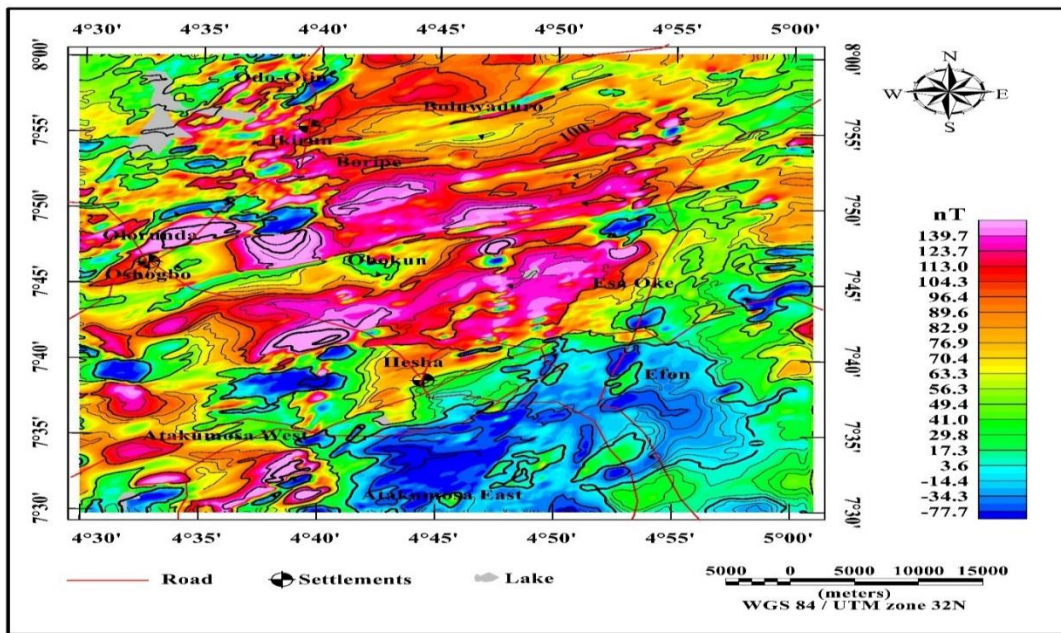


Figure 2. Total magnetic intensity map of the study area

The magnetic intensity value of the field ranged from -77.7 to 139.7 nT. Total magnetic field intensities map indicates high magnitude magnetic intensity values in the north, east, parts of the west and the central mapped area. Regions of magnetic lows (low amplitude magnetic anomaly) and highs (high amplitude anomaly) are apparent on the magnetic map. The defined magnetic highs and lows as visible on the map are in real sense relative. The north-eastern part of the study area is characterized by high intensity which related to lithological variation in the basement. The sharp contrast is enhanced due to sharp magnetic intensity contrast between the crystalline and the sedimentary rocks magnetic susceptibilities. Spectral energy

peaks which were clearly noticeable in graphs of the logarithms of the spectral energies against wavenumbers were plotted for each block, and the connotation of this is the indication of the fact that Curie temperature isotherm depths are demonstrable as it defines the target source bottoms., from which Curie point depths (Isotherm depth) were evaluated, and the depth to the Centroid ( $Z_0$ ) ranges from 9.77 km to 22.51 km.

On the other hand, the values of depth to the top ( $Z_t$ ) of magnetic sources ranged from 2.51km to 4.72km as presented in Table 1. The corresponding curie depth ranges from 16.47 km to 41.47 km, these values were in agreement with earlier work by [41]. The calculated values of Curie point depth (CPD) obtained reveal the mean local curie depth point values below each block. The estimated Curie point depths values for the blocks were used to create Curie isotherm in the Ilesha (Figure 3). The CPD reveals the innumerable depths to curie points which define the thermal nature of the Earth crust. Previous studies by [41,44-48] presented that the geological context of an area is linked to the Curie point depth.

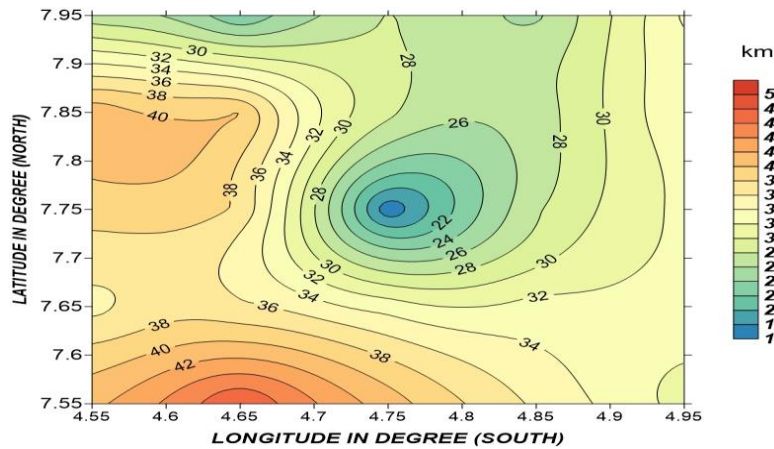


Figure 3. Curie point Depth (Curie Isotherm) map of the Ilesha and its environs

Using a standard value of Curie temperature of Igneous rock (magnetite, 580°C) and the estimated depth to bottom (Curie point depths), variation in a geothermal gradient within Ilesha and its environs were evaluated from where the geothermal gradient map was generated as shown in Figure 4. This is linked to the heat flow map (Figure 5), meaning that most areas of high heat flow relate to high geothermal gradient as shown in Figure 4

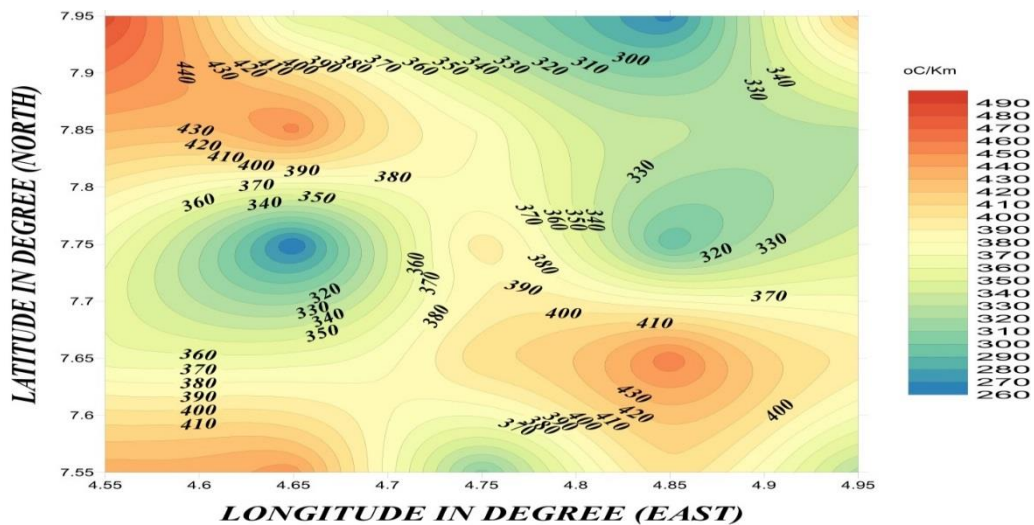


Figure 4. Geothermal gradient map of Ilesha and its environs

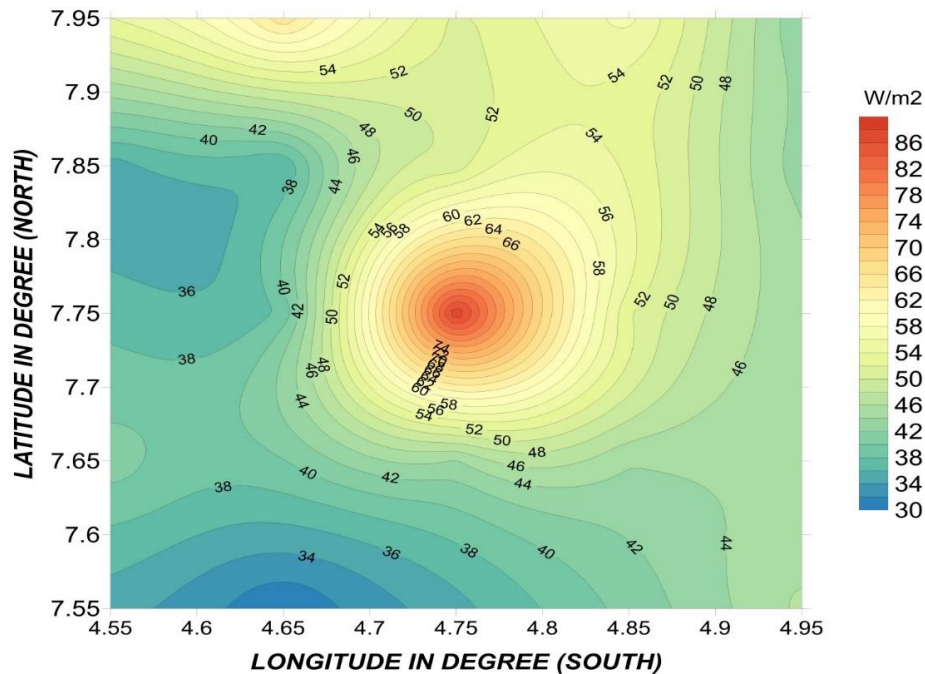


Figure 5. Heat flow map of Ilesha and its environs

Analysis of the potential field data in conjunction with heat flow values using Power spectral has shown a virtually inverse linear correlation between heat flow and Curie depths. The relationship was used to construct the Curie isotherm regime from the current data. It was noticed from the heat flow map of Ilesha were found to be less than  $60 \text{ mWm}^{-1}$ . This suggests that the heat flows in Ilesha are not uniform, which conceivably designate that the magma tubes were indiscriminately distributed.

The mean heat flow values using Curie point depth were derived from Equation (11) with the average thermal conductivity  $k$ .

The mean heat flow obtained for Ilesha and its environs is  $46.008 \text{ Wm}^{-1}$  which may possibly be painstaking as distinguishing of continental crust. Most of the recent literature state that the heat flow and Curie point depth is greatly reliant on upon geological situation. In geothermal exploration heat flow is the primary observable parameter in geothermal exploration. Generally, the units that comprise of high heat flow values correspond to metamorphic regions since the rock unit has high heat conductivity [48]. Therefore the finding makes the study area to have geothermal regime potentials.

## 5. Conclusion

High resolution airborne geophysical approach was used to delineate the subsurface structure of the studied area (Ilesha and its environs) in order to determine geothermal regime using power spectral analysis of magnetic data. The result of the finding using power spectrum display clearly the variant along the blocks in the magnetic basement across the study area. The source depth of the deeper (regional) sources ranges from  $1.19 \text{ km}$ -  $2.25 \text{ km}$  and is assumed to relate to the apparent of the magnetic basement in the Ilesha and its environs. The shallower depth of anomaly, ranging from  $0.45 \text{ km}$  to  $1.165 \text{ km}$  might denote main magnetic components, to improved basement apparent magnetic structures. The CPD for Ilesha and its environment estimated using HRAD via filtering technique (Power Spectrum). The end result divulges that the CPD be at variance contrariwise with heat flow. The inference drawn from the output results show that CPD acquired in all blocks ranges from  $16.479 \text{ km}$  to  $41.47 \text{ km}$  which stemmed from the emergence of the asthenosphere. The obtained results compared favorably in agreement with earlier work done (Nur *et al.* [49]). The mean heat flow value

acquired is  $46.008 \text{ Wm}^{-1}$  which can be utilized for exploration of substitute source of geothermal energy. The analysis of HRAD investigate the extent to Curie Point Isotherm (CPI) and heat flow anomaly over Ilesha and its environs, added greatly to the improved understanding of geothermal anomaly regime in this study which indications a prospect for geothermal possibilities to reconnoiter for new and more energy locations in Nigeria.

## References

- [1] Reeves C. Aeromagnetic Surveys: principle, practice and interpretation. Geosoft INC., 2007.
- [2] Pipan M. Remote sensing and geophysical methods for geothermal exploration. Presented at the School on Geothermic, organized by ICTP, ICS-UNIDO and IAEA, Trieste, Italy, 2009.
- [3] Ochieng L. Overview of geothermal surface exploration methods. Presented at Short course VIII on exploration for geothermal resources, organized by UNU-GTP at Lake Bogoria/Naivasha, Kenya, Oct. 31 – Nov 22, 2013.
- [4] Manzella A. Geophysical methods in geothermal exploration. Unpublished. Lecture notes of International Institute for geothermal research, Pisa, Italy, 1999.
- [5] Chapman DS, and Furlong KP. Thermal state of continental lower crust. In: Fountain DM, Arculus R, Kay RW. (Eds.), Continental Lower Crust. Elsevier Science, Amsterdam, 1992: 179-199.
- [6] Ross HE, Blakely RJ, and Zoback MD. Testing the use of aeromagnetic data for the determination of Curie depth in California: Geophysics, 2006; 71(5): 51 – 59
- [7] Bansal AR, and Anand SP. Estimation of depth to the bottom of magnetic sources using modified centroid method from aeromagnetic data of Central India, 9th Biennial International Conference, and Exposition on Petroleum Geophysics 2012, Hyderabad India.
- [8] Bansal, AR, Anand SP, Rajaram M, Rao VK, and Dimri VP. Depth to the bottom of magnetic sources (DBMS) from aeromagnetic data of central India using modified centroid method for fractal distribution of sources, Tectonophysics, 2013; 603: 155-161
- [9] Spector A, and Grant F. Statistical models for interpreting aeromagnetic data: Geophysics; 1970; 35: 293-302.
- [10] Bhattacharyya BK, Morley LW. The delineation of deep crustal magnetic bodies from total field aeromagnetic anomalies. J. Geomagn. Geoelectr., 1965; 17: 237-252.
- [11] Bhattacharyya BK, and Leu LK. Analysis of magnetic anomalies over Yellowstone national park: mapping and curie point isothermal surface for geothermal reconnaissance. Journal of Geophysical Research, 1975; 80: 4461-4465.
- [12] Bhattacharyya BK, and Leu LK. Spectral analysis of gravity and magnetic anomalies due to two-dimensional structures. Geophysics, 1975; 40: 993-1013.
- [13] Bhattacharyya BK, and Leu LK. Spectral analysis of gravity and magnetic anomalies due to rectangular prismatic bodies: Geophysics, 1977; 42: 41-50.
- [14] Okubo Y, Graff RG, Hansen RO, Ogawa K, and Tsu H. Curie point depths of the Island of Kyushu and surrounding areas, Geophysics, 1985; 53: 481-494.
- [15] Blakely RJ. Curie temperature isotherm analysis and tectonic implications of aeromagnetic data from Nevada. J. Geophys. Res., 1988; 93, 817-832.
- [16] Blakely RJ. Potential Theory in Gravity and Magnetic Applications. Cambridge University Press 1995, Cambridge.
- [17] Blakely RJ, Hassanzadeh S. 1981. Estimation of depth to the magnetic source using maximum entropy power spectra with application to the Peru-Chile trench. Geol. Soc. Am. Mem. 1981; 154: 667-681.
- [18] Maus S, Gordon D, and Fairhead JD. Curie temperature depth estimation using a self similar magnetization model. Geophysical Journal International, 1997; 129: 163-168.
- [19] Tanaka A, Okubo Y, Matsubayashi O. Curie point depth based on spectrum analysis of the magnetic anomaly data in East and Southeast Asia. Tectonophysics, 1999; 306: 461-470.
- [20] Russ P. Airborne electromagnetics in review. Geophysics, 1957; 22: 691- 713.
- [21] Bouligand C, Glen JMG, and Blakely RJ. Mapping Curie temperature depth in the western United States with a fractal model for crustal magnetization. Journal of Geophysical Research, 2009; 114: B 11104.
- [22] Gabriel G, Dressel I, Vogel D, Krawczyk CM. Depths to the bottom of magnetic sources and geothermal prospectivity in southern Germany. First Break, 2012; 30(4): 39-47.
- [23] Kasidi L, and Ndatuwong L. Spectral analysis of aeromagnetic data over Longuda Plateau and environs north eastern Nigeria. Continental Journal of Earth Science, 2008; 3: 28 – 32.

- [24] Nwankwo LI, Olasehinde PI, and Akoshile CO. Heat flow anomalies from the spectral analysis of Airborne magnetic data of Nupe Basin, Nigeria. *Asian Journal of Earth Sciences* 2011.
- [25] Ravat D, Pignatelli A, Nicolosi I, and Chiappini M. A study of spectral methods of estimating the depth to the bottom of magnetic sources from near-surface magnetic anomaly data, *Geophysical Journal International*, 2007; 169: 421-434.
- [26] Guimarães SNP, Hamza VM, Ravat D. Curie depths using combined analysis of centroid and matched filtering methods in inferring thermomagnetic characteristics of central Brazil. In: 13th International Congress of the Brazilian Geophysical Society, Rio de Janeiro, Brazil, 26–29 August 2013, Rio de Janeiro, Brazil.
- [27] Nwankwo L. Estimation of depths to the bottom of magnetic sources and ensuing geothermal parameters from aeromagnetic data of Upper Sokoto Basin, Nigeria, *Geothermics*, 2015; 54: 76–81.
- [28] Badejo AO, Adekunle AA, and Oyerinde AO. Pollution studies on groundwater contamination: water quality of Abeokuta, Ogun State, Southwest Nigeria. *Journal of Environment and Earth Sciences*, 2013; 3:162 -166.
- [29] De Swardt AMJ. The Ife-Ilesa goldfield (Interim report number 2) Geology of Survey of Nigeria annual report. 1947; 14-19
- [30] De Swardt AMJ. The geology of the country around Ilesa. *Geological Survey of Nigeria Bulletin*, 1953; 23: 55
- [31] Russ P. Airborne electromagnetics in review. *Geophysics*, 1957; 22: 691- 713.
- [32] Rahaman MA. A review of the basement geology of Nigeria in kogbe, C.A (ed), *geology of Nigeria* Elizabeth Publishing Co. 1976, pp. 41-58.
- [33] Hann A, Kind G, and Mishra DC. Depth estimation of magnetic Source by means of Fourier amplitude spectral. *Geophysical Prospecting*, 1976; 24: 287–305.
- [34] Connard G, Couch R, and Gemperle M. (1983): Analysis of aeromagnetic measurements from the Cascade Range in central Oregon, *Geophysics*; 1983; 48: 376–390.
- [35] Garcia-Abdeslem J, and Ness GE. Inversion of power spectrum from Magnetic anomaly, *Geophysics*; 1994; 59: 381–401.
- [36] Okubo Y, and Matsunaga T. Curie point depth in northeast Japan and its Correlation with regional thermal structure and seismicity, *Journal of Geophysics Research*, 1994; 99, 22363–22371.
- [37] Shuey RT, Schellinger DK, Tripp AC, and Alley LB. Curie depth determination from aeromagnetic spectra, *Geophysical Journal of the Royal Astronomical Society*, 1977; 50: 75-101.
- [38] Taha R. Prospecting for the ferromagnetic mineral accumulations using the magnetic method at Eastern desert, *Egyptian Geophysics Society*, 2009; 6: 401-411.
- [39] Phillips JD. Potential field geophysical software for the PC, version 2.2: U.S. Geological Survey Open-File Report, 1997; 97-725, 34pp.
- [40] Stampolidis A, Kane I, Tsokas GN, Tsourlos P. Curie point depths of Albania inferred from ground total field magnetic data. *Survey Geophysics*, 2005; 26: 461– 480.
- [41] Maden N. Curie-point depth from spectral analysis of magnetic data in Erciyes stratovolcano (Central TURKEY). *Pure and Applied Geophysics*, 2010; 167: 349–358.
- [42] Turcotte DL, and Schubert G., *Geodynamics Applications of Continuum Physics to Geologic Problems* (Wiley, New York, 1982), p 450.
- [43] Stacey FO. *Physics of the Earth*. John Wiley and Sons 1977, New York
- [44] Hsieh H H, Chien HC, Pei-Ying L, and Horng YY. Curie point depth from spectral analysis of magnetic data in Taiwan. *Journal of Asian Earth Sciences*, 2014; 90: 26–33
- [45] Abraham EM, Lawal MK, Ekwe AC, Alile O, Murana KA, and Lawal AA. Spectral analysis of aeromagnetic data for geothermal energy investigation of Ikogosi Warm Spring - Ekiti State, southwestern Nigeria. *Geothermal Energy*, 2014; 2:6.
- [46] Kasidi S, and Nur A. Curie depth isotherm deduced from spectral analysis of Magnetic data over sarti and environs of North-Eastern Nigeria, *Scholarly Journal of Biotechnology*, 2013; 1: 49 – 56
- [47] Nwankwo LI, and Shehu AT. Evaluation of Curie-point depths, geothermal gradients and near-surface heat flow from high- resolution aeromagnetic (HRAM) data of the entire Sokoto Basin, Nigeria, *J. Volcanol. Geoth. Res.*, 2015; 305: 45–55.
- [48] Nwankwo LI, and Sunday JA. 2017. Regional estimation of Curie-point depths and succeeding geothermal parameters from recently acquired high-resolution aeromagnetic data of the entire Bida Basin, North-central Nigeria. *Geothermal Energy Science*, 2017; 5: 1 –9.
- [49] Nur A, Ofeogbu CO, and Onuha KM. Estimation of the depth to the Curie point isotherm in the upper Benue trough, Nigeria. *Journal of Mining and Geology*, 1999; 35(1): 53-60.

*To whom correspondence should be addressed: Dr. O. T. Olurin, Department of Physics, Federal University of Agriculture Abeokuta, Ogun State, Nigeria*

## REDUCING SULFUR EMISSION IN A COMMERCIAL SCALE SULFUR RECOVERY UNIT (SRU) USING ARTIFICIAL NEURAL NETWORK: R APPLICATION

Sepehr Sadighi<sup>1\*</sup>, S. Reza Seif Mohaddecy<sup>1</sup>, Yasser Arab-Ameri<sup>2</sup>

<sup>1</sup> Research Institute of Petroleum Industry (RIPI), Catalysis Technologies Development Division, P.O. Box 14665137, Tehran, Iran

<sup>2</sup> Islamic Azad University, South Tehran Branch, Chemical Engineering Department, Tehran, Iran

Received August 21, 2018; Accepted November 19, 2018

---

### Abstract

The main objects of this research are developing an artificial neural network (ANN) model in R environment for simulating an industrial scale modified Claus unit, and optimizing temperatures of Claus catalytic reactors to achieve the minimum sulfur emission. The input layer of the ANN model consists of acid gas flow rate, reactors inlet temperatures, and H<sub>2</sub>S and SO<sub>2</sub> contents of acid gas, while the output neuron is the sulfur content of the tail gas (TG). The results confirmed that the AAD% (average absolute deviation) of the ANN model for training and validating data are 1.164% and 3.429%, respectively. After validating the model, optimal temperatures of input streams to the catalytic bed are calculated considering the sulfurous compounds of the TG as the objective function. Simulation results prove that the sulfur content of the TG decreases from the average value of 0.6 mol% to about 0.3 mol% that considerably reduces the sulfur emission of the target Claus process.

**Keywords:** Claus process; artificial neural network; optimization; sulfur emission; R software.

---

## 1. Introduction

H<sub>2</sub>S (hydrogen sulfide) is a byproduct of processing natural gas and refining high sulfur crude oils [1]. This species is a toxic gas, and consequently, its present in any exhaust gas is under stiff environmental regulations. To meet these requirements, H<sub>2</sub>S must be converted to elemental sulfur which is mainly accomplished in a sulfur recovery unit (SRU). To do such a task, Claus process is widely used nowadays in a modern configuration succeeds the one pioneered in 1883 based on the reaction of H<sub>2</sub>S over a catalyst with air (oxygen) to produce sulfur and water [2] that typically recovers 95 to 97 percent of the H<sub>2</sub>S feed stream [3]. Approximately 90 to 95 percent of recovered sulfur is produced by this technology.

Few articles have been reported on the fundamental modeling and simulation of the Claus process [4-7]; however, there are scarce studies on using black-box modeling approach for this process. In recent years, there has been a significant increase in the use of artificial intelligence based techniques in the field of industrial control. Different intelligent techniques (black-box modeling approaches) like fuzzy logic, artificial neural network (ANN) and other hybrids were successfully implemented for various control problems. Prakash et al. studied optimal control of incinerator in a sulfur recovery unit by an ANN model [8]. This model had four inputs including O<sub>2</sub> and SO<sub>2</sub> concentration, the temperature of the incinerator and total flow rate of the tail gas. The outputs of the network controlled parameters of the process i.e., fuel gas and air flow rates and oxygen concentration in the input air. It was found that the model was able to successfully approximate the training data and generate the inputs for the plant for its optimal operation. Abdali et al. studied estimation of the temperature of Claus furnace using ANN and control of the Claus reactions. In this research, the amount of H<sub>2</sub>S content was

adjusted aware of the air flow rate [9]. Moreover, output temperatures of Claus reactors was estimated via adaptive linear neuron networks.

In this research, based on data collected from a modified SRU in an Iranian gas refinery, the sulfur content of the tail gas (TG) is modeled applying the ANN modeling methodology. This model which is implemented in R has a feed-forward structure, and it is composed of 6, 3 and 1 neurons in the input, hidden and output layers, respectively. By using the proposed model, the sulfur emission from the target plant is minimized. Due to the importance of the SRU from the environmental viewpoint, this research and the proposed methodology is significant.

## 2. Process description

A block flow diagram of the understudy Claus process unit is presented in Figure 1. The acid gas from the upstream (i.e., sweetening unit) is directed to the acid gas KO drum D-01. The gas comes from this KO drum is warmed up to 220°C in the E-01 by using HP steam, and then goes through the reaction furnace burner (H-01). By using the compressor (K-01 A/B), the required air is introduced to the pre-heater (E-02), and heated by high pressure steam before entering the furnace burner H-01.

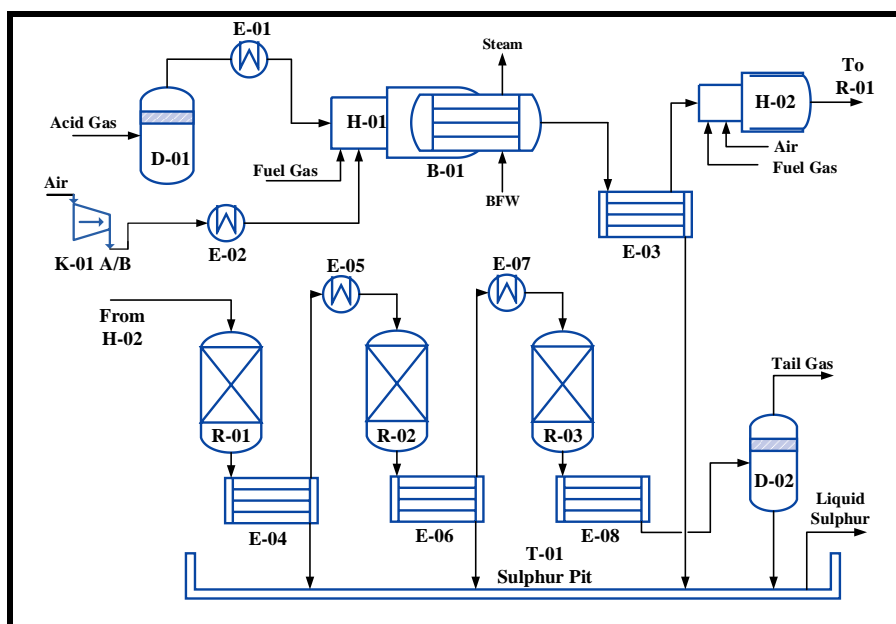


Figure1. Block flow diagram of the target Claus unit

The process gas from furnace burner (H-01) is cooled in passing through the reaction furnace boiler (B-01), and then routed to the 1<sup>st</sup> condenser (E-03) where the gases are cooled, and sulfur is formed. The condensed sulfur is removed through a seal pot to the sulfur degassing pit (T-01). The process gases pass through the auxiliary burner (H-02), where they are reheated up to 235°C before introducing the first catalytic reactor (R-01). In this reactor, additional sulfur is produced and scraped in the vapor phase by the process of hot gases. Due to the exothermic nature of Claus reactions, the temperature increases across the catalytic bed. However, the inlet temperature of the reactor should be adjusted such that the outlet temperature of the reactor reaches to at least 300°C for promoting the hydrolysis of COS and CS<sub>2</sub>.

The hot gases leaving the 1<sup>st</sup> reactor are cooled in the 2<sup>nd</sup> condenser (E-04) by generating LP steam. The condensed sulfur is also sent to the sulfur degassing pit (T-01). The gases leaving the condenser (E-04) first are reheated up to 215°C by the heater (E-05) and then routed to the 2<sup>nd</sup> catalytic reactor converter (R-02). The hot gases leaving the second converter (R-02) are cooled in the 3<sup>rd</sup> condenser (E-06) by generating LP steam. The condensed sulfur flows through a seal pot to the sulfur degassing pit (T-01). Process gases leaving the

3<sup>rd</sup> condenser is reheated up to 200°C by HP steam in the heater (E-07), prior to entering the 3<sup>rd</sup> catalytic reactor (R-03). The process gases pass downwards through the catalyst bed of third reactor (R-03). The gases are then cooled to 130°C in the last condenser (E-04) in order to condense the sulfur and to decrease its losses by vapor pressure in the tail gas. The last condenser ensures cooling of gases by generating very low LP steam, which is condensed in an air cooler. Prior to being incinerated, the effluent gas from E-03 introduces to the last equipment (D-02), and any mists and drops of liquid sulfur are collected.

### 3. Process modeling and optimization

The modeling strategy used in this research is the same as the methodology presented in the previous works [10-11]. In the current study, an ANN model is implemented in R software (Version 3.4.1, Copyright 2017) for simulating the sulfur content of TG (i.e. sum up molar percentages of H<sub>2</sub>S and SO<sub>2</sub>). R is a language and environment for statistical computing and graphics which was developed at Bell Laboratories (formerly AT&T, now Lucent Technologies) by John Chambers and colleagues. The significant benefit of using R is its opportunity as free software under the terms of the Free Software Foundation's GNU General Public License in source code form. To develop and construct the corresponding ANN model, the package 'neuralnet' (Version 1.33) obtained from the CRAN repository is applied. This package permits resilient settings through custom-choice of error and activation function, and also the calculation of generalized weights is implemented [12]. The globally convergent algorithm of 'neuralnet' is based on the resilient back-propagation without weight back-tracking, and additionally modifies one learning rate, either the learning rate associated with the smallest absolute gradient [13].

The most widely employed networks have one hidden layer only. Each node within a given layer is connected to all of the nodes of the previous layer. The node sums up the weighted inputs and bias, and it passes the result through a linear function as follows [14]:

$$a_j = \sum_{i=0}^m w_{ji}y_i + b_j \quad (1)$$

In Eq. (1),  $w_{ji}$  is the weight that goes from the input ( $i$ ) to the hidden neuron ( $j$ );  $b$  is the bias to the node, and  $y_i$  is the input unit of the neuron. By utilizing an activation function ( $f$ ), the output of the neuron can be written as follows:

$$Z_j = f(a_j) \quad (2)$$

By using 'neuralnet' package, a feed-forward ANN with one hidden layer is developed to simulate the sulfur content of the TG. The input layer of Claus ANN model is contained in acid gas flow rate ( $F_{in}$ ), temperatures of input streams to the catalytic reactors ( $T_{inR1}$ ,  $T_{inR2}$ , and  $T_{inR3}$ ), and H<sub>2</sub>S and SO<sub>2</sub> contents of acid gas. The output layer has one node which is the summation of SO<sub>2</sub> and H<sub>2</sub>S contents of the TG ( $InH_2S$  and  $InSO_2$ ). To inhibit from memorizing instead of learning, only 3 neurons are selected for the hidden layer such that the number of coefficients should be less than the number of real data points obtained from the target SRU plant.

To evaluate the accuracy of the model, the absolute average deviation (AAD%) and mean squared error (MSE) between the actual and predicted data are calculated as follows:

$$AAD\% = \frac{\sum_{n=1}^{N_t} \sqrt{\frac{(y_n^{actual} - y_n^{model})^2}{y_n^{actual^2}}}}{N_t} \times 100 \quad (3)$$

$$MSE = \frac{1}{N_t} \sum_{n=1}^{N_t} (y_n^{actual} - y_n^{model})^2 \quad (4)$$

where  $y$  and  $N_t$  are output variables (i.e. sulfur content of TG) and number of data points, respectively; superscripts *actual* and *model* indicate the actual (or real) and the simulated values, respectively.

Finally, to optimize the target modified Claus process, the sum of H<sub>2</sub>S and SO<sub>2</sub> content of the TG is minimized by manipulating the temperatures of the input temperatures to the catalytic reactors (1<sup>st</sup>, 2<sup>nd</sup> and 3<sup>rd</sup> Claus reactors). To be engaged such a problem, 'optimx' package available in R software is applied. This package provides a replacement and extension of the

'optim' function of R toolbox to unify and streamline optimization capabilities for smooth [15]. In this study to carry out the optimization procedure, Large-scale Bound-constrained (L-BFGS-B) method is utilized which is a limited-memory quasi-Newton code for bound-constrained optimization.

#### 4. Results and discussions

##### 4.1. Modeling the target SRU

During 90 days, 90 data points including acid gas flow rate, temperatures of input streams to the catalytic reactors, H<sub>2</sub>S and SO<sub>2</sub> contents of acid gas, and sulfur content of TG were obtained from the understudy Claus plant. These data points were divided into two categories: training and validating groups which were included 63, and 27 points (70% and 30% of total data), respectively. The topology of ANN constructed by R for modeling sulfur content of TG is demonstrated in Figure 2. As seen, each network has 21 weights and 4 biases, totally 25 coefficients; therefore, the number of model variables is less than the half of the training data, and the degree of freedom (DOF) for training the network is equal to 38. It seems that this positive DOF restrains from over learning instead of training.

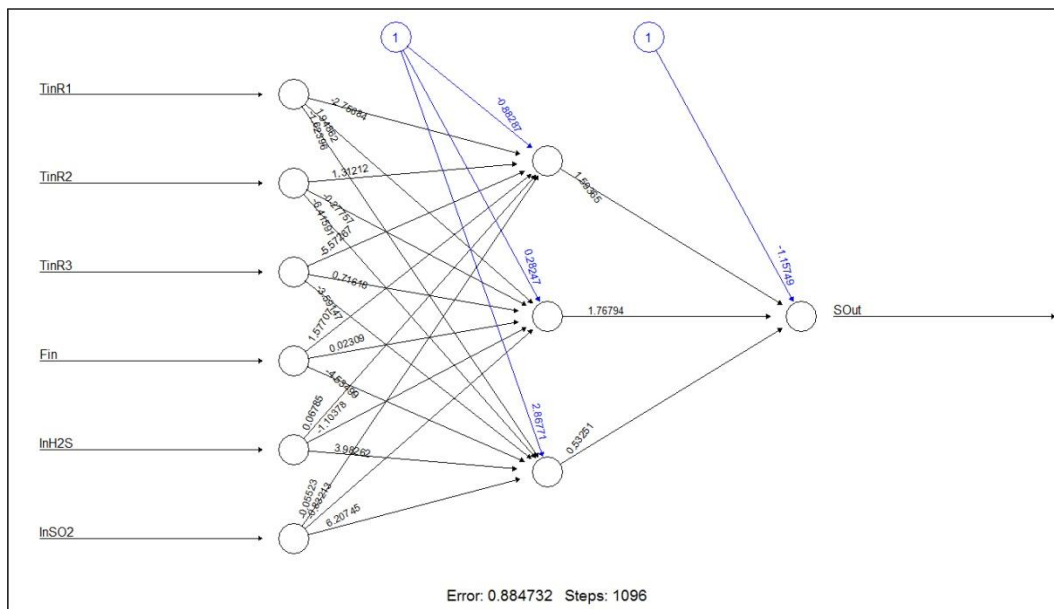


Figure 2. The topology of ANN constructed by R for predicting total sulfur of TG in the target SRU

The results obtained for simulating the sulfur content of TG is presented in Table 1. From this table, it is concluded that the AAD% and MSE of training data (1.164% and 0.057, respectively) are less than those of belong to testing or unforeseen data points (3.429% and 0.095, respectively), and they are relatively close together. To further explore the validity of the model, in Figure 3, the actual data on the sulfur content of TG are sketched against trained and validated values obtained from the developed ANN model. As seen, the ANN model has acceptable accuracy, and therefore it can be applied for the purpose of optimizing the modified Claus process. We believe that the observed deviation is mainly due to the error of measuring H<sub>2</sub>S and SO<sub>2</sub> concentrations of the TG.

Table 1. AAD% and MSE of the ANN model in comparison to the actual data

Product	Training data (%)	Validating data (%)
AA%D%	1.164	3.429
MSE	0.057	0.095

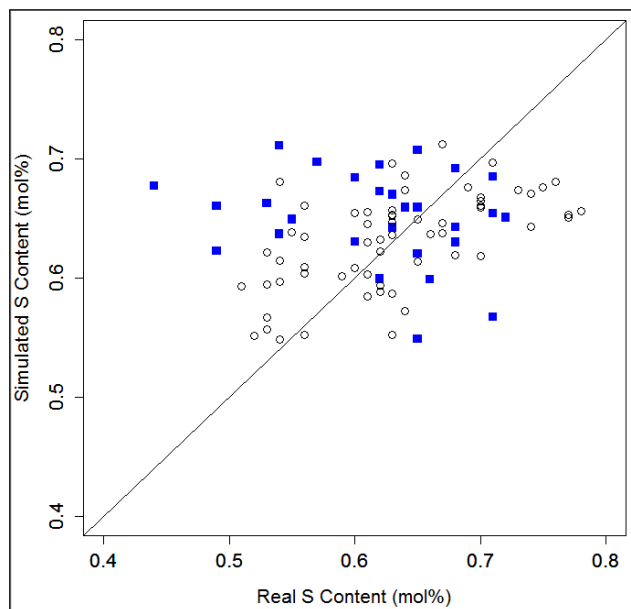


Figure 3. Comparison of real and simulated (trained (○) and validated (■)) values of the total sulfur of TG

#### 4.2. Reducing the sulfur emission

After developing and validating the ANN model for the target modified Claus process, this model is ready for being applied to reduce the sulfur emission of the SRU. Therefore, for all 90 test runs, the optimized feed temperatures of Claus convertors are calculated by using the proposed model. Then, for each case, temperatures are adjusted to minimize the sulfur content of the TG. After applying the optimal decision variables, the comparison between the optimal values of TG sulfur content versus the current (actual) ones is presented in Figure 4. As seen, the obtained optimum inlet temperatures can decrease the sulfur content of TG by approximately 0.3 mol% which is equal to 50% decrease in sulfur emission. It is obvious that lowering the concentration of sulfurous compounds in the TG is a momentous achievement both from the environmental and economic viewpoints.

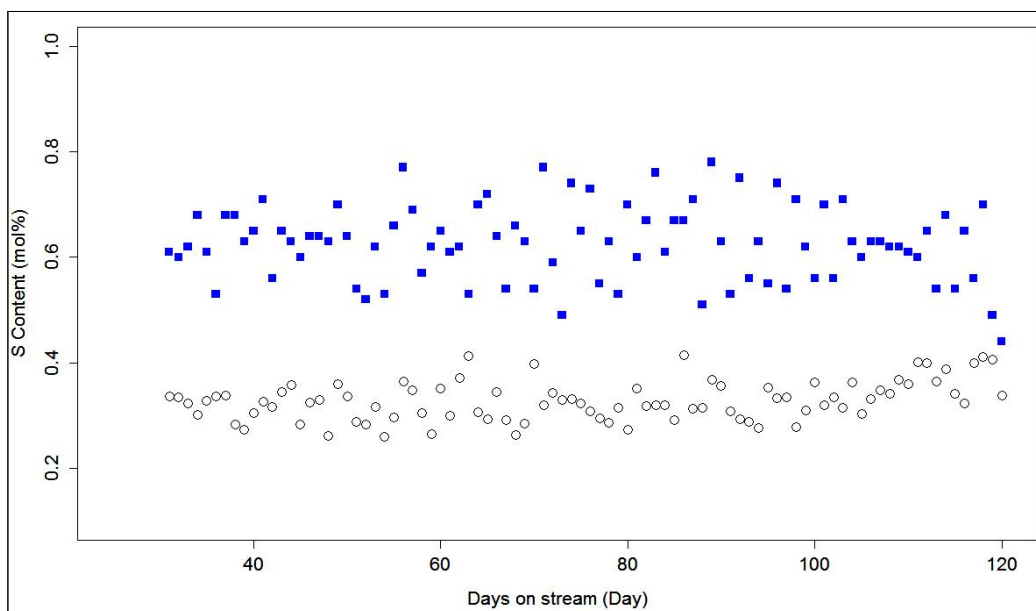


Figure 4. Comparison of the actual (■) and optimized (○) values of the total sulfur of TG

The results related to the optimum values of the input stream temperatures of catalytic beds against the actual values are presented in Figures 5 to 7. As seen in Figure 5, the optimum temperature of the first convertor should be adjusted to the values lower than the actual temperature. This phenomenon is expectable due to the exothermic nature of the Claus reactions; therefore, a lower temperature is desired to supply a suitable thermodynamic condition for higher SO<sub>2</sub> and H<sub>2</sub>S conversion [16]. On the other hand, in the 2<sup>nd</sup> and 3<sup>rd</sup> catalytic reactors, the degree of temperature reduction is limited by the sulfur dew point such that below this constraint, the sulfur conversion decreases because of the blockage of the catalyst surface, and the plausible deactivation [17]. Therefore, in opposite to the thermodynamic equilibrium, the temperature of the feed introduced to the 2<sup>nd</sup> and 3<sup>rd</sup> convertors should be meticulously elevated (see Figures 6 and 7).

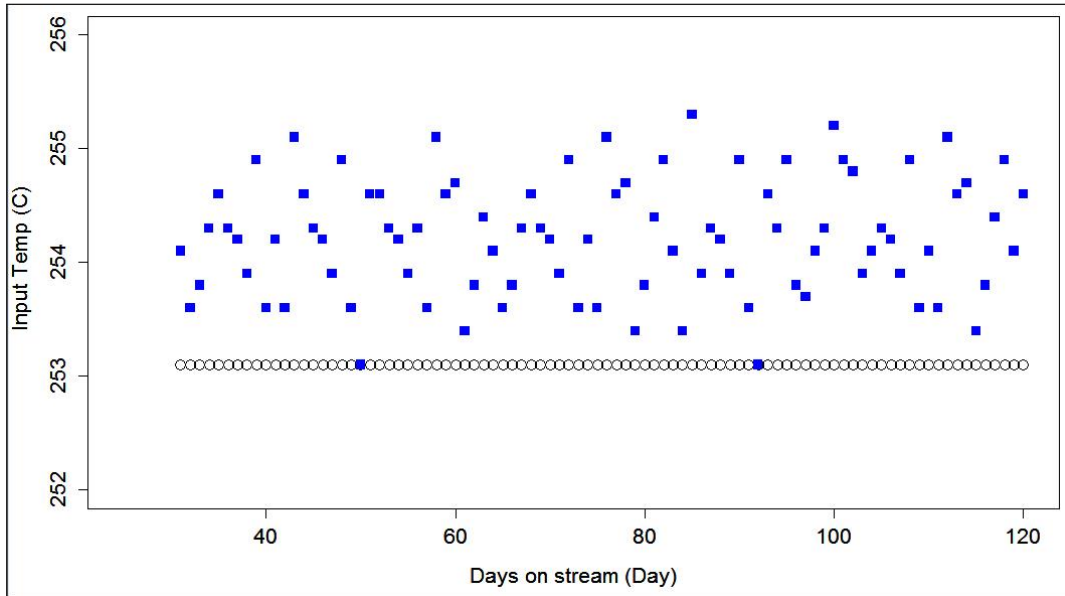


Figure 5. Comparison of the actual (■) and optimized (○) values of the inlet temperature to the 1<sup>st</sup> Claus reactor

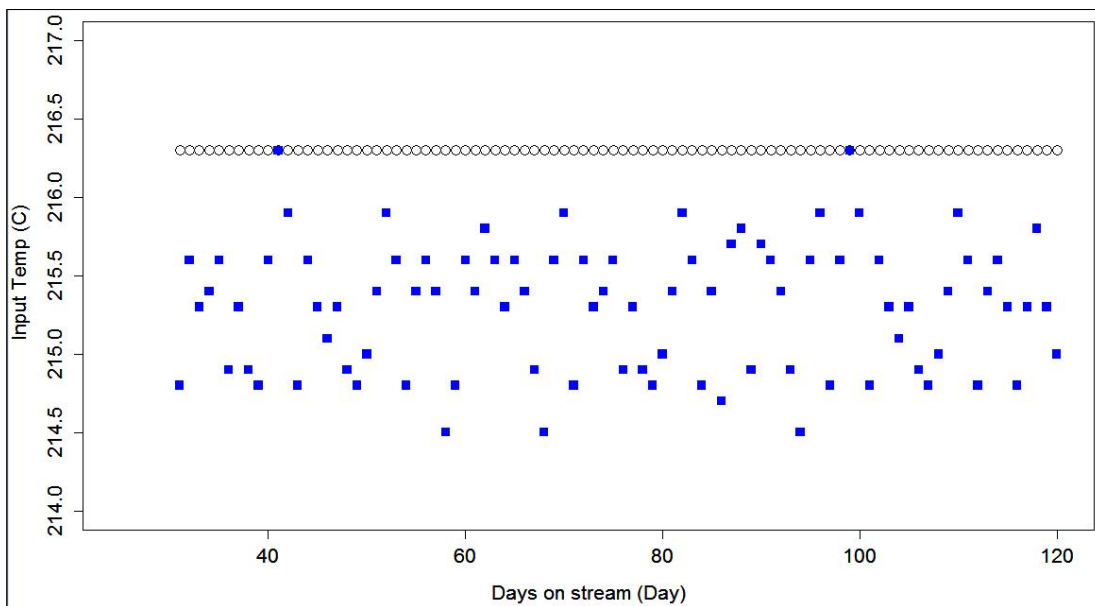


Figure 6. Comparison of the actual (■) and optimized (○) values of the inlet temperature to the 2<sup>nd</sup> Claus reactor

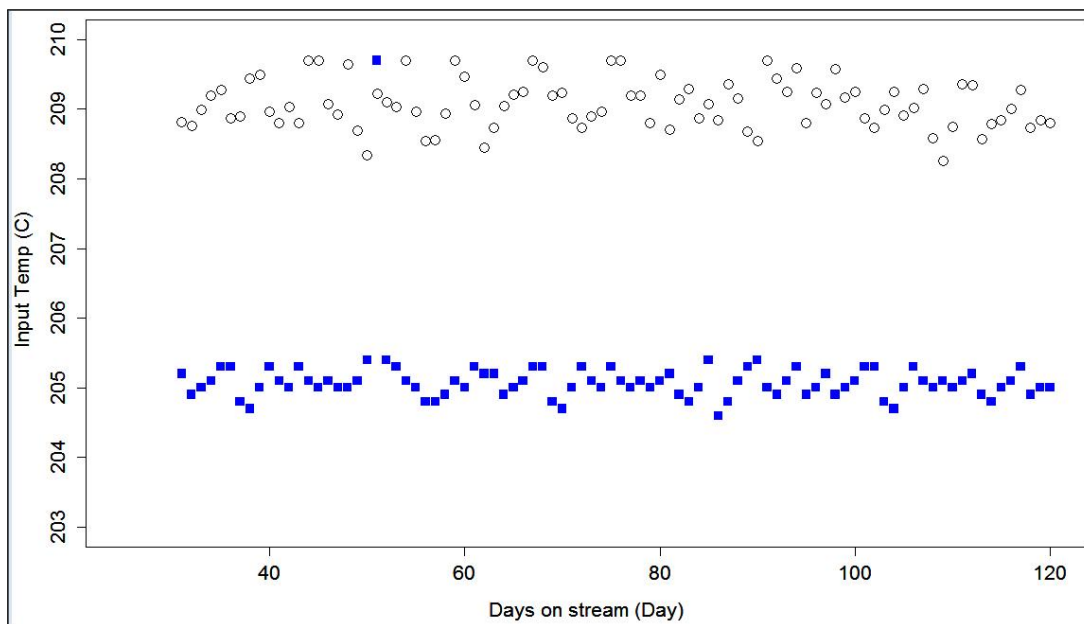


Figure 7. Comparison of the actual (■) and optimized (○) values of the inlet temperature to the 3<sup>rd</sup> Claus reactor

## 5. Conclusions

A commercial-scale modified Claus unit was modeled based on the ANN methodology developed in R software. This model was a feed-forward neural network including six neurons in the input layer (i.e. acid gas flow rate, temperatures of input streams to the catalytic reactors, and H<sub>2</sub>S and SO<sub>2</sub> contents of acid gas), three neurons in the hidden layer, and one neuron in the output layer (i.e. sum of SO<sub>2</sub> and H<sub>2</sub>S contents of TG). The model was trained and validated against the actual data points which were gathered from the target plant during 90 days. The results showed that ANN could simulate the sulfur content of training and validating data (63 and 27 data points, respectively) with an AAD% of 1.164% and 3.429%, respectively. The MSEs of the model for those data were 0.057 and 0.095, respectively. These results confirmed the reliability of the constructed ANN model.

To suggest an application for the developed ANN model, the sulfur content of the TG was minimized by manipulating the temperatures of feed streams entered to the catalytic converters of Claus process. The results proved that within the admissible range for the adjusted variables, the average sulfur content of the TG could be decreased from 0.6 mol% to 0.3 mol% (about 100% reduction in sulfur emission).

It is supposed that applying optimal decision variables in the target modified Claus process can decrease sulfur contaminant emission which has a great impact on the environmental and economic aspects of the process.

## References

- [1] Sassi M, Gupta A. *American Journal of Environmental Sciences*, 2008; 4(5): 502.
- [2] ZareNezhad B, Hosseinpour N. *Applied Thermal Engineering*, 2008; 28: 7.
- [3] Abedini R, Koolivand Salooki M. *Pet Coal*, 2010; 52(3): 173.
- [4] Sadighi S, Seif Mohaddecy SR. *Pet Coal*, 2018; 60(1): 71.
- [5] Abedini R, Koolivand M, Ghasemian S. *Chemical Engineering Research Bulletin*, 2010; 14: 110.
- [6] Pahlavan M, Fanaei M. *Iranian Journal of Oil & Gas Science and Technology*, 2015; 5: 42.
- [7] Eghbal Ahmadi MH, Rad A. *Chemical Engineering Transactions*, 2017; 57: 997.
- [8] Prakash GL, Samson S, Snehil M, Vedant S. *Neural Network based Decision Support System for Optimal Incinerator Control*, International Symposium of Signal Processing and Information Technology, December 2014.

- [9] Abdali GA, Suratgar AA. Separating Impurities of Acid Gas from Hydrogen Sulfide by Using Adaptive Filter for Estimating of Claus Reaction Temperature by Neuron Networks, International Multi Conference of Engineers and Computer Scientists, 2009, March 18 - 20, Vol. II, Hong Kong.
- [10] Sadighi S, Mohaddecy SR. *Pet. Coal*, 2018; 60(3): 358.
- [11] Sadighi S, Faraji D. *Pet. Coal*, 2018; 60(4): 688.
- [12] Intrator O, Intrator N. Using Neural Nets for Interpretation of Nonlinear Models. Proceedings of the Statistical Computing Section, 1993, 244-249, San Francisco: American Statistical Society.
- [13] Fritsch S, Guenther F, Suling M, Mueller SM. Package `neuralnet`: Training of Neural Networks, 2016, <https://cran.r-project.org/web/packages/neuralnet/neuralnet.pdf>.
- [14] Haykin S, Hamilton O. *Neural Networks*. 2nd ed., Prentice Hall International, Upper Saddle River, NJ, 1998.
- [15] Nash JC, Varadhan R, Grothendieck G. A Replacement and Extension of the optim() Function, Version 2013.8.7, February 2015.
- [16] Sadighi S, Mohaddecy SR. *Petrol. Coal*, 2018; 60(1): 71.
- [17] Zagoruiko AN, Matros TuSh. *Chem. Eng. J.*, 2002; 87: 73.

---

*To whom correspondence should be addressed: Dr. Sepehr Sadighi, Research Institute of Petroleum Industry (RIPI), Catalysis Technologies Development Division, P.O. Box 14665137, Tehran, Iran*

## PREPARATION OF SORBITOL PALMITATE BY ORGANIC CATALYSIS AND ITS APPLICATION FOR BASE OIL STABILIZATION

Noura el Mehad

Najran University, Faculty of Science and Arts, Kingdom of Saudi Arabia

Received September 29, 2018; Accepted October 19, 2018

---

### Abstract

Esters are excellent lubricants and high performance industrial fluids, but they are often costly. We prepared the ester sorbitol palmitate via an inexpensive phase-transfer catalysis method as an additive for the retardation of oil oxidation. The effects of the sorbitan palmitate content on the lubricant properties and oxidation stability of a base oil were determined. The addition of sorbitan palmitate to the oil retarded oxidation and enhanced the pour point depression. A novel method for inhibiting oxidation through the action of micellar cores was suggested. This micellar inhibition offers a new concept for the protection of lubricants against oxidative degradation.

**Keywords:** Hydrocarbon; Oxidation; Alkylation; Esterification; Wear.

---

### 1. Introduction

Esters are widely used as lubricants and high performance industrial fluids. They are characterized by good biodegradability, low volatility, good lubricity, good thermal stability, and low pour points [1]. Ester oils are now used in many applications, including as automotive engine oils, hydraulic fluids, and compressor oils [2]. The antiwear and antifriction characteristics of alkyl octadecenoates increase with an increase in the number of polar linkages in the alkyl octadecenoate backbone. This is primarily due to the increase in a number of sites amenable to chemisorption on the surface and, consequently, their reactivity. The antiwear and antifriction characteristics of derivatives of ethyl octadecenoates are inferior to the corresponding methyl 12-hydroxyoctadecenoate derivatives. This can be attributed to the increased reactivity of the latter at surfaces due to the additional hydroxyl moiety [3].

The properties of a non-ionic surfactant are related to its chemical structure. In particular, the structure of its hydrophobic and hydrophilic groups and their interactions are of great importance. The oxidative stability of lubricating oil has a critical influence on its performance during service. In this paper, the non-ionic surfactant sorbitan palmitate (SPT) was prepared by phase-transfer catalysis, and its physicochemical (e.g., cloud point, critical micelle concentration (CMC) [4-5] and performance properties [6] as an antioxidant were investigated.

Ester oils are typically prepared by alcoholysis reactions catalysed by simple inorganic compounds [7]. Transesterification can be catalysed by both acids and bases, with the latter usually proceeding at much faster rates [7]. Aqueous solutions of sodium alkanoates will react with alkyl halides in a second phase provided an amine is added as a catalyst [8-9]. Hennis *et al.* [9] showed that the catalyst must have at least one moderately long alkyl group to function well. The poor nucleophilicity of acetate ion toward various substrates in condensed systems has been attributed to a combination of polarizability, basicity, and solvation factors. Liotta *et al.* [10] reported that the acetate ion, solubilized as the potassium salt in acetonitrile or benzene containing 18-crown-6, becomes sufficiently nucleophilic to react smoothly and quantitatively, even at room temperature, with a wide variety of organic substrates. Because of the cost of

some esterification methods, we explored a phase-transfer catalysis approach for the preparation of SPT.

The aim of this work was to study the preparation and performance of SPT as an additive which can act as an antioxidant and affect the pour and cloud points for a base oil. SPT was added to the base oil in different concentrations, and its antioxidant activity was evaluated as a function of time. The degradation of the oil was monitored by total acid formation. A mechanism of action based on the formation of micelles and micellar inhibition of radical propagation was suggested. The oxidation stability of the lubricating oil was largely affected by the sulfur and aromatic hydrocarbon concentration in the oil, with an increased sulfur content leading to increased oxidative stability. The prepared compounds gave higher oxidation stability than imported compound (IRGANOX® L 135, Ciba) [11].

## 2. Experimental

### 2.1. Base oil sample

The physicochemical properties of the base oil are listed in Table 1.

Table 1. Physicochemical properties of the base oil

Property	Base oil	Test
Density (g/mL) at 15.5°C	0.8918	D. 1298
Refractive index (nD20)	1.4945	D. 1218
ASTM colour	4.5	D. 1500
Kinematic viscosity (cSt)		D. 445
at 40°C	18.56	
at 100°C	27.15	
Pour point (°C)	12	ASTM D 97
Molecular weight (g/mol)	450	GPC
Total paraffinic content (wt%)	61.353	Urea adduction [7]
Carbon residue content (wt%)	1.5	ASTM D524
Ash content (wt%)	0.0311	ASTM D482
Naphthenes (wt%)	24.49	ASTM 3238/85
Aromatics (wt%)	9.51	ASTM 3238/85

### 2.2. Preparation of the additive by phase-transfer catalysis

**Method 1.** Anhydrous aluminium chloride (1 mol) was added with stirring over 1 h to 1-chloropalmitoyl chloride (1 mol) in CCl<sub>4</sub> (100 mL). The reaction temperature was kept at 20°C, and stirring was continued for another hour to form the aluminium chloride complex. Sorbitan (0.1 mol) was condensed with palmitoyl chloride (0.6 mol) in a three-necked flask in the presence of tetraethylammonium bromide (0.01 g) as a phase-transfer catalyst. The reaction mixture was heated with continuous stirring until the theoretical amount of water was collected. The product was purified by washing with a hot solution of 5% sodium carbonate and was then dissolved in petroleum ether (b.p. 40–60°C). The sorbitol palmitate was completely characterized by IR, <sup>1</sup>H NMR, and mass spectroscopy.

The esters can be also prepared from haloalkanes by phase-transfer catalysis (ptc), as follows: A mixture of 1-bromohexadecane (0.25 mol), sodium acetate trihydrate (0.2 mol), and tetraethylammonium bromide (1 g) was heated at 105°C with vigorous stirring for 1 h. Then, water (300 mL) was added, the organic layer was separated and dried over anhydrous Na<sub>2</sub>SO<sub>4</sub>, and 1-hexadecyl acetate was recovered in 97% yield.

**Method 2.** The transesterification of methyl palmitate with 1-sorbiton was catalysed by calcium oxide. The ester was charged with the 1-sorbiton complex in a glass reactor equipped with a Dean-Stark trap. Methanol was removed by azeotropic distillation with isooctane, as per the following equation:



### 2.3. Oxidation stability study

The oxidation tests were carried out at 120°C according to the ASTM D 943 standard method. The base stock sample was subjected to oxidation with pure oxygen at a flow rate of 0.1 L/h for a maximum of 70 h. The SPT additive was added in different concentrations (from  $1 \times 10^{-6}$  to  $1 \times 10^{-3}$  mol/L). The viscosity, pour point depression, and total acid number was determined.

### 3. Results and discussion

The successful preparation of SPT was confirmed by IR and NMR spectroscopy (Fig. 1). In the IR spectrum characteristic  $\text{CH}_2$  and  $\text{CH}_3$  stretching bands at  $2916\text{--}2860\text{ cm}^{-1}$  is observed, as is a band at  $1750\text{ cm}^{-1}$  typical for a carbonyl group. The molecular weight was confirmed by mass spectroscopy, with the product affording a parent ion at  $m/z$  402.5. The melting point is 47°C.

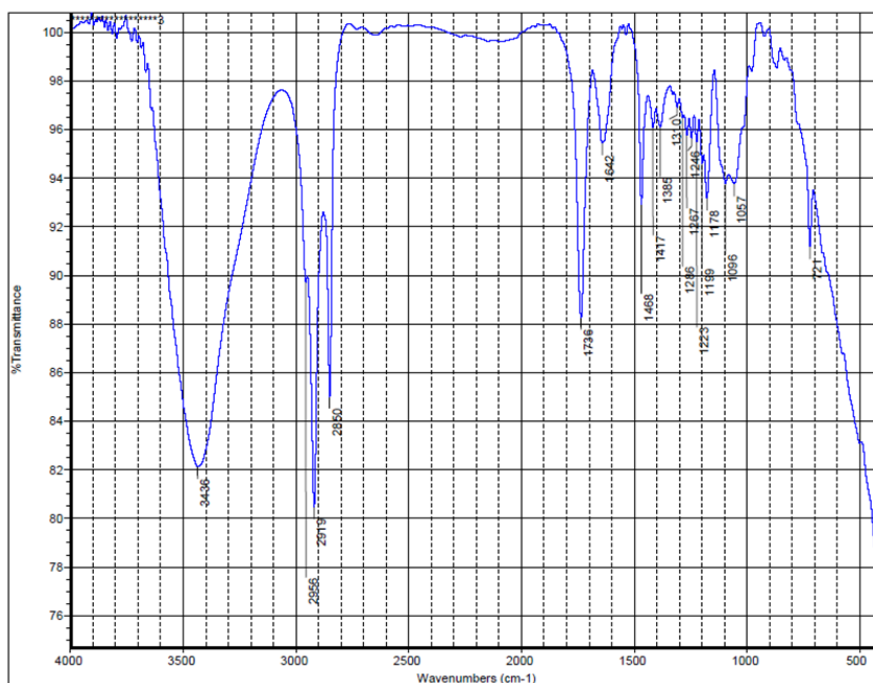
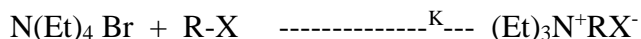


Figure 1. IR spectrum of the prepared compound

The synthesis conditions for SPT were probed by studying the rate of product formation as a function of the catalyst loading. The preparation of SPT from alkyl carboxylates depends on the rate of quaternization relative halides and aqueous sodium (Figure 2).

According to Hennis *et al.* [9], the rate can be determined according to the following:



$$(\text{Et})_3\text{N}^+\text{RX}^-/\text{dt} = \text{K}[(\text{Et})_3\text{N}/\text{RX}]$$

#### 3.1. Evaluation of SPT as a pour and cloud point depressant and a flow improver for the base oil

Figures 3 and 4 present the data for the changes in the pour and cloud points as a function of the SPT additive concentration. The additive clearly depresses both the pour and cloud points. This indicates that SPT prevents aggregation of the wax nuclei, but the value is nearly equal to the critical micelle concentration (CMC) in the oil phase ( $5 \times 10^{-5}$  mol/L). Thus, the additive disperses the wax molecules and disrupts the formation of aggregates, in accordance

with the findings in a previous report [11]. The onset of the effect is observed at a concentration below the critical micelle concentration (CMC) and reaches a maximum at the CMC. Further increases in the concentration of the additive lead to the reversal of its adsorption orientation, as confirmed by Omar and Khidr [12].

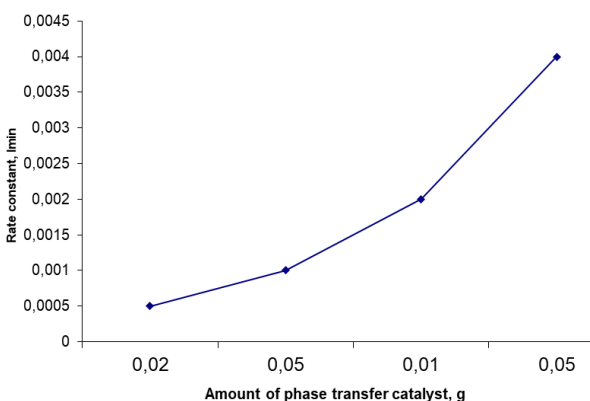


Figure 2. Relationship between the esterification rate and concentration of the phase transfer catalyst

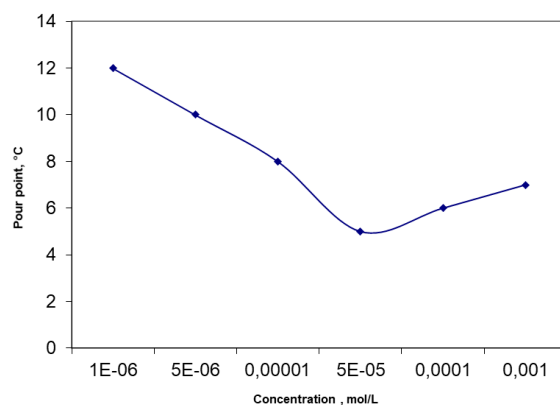


Figure 3. Effect of SPT concentration on pour point (°C)

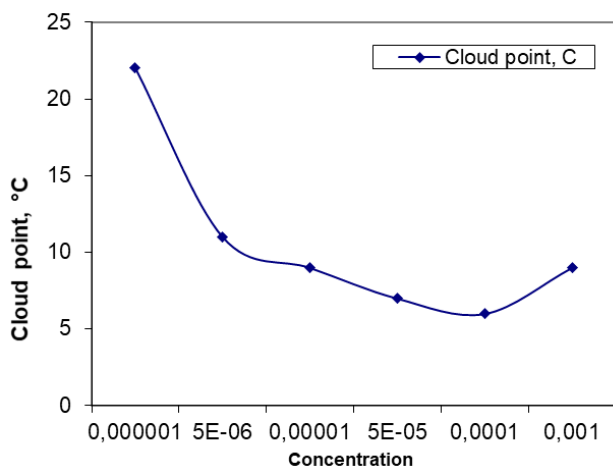


Figure 4. Effect of SPT concentration on cloud point (°C)

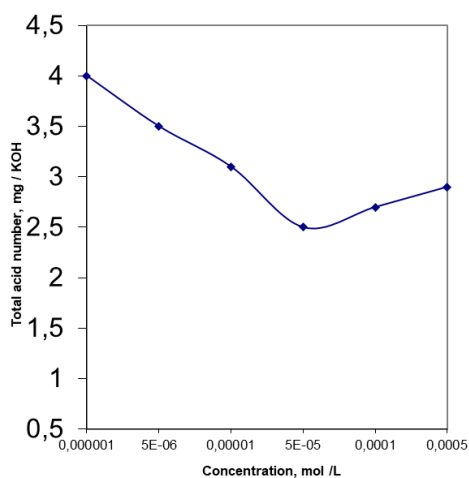


Figure 5. Effect of SPT concentration on total acid number after 72 h

There is a good relationship between the oxidation stability of an oil and its viscosity. The oxidation behaviour of the oil was studied by oxidizing it at 120°C and determining the total acid number at different times, whereas the viscosity was determined at 100°C. The results in Table 1 show that the viscosity and total acid number increase slightly over time during oxidation. These data confirm that the addition of SPT retards hydrocarbon degradation and the increasing of the oil viscosity with time. Thus, SPT increases the oil's stability toward oxidation and extends its lifetime. These results can be clearly observed in Figure 5. From this diagram, the addition of the additive to the oil retards the increase in the total acid number through oxidation. The best results are obtained at  $5 \times 10^{-5}$  mol/L (the CMC of the additive).

To explain these results, the author suggests a concept of revised micelle formation during hydrocarbon oxidation. The formation of micelles and their aggregation may take part in the oxidation process by inhibiting the chain propagation of the alkoxy free radicals  $R-O\cdot$ . The author believes that the micelles have cores in which the alkoxy free radicals are trapped. This means that the radicals that form oxidatively lose their ability to attack other species. Moreover, increasing the concentration of the additive does not change the degree of oxidation stability. It can be suggested that the possibility of micelle to aggregates or destruct of micelle lead to a free molecule of this additive tend to adsorbed at oil interface. This mechanism

implies that before an additive is added into oil, the critical value of micellization must be determined. This work agrees with early research by the author [11].

To elaborate on this concept, further work will be needed to calculate the aggregation number of the micelles and their geometry at the oil interface. Moreover, the effects of non-ionic polymers on the degree of stability of the micelles, which can have a predominant role in oxidation processes, should be studied.

#### 4. Conclusion

The mechanism of action for sorbitan palmitate as a multifunctional additive for the modification of the pour and cloud points and viscosity improver for a base oil was examined. The efficiency of this additive depends on its critical micelle concentration. The micelle cores act as traps for hydrocarbon oxide radicals in which to terminate hydrocarbon oxidation chains. The micellar inhibition depends on the incorporation of hydroperoxide or other polar oxygen-containing molecules in the reversed micelle, as the results revealed the increased oxidation stability of the oil. This information may be useful in further efficiency improvements for antioxidant additives.

#### References

- 1 Shubkin RL. Synthetic lubricants and high performance functional fluids. New York: Marcel Dekker 1993.
- 2 Brown M, Fotheringham JD, Hoyes TJ, Mortier RM, Orszulik ST, Randles SJ, and Stroud PM. Synthetic base fluids, in Chemistry and technology of lubricants, Mortier, R. M., Fox, M. F., Orszulik, S. T., eds. London: Springer 2010.
- 3 Chibber VK, Chaudhary RB, Tyagi OS, and Anand ON. 2<sup>nd</sup> World Tribology Congress, Sep. 3-17 2001, Austria. pp. 193–202.
- 4 Rosen MJ. The relationship of structure to properties in surfactants. Journal of the American Oil Chemists' Society, 1972; 49: 293–297.
- 5 Rosen MJ. Relationship of structure to properties in surfactants: II. Efficiency in surface or interfacial tension reduction. Journal of the American Oil Chemists' Society, 1974; 51: 461–465.
- 6 Marszall L. Cloud point of mixed ionic-nonionic surfactant solutions in the presence of electrolytes. Langmuir, 1988; 4: 90–93.
- 7 Gryglewicz S. Synthesis of dicarboxylic and complex esters by transesterification. 12th International Colloquium, January 11-13, 2000, Germany, 279–285
- 8 Huang ID, and Dauermann L. Exploratory process study. Base-catalyzed reaction of organic chlorides with sodium acetate. Industrial and Engineering Chemistry Product Research and Development, 1969; 8: 227–232
- 9 Hennis HE, Thompson LR, and Long JP. Esters from the reactions of alkyl halides and salts of carboxylic acids. Comprehensive study of amine catalysis. Industrial and Engineering Chemistry Product Research and Development, 1968; 7: 96–101.
- 10 Liotta CL, Harris HP, McDermott MC, Gonzalez T, and Smith K. Chemistry of "naked" anions II. Reactions of the 18-crown-6 complex of potassium acetate with organic substrates in aprotic organic solvents. Tetrahedron Letters, 1974; 15: 2417–2420.
- 11 El-Mehbad N. Development antioxidants synthesized by phase transfer catalysts for lubricating oil. Journal of Surface Engineered Materials and Advanced Technology, 2014; 4, 29-32.
- 12 Khidr TT, and Omar AMA. Anionic/non-ionic mixture of surfactants for pour point depression of gas oil. Egyptian Journal of Petroleum, 2003; 12: 21–26.

*To whom correspondence should be addressed: Dr. Noura el Mehbad, Najran University, Faculty of Science and Arts, Kingdom of Saudi Arabia*